CRANFIELD UNIVERSITY

COLLEGE OF AERONAUTICS

Hypersonic Control Effectiveness

D KUMAR

PhD Thesis
Academic year 1994 - 1995

Supervisors - Professor J L Stollery & Mr J Mapes

January 1995

This thesis is submitted as a partial requirement for the degree of Doctor of Philosophy

ACKNOWLEDGEMENTS

I would like to thank Professor J L Stollery and Mr John Mapes for their helpful discussions and assistance during the preparation of this thesis. I would also like to thank Prof. J C Clarke, Dr P A T Christopher, Mr A J D Smith (Fluid Gravity Engineering) and my co-workers in the Cranfield Hypersonics facility - Dr H Babinsky and Mr P A Attcliffe.

Finally, I would like to thank the workshops staff at the College of Aeronautics for their dedication and excellent work in preparing the experiments.

SUMMARY

The present study analyses the effects of a number of geometric parameters on the performance of a trailing edge control flap on a hypersonic body. The tests were conducted in a gun tunnel at Mach 8.2 and Mach 12.3.

The study revealed that flap deflection promoted separation lengthscales and boundary layer transition. The latter significantly increased the local aerothermal loads on the flap. For well separated flows, flap heat transfer rates were successfully predicted by reference temperature theory. The promotion of transition caused a progressive reduction in the lengthscales of separated flows.

In a free-flight environment, vehicle incidence varies considerably. Incidence was found to promote transition on both flat plates and control flaps. The latter resulted in a considerable increase in flap heat transfer. A modified version of reference temperature theory successfully predicted the aerothermal loads on the flap. For laminar and transitional interactions, the separated flow lengthscale was found to have a complex variation with incidence. A number of relevant flow parameters were identified.

The intense heat loads on a vehicle in hypersonic flight dictates the blunting of the leading edge. This strengthens the leading edge shock structure and generates an entropy layer. Bluntness was found to significantly decrease the separation interaction scales on the flap. This was due to a reduction in the pressure recovered on the flap. The latter adverse affects control effectiveness. The aerothermal loads on the control flap was successfully predicted by reference temperature theory.

An investigation into the efficiency of an under-expanded transverse jet controls was conducted on an axi-symmetric slender blunt cone. Force measurements found that the interaction augmented the jet reaction force by 70% at zero incidence. This increased to 110% at low incidence. The experiments found that the scale of the interaction region was determined by P_{oj}/p_{∞}. Using this parameter, a closed loop algorithm for the shape of the separation front was developed. The latter can be used to predict jet reaction control effectiveness.

CONTENTS

SYMBOLS

Alphanumeric letters

A_1	$0.332(\gamma-1)\left[1+2.6(T_w/T_o)\right]$
A_2	$0.166\gamma(\gamma-1)+\gamma\left(0.865T_w/M_\infty{}^2T_\infty\right)$
A_3	Constant
a	Speed of sound
A	Axial force (measured along the model axis)
B	Base Diameter
b	Width of model
C_1, C_2 etc.	Constants
C_A	Axial force coefficient $D/(\frac{1}{2}\rho_\infty U_\infty{}^2S)$
C_{an}	Effective capacitance of analogue
C_D	Leading edge drag coefficient $D/(\frac{1}{2}\rho_\infty U_\infty{}^2S_{LE})$
C_H	Heat transfer rate coefficient
$\overline{C}_H$	Mean Heat transfer rate coefficient
C_H'	Fluctuating component of heat transfer coefficient
$[C_H']_{rms}$	Root mean square value of fluctuating component of heat transfer
C_M	Moment coefficient $M/(\frac{1}{2}\rho_\infty U_\infty{}^2SL_{CO})$
C_N	Moment coefficient $M/(\frac{1}{2}\rho_\infty U_\infty{}^2S)$
C_W	Chapman-Rubesin constant
c_f	Skin friction coefficient
c_{fe}	Skin friction coefficient $(\tau_w/\frac{1}{2}\rho_e u_e{}^2)$
c_p	Specific heat capacity (at constant pressure)
d	Diameter of leading edge
d	Base diameter of cone
d(y)	Derivative of y
E	Disturbance energy = $(u'^2 + [v'^2 + w'^2]/Re)dy$
f	Frequency
F	Fluctuation amplitude
G	Gain of analogue circuits
G_{amp}	Gain of amplifier
G_{cal}	Gain of amplifier during transducer calibration
G_{run}	Gain of amplifier during tunnel run
i	current
k	Thermal conductivity
L	Hingeline
L_{CO}	Length of cone
L_c	Launch cost
L_m	Interaction length
m	Mass flow rate
M	Mach number
M	Moment (measured with respect to moment reference)

N	Normal force (measured with respect to model axis)
p	Static pressure
P	Reservior pressure
P_m	LEO Payload mass
P_4	Reservior pressure
P_l	Barrel pressure
Pr	Prandtl number
Q	Momentum
q	Heat transfer rate
r	Recovery factor
r_b	Base radius
R	Gas constant
R	Electrical resistance
R	Reattachment
RMS/rms	Root mean square $\sqrt{X^2}$
R_F	Analogue feedback resistance
R_T	Thin-film gauge resistance
R_{an}	Effective resistance of analogue
$Re_{\infty x}$	Reynolds number ($\rho_\infty u_\infty x/\mu_\infty$)
Re_{ex}	Reynolds number ($\rho_e u_e x/\mu_e$)
S	Reference area (base area for cone)
S	Separation
S_{LE}	Reference area of leading edge
T	Temperature
T*	Reference temperature
TR	Digitised output of transient recorder
t	time (measured from the start of the run)
u	Velocity along x-axis
v	Velocity along y-axis
V	Voltage
w	Wall
w	Velocity along z-axis
x	Distance along body axis
y	Distance normal to body axis
z	Distance normal to freestream in the plane of the body axis
Z	Impedence

Greek letters

α	Incidence relative to freestream (°)
α_T	Thermal coefficient of resistance of thin-film gauge
β	Flap deflection angle relative to flap plate
δ	Velocity boundary layer thickness (measured at $u/u_e = 0.99$)
δ^*	Displacement boundary thickness

δ_{EN}	Entropy layer thickness
Δ	Change in property
ε	Density ratio for a strong shock $[(\gamma-1)/(\gamma+1)]$
η	Defined in equation
θ	Shock angle
θ_m	Meridian angle (measured from the jet meridian)
φ	Defined in equation
γ	Ratio of specific heats
ρ	Density
$\Re_\nu$	Reflection pressure coefficient
τ	Shear stress
Γ	Mach number coefficient
$\overline{\chi}$	Viscous interaction parameter
μ	Dynamic viscosity
μ_m	Mach angle
ν	Kinematic viscosity
υ	Prandtl-Meyer function
ω	Angular frequency $2\pi f$
ξ	Blast analogy parameter $M_\infty^{-2}[x/dC_D]^{2/3}$

Superscripts and subscripts

atm	Atmospheric conditions
B	Base diameter
d	Dead air
d	Leading edge diameter
e	Local
FS	Full scale
i	Initial conditions prior to start of run
in	Input
incip	Incipient condition
inf	Infinite subatrate thickness
j	Jet
o	Reservoir
o	Start of interaction
out	Output
rt	Reattachment
RMS/rms	Root mean square
s	Shock
sep	Separation
ss	Separation streamline
st	Start of interaction
sub	Thin-film gauge substrate

t	time
w	wall
vac	Vacuum conditions prior to run
x/L	Location defined with respect to hingeline
1	Conditions immediately downstream of leading edge shock
2	Conditions immediately upstream of the hingeline shock
3	Conditions immediately downstream of the hingeline shock
4	Conditions some distance downstream of the hingeline shock
*	Conditions at reference temperature
∞	Freestream
'	Time dependent fluctuating component

Chapter 1

INTRODUCTION

The work presented in this thesis was conducted as part of a Total Technology PhD programme and an industrial research contract. Its aims were to experimentally study the effects of a number of parameters on the performance of mechanical flaps and reaction jet mechanisms for active aerodynamic control during high speed flight. A parallel analytical study forwards procedures for predicting the observed effects.

The study includes an assessment of the present state of the satellite launch services market and forwards mechanisms for modelling the commercial demand on its services from associated markets and products.

1.1 TECHNICAL STUDY

The Space Shuttle Orbiter vehicle, in addition to its routine commercial launch operations has been used for studying the aerothermodynamics of re-entry configurations in hypersonic flight. This has proved to be an invaluable tool for aerothermodynamacists as it allows a direct evaluation of the accuracy of semi-empirical tools developed from wind tunnel and computational fluid dynamics studies. Inconsistencies between flight and experimental predictions highlights technology areas which require further evaluation for the formulation of more accurate analytical/numerical predictive tools.

The technical work presented in this thesis has been focused on two of the aerodynamic control problems encountered during the re-entry descent phase of the Orbiter's flight envelope.

The phenomenon of boundary layer separation generally arises as a result of the formation of a strong adverse pressure gradient. In supersonic flows, this is present as a result of compression waves generated either external to or from within the boundary layer. These originate from the edge of the subsonic region of the boundary layer and deflect its supersonic portion as well as the inviscid flow around a local protrusion.

The ability of the boundary layer to penetrate an adverse pressure gradient depends on the local wall skin-friction distribution. In perfect gases, the skin-friction distribution depends on

the local flow properties of Mach and Reynolds numbers, wall to freestream temperature ratio as well as on its laminar or turbulent character.

The separation of a boundary layer has an appreciable effect on the local flow characteristics of pressure, heat transfer and skin-friction. The changes in these properties alter the aerodynamic performance (lift, drag, moment etc.) characteristics of the vehicle.

The present study analyses the effects of an entropy layer, generated by a blunt leading edge, on the performance of a quasi two-dimensional trailing edge flap. The investigation focuses on its effects on boundary layer separation and transition in the interaction region. The experiments were designed to directly identify separation whilst comparisons of experimental heat transfer distributions with laminar and turbulent theories allow diagnosis of the laminar or turbulent state of the flap boundary layer.

In a free-flight environment, vehicle incidence varies considerably. Incidence has a significant effect on flow properties close to the body and hence in the performance of a trailing edge flap embedded within the body flowfield. The effects of incidence have been investigated experimentally for both sharp and blunt leading edge control flap configurations.

In the high altitude portion of the flight envelope, aerodynamic control at high speeds is achieved using transverse jets located strategically around the body. The presence of a jet creates a highly three-dimensional adverse pressure gradient which generates a three-dimensional separated interaction region. The resulting viscous-inviscid interaction produces an increase in pressure in the separation region. This increases the 'effective jet reaction force' and thus augments the desired control force.

An investigation into the efficiency of an under-expanded transverse jet controls was conducted on an axi-symmetric slender blunt cone. The experiments were designed to identify aerodynamic parameters which have an influence on separation. The effects of jet nozzle geometry and body incidence on normal force and moment augmentation were studied using pressure and force measurements.

1.2 MARKET STUDY

The present single-use throw-away satellite launch systems are highly inefficient, with payload to gross mass ratios of the order of 1%. To enable further growth of space based industries as well as the development of new applications, a reduction in launch costs has become imperative.

The ideal solution for attaining this goal remains the development of an "aerodynamically efficient" reusable launch vehicle. The enormous investments required for development and manufacture of such vehicles can only be justified when the associated technologies are mature and market demands ensure that its operations accommodate an adequate short-term return. The long lead times required for the development of associated technologies means that the need for modelling the long term demands on the launch services market becomes essential.

The modelling of any service based market requires accurate knowledge of the behaviour and influence of its associated secondary markets. For satellite launch services, these secondary markets, in the medium to long term are telecommunications and Earth observation.

This thesis presents a model for the long term development of the relatively mature Satellite Telecommunications market and a survey of the launcher requirements of the Earth Observation industry over this period. By integrating the development of these markets, the latent demand for satellite launch services up to the year 2005 has been estimated.

Chapter 2

MARKET FOR SATELLITE LAUNCH VEHICLES

2.1 INTRODUCTION

The satellite launch industry was conceived in the fifties as a result of political and national rather than market aspirations. The technical complexity of launch systems provided an excellent arena for governments to demonstrate their technical and political prowess. Access to space also provided government agencies a platform for conducting covert reconnaissance operations outside the reach of conventional interception systems.

The funding for the development of the industry in its early years was directed towards technology development programs which appeased the political aspirations of its sponsors. This resulted in a rapid technology push aimed at increasing the total launch mass capability of launchers. This technology push is reflected in the typical S-curve of the low Earth orbit performance capabilities of the Delta launch vehicle, shown in figure 2-1.

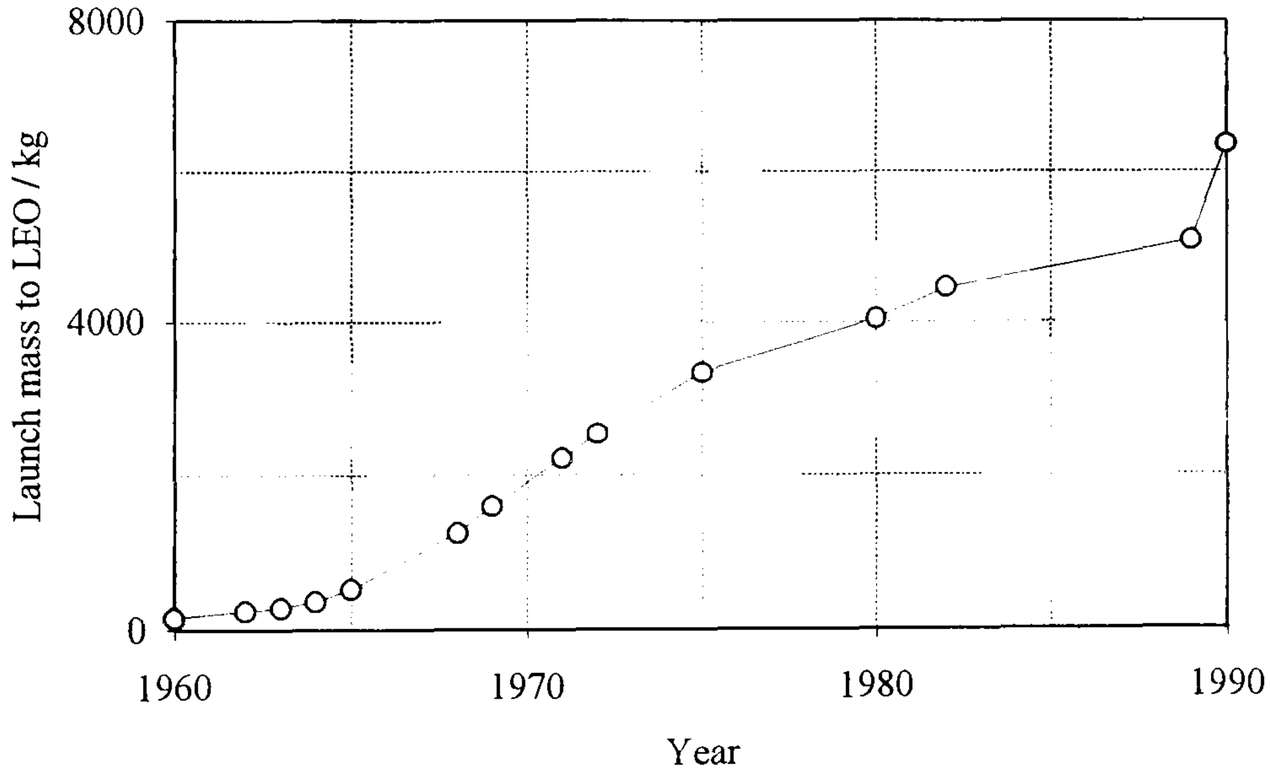

Figure 2-1 Low Earth orbit launch mass capability of the McDonnell Douglas Delta launch system (Isakowitz, 1991)

Along with payload growth, the technology push also produced a rapid initial growth in the number of launches per year, as shown in figure 2-2. However, the growth rate decreased as initial technology goals were realised and the exorbitant costs of the next generation of technology objectives became apparent.

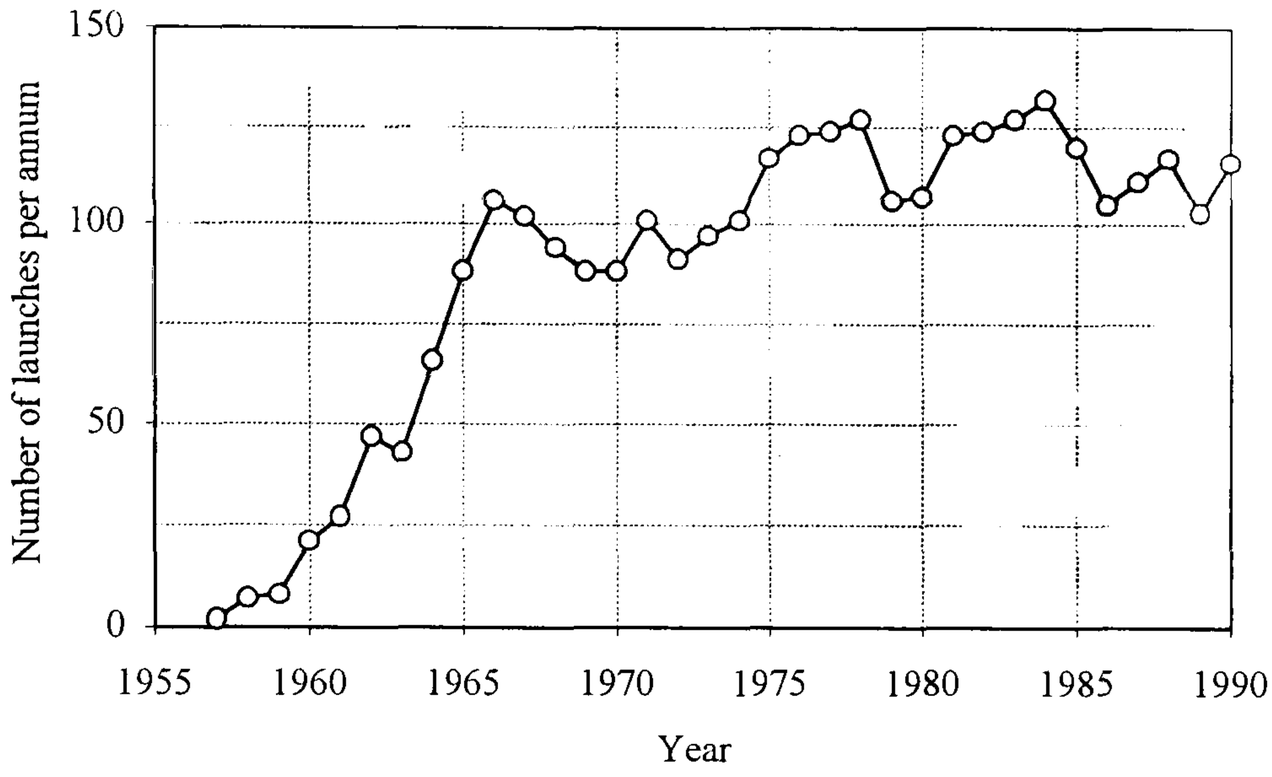

Figure 2-2 Growth of the global satellite launch services industry since its inception (Isakowitz, 1991)

This realisation led to a consolidation of technologies by the commercial launch service operators whilst government agencies shifted their emphasis away from large scale technology demonstration programs to focus on developing technologies directly relevant to the growth of associated terrestrial markets. One of the goals of the latter was the development of technologies associated with a more cost efficient launch system and led to the development of the Space Shuttle Orbiter vehicle.

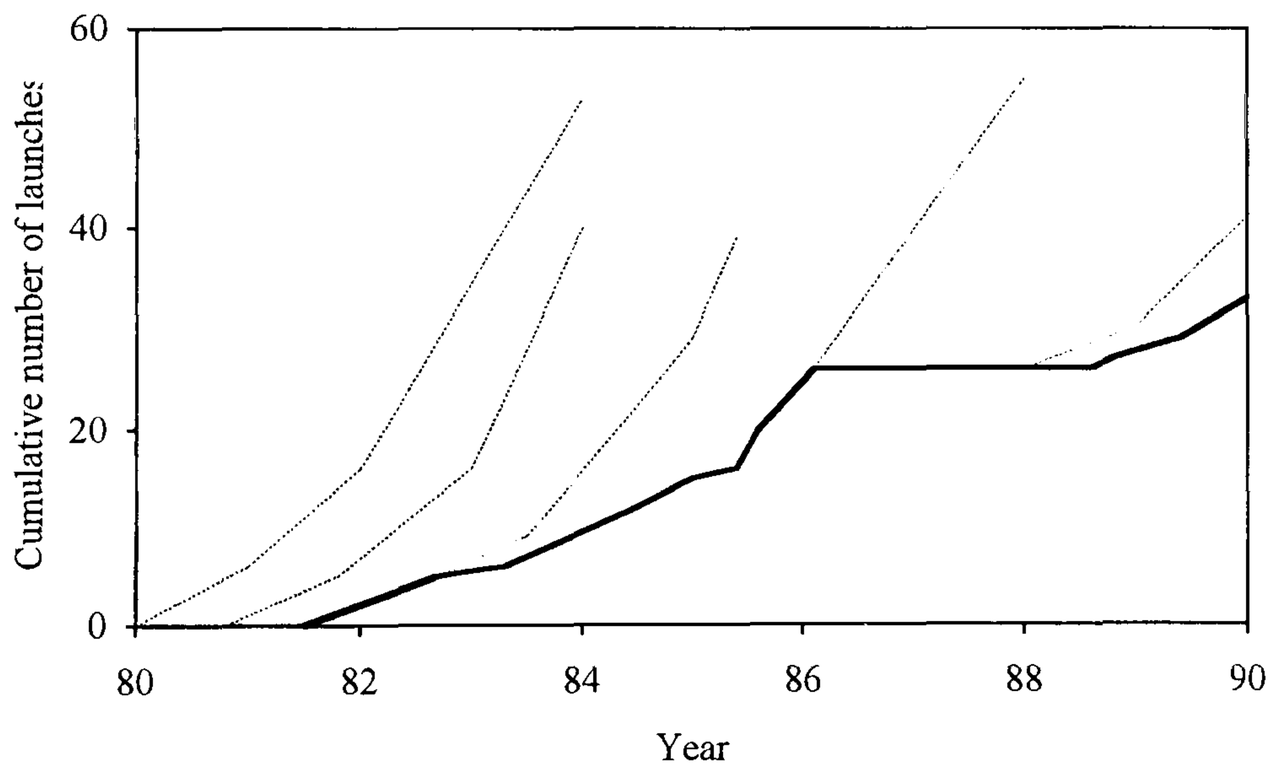

Figure 2-3 Scheduled and actual operational performance of the Space Shuttle Orbiter fleet (The Economist, 1991)

However, although operational cost performance (cost per kg) was improved by the partial reusability of the vehicle, the costs associated with its ground support systems led to a

launch cost similar to that of conventional systems. Along with its failure to improve launch cost performance, the Shuttle vehicle also failed to attain its objective of providing scheduled and regular access to space. This is illustrated by the desired against actual operational performance of the fleet shown by figure 2-3.

A second approach to the reduction of launch costs was adopted by the much smaller Pegasus booster vehicle. This vehicle is launched at an altitude of 13200m from a conventional aircraft. A swept wing together with the high altitude launch allows a 10-15% improvement in the aerodynamic efficiency over terrestrial launch systems.

These performance improvements allow the Pegasus vehicle to offer net payload fractions of 2.2% (approximately double that of comparable terrestrial launchers). Along with improved technology performance, simple streamlined assembly and a designed capability for rapid launches allow the Pegasus to offer a substantial reduction in the per kg launch cost for the vehicle.

2.2 LAUNCHER MARKET DEMAND STRUCTURE

To satisfy demand for their services, satellite operators look to launcher companies for compatible launch vehicles to allow them to place required platforms into orbit within a specified cost and time period. Thus, for developed markets, demand for launch systems transpires indirectly from satellite operators who respond to demand from users.

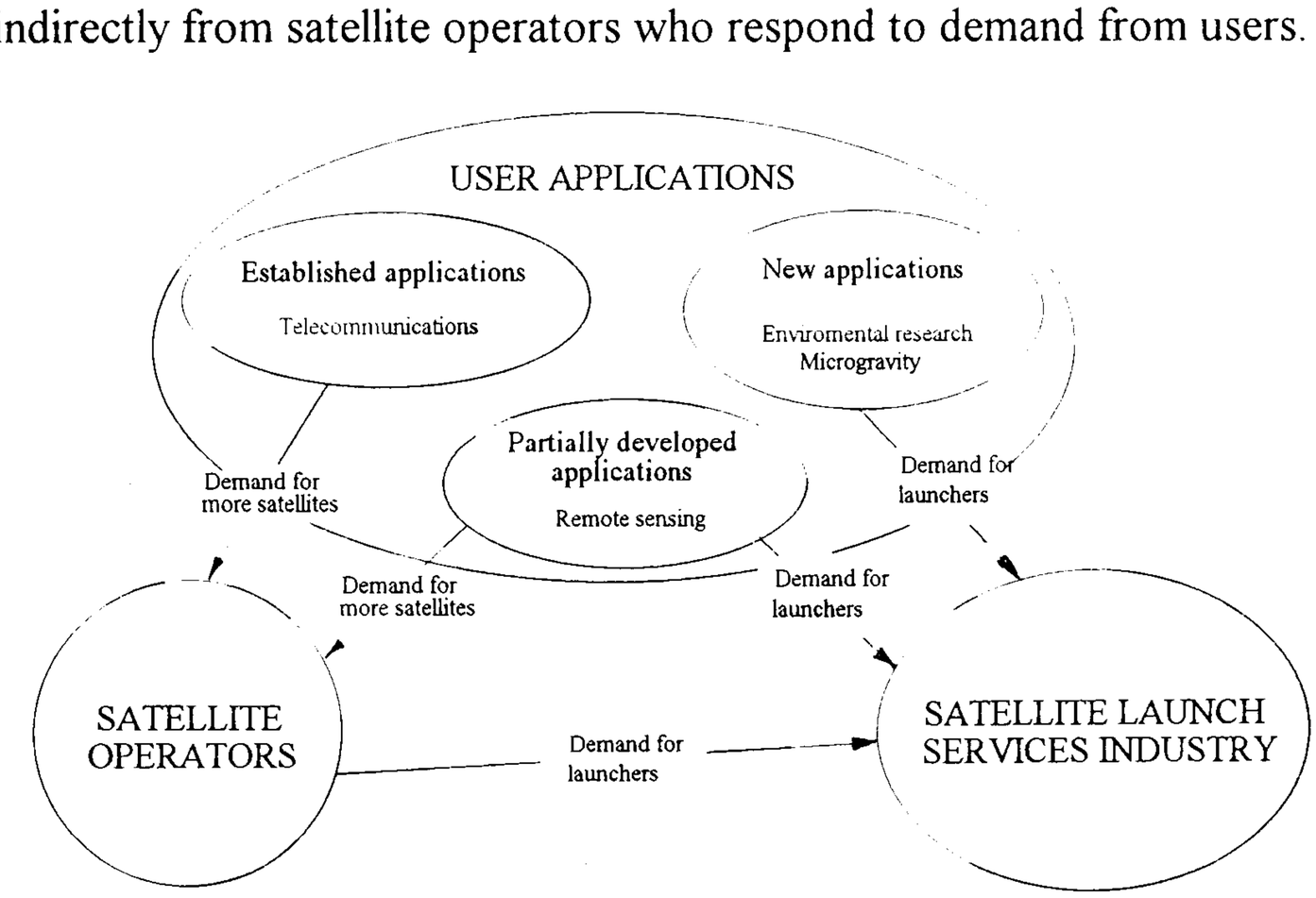

Figure 2-4 Derived demand chain structure for satellite launch services markets

For markets where the technology and market structures are partially developed, demand transpires both indirectly through satellite operators and directly from the user for undeveloped sectors. This derived demand structure is shown in figure 2-4. A similar "derived demand" structure was established by Benton (1987) for the satellite communications market.

2.3 DEVELOPMENT OF COMMERCIAL LAUNCH MARKETS

The first demonstration of transoceanic satellite telecommunications was by the Telstar satellite confirmed the theory that satellite repeaters were a viable alternative to terrestrial repeaters for long distance telecommunications. This demonstration produced the primary driving impetus for the commercialisation of space.

The commercial success of satellite telecommunications followed rapidly after the AT&T technology demonstration and was attributed by Edelson (1984) to the combination of three ingredients; technology to create the system, communications requirements to form a market, management structure to implement the system

The satellite communications industry saw a rapid growth in its space based infrastructure (number of telephone paths) with an 800% increase in capacity in its first four years. However, a large proportion of this infrastructure growth was absorbed by an increase in the number of links per satellite (see figure 3-5) and thus did not translate into a similar growth in the number of commercial satellite launches. The reversal of this trend in the mid-late eighties occurred due to the revenue and capital loss associated with the malfunction of a number of large satellites during the early and late phases of their launch. If this view is sustained, then future space telecommunication infrastructure demand is likely to be met by an increase in the number rather than the capacity of satellites.

2.4 LAUNCHER MARKETS

2.4.1 General structure of the market

The present launcher market can be segmented into three distinct categories according to the payload mass. These are shown in figure 2-5.

The market for commercial launch services remains dominated by the requirement to launch communications satellites. The payloads associated with this sector of the market are in the

medium lift segment of the market. As a result, the greatest density of launchers exists in this category. All countries with launch capabilities are present in this segment of the market apart from India, whose capabilities remain at an embryonic stage.

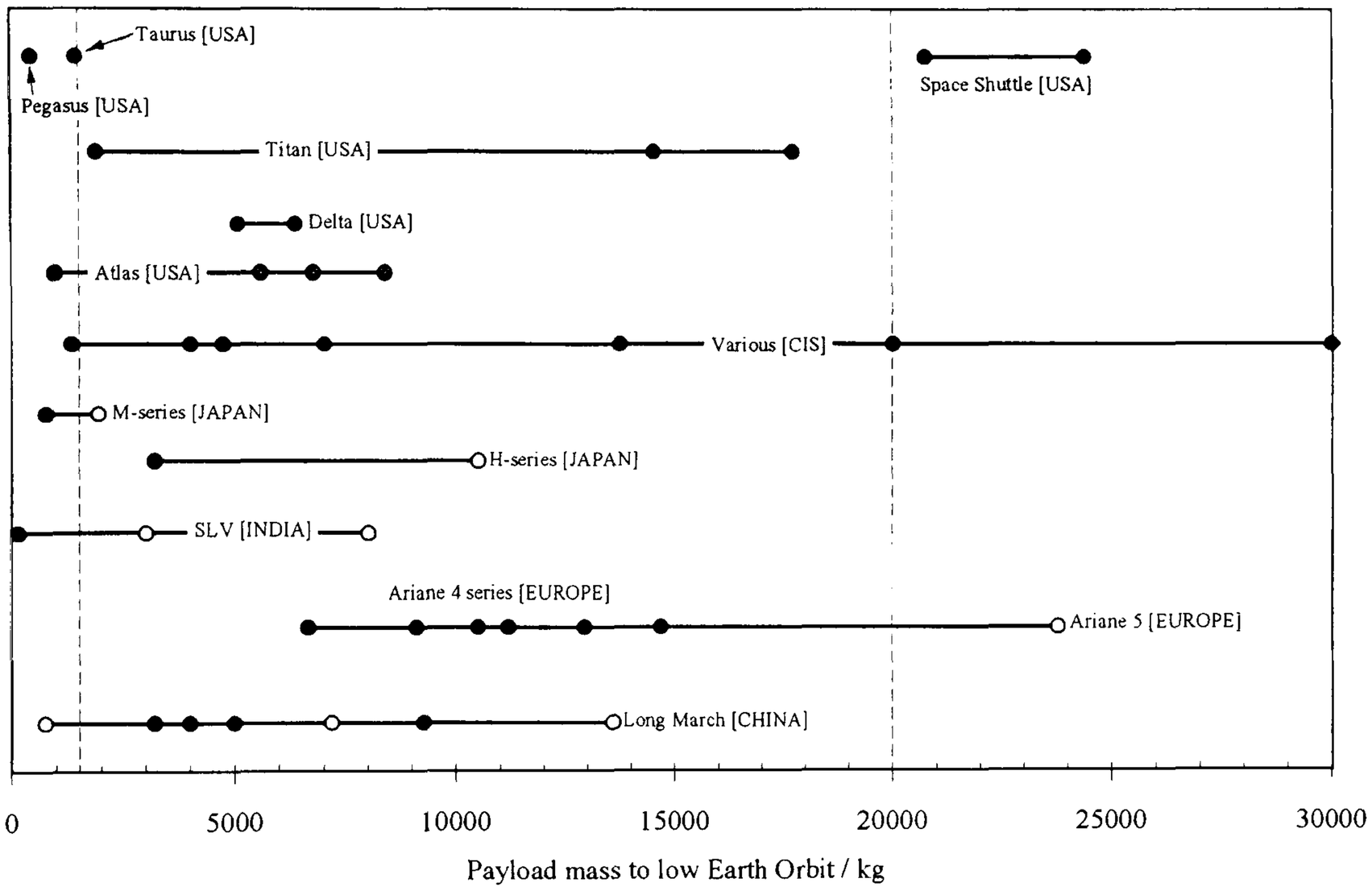

Figure 2-5 Structure of the launch services market according to payload mass to low Earth orbit capability (Isakowitz, 1991)

Alongside payload capability, the option to use a launcher may be further limited by payload volume capacity, post-launch facilities, launcher availability as well as a nationalistic concern to use a domestic launcher. These restrictions limit the market access for a given launcher. Due to the globalisation of launch services and the desire for launch cost reduction, commercial satellite operators are beginning to disregard the latter parameter. However, for government agencies, launch using a domestic launcher remains one of the primary parameters. The reasons associated with this are discussed in section 2.5.2.

2.4.2 Operators in the launcher markets

The United States and the countries of the Commonwealth of Independent States (CIS) remain the primary launchers of satellites, as shown by figure 2-6. According to Isakowitz (1991) and Arianespace (1990), launches by the CIS during the period 1985-89 accounted

for nearly 75% of the total number of global launches during that period. This high rate of launch was attributed by Arianespace (1990) to

(a) elliptical orbits required for high latitude telecommunications doubling the number of satellites required for 24 hour coverage

(b) inferior technology of the satellites limiting their life-span and thus increasing the requirement for frequent replacement

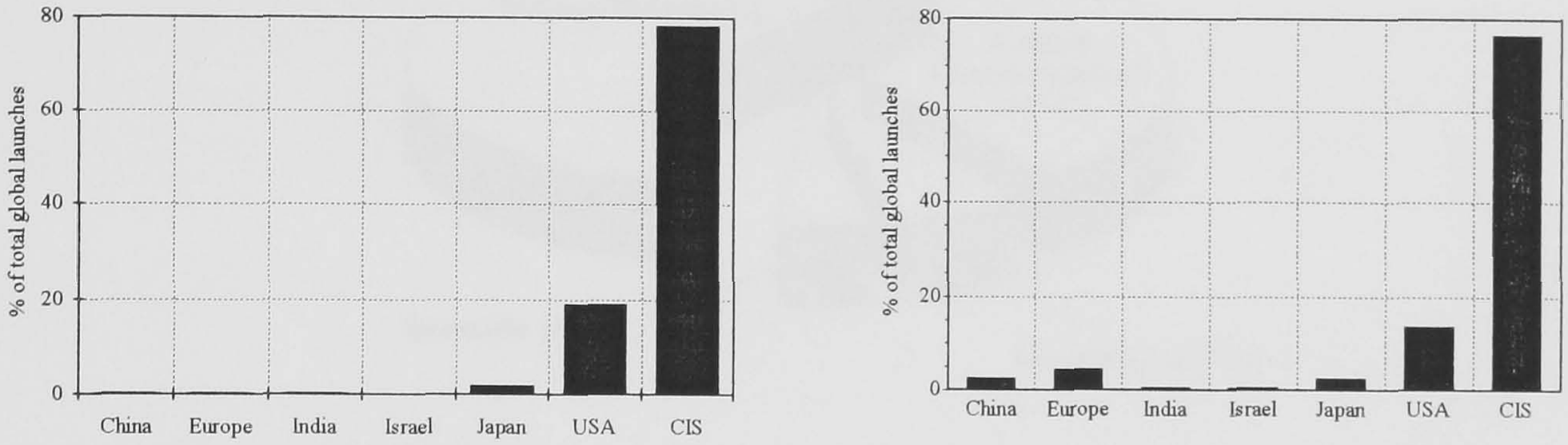

(a) 1975 - 1979

(b) 1985-1989

Figure 2-6 Development of satellite launch services market share (Isakowitz, 1991)

Although the total number of launches per year provides an indication of the market share, it does not provide an absolute value for the number of satellites being launched. This is due to multi-satellite launches from a given launch vehicle as practised by the medium-heavy lift Titan, Space Shuttle and Ariane vehicles. This method is favourable in that it reduces the effective per kilogram launch cost per satellite. However, it may increase the insurance costs associated with a given satellite due to the proximity of its companion satellite which may not be manufactured to the same standard.

A number of new countries have entered the launch services market, with China, Japan and Europe showing an increase in their market share, as shown in figure 2-6. The proliferation of technologies for launching satellites reflects a globalisation of the technology base associated with the market. This is partly a result of the military importance of satellites for observing troop concentrations and aggressor missile flight paths (demonstrated by US anti-Scud operations in the Gulf War). The proliferation of launcher technologies reflects a desire for governments to have direct rather than intermediate access to space in order to retain confidentiality for covert operations.

2.4.3 Restrictive practices

The requirements of military and government operators for satellites dominates the launch manifest, as shown by figure 2-7. A large proportion of the demand for western launchers in

these sectors originates from agencies of the US government. These agencies, such as National Aeronautics and Space Administration (NASA), National Ocean and Atmosphere Administration (NOAA) and the Department of Defence (DoD), restrict bidding and procurement of launch vehicles for their spacecraft to US launchers operators only.

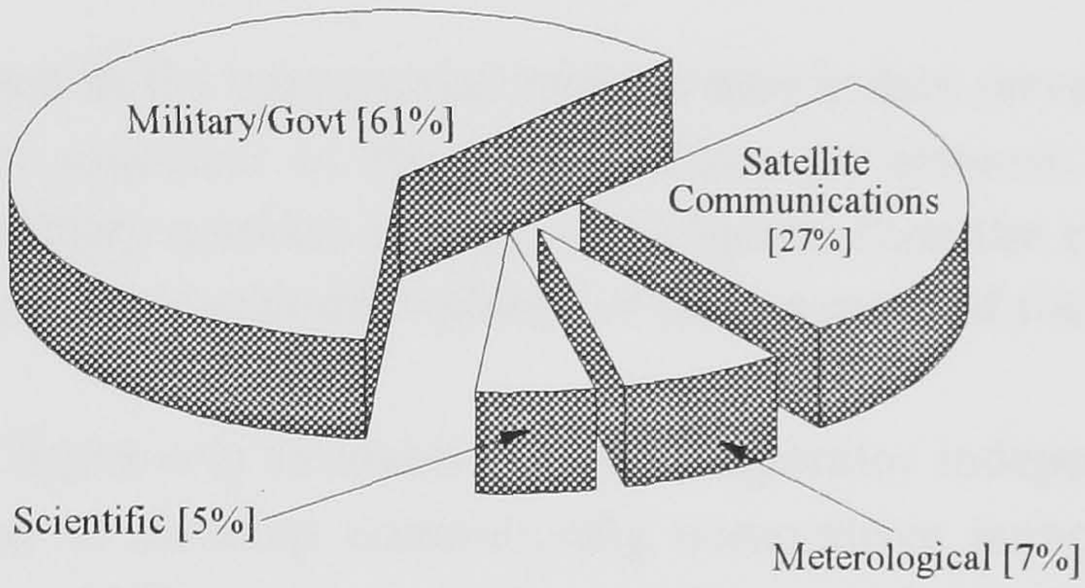

Figure 2-7 Origins of business for operators in the launch service industry

Due to these restrictive practices, launches of military and government agency satellites, shown in figure 2-8 are dominated by the US launchers Titan, Atlas and Delta. The European operator Arianespace is denied access to bid for launching most of the military spacecraft.

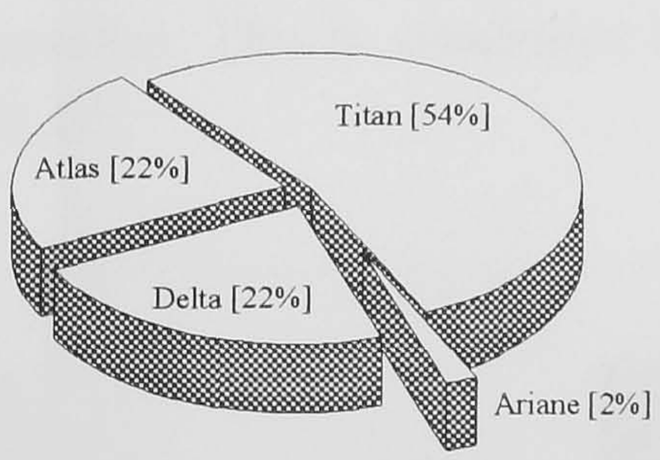

(a) military

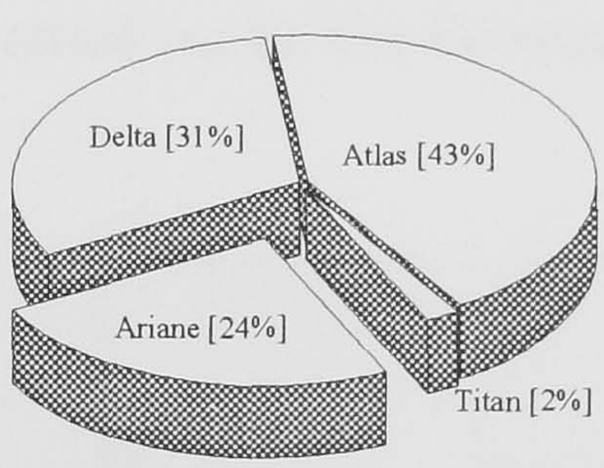

(b) government agencies

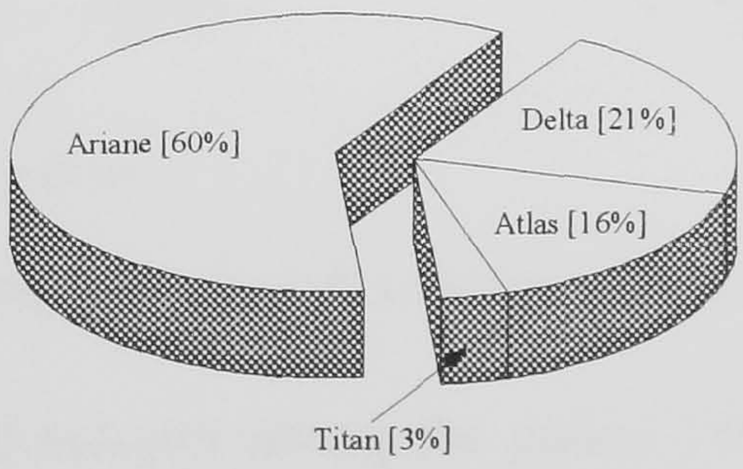

(c) commercial

Figure 2-8 Types of satellites launched using various launchers 1980-90 (The Economist, 1991)

However, Arianespace has access to satellites from European government agencies which have similar restrictive practices as their US counterparts. Thus, the market share of Arianespace for government agency launches is improved. The European operator dominates in the commercial satellite sector. This may be due to the non-availability of US launchers due to demands for launchers from the US military and government agencies.

The success of Arianespace in the commercial markets may in fact serve as a deterrent to the removal of the restrictive practices of the United States government. If Arianespace was given full access to the military markets in the United States, then the competition may raise questions with regards to the commercial viability of one or more of the US launchers.

Therefore, if the United States was to maintain a multi-operator independent launch system, an increase in investment to develop commercially competitive launch systems would be required by the operators of US launch systems in order to maintain their market share, the latter being an unfavourable option in the short term.

2.4.4 Growth of launcher markets

The commercial sector of the launch services market has shown significant growth both in terms of the number of satellites launched and the total operational revenue generated from these launches. This is confirmed by a survey carried out by The Economist (1991), shown in figure 2-9.

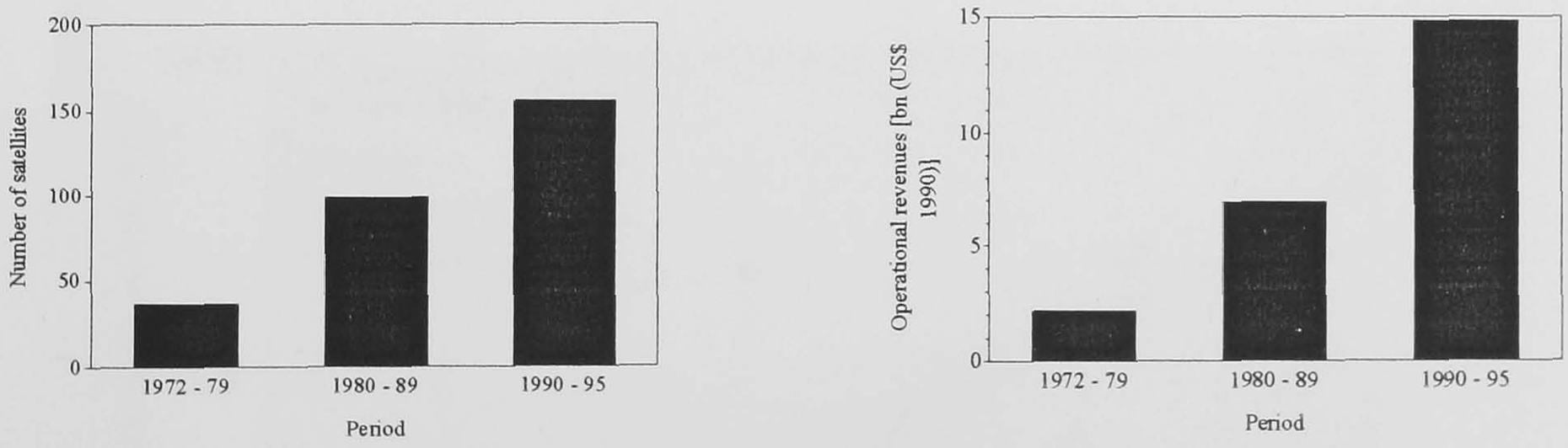

(a) number of satellites

(b) Operational revenues

Figure 2-9 Growth of the launch services market (The Economist, 1991)

The predicted growth of the industry during the period 1990-1995 indicates a decrease in the growth rate for the number of satellites. This may be a result of the increase in the life expectancy and capacity of satellites as well as the entrance of rival terrestrial based technologies. A decrease in the growth rate for operational revenues is also forecast. A

survey by Furniss (1990) suggests a similar growth rate behaviour for the industry in the medium-long term.

2.5 LAUNCH SERVICE PRICING POLICIES

As has been illustrated in section 2.4.3, a number of restrictive practices are exercised by the satellite manufacturing countries to support and promote their domestic launcher. This results in a departure of pricing policy from a purely cost based commercial competition between international launchers. The fear of uncompetitive national launchers being priced out of the international commercial satellite launches services market and the resulting loss of revenue results in indirect subsidies for launch operations.

Chenard (1990) has identified a number of mechanisms for subsidising launch operations. They range from subsidised launch pad maintenance costs, cross-subsidising commercial launches through a pool of assured government launch contracts to subsidising launcher technology improvements and the writing off of initial development costs.

There is a strong correlation between the payload launch mass and launch costs for both the United States and European launch vehicles. This is shown in figure 2-10. The launch cost L_c correlates with the payload mass P_m according to the relationship

$$\text{Launch cost } L_C = 0.55 P_m^{\,0.57}$$

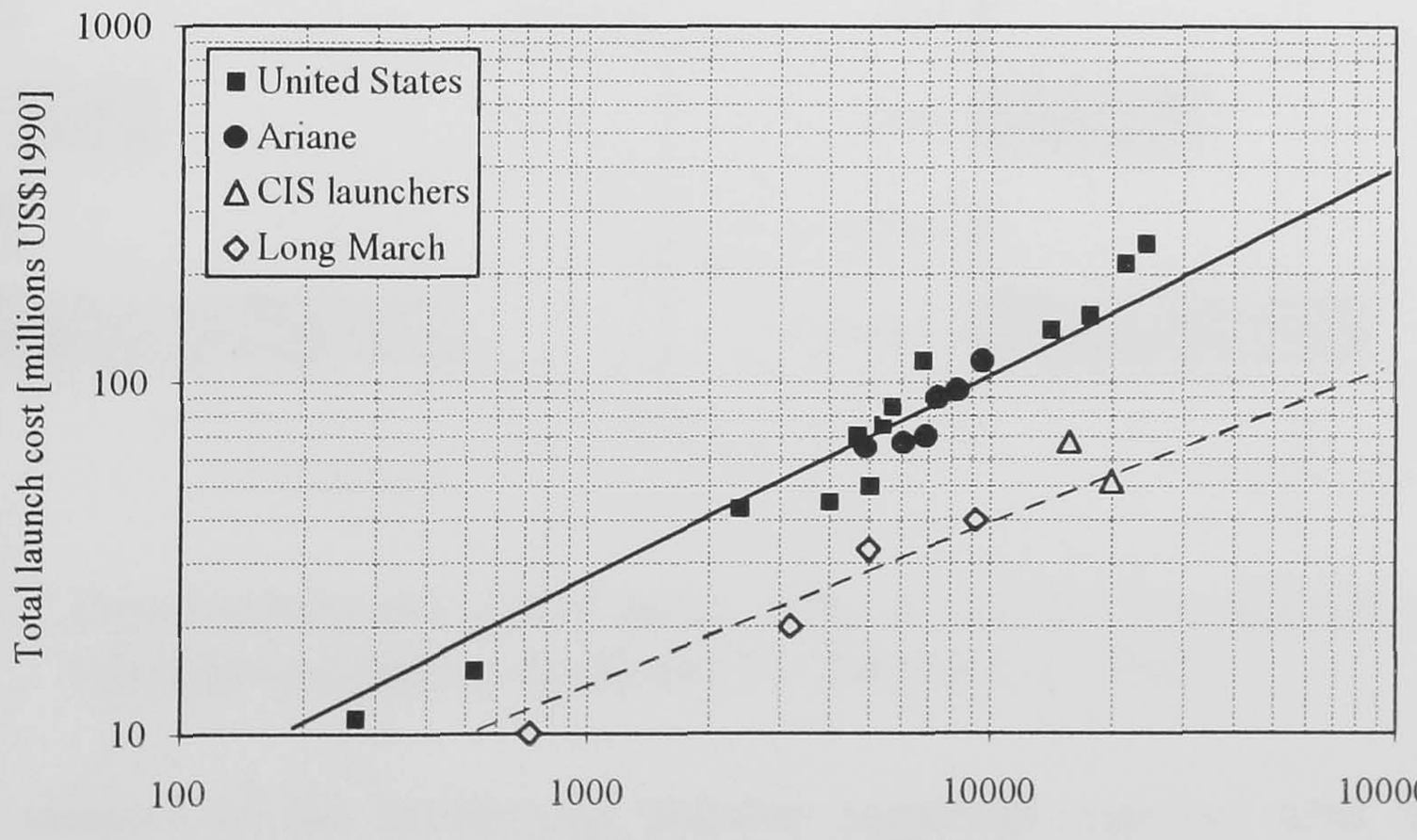

Figure 2-10 Launch costs associated with medium lift capacity launcher (Isakowitz, 1991)

The variations in launch price for Western launch vehicles fall within a ± 15% band around this relationship through the payload range. The fluctuations within this band may be due to launcher efficiency, operations cost or insurance costs.

2.5.1 Launch cost subsidy

Due to the end of the cold war, the commercial launch market has gained access to a number of new launchers from the CIS and Chinese government agencies. As shown in figure 2-10, the launch prices for commercial launches using Chinese or CIS launchers are significantly lower than western vehicles.

In the absence of published cost breakdowns, it remains unclear whether the reduction in launch price is due to increased vehicle and/or ground operations efficiency, reduced manufacturing costs or whether the commercial launch cost of the vehicle is directly subsidised to promote market access.

In some cases, access to these cheaper launchers has been restricted with technology transfer concerns being cited by the satellite manufacturing countries as a primary factor. The domination of satellite manufacturing by a limited number of countries (see figure 2-11) has allowed their governments to restrict market access to launchers from politically unfavourable sources.

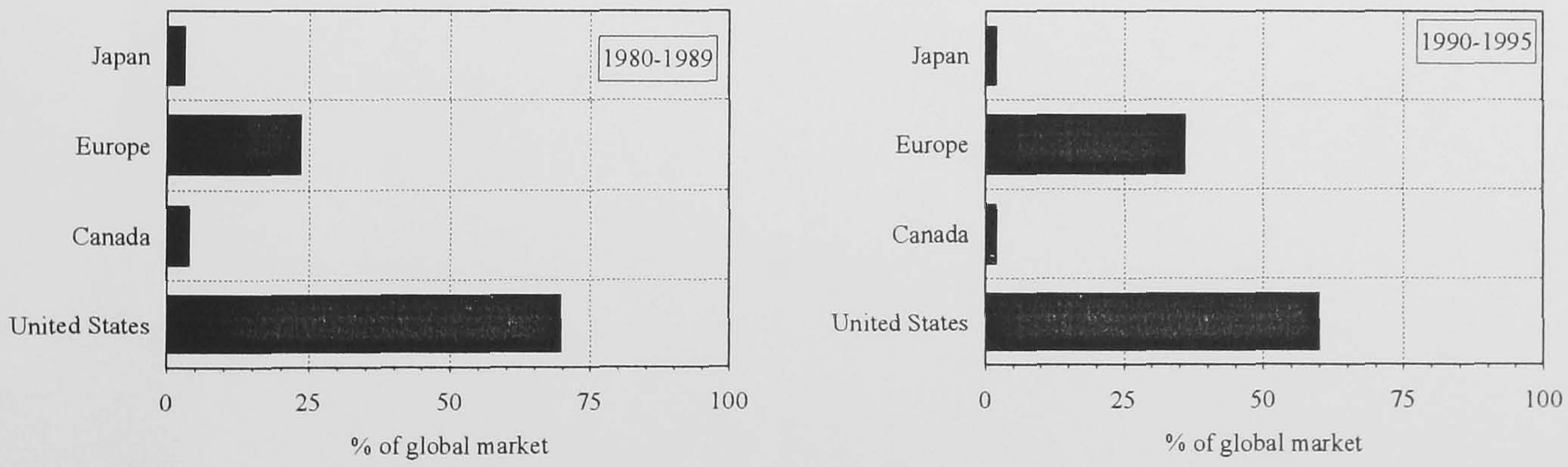

Figure 2-11 Development and globalisation of the market for manufacturing commercial telecommunications satellites (The Economist, 1991)

The steady erosion of the technology transfer argument together with proliferation of technology for manufacturing satellites will improve access to the commercial satellite market for launch service operators. Until most of the satellites launches originate from

commercial rather than the military/government segment of the market, true cost based pricing of launch services is unlikely.

Chapter 3

SATELLITE TELECOMMUNICATIONS

3.1 INTRODUCTION

The concept of satellite telecommunications was originally forwarded by Clarke (1945). This considered three satellites located in geostationary orbit, 22300 miles above the equator acting as repeater stations for terrestrial point-to-point communications. The first communications satellite was launched in the late fifties. It functioned as an indirect repeater, storing a message on one part of its orbit and then transmitting it during another part of its orbit.

In order to attain direct point-to-point communications, experiments were conducted using aluminium coated balloons (approximately 100 ft in diameter). Ground stations, located at a large distance from each other were able to communicate by using the balloons as reflectors. These systems had limited success as a very powerful transmitter and a highly sensitive receiver were required.

In order to overcome the power limitations of passive systems, satellites needed to act as active transmitters, receiving a signal, amplifying it and then transmitting it to an appropriate Earth station. This principle was employed in 1962 by TELSTAR 1 which, operating from a low Earth orbit, allowed pictures to be transmitted across the Atlantic. However, as a result of its altitude, TELSTAR 1 was unable to remain simultaneously in the line of sight of two Earth stations for more than ten minutes during its two hour orbit.

The subsequent development of more powerful launcher rockets allowed the RELAY series of satellites to be placed at a greater altitude. This increased the connection period between the satellites to thirty minutes. However, even at this altitude, in order to provide a permanent link between two Earth stations, forty eight equally spaced RELAY satellites would be required. Moreover, ground stations would require large, highly accurate moving antennae for tracking the satellites along with antennae for telecommunications. Due to the prohibitive costs associated with the antennae, the approach of low altitude satellites providing permanent links between Earth stations was abandoned.

Finally in 1964, the continued advances in launcher technology as well as a satellite which incorporated innovative electronics and stabilisation systems allowed a communications satellite to be placed into geostationary orbit. Since the time period at this altitude is equal to the period of rotation of the Earth, the satellite remains at a fixed location above the Earth. Geostationary satellites allowed ground stations located within the footprint of the satellite to be connected permanently and thus demonstrated that satellites were viable repeaters for long distance terrestrial telecommunications links.

3.1.1 Formation of a global communications network

By the early sixties, national terrestrial telecommunications industry was well established in developed countries. However, long distance "international" telecommunications were limited to poor quality high frequency radio services and a few point-to-point submarine cables. Overland communications employed microwave line-of-sight links on high volume routes. As a result of these technology limitations for long distance telecommunications, the commercial potential of satellite telecommunications was recognised early by the industry.

The ability of satellite telecommunications to overcome political as well as geographical boundaries led to ownership problems for an international telecommunications system. In order to reach a compromise solution, the Communication Satellite Corporation, (COMSAT) was established in 1962 by the US Federal Communications Commission (FCC).

COMSAT had a mandate to establish a global satellite telecommunications network. Its work led the United States along with twelve other nations to form the International Telecommunications Satellite Organisation, INTELSAT. The organisation owned and operated the global satellite telecommunications network on a non-profit basis. The introduction of INTELSAT allowed developed national telecommunication infrastructures to be linked to form a global telecommunications network.

3.2 COMMUNICATIONS TECHNOLOGY

The development of the telecommunications industry is typical of any technology intensive industry. Although it is regarded as being global, the relative quality, cost and number of services differs tremendously from one country to another.

3.2.1 Multimedia evolution

Until the mid-eighties, the global telecommunications transmission infrastructure in developed countries consisted of analogue transmission lines dedicated to voice communications and telex lines for dedicated data transfer. The introduction of voice integrated digital networks (IDN) allowed a number of improvements to be incorporated into voice telecommunications transmission systems. A number of these are listed below

(i) increase in cable bandwidth by digital compression techniques
(ii) improved signal quality by reduction of noise
(iii) low power compact transmitters

The technological progress and diffusion of personal computer systems and terminal equipment has led to the introduction of Integrated Services Digital Networks (ISDN's) mainly in the developed telecommunications regions of Western Europe and the United States. Knight et al (1986) have highlighted a number of benefits due to these networks

- global standard for interconnection of domestic transmission systems to form standard international networks
- terminal-to-terminal digital connections
- supports a wide range of services
- multi-purpose customer interface

The advantages of ISDN's over conventional segregated networks are illustrated by figure 3-1. Along with a reduced capital cost in transmission equipment and paths, these networks also reduce maintenance and operational costs as well as increasing the quality of the service to the end user.

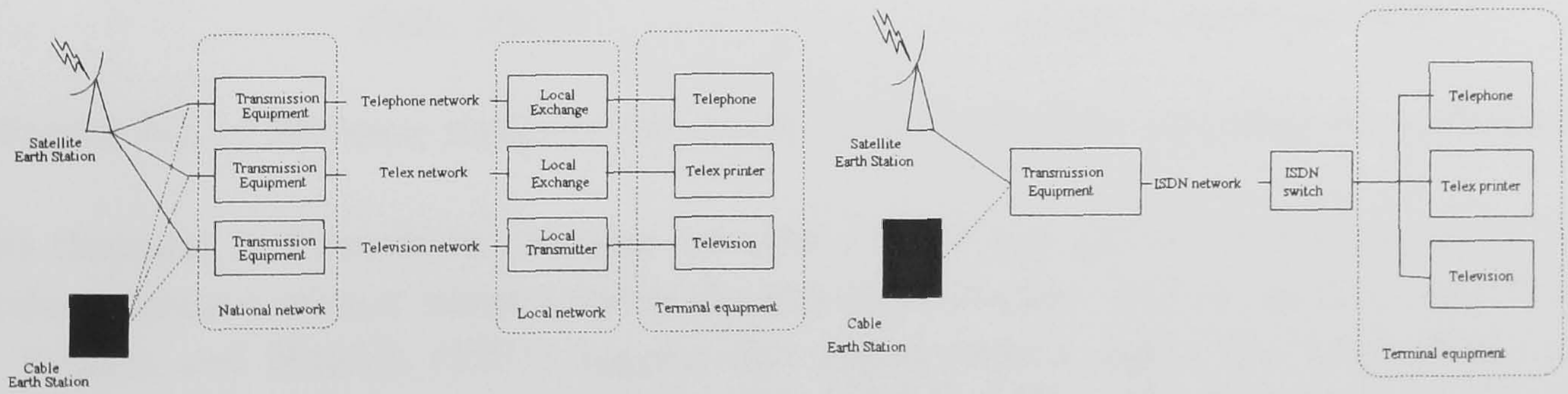

(a) discrete network (b) ISDN transmission

Figure 3-1 Effect of ISDN's on communications transmission infrastructure (Knight et al 1986)

The introduction of national ISDN's has increased the range and quality of services which can be offered over the same network. This has resulted in the so called "multi-media evolution" with a diversification in the product portfolio and an increased user access to the portfolio, as shown in figure 3-2.

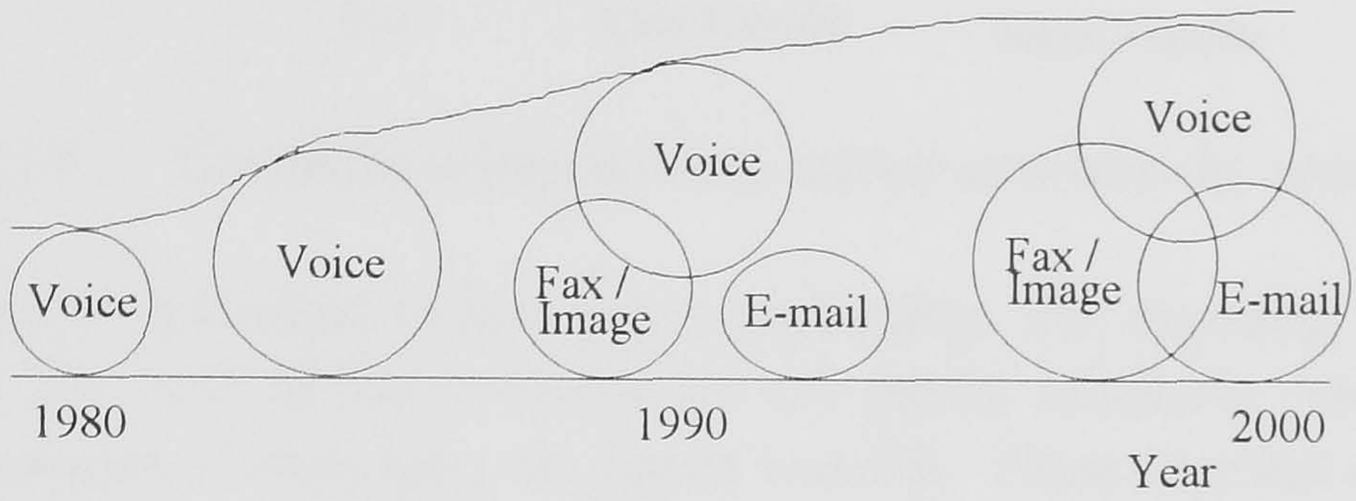

Figure 3-2 Development of multimedia products - an ever broader electronic pipe
Uehara & Nashida (1991)

The diversification of the industry product portfolio has resulted in a steady decrease in the total revenue fraction generated by voice telephony, as shown in figure 3-3.

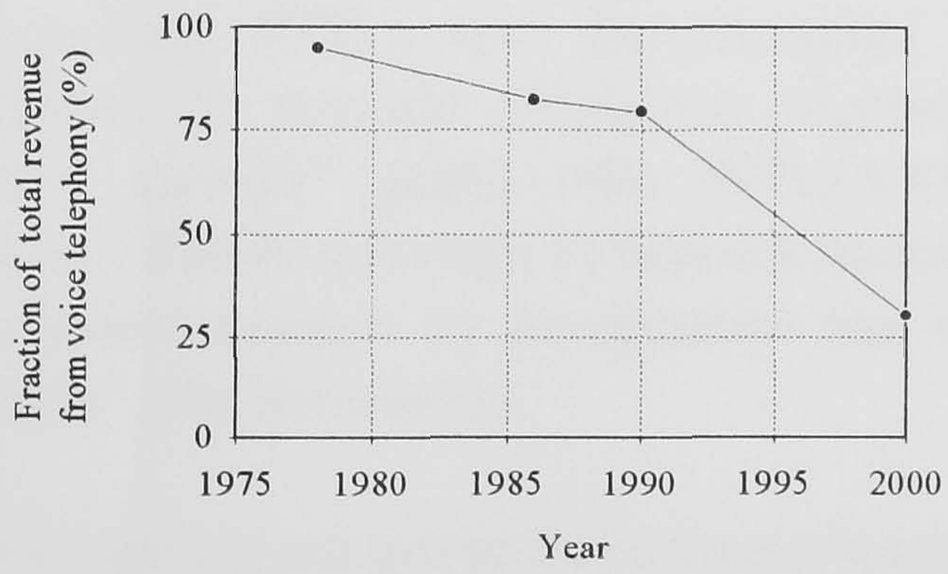

OECD countries
(Kelly, 1990)

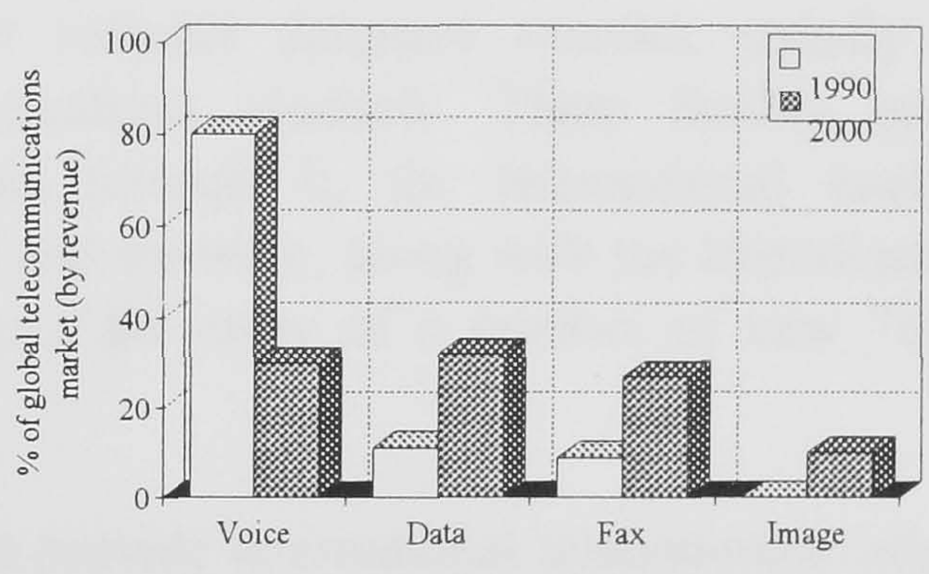

Global
(Uehara and Nishida 1991)

Figure 3-3 Revenue structure for communication services according to application

This decrease is forecast to continue for both OECD and global markets until the new products attain a mature status towards the end of the decade. Following this, predictions by Uehara and Nishida (1991) suggest that approximately equal fractions of the total revenue are to be generated by voice, data and fax. The overall telecommunications services markets can be segmented by applications. These are shown in figure 3-4.

The sectors consist of voice telephony, data/fixed image transfer and moving image transfer with further subsections in each segment.

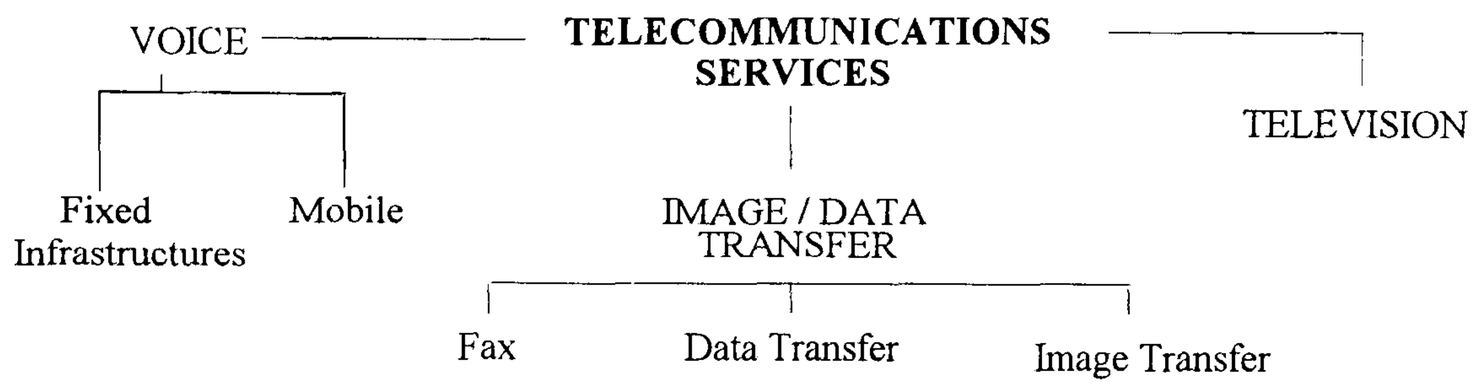

Figure 3-4 Communications services market structure (by application)

The relative sizes of individual sectors vary considerably. For example, data transfer, in 1989 accounted for 20% of the revenues for US public telephone operators (PTO's), whilst in the European Community, the figure was 9%. These regional differences arise due to regional technical, regulatory and economic differences.

3.2.2 Interconnection of markets

The market for international telephony has been described by Staple (1991) as undergoing a "paradigm shift". A few years ago, international telecommunications was operated by the national PTO's who interconnected their national domestic circuits, usually by satellites, to provide end-to-end telecommunications channels. These facility based "heavy carriers" jointly own INTELSAT and through it, the international satellite systems. Recent advances in network hardware and software, along with the liberalisation of national markets by deregulation has led to a the entry of a number of new "light carriers" into the market.

These carriers are primarily software based and provide international telecommunications by re-programming the route offered by the PTO's. This allows the user to choose the cheapest route over the interconnected international network. The behaviour is well illustrated well by the behaviour of the Canadian carriers who in order to take advantage of cheaper satellite link charges in the United States, transmit Canadian international calls via terrestrial telecommunications links to the United States before transmission to satellites.

3.2.2.1 Pricing policies for interconnected markets

The international public telecommunications system remains a monopoly with its pricing is determined by cartel practices. This requires the operator from the origin country to pay the operator in the receiving country approximately four times the cost of the call.

The operator in the source country, in turn, charges the caller an inflated rate for international telecommunications. For example, although the distance from London to Paris is similar to that from London to Birmingham, the cost to the user of a call from London to Paris is approximately three times the cost for a call from London to Birmingham.

The pricing policy between PTO's offering international telecommunications has been in place since the inception of the satellite telecommunications. An analysis of the cost of the space segment by Mahle (1992) suggests that the transmission cost is an order of magnitude lower than the user cost. The estimates show the transmission cost via satellite for the London to Paris call is 10 p/min (1991) whilst the user cost, determined by the accounting practices of PTO's is approximately 30p/min. To decrease the user cost, Dixon (1990) suggests a reform of the accounting rate of the cartel and that the international telecommunications market should be accessible to private operators to ameliorate current monopolistic practices.

3.2.3 Satellite communications technology

The technology for satellite telecommunications has developed significantly since the early years. The technology developments can be analysed by considering the progress of the INTELSAT satellite series, as shown in figure 3-5.

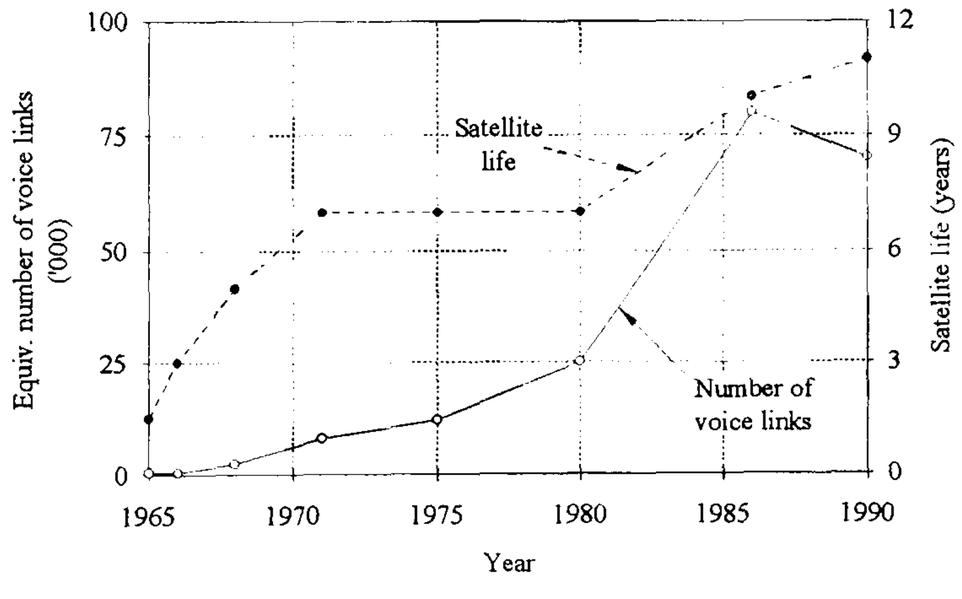

Figure 3-5 Evolution of satellite technology for the INTELSAT series of satellites (Staple 1991)

In addition to having a transmission capacities which are an order of magnitudes greater than that of the early satellites, present day satellites also have much greater design lives. Both of these factors are a direct result of more robust electronics and contribute to the reduced cost per voice path over the life span of the satellite. As a result, the cost per link

via satellites has decreased dramatically since the inception of the commercial satellite telecommunications market, as shown in figure 3-6.

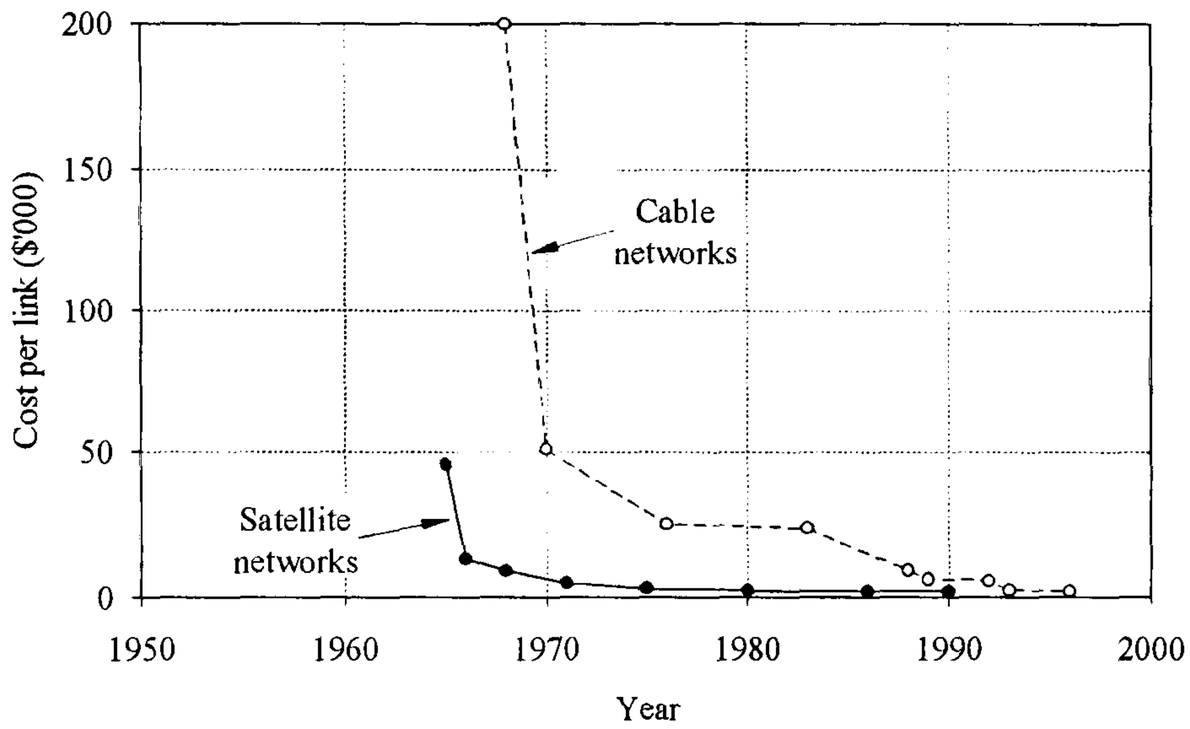

Figure 3-6 Evolution of the cost per equivalent voice link for transmission satellites and cables (Staple 1991, Wilson 1991 & Mahle 1992)

For the INTELSAT series of satellites, the decrease in the cost per voice link can be achieved by progressively increasing the total transmission bandwidth available on each satellite. This technology driven growth continued until in the late eighties, the INTELSAT VI series had a total voice transmission capacity of 80000 lines. This figure attained a maximum as fears of placing too great an investment in one satellite arose and the severe consequences of its failure. Given the fears, the future bandwidth capacity is unlikely to exhibit the high technology driven growth rates which have been observed to date.

Any future growth in capacity is likely to result from improvements in electronics and transmission software rather than through an increase in the number of transponders per satellite. The estimates by Mahle (1992) suggest that a significant reduction in the cost per voice link can be realised if these improvements in technology are embodied into satellites.

3.2.4 Satellite versus Cable

In the early sixties, immature cable technology resulted in the cost per link of cable infrastructures being an order of magnitude in excess of comparable satellite infrastructures. In the eighties, the maturing of fibre-optic technology allowed a dramatic increase in bandwidth of cable links. This produced an order of magnitude increase in the

capacity (number of voice paths) of trans-oceanic cables and as a result, a large decrease in the cost per voice link, as demonstrated by figure 3-6.

Pearce (1988) concluded that satellite and cable technologies are complementary with cables having the advantage over short distance, high volume routes. The study also suggests that the future costs of voice links via cable networks are likely to be much cheaper than comparable satellite links. Other studies by Bradshaw (1990), Pelton(1989) and Gilhooly (1991) have concluded that the cost per voice link for satellite systems were favourable compared to the per link cable costs and that satellites were likely to remain competitive with fibre optic cables on a cost basis during the period 1990-2005.

In the short-medium term, satellite and cable transmission technologies will complement each other. This is illustrated by a breakdown of the planned trans-oceanic cable and satellite capacity (based on INTELSAT's planned launches) up to the next century and is shown in figure 3-7.

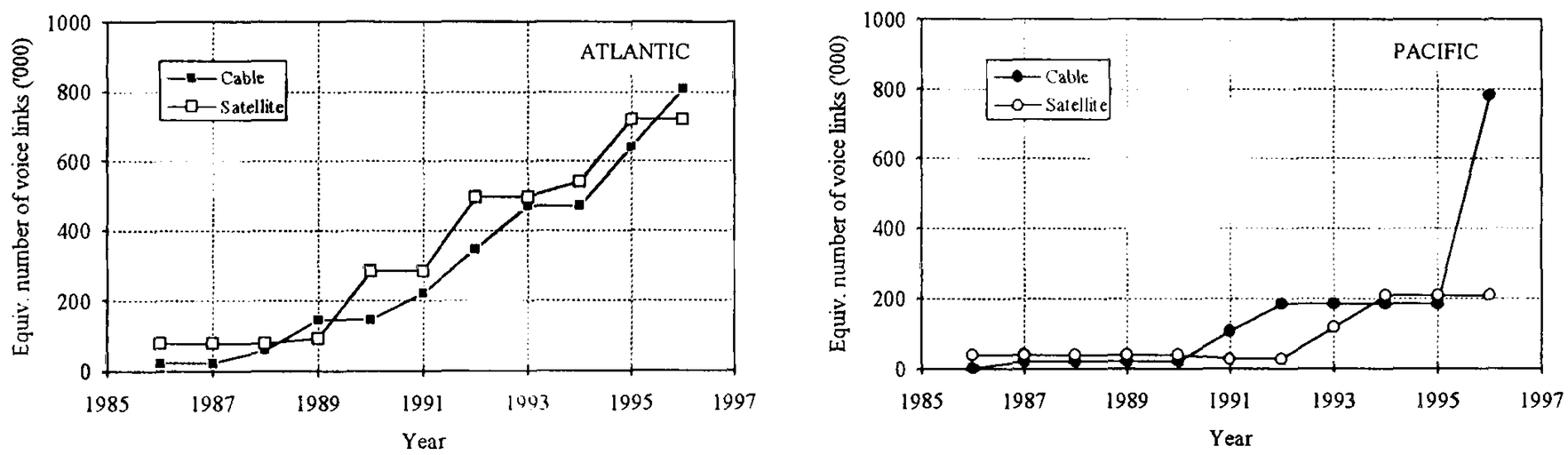

Figure 3-7 Estimated growth of trans-oceanic satellite and cable infrastructures (Uehara & Nishida 1991, and Staple 1991)

In the long term, cables are likely to provide the majority of point-to-point telecommunications links over long distances whilst satellites will continue as the primary medium for broadcast signals such as television transmissions, mobile telecommunications etc., which are often aimed simultaneously at multiple destinations.

3.3 MODELLING OF TERRESTRIAL COMMUNICATIONS MARKETS

The global telecommunications market is immense, with total revenues in 1990 of US$ 400 bn. The market for telecommunications services constitutes approximately 67% of the overall revenues with equipment sales accounting for the remainder. This breakdown has remained constant since 1985.

Along with the economic growth, technical and regulatory changes also have a significant effect on the regional structure of telecommunications services. Due to regional variations in these factors, the relative technical and regulatory complexities of regional telecommunications infrastructures vary considerably.

Studies by Singh (1988) and Kelly (1989) indicate a strong correlation between regional telecommunications investment and economic growth. A good telecommunications infrastructure is perceived in the same light as a good transport structure. Underdeveloped countries and regions are looking to rapidly establish an adequate national and international telecommunications infrastructure in order to compete for investment with other more developed countries.

A number of assumptions regarding regional zones and their relative infrastructure magnitudes have been made in order to model the global telecommunications market. For the present study, it has been assumed that

a) The global telecommunications market can be divided into regional markets structured according to economic boundaries

b) In a given regional market, there are two types of telecommunications traffic
   - intra-regional traffic (within regional boundaries)
   - inter-regional traffic (across the regional boundaries out of a region)

c) The two types of telecommunications traffic are composed of voice, data and television signals

d) Regional satellite bandwidth capacity has been measured by counting the total satellite transponder bandwidth in the region

e) The total transponder bandwidth of the satellites owned by the international consortia, INTELSAT and INMARSAT has been factored by the inter-regional traffic distribution and added to the regional satellite bandwidth distribution of (d).

3.3.1 Intra-regional communications market structure

The relative magnitudes of the intra-regional telecommunications markets has been estimated by considering the number of fixed voice lines in a given region. This, along with the frequency of use of the lines, will determine the operational revenue generated per line, and thus the intra-regional market size, assuming that a large proportion of the calls are intra-regional.

The relative size of the intra-regional market, based on the regional number of fixed voice links is given by Hay and Roberts (1988). This infrastructure distribution, coupled with the regional population distribution gives the regional penetration rates. This is shown in figure 3-8.

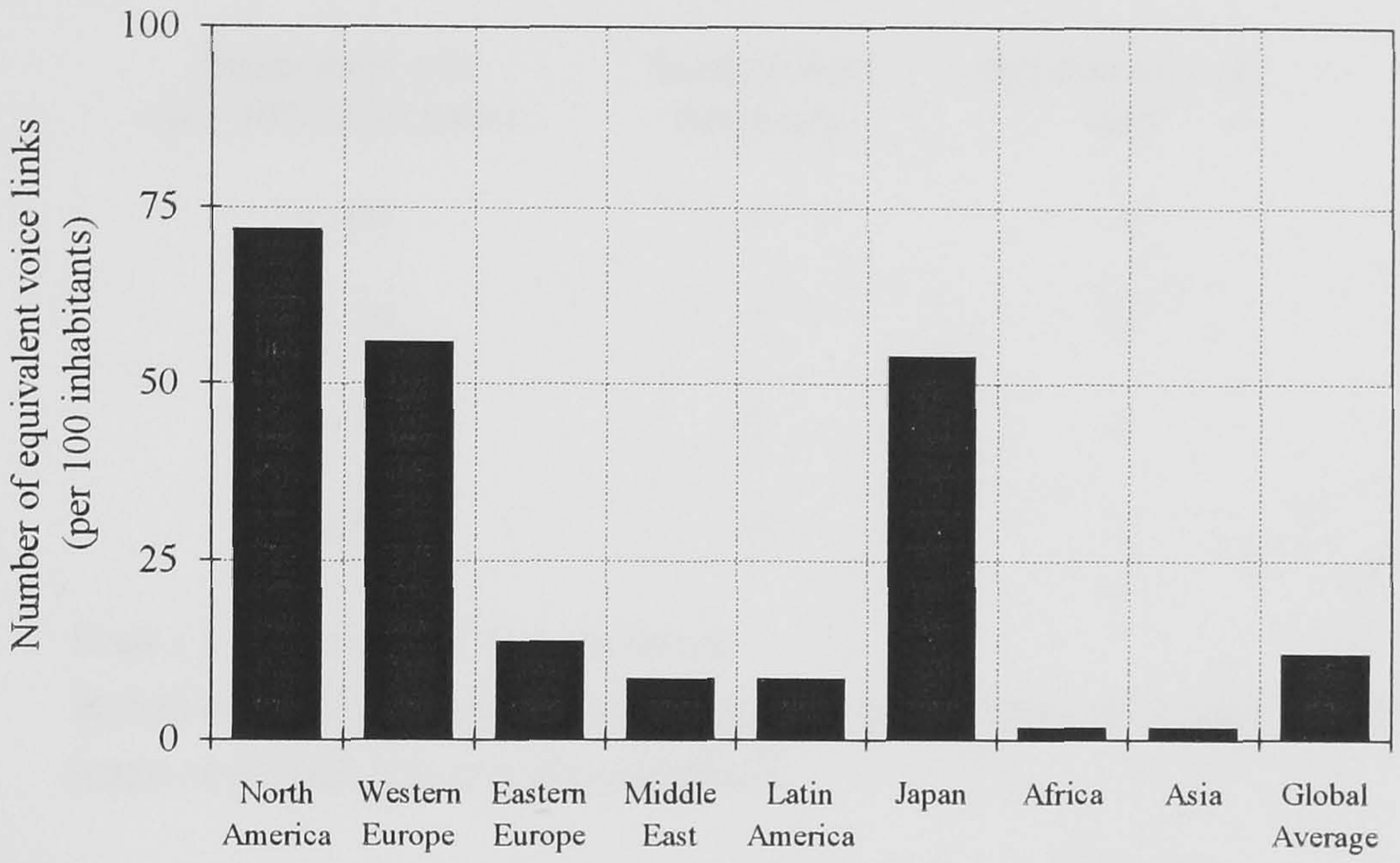

Figure 3-8 Regional penetration of fixed communications infrastructure

The average global penetration is 12 lines per 100 inhabitants. Regional markets with penetration rates at or below the global average are under-developed, both from a telecommunications and from an economic perspective. As a result, these markets have the greatest potential for growth.

Three markets, North America, Western Europe and Japan exceed the global average penetration and are regarded as having the most developed regional telecommunications infrastructures. This correlates with the economically developed nature of these regions. The low penetration rates of the African and Asian markets reflect their relatively under-developed economies. The figures used for these regions assessed the overall penetration.

Telecommunications "hot-spots" within these regions such as South Africa and the Pacific Rim countries have penetration rates substantially above the global average, and hence a telecommunications behaviour which reflects those of developed markets. However, it was considered that since these "hot-spots" represent a modest fraction of the overall regional market, they are unlikely to impact significantly on the long-term growth of the market. The low penetration rates of the Eastern European, Latin American and Middle Eastern markets reflects the relatively under-developed economies of these regions.

Since the revenues generated in a given region from intra-regional telecommunications are proportional to the frequency of usage and user cost per call, a series of factors for these variables were established in order to assess their effects on the regional telecommunications revenue. These factors were considered to be a direct function of the regional fixed infrastructure distribution and are given in table 3-1.

Penetration rate (per 100 inhabitants)	Relative user frequency	Relative overall cost
< 10	1	3
10 - 30	2	2
31 - 60	3	1
>60	4	1

Scale : 1 = minimum, 4 = maximum

Table 3-1 Relative factors used for estimating operational revenues generated from intra-regional telecommunications

The combination of these factors along with the relative magnitudes of the regional fixed infrastructure yields the relative magnitudes of the revenues generated from intra-regional telecommunications.

In terms of revenue generated, the global intra-regional market is dominated by the North American and European regional markets, which together comprise 60% of the global market. Japan, the former Eastern European countries (including the former Soviet Union) and Asia (including Australia and New Zealand) have similar sized markets while Africa and the Middle East have the smallest markets and together generate only 5% of global telecommunications services revenues.

3.3.1.1 Inter-regional market growth rates for various telecommunications products

The growth rates for voice and data telecommunications are shown in figure 3-9. These were obtained from a variety of references. The limits of the growth rates reflect the variation in predictions in the literature.

As voice telecommunications is a mature product, its growth in the developed markets is relatively low whilst in the under-developed markets, its growth rate is substantially

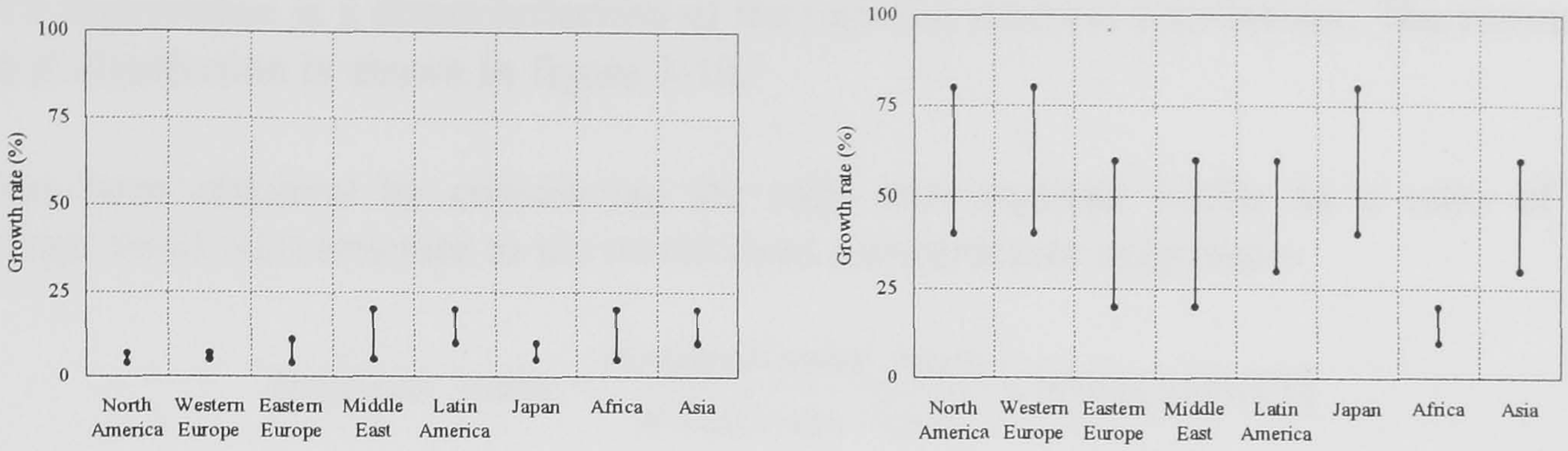

(a) voice communications

(b) data communications

Figure 3-9 Estimated regional growth rates for various telecommunications products in the intra-regional markets

greater. However, as data telecommunications is a relatively new and more sophisticated product, its growth rate is greatest in the developed regions. In modelling the market, these growth rates have been assumed as annual compound rates over the entire period of the study.

3.3.2 Market for inter-regional communications

The inter-regional telecommunications market has been estimated from traffic flow surveys carried out by Staple (1991). The survey considered the total number of minutes of telecommunications traffic (miTT) originating from the various regional markets.

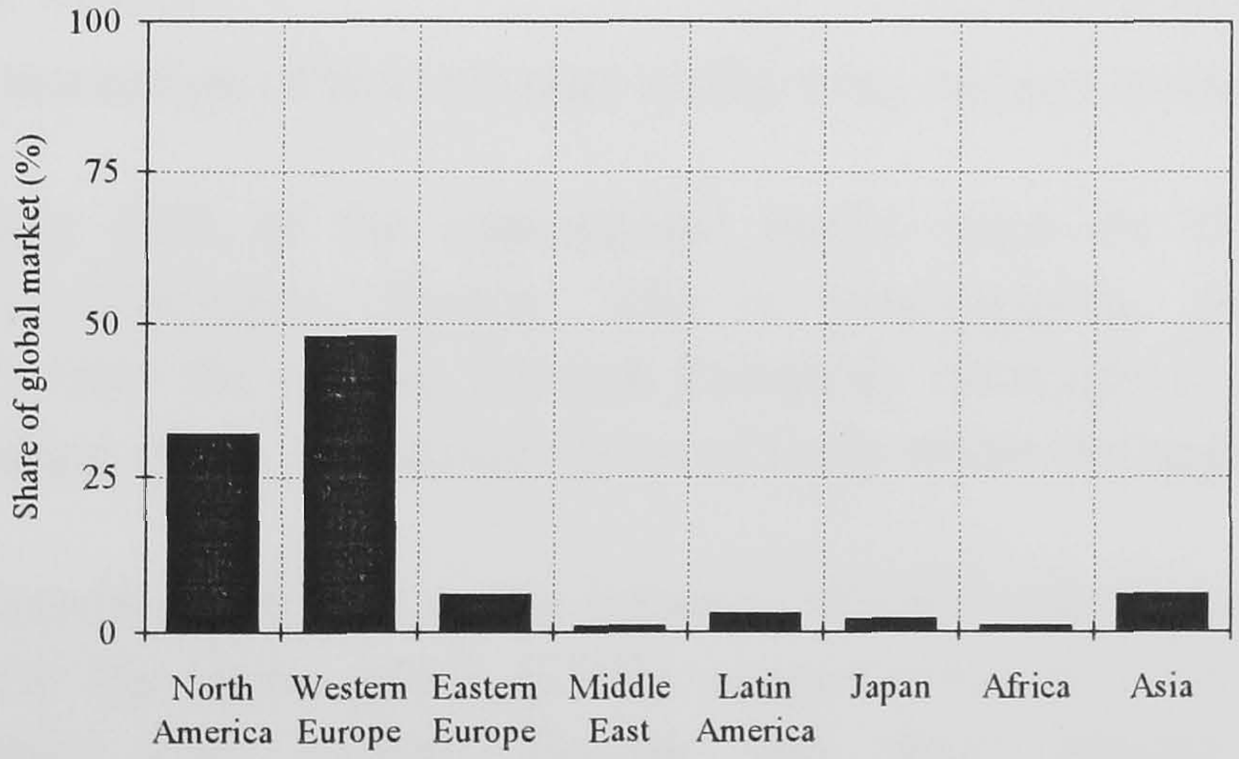

Figure 3-10 Relative market size for inter-regional telecommunications

This incorporates the frequency of calls made over a given line as well as the total number of lines in a region. Assuming that the cost per unit time is the same globally, the

miTT distribution is a direct reflection of the regional revenue distribution. The estimated global distribution is shown in figure 3-10.

It has been obtained by considering the total inter-regional traffic as a ratio of the regional fixed infrastructure to the world fixed infrastructure magnitude

$$\text{Regional traffic} = \frac{\text{Regional(voice lines)}}{\text{World(voice lines)}} \times \text{WORLD[miTT]}$$

Western Europe dominates the market with nearly 50% of the global traffic originating from this region. A large proportion of this traffic originates from the three major countries, Germany, United Kingdom and France and reflects their relatively developed economies within the region. A large volume of international telecommunications traffic from the developed market regions remains intra-regional, as seen by figure 3-11.

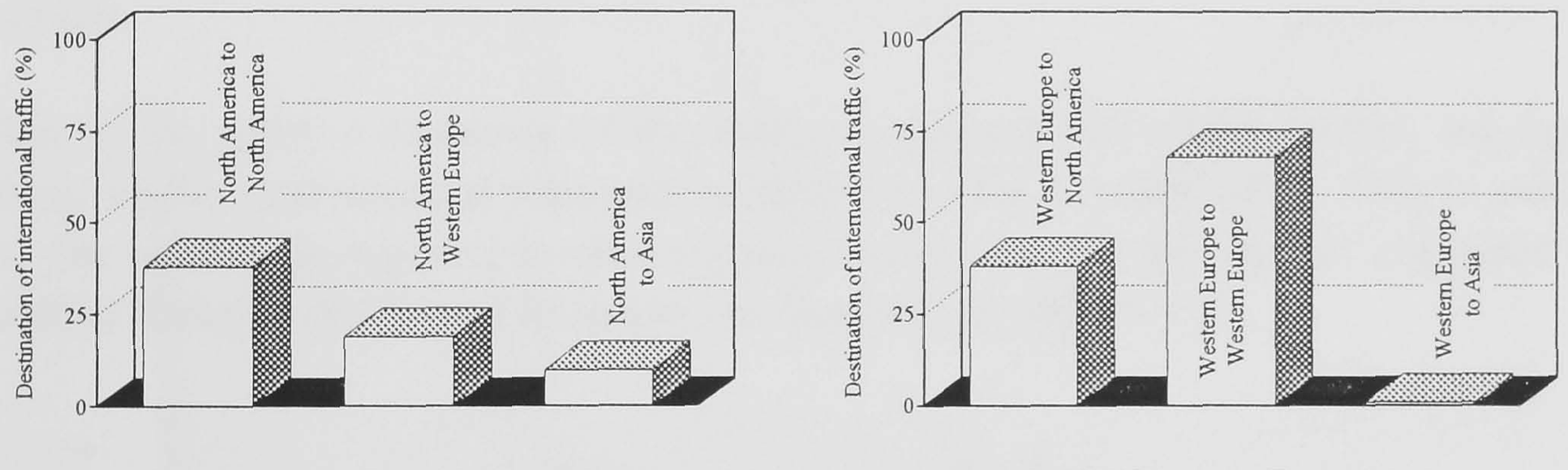

(i) North America (ii) Western Europe

Figure 3-11 Destination of international traffic from various markets (Staple 1991)

While approximately 40% of the international traffic from the three main Western European countries (Germany, France, UK) is intra-regional, nearly 80% of the international traffic from the smaller Western European countries is intra-regional. This may be a manifestation of the incestuous nature of trade within the region.

The volume of telecommunications traffic between Western and Eastern Europe remains small. A survey by the Sema group (1991) suggests that the movement of western European companies into Eastern Europe and their inherent dependence on telecommunications will act as a catalyst for upgrading the local infrastructure. At the moment, the demand for links between the two regions is partially compensated for by mobile telecommunications infrastructures.

In order to expand the Eastern European telecommunications infrastructure to western European standards, estimates by Dandelot (1991) indicate that an annual investment of US$ 6 billion is required over the next ten years. However, due to the recession in Western Europe and political uncertainties in Eastern Europe, investments to date (1991) in telecommunications have averaged US$ 3 billion per annum. Therefore, it is unlikely that traffic growth between the two regions will display a sudden departure from this level. Until the problems of the reduced investment levels are redressed, short to medium term requirements, especially for broad band telecommunications are likely to be served by temporary infrastructures such as satellites.

The North American market is also well developed for inter-regional telecommunications. The distribution of traffic destinations for this market is much greater than for either Western Europe or the Asian market. A large fraction of the latter traffic originates from countries bordering the Pacific rim, as shown by figure 3-11. This was attributed by Staple (1991) to increasing economic and cultural ties between the two regions.

Due to the relative insularity of the Japanese telecommunications market, the Japanese share of the inter-regional telecommunications market remains small. This is evidenced by the small inter-regional to intra-regional traffic ratio for this market compared to the United States or the United Kingdom, as illustrated by the table 2.

Japan	0.2%
North America	1.0%
Western Europe	2.0%

Table 2 Regional Traffic volume ratio between intra-regional and inter-regional telecommunications (Staple, 1991)

3.3.2.1 Inter-regional market growth rates for various telecommunications products

The global market for international telecommunications is estimated by Staple (1991) to grow at an average rate of 16-26 % per annum until 1995. The growth rates for the main markets for inter-regional voice and data telecommunications has been obtained from a variety of sources and are shown in figure 3-12

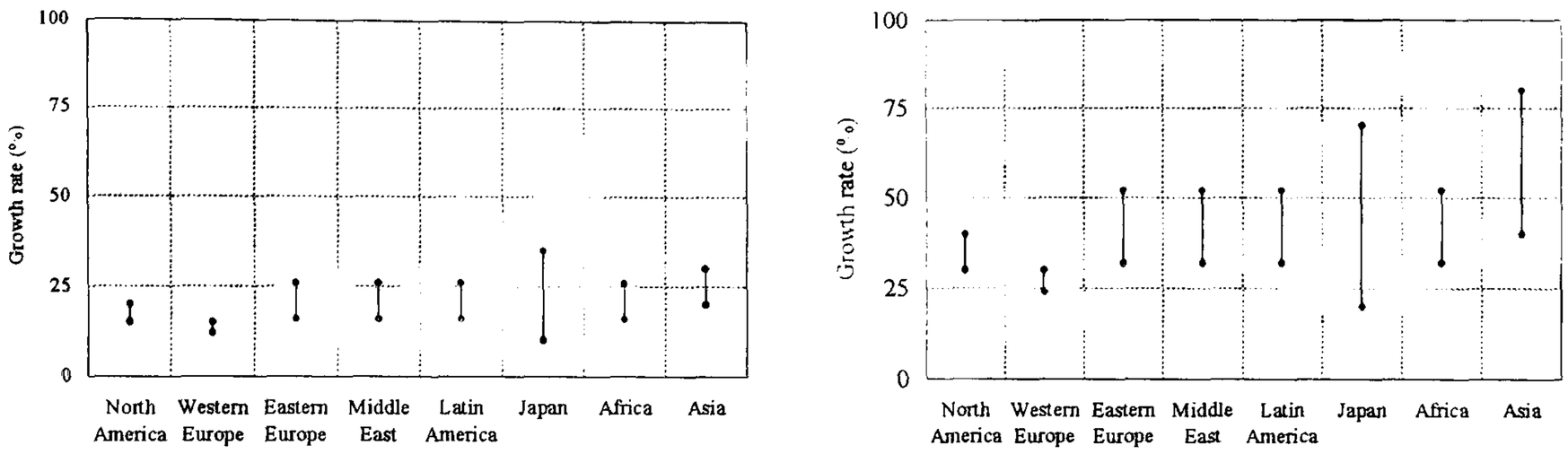

(a) voice communications (ii) data communications

Figure 3-12 Regional growth rates for various communications products in the inter-regional market

The upper and lower limits of the growth rates were determined from a literature survey. For regions where growth rates are not available in the literature, the average global growth rate has been assumed over the entire period of the study. The inter-regional data traffic growth rates have been assumed to be approximately double the voice traffic growth rates.

3.4 SATELLITE COMMUNICATIONS

As described in section 3.1, the satellite telecommunications infrastructure was established by public telecommunications operators to interconnect national telecommunications infrastructures. In its embryonic stages, the market had a single operator, INTELSAT.

INTELSAT operates by selling capacity to its customers, namely the PTO's who in turn resell it to users. The operating revenues generated by INTELSAT in 1990 was $US 600 million, while estimates indicate that this capacity is resold by the PTO's to the user for $US 7 billion.

INTELSAT has a monopoly on transmitting international public traffic via satellites. This monopoly is protected by legislation which prohibits separate satellite systems from carrying public traffic. An article proposed by the United States at the inception of INTELSAT requires member telecommunications operators to co-ordinate with INTELSAT before initiating competitive satellite systems.

Although private satellite systems are beginning to make an appearance onto the market, regulatory constraints prevent them from transmitting end-to-end public telecommunications. However, with the deregulation of terrestrial markets, increasing pressures are being exerted on governments and regulatory bodies to relax regulations governing satellite transmission.

3.4.1 Modelling of satellite communications

The maximum telecommunications volume which a satellite can administer is dependent on the overall bandwidth of the satellite. This in turn depends on the number and type of transponders on board the satellite. In the present study, it has been assumed that satellites contain either C-band transponders (maximum bandwidth of 36 MHz) or Ku-band transponders (maximum bandwidth of 72 MHz).

The number of satellites and the number and type of transponders in a given market region was obtained from Interavia (1991). From this the bandwidth of the space segment of a regional market was estimated. The total global space segment bandwidth was 103280 MHz (1990).

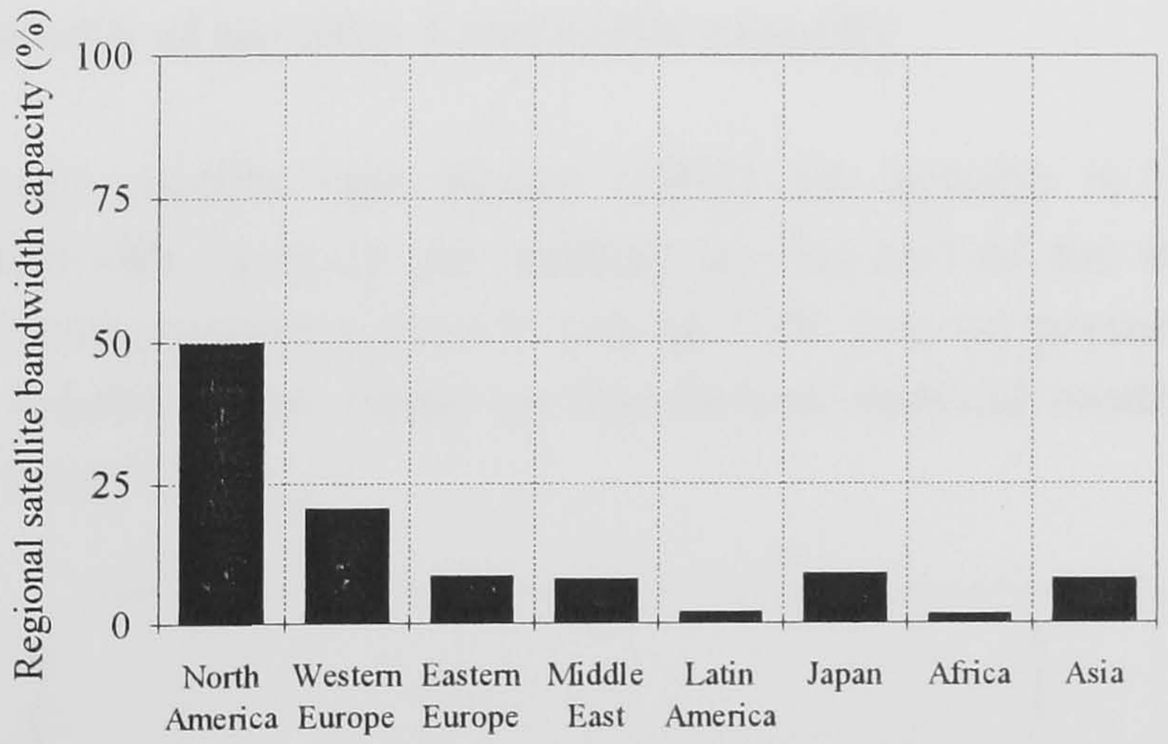

Figure 3-13 Regional fraction of global satellite bandwidth capacity in a given region

The bandwidth capacities of the international operators have been divided regionally according to the inter-regional telecommunications market distribution shown in figure 3-10. These were subsequently added to the dedicated regional satellite bandwidths to obtain the overall bandwidth serving a given market region. This distribution is shown as a fraction of the global total in figure 3-13.

For a given region, the study assumed a bandwidth distribution according to traffic and application as shown in figure 3-14. The growth rates for satellite television has been based on the growth rates for television terminals as estimated by the British Broadcasting Corporation (1991)

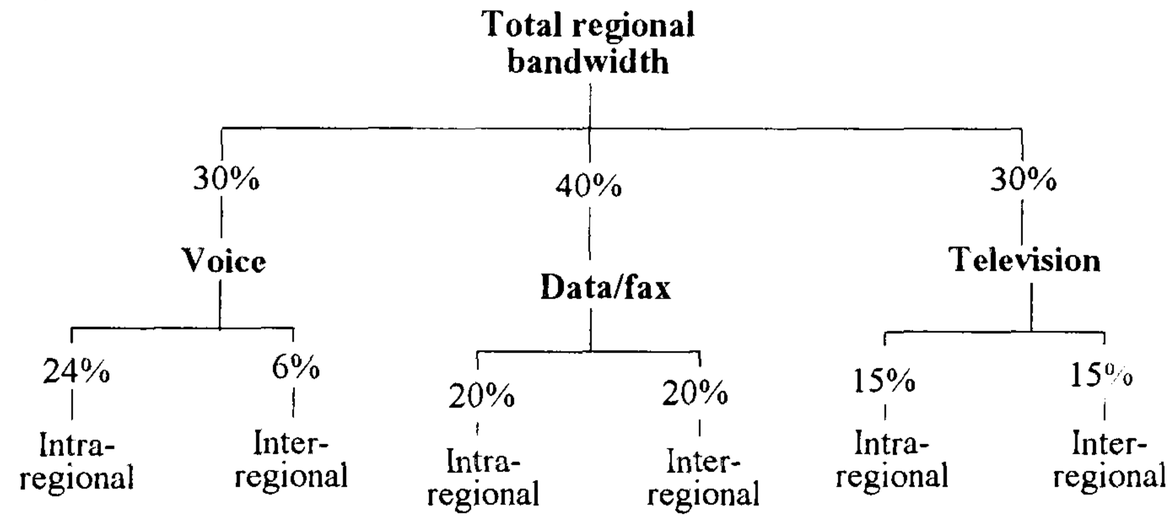

Figure 3-14 Assumed distribution of satellite bandwidth capacity by application in a given region

Following the sectoring, the regional growth rates for a given application for terrestrial telecommunications was imposed on the space segment bandwidth. These growth rates were assumed to be constant for the period of the study.

3.4.2 Development of satellite bandwidth capacity

The advanced concept satellite (see Mahle (1992) for details) is likely to result in a doubling of the bandwidth capacity per satellite by the end of the decade. This type of growth is attained if one assumes a growth rate of 10% p.a. on present day satellites. The satellite bandwidth requirements, based on the derived demand model over the period of study are shown in figure 3-15.

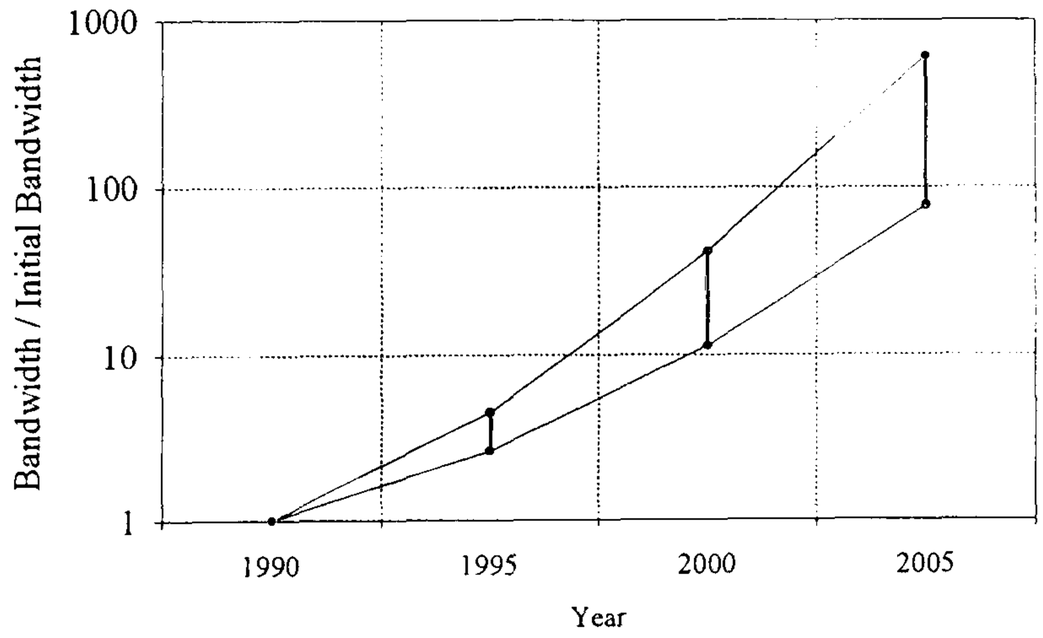

Figure 3-15 Growth of global satellite bandwidth capacity required to satisfy latent telecommunications demand

An order of magnitude increase in global space based bandwidth capacity is required over the period of the study to furnish latent demand. The majority of this growth will emerge from bandwidth intensive products such as data and television telecommunications as these services mature. A part of this growth will be absorbed by an increase in satellite bandwidth capacity but an increase in the number of satellites from 100 to approximately 1000 will still be required to furnish the total latent demand.

Chapter 4

SATELLITE EARTH OBSERVATION MARKET

Satellite Earth observation is a technique for qualitative as well as quantitative analysis of the properties of the Earth's land, ocean and atmosphere from space. The technique was originally conceived with aircraft and balloons being used as the platform for sensing elements.

However, improvements in sensor technology, data transmission and image processing have made it more advantageous to use space based platforms. The benefits and drawbacks of a space based Earth observation systems are given in table 4-1.

ADVANTAGES	DISADVANTAGES
Data acquisition over a wide range of spatial scales	Poor spatial resolution - political/national restrictions result in high resolution data being classified
Data collection regardless of political/geological boundaries	Satellites follow fixed paths. Thus, instantaneous data with dynamic changes can only be acquired on the next nadir sweep
Repetitive coverage over a wide time span	
Data acquisition regardless of weather/operator problems	

Table 4-1 Advantages and disadvantages of a space based Earth observation systems (Harr & Kohli, reference 1990)

The technique of satellite Earth observation employs sensors located on-board the sensing platform to analyse emissions and/or reflections from the object under investigation. The sensors are repeatedly calibrated against objects of known emissivity/reflectivity. The calibration factors obtained allow the qualitative measurement of the changes imposed by

the object onto the surrounding electromagnetic radiation field to be converted into absolute electromagnetic radiation intensities. Sensors on-board the platform allow the intensity to be digitised. By coupling this information with the spatial location of the object, a map of the radiation intensity from a particular area can be constructed. Analysis of the digitised emissivity/reflectivity measurements against known data allows the user to comment on the state of the objects physical and chemical structure.

4.1 TECHNOLOGY STRUCTURE FOR SATELLITE REMOTE SENSING

The satellite remote sensing industry can be divided into two distinct sectors. These sectors are based upon the particular technologies involved.

Space component	This sector involves the satellites bus, ground systems for control of the satellite and launchers
Data collection	This includes ground stations involved in collection and pre-processing of data to produce raw data on computer compatible tapes
Value added products industry	This sector is involved in the manipulation of raw data by computer processing in order to extract particular types of information. Integration of this processed data with other databases results in analytical / predictive products.

The overall technology structure for satellite remote sensing in shown in figure 4-1.

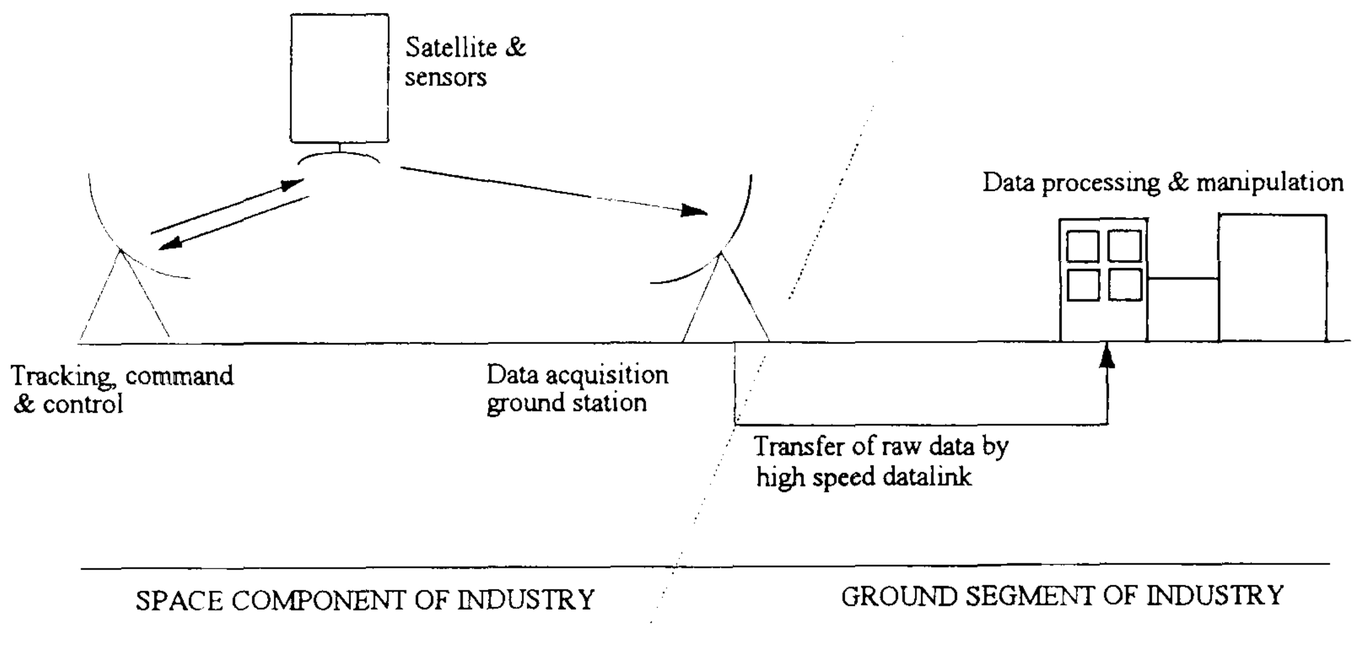

Figure 4-1 Overall technology structure for satellite remote sensing industry

There are two distinct technology structures present in the industry.

Space component : The fundamental technology of this industry consists of the space component and its associated ground equipment. This involves the satellite bus and associated sensors, tracking, command and control structures as well as the ground stations established for receiving and collating data from satellites.

The development of technologies involved in the space component part of this sector arises from new applications and involves large capital investments. Due to the commercially immature status of this sector, the commercial yields on the capital investments are negligible in the short to medium term.

The primary sources of funding for these programs are large government agencies who justify their support for the development of new space technology applications in terms of their political and economic importance, as well as the social/ecological benefits. Another reason for the considerable involvement of governments in this sector of the industry is the high risks and limited short-medium term returns associated with the research and development of new technologies. Due to these factors, these projects are rarely funded by private industry.

Ground segment : The ground segment of the industry is directly user oriented. The technology developments in this sector are modest and require much lower injections of capital than the space component. These developments are highly influenced by commercial as well as by legislative considerations. Alongside this, the commercial technological limits of this sector are derived primarily from the space component sector of the industry.

The primary developments in this sector of the industry arise from software as well as hardware developments in the computer industry. The improvements in telecommunications with the considerable improvements in the performance of data transfer links will give rise to a more flexible technological structure to this sector of the industry.

4.2 MARKET STRUCTURE FOR THE SATELLITE REMOTE SENSING INDUSTRY

The market for remote sensing can be divided along similar lines to the overall technology structure of the industry. Harr & Kohli (1990) consider the main commercial thrust in the industry during the period of concern for the present study to arise from the user section of the industry. However, the growth and development of this section of the industry is constrained by two technological limits.

4.2.1 Development of the user component of the industry

The maximum resolution of data available commercially at the moment is 30 to 120 m. A large number of potential customers require Earth resources data at a resolution of < 10 m. The potential application areas are given in table 4-2 along with the anticipated long term demand for this type of data.

Application area for remote sensing data	Present market size	Potential for application	Potential demand (long term)
Agriculture	small	high	high
Fisheries	non-existent	medium	medium
Environment	small	high	medium
Geology	large	high	high
Cartography	small	medium/high	high

Table 4-2 Potential demand from application areas (Harr & Kohli, 1990)

Although sensor technology for this high level of resolution is available, the data obtained is often classified for reasons of national security. This level of resolution is likely to become commercially available in the mid-1990's with the launch of the LANDSAT 6 satellite. The future market size of the user segment of remote sensing is also likely to be determined by the frequency of coverage of a particular point. A high frequency of coverage is essential for some applications, as shown in figure 4-2.

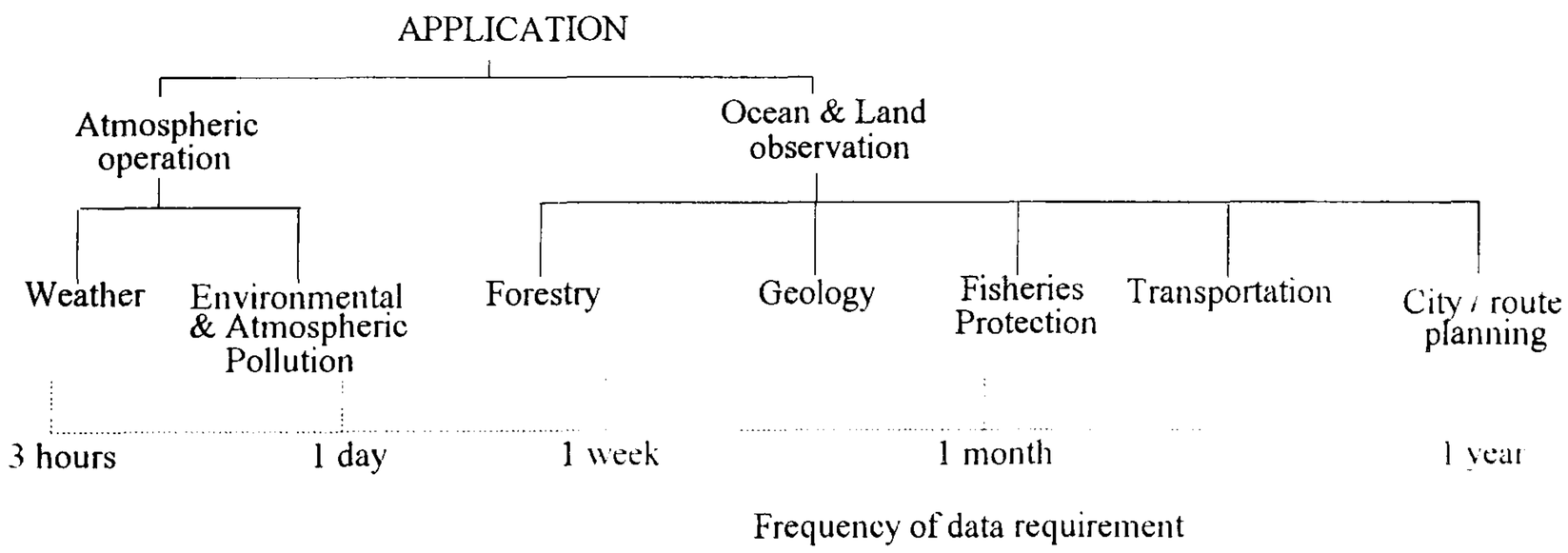

Figure 4-2 Frequency of data requirements for applications (Harr & Kohli, 1988)

4.2.2 Data collection and interpretation

This is a part of the user component of the industry. It is characterised by two types of businesses. The types are identified by the level to which they process the raw data obtained from satellites.

Non-enhanced data	This type of business involves the sale of minimally processed data
Value added products and services	This involves the sale of processed data which has been integrated with other databases to form predictive tools. The data is primarily used by the ultimate user as part of a decision forming tool.

The non-enhanced data market has a small number of usually government owned companies/agencies involved. They own ground stations which receive data from orbiting platforms. This data undergoes minimal processing following which it is stored on computer compatible tapes. These tapes are subsequently sold to companies involved in the value added services market. They in turn further process/enhance the data before selling it to the ultimate customer.

The first remote sensing system, LANDSAT, was established by the United States in 1972. This system consisted of a polar orbiting satellite and a number of ground stations spread globally. These stations were owned either directly or indirectly by local governments who paid $600,000 annually to receive and sell regional remotely sensed data from the LANDSAT system.

Although the system remained experimental until 1983, a phased commercialisation of the data marketing was undertaken in 1983. the operation and data handling of the system was given to a commercial contractor company. Alongside the privatisation of the system in 1984, the LANDSAT act was passed. This obliged all operators of ground stations to make public all unenhanced data obtained from LANDSAT satellites to potential users on a non-discriminatory basis.

At the moment, there are 15 ground stations. The capital cost breakdown for these stations is given below

Construction	Total = $ 20m (Antennae = $ 5m, Image processing equipment = $ 15m)

Operation Total = $ 3m (including $0.6 m for "right to receive")

An additional cost of $2m per station is required for fitting additional equipment to receive data from the SPOT system. The image processing associated with the LANDSAT system can also be used by the SPOT system. In 1990, 13 of the 15 ground stations were fitting additional equipment to receive data from the SPOT system. The data obtained by these ground stations will again be a subject of the "open skies policy" although the SPOT image corporation

This sector has seen a sales move in recent years from the non-enhanced data market to the value added products and services market. This move has been attributed to both a decrease in the hardware/software costs associated with the processing of data as well as an increasing sophistication of users. The former is illustrated well by three developments

a) in 1990, there were 50 companies in the US involved in selling hardware/software for information processing. This is a tripling in numbers since 1980. A number of major oil companies are involved in this activity. They have established their own Earth observation laboratories and process the data using in-house developed software.

b) capital investment costs for entry into the image processing market have decreased from $150,000 in 1987 to $40,000 in 1990

c) in 1990, there were 125 companies servicing the demand for value added services. This is a doubling in numbers since 1980.

The companies involved in this sector of the market purchase computer compatible tapes of raw data manufactured by the ground stations. The price of these tapes varies depending upon the quality (cloud free etc.), as well as the age of the data.

The costs associated with the raw data tapes remain prohibitive ($ 5000 for LANDSAT data) although agreements have been reached to return LANDSAT data older than two years to the public domain. At the moment, only two operators commercially generate remotely sensed data. Along with this, ground stations have a virtual monopoly on local remotely sensed data. As a result, a dramatic decrease in the costs of raw data is not conceived.

4.2.3 Demand for data products and services

There are three basic user groups for commercial remote sensing data. These are categorised as the various departments of the United States government (Department of Agriculture, Department of Defence etc.), commercial users of remote sensing data in the

United States and foreign users. The market share of these groups (as derived from their purchasing of raw data) is shown in figure 4-3.

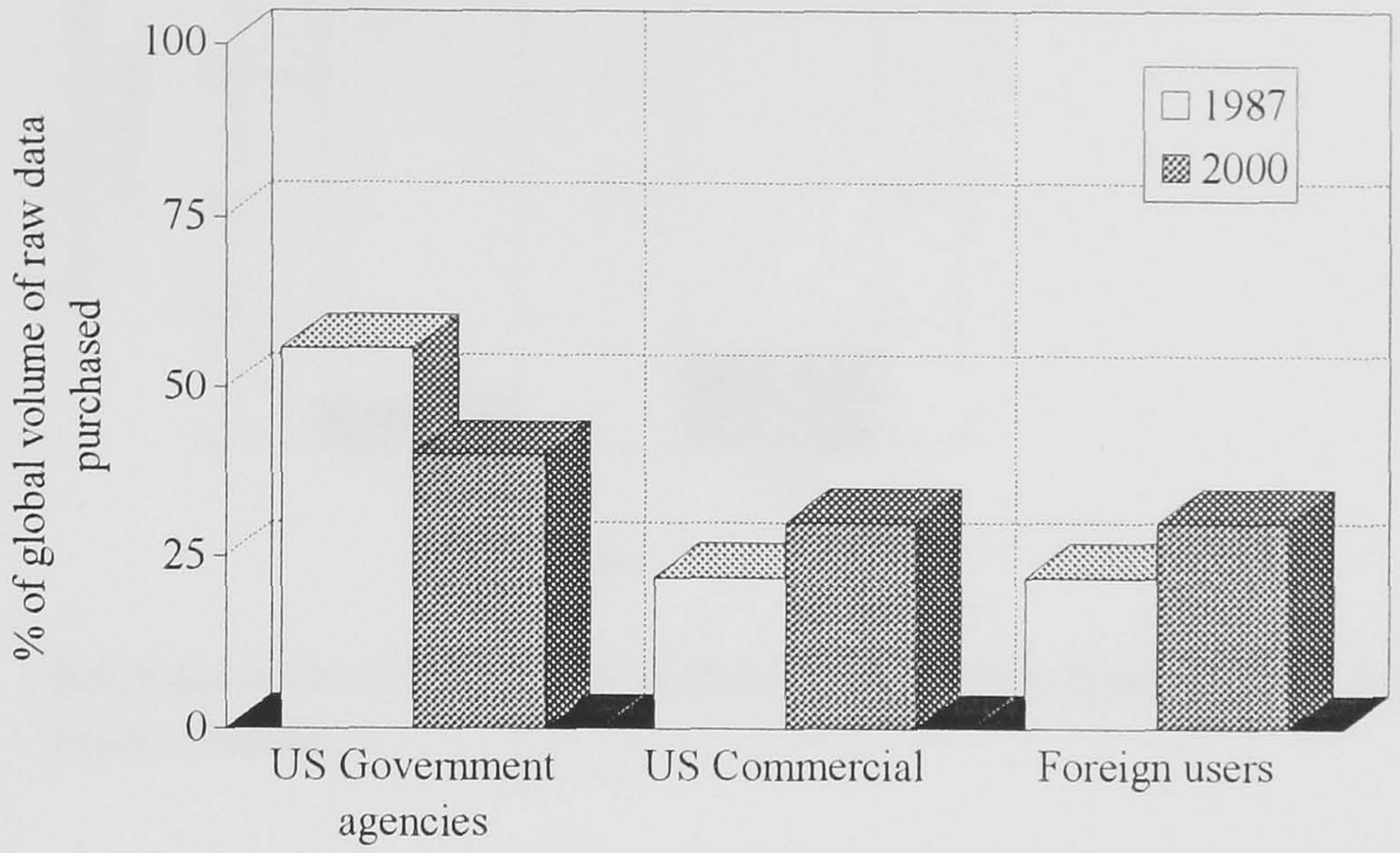

Figure 4-3 Development of demand for raw data from remote sensing satellites in the period 1987 - 2000 (Harr & Kohli, 1988)

This shows that the major users of raw data from remote sensing satellites are government departments in the United States. Altogether, they account for well over 50 % of the user demand for raw data. The majority of the data enhancement/integration is undertaken in-house by these agencies.

The sophistication of the US commercial sector in utilising remotely sensed data is illustrated by the fact that they alone account for 22% of the global sales of raw data. Non-US countries and international agencies ("Foreign users") accounted for the remainder of the sales of raw data. The breakdown between the three sectors is forecast to decrease by the year 2000 (see figure 4-3) due to easier access for less sophisticated users through reductions in costs of data processing hardware.

The reduction in costs of image processing equipment and an increase in their real-time capabilities will lead to a more rapid growth of sales of value added rather than raw data products. Arianespace (1990) estimates this to be by a factor of ten in the 1987 to 1997 period, as shown in figure 4-4.

Due to the lower sophistication level in both computer hardware/software and domestic market structure for remotely sensed data, foreign users, a large fraction of which are developing countries, are likely to have a value added data to raw data sales ratio of five. This is lower than the ratios for the US sectors.

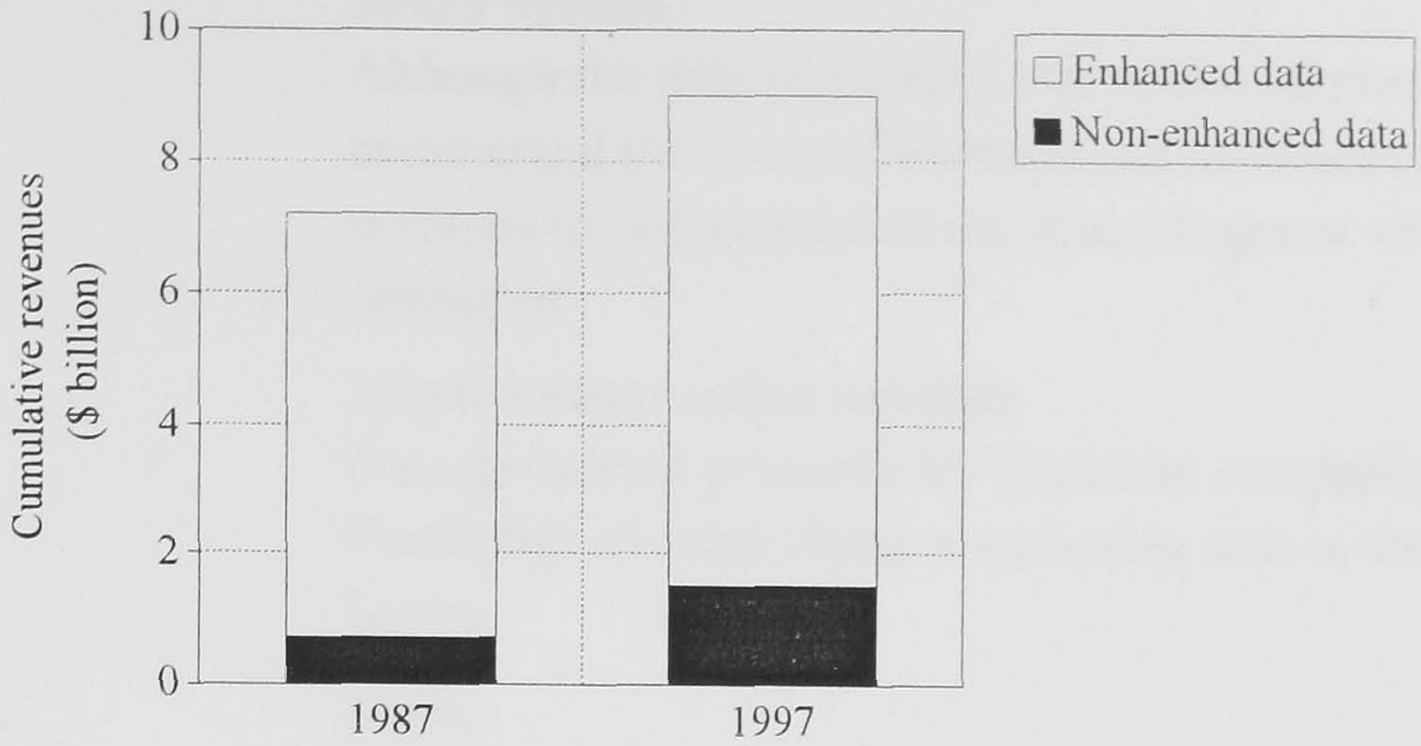

Figure 4-4 Estimated development of cumulative revenues from remote sensing market sectors

The cumulative revenues from sales of non-enhanced and enhanced data was $US 7.2 billion in 1987 (Arianespace, 1990). The revenues from enhanced data / value added services sales accounted for 90% of this figure. The cumulative revenue is forecast to have an average growth rate of 1.7 % per annum during the ten year period of 1987-1997 to yield cumulative sales revenues from the market of $US 9.0 billion. The sales of enhanced data is forecast to account for 83.3% of the total cumulative revenues for 1997. The increase in the percentage of sales from non-enhanced data is as a result of the increase in data processing and image analysis ability brought about as a result of improvements in image processing hardware and software.

4.2.4 Operators in the space component of the industry

The space component of the industry can be sectored in terms of the primary objective of the satellite operators - whether commercial or scientific. The sectoring is based as much on the will of the operator as on the hardware. Although a steady growth in the various sectors of the user component of the industry is forecast, it is unlikely to affect the space component of the industry. This component of the industry is dominated by a number of government agencies. The principal operators and their associated hardware involved in commercial remote sensing are shown below

a) **United States** **LANDSAT (2 satellites)**
This was privatised in 1984, although there is speculation of either partial (the space component only) or full (the space component and the data marketing)de-commercialisation of the system

b)	**France**	**SPOT system** Although the data marketing arm of the corporation is commercial (in terms of financial self sufficiency), there are no plans to commercialise the space segment of the operation
c)	**Japan**	**Marine observation satellite** Data generated primarily for Japanese companies. Possibility of establishing a marketing arm in the United States.
d)	**India**	**Insat** Satellite operated on a non-commercial basis
e)	**Commonwealth of Independent States**	High resolution photographs in visible range of spectrum. Do not observe international "open skies" policy.

Although the raw data generation arm of these operators is usually either directly or indirectly state owned, the marketing arm for this non-enhanced data is usually commercially independent. The demand structure is also subject to the political pressures of its ultimate sponsors.

Due to the uncertainty associated with this factor, it is difficult to undertake a conventional analysis to estimate the growth of the market using a derived demand model. As a result, the future impact of developments in the remote sensing market on the launcher market has been assessed using data provided by references Arianespace (1990), Kramer (1992) and CEOS (1992). These documents summarise the future launch schedules for remote sensing satellites. The results are shown in figure 4-5.

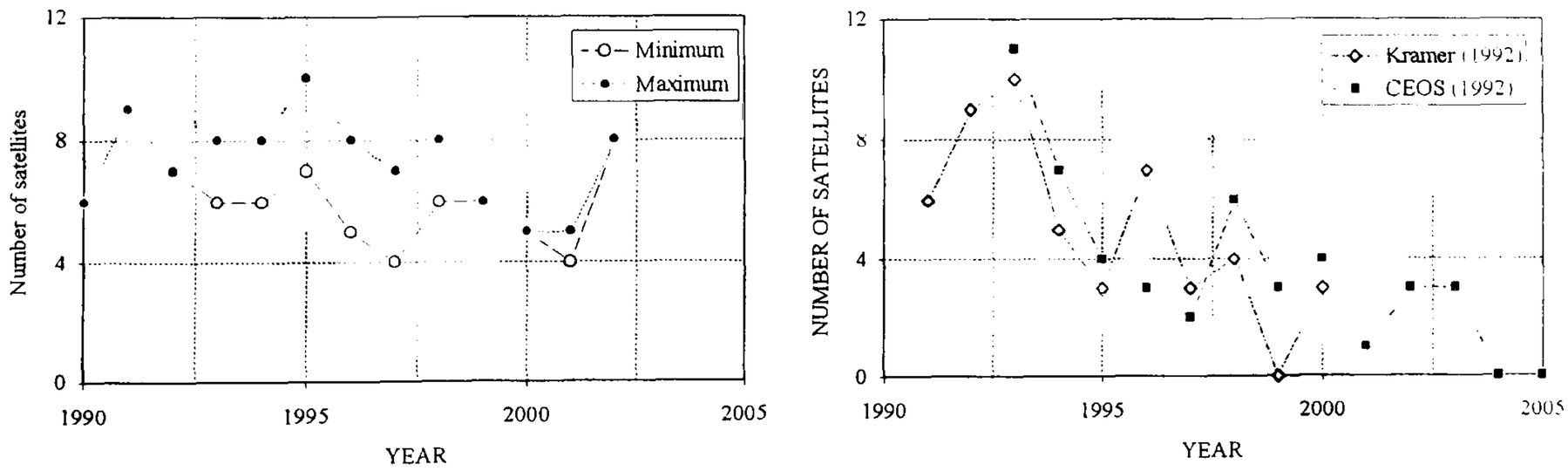

(a) Arianespace (b) Various references

Figure 4-5 Summary of the number of satellites to be launched for remote sensing purposes during the period 1990 - 2005

The results are biased towards the near term period of the study due to more confirmed nature of satellite programs in the near term of this period as compared to the long term.

4.2.5 Demand for launcher services from satellite Earth observation markets

The results of the study indicate an average of 7 Earth observation satellites per annum will be available for launch during the period 1990-2005. However, due to the tremendous level of involvement of governments in the space component of this industry, it is unlikely that any foreign launch system will be given precedence over domestic launch systems for these satellites.

The developments in the user component of this industry are unlikely to generate sufficient demand to affect this figure through the derived demand structure to the space component of the market during the period of study.

Chapter 5

REVIEW OF CURRENT LITERATURE

5.1 BOUNDARY LAYER TRANSITION

Boundary layer transition has been identified by Holden (1986) and Malik (1990) as being critical to the aerodynamic optimisation hypersonic vehicles.

Although its underlying mechanisms remain ill understood, transition affects a number of surface properties such as heat transfer and skin friction as well as the drag and payload performance of the vehicle.

5.1.1 Development of transition

The transition process has been described by Malik et al (1990) as an initial boundary value problem. It arises due to the entry of disturbances, from an initial disturbance field, into the boundary layer. Stetson (1983 b and 1988 b) has experimentally shown that this is followed by linear and non-linear amplification of selected disturbances (within a mean flow boundary layer which exhibits laminar characteristics).

Following a considerable amplification of the disturbances, White (1974) suggests that intense local fluctuations (known as turbulent spots) appear randomly within the boundary layer. From these, true turbulence (in the form of high frequency eddies) is generated and convected downstream.

The random generation and passing of these concentrated regions of turbulence over surface mounted sensors produces an intermittent increase in the amplitude of fluctuations on the surface. Using surface mounted thin-film gauges, Owen (1970 and 1975) observed the increase in fluctuation associated with the synthesis of turbulent spots as an increase in the RMS voltage component. These are shown together with oscilloscope traces in figure 5-1. The RMS voltage component is non-dimensionalised with respect to the noise on an entirely laminar signal. An increase in fluctuation above this level is attributed to the shedding of turbulent spots.

The increased frequency of synthesis of turbulent spots in the transition region results in an increase in intermittency. This increases until the spots coalesce at which point a peak in intermittency is observed.

Following the merger of the spots, the boundary layer is made up of high frequency turbulent eddies (originally present within the confines of the spot). The frequencies of these eddies are outside the sensing range of thin-film gauge instrumentation. As a result, the fluctuations are not registered and the fluctuating component of the signal is reduced.

Mean heat transfer measurements by Owen et al (1972) and by Legraff (1972) have shown that the increase in heat transfer due to transition starts from close to the peak fluctuation point. This is because of the coalescing of turbulent spots in this region.

As will be demonstrated later in the thesis, the heat transfer rate increases from the laminar to the turbulent level as a turbulent spot passes over the surface of a thin-film sensor.

5.1.2 Parameters which affect transition

5.1.2.1 Mach number

The effect of Mach number on the transition of a sharp flat plate boundary layer has been studied experimentally by Korkegi (1956), Potter et al (1960) and by Coleman (1973). These tests concluded that an increase in Mach number delays the onset of transition of a laminar boundary layer (see figure 5-2). The transition studies by Nagamatsu et al (1967) on an axi-symmetric conical attained a similar conclusion.

These studies showed that for both flat plate and conical boundary layers, the length of the transition region increased with Mach number. For hypersonic Mach numbers, the length of the transition region on both flat plates and on cones was of the order of the length of the laminar region.

Spall and Malik (1989) and Mack (1975) have shown that the growth rates of Tollmien-Schlichting waves and Gortlër instabilities are reduced by an increase in Mach number. The slower growth of disturbances within the boundary layer may be responsible for the observed delay in transition with Mach number.

An anomaly of the delaying of transition by Mach number in the range $5 \leq M_e \leq 6.8$ was found by Mateer et al (1969). Tests on sharp cones with $\delta_c = 5°$ and $\delta_c = 15°$ showed a

promotion of transition by Mach number. This contradictory behaviour was attributed to the low molecular weight helium-air flow unique to the test facility.

5.1.2.2 Unit Reynolds number

As is shown by the data of Coleman (1973) in figure 5-2, the transition Reynolds number and the length of the transition region exhibit considerable variation with changes in the freestream unit Reynolds number. A similar unit Reynolds number effect has been observed by Potter (1960) Richards (1967) and by Stetson (1993) on both flat plate and conical boundary layers.

However, the rate of increase of the transition Reynolds number (at a given Mach number) with unit Reynolds number is less than unity. Therefore, the distance to transition progressively decreases with increasing unit Reynolds number, as shown in figure 5-3.

These tests at M_∞ = 8.0 by Potter (1960) and by Stetson (1991, 1993), shown in figure 5-3, were conducted in a "low" noise closed loop hypersonic facility using the same nozzle. Thus the freestream environment associated with these measurements was similar. The correlation of the measurements underlines the importance of the forcing effect of freestream disturbances on boundary layer transition. In comparison, the tests of Richards (1967) and of Coleman (1973), despite being at a similar Mach number, were conducted in the noisy freestream environment of a gun tunnel. As a result, these show the onset of transition to be much further upstream.

5.1.2.3 The effect leading edge diameter on transition - Small bluntness

Heat transfer distributions on a flat plate with various leading edges are shown in figure 5-4. This shows that an increase in leading edge diameter from a sharp leading edge to d = 0.25 cm delays the onset of transition. The delaying of transition by "small" bluntness has also been observed by Brinich (1956), Potter et al (1960), Deem et al (1965) and Richards (1967).

Reshotko and Khan (1979) modelled the flow over a blunt flat plate using a method of multiple scales. Stability analysis of the boundary layer and the entropy layer using this model showed that although the boundary layer was stabilised by bluntness, the inner part of the entropy layer was relatively unstable.

Stetson (1984) conducted hot-wire anemometry surveys at M_∞ = 8.0 of the disturbance structure normal to the surface of a 7° cone with a sharp and a hemi-spherically blunt leading edge with d = 0.76 cm ($Re_{\infty d}$ = 6.25 × 10^4). The latter typically represented a "small" bluntness condition. For small bluntness, the growth of the boundary layer leads to a rapid swallowing of the relatively thin entropy layer (see figure 6-5).

Stetson's tests revealed that well upstream of the entropy layer swallowing point, disturbances present within the boundary layer on a sharp cone were absent from the boundary layer of the cone with small bluntness. For the latter, the surveys revealed large disturbances to be present in the entropy layer. These disturbances were found within the boundary layer downstream of the entropy layer swallowing point after which a rapid transition of the boundary layer was observed.

From these tests, it was concluded that although small bluntness stabilised the boundary layer, the inviscid shear associated with the entropy layer led to a growth of disturbances. These subsequently entered the boundary layer and forced transition.

For small bluntness, an increase in leading edge diameter increases the thickness of the entropy layer. This delays the entry of the disturbances into the boundary layer. Thus, for small bluntness, progressive blunting of the leading edge delays transition of the boundary layer (see figure 5-5).

5.1.2.4 The effect leading edge diameter on transition - Large bluntness

In figure 5-4, the heat transfer measurements of Neal (1966) show that increasing the leading edge diameter from d = 0.25 cm to d = 1.27 cm promotes the onset of transition. This promotion of transition by "large" bluntness has also been observed by Brinich et al (1957), Muir et al. (1972) and by Softley et al (1969). It is a reversal of the delaying effect of "small" bluntness on transition, as discussed in section 5.1.2.3.

In the "small" bluntness tests of Stetson (1984), the relatively thin entropy layer meant that the boundary layer edge Mach number remained close to the freestream hypersonic value of M_∞ = 8.0. Thus the boundary layer remained stable and was only de-stabilised by disturbances from the entropy layer.

However, for large bluntness, the entropy layer is an order of magnitude thicker than the boundary layer and thus envelops the boundary layer. As will be shown in section 6.5, the Mach number at the across an entropy layer in hypersonic flow is reduced from the

hypersonic value at the upper edge of the entropy layer to a supersonic Mach number at the lower limit of the entropy layer.

The disturbances in the entropy layer, together with the destabilising influence of the reduced boundary layer edge Mach number (see figure 5-2) results in a promotion of transition by large bluntness.

The reduced boundary layer edge Mach number also reduces the length of the transition region for large bluntness. This is evident in figure 5-4 for the d = 1.27 cm leading edge configuration. The effect of small and large bluntness on the Reynolds number for the onset transition of planar and axi-symmetric boundary layers is shown in figure 5-5. For both configurations, small bluntness delays transition and large bluntness promotes transition.

The correlation shows that for "small bluntness" condition with a given leading edge diameter under the same local conditions, a planar boundary layer becomes transitional earlier than a conical boundary layer. This effect also appears to hold for the large bluntness condition although given the lack of transition data for planar boundary layers at high $Re_{\infty d}$, the condition requires further verification.

The complex mechanisms associated with the effects of bluntness on transition, together with the lack of blunt flat plate "large" bluntness data makes it difficult to forward definitive quantitative arguments for exact identification of transition. However, it is evident that the unstable nature of the entropy layer is fundamental to the transition of the boundary layer on surfaces submerged either partially or completely within the layer.

5.1.2.5 The effect leading edge shape on transition

The effect of the shape of the leading edge on transition of the boundary layer on a blunted hollow cylinder was studied by Brinich and Sands (1957) at M_∞ = 3.1. The results are shown in figure 5-6. As for the small bluntness case discussed in section 5.1.2.3, an initial increase in $Re_{\infty d}$ stabilises transition for both leading edges. This is due to a downstream movement in the entropy layer swallowing point delaying the entry of disturbances into the boundary layer.

The promotion of transition by the flat leading edge was attributed by Brinich et al (1957) to the shedding of vortices from sharp corners of the leading edge. These vortices increase the disturbances within the entropy layer and hence promote transition for both the small and the large bluntness conditions.

5.2 BOUNDARY LAYER SEPARATION

5.2.1 Introduction

The flow over a hypersonic vehicle separates due to abrupt changes in the local inviscid flow pressure distribution. These changes may be due to gradients in the surface geometry, displacement bodies associated with the ejection of reaction control gases or due to external agencies such as impinging shockwaves.

In all cases, the incident flow is required to tolerate a pressure gradient associated with the flow field modification. Separation occurs when the low momentum fluid contained in the lower portions of the boundary layer is unable to penetrate the external pressure gradient. It results in a considerable modification of the inviscid flow field pressure and heat transfer distributions and thus of the aerothermal loads on the surface.

In the present study of control effectiveness of mechanical flaps on quasi two-dimensional bodies, these controls have been simulated using a full span wedge located at the trailing edge of a low aspect ratio flat plate. The separation and reattachment fronts associated with these separations are quasi two-dimensional and are free to move relative to each other.

For wedge type flows, an adverse pressure gradient is generated by the change in the wall geometry. The interaction between the wall skin friction and the adverse pressure gradient determines whether the flow separates.

5.2.2 Parameters affecting separation

Popinski and Ehrlich (1966) have identified the main factors governing the two-dimensional interaction between a shock wave and a boundary layer to be

a) Mach number
(b) Reynolds number
(c) Overall pressure rise
(d) State of the boundary layer (laminar, transitional or turbulent)

Additional effects which influence the interaction scales for laminar, transitional and turbulent interactions are the wall-to-freestream temperature ratio and the geometrical incidence of the configuration.

The laminar or otherwise state of the boundary layer was also identified by Chapman et al (1958) and by Delery (1986) as one of the fundamental parameters governing the properties and the streamwise extent of the flap interaction region.

The state of the boundary layer produces four distinct classifications of the interaction region according to the location of transition relative to the point of separation. These classifications are

(i)	Pure laminar	A laminar separation with transition occurring well downstream of the interaction region. In these cases, the boundary layer is laminar at separation and reattachment
(ii)	Transitional (Type 1)	Transition beginning between the separation and reattachment point. In these cases, the boundary layer is laminar at separation but reattachment is either transitional or turbulent
(iii)	Transitional (Type 2)	Transition beginning upstream of the separation with fully turbulent conditions developing either downstream of separation or downstream of reattachment
(iv)	Turbulent	Transition being complete and a fully turbulent boundary layer being established from upstream of separation

5.2.3 Incipient separation for laminar interactions

Needham (1966) and Holden (1978) have shown that for low flap deflection angles, the flow remains attached. The flow structure resembles that for inviscid flows with a single flap shock present at the hingeline.

An increase in the flap deflection angle increases the associated pressure gradient and causes the incipient separation condition to be attained. At this condition, the wall skin friction at the hingeline is reduced to zero. Experimental studies by Needham & Stollery (1966) of incipient separation in hypersonic flow has shown that

$$M_\infty \beta_{incip} = 80 \bar{\chi}_{\infty_L}^{1/2} \qquad [5.01]$$

This variation is also given by Hankey and Holden (1975) and by Delery (1986).

Using a triple deck formulation of the incipient separation interaction region, Inger (1993) has extended the incipient separation model to supersonic Mach numbers and gives the incipient separation flap deflection angle as

$$M_\infty \beta_{incip} = k_1 \left[\frac{\sqrt{M_\infty{}^2 - 1}}{M_\infty} C^{*1/2} \chi_{\infty_L} \right]^{1/2} \qquad [5.02]$$

The experiments of Needham (1967) have shown that a reduction in the wall temperature increases the incipient separation flap angle. Inger's formulation suggests that the wall temperature effect is governed by the Chapman-Rubesin constant which is given by

$$C_{ref}{}^{1/4} = \left[0.5 + 0.5 \frac{T_w}{T_\infty} + 0.039 M_\infty{}^2 \right]^{(\varpi - 1)/4} \qquad [5.03]$$

and $0.5 \leq \varpi \leq 0.7$.

Delery (1986), Katzer (1989) and Simeonides (1992) suggest that the flap pressure rise required for incipient separation can be scaled according to the laws of free interaction, that is

$$\frac{p_{incip} - p_1}{q_1} = k_2 \frac{\left(c_{f,1}\right)^{1/2}}{\left(M_1{}^2 - 1\right)^{1/4}} \qquad [5.04]$$

The studies of Simeonides (1992) and of Katzer (1989) suggest that $k_2 = 2.6 \pm 15\%$.

5.2.3.1 The effect of transition on incipient separation

Potter et al (1960) have shown that transition of the flat plate boundary layer is accompanied by an increase in boundary layer thickness. Coles (1953) has shown that the increase in viscous/inviscid interaction due to the thickening of the boundary layer during transition results in an increase in static pressure.

On a laminar configuration with $\beta = \beta_{incip}$, an increase in Reynolds number will promote transition of the flap boundary layer. As a result of the pressure rise associated with transition, this will increase the overall flap pressure rise and hence promote separation.

Further increasing the Reynolds number will promote transition well upstream of the hingeline. The increased energisation of the boundary layer from well ahead of the hingeline will delay separation and hence increase the incipient separation flap deflection angle. These effects are further discussed by Needham (1965) and by Needham and Stollery (1966).

5.2.4 Parameters which affect the scale of the separation interaction region

5.2.4.1 Flap deflection

Miller et al (1964) and Needham (1965) have shown that flap deflection promotes separation and increases the length of the separation interaction region of a laminar boundary layer. Johnson (1970), Simeonides(1992) and Smith (1993) have shown a similar effect for TYPE 1 and TYPE 2 transitional interactions.

Needham & Stollery (1966) suggest that the scale of the separation interaction region is principally determined by the pressure rise associated with the reattachment process. The increase in inviscid flap pressure ratio with flap deflection is responsible for the promotion of separation for both laminar and transitional interactions.

5.2.4.2 Mach number

For fully laminar interactions, experiments by Miller et al (1964), Needham (1965) and by Hankey and Holden (1975) have shown that an increase in Mach number (whilst maintaining a constant flap deflection angle and freestream unit Reynolds number) reduces the separation length.

For TYPE 1 transitional interactions , Kaufman (1966) has shown that the length of the separation interaction region increases with Mach number. This is due to the delay in transition (by the increased Mach number) reducing the energisation of the shear layer by transition.

5.2.4.3 Unit Reynolds number

For fully laminar interactions, Miller et al (1964), Needham et al (1966) and Hankey and Holden (1975) have shown an increase in the length of the separation interaction region with

unit Reynolds number. The Reynolds number influence occurs due to its effect on plateau pressure and hence on the reattachment pressure ratio. An increase in Reynolds number decreases the angle of the separation streamline and hence decreases the plateau pressure. This in turn increases the pressure rise across the reattachment shock and hence promotes separation.

For TYPE 1 transitional interactions as studied by Needham (1965), Johnson (1970), Simeonides (1992) and Smith (1993), an increase in unit Reynolds number promotes early transition and thus decreases the length of the separation region. This is due to the earlier transition of the shear layer increasing the length over which its energised.

For TYPE 2 transitional interactions studied by Johnson (1970), the increased energisation resulting from shear layer transition decreases the length of the interaction region by delaying separation and by promoting the early reattachment of the boundary layer.

5.2.4.4 Incidence

Poisson-Quinton et al (1966) have shown that an increase in incidence of a $\beta = 15°$ control flap configuration from $\alpha = 0°$ to $\alpha = 10°$ delays separation of the boundary layer. This was attributed to the promotion of flat plate transition by incidence resulting from the development of a TYPE 2 transitional interaction structure. The increased energisation of the flat plate boundary layer by transition delayed separation on this configuration.

5.2.4.5 The effect of leading edge bluntness on separation - "Small" bluntness

The effects of leading edge bluntness on boundary layer separation were studied using surface pressure measurements by Sanator et al (1968). Their tests revealed that the introduction of leading edge bluntness to 2D-inlet type flows at $M_\infty = 10.55$ and $Re_\infty/cm = 6.1 \times 10^4$ promoted separation. This promotion of separation was attributed to the reduced boundary layer edge Mach number. In the absence of heat transfer measurements, it is not possible to diagnose the state of the boundary layer as either laminar or turbulent although given the freestream conditions, the boundary layer was probably laminar at separation.

The promotion of separation by leading edge bluntness was also observed by Edwards et al (1968) in low density tests at $M_\infty = 12.5$ and $Re_\infty/cm = 6.2 \times 10^2$. Again the freestream conditions indicate a laminar boundary layer at the hingeline.

Pressure distribution measurements conducted by Vermeulen et al (1992) at M_∞= 6 on a compression corner with a slightly blunt leading edge also showed the promotion of separation due to bluntness. Heat transfer tests on corresponding configurations showed that bluntness decreased the heat transfer rate for some distance downstream of the reattachment compression. This was attributed to an increased resistance to transition in the reattachment region due to bluntness. The measurements on the flat plate upstream of the interaction region correlated with heat transfer predictions for laminar boundary layers.

5.2.4.6 The effect of leading edge bluntness on separation - "Large" bluntness

Pressure measurements conducted upstream of the hingeline by Townsend (1966) on a blunted flat plate / flap configuration (d = 5.0 mm) at M_∞ = 10.0 and $Re_\infty/cm = 5.0 \times 10^4$ showed an appreciable reduction in the extent of the separated flow region when leading edge bluntness was introduced. The state of the boundary layer was diagnosed as being entirely laminar.

In tests at M_∞= 10.0 and $Re_\infty/cm = 8.4 \times 10^4$ on a compression corner, Coet et al (1993) observed a delay in separation due to the introduction of d = 2.5 mm and d = 5.0 mm hemicylindrical leading edge bluntness. Along with a reduction in the extent of the separation region, these tests showed an order of magnitude decrease in the flap heat transfer due to leading edge bluntness. This was attributed by the authors to losses in stagnation pressure sustained at the leading edge.

Measurements on blunt compression corners by Holden (1992) at M_∞= 19 and $\beta = 25.7°$ showed that the extent of the laminar separated region was related to the viscous bluntness interaction parameter, $\chi_\varepsilon/\kappa_\varepsilon^{2/3}$. This effectively accounted for the relative effects of changes in Mach number and Reynolds number on the extent of the interaction.

Holden's results indicate that for $\chi_\varepsilon/\kappa_\varepsilon^{2/3} \leq 0.1$, the introduction of leading edge bluntness results in a dramatic reduction in the extent of boundary layer separation. This is similar to the "large" bluntness condition discussed above. For $0.1 \leq \chi_\varepsilon/\kappa_\varepsilon^{2/3} \leq 0.5$, Holden observed that leading edge bluntness promotes separation. This is typical of the "small" bluntness condition discussed above. Due to the relatively high Mach number and the low freestream unit Reynolds number, it is believed that these tests were entirely laminar.

In summary, bluntness has a dual effect on laminar separation. "Small" bluntness promotes separation of a laminar boundary layer (with respect to equivalent sharp configuration) while "large" bluntness delays separation.

Chapter 6

THEORETICAL STUDY

6.1 EFFECT OF INCIDENCE ON LOCAL BOUNDARY LAYER "EDGE" CONDITIONS ON A SHARP FLAT PLATE

Parametric study of the effects of incidence on compression corner induced interactions requires a understanding of the effect of incidence on the hingeline Mach and Reynolds. In the absence of strong viscous interaction effects, these parameters are dependent on the strength of the leading edge shock. This is a function of the freestream Mach number and the geometrical incidence of the flat plate.

6.1.1 Mach number

For a given incidence, the local Mach number downstream of a shockwave is given by the Ames tables (1953) as

$$M^2 \sin^2(\theta-\alpha) = \frac{(\gamma-1)M_\infty{}^2 \sin^2\theta + 2}{2\gamma M_\infty{}^2 \sin^2\theta - (\gamma-1)} \qquad [6.01]$$

The effect of incidence on the local Mach number is shown in figure 6-1. For a given freestream Mach number, incidence increases the strength of the leading edge shock. This reduces the reservoir pressure (the pressure attained if the flow is reduced isentropically to rest) downstream of the shock and thus decreases the local Mach number. The rate of decrease of the local Mach number with incidence increases with the freestream Mach number. This is due to the increase in reservoir pressure loss sustained at the leading edge.

6.1.2 Unit Reynolds number

The ratio of the local to freestream unit Reynolds number is

$$\frac{Re_e}{Re_\infty} = \left[\frac{\rho_e}{\rho_\infty}\right]\left[\frac{M_e}{M_\infty}\sqrt{\frac{T_e}{T_\infty}}\right]\left[\frac{\mu_\infty}{\mu_e}\right] \qquad [6.02]$$

Assuming a linear viscosity-temperature relationship ($\mu \propto T$) and a perfect gas flow, the unit Reynolds number ratio becomes

$$\frac{Re_e}{Re_\infty} = \frac{p_e M_e}{p_\infty M_\infty}\left[\frac{T_\infty}{T_e}\right]^{3/2} \qquad [6.03]$$

The effect of incidence on the local unit Reynolds number is thus a combination of the effects of incidence on the changes in pressure, temperature and Mach number across the leading edge shock. These changes are a function of the leading edge shock strength.

The pressure and temperature ratio across an oblique shock increase with incidence while the Mach number ratio decreases with incidence. The combination of these competing effects leads to a complex unit Reynolds behaviour with incidence, as shown in figure 6-2.

At low incidences, the increase in pressure dominates and produces an increase in unit Reynolds number. At high incidences, the effects of the heating from the strong leading edge shock dominates and causes a decrease in the unit Reynolds number.

6.2 THE EFFECTS OF PRESSURE ON BOUNDARY LAYER THICKNESS IN COMPRESSIBLE FLOWS

Bertram et al.(1961) give the displacement thickness of a compressible laminar boundary layer in a region of varying pressure gradient as

$$\frac{\delta^*}{x}\sqrt{Re_{\infty x}} \approx 0.865\left[\frac{T_w}{T_r} + 0.38\right](\gamma - 1)M_\infty{}^2\sqrt{\frac{p_\infty}{p_e}} \qquad [6.04]$$

Stollery (1975) gives the ratio of the displacement to boundary layer thickness as

$$\frac{\delta^*}{\delta} = 1 - \frac{n-2}{(1+n)\left[\left\{1+\frac{\gamma-1}{2}M_\infty{}^2\right\}\left\{\frac{T_r}{T_o} + \frac{T_w}{T_o}\left(\frac{n+2}{n}\right)\right\}\right]} \qquad [6.05]$$

where n = 0.5 for laminar and n = 0.2 for turbulent boundary layers. For compression corner configurations, the increase in pressure on the flap compresses and thus reduces the thickness of the local boundary layer. Under hypersonic conditions, this decrease is primarily

due to a compression of the streamtubes in the outer supersonic portion of the boundary layer.

6.3 THE EFFECT OF LEADING EDGE BLUNTNESS ON FLAT PLATE FLOW STRUCTURE

The flow structure over a sharp and a blunt leading edge flat plate is shown in figure 6-3.

For the sharp flat plate at $\alpha = 0°$, the growth of the boundary layer at the leading edge produces a weak leading edge shock. This deflects the flow over the displacement body. The shock causes negligible loss in reservoir pressure. Thus, the boundary layer edge Mach number remains close to freestream values.

For the blunt flat plate at $\alpha = 0°$, streamlines close to the body axis require large deflections. This is achieved by the formation of a strong near normal shock close which decelerates the flow to subsonic speeds, allowing it to negotiate the finite leading edge. Following this, the flow accelerates back to supersonic speeds. Further turning downstream of the sonic line is achieved by Prandtl-Meyer expansion fans. Away from the body axis, the deflection angles required are small. As a result, streamlines in this region of the flowfield are processed by weaker oblique shockwaves.

The variation in the strength of the leading edge shock produces a gradient in reservoir pressure normal to the surface of the body. The boundary layer edge streamlines, having passed through the strong normal shock at the leading edge are subject to the greatest reservoir pressure loss. Away from the body axis, the loss of reservoir pressure is lower due to a decrease in the local shock strength. These variations in reservoir pressure are confined to a region of flow known as the "entropy layer".

In inviscid flows, the lower limit of the entropy layer is defined by the surface streamline whilst in viscous flows, this limit is defined by the upper edge of the boundary layer.

The upper limit of the entropy layer is defined by the streamline at which the normal gradient in reservoir pressure is reduced to zero. In bluntness dominated flows, the reservoir pressure at the lower limit of the entropy layer is equal to that immediately downstream of a normal shock, whilst the reservior pressure at the upper limit of the entropy layer is equal to the reservior pressure in the shock layer over an equivalent sharp leading edge flat plate.

Since streamline curvature within the entropy layer over a flat plate is small. the static pressure gradient normal to the flat plate is negligible. Thus, the variation in reservoir pressure introduced into the inviscid flow field by the leading edge shock generates Mach shear over the flat plate.

6.3.1.1 Boundary layer thickness on blunt flat plates

On blunt flat plates, Creager (1957) and Stone (1969) have found good agreement between laminar boundary layer thickness and the equation

$$\frac{\delta}{d}\sqrt{Re_{\infty d}} = \left[\frac{1.73}{M_\infty{}^2}\left(\frac{T_w}{T_\infty}\right) + 0.332(\gamma - 1) + \frac{4.27}{M_\infty{}^2}\right] M_\infty{}^2 \sqrt{C_w}\sqrt{\frac{x}{d}} \qquad [6.06]$$

The data was in the blast analogy parameter range $0.04 \leq \xi \leq 4.95$. This correlation also shows that the boundary layer thickness is independent of the leading edge diameter.

6.3.1.2 Entropy layer swallowing

The thickness of the entropy layer is a function of the curvature of the leading edge shock and hence of the leading edge diameter. The effects of bluntness are limited to the point at which the entropy layer is swallowed by the boundary layer.

Small bluntness : For small bluntness, the thickness of the entropy layer is small $\delta_{EN} = o(\delta)$. Thus the streamline at the upper edge of the entropy layer is rapidly swallowed by the boundary layer, as shown in figure 6-5(a). Upstream of the entropy layer swallowing point, the reservior pressure gradient within the entropy layer generates an axial variation in the boundary layer edge Mach number. Downstream of the swallowing point, the reservior pressure gradients outside the boundary layer disappear and the Mach number profile returns to that on a sharp flat plate.

Moderate bluntness : An increase in leading edge diameter produces an entropy layer whose thickness is of the order of that of the boundary layer $\delta_{EN} = O(\delta)$. Although the thicker entropy layer envelops the boundary layer, as shown in figure 6-5 (b), the growth of the boundary layer swallows streamlines in the lower portion of the entropy layer. The swallowing causes considerable variations in the boundary layer edge conditions along the plate.

Large bluntness : Further increasing the leading edge diameter increases the thickness of the entropy layer such that $\delta_{EN} \gg \delta$. This results in the boundary layer edge conditions being characterised by the supersonic low Mach number conditions in the lower portion of the entropy layer, as shown in figure 6-5(c). The large thickness of the entropy layer means that the boundary layer is unable to swallow any significant portion of the entropy layer. Thus the boundary layer edge Mach number remains well below the freestream value along the length of the flat plate.

The three degrees of bluntness cause considerable changes in the inviscid flow reservoir pressure profile over a flat plate. This is shown in figure 6-4. An initial increase from the small (sharp) to moderate (d = 0.16 cm) bluntness increases the leading edge shock strength close to the body axis. This creates a thin entropy layer across which reservoir pressure properties change rapidly from the blunt level at the edge of the boundary layer to the sharp level. Further increases in leading edge diameter considerably thickens the entropy layer, reducing the reservoir pressure at the edge of the boundary layer well below the sharp flat plate level.

6.4 THE EFFECTS OF BLUNTNESS ON FLAT PLATE PRESSURE DISTRIBUTION

6.4.1 Blast wave analogy

The blast wave analogy of hypersonic flow over blunt bodies is based on the hypersonic equivalence principle. This states that "the steady hypersonic flow over a slender body is equivalent to an unsteady flow in one less space dimension."

On this basis, the steady physical effects of the blunt leading edge in the x-y plane are considered to be analogous to the unsteady effects in the y-t plane associated with the propagation of a blast wave, as shown in figure 6-6.

6.4.2 Blast wave theory (inviscid flows)

6.4.2.1 First order blast analogy

By equating the work done by a blunt leading edge to the energy released by a blast, Anderson (1989) has shown the pressure distribution on a blunt flat plate varies as

$$\frac{p_e}{p_\infty} = C_1 \frac{M_\infty{}^2 C_{DN}{}^{2/3}}{(x/d)^{2/3}} = \frac{C_1}{\xi} \qquad [6.07]$$

where ξ is the blast analogy parameter and C_{DN} is the nose drag coefficient. The constant of proportionality C_1 found by a number of studies is given in table 6.1.

Anderson (1989)	$C_1 = 0.127$
Lukasiewicz (1961)	$C_1 = 0.121$
Cheng et al. (1956)	$C_1 = 0.112$

Table 6.1 Empirical constants for the distribution of pressure over a blunt flat plate hypersonic flow blast analogy

Although the first-order analogy provides good agreement with experimental pressure measurements in the bluntness dominated region, it breaks down in the limit $x \rightarrow \infty$ where the predicted pressure level $p/p_\infty = 0$ is below the inviscid flat plate value. Blast wave theory also becomes invalid at $x = 0$ where it predicts an infinite pressure ratio. In the actual flow, the pressure ratio at $x = 0$ is the normal shock value.

6.4.2.2 Second-order blast analogy

Lukasiewicz (1961) and Bertram (1960) found that experimental pressure measurements in the range $0.001 \leq \xi \leq 1$ correlated well with a modified form of the blast analogy relationship. These empirical correlation give the pressure distribution as

$$\frac{p_e}{p_\infty} = \frac{C_1}{\xi} + C_2 \qquad [6.08]$$

The best agreement was for $C_2 = 0.735$. Although the second order analogy improves the solution, it fails to predict the pressure in the limit $x \rightarrow \infty$ where it predicts $p/p_\infty < 1$. The breakdown of the solution in the limit is due to the limited range of the blast analogy parameter over which the data was acquired.

6.4.2.3 Quasi-similarity blast analogy

In order to satisfy the condition in the limit $x \rightarrow \infty$, a further refinement of the blast analogy solution was proposed by Lewis (1961). This considers the hypersonic equivalence principle

to be applicable in the vicinity of the shockwave only with the flow relaxing asymptotically to the freestream pressure at a large distance from the leading edge. The modified blast wave pressure distribution given by Lewis (1961) is

$$\frac{p_e}{p_\infty} = 0.12003 \cdot \exp[\eta] / \xi^{0.98152} \qquad [6.09]$$

where

$$\eta = \frac{2.1595 + 2.26 \log_{10} \xi}{1 - \exp[-5.404(\log_{10} \xi + 0.955551)]} \qquad [6.10]$$

Numerical investigation of the behaviour of equation 6.10 shows that in the bluntness dominated regime close to the leading edge, as $\xi \rightarrow 0$ so $\eta \rightarrow 0$. Thus the pressure distribution close to the leading edge is equal to that given by first-order blast analogy (given in equation 6.07). Away from the bluntness dominated regime, $p/p_\infty \rightarrow 1$ as $x \rightarrow \infty$. This is the correct inviscid pressure level on a flat plate in inviscid flow.

6.4.3 The effect of weak viscous interaction on blunt flat plate pressure distribution

In region of strong viscous interaction, Stollery (1970) has shown that the growth of a laminar boundary layer on a sharp flat plate severely distorts the external flowfield and produces a significant increase in pressure above the inviscid flat plate value.

The pressure distribution over a blunt flat plate ($\alpha = 0°$) in viscous hypersonic flow is a combination of the inviscid blast effect associated with the leading edge and the viscous interaction effect associated with the growth of the boundary layer. Creager (1957) suggests that the viscous interaction effect on pressure distributions is superimposed upon the variations induced by the blast effect of the leading edge shock. This gives

$$\frac{p}{p_\infty} = 1 + C_3 \bar{\chi} + \frac{C_4}{\xi} \qquad [6.11]$$

where

$$C_3 = \gamma \left[\frac{0.865}{M_\infty{}^2} \left(\frac{T_w}{T_\infty} \right) + 0.166(\gamma - 1) \right] \qquad [6.12]$$

and $C_4 = 0.112$ (as in first order blast wave theory). In this, the term $[1 + C_3 \chi_{ex}]$ accounts for the effect of weak viscous interaction whilst term C_4/ξ accounts for effect of the inviscid blast effects associated with the leading edge.

6.4.4 Comparison of the predictions of blast wave theory with experimental measurements

The theoretical pressure distributions the various approximations of inviscid blast wave theory are compared with experimental measurements from the present study in figure 6-7. The agreement the measured experimental distributions and the theoretical predictions of first order blast wave theory suggests that the flow over entire the length of the model is dominated by the blast effect of the leading edge shock.

In the present study, the viscous interaction parameter $\chi_{\infty X}$ at x/d = 10 is 0.75. This is in the weak interaction category. Due to the limited effects of viscous interaction under the present test conditions, the pressure distribution is adequately predicted by blast wave theory (inviscid).

6.5 THE EFFECTS OF BLUNTNESS ON FLAT PLATE MACH NUMBER

6.5.1 Flat plate at zero incidence ($\alpha = 0°$)

For a blunt body with large bluntness, the boundary layer edge streamtube is processed by the strong near normal portion of the leading edge shockwave (see figure 6-3). This reduces the reservoir pressure at the edge of the boundary layer edge to that downstream of a normal shock.

From the Ames tables (1953), the reservoir pressure downstream of a normal shock is given by the Rayleigh-pitot relationship as

$$\frac{P_{o1}}{p_\infty} = \left[\frac{(\gamma+1)M_\infty{}^2}{2}\right]^{\frac{\gamma}{\gamma-1}} \left[\frac{\gamma+1}{2\gamma M_\infty{}^2-(\gamma-1)}\right]^{\frac{1}{\gamma-1}} \qquad [6.13]$$

Assuming the flow at the edge of the boundary layer to be isentropic, the boundary layer edge Mach number is

$$M_e = \sqrt{\left(\frac{2}{\gamma-1}\right)\cdot\left[\left(\frac{P_{o1}}{p_\infty}\cdot\frac{p_\infty}{p_1}\right)^{\frac{\gamma-1}{\gamma}}-1\right]} \qquad [6.14]$$

Substitution of the reservoir pressure relationship given by equation 6.13 together with the quasi-similarity blast wave pressure distribution of equation 6.09 gives the local Mach number as

$$M_e = \left(\frac{2}{\gamma-1}\right)^{1/2} \cdot \left[\left(\left[\frac{(\gamma+1)M_\infty{}^2}{2}\right]^{\frac{\gamma}{\gamma-1}}\left[\frac{\gamma+1}{2\gamma M_\infty{}^2-(\gamma-1)}\right]^{\frac{1}{\gamma-1}} \cdot \frac{\xi^{0.98152}}{0.12003} \cdot \frac{1}{\exp(\eta)}\right)^{\frac{\gamma-1}{\gamma}} - 1\right]^{1/2} \quad [6.15]$$

6.5.1.1 Surface Mach number in bluntness dominated regions of hypersonic flows

In the hypersonic Mach number domain with $M_\infty \geq 4$, it may be assumed that $2\gamma M_\infty{}^2 \gg (\gamma - 1)$. Substitution of this condition into equation 6.13 yields the approximated hypersonic flow reservoir pressure relationship

$$\frac{P_{01}}{p_\infty} = \left(\frac{1}{\gamma}\right)^{\frac{1}{\gamma-1}}\left(\frac{\gamma+1}{2}\right)^{\frac{\gamma+1}{\gamma-1}} M_\infty{}^2 \quad [6.16]$$

Substitution of this together with the quasi-similarity blast wave approximation of equation 6.09 into the isentropic Mach number relationship of equation 6.14 gives the boundary layer edge Mach number in hypersonic bluntness dominated flows as

$$M_e = \left(\frac{2}{\gamma-1}\right)^{1/2} \cdot \left[\left(\left(\frac{1}{\gamma}\right)^{\frac{1}{(\gamma-1)}}\left(\frac{\gamma+1}{2}\right)^{\frac{\gamma+1}{\gamma-1}} M_\infty{}^2 \cdot \frac{(x/dC_D)^{2/3}}{0.12M_\infty{}^2} \cdot \frac{1}{\exp(\eta)}\right)^{\frac{\gamma-1}{\gamma}} - 1\right]^{1/2} \quad [6.17]$$

In bluntness dominated regions very close to the leading edge, $\eta \rightarrow 0$ as $\xi \rightarrow 0$ (see section 6.4.2.3). This gives the boundary layer edge Mach number as

$$M_e = \left(\frac{2}{\gamma-1}\right)^{1/2} \cdot \left[\left(\left(\frac{1}{\gamma}\right)^{\frac{1}{(\gamma-1)}}\left(\frac{\gamma+1}{2}\right)^{\frac{\gamma+1}{\gamma-1}} \cdot \frac{(x/dC_D)^{2/3}}{0.12003}\right)^{\frac{\gamma-1}{\gamma}} - 1\right]^{1/2} \quad [6.18]$$

Thus, under hypersonic freestream conditions in regions dominated by the inviscid effects of leading edge bluntness, the local boundary layer edge Mach number is independent of the freestream Mach number.

Under these conditions, the local Mach number is a function of

$$M_e = f_1[x, C_{DN}, d, \gamma] \qquad [6.19]$$

The exact and approximate boundary layer edge Mach number solutions as given by equations 6.15 and 6.18 respectively are shown in figure 6-8.

Close to the leading edge, the surface Mach distribution is independent of the freestream Mach number. This is because the increased reservoir pressure loss across the normal shock is compensated for by an increase in the local static pressure due to the blast effect of the leading edge shock.

6.5.1.2 Comparison of theoretical predictions with experimental measurements of the surface Mach number on blunt plates

A number of studies have measured the pitot pressure distribution across the entropy layer on blunt flat plates in hypersonic flows. The pitot pressure distributions of Stone (1969) on a blunt flat plate with various leading edges at $M_\infty = 10.4$ are shown in figure 6-4. Similar tests were conducted by Creager (1957) at $M_\infty = 3.95$ and by Deveikis et al. (1973) at $M_\infty = 7.0$. The experimental set-up employed for these studies and is shown schematically in diagram 6-1.

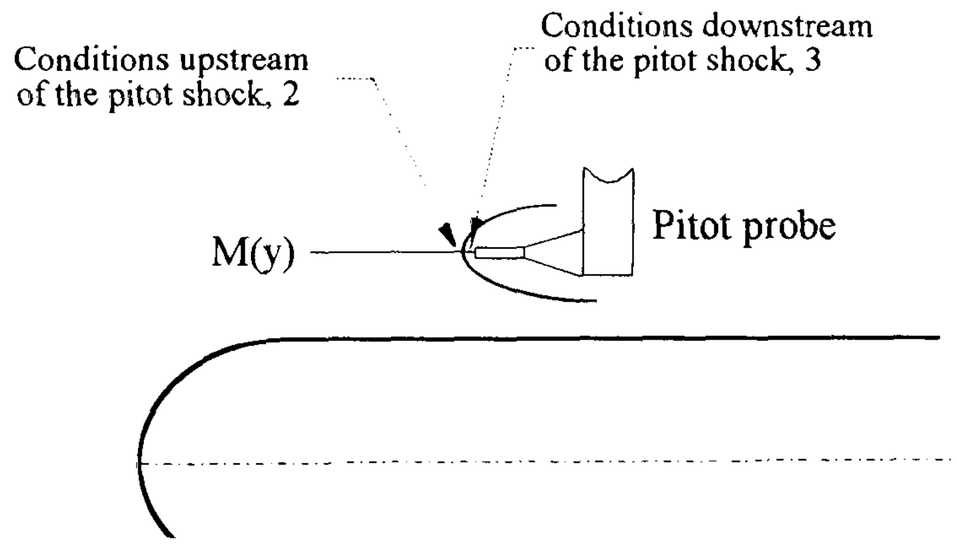

Diagram 6-1 Experimental set-up employed to study entropy layer reservoir pressure distributions - Creager (1957), Stone (1969) and Deveikis (1973)

The results given by Stone (1969) are in the form P_{o3}/p_2. The static pressure p_2 was measured at the wall. Assuming the local streamline curvature in the entropy layer to be small, the pressure gradient in the entropy layer is negligible.

The local Mach number M(y) immediately upstream of the pitot shock was thus evaluated from the local Rayleigh-pitot relationship

$$\frac{P_{o3}(y)}{p_2} = \left[\frac{(\gamma+1)M(y)^2}{2}\right]^{\frac{\gamma}{\gamma-1}} \left[\frac{\gamma+1}{2\gamma M(y)^2-(\gamma-1)}\right]^{\frac{1}{\gamma-1}} \qquad [6.20]$$

The results of Creager (1957) are in the form P_{o3}/P_{o2}. This can be re-written as

$$\frac{P_{o3}(y)}{P_{o2}(y)} = \frac{P_{o3}(y)}{p_2} \cdot \frac{p_2}{P_{o2}(y)} \qquad [6.21]$$

Assuming the flow immediately upstream of the pitot shock to be isentropic, equation 6.21 can be expanded using the Rayleigh-pitot reservoir pressure relation (equation 6.20) and the isentropic pressure relationship to give

$$\frac{P_{o3}(y)}{P_{o2}(y)} = \left[\frac{(\gamma+1)M(y)^2}{2}\right]^{\frac{\gamma}{\gamma-1}} \left[\frac{\gamma+1}{2\gamma M(y)^2-(\gamma-1)}\right]^{\frac{1}{\gamma-1}} \left[1+\frac{\gamma-1}{2}M(y)^2\right]^{\frac{\gamma-1}{\gamma}} \qquad [6.22]$$

The pitot pressure measurements of Creager (1957) were converted into corresponding Mach numbers by a Newton-Rhapson solution of equation 6.22.

In figure 6-8, the inferred boundary layer edge Mach number from these measurements are compared with predictions from equations 6.15 and 6.18. The agreement between the experimentally inferred surface Mach number and the theoretical predictions allows the conclusion that the reservoir pressure at the edge of the boundary layer in bluntness dominated flows is well approximated by the reservoir pressure downstream of a normal shock.

6.5.2 Theoretical prediction of the surface Mach number on blunt flat plates at incidence ($\alpha > 0°$)

Cheng et al (1961) have shown that the shock structure close to the axis of a blunt flat plate at incidence $\alpha > 0°$ is determined by the shape of the leading edge.

As with the zero incidence case, the surface streamtubes on a blunt flat plate at incidence $\alpha > 0°$ are processed by a normal shock. Therefore, the reservoir pressure within these streamtubes can be approximated to that immediately downstream of a normal shock. This is given in equation 6.13.

Bade (1975) gives the local pressure ratio on a blunt flat plate at incidence as

$$\frac{p_1}{p_\infty} = \frac{(\gamma+1)\gamma M_\infty{}^2\alpha^2}{2}\left[1+\frac{0.382}{\alpha^2}\left(\frac{2\varepsilon C_D d}{(\gamma+1)x}\right)^{2/3}\right] \qquad [6.23]$$

As is shown by figure 8-46, this equation provides a satisfactory approximation to the pressure distribution on a blunt flat plate at incidence.

The Mach number distribution on a blunt flat plate at incidence is thus determined by substituting from equation 6.13 and equation 6.23 into the Mach number relationship of equation 6.14.

6.6 ENTROPY LAYER MACH NUMBER PROFILE ($\alpha = 0°$)

As was described in section 6.3, the curvature of the leading edge shockwave associated with a blunt body generates Mach shear over the flat plate. This shear is most noticeable in the entropy layer.

Entropy layer Mach shear profiles derived from the pitot measurements of Creager (1957) and Stone (1969) are shown in figure 6-9. These profiles were derived from pitot pressure profiles using the methods described in section 6.5.1.2.

The Mach number profile is a direct function of the shape of the leading edge shock. The similarity in the shape of the leading edge shock produces a qualitative similarity of the Mach number profiles. The quantitative variations in the profiles are due to different freestream Mach numbers and axial locations.

6.6.1 Parameters affecting the Mach profile in the entropy layer

A model for the flow over a blunt flat plate is shown in diagram 6-2. The leading edge curved shock is approximated by a series of straight line segments. The shape of the curved leading edge shock on a blunt flat plate is given by blast wave theory (Anderson, 1989) as

$$\frac{Y_s}{d} = 0.774 C_D{}^{1/3}\left(\frac{x}{d}\right)^{2/3} \qquad [6.24]$$

Differentiating equation 6.24 with respect to x, the shock angle at a given height $y = Y_s$ is

$$\left[\tan\theta_s\right]_{y=Y_s} = \left[\frac{dY_s}{dx}\right]_{y=Y_s} = 0.516\left(\frac{C_D}{x/d}\right)^{1/3} \qquad [6.25]$$

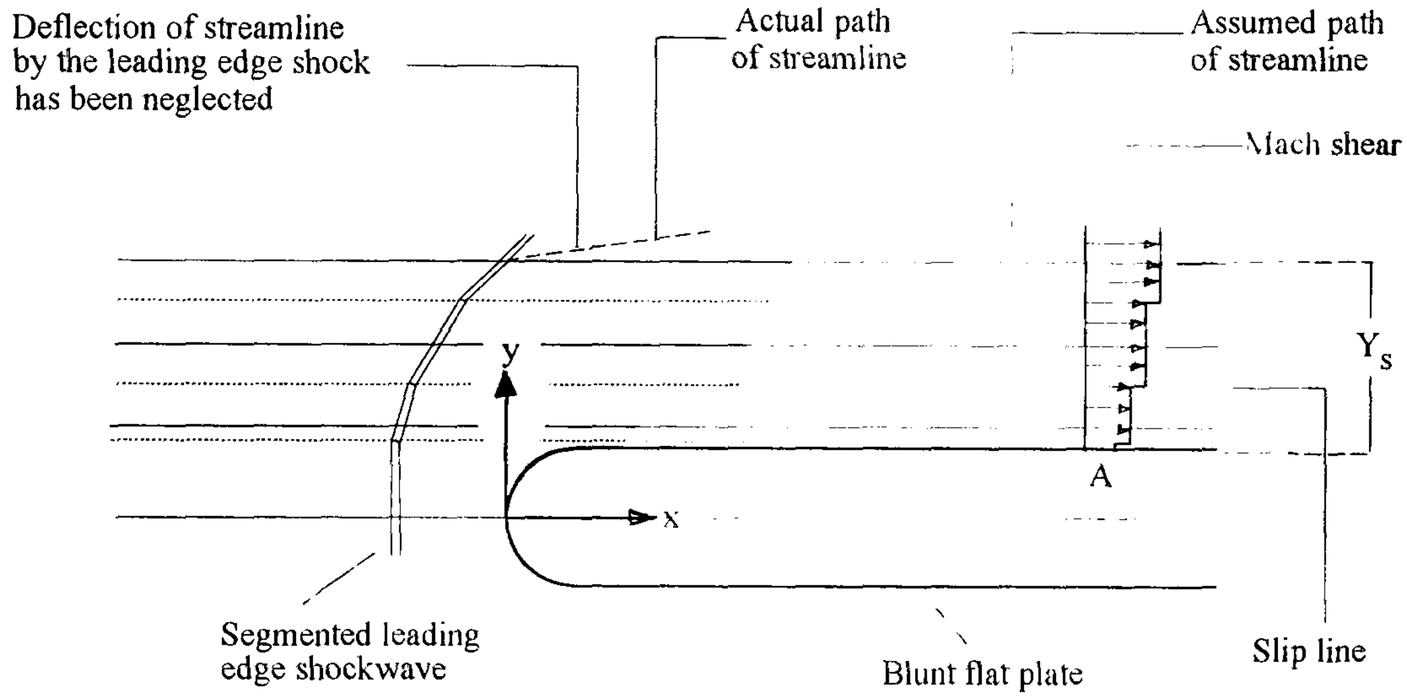

Diagram 6-2 Model of the flow structure in the entropy layer over a blunt flat plate

Substitution for x from equation 6.24 into equation 6.25 gives

$$\left[\tan\theta_s\right]_{y=Y_s} = 0.45\left(\frac{dC_D}{Y_s}\right)^{1/2} \qquad [6.26]$$

The reservoir pressure downstream of an oblique shock (for $\gamma = 1.4$) is given by the Ames tables (1953) as

$$\left[\frac{P_{o1}}{p_\infty}\right]_{y=Y_s} = \left(\frac{6}{7M_\infty{}^2\sin^2\theta_s - 1}\right)^{5/2}\left(\frac{6M_\infty{}^2\sin^2\theta_s(M_\infty+5)}{5(M_\infty{}^2\sin^2\theta_s+5)}\right)^{7/2} \qquad [6.27]$$

Since the flow downstream of the shock segment is isentropic, the reservoir pressure along the streamline passing through the shock facet remains constant. Therefore, the reservoir pressure distribution within the entropy layer (neglecting the deflection of the streamline due to the leading edge shock) is given by

$$\left[\frac{P_{o1}}{p_\infty}\right]_{y=Y_s} = f(Y_s) \qquad [6.28]$$

From the isentropic flow relations, the local Mach number on a streamline is a function of the local reservoir and static pressures. Since the axial static pressure distribution is a function of the blast analogy parameter, the Mach number profile in the entropy layer associated with a blunt leading edge is thus given by

$$M_e = f[M_\infty, C_D, Y_s, \xi, \gamma] \qquad [6.29]$$

A correlation of the entropy layer Mach number profiles, derived from the pitot pressure measurements of Deveikis (1973) and of Stone (1969) is shown in figure 6-10. The correlation between these profiles confirms the hypothesis that the Mach number distribution in the entropy layer is a direct function of the shape of the leading edge shock. However, given the limited data sources, the correlation is only applicable in the range $7 \leq M_\infty \leq 10.4$.

6.6.2 The effect of entropy layer Mach shear on surface pressure distribution

Hayes and Probstein (1959) have shown that the interaction of an incident compression wave or a shock with a region of Mach shear produces a series of transmitted and reflected waves, as shown in diagram 6-3.

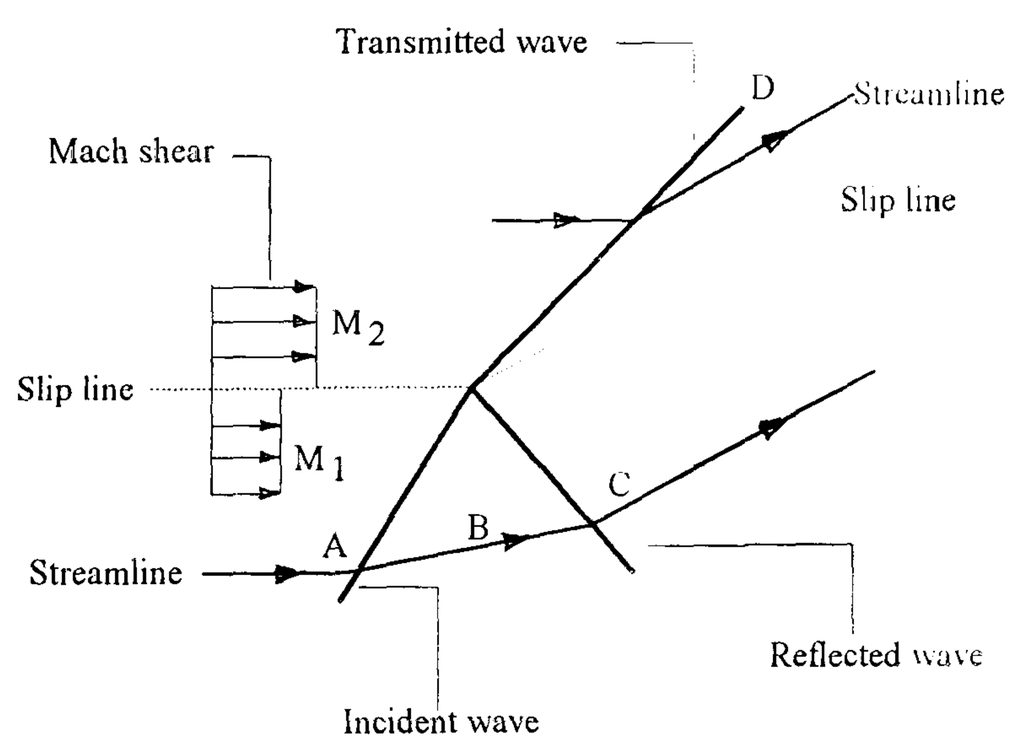

Diagram 6-3 Interaction between an incident wave and a Mach shear

Using an argument based on the method of characteristics with the pressure and deflection either side of the slip line assumed to be constant, they showed that the pressure rise across the reflected wave to that across the incident wave was

$$\Re_{\upsilon} = \frac{p_C - p_B}{p_B - p_A} = \frac{\Gamma_2 - \Gamma_1}{\Gamma_2 + \Gamma_1} \qquad [6.30]$$

where the Mach number coefficient Γ is defined as

$$\Gamma = \frac{\gamma_e M_e^{\,2}}{\sqrt{M_e^{\,2} - 1}} \qquad [6.31]$$

The effect of the strength of the Mach shear on the coefficient $\Re_{\upsilon}$ is shown in diagram 6-4.

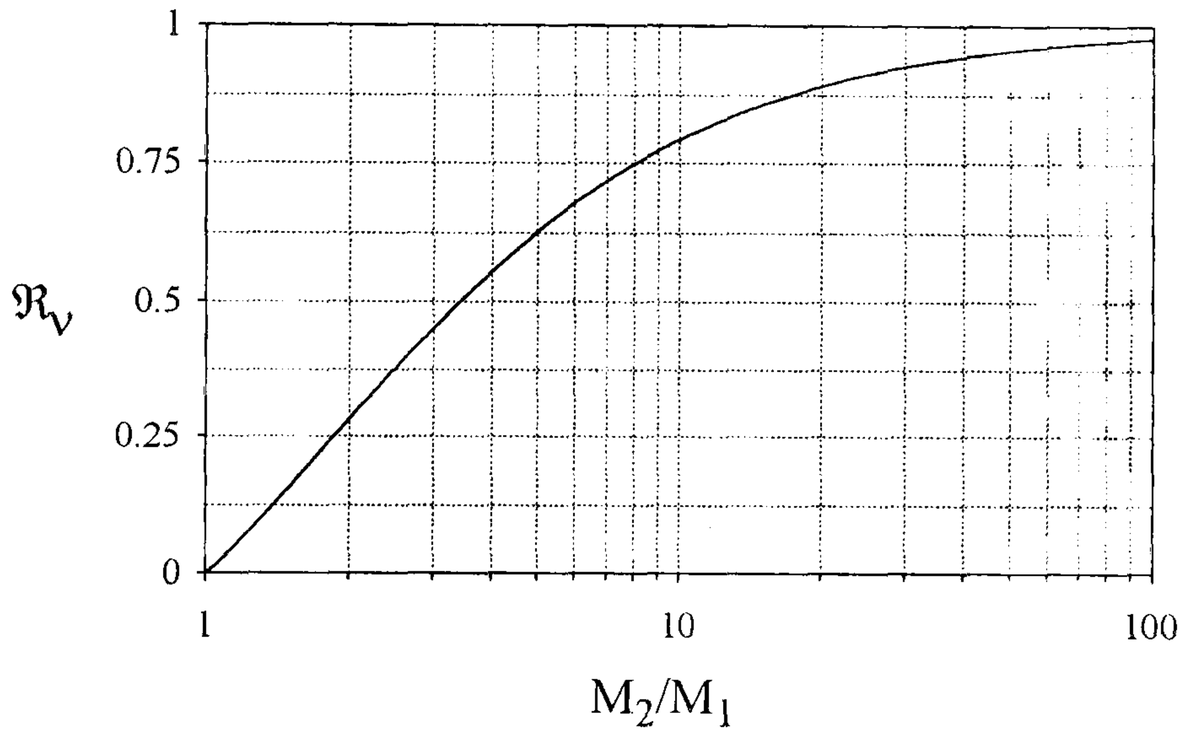

Diagram 6-4 Variation of Reflection coefficient $\Re_{\upsilon}$ with Mach shear

For a weak shear layer, $M_2 \rightarrow M_1$, $\Re_v \rightarrow 0$ so the strength of the reflected shock is negligible. However, for a strong shear layer, $M_2 \gg M_1$ so $\Re_v \rightarrow 1$. For a shear layer characterised by high Mach number gradients, the pressure rise across the reflected wave is equal to the pressure rise across the incident wave.

6.6.2.1 Model of the entropy layer Mach shear effect

For a blunt leading edge the finite strength of the Mach shear in the entropy layer and its interaction with a flap generated shock will produce reflected and transmitted waves. The reflected waves will increase the pressure above the level immediately downstream of the flap shock. The effect is discussed by Bird (1963).

The entropy layer Mach number profile can be determined from a characteristics solution involving the streamline deflection at the leading edge shock followed by its interaction with

the expansion fan generated by the curvature of the leading edge. Using this Mach shear profile, a characteristics solution (based on the Hayes and Probstein model of reflected and transmitted waves) can be affected at the hingeline to calculate the effects of Mach shear interaction on the flap pressure distribution.

The inherent complexities of a multiple characteristic solution make such an approach computationally intensive. A simpler model for estimating the effects of an interaction between a shear layer and a shock was proposed by Elfstrom (1972) and is shown in diagram 6-5.

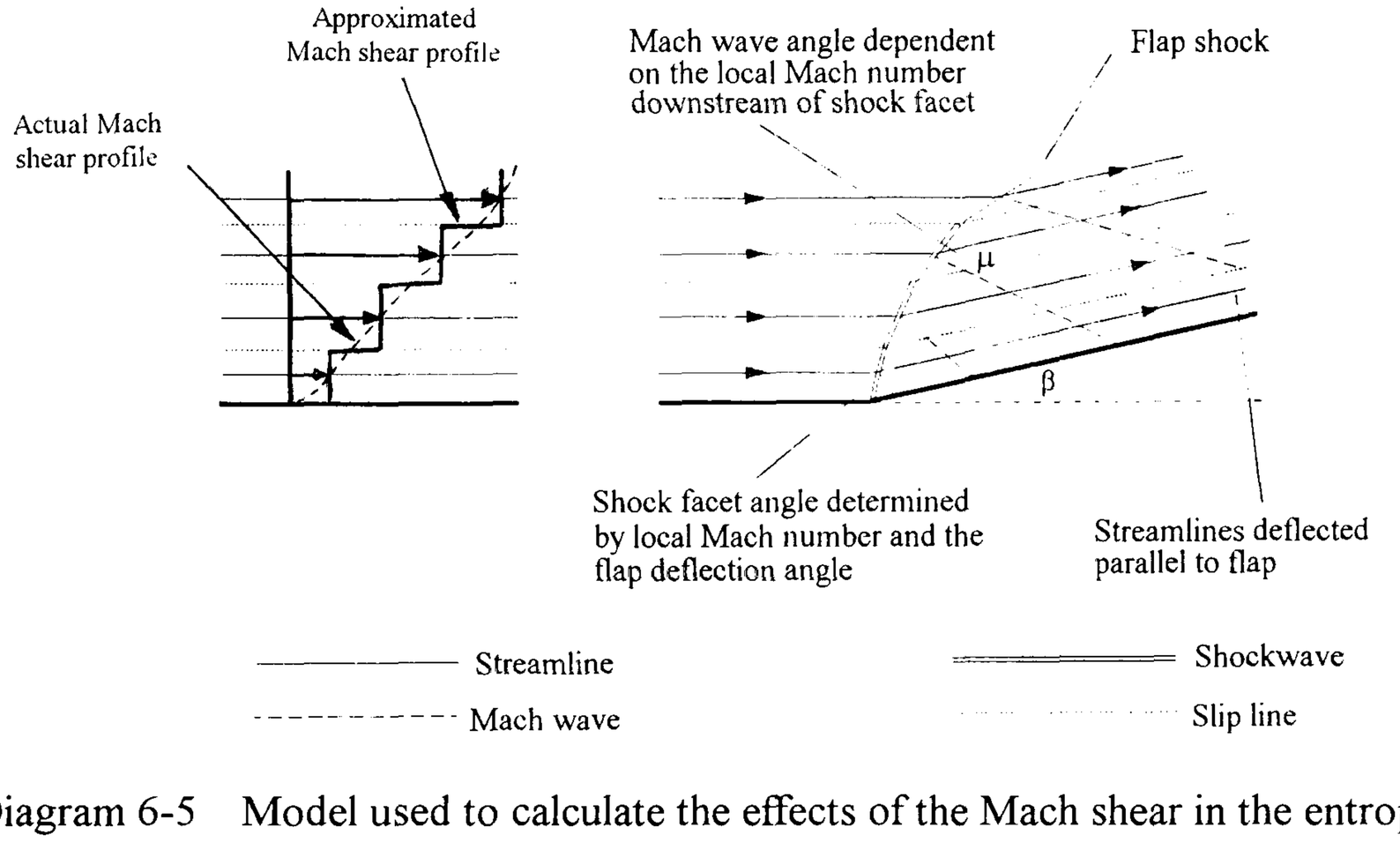

Diagram 6-5 Model used to calculate the effects of the Mach shear in the entropy layer on the flap pressure distribution

The model considers the hingeline shock to be segmented in accordance with the entropy layer Mach number profile. The shock is assumed to turn the streamlines parallel to the flap to satisfy the no flow boundary condition on the surface.

The angle of the shock segment is dependent on the local Mach number (within the entropy layer Mach number profile) and on the required streamline deflection. It is assumed that the pressure immediately downstream of the shock segment is communicated to the flap surface by Mach waves. The angle of these waves depends on the local Mach number immediately downstream of the shock segment.

This model was used to make estimates of the pressure distribution on the control flap of the present blunt configuration. The results are discussed in section 8.15.

6.7 SKIN FRICTION & HEAT TRANSFER IN COMPRESSIBLE FLOWS

6.7.1 The concept of a reference temperature

The concept of a reference temperature was proposed by Eckert (1955) to allow analysis of high speed compressible flows using solutions obtained for low speed flows. It considers the effect temperature variations in a compressible boundary layer to be equivalent to that of an average "reference" temperature. This reference temperature is given by Eckert (1955) as

$$T^* = T_e + 0.5(T_w - T_e) + 0.22 r T_e \left(\frac{\gamma - 1}{2}\right) M_e{}^2 \qquad [6.32]$$

6.7.2 Flat plate skin friction and heat transfer in compressible flows

From boundary layer theory, the classic expression for the local skin-friction coefficient for incompressible flow over a flat plate is of the form

$$\frac{c_f}{2} = \frac{A}{Re^n} \qquad [6.33]$$

where A = 0.332, n = 0.5 for laminar boundary layers and A = 0.0296 and n = 0.2 for turbulent boundary layers. Generalising the incompressible solution to reference temperature conditions gives

$$\tau_w = c_{f_e} \cdot \frac{\rho_e u_e{}^2}{2} = A \rho^* u_e{}^2 \left[\frac{\mu^*}{\rho^* u_e x}\right]^n \qquad [6.34]$$

Assuming constant pressure and a linear viscosity-temperature relationship, this can be simplified to

$$\frac{c_{f_e}}{2} = A \left(\frac{T_e}{T^*}\right)^{(1-2n)} \left[\frac{1}{Re_{ex}}\right]^n \qquad [6.35]$$

Referencing the coefficient to freestream conditions gives the skin friction coefficient distribution for laminar and turbulent boundary layers as

$$\frac{c_{f\infty}}{2} = \frac{A}{Re_{\infty x}{}^n} \left[\frac{p_e}{p_\infty}\right]^{(1-n)} \left[\frac{u_e}{u_\infty}\right]^{(2-n)} \left(\frac{T_e}{T^*}\right)^{(1-2n)} \qquad [6.36]$$

where the skin-friction coefficient $c_{f\infty}$ is defined as

$$c_{f\infty} = \frac{\tau_w}{\frac{1}{2}\rho_\infty u_\infty{}^2} \qquad [6.37]$$

A full derivation of equation 6.36 is given in Appendix 1.

From Reynolds analogy, the local heat transfer is a direct function of the local skin-friction distribution. Using this analogy with the local skin friction coefficient c_{fe} gives the heat transfer coefficient as

$$C_{H\infty}(Re_{\infty x})^n = \frac{2A}{s}\left(\frac{p_e u_e}{p_\infty u_\infty}\right)^{(1-n)}\left(\frac{T_\infty}{T^*}\right)^{(1-2n)}\left[\frac{T_r - T_w}{T_o - T_w}\right] \qquad [6.38]$$

The heat transfer coefficient $C_{H\infty}$ given in equation 6.38 is defined as

$$C_{H\infty} = q/\left[\rho_\infty u_\infty c_p (T_o - T_w)\right] \qquad [6.39]$$

A full derivation of equation 6.38 is given in Appendix 2. For laminar boundary layers, $s = Pr^{2/3}$ and for turbulent boundary layers, $s = 1$.

6.7.3 Local Similarity

The concept of local similarity suggests that axial variation of surface flow properties of skin-friction and heat transfer exhibited by the boundary layer will be as that exhibited on a flat plate provided the velocity profiles are similar. In a region characterised by an axial pressure gradient, the local velocity profiles are no longer similar. Thus, the loss of similarity of the velocity profile in regions characterised by an axial pressure gradient invalidates the local similarity concept.

6.7.4 The effect of incidence on flat plate heat transfer

In regions characterised by weak viscous interaction, incidence increases the boundary layer edge pressure. However, since the axial pressure gradient on the flat plate remains zero, the boundary layer velocity profiles on the flat plate at incidence exhibit local similarity. The effect of incidence (and the associated changes in boundary layer edge properties) on the flat

plate heat transfer can be evaluated using the reference temperature concept evaluated at the local boundary layer edge conditions.

The effect of incidence on the local pressure and velocity ratio can be evaluated from the oblique shock relations. These are given by the Ames tables (1953) as

$$\frac{p_e}{p_\infty} = \frac{2\gamma M_\infty{}^2 \sin^2\theta - (\gamma - 1)}{\gamma + 1} \qquad [6.40]$$

$$\frac{u_e}{u_\infty} = \left[1 - 4\frac{\left(M_\infty{}^2 \sin^2\theta - 1\right)\left(\gamma M_\infty{}^2 \sin^2\theta + 1\right)}{(\gamma+1)^2 M_\infty{}^4 \sin^2\theta}\right]^{1/2} \qquad [6.41]$$

Local temperature changes due to incidence manifest indirectly on the heat transfer through the reference temperature. Eckert's reference temperature, as given by equation 6.32 may be expressed as

$$\frac{T^*}{T_\infty} = \frac{T_e}{T_\infty}\left[1 + 0.5\left(\frac{T_w}{T_\infty}\frac{T_\infty}{T_e} - 1\right) + 0.22r\left(\frac{\gamma-1}{2}\right)M_e{}^2\right] \qquad [6.42]$$

The local temperature ratio T_e/T_∞ and the local Mach number M_e are direct functions of incidence, and given by the oblique shock relations of the Ames tables (1953).

6.8 THE EFFECT OF AN AXIAL PRESSURE GRADIENT ON HEAT TRANSFER

6.8.1 Attached laminar flow

In the presence of a region of flow characterised by an axial pressure gradient, the local velocity profiles in a laminar boundary layer lose local similarity with that on corresponding flat plates (see figure 6-11). The loss of similarity occurs due to the adverse pressure gradient producing a loss of momentum in the sublayer.

The loss of momentum decreases the skin friction in a region of increasing pressure. This is contradictory to the behaviour of flat plate boundary layers which show an increase in skin-

friction with increased compression. The contradiction occurs due to the loss of similarity of velocity profiles in the interaction region.

The "regeneration" of the velocity profile by the shock compression process means that the local similarity condition is again satisfied. Thus, the skin-friction distribution exhibits similarity with that on a flat plate under equivalent boundary layer edge conditions.

6.8.2 Attached turbulent flow

Pressure and skin-friction measurements on a attached turbulent boundary layer in a region of variable axial pressure gradient were conducted by Gran et al (1972) at $M_\infty = 4.0$. The results are shown in figure 6-12.

The predicted skin friction levels are based on the turbulent form of the reference temperature skin friction distribution (equation 6.36). The experimental pressure ratios were used for the theoretical calculation.

Velocity profiles in the boundary layer given by Gran et al (1974) show that the adverse pressure gradient has little effect on the velocity profile in the interaction region. The similarity led the authors to conclude that in regions of zero and adverse pressure gradients, turbulent boundary layers are insensitive to the upstream history and maintain local similarity with flat plate profiles.

Thus, for turbulent interactions, local similarity is maintained through an interaction region due to the greater resistance of turbulent boundary layers to adverse pressure gradients.

6.9 ESTIMATION OF FLAP HEAT TRANSFER ON CONTROL FLAP CONFIGURATIONS

6.9.1 Sharp leading edge ($\alpha \geq 0°$)

The general inviscid flow structure over a compression corner configuration at incidence is shown in diagram 6-6. The leading edge shock is generated due to incidence of the flat plate whilst the flap shock is generated due to the local flap deflection.

In the absence of strong viscous interaction effects, the hingeline Mach number at 2 is equal to the Mach number immediately behind the leading edge shock. The latter is given by

$$M_2 = M_1 = \frac{1}{\sin(\theta-\alpha)}\sqrt{\frac{(\gamma-1)M_\infty{}^2\sin^2\theta+2}{2\gamma M_\infty{}^2\sin^2\theta-(\gamma-1)}} \qquad [6.43]$$

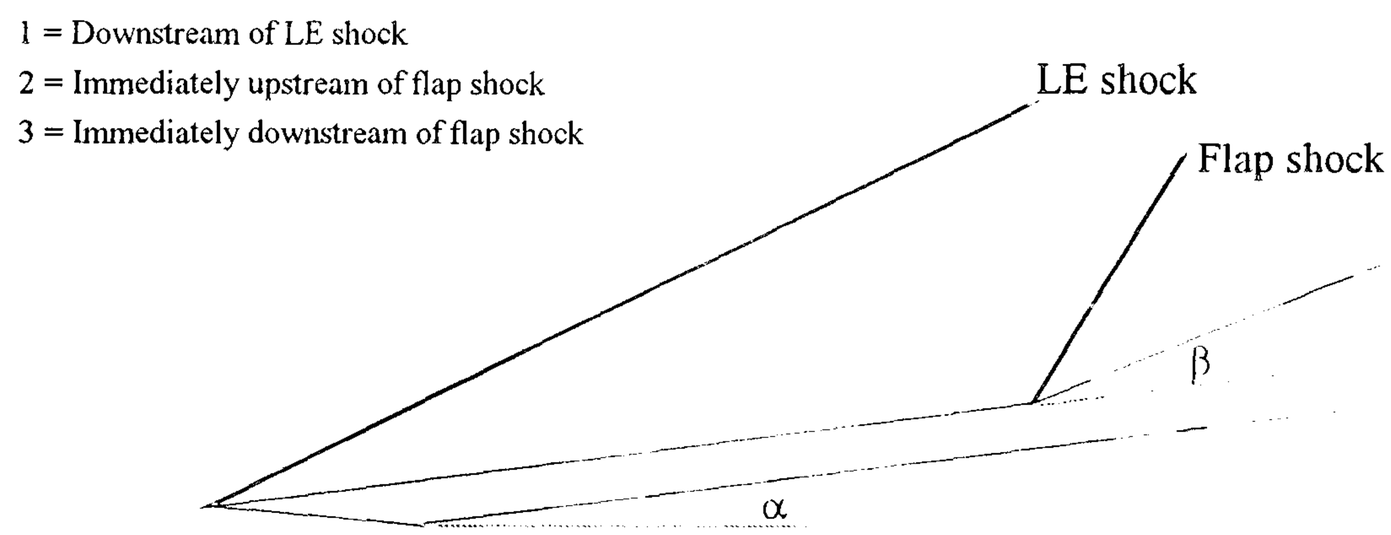

Diagram 6-6 Schematic diagram for the inviscid flow structure over a sharp leading edge flat plate-flap configuration

The temperature ratio across the leading edge shock is

$$\frac{T_2}{T_\infty} = \frac{T_1}{T_\infty} = \left[2+(\gamma-1)M_\infty{}^2\sin^2\theta\right]\left[\frac{(\gamma+1)+2\gamma\left(M_\infty{}^2\sin^2\theta-1\right)}{\left[(\gamma+1)M_\infty\sin\theta\right]^2}\right] \qquad [6.44]$$

From the oblique shock relations given by Anderson (1985), the flap shock angle θ_f is obtained from

$$\tan\beta = 2\cot\theta_f\frac{M_2{}^2\sin^2\theta_f-1}{M_2{}^2(\gamma+\cos2\theta_f)+2} \qquad [6.45]$$

where β is the flap deflection angle (relative to the flat plate). Thus, the Mach number M_3 on the flap is

$$M_3 = \frac{1}{\sin(\theta_f-\beta)}\sqrt{\frac{(\gamma-1)M_2{}^2\sin^2\theta_f+2}{2\gamma M_2{}^2\sin^2\theta_f-(\gamma-1)}} \qquad [6.46]$$

and the temperature ratio T_3/T_2 across the flap shock is

$$\frac{T_3}{T_2} = \left[2 + (\gamma - 1) M_2{}^2 \sin^2 \theta_f\right] \left[\frac{(\gamma + 1) + 2\gamma\left(M_2{}^2 \sin^2 \theta_f - 1\right)}{\left[(\gamma + 1) M_2 \sin \theta_f\right]^2}\right] \qquad [6.47]$$

From equations 6.44 and 6.47, the flap to freestream temperature ratio T_3/T_∞ can be determined. The flap reference temperature, given by

$$\frac{T^*}{T_\infty} = 1 + 0.5\left(\frac{T_w}{T_\infty} - \frac{T_3}{T_\infty}\right) + \frac{0.22 r T_3 (\gamma - 1) M_3{}^2}{2 T_\infty} \qquad [6.48]$$

can therefore be determined.

The laminar and turbulent flap heat transfer predictions from this method are compared with experimental heat transfer measurements in figure 8-6, 8-17 and 8-18. The results for attached flows on sharp configurations at $\alpha \geq 0°$ are discussed in section 8.8.3 whilst the results for separated flows are discussed in section 8.9.1.

The laminar and turbulent predictions were made from experimentally derived flap pressure distributions together with a reference temperature estimated from equation 6.48.

6.9.2 Virtual origin for attached and separated flows

For attached laminar and turbulent flows, the heat transfer predictions made using equation 6.38 and shown in figures 8-6, 8-17 and 8-18 employed the leading edge of the body as the origin. Thus, the Reynolds number $Re_{\infty X}$ was calculated on the basis of x measured from the leading edge.

For separated flows, the leading edge of the body was used to predict the laminar flap heat transfer rate. The turbulent flap predictions in separated flows employed the hingeline as the virtual origin of the solution. Thus the x used for Reynolds number calculations in the latter case was measured from the hingeline.

The move of the origin of the solution from the leading edge to the hingeline was based on the observations of Stollery (1975) and of Simeonides (1992). These results suggest that turbulent flap boundary layers grow in accordance with a virtual origin at the mid-point of the transition region. In the present study, since transition occurred within the separated

shear layer, the choice of the hingeline as the virtual origin was considered as a good first approximation for the virtual origin.

6.9.3 Method for esitmation of flap heat transfer on blunt leading edge control flap configurations

6.9.3.1 At zero incidence ($\alpha = 0°$)

The entropy layer generated by a blunt leading edge considerably modifies the boundary layer edge conditions on a flat plate. This modifies the flow structure associated with a flap submerged under the entropy layer.

The general flow structure over a blunt leading edge control flap configuration is shown in diagram 6-7.

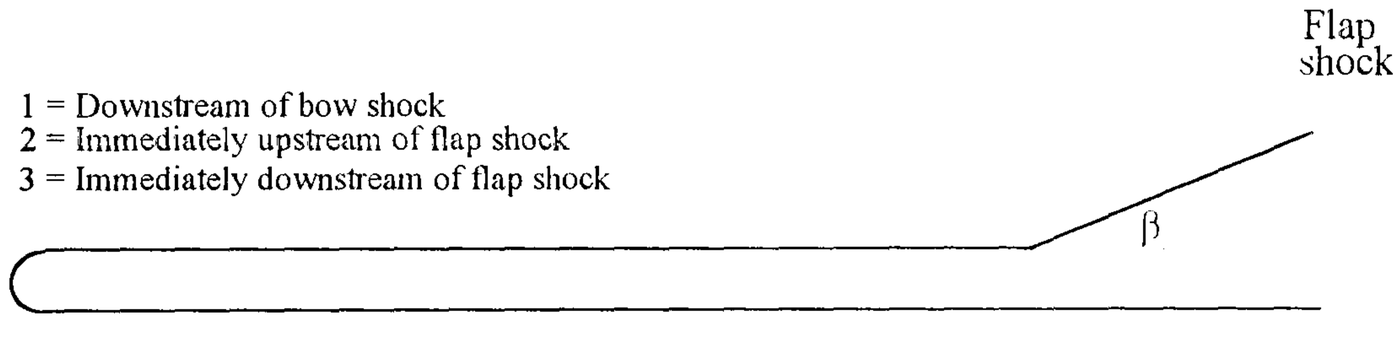

Diagram 6-7 Schematic diagram for the inviscid flow structure over a blunt leading edge flat plate-flap configuration

The boundary layer edge Mach number M_2 immediately upstream of the hingeline shock can be determined from the method described in section 6.5.

Since the flow outside the boundary layer is homenergic, the local boundary layer edge temperature at the hingeline can be determined from isentropic flow relations. Richards (1978) showed that the performance of a flap submerged within the entropy layer of a bluntness dominated flow was determined by conditions at the lower limit of the entropy layer.

Thus, assuming the control flap in diagram 6-4 to be submerged in an "effective" supersonic flow at a Mach number M_2, the local Mach number M_3, flow velocity ratio u_3/u_2 and temperature ratio T_3/T_2 at the start of the flap can be determined from the oblique shock

relations as given by the Ames tables (1953). From these conditions, the flap reference temperature can be estimated.

Substitution of these conditions and the measured pressure distributions into equation 6.38 allows estimates the flap heat transfer coefficient for laminar and turbulent flows. The virtual origin condition described in section 6.9.2 needs to be taken into consideration.

6.9.3.2 At incidence ($\alpha > 0°$)

For a blunt leading edge control flap configuration at incidence, the local Mach number M_2 at the hingeline (immediately upstream of the shock) can be evaluated using the method described in section 6.5.2. Using this, the local temperature ratio immediately upstream of the flap shock can be determined from isentropic flow equations.

With these as conditions as the effective freestream, the reference temperature on the flap can be determined. Hence the heat transfer on the flap can be determined from the method described in section 6.9.3.1.

Chapter 7

EXPERIMENTAL SET-UP

7.1 CRANFIELD HYPERSONIC FACILITY

7.1.1 Wind tunnel facility

The experimental studies presented in this thesis were conducted in the Cranfield hypersonic gun tunnel. It consists of a free-piston compression driver feeding an intermittent open-jet blowdown facility.

The fundamental principles of operation of this facility are based on those of free-piston shock tunnels. These principles are discussed in detail by Groth et al (1969), Lukasiewicz (1973) and by Derksen et al (1973).

Briefly, high pressure gas from a reservoir is used via a double diaphragm set-up to accelerate a piston (mass = 0.1 kg) to supersonic speeds down a compression tube. The incident and reflected shock systems associated with the supersonic piston compress and heat up the working gas by a non-isentropic process. The release and subsequent expansion of the working gas through a contoured nozzle produces uniform high Mach number flow in the working section for short durations.

The general set-up of the Cranfield facility is shown in figure 7-1. A full description of the facility is given by Stollery (1960). Subsequent modifications and calibration of the driver section of the facility are reported by Needham (1963).

The detailed freestream environment associated with the Mach 8.2 contoured nozzle was studied by Opatowski (1967, 1969) and by Ledford (1973) using pitot pressure measurements. A similar study was conducted for the Mach 12.3 nozzle by Mommahadian (1968).

7.1.2 Calibration of the driver section

The time variation of reservoir pressure in the facility is shown in figure 7-2. Following the initial peak, the reservoir pressure ratio P_0/P_4 was 0.78 ± 0.04 for a driver pressure of 2000 psig. These conditions were attained during the time interval $10 < t < 30$ ms after which the arrival of expansion and reflected compression waves from the driver

vessel produced secondary compressions. The reservoir pressure measured for the Cranfield facility is similar to that obtained by Needham (1963).

The reservoir temperature of the facility was inferred from stagnation point heat transfer measurements on a hemispherical body using the Fay-Riddell stagnation point heat transfer formula given by Anderson (1989).

It was also estimated from run time measurements assuming choked nozzle conditions. The measurements were conducted for various driver pressures whilst maintaining the barrel pressure at atmospheric conditions.

The variation of reservoir temperature with the driver to barrel pressure ratio is shown in figure 7-3. The measurements agree with previous measurements made by Needham (1963) using these techniques. The best fit line showed the reservoir temperature variation with the driver to barrel pressure ratio as

$$T_O = 110\ (P_4/P_1)^{1/2} \pm 10\% \qquad [7.01]$$

7.1.3 Off-design operation

In its design, the Mach 8.2 contoured nozzle expansion profile was corrected for the displacement body associated with nozzle conditions generated for $P_4/P_1 = 137$. Thus, operation of this nozzle at driver pressures off the design condition leads to an incorrect expansion profile.

Pitot pressure measurements in the driver pressure range $34 \leq P_4/P_1 \leq 137$ showed the exit plane Mach number variation to be $8.2 \pm 4\%$ with a repeatability of 1.2%. Thus the off-design operation of the facility generates nominal Mach 8.2 conditions for the unit Reynolds number range $4.6 \times 10^4 \leq Re_\infty/cm \leq 9.0 \times 10^4$.

7.2 DATA ACQUISITION AND RECORDING SYSTEM

A digital data acquisition has been established for the facility to allow rapid primary analysis and storage of data following the run and to allow for the application of numerical techniques (Fourier analysis etc.) in secondary analysis of the run histories. The system is shown schematically in its pressure, force and heat transfer measurement modes in figure 7-4.

7.2.1 Power source

A ± 12 V rechargeable DC power source was constructed from lead-acid car batteries. The system incorporated a Thevinin transistor circuit to provide a voltage stabilised power source for the diagnostic instrumentation and effectively isolated the instrumentation from the electrical noise associated with the mains system.

7.2.2 Transient Recorder

For pressure, force and heat transfer measurements, the data recording system consisted of a low-noise 8-channel amplifier coupled to a digital transient recorder. The recorder allowed a maximum sampling rate of 50 kHz and a 10-bit digitisation of the voltage history. The digitised output of the transient recorder is proportional to the change in voltage with respect to the level before the run. This is given by

$$\Delta V = (V - V_i) = \frac{(T - T_i)}{1023} \cdot V_{FS} \qquad [7.02]$$

The output for each channel was a 12-bit data string. These data strings were dumped via an RS-232 Kermit interface into a data file on the Personal Computer. This file was stored on the hard disk and on 1.44 Mb 3.5" floppy discs. An SCDUMP.EXE file was used to rearrange the raw digitised data prior to its primary processing in a spreadsheet.

7.2.3 Pressure measurement system

KULITE XCS-190 series transducers (0 - 15 psia range) were used for pressure measurements during the run. These were mounted in sealed brass-housings located on the floor of the sting. The pressure tappings of the model were connected to the transducers using 10-15 cm long plastic PORTEX tubes.

For each run, the transducers were calibrated during the evacuation phase of the tunnel between the initial atmospheric and final vacuum pressures. These pressures were measured using the tunnel vacuum pressure gauge. The pressure-voltage calibration of the transducer was assumed to be linear and was calculated from the relationship

$$A_3 = \frac{p_{atm} - p_i}{G_{cal}(V_{atm} - V_i)} \qquad [7.03]$$

The 10-bit voltage (given by equation 7.02) during the run was converted into the absolute pressure level using the relation

$$p = p_{vac} + A_3 \frac{\Delta V}{G_{run}} \qquad [7.04]$$

Typical pressure histories during the run is shown in figure 7-5. For both high and low pressure ratio measurements, a number of periodic waves are evident after the run. These are due to reflections from the dump tank. Since supersonic flows are insensitive to downstream history, these waves do not affect the core flow through the working section during the run.

7.2.4 Heat Transfer measurements

For heat transfer measurements, the battery power supply discussed in section 7.2.1 was used with the 8-channel CONTECH analogue circuits. Input currents of approximately 20 mA were used to power thin-film gauges during the run.

The voltage rise associated with the temperature rise of the gauges was integrated using a C-R analogue integrator circuit. This was digitised and stored on the 386 SX PC. Subsequent calibrations for the gain of the analogue circuits and the voltage-temperature response of the thin-film gauges were applied to convert the stored digitised voltage history into heat transfer rate history.

7.2.4.1 Theory of the analogue circuits

The channels of the CONTECH analogue integrator circuits consist of a constant current supply which energises the gauges. Heat transfer to the gauge during the run changes its temperature and hence its resistance. Since a constant current source is used, this produces a voltage history which is integrated using an analogue R-C network. The integrated output is amplified and passed through an analogue 0.02 Hz - 100 kHz band-pass filter.

The overall equivalent integrator-amplifier circuit (Oldfield et al, 1984) can be modelled as a direct coupled differential amplifier with a feedback resistor R_F (see figure 7-10). It is noted that the resistor R_F shown in the equivalent circuit is not a physical resistor but a model for the amplifier calibration. The bandpass filter has been neglected in the equivalent circuit. From Oldfield (1993), the gain of the equivalent circuit can be written as

$$\frac{V_{out}}{V_{in}} = \frac{-R_F}{Z} \qquad [7.05]$$

The impedance of the finite length R-C network is given by Oldfield et al (1984) as

$$|Z| = \sqrt{\frac{R}{\omega C}} \qquad [7.06]$$

Therefore, by substitution into equation 7.05, the gain of the equivalent circuit can be rewritten as

$$\frac{V_{out}}{V_{in}} = -R_F\sqrt{\frac{\omega C}{R}} \qquad [7.07]$$

For a signal with a known input angular frequency $\omega = 2\pi f$, the value of the modelled resistance $R_F[C/R]^{1/2}$ can be evaluated from

$$|G| = \left|-R_F\sqrt{\frac{C}{R}}\right| = \frac{V_{out}}{V_{in}}\frac{1}{\sqrt{\omega}} \qquad [7.08]$$

Using the electrical analogy for heat transfer Oldfield et al. (1984) showed that the current is given by

$$i = q\frac{V_i\alpha_T}{\sqrt{\rho ck}}\sqrt{\frac{C}{R}} \qquad [7.09]$$

and for a constant analogue current i, the output of the analogue is given by the feedback relationship

$$V_{out} = -R_F i \qquad [7.10]$$

Thus, by substitution from equations 7.08 and 7.09 into equation 7.10, the heat transfer rate associated with the thin-film gauge voltage change is given by

$$q = \frac{1}{G}\cdot\frac{\sqrt{\rho ck}}{V_i\alpha_T}\cdot V_{out} \qquad [7.11]$$

7.2.4.2 Calibration of the analogue circuit

The gain G of a channel of the analogue circuit was determined using the frequency response circuit shown in figure 7-10. A signal generator and an input resistance approximately equal to that of the thin-film gauge were used to input an a.c. sinusoidal signal. The frequency of the input signal was measured using a frequency meter. The peak to peak voltage of the input and output signals was measured using an oscilloscope. From this, the analogue gain was evaluated from equation 7.08. The variation of the analogue gain with frequency for two channels is shown in figure 7-10.

The mean value of the gain was 3.0 ± 4% in the frequency range $0.1 \leq f \leq 40$ kHz. The upper 3dB point (the value at which the gain is attenuated to 70% of its value) was at 95 kHz. The reduced frequency response at high frequencies is due to a low pass filter.

The present calibration set-up did not allow investigation of the gain performance at the lower 3dB frequency limit. This has been estimated by Oldfield (1984) to be at 0.02 Hz. The constant response of the circuits in the frequency range $0.1 \leq f \leq 20$ kHz allowed quantitative heat transfer studies within these frequency limits.

In order to further attenuate the electrical noise, a second low pass R-C filter with a 3dB point at 5 kHz was incorporated downstream of the analogue output as shown in figure 7-4. Together with an common Earth network (which incorporated the gun tunnel), the amplitude of the electrical noise associated with the measurement system was reduced to a minimum of 5 mV on all channels. The minimum signal amplitude in the present heat transfer study was approximately 100 mV.

7.3 PRIMARY AND SECONDARY DATA PROCESSING

The recorded data was processed in primary and secondary stages. The former involved analysis of the run time history immediately after the run to study values such as pressure, heat transfer and force variation with time during the run. Typical traces are shown in figure 7-5. Secondary processing typically involved spectral analysis and the application of digital filtering techniques for selected measurements. The techniques employed the MSPECTE signal processing package developed by Russell and Wyatt (1993). Frequency spectra of various signals are shown in figure 7-6.

7.4 SCHLIEREN SYSTEM

A single pass schlieren flow visualisation system was used to observe density gradients associated with the flow structure. These tests provided essentially a two-dimensional picture of the flowfield.

An argon stabilised source was used to produce a high-intensity beam of light with a duration of a few microseconds. The single pass schlieren set-up employed for the Cranfield facility is similar to that given by Needham (1965). A Land Polaroid camera with high speed Type 667, 3000 ASA black and white film was used for the study. The system was triggered 15 ms after the start of the run. A horizontal source-knife edge set-up was used to study density gradients normal to the freestream whilst a vertical source-knife edge set-up was employed for studying density gradients parallel to the freestream.

7.4.1 Identification of separation and reattachment points from schlieren photographs

Due to the sweep of the compression fans within the boundary layer (see figure 8-7), there is a lag between the start of the thickening of the sublayer and the deflection of the outer edge of the boundary layer. The lag results in the separation shock emerging some distance downstream of the start of the thickening of the sublayer.

In schlieren studies where the separation streamline cannot be clearly visualised, it was assumed that the axial location of upstream limit of the separation shock at the edge of the boundary layer provided a good approximation for the location of the separation streamline. The upstream limit of the reattachment shock was assumed to provide a good approximation for the reattachment point.

7.5 LIQUID CRYSTAL SYSTEM

Encapsulated thermochromic liquid crystals have been employed for qualitative analysis of the surface temperature distribution. Their use in the present study augments the schlieren data and provides a means for studying the temperature and hence heat transfer variations produced by localised highly three-dimensional flow structures as well as information with regards to the laminar or otherwise structure of the boundary layer.

The models used for these tests were made of mild steel and were painted matt black using commercial grade aerosol paint. The thickness of the paint layer was approximately 0.5 mm. A number of layers of diluted liquid crystals were applied using an air brush (at a pressure of 50 psig). The thickness of the crystals together with that of the paint layer was sufficient to satisfy the requirement for an insulating substrate and hence provide a sufficient temperature rise during the run. An Olympus OM-10 camera equipped with 35/105 mm zoom lens was used for the tests. The camera was on an open shutter during the run. A constant intensity flash of white light with a duration of 2.5 ms was used to illuminate the model 25 ms after the start of the run. The surface colour distribution was captured using 100-ASA Fuji film.

7.5.1 Colour temperature response of liquid crystals

In diagram 7-1, the colour temperature response for the well separated flow structure on the $\alpha = 0°$, $\beta = 25°$ configuration is compared against the corresponding thin-film heat transfer measurements.

The relatively coarse colour response of the crystals produces a lag in the colour change i.e. the start of the interaction (diagnosed by a colour change of the liquid crystals) starts downstream of the actual start of the interaction (see diagram 7-1).

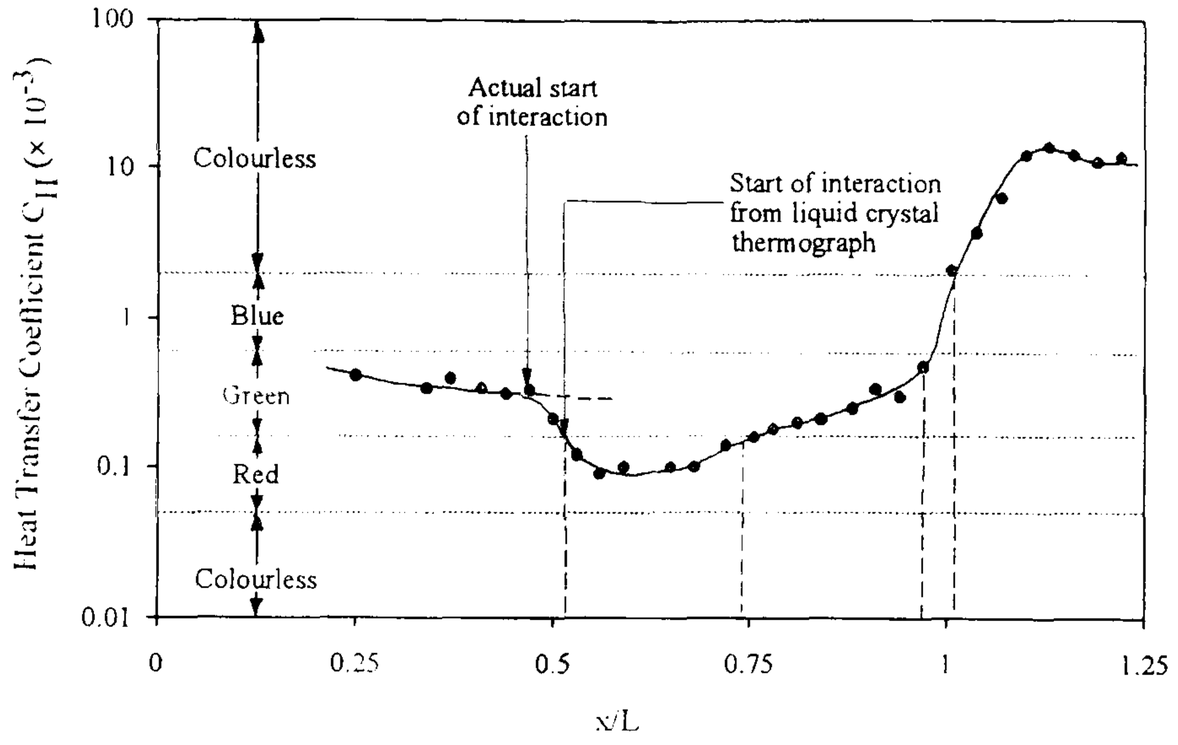

Diagram 7-1 Comparison of the colour temperature response of liquid crystals with heat transfer measurements ($M_\infty = 8.2$, $Re_\infty/cm = 9.0 \times 10^4$, $\beta = 25°$)

However, the thermographs do reveal the salient features of the heat transfer distribution and provide invaluable information on the three-dimensionality of the heat transfer distribution.

7.6 MODELS USED FOR WIND TUNNEL TESTS

7.6.1 Pressure measurement models

7.6.1.1 Control flap

The models employed for pressure tests over the sharp and the blunt leading edge control flap configurations are shown in figure 7-7.

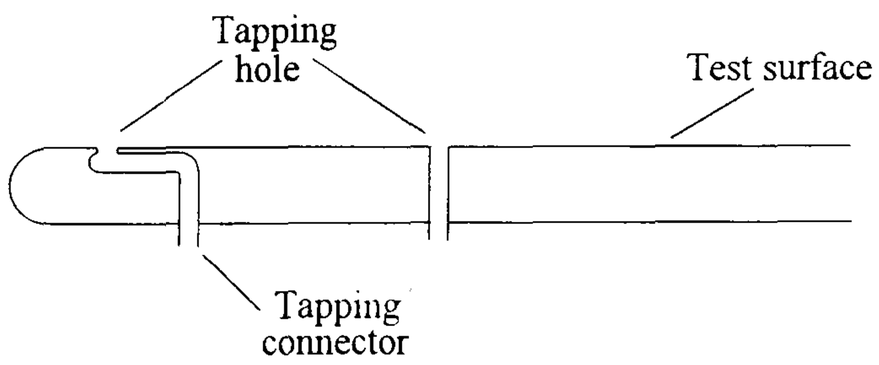

Diagram 7-2 Design of pressure tappings on the blunt leading edge flat plate

Two separate flat plates, one with a sharp and the other with a 6.0 mm blunt leading edge were manufactured from mild steel. The flat plates were equipped with 2.0 mm diameter pressure tappings. These were located at intervals of 5.0 mm at spanwise

locations 10.0 mm either side of the centreline. The flap was equipped with similar tappings at the same spanwise locations.

The tappings close to the leading edge of the body had a number of bends, as shown in diagram 7-2. This was designed to prevent interactions between the tapping connector and the leading edge shock. The response of these tappings to a given pressure input was poorer than that of straight through tappings away from the leading edge.

7.6.1.2 Jet interaction models

The models employed for the jet interaction studies are shown in figure 7-8. These were equipped with a single row of 2.0 mm diameter tappings located directly ahead of the 0° jet meridian. The tappings were connected to 'PORTEX' pressure tubes which emerged from the base of the model.

A number of the connectors for tappings located close to the jet passed through the high pressure plenum chamber located within the model. In order to sustain the higher plenum chamber pressure, the connector tubes associated with these tappings were thicker walled as compared to normal connector tubes. The cross-sectional view of the tapping structure in the model is shown in diagram 7-3.

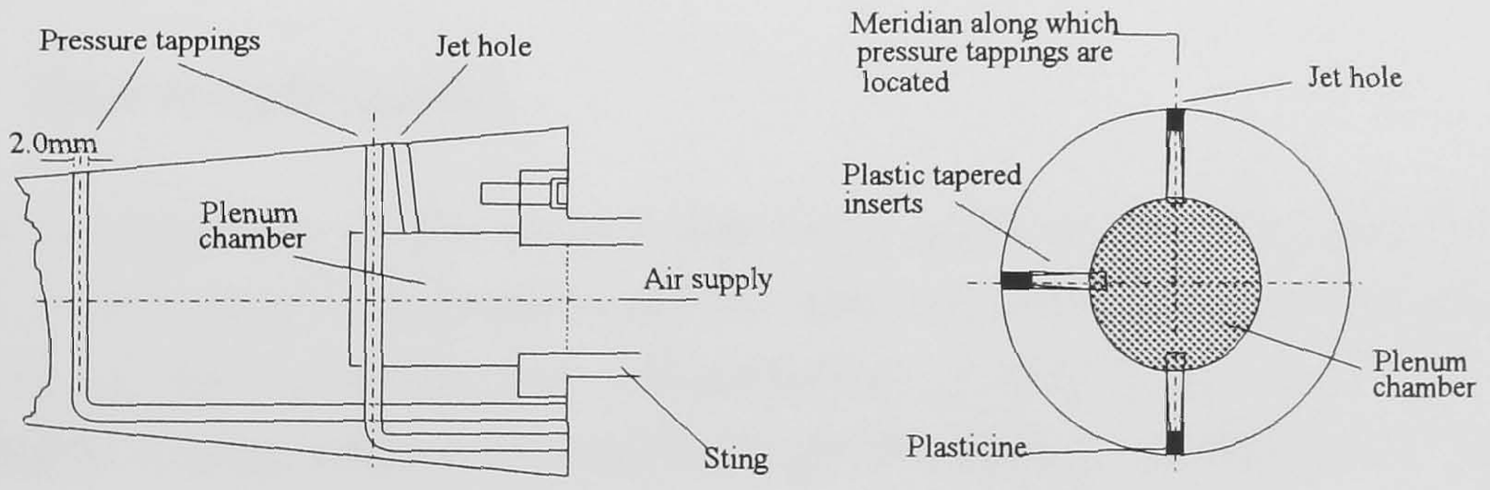

(i) tapping structure in model measurements

(ii) jet geometry used for pressure

Diagram 7-3 Structure of the jet interaction model used for pressure measurements

A number of jet holes located at the same axial position but at selected angular intervals were drilled into the common plenum chamber. These jets allowed the relative angle between the jet and the tapping meridian to be altered.

For a given run, only a single jet hole was used. The remainder of the jets were sealed from within the plenum chamber using tapered plastic inserts, as shown in diagram 7-3. 'Plasticine' was used to ensure a good surface finish. The variable location of the jet

allowed the single line of pressure tappings to be used for pressure measurements along selected meridians.

7.6.2 Control flap heat transfer model

7.6.2.1 Manufacture and calibration of temperature sensors

Thin-film platinum gauges mounted on an insulating semi-infinite MACOR substrate were employed as surface temperature sensors. The gauges were fired onto the substrate at a temperature of 600°C for 1 hour. Additional layers of platinum were added and fired to attain a desired gauge resistance of 50 ± 10Ω. The gauges were as part of an Whetstone bridge circuit. The gauge connections were established using insulated copper wires and epoxy silver. This was fired at 70°C for 1 hour.

The temperature/voltage response of the gauges was measured by placing the model (whilst covered in vacuum sealed plastic) in a bath of water. The temperature of the bath was varied by the addition of hot water upto a maximum temperature of 70°C. The voltage response of the gauge for a constant input current was measured using a voltmeter. The thermal coefficient of resistivity (dR/dT = (dV/dT)/i) was evaluated as the gradient of the best fit line.

7.6.1.2 Heat transfer model

The general arrangement of the control flap heat transfer model is shown in figure 7-9. The inserts were located into grooves cut into the steel model and held in place by pitch. The location of the centreline and off-centreline gauges is given in figure 7-9. An interchangeable leading edge was used to study the effects of changes in leading edge geometry.

7.7 FORCE MEASUREMENT SYSTEM

7.7.1 Model

The force model used for jet interaction study was constructed in two separate parts. The overall configuration has the same dimensions as the flow visualisation and the pressure models. This ensured a matching of the aerodynamic interaction scales.

Various aspects of the force model are shown in figure 7-14. The construction of the model focused on minimising its mass and moment of inertia (in the pitch plane). The total mass of the forecone was 20g and that of the jet feed system was 42g. This mass

gave a natural frequency of mechanical oscillations of 180 Hz. This frequency was sufficiently high to allow implementation of digital filtering techniques (see figure 7-6).

7.7.2 Wind tunnel set-up

The set-up employed for force tests on the jet interaction configuration is shown in figure 7-14. A variable incidence cantilever mounting system was designed to locate the force balance and the model along the centreline and allowed the incidence of the model to be changed whilst the location of the jet remained fixed relative to the nozzle.

The air feed system for the plenum chamber used two injection ports located in the horizontal axis plane of the model. This set-up imposed yaw moments onto the model due to differences in feed pipe pressure. For the balance, the coupling of the pitch moment to the yaw moment was negligible. The pressure feed employed coiled tubes, as shown in figure 7-14. These coils allowed movement similar to a spring and thus reduced the coupling forces associated with interaction between the jet feed system and the model.

7.7.3 Force measurement data acquisition system

The force measurement system employed a 3-component strain gauge balance. A full description of the design and construction of the balance is given by Opatowski (1967). All three components of the balance were equipped with 1000Ω semi-conductor strain gauges (Maywood Instruments, Basingstoke). Due to the short run-time of the tunnel and the relative thermal isolation of the gauges, the components were not temperature compensated. The balance was energised using a stabilised 5.0 volt lead-acid battery power source (described in section 7.2.1).

7.7.4 Calibration of the force balance

The calibration set-up used the rig shown in figure 7-15. This allowed calibrated weights to be applied normal and parallel to the axis of the balance sting using a system of pulleys. A non-isotropic force calibration bar was employed to apply forces to the sting. The bar was designed so that its COG was coincident with the plane of the bending moment gauges, as shown in diagram 7-4.

The application of a pure normal load (primary load) to the balance results in a strain and hence output voltage change from the normal force component (primary component) of the balance.

However, due to coupling effects between the components, the applied normal force also produces a strain in the axial force and moment components (secondary components) of the balance. This coupling between the components is also present when axial and moment loads are applied.

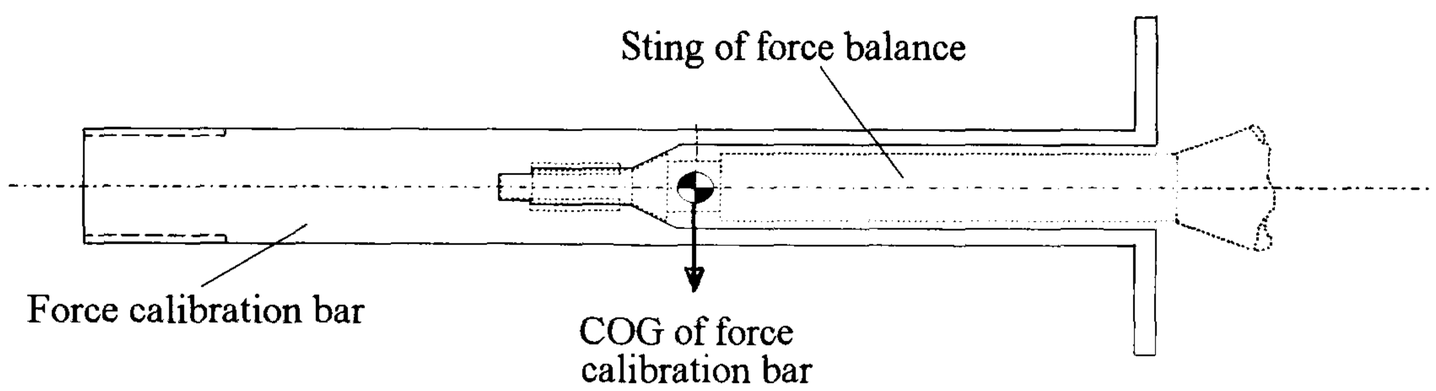

Diagram 7-4 Location of the COG of the force calibration bar

The coupling effect changes the voltage response of a given component to its primary load. In order to eliminate this error, the matrix calibration method proposed by Rae and Pope (1984) was implemented. This is described in section 7.7.5.

Normal force calibration : Normal loads upto 25 N were applied normal to the calibration bar using nylon ropes. This is shown in figure 7-15(c). These loads were applied at the COG of the calibration bar (located in the plane of the bending moment gauges). This was done in order to prevent the application and hence the interference effects associated with the application of a pitching moment. The voltage-force output response was amplified and measured for all three components.

Axial force calibration : The axial force component was calibrated by attaching a horizontal pan to the end of the calibration bar while the balance sting was vertical. Loads placed on the pan allowed the axial force component to be calibrated in compression. The difficulty associated with placing weights directly along the axis of the sting meant that the component interactions were neglected. A second calibration of this component using a hook attached to the end of the calibration bar was carried out by Courtis (1994). This set-up is shown in figure 7-15(a) and allowed tension loads to be applied to the axial force component along the axis of the sting. Both of these calibrations showed similar responses to an axial load for the primary component. Thus, the response of the axial component to loads in tension and in compression is similar. The coupling response of the secondary components to an axial load was found by Courtis (1994) to be negligible.

The axial force component was also calibrated in the gun tunnel by measuring the drag coefficient history on a a hemispherical cylinder. This is shown alongside the corresponding pitot pressure history in diagram 7-5. The qualitative similarity between these histories illustrates the rapid response of the force system to freestream conditions.

The mean axial force coefficient of the system was measured as 0.89 between 25 and 30 ms after the start of the run. This compares with a theoretical coefficient of 0.92.

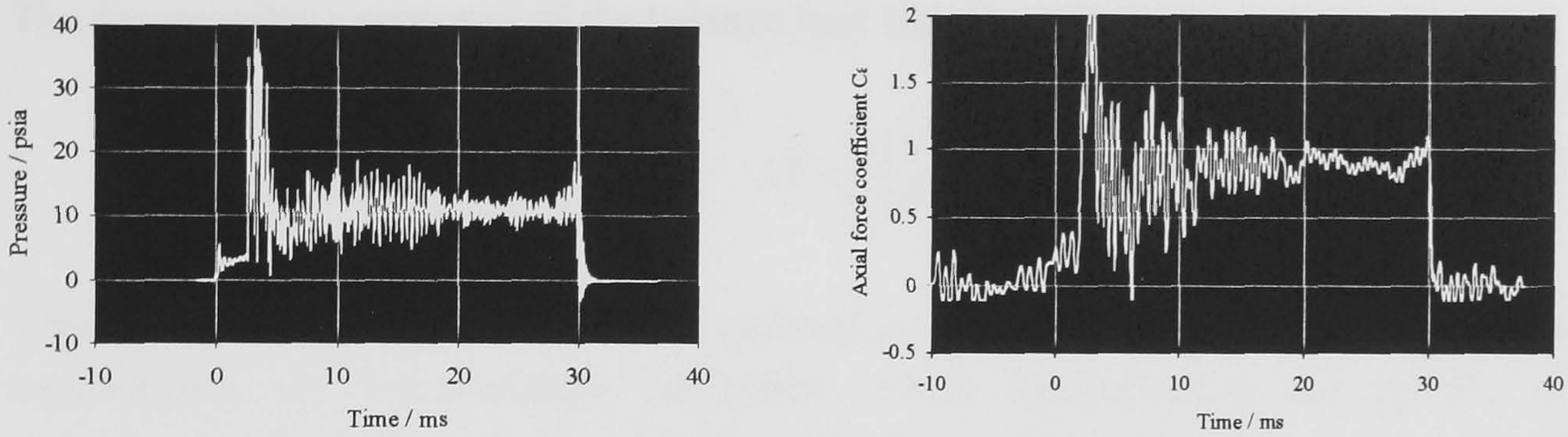

(i) pitot pressure history (ii) axial force history

Diagram 7-5 Comparison of the pitot pressure and axial force history on a hemisphere-cylinder ($M_\infty = 8.2$, $Re_\infty/cm = 9.0 \times 10^4$, $d_B = 2.26$ cm)

Moment calibration : The moment component was calibrated by applying a couple about the plane of the bending moment gauges. The moment was created by applying a positive and a negative lift about the calibration bar. The set-up employed is shown in figure 7-15(d).

7.7.5 Component interactions

The voltage output from the normal force component of the balance is a function of the response of the normal force component to normal loads and as a result of the coupling between the components, to axial loads and to moments. Thus the overall response of the normal force component may be written as

$$\Delta V_N = \left(\frac{dV_N}{dN}\right)_N \Delta N + \left(\frac{dV_N}{dA}\right)_A \Delta A + \left(\frac{dV_N}{dM}\right)_M \Delta M \qquad [7.12]$$

Similar equations can be set-up for the voltage outputs from the axial and the normal force components and total response of the three-components may be written as the matrix equation

$$\begin{bmatrix} \Delta V_N \\ \Delta V_A \\ \Delta V_M \end{bmatrix} = \begin{bmatrix} [dV_N/dN]_N & [dV_N/dA]_A & [dV_N/dM]_M \\ [dV_A/dN]_N & [dV_A/dA]_A & [dV_A/dM]_M \\ [dV_M/dN]_N & [dV_M/dA]_A & [dV_M/dM]_M \end{bmatrix} \begin{bmatrix} \Delta N \\ \Delta A \\ \Delta M \end{bmatrix} \qquad [7.13]$$

Thus the overall voltage-force response of the balance may be written in vector representation as

$$\Delta\overline{V} = \left[\frac{d\overline{V}}{d\overline{F}}\right] \cdot \overline{F} \qquad [7.14]$$

The force-voltage response of the balance may thus be written as

$$\Delta\overline{F} = \left[\frac{d\overline{V}}{d\overline{F}}\right]^{-1} \cdot \overline{V} \qquad [7.15]$$

Thus by inverting the voltage-force calibration matrix which incorporates the balance interactions, the force-voltage calibration matrix incorporating the effects of the component interactions can be derived. Using this method, the calibrations of the three-components were derived as

$$\Delta N = 0.467\Delta V_N + 0.008\Delta V_A - 0.042\Delta V_M \qquad [7.16]$$

$$\Delta A = 0.008\Delta V_N + 0.867\Delta V_A + 0.002\Delta V_M \qquad [7.17]$$

$$\Delta M = -0.00073\Delta V_N + 0.00004\Delta V_A + 0.00483\Delta V_M \qquad [7.18]$$

The voltage changes in equations 7.16 to 7.18 are in mV.

7.7.6 Data analysis and filtering

During the running of the tunnel, the working section is subjected to significant mechanical oscillations. As a result of the mass inertia of the model, these oscillations cause the model and sting to exhibit damped harmonic oscillations. The natural frequency of these oscillations was determined by a tare calibration. In this, the tunnel was run with the flow blocked off by means of a 5 cm thick brass disc placed over the nozzle entry plane, as shown in diagram 7-6.

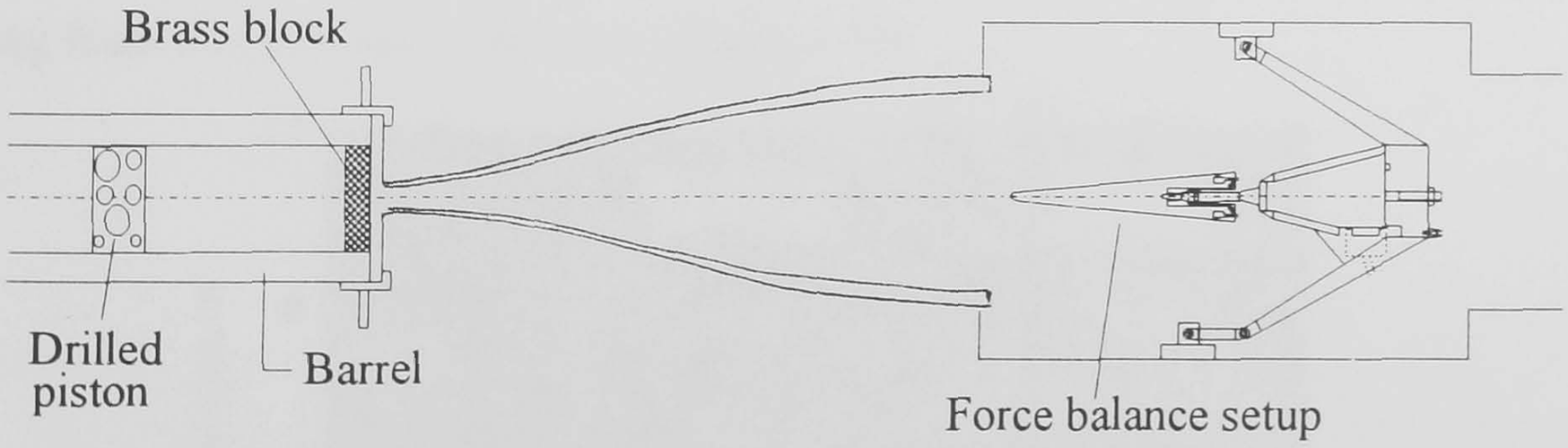

Diagram 7-6 Set-up employed for tare calibration to identify natural frequency of oscillation of normal force and pitching moment components

FFT analysis of the resulting signals (from the tare calibration) showed natural frequency oscillations due to mechanical vibrations only. These were observed on the normal force

and pitching moment components at 180 Hz. The power density spectra of the normal force and pitching moment components during a run with the flow on are shown in diagram 7-7.

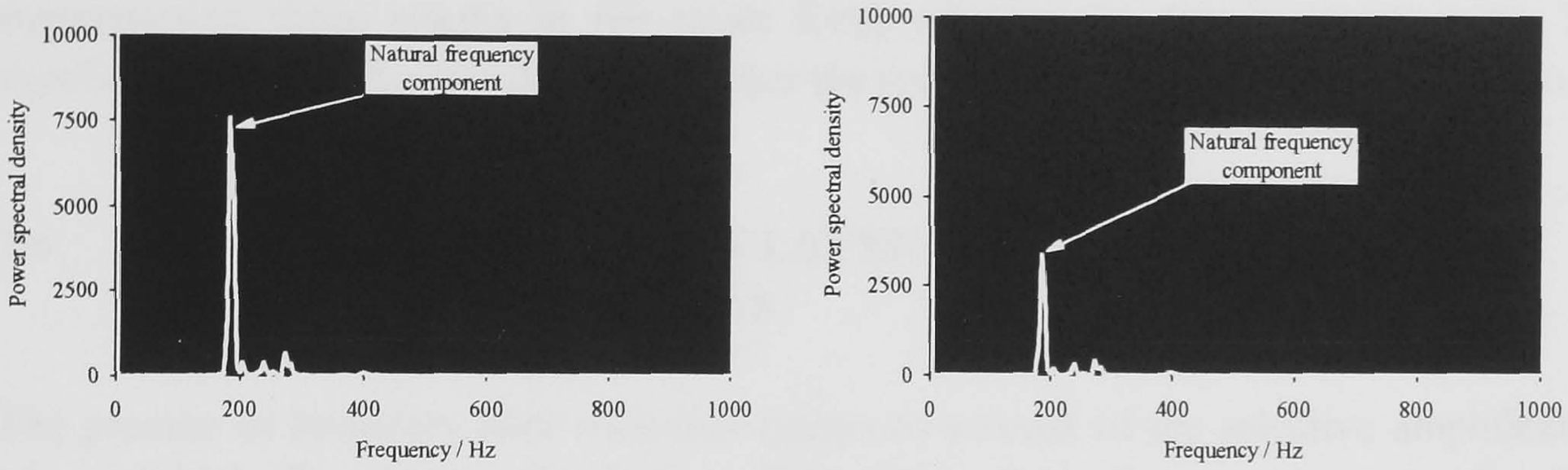

(i) Normal Force (ii) Pitching moment

Diagram 7-7 Power Density Spectra for the Normal Force and Moment components

The removal of the natural frequency oscillation component using a digital filter and the re-inversion of the signal back to its time history produces a significant increase in the signal to noise ratio and hence in the accuracy of the measurements. The effects of the digital filter on the time history of the normal force component during the run is shown in figure 7-6. The mean force measurements were taken between 10 and 25 ms during the run.

7.7.7 Force measurements history for jet interaction studies

The tests to study the effects of the jet/crossflow interaction on the total reaction force generated by the jet were conducted by first establishing a steady jet and then firing the hypersonic crossflow generated by the tunnel across the jet. The normal force history resulting from this process is shown in diagram 7-8.

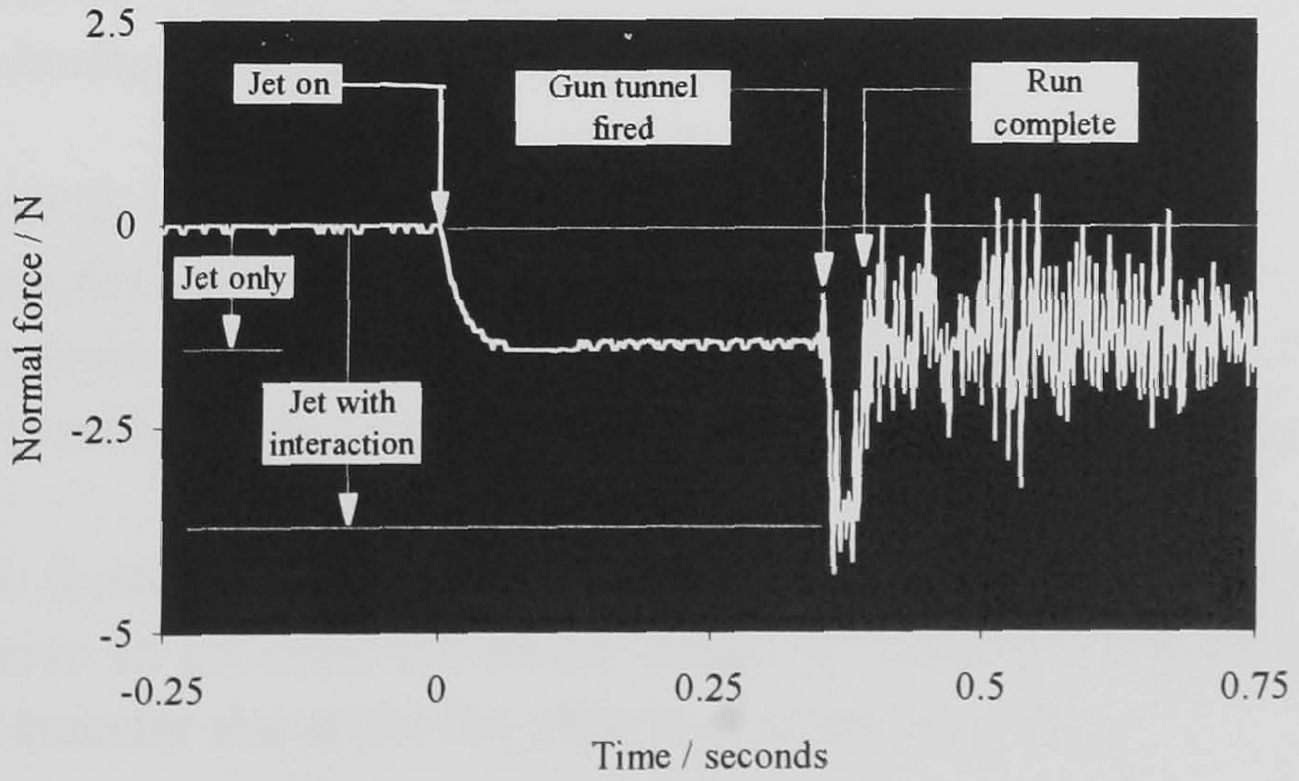

Diagram 7-8 The effects of the jet and the jet/crossflow interaction on normal force

The presence of the jet at t = 0 produces a negative force, the magnitude of which becomes constant after 100 ms as the jet plenum chamber becomes choked. The firing of the tunnel and the establishment of a separated interaction region in the vicinity of the jet augments the jet force. The completion of the tunnel run and the removal of the augmentation force results in the mean force returning to the jet force level. The significant increase in noise during and after the run is due to the mechanical oscillations.

7.8 DIAGNOSIS OF BOUNDARY LAYER TRANSITION USING HEAT TRANSFER FLUCTUATIONS

The process of boundary later transition occurs as a result of the selective amplification of an initial disturbance distribution. The fluctuations impose an unsteady, time dependent fluctuation on the quasi-steady surface velocity, pressure and heat transfer distributions.

Holden (1986) has observed a qualitative increase in the amplitude of surface heat transfer fluctuations in the transition region. Quantitative analysis by Owen (1970) of the voltage output from a constant temperature thin film gauge showed a factor of 14 increase in the rms voltage distribution through the transition region in hypersonic flows (see figure 5-1).

The following method proposes a quantitative method for the experimental detection of transition using heat transfer fluctuations detected using surface mounted constant current thin film gauges.

7.8.1 Flat plate boundary layer transition

From figure 8-14, the agreement between the measured heat transfer rates on a flat plate at $\alpha = 0°$ and the predictions of reference temperature theory means that the boundary layer is entirely laminar.

At $\alpha = 5°$, there is an increase in the measured heat transfer level above that of the predicted laminar flat plate from x/L = 1.05. The increase is associated with a transition of the boundary layer which is promoted by incidence due to the combined effects of a decrease in the local Mach number and an increase in the local unit Reynolds number.

At $\alpha = 10°$, the further reduction in local Mach number and increase in local Reynolds number both serve to promote the earlier onset of transition. This is evident from the increase in heat transfer above the flat plate level from x/L = 0.6.

The heat transfer rate time history and frequency spectra at selected locations along the $\alpha = 10°$ sharp flat plate configuration is shown in figure 7-11. The time histories show that at x/L = 0.25, close to the leading edge, there is little variation from the mean laminar heat transfer level during the run. The corresponding frequency spectra shows that the signal is composed of mainly low frequencies associated with the operation of the tunnel.

Further downstream at x/L = 0.41, the time history again shows that there is little variation in the time history during the run with the mean heat transfer level again corresponding with the predicted laminar heat transfer level. The frequency spectra at this location shows an increase in amplitude of a group of frequencies around 2 kHz.

At x/L = 0.81, a number of short-duration spikes in heat transfer are observed. The mean heat transfer rate remains at the predicted laminar value but, for short durations, it increases above the laminar level. The spikes are associated with the passing of turbulent spots. These cause an intermittent increase in heat transfer above the laminar level as they pass over the gauge. The corresponding frequency spectra shows an amplification of the amplitudes of the frequencies located at 2 kHz. It also shows the amplification of the amplitudes of additional lower frequencies.

At x/L = 1.23, the time history shows large and sustained increases from the laminar level throughout the run. These are again in the form of spikes although the relative duration between the spikes is decreased suggesting that the frequency at which turbulent intermittencies pass over the gauge has increased. The associated frequency spectra shows an increase in the amplitudes of low frequency disturbances around 1 kHz. There is also an increase in the amplitude of high frequency (> 2 kHz) disturbances relative to x/L = 0.81.

As the time histories show, the process of boundary layer transition is accompanied by an increase in the time-dependent fluctuation in heat transfer. This property is measured by the root mean square value which is defined by

$$[C_H{}']_{rms} = \left[\sum_{t=15ms}^{t=25ms} \left[[C_H]_t - [\bar{C}_H] \right]^2 \right]^{1/2} \qquad [7.19]$$

In a region of variable mean heat transfer such as that on a flat plate, the fluctuating component of heat transfer is likely to be a function of the mean heat transfer level. Therefore, comparison of the fluctuating component is possible only if it is a ratio of the mean heat transfer level, i.e. the value of

$$\text{Fluctuation amplitude } F_x = [C_H{}']_{rms} / \bar{C}_H \qquad [7.20]$$

is a function of the transitional status of a boundary layer.

In an entirely laminar boundary layer, the value of F_x remains constant. For the present compression corner configuration, shown in figure 7-9, the first gauge is located at x/L = 0.22. Thus, for an entirely laminar boundary layer on this configuration, the relative fluctuation amplitude at x/L must be the same as the relative fluctuation amplitude at x/L = 0.22, i.e. $[F_{x/L}]/[F_{x/L=0.22}] = 1$.

For a transitional boundary layer, due to an increase in the root mean square fluctuation level, the relative fluctuation amplitude $F_{x/L}/F_{x/L=0.22}$ must increase. Therefore, for transitional boundary layers $F_{x/L}/F_{x/L=0.22} > 1$.

For the sharp leading edge flat plate at various incidences, the distribution of the relative fluctuation parameter $F_{x/L}/F_{x/L=0.22}$ at a given point is plotted in figure 7-13.

At $\alpha = 0°$, the relative value of the fluctuation parameter remains 1 ± 0.15 along the flat plate. Thus, the boundary layer is laminar along the entire length of the flat plate. The heat transfer time history at x/L = 1.23 for the flat plate at $\alpha = 0°$ is shown in figure 7-13. This shows no evidence of turbulent intermittencies which are characterised as short duration increases in heat transfer during the run. The relative fluctuation parameter remains at 1 ± 0.15 along the flat plate. Thus, the boundary layer is laminar along the entire length of the flat plate. This reinforces similar conclusions drawn in section 8.1.

At $\alpha = 5°$, the relative fluctuation parameter distribution $F_{x/L}/F_{x/L=0.22}$ remains at 1 ± 0.15 along the length of the flat plate upto x/L = 1.12. Following this, it shows a sustained increase in the relative fluctuation level. The mean heat transfer distributions for this configuration also show an increase in heat transfer above the laminar level in this region. The time history of heat transfer at x/L = 1.23 for the flat plate at $\alpha = 5°$ is shown in figure 7-12. This shows a number of short duration intermittencies causing varying increases in heat transfer from the mean laminar to the mean turbulent level during the run.

At $\alpha = 10°$, the relative fluctuation amplitude distribution, shown in figure 7-13 remains at 1 ± 0.15 upto x/L = 0.6. The mean heat transfer rates in this region agree with the predictions of laminar reference temperature theory. The onset of boundary layer transition at this point results in the mean heat transfer level increasing above the laminar level. The region is also characterised by the relative increase in the relative fluctuation amplitude. This confirms that following the onset of transition, there is an increase in the relative heat transfer fluctuation amplitude.

In the region $0.6 < x/L < 1.0$, the intermittency of associated with the passing of turbulent spots over the gauge increases gradually as the laminar structure of the boundary layer breaks down. The time history of heat transfer at x/L = 1.23 for this

configuration, shown in figure 7-12, shows that the laminar heat transfer level is attained for short durations only. The high degree of intermittency increases the mean heat transfer rate above the laminar level.

7.8.2 Compression corner boundary layer transition

The diagnosis of boundary layer transition in a compression corner configuration is critical for the efficient aerothermal performance of the control surface. This is because transition causes a large increase in the flap heat transfer rate.

In figures 8-6, 8-17 and 8-18, flap boundary layer transition has been diagnosed by comparison of the measured heat transfer rates with predictions from laminar and turbulent reference temperature theory. Such a diagnosis requires accurate knowledge of the reference laminar and turbulent levels. The absence of the theoretical levels would make the diagnosis of transition difficult.

In section 7.8.1, the relative fluctuation amplitude on a flat plate at $\alpha = 0°$ and $\alpha = 10°$ was found to be unity for regions characterised by laminar boundary layers. This was in spite of large changes to the pressure as the incidence of the flat plate was increased from $\alpha = 0°$ to $\alpha = 10°$.

It is therefore reasonable to assume that, in an entirely laminar region characterised by an axial pressure gradient, the relative fluctuation parameter will remain at unity. Any subsequent changes in the laminar status of a boundary layer will be reflected by an increase in the value of the relative fluctuation amplitude.

The heat transfer rate histories at $x/L = 1.23$ on the $\beta = 0°$ and the $\beta = 5°$ flap are shown in figure 7-12. The undeflected and deflected flap histories are shown for incidences of $\alpha = 0°$, $5°$ and $10°$. The mean heat transfer rates have been estimated assuming fully laminar and fully turbulent interactions using the method described in section 6.9.1.

In figure 8-6, the measured flap heat transfer rates for the $\alpha = 0°$, $\beta = 5°$ configuration are shown alongside predictions from laminar and turbulent theories. The agreement between the laminar predictions and the measured heat transfer rates for the $\alpha = 0°$, $\beta = 5°$ configuration means that the flap boundary layer for this configuration is laminar.

The axial distribution of the relative fluctuation amplitude for the $\alpha = 0°$, $\beta = 0°$ and for the $\alpha = 0°$, $\beta = 5°$ configuration are shown in figure 7-13. The small increase in the relative fluctuation ratio on the flap is due to an increase in intermittency on the flap.

In figure 7-12, the heat transfer rate time history at x/L = 1.23 for $\alpha = 0°$, $\beta = 0°$ and the $\alpha = 0°$, $\beta = 5°$ are shown. This shows that increasing flap deflection from $\beta = 0°$ to $\beta = 5°$ increases the number and amplitude of intermittent heat transfer spikes during the run. The relatively small amplitude of the intermittencies together with the infrequency of their shedding suggests that the laminar boundary layer is just starting to breakdown.

The $\alpha = 5°$, $\beta = 0°$ the flat plate boundary layer already exhibits intermittency at x/L = 1.23, as shown in figure 7-12. This suggests that the onset of transition has occurred. The corresponding heat transfer rate history for $\alpha = 5°$, $\beta = 5°$, shown in figure 7-12 shows a mean heat transfer level in excess of the predicted laminar level throughout the run. This suggests that, at x/L = 1.23, transition is well advanced on the deflected flap configuration.

The axial distribution of the relative fluctuation parameter for the $\alpha = 5°$, $\beta = 0°$ and the $\alpha = 5°$, $\beta = 5°$ configuration are shown in figure 7-13. These show the laminar level of unity upstream of the flap interaction region for both configurations. However, the promotion of transition by the flap increases the local relative fluctuation amplitude well above that on the corresponding flat plate.

For the $\alpha = 10°$, $\beta = 0°$, the flat plate boundary layer at x/L = 1.23 exhibits intermittency throughout the run, as shown in figure 7-12. This suggests that the transition process is well advanced. The heat transfer rate history for the $\alpha = 10°$, $\beta = 5°$ configuration at x/L = 1.23 (see figure 7-12) shows a decrease in the fluctuation amplitude relative to the $\alpha = 10°$, $\beta = 0°$ configuration. The mean heat transfer level remains close to the predicted turbulent level during the run. Thus the transition process for the $\alpha = 10°$, $\beta = 5°$ is either complete or close to completion.

The axial distribution of the relative fluctuation amplitudes for the $\alpha = 10°$, $\beta = 0°$ and the $\alpha = 10°$, $\beta = 5°$ configurations are shown in figure 7-13. Similar fluctuation levels are realised on the flat plate well ahead of the hingeline for the two configurations. However, on the flap there is a decrease in intermittency and hence in the fluctuation level as the boundary layer attains a fully turbulent status.

The agreement between the transitional status as inferred from fluctuation amplitude measurements and that inferred from heat transfer measurements suggests that the proposed fluctuation amplitude method provides an accurate reflection of the laminar or otherwise status of the boundary layer. Indeed, it allows the detection of the early stages of development of boundary layer transition.

The fluctuation amplitude method for detecting transition therefore forms a new and accurate tool in the diagnosis of boundary layer transition in flow regions characterised by strong axial pressure gradients.

Chapter 8

FLAP CONTROL EFFECTIVENESS

8.1 SHARP LEADING EDGE FLAT PLATE STUDIES [$\alpha = 0°$]

The pressure and heat transfer distributions along a sharp flat are shown in figure 8-1. These measurements were obtained with the leading edge of the flat plate located at the exit plane of the nozzle. The centreline pressure distribution is similar to that obtained by Needham (1965) and agrees with laminar weak interaction theory given by Beyer (1989).

The centreline heat transfer distribution agrees with predictions of Eckert's laminar reference temperature theory and remains well below the turbulent level along the entire length of the flat plate. The theoretical solutions are described in section 6.7. Thus, at $M_\infty = 8.2$, $Re_\infty/cm = 9.0 \times 10^4$, the boundary layer on a sharp flat plate at $\alpha = 0°$ is laminar.

8.1.1 Nozzle centreline flow characteristics

Although the centreline flat plate heat transfer distribution in figure 8-1 agrees with the predicted laminar variation, it exhibits periodic departures at x = 5 cm and x = 15 cm downstream of the nozzle exit plane. Richards (1967) observed similar variations in heat transfer on flat plates mounted on the nozzle centreline. The variations were also observed in centreline pitot pressure distributions conducted by Ledford (1973). The amplitude of the heat transfer variations was reduced when the model was mounted above the nozzle centreline. This is shown in figure 8-1 and confirms the focusing effects to be a highly localised centreline phenomena.

The contour of the Mach 8.2 nozzle is known to have an annular imperfection in its geometry upstream of the test rhombus. The interaction of this imperfection with the supersonic portion of the local boundary layer may generate characteristics which, due to the annular nature of the proturbance, are focused onto the centreline within the test rhombus.

In order to minimise the effects of the centreline flow variations on flat plate heat transfer distributions, all heat transfer studies presented in this thesis were conducted with the model mounted 0.5" above the nozzle centreline.

8.2 ATTACHED FLOW COMPRESSION CORNER INTERACTION [$\alpha = 0°$]

8.2.1 Flap shock structure

The presence of a flap or any sudden compressive deflection of the inviscid flow field creates an adverse pressure gradient. This pressure rise feeds upstream via the relatively thin subsonic portion of the boundary layer, referred to as the sublayer.

The adverse pressure gradient causes a loss of momentum and a subsequent thickening of the sublayer some distance upstream of the agency responsible for the pressure rise. Within the supersonic portion of the boundary layer, compression fans are generated to deflect the local streamlines past the thickening sublayer.

The fans induce a pressure rise which proceeds to further thicken the sublayer. The mutual interaction process between the pressure rise and the thickening boundary layer continues until equilibrium is attained.

Along with an increase in pressure, compression fans also cause an increase in the local temperature hence in wave speed. For supersonic flows, the small increase in wave speed together with the relatively high local Mach angles results in the compression waves coalescing well outside the boundary layer to form an oblique shock wave. This is evidenced in the $M_\infty = 1.5$ shockwave boundary layer interaction studies of Chapman (1957).

Under hypersonic conditions, the high Mach number increases the temperature ratio and hence the wave speed across a compression fan. Moreover, because of the high Mach number, the Mach angle is relatively small.

The combination of these effects results in the rapid coalescing of the compression waves close to, and ultimately, within the boundary layer. A schlieren flow visualisation of the latter case, along with a schematic diagram is shown in figure 8-2.

8.2.2 Pressure distribution

In figure 8-2, the single hingeline shock confirms the flow on the $\alpha = 0°$, $\beta = 5°$ configuration to be attached. The corresponding pressure distribution shows an increase in pressure from some distance upstream of the hingeline. The increase is due to the pressure rise associated with the thickening sublayer.

The final pressure level attained on the flap agrees well with the inviscid pressure rise associated with a Rankine-Hugoniot shock. The location at which the pressure gradient returns to zero after the hingeline interaction region is the downstream limit of the interaction. At this point, the streamlines at the outer edge of the boundary layer and in the inviscid flow field are turned parallel to the flap.

8.2.3 Flap boundary layer thickness

In the schlieren photograph of the $\alpha = 0°$, $\beta = 5°$ configuration, shown in figure 8-2, the thickness of the flap boundary layer is less than that on the flat plate. The decrease is due to the compressive effects of the increase in pressure on the flap decreasing the thickness of the supersonic portion of the boundary layer. The effect is further discussed in section 6.2.

8.2.4 Heat transfer distribution

For the $\alpha = 0°$, $\beta = 5°$ configuration shown in figure 8-2, the adverse pressure gradient in the laminar interaction region decreases the local heat transfer below that on a flat plate. This is due to the thickening of the boundary layer reducing the local wall temperature gradient. On the flap, the compression from the flap shock increases the local heat transfer above the flat plate level.

Using the measured pressure distribution, the laminar and turbulent flap heat transfer distribution were estimated from reference temperature theory using the method described in section 6.9.1. The theoretical estimates are shown alongside the measured flap heat transfer levels in figure 8-6. The agreement between the measurements and the predictions of laminar reference temperature theory confirm the flap boundary layer as laminar.

8.3 INCIPIENT SEPARATION FOR LAMINAR INTERACTIONS

An increase in the flap deflection angle from an initial attached flow condition increases the associated adverse pressure rise. This increases the loss of momentum in the upstream interaction region. If the strength of the adverse pressure gradient is sufficient, then the wall velocity gradient and hence the wall skin friction is reduced to zero at the hingeline. This is the limiting case between attached and separated flow and is referred to as the incipient separation condition. The incipient separation condition represents the design limit of a control surface. A discussion of the condition is given in section 5.2.3.

8.4 GENERAL CHARACTERISTICS OF WELL SEPARATED FLOWS

Increasing the flap deflection beyond the incipient separation angle causes the flow to separate. In well-separated flows, the skin friction is reduced to zero at locations some distance upstream and downstream of the hingeline. This is shown from the measurements of Holden (1992) in figure 8-4.

The computational study of Katzer (1989) has shown that in a well-separated interaction region, there is a significant increase in displacement thickness but little change in the associated momentum thickness. Thus, the recirculating fluid within the separation bubble is slow moving and possesses negligible momentum. As a result, the magnitude of the wall skin-friction in the separation region is small.

In entirely laminar interactions, the thickening of the boundary layer in the separated flow interaction region reduces the wall temperature gradient. This reduces the heat transfer within the separation region below the local flat plate level.

In the vicinity of the reattachment point, the shear layer is turned parallel to the flap by a strong reattachment shockwave. The strength of this shock causes a large increase in the local pressure, with reattachment occurring at the point of maximum pressure gradient.

On the flap, the compression from the reattachment shock regenerates the local velocity profile. In these regions, the flap skin friction and heat transfer signatures also increase and resemble their equivalent flat plate distributions.

8.5 THE EFFECT OF FLAP DEFLECTION

8.5.1 Three-dimensionality of the interaction region

A liquid crystal thermographs of the sharp leading edge $\alpha = 0°$, $\beta = 10°$ compression corner configuration is shown in figures 8-3. The thermograph was taken 25 ms after the start of the run whilst the equivalent schlieren photograph shown was taken 15 ms after the start of the run. Needham (1965) has shown that the variation in the length of separated flow during these periods is negligible.

8.5.1.1 Three-dimensional flow structures on the flat plate

In the thermograph of figure 8-3, a number of distinct streamwise striations are present upstream of the separation interaction region. The application of a uniform heat source prior to the run did not show any evidence of these striations. It was thus concluded that the striations arise due to the three-dimensionality of the aerodynamic heat transfer distribution during the run. The spanwise locations of the aerodynamic striations were repeatable.

Under the present hypersonic conditions, the leading edge displacement body is finite and causes a concave curvature of streamlines at the leading edge. Streamline concavity has been identified by Inger (1975) as a mechanism for the generation and amplification of spanwise arrays of Taylor-Goertler vortices. These vortices cause localised variations in heat transfer, and hence in surface temperature, leading to striations in surface temperature as observed on the flat plate section (upstream of the separation interaction region) in figure 8-3.

Simeonides (1992) found a strong correlation between spanwise variations in heat transfer and microscopic manufacturing imperfections in the sharp leading edge. The correlation led to the conjecture that the vortices are generated by these imperfections.

For the present study, in the absence of additional information (such as a microscopic analysis of the leading edge), it is conjectured that the striations on the flat plate are probably due to a combination of the effects of leading edge imperfections and of the concavity of streamlines leading to the birth and amplification of streamwise arrays of Taylor-Goertler vortices.

8.5.1.2 Three-dimensional flow structures in the interaction region

The thermograph for the $\alpha = 0°$, $\beta = 10°$ configuration, shown in figure 8-3 shows a number of periodic striations of high heat transfer downstream of the reattachment line. The spanwise wavelength of these striations is 0.7 ± 0.2 cm.

The flap striations in temperature are between the dark green and blue/colourless phase of the temperature response of the crystals and represent a 30% variation in spanwise temperature (°K) and hence in the heat transfer distributions. There is a correlation between the spanwise disturbances on the flat plate and those on the flap.

By assuming an initial periodic spanwise disturbance distribution in velocity (u', v' and w'), pressure and temperature of the form $u'(x,y,z,t) = u'(x,y,t)e^{i\phi z}$, Spall and Malik (1989) have shown that during the development of a hypersonic boundary layer on a curved compression ramp, the growth rate of the energy E associated with Taylor-Goertler vortices increases due to an adverse pressure gradient.

Based on these results, it is conjectured that the large spanwise variations in temperature observed on the flap in figure 8-3 are due to amplification of Taylor-Goertler vortices by the adverse pressure gradient of the interaction region.

8.5.2 Effect of flap deflection on separation

8.5.2.1 Laminar separation

The effect of flap deflection on the separation of a laminar boundary layer was studied by Holden (1992) at $M_\infty = 18.9$, $Re_\infty/cm = 0.6 \times 10^4$. The relatively high Mach number and the low freestream unit Reynolds number ensured that the interaction region was fully laminar. The skin-friction distribution in the separation interaction region is shown in figure 8-4.

The increase in flap angle results in earlier separation of the flow and a downstream movement of the reattachment point. The combined effect of these changes is an increase in the length of the separated flow region.

8.5.2.2 Transitional separation

In the present study, the effect of flap deflection on separation was studied at $M_\infty = 8.2$, $Re_\infty/cm = 9.0 \times 10^4$. In comparison to the tests of Holden (see section 8.5.2.1), the lower freestream Mach number and the higher freestream unit Reynolds number of the present study combine to produce interactions which rapidly become transitional following separation.

From the Needham & Stollery (1966) incipient separation correlation given in equation 5.01, the incipient separation condition for the present test configuration is attained at $\beta_{incip} = 6.6°$. In figure 8-5, an increase in the flap deflection angle from $\beta = 5°$ to $\beta = 10°$ changes the shock structure region from an attached-flow, single-shock structure for the former to a separated flow, dual-shock structure for the latter. The promotion of separation between these flap deflection angles is in agreement with the predictions of the Needham & Stollery (1966) incipient separation correlation.

The increased pressure rise associated with flap deflection causes a progressive upstream movement in the location of separation, as shown in figure 8-5. These photographs also show a small upstream movement in reattachment. This behaviour of reattachment contrasts the downstream movement of reattachment in fully laminar interactions, as shown in figure 8-4.

The small upstream movement in reattachment is due to the transition process increasing the lateral transfer of energy in the separated shear layer. This causes an earlier reattachment in comparison to an equivalent laminar boundary layer. This effect is further discussed in section 8.6.3.

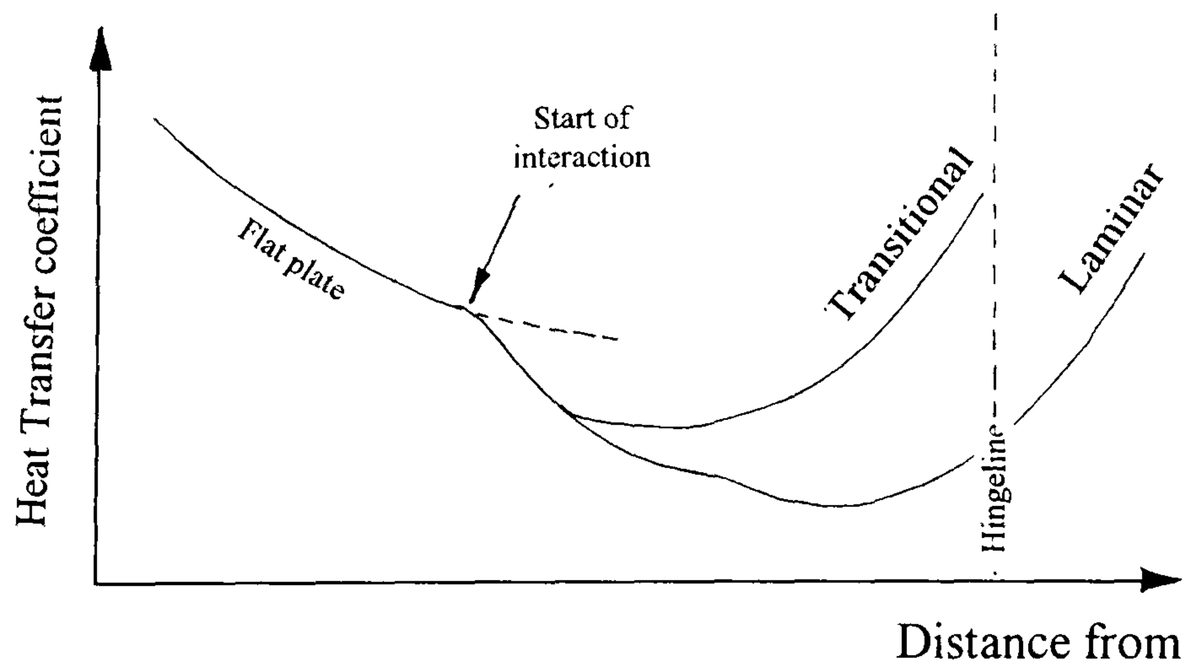

Diagram 8-1 The effect of shear layer transition on heat transfer distribution within the separated flow region

Heat transfer measurements in transitional interaction regions, shown in figure 8-6, show that the heat transfer rate at separation drops below the flat plate level. This is due to the laminar structure of the flat plate boundary layer.

However, it rises within the separation interaction region as transition of the shear layer occurs. Though still below the attached flow flat plate value, the heat transfer rate is now considerably greater than the fully laminar separated value, shown typically in diagram 8-1.

8.5.3 The effect of flap deflection on boundary layer transition

The current database on boundary layer transition suggests that for an attached interaction region, transition of the flap boundary layer is promoted by the presence and magnitude of the adverse pressure gradient (Spall and Malik, 1989) in the interaction region.

However, in a separated interaction region, alongside the destabilising effects of the adverse pressure gradient, transition is also promoted by the destabilising effects of the length of shear layer and of flow concavity in the reattachment region (Inger, 1975). A model of the transition process in a compression corner is shown in diagram 8-2. The flow on the flap displays transitional characteristics if the mechanisms in the interaction region produce sufficient destabilisation of the laminar boundary layer.

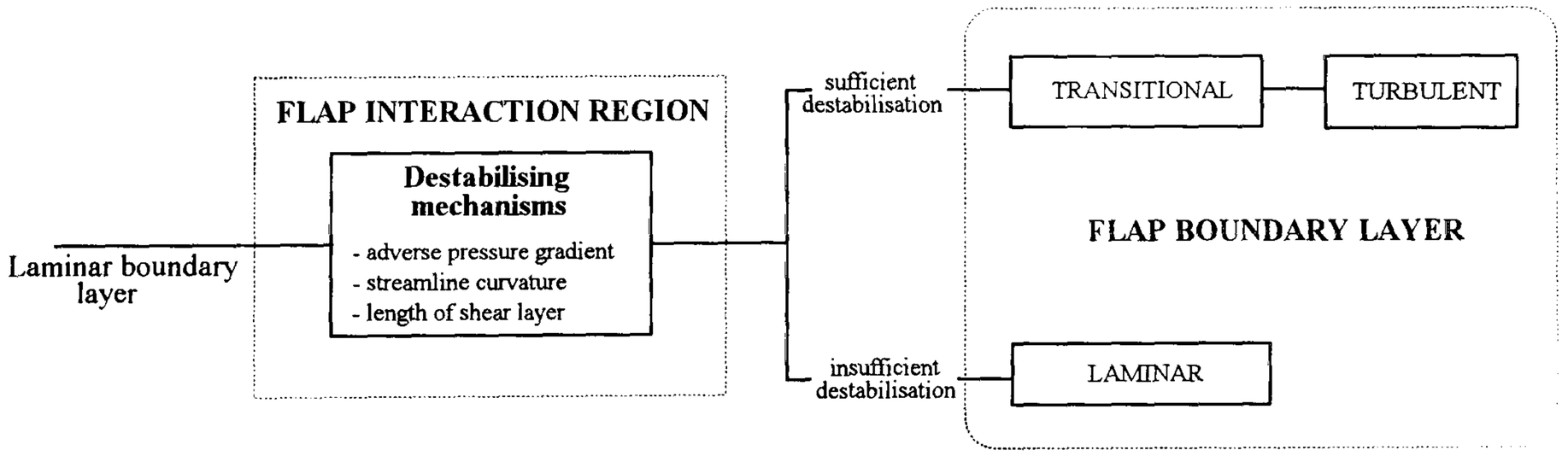

Diagram 8-2 Model of the transition process in an interaction region

8.5.3.1 Attached flow

In figure 8-6, the flap heat transfer distributions on the $\alpha = 0°$, $\beta = 5°$ configuration are compared with theoretical laminar and turbulent predictions. The absence of a plateau pressure in the interaction region of this configuration confirms the flow to be attached.

The measured flap heat transfer distributions agree with the predictions of laminar theory and remain well below the turbulent level along the entire length of the flap. Thus, the flap boundary layer on this configuration is laminar. As the flow is attached, the only mechanism promoting transition is the adverse pressure gradient in the interaction region. However, due to its relatively small magnitude, this pressure gradient is insufficient to promote flap boundary layer transition and hence the flap boundary layer remains laminar.

8.5.3.2 Separated flow

In figure 8-6, if the flap boundary layer for the $\alpha = 0°$, $\beta = 10°$ had remained fully laminar, then the increase in heat transfer on the flap (due to the local increase in pressure) would result in the laminar heat transfer level being realised.

Since the heat transfer measured on the flap of the $\alpha = 0°$, $\beta = 10°$ configuration exceeds the theoretical laminar level, the boundary layer must have become transitional following separation.

The heat transfer distributions shown in figure 8-9 show that at $M_\infty = 8.2$, $Re_\infty/cm = 9.0 \times 10^4$, the shear layer on a control flap configuration becomes transitional if its length increases beyond $(x-x_o)/L = 0.19$. For a flap deflection of $\beta = 10°$, the length of the shear layer is insufficient to cause transition. Therefore, the shear layer for this configuration is laminar upto reattachment and transition is triggered by the reattachment adverse pressure gradient.

Although the flap heat transfer on the $\beta = 10°$ configuration exceeds the laminar level, it remains below the theoretical turbulent level upto the end of the flap. Therefore, the transition process is incomplete at the end of the flap.

For $\beta = 15°$, figure 8-6 shows agreement between the measured and predicted turbulent heat transfer rates towards the end of the flap. This suggests that the transition process is complete at $x/L = 1.23$. Further deflection of the flap to $\beta = 20°$ produces turbulent heat transfer rates from $x/L = 1.125$. For $\beta = 25°$ and $\beta = 28°$, turbulent heat transfer rates are realised along the entire length of the flap. This suggests that for these configurations, transition to a fully turbulent flow must be complete within the separated shear layer prior to reattachment.

In summary, for transitional interactions, the heat transfer realised on the flap is a function of the flap pressure level and of the degree to which the transition process is complete. As the flap deflection angle is increased, the progressive improvement in agreement between the measured and predicted turbulent flap heat transfer level means that along with promoting the onset of transition, flap deflection also promotes the completion of the transition process.

8.6 FREE-INTERACTION REGION

Well-separated flows are characterised by a pressure plateau between the separation and reattachment points. The plateau signals that the separation streamline in this region has become straight.

In these cases, the pressure rise in the vicinity of separation is a function of the mutual interaction between the pressure rise and a local thickening of the boundary layer. Chapman et al (1957) describe this as a region of "free-interaction". The interaction is free in the sense that the pressure distribution in the separation region is independent of the cause of separation.

8.6.1 Shear layer separation angle for laminar interactions

In laminar studies at $M_\infty = 9.7$, Needham (1965) observed that under given freestream conditions, the pressure rise upto the hingeline for incipient separation [$\beta = \beta_{incip}$] is the same as the pressure rise upto the point of separation in a well-separated flow [$\beta > \beta_{incip}$]. This is shown schematically in figure 8-7. Thus, it is conjectured that the flow in the vicinity of the separation point for well-separated flows is analogous to the flow at the hingeline for the incipient separation condition.

Assuming this similarity, the laminar incipient separation model of Needham and Stollery (1966), which is described in section 5.2.3, is applicable to the free-interaction region of well- separated flows. This implies that at separation,

$$M_e \beta_{sep} \propto \bar{\chi}_{sep}^{1/2} \qquad [8.01]$$

In figure 8-8, a correlation of the separation streamline angle based on the parameters of equation 8.01 is shown alongside Needham & Stollery's incipient separation data.

Thus, for laminar interactions, an increase in the viscous interaction parameter by either an increase in Mach number or a decrease in the local Reynolds number increases the separation streamline angle. This moves the reattachment point away from the hingeline.

The similarity between the separation streamline and the incipient separation criterion has been illustrated by the Inger (1993) using a triple deck formulation of incipient and well-separated flows.

8.6.2 Shear layer transition in the interaction region

Using the start of the separation interaction region as the origin, pressure and heat transfer distributions in the interaction region have been plotted in non-dimensional form. These are shown in figure 8-9.

For well separated flows, i.e. with $\beta \geq 10°$, the pressure and heat transfer distributions exhibit similarity. In all cases, separation (identified as the point at which the pressure gradient upstream of the pressure plateau increases to a local maximum) occurs at $(x-x_0)/L = 0.12$.

Due to the laminar structure of the flat plate boundary layer, the heat transfer decreases at the start of the interaction region. Following separation, the heat transfer in the separated shear layer starts to increase from its initial laminar minimum at $(x-x_0)/L = 0.19$. This increase in heat transfer within the separation interaction region is due to the onset of shear layer transition.

The similarity of the heat transfer profiles in the interaction region suggests that at $M_\infty = 8.2$, $Re_\infty/cm = 9.0 \times 10^4$, shear layer transition is influenced by factors associated with the separation region only and appears to be independent of the reattachment process.

8.6.2.1 The effect of shear layer transition on the reattachment shock

In figure 8-10, for $Re_\infty/cm = 4.5 \times 10^4$, the absence of shock waves at the edge of the shear layer suggests that the shear layer is laminar upto reattachment. The reattachment shock angle (measured with respect to the freestream) is 35°.

An increase in the freestream unit Reynolds number to $Re_\infty/cm = 7.0 \times 10^4$ and to $Re_\infty/cm = 9.0 \times 10^4$ promotes transition within the shear layer. This is confirmed by the multiple shock waves present along the length of the shear layer. The reattachment shock angle (measured with respect to the freestream) for both of these configurations is 42°.

The increased energisation of the shear layer by transition causes early reattachment of the separated shear layer. This reduces the angle of the separation streamline and consequently increases the deflection required at reattachment. The latter increases the strength of the reattachment shock which, in turn, increases the reattachment pressure rise p_r/p_2 of transitional shear layers above those of comparable laminar layers.

8.6.3 The effect of shear layer transition on the length of separated flow

According to Mallinson et al. (1993), Katzer (1989) and Delery (1989), the length of separated flow in fully laminar interactions decreases with increasing Mach number and increases with increasing boundary layer thickness, Reynolds number, flap deflection angle, and wall to total temperature ratio. That is

$$\frac{L_{sep}}{\delta} = F\left[Re_{x_{st}}, \beta, \frac{T_w}{T_o}, \frac{1}{M_\infty}\right] \qquad [8.02]$$

Mallinson et al. (1993) suggest that small changes in the wall to stagnation temperature ratio have a negligible effect on the separation length and thus can be ignored. Katzer (1989) suggests that under hypersonic conditions, the non-dimensional separation length correlates as

$$\frac{L_{sep}}{\delta} \propto \left[\frac{M_{e,st}{}^3}{Re_{x,st}{}^{1/2}}\right]^{-1} \propto \left[\bar{\chi}_{e,st}\right]^{-1} \qquad [8.03]$$

Since $\beta \propto p_3/p_1$ and assuming that $\delta \approx \delta^*$ (valid for hypersonic flows only), the non-dimensional separation length variation is

$$\frac{L_{sep}}{\delta^*} = F\left[\bar{\chi}_{e,st}{}^{-1}, \frac{p_3}{p_1}\right] \qquad [8.04]$$

In figure 8-11, a variety of laminar well separated flow data in the hypersonic Mach number range $8.0 \le M_\infty \le 19$ is correlated using the parameters given in equation 8.04. For Holden's data, the flap pressure ratio was taken as the pressure well downstream of the reattachment

peak. The data of Johnson (1970), the flap pressure ratio was determined from inviscid shock theory with $M_\infty = 8.0$. Due to the relatively high Mach number and low unit Reynolds number of these studies, the associated interaction regions are fully laminar.

The laminar interaction data shows a correlates as

$$\frac{L_{sep}}{\delta^*_{x,st}} \propto \frac{1}{\chi_{e,st}} \left[\frac{p_3}{p_1}\right]^2 \qquad [8.05]$$

As was described in section 8.5.3.2, transition on the $\beta = 10°$ configuration occurred downstream of the reattachment. For this configuration, the laminar structure of the separated shear layer is reflected in the correlation of the separated flow length with that of entirely laminar interactions. Thus, for configurations with transition occurring downstream of reattachment, the separated shear layer acts as a fully laminar interaction upto the point of transition.

For the $\beta = 15°$, the non-dimensional separation length parameter $\left[L_{sep}\,\chi_{e,st}\right]/\delta^*_{e,st}$ is well below that for an equivalent laminar separation. Transition of the shear layer for this configuration was identified (see section 8.5.3.2) to be upstream of reattachment.

Needham (1965) and Roberts (1970) suggest that following separation in laminar interactions, the separation streamline is energised by velocity shear upto its reattachment on the flap. The occurrence of shear layer transition increases the lateral transfer of energy within the shear layer. This increases the energisation of the separation streamline and causes early reattachment, which decreases the length of separated flow relative to that for an equivalent fully laminar separation.

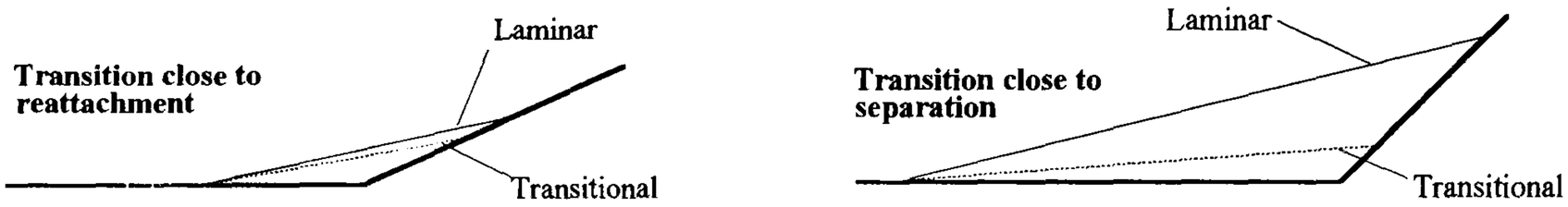

(a) low flap deflection (b) high flap deflection

Diagram 8-3 The effect of flap deflection and subsequent transition of the shear layer on reattachment

In section 8.5.3.2, it was shown that increasing the flap deflection angle promotes both separation and transition. For these configurations, the rapid occurrence of transition close to separation increases the length over which transition energises the separated shear layer. This causes a greater reduction in the separated flow length with respect to that on an

equivalent laminar interaction. Thus, the reduction in separated flow length from its laminar level increases with flap deflection, as shown schematically in diagram 8-3.

8.7 THE EFFECT OF INCIDENCE ON SHARP FLAT PLATE FLOWS

8.7.1 Pressure distribution

Pressure measurements on the flat plate at incidence are shown in figure 8-12. The measured distributions are compared with the predictions of weak interaction theory for a body at incidence. For a given incidence α, the generic theoretical form of this expression is

$$\frac{p}{p_\infty} = \left[\frac{p_e}{p_\infty}\right]_\alpha + \frac{A\bar{\chi}_{ex}}{2} \qquad [8.06]$$

where $(p_e/p_\infty)_\alpha$ is the inviscid flat plate pressure ratio from oblique shock theory. The flat plate pressure distributions at incidences of at $\alpha = 5°$ and $\alpha = 10°$ compare well with the predictions of weak interaction theory (see figure 8-12).

In section 6.1, it was shown that for a freestream Mach number $M_\infty = 8.2$, an increase in incidence decreases the local Mach number and increases the local unit Reynolds number. These effects combine to decrease the local viscous interaction parameter and hence to reduce the effects of viscous interaction with incidence.

8.7.2 Boundary layer thickness

The effect of incidence on the flat plate boundary layer was studied using schlieren flow visualisation with the limiting cut-off level. This enhanced the contrast between the strong density gradients present in the boundary layer and the density gradients of the shock layer. The photographs are shown in figure 8-13.

The thickness of the compressible boundary layer is reduced by incidence. This occurs due to the increase in compression with incidence and agrees with the observations of Bertram et al. (1961) and .

8.7.3 The effect of incidence on flat plate boundary layer transition

The effects of incidence on the transition of the flat plate boundary layer has been studied using schlieren flow visualisation, heat transfer distributions and root mean square (rms) fluctuations in the surface heat transfer distribution. The algorithms used in the rms analysis of heat transfer signals are discussed in section 7.8.

8.7.3.1 Flat plate at $\alpha = 0°$

The schlieren photograph of the flat plate at $\alpha = 0°$, shown in figure 8-13, shows the edge of the boundary layer to be well defined along its entire length. This suggests that the boundary layer is laminar. This is confirmed by the corresponding heat transfer distribution, shown in figure 8-14 which agrees with the predictions of laminar reference temperature theory. As the boundary layer remains laminar, the relative rms heat transfer fluctuation distribution remains constant along the length of the flat plate.

8.7.3.2 Flat plate at $\alpha = 5°$

The heat transfer distribution on the flat plate at $\alpha = 5°$, shown in figure 8-14, agrees with the predictions of laminar reference temperature theory upto $x/L = 1.05$. Therefore the boundary layer upto this point is laminar.

The observed increase in heat transfer from $x/L = 1.05$ is accompanied by an increase in the relative rms component of heat transfer in this region. The heat transfer time history at $x/L = 1.23$, shown in figure 7-12, shows that although the mean heat transfer rate remains at the laminar level, it increases to the turbulent level for short durations.

These intermittent increases are due to the generation of turbulent spots and characteristic of the onset of transition in a boundary layer (see section 5.1.1). The small but consistent changes in heat transfer and RMS fluctuation leads to the conclusion that the boundary layer on the $\alpha = 5°$ flat plate has become transitional at $x/L = 1.05$.

In spite of the onset of transition, the corresponding schlieren photograph for the $\alpha = 5°$ flat plate, shown in figure 8-13, does not show a sudden thickening of the boundary layer. The latter is a characteristic associated with transition of the boundary layer.

In flat plate transition experiments of Potter (1960) and Richards (1967) have demonstrated that the thickening of the boundary layer due to transition starts well downstream of the onset of transition. The delay between the onset of transition and the associated thickening of the boundary layer is responsible for its absence from the schlieren photograph of the $\alpha = 5°$ flat plate.

8.7.3.3 Flat plate at $\alpha = 10°$

For $\alpha = 10°$, the schlieren photograph, shown in figure 8-13 shows a sudden increase in boundary layer thickness from x/L = 0.75. This suggests that this boundary layer is transitional.

The heat transfer distribution for $\alpha = 10°$ flat plate is shown in figure 8-14. In the vicinity of the leading edge, the heat transfer distributions are in agreement with the predictions of laminar reference temperature theory and well below the corresponding turbulent level. Thus, close to the leading edge, the boundary layer on this configuration in initially laminar. From x/L = 0.65, there is a sustained increase in heat transfer. The rate of increase of the heat transfer rate in this region is initially small. However, after x/L = 1.1, it increases rapidly.

The spatial evolution heat transfer rate time histories on the $\alpha = 10°$ flat plate is shown in figure 7-11. The histories at x/L = 0.25 and at x/L = 0.41 show the mean heat transfer rate to remain at the laminar level. Thus the local boundary layer is fully laminar. The history at x/L = 0.85 shows that whilst the mean heat transfer rate stays at the laminar level, it increases close to the turbulent level for short durations. These intermittent increases arise due to the spontaneous formation and passing of turbulent spots over the surface mounted thin-film heat transfer gauges. Some of the underlying mechanisms associated with the formation of spots is discussed in section 5.1.1.

Further downstream, the increased shedding and passing of turbulent spots over the gauge causes large fluctuations in heat transfer between the local laminar and the local turbulent level. This is evidenced from the heat transfer rate history at x/L = 1.23. The increase in rms fluctuation distribution from x/L = 0.65 to x/L = 1.1 (see figure 8-14) is due to a build-up of turbulent spot behaviour as the boundary layer becomes transitional.

The high level of intermittency increases the mean heat transfer rate in the transition region above the corresponding laminar heat transfer level. However, as the heat transfer rate at the

trailing edge of the $\alpha = 10°$ flat plate, shown in figure 8-14, is below the predicted turbulent level, the transition process on this configuration is incomplete.

8.7.3.4 Flat plate at $\alpha = 15°$

The schlieren photograph for the $\alpha = 15°$ flat plate configuration is shown in figure 8-13. The location of the start of transition, derived from the thickening of the boundary layer, is upstream of its location at $\alpha = 10°$. Thus, transition is promoted by increasing incidence.

In summary, incidence promotes transition of the flat plate boundary layer. The promotion is due to the decrease in the local Mach number and the increase in the local unit Reynolds number which follow as the incidence is increased.

8.8 THE EFFECT OF INCIDENCE ON ATTACHED COMPRESSION CORNER FLOWS

8.8.1 Shock structure

Schlieren photographs of the $\beta = 5°$ configuration at incidences of 0, 5 and 10° are shown in figure 8-15. The photographs show an increase in the strength of the leading edge shock with incidence.

At $\alpha = 0°$, the leading edge shock is generated by viscous interaction. Due to the weak interaction conditions of the present tests, this leading edge shock is weak. At incidence, the shock is generated by geometrical incidence of the body and consequently its strength increases with incidence.

The schlieren photographs also show a single flap shock located at the hingeline. This indicates that for $\beta = 5°$, the flow remains attached at all the incidences tested. This is confirmed by the corresponding pressure distributions, shown in figure 8-16 which do not show the pressure plateau associated with separated flows.

8.8.2 Flap pressure ratio

Due to the attached flow structure on the $\beta = 5°$ configuration, the inviscid flow structure on the control flap configuration at incidence can be modelled as shown in diagram 8-4.

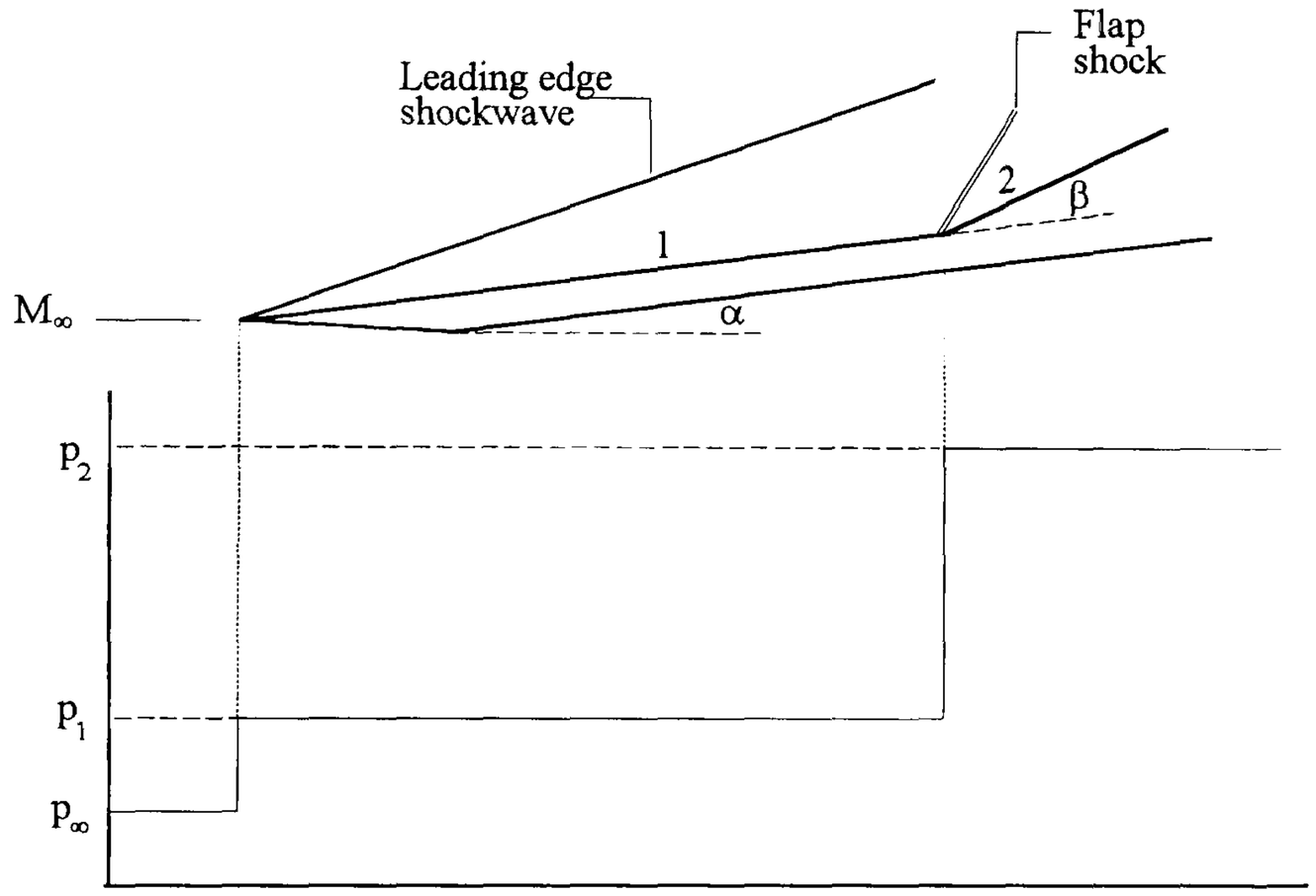

Diagram 8-4 Model of the inviscid flow structure on a control flap configuration at incidence

From oblique shock theory relations given by the Ames charts (1953), the angle of the leading edge shock (relative to the freestream) is

$$\cot\alpha = \tan\theta_1\left[\frac{(\gamma+1)M_\infty{}^2}{2\left(M_\infty{}^2\sin^2\theta_1\right)}-1\right] \qquad [8.07]$$

Also from oblique shock theory, the inviscid pressure ratio on the flat plate is

$$\frac{p_1}{p_\infty} = \frac{2\gamma M_\infty{}^2\sin^2\theta_1-(\gamma-1)}{\gamma+1} \qquad [8.08]$$

and the local Mach number on the at incidence is

$$M_1 = \frac{1}{\sin(\theta_1-\alpha)}\left[\frac{(\gamma-1)M_\infty{}^2\sin^2\theta_1+2}{2\gamma M_\infty{}^2\sin^2\theta_1-(\gamma-1)}\right]^{1/2} \qquad [8.09]$$

Considering the flap to be submerged in an "effective" freestream at the local flat plate Mach number, the flap shock angle is then given by the relationship

$$\cot\beta = \tan\theta_2\left[\frac{(\gamma+1)M_1^{\,2}}{2\left(M_1^{\,2}\sin^2\theta_2\right)}-1\right] \qquad [8.10]$$

and the flap pressure ratio (relative to the flat plate) is

$$\frac{p_2}{p_1} = \frac{2\gamma M_1^{\,2}\sin^2\theta_2-(\gamma-1)}{\gamma+1} \qquad [8.11]$$

The flap pressure ratio (relative to the freestream) can then be derived by combining equations 8.08 and 8.11. For a $\beta = 5°$ control flap configuration, the effects of incidence on the flat plate and the flap pressure distribution has been derived using the two shock model described above. This is shown in diagram 8-5.

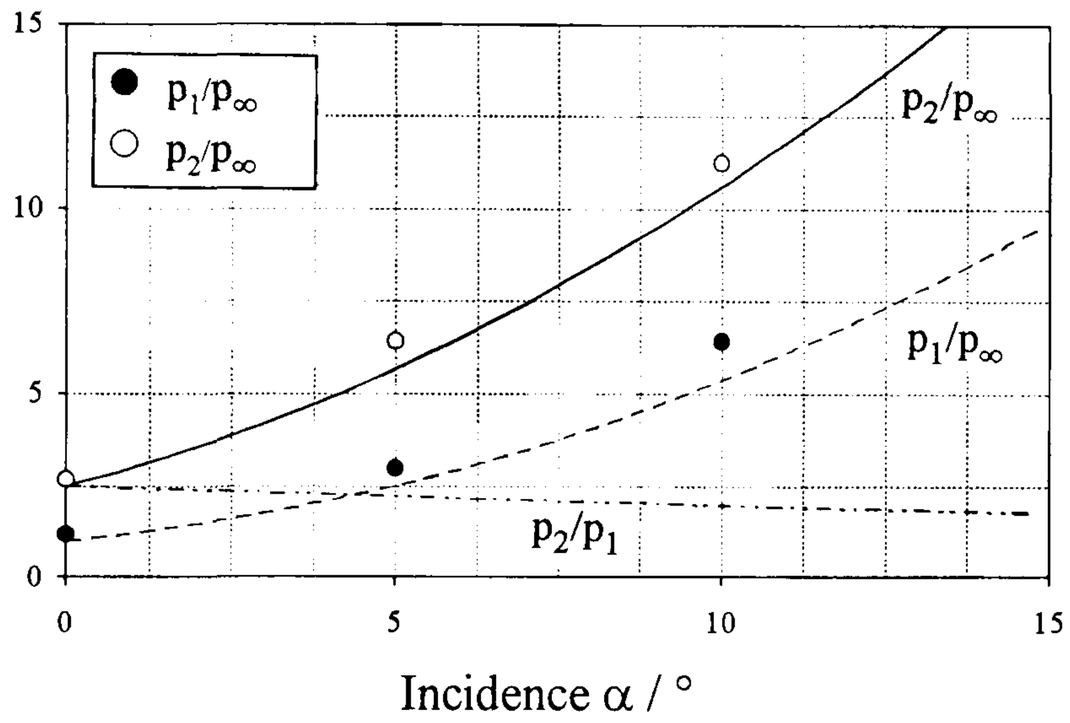

Diagram 8-5 The effect of incidence on inviscid flow pressure distribution on a control flap configuration ($M_\infty = 8.2$, $\beta = 5°$)

Due to an increase in the strength of the leading edge shock, the compression p_1/p_∞ increases with incidence. However, increasing incidence reduces the flat plate Mach number M_1. This reduces the compression ratio p_2/p_1 across the flap shock.

The experimental pressure distributions in the hingeline interaction region for the $\beta = 5°$ configuration at various incidences are shown in figure 8-16. In diagram 8-5, the pressure ratios well upstream and well downstream of the interaction region are compared with the predictions of the inviscid shock theory model.

For both the flat plate and the flap, the measured pressure ratios agree with the predictions of the approximate theory. Thus for the present tests, inviscid effects dominate the pressure distributions on the flat plate and on the flap.

8.8.3 Flap heat transfer and boundary layer transition

The effects of incidence on the transition of the flap boundary layer for the $\beta = 5°$ configuration was studied using surface heat transfer measurements. These are shown in figure 8-16. In figures 8-6, 8-17 and 8-18, the measured flap heat transfer levels are compared with theoretical predictions for fully laminar and turbulent interactions. The theoretical estimates were derived using the methodology described in section 6.9.1.

8.8.3.1 $\alpha = 0° \beta = 5°$ configuration

In the schlieren photograph of figure 8-15, the flap boundary layer for $\alpha = 0° \beta = 5°$ is well defined. The boundary layer thins through the interaction region due to the increase in pressure on the flap. Both of these effects suggest that the boundary remains laminar on the flap.

Due to the laminar structure of the flat plate boundary layer, the heat transfer rate at the start of the interaction decreases below the flat plate level. The correlation of the measured flap heat transfer rate with predictions from laminar boundary layer theory (see figure 8-6) confirms the flap boundary layer as laminar.

8.8.3.2 $\alpha = 5° \beta = 5°$ configuration

The schlieren photograph for the $\alpha = 5°$, $\beta = 5°$ configuration (see figure 8-15) shows the boundary layer to be well defined upto the hingeline. Immediately downstream of the hingeline, the boundary layer thins. This is due to the increase in pressure associated with the compression of the flap shock. The thinning behaviour is characteristic of a laminar boundary layer. The corresponding heat transfer distribution (see figure 8-16) shows a decrease in heat transfer below the flat plate level at the start of the interaction. This confirms the state of the boundary layer at the start of the interaction to be laminar.

The measured flap heat transfer distribution is well above the predicted laminar level from the start of the flap (see figure 8-17). Therefore, the flap boundary layer is transitional with the onset of transition being at the hingeline. The promotion of transition is due to the adverse pressure gradient in the interaction region imposed by the flap. The occurrence of transition is also evident in the corresponding schlieren photograph in figure 8-15. This shows a thickening of the flap boundary layer from x/L = 1.12. After this, the edge of the flap boundary layer becomes increasing irregular.

Since the measured heat transfer level at the end flap remains below the predicted turbulent level, the transition process is incomplete at the trailing edge.

8.8.3.3 $\alpha = 10°$ $\beta = 5°$ configuration

In the heat transfer distribution for the $\alpha = 10°$, $\beta = 5°$ configuration (see figure 8-16), the decrease in heat transfer in the upstream interaction region observed at lower incidences is absent.

In section 8.7.3, transition of the $\alpha = 10°$ flat plate boundary layer was confirmed to be well upstream of the hingeline. By increasing the lateral transfer of energy, transition generates a much fuller velocity profile. This makes the boundary layer more resistant to the flap adverse pressure gradient and thus limits the thickening of the interaction region upstream of the hingeline. This restriction of the interaction region is also reflected by the corresponding pressure distribution, shown in figure 8-16, which shows the flat plate pressure ratio to be maintained upto the hingeline.

The schlieren photograph of the $\alpha = 10°$, $\beta = 5°$ configuration (see figure 8-15) shows the flap boundary layer to be significantly thicker than on the flat plate. The edge of the flap boundary layer is ill-defined. Since the flat plate boundary layer is already transitional at the hingeline, the flap boundary layer is entirely transitional/turbulent.

Since the flap boundary layer is already transitional at the hingeline, the measured flap heat transfer level is always greater than the predicted laminar flap heat transfer level. This is shown in figure 8-18. At the end of the flap, the agreement between the measured and the turbulent heat transfer rates means that transition is complete and fully turbulent flow has been established.

In summary, for the $\beta = 5°$ attached flow configuration, small increase in body incidence promotes the transition of an initially laminar flap boundary layer. Further increasing the incidence promotes transition on the flat plate and accelerates the transition process on the flap. The latter may result in fully turbulent flow conditions being attained on the flap.

The promotion of flap boundary layer transition at incidence is due to an increased susceptibility of the initial flat plate boundary layer to transition and due to an increase in the adverse pressure gradient in the interaction region.

8.9 THE EFFECT OF INCIDENCE ON WELL SEPARATED FLOWS

The effects of incidence on well separated flows were studied at incidences of 0, 5 and 10° with a variety of flap deflection angles. The results of schlieren, pressure and heat transfer studies are shown in figures 8-6, 8-17 and 8-18 respectively.

For all the configurations studied, the measured heat transfer levels on the flap are compared with the predictions of laminar and turbulent reference temperature theories. The methodology of these predictions are described in section 6.9.1.

8.9.1 The effect of incidence on flap boundary layer transition in separated flows

The flap heat transfer distributions for the $\beta = 10°$ flap at incidences of 0°, 5° and 10° are shown in figure 8-20.

Since the measured flap heat transfer rate on the $\alpha = 0°$, $\beta = 10°$ configuration is between the predicted laminar and turbulent levels (see figure 8-6), the flap boundary layer is transitional. However, as the measured heat transfer level at the end of the flap is well below the turbulent level, the transition process at the end of the flap is incomplete.

For the $\alpha = 5°$, $\beta = 10°$ configuration, the measured flap heat transfer rates are well above the predicted laminar and close to the predicted turbulent level. Therefore, the flap boundary layer is transitional. The proximity of the measured heat transfer levels to the predicted turbulent level indicates that the transition process for this configuration is close to completion by the end of the flap.

Since the flat plate boundary layers for the $\alpha = 0°$ and the $\alpha = 5°$ configurations are laminar at the start of the interaction, the near completion of the transition process for the latter suggests that the promotion of transition of an initially laminar boundary layer is accelerated by incidence.

As was discussed in section 8.7.3.3, the $\alpha = 10°$ flat plate boundary layer became transitional from upstream of the hingeline. The energisation of the flat plate boundary layer by transition suppresses separation and thus produces a modest interaction region. The latter is evidenced by the merging of the separation and reattachment shocks (see schlieren photograph in figure 8-19) and by the absence of a plateau in the corresponding pressure distribution (see figure 8-20).

The flat plate heat transfer distributions of figure 8-14 show the trailing edge heat transfer rates to be below the predicted turbulent level. Therefore, the transition process on the $\alpha = 10°$ configuration is incomplete at the end of the flat plate. The heat transfer rates at the end of the flap of the $\alpha = 10°$, $\beta = 10°$ are well above the predicted laminar and close to the predicted turbulent level, as is shown in figure 8-18. Thus, transition of the flap boundary layer is well advanced and close to attaining a fully turbulent state. Therefore, the adverse pressure gradient of the interaction region for the configuration accelerates the transition process.

In summary, incidence accelerates the transition of the flap boundary layer for both laminar and transitional separations.

8.10 THE EFFECT OF INCIDENCE ON SEPARATION LENGTH SCALES

8.10.1 Laminar separation

In section 8.6.3, it was shown that the length of separated flow is affected by transition, flat plate to flap pressure ratio, $\chi_{e,st}$ and δ^*. Given the influence of incidence on all of these parameters, the effect of incidence on the length of separated flow is likely to be highly complex.

Hence, it was decided to investigate the effects of incidence on separation when the state of the boundary layer was known to be unaffected by transition. This was achieved using

the $M_\infty = 12.3$, $Re_\infty/cm = 3.3 \times 10^4$ nozzle. The higher Mach number and the lower unit Reynolds number produces by this nozzle delays boundary layer transition (see section 5.1).

Schlieren photographs of the $\beta = 15°$ configuration at incidences of 0°, 5° and 10° are shown in figure 8-22. The entirely laminar structure of the interaction is reflected in the well defined outer edge of the flat plate and the flap boundary layer at all incidences. The schlieren photographs show a decrease in the thickness of the flat plate boundary layer with incidence. This is due to the increased compression from the stronger leading edge shock. The photographs also show a dual shock separated flow structure for all configurations.

Using the location of the intersection of the separation shock and the flat plate boundary layer edge to identify separation suggests a modest delay in separation with incidence. Centreline pressure measurements are required to confirm this effect. The photographs conclusively show an upstream movement of reattachment. The combined effects of movements in separation and reattachment are a decrease in the length of the separated flow with incidence.

The laminar flow separated length correlation of figure 8-11 shows that for laminar interactions, the separation length varies as

$$\frac{L_{sep}}{\delta^*_{e,st}} \propto \frac{1}{\chi_{e,st}} \left[\frac{p_3}{p_1}\right]^2 \qquad [8.12]$$

Due to the high hingeline viscous interaction parameter generated by the Mach 12.3 nozzle ($\chi_{\infty L} \approx 2.6$), viscous interaction effects significantly alter the hingeline pressure and hence Mach number distribution on the flat plate.

The hingeline pressure ratio p_1/p_∞ on the viscous flat plate at incidence was determined by equation 8.06. The pressure ratio p_1'/p_∞ and Mach number M_1' (for the inviscid flow condition) was estimated from oblique shock theory.

Assuming the flow from downstream of the leading edge shock to the hingeline to be isentropic, the boundary layer edge Mach number at the hingeline of the viscous flat plate is

$$M_1^2 = \frac{2}{\gamma - 1}\left[\left(1 + \frac{\gamma - 1}{2} M_1'^2\right)\left(\frac{p_1}{p_1'}\right)^{-\frac{\gamma-1}{\gamma}} - 1\right] \qquad [8.13]$$

Using this hingeline Mach number, the flat plate to flap pressure ratio p_3/p_1 was derived using the methodology described in section 8.8.2. With this pressure ratio and a displacement thickness estimated from Bertram's (1961) relationship (given in section 6.2), the separation lengths for the laminar tests at incidence, derived from figure 8-22, were correlated with other laminar test data. This is shown in figure 8-23.

The correlation shows that due to the decrease in flap pressure ratio and δ^*, the separated flow length L_{sep} decreases with incidence. Further schlieren and pressure studies are required on laminar interactions at incidence to confirm this conclusion.

8.10.2 Scaling parameters for separated length scales in transitional interactions

The present study at $M_\infty = 8.2$, $Re_\infty/cm = 9.0 \times 10^4$ at various incidences revealed two distinctly different effects of transition on the length of the separation flow region. The length of separated flow for the transitional conditions of the present study are correlated using the parameters given in equation 8.05. This is shown in figure 8-26.

For laminar, type 1 and type 2 transition interactions, the viscous interaction parameter was taken as $\chi_{e,st} = M_e^3 C^{1/2}/(Re_{ex})^{1/2}$. For fully turbulent interactions, the viscous interaction parameter of Stollery and Bates (1974), $\chi_{e,st} = [M_e^9 C/Re_{ex}]^{2/7}$ was adopted. The boundary layer thickness of the turbulent boundary layer was estimated using the expression given by Anderson (1985). This was converted into a displacement thickness using Spence's correction factor given by Stollery (1975).

The correlation of figure 8-26 reveals four distinct modes of separated flow length scales.

Laminar interactions : For fully laminar interactions, the separation length increases rapidly with the flap pressure ratio. This is reflected by the results of Holden (1992) and by Johnson (1970). For these interactions, separation typically occurs close to the hingeline whilst the flow reattaches well downstream of the flap. This is shown in figure 8-4. The scaling suggests that for a given flap pressure ratio and boundary layer thickness, an increase in Mach number will decrease the length of separated flow in fully laminar and fully turbulent interactions. This is consistent with the observations of Miller et al (1964), Needham (1965) and Holden (1992).

Transitional interactions : For a transitional interactions, the adopted mode of behaviour of the separation length depends on the degree to which the interaction region has become

transitional. For type 1 transitional interactions, the length of separated flow decreases due early reattachment of the shear layer. This was discussed in section 8.6.3. For type 2 transitional interactions, transition occurs upstream of separation. The increased energisation of the boundary layer by transition delays separation and causes early reattachment. This dual effect of transition on both separation and reattachment reduces the separated length scale well below the corresponding laminar length scale.

Turbulent interactions : For fully turbulent interactions, the increased lateral transfer of energy makes the boundary layer more resistant to adverse pressure ratios. This produces an order of magnitude decrease in the length of the separated flow region as compared to corresponding laminar interactions.

8.10.3 The effect of incidence on transitional interaction length scales

In section 8.10, it was shown that the effects of incidence on laminar flow lengthscales are governed by the non-dimensional parameter $L_{sep}\chi_{e,st}/\delta^*$. In figure 8-26, the separated flow lengthscales derived from transitional studies at incidences of 5° and 10° (see figures 8-17 and 8-18) are correlated with other transitional studies at zero incidence.
The correlation shows for both type 1 and type 2 transitional interactions, the separated flow lengthscales observed on a body at incidence mimics that on a corresponding transitional configuration at zero incidence. Thus, the reduction in the length of separated flow by incidence for transitional interactions (see figures 8-24 and 8-25) occurs due to changes in the local viscous interaction parameter and displacement body thickness with incidence.

8.11 BLUNT FLAT PLATE FLOWS ($\alpha = 0°$)

8.11.1 Pressure distribution

The blast effect (described in section 6.4) of a blunt leading edge creates a strong near normal leading edge shock. This increases the pressure levels over the flat plate, as shown in figure 8-27 and creates a favourable pressure gradient along the flat plate. The experimental pressure measurements are well predicted by second order blast wave theory Lukasiewicz (1961) and by zero-order theory as proposed by Cheng et al (1961). The blast analogy and its various approximations are discussed in section 6.4.

8.11.2 Heat transfer distribution

The surface heat transfer distributions for sharp and blunt leading edge flows are compared in figure 8-27. The increase in heat transfer near the leading edge of the blunt flat plate is due to the increase in pressure and suggests the prevalence of strong bluntness effects in this region of the body.

From zero order theory, Cheng et al (1961) give the laminar heat transfer over a blunt flat plate as

$$C_H = \frac{0.119\kappa_\varepsilon^{1/3}\sqrt{\gamma\chi_\varepsilon}}{\varepsilon M^3\left[0.664+1.73\left(\frac{T_w}{T_o}\right)\right]} \qquad [8.14]$$

The predictions of this theory are shown alongside the measured heat transfer values in figure 8-27.

The agreement between the measured heat transfer rates and the predictions of equation 8.14 means that the blunt flat plate boundary layer is entirely laminar. In section 8.1, it was shown that the boundary layer over the sharp flat plate at $\alpha = 0°$ was laminar. Thus, under the present test conditions, bluntness ($Re_{\infty d} = 5.4 \times 10^4$) does not promote transition of the flat plate boundary layer.

8.12 THE EFFECT OF BLUNTNESS ON ATTACHED FLOWS ($\alpha = 0°$)

8.12.1 Flap shock structure

In section 6.6, it was shown that bluntness significantly alters the Mach number profile on a flat plate. The effects of the changes in bluntness on the flap shock structure are shown schematically in figure 8-28.

For supersonic flows over sharp flat plates, the small Mach number gradient between the sublayer and the edge of the boundary layer results in a small curvature of the compression wave within the boundary layer. Due to the absence of Mach number gradients outside the boundary layer, the compression fans become straight. The large Mach angle means that the compression waves are upright. The low freestream Mach number in supersonic flows

produces a small increase in temperature and hence wave speed across the compression fans. This delays coalescence of the waves and produces a well spread out flap shock.

For hypersonic flows over sharp flat plates, the compression waves generated by the flap interaction process become highly swept (due to the low freestream mach angle) and lie close to the edge of the boundary layer. The absence of any Mach number gradients outside the boundary layer produces a straight flap shock in the inviscid flow outside the boundary layer.

In section 6.5, it was shown that the boundary layer edge Mach number on blunt flat plate is reduced from the hypersonic freestream value to supersonic values. This is due to a loss of reservoir pressure through the bow shock.

The reduction in local Mach number reduces Mach number gradients in the outer portion of the boundary layer and so reduces the sweep of the compression fans within the boundary layer. As a result, the boundary layer edge shock structure resembles that of a supersonic rather than a hypersonic flow.

The Mach number gradients in the entropy layer cause a curvature of the compression fans within the entropy layer. Well away from the surface of the blunt flat plate, the compression waves eventually coalesce to form a shockwave.

The effect of varying leading edge bluntness on the flap shock structure is shown in the schlieren photographs of figure 8-29. Even at the smallest bluntness tested (d = 2 mm), the angle of the flap shock increases above that on the sharp leading edge configuration. The increase in the shock angle is due to the reduced Mach number within the entropy layer.

Further increases in leading edge diameter thickens the entropy layer. This decreases the Mach number at a given height within the entropy layer and results in the flap shock becoming more upright.

8.12.2 Flap pressure distribution

The pressure distributions in the flap interaction region for the $\beta = 5°$ configuration with a sharp and a blunt leading edge are shown in figure 8-30.

For the blunt body, the pressure distribution upstream of the interaction region behaves in accordance with blast wave theory. Therefore, as with the sharp leading edge flat plate, the effects of the flap are limited to the interaction region.

For the blunt leading edge configuration, the final flap pressure level p_3/p_∞ is a function of the pressure rise across the flap shock p_3/p_2 and of the hingeline pressure p_2/p_∞ due to the blast effect of the leading edge.

From the Ames tables, the angle of the flap shock is given by

$$\cot\beta = \tan\theta_{eL}\left[\frac{(\gamma+1)M_{eL}{}^2}{2\left(M_{eL}{}^2\sin^2\theta_{eL}-1\right)}-1\right] \qquad [8.15]$$

where M_{eL} is the local Mach number at the edge of the hingeline boundary layer. From oblique shock theory, the pressure ratio across the flap shock is given by

$$\frac{p_3}{p_2} = \frac{2\gamma M_{eL}{}^2\sin^2\theta_{eL}-(\gamma-1)}{(\gamma+1)} \qquad [8.16]$$

It was shown in section 6.5 that the loss of reservoir pressure across the normal leading edge shock reduces the hingeline Mach number on the blunt configuration to $M_{eL} = 3.4$. Assuming the flap on the blunt configuration to be submerged in an "effective" supersonic freestream at the hingeline Mach number, the pressure ratio p_3/p_2 across the flap shock is 1.7.

From Oshima's blast analogy given in equation 6.09, the hingeline pressure ratio on the blunt leading edge configuration is $p_2/p_\infty = 1.4$. Thus the flap pressure ratio for the blunt configuration is $p_3/p_\infty = 2.4$. This compares well with the measured flap pressure level, as shown in figure 8-30.

The reduction in the flap pressure ratio p_3/p_∞ due to bluntness occurs due to the reduced hingeline Mach number. This decreases the pressure ratio p_3/p_2 across the flap shock and thus decreases the overall pressure realised on the flap.

It is noted that, for this configuration the effects of the entropy layer Mach shear interaction (see section 6.6) on the flap pressure distribution are negligible. This is due to relative weakness of the flap shock.

8.12.3 Flap heat transfer distribution

The heat transfer distributions for the $\alpha = 0°$, $\beta = 5°$ configuration with a sharp and d = 6 mm blunt leading edge is shown in figure 8-30. The upstream interaction region shows the characteristic initial decrease in heat transfer associated with a laminar boundary layer. The decrease is due to laminar structure of the respective flat plate boundary layers.

The compression associated with the flap shock increases the heat transfer on the flap. In figure 8-6, the measured flap heat transfer level for the sharp leading edge configuration agrees with the prediction of laminar theory. Thus the flap boundary layer for the sharp configuration is laminar. A similar comparison of the flap heat transfer measurements for the d = 6 mm blunt leading edge configuration (shown in figure 8-34) confirms the flap boundary layer on the blunt configuration to also be laminar. The theoretical predictions for the blunt configuration were based on the theory described in section 8.12.2.

Thus, for the $\alpha = 0°$, $\beta = 5°$ configuration, the flap boundary layer is laminar for both the sharp and the blunt leading edges. In both cases, the strength of the flap adverse pressure gradients is insufficient to promote transition of the flap boundary layer.

8.12.4 The effect of bluntness on spanwise heat transfer variations

Surface thermographs of the $\alpha = 0°$, $\beta = 5°$ configuration with the sharp and 6.0 mm blunt leading edges are compared in figure 8-31. These thermographs were obtained using HALLCREST R18C10W liquid crystals. The technique employed is described in section 7.5.

For the sharp configuration, the thermograph shows small variations in the spanwise temperature distribution upstream of the flap interaction region. These arise due to the presence of streamwise vortices, generated by leading edge imperfections and by streamline curvature associated with a finite displacement body.

The flap of the sharp configuration shows a number of highly localised striations with a wavelength between 8 and 15 mm. The correlation of the spanwise locations of the striations on the flap with striations on the flat plate implies that the flat plate vortices are convected through the adverse pressure gradient interaction region.

The thermograph for the blunt leading edge configuration, shown in figure 8-31, shows an increase in the intensity of the spanwise variations in temperature on the flat plate. These variations are highly periodic with a wavelength of 14 mm.

These spanwise variations in heat transfer may be associated with streamwise vortices, similar in structure to that shown in figure 8-32. The vortices arise due to streamline curvature associated with the blunt leading edge region of the body. These vortices are similar to the contra-rotating Taylor-Goertler vortices which arise due to streamline concavity in the reattachment region of separated supersonic and hypersonic flows. The latter have been observed by Ginoux (1969), Coet (1992) and by Simeonides (1992).

8.12.4.1 Streamwise heat transfer fluctuations

In section 7.8, it was demonstrated that heat transfer fluctuation observations from thin-film gauges are an accurate means of diagnosing the intermittency from turbulent spots and so provide an early indication of boundary layer transition on flat plates and on compression corners.

The thin-film heat transfer rate histories at various streamwise locations on the sharp and the d = 6.0 mm blunt leading edge $\alpha = 0°$, $\beta = 5°$ configurations are shown in figure 8-33. The RMS heat transfer fluctuation ratio is also shown. The steady increase in fluctuation amplitudes from x/L = 1.12 for the $\alpha = 0°$, $\beta = 5°$ sharp leading edge configuration means that the onset of transition of the boundary layer has started.

In spite of the increase in heat transfer disturbances during the run, the mean heat transfer rate remains at the predicted laminar level (see figure 8-6). Thus, the transition process remains in its infancy at the end of the flap.

The increase in fluctuation amplitude from the hingeline for the d = 6.0 mm blunt leading edge configuration means that the onset of intermittency occurs immediately upon interaction with the flap adverse pressure gradient. Stability analysis by Spall and Malik (1989) has shown that adverse pressure gradients cause a significant destabilisation of Taylor-Goertler vortices.

Therefore, it is conjectured that the increased heat transfer disturbances on the flap is due to the breakdown of the streamwise vortices by the flap adverse pressure gradient.

8.13 THE EFFECT OF BLUNTNESS ON MODERATELY SEPARATED FLOWS

8.13.1 Flap pressure distribution

The pressure distributions on the $\alpha = 0°$, $\beta = 10°$ configuration are shown in figure 8-37. This shows that the final pressure realised on the flap is significantly decreased by leading edge bluntness.

The predicted flap pressure level shown for the blunt configuration is based on the "effective" supersonic freestream model described in section 8.12.2. The agreement between the predictions of this model and the measured flap pressure ratio means that the decrease in the flap pressure ratio due to bluntness is due to the reduction in hingeline Mach number. The latter occurs due to the loss of reservoir pressure across the bow shock.

8.13.2 Flap heat transfer distribution

The heat transfer distributions for the $\alpha = 0°$, $\beta = 10°$ sharp and blunt leading edge configurations are shown in figure 8-37. For both configurations, there is a reduction in heat transfer in the upstream interaction region. This is due to the laminar state of their respective flat plate boundary layers.

The flap heat transfer measurements for the sharp leading edge configuration are compared with the predictions of laminar and turbulent theories in figure 8-6. Since the measured heat transfer rates on the flap exceed the predicted laminar level, the flap boundary layer is transitional.

Thus , as the boundary layer was laminar at the start of the interaction, transition has been promoted by the separated interaction region. However, since the measured heat transfer level at the end of the flap is below the predicted turbulent heat transfer level, the transition process is incomplete at the trailing edge.

The heat transfer measurements for the d = 6.0 mm blunt leading edge $\alpha = 0°$, $\beta = 10°$ configuration are compared with laminar and turbulent predictions in figure 8-34. As the

measured flap heat transfer rates are well above the predicted laminar level, the flap boundary layer on the blunt configuration is transitional.

The proximity of the measured rates to the predicted turbulent rates indicates that the transition process is well advanced and may be close to completion at the end of the flap. Therefore, the flap transition process on the blunt configuration is further advanced compared to the corresponding sharp leading edge configuration.

In spite of the more advanced state of transition on the blunt configuration, the comparison of figure 8-37 shows the heat transfer rate on the blunt configuration to be well below that on the sharp configuration.

The flap heat transfer rate is directly proportional to the local pressure ratio. The reduction in the flap pressure ratio for the blunt leading edge configuration (due to the lower hingeline Mach number) is responsible for the observed reduction in flap heat transfer rate.

8.13.3 The effect of bluntness on separation

In figure 8-36, the dual interaction shock structure of the sharp configuration indicates the flow to be well separated. Separation is confirmed by the presence of a plateau in the pressure between the separation and reattachment points (see figure 8-37).

An increase in the leading edge diameter to d = 2.0 mm delays separation from x/L = 0.85 to x/L = 0.93 and causes early reattachment on the flap (see figure 8-36). Further increasing the leading edge diameter suppresses separation.

The suppression of separation is characterised by the presence of a single shock at the hingeline and is evident in the photographs for the 4 mm and the 6 mm configurations. For the d = 6 mm configuration, the suppression of separation is confirmed by the absence of a pressure plateau in the corresponding pressure distribution, shown in figure 8-37.

The flap pressure ratio is critical to boundary separation on bluntness dominated configurations. For the $\beta = 10°$ configuration, the reduction in the flap pressure ratio by increasing leading edge bluntness causes the progressive reduction and the ultimate suppression of separation. This effect is further discussed in section 8.14.3.

8.14 THE EFFECT OF BLUNTNESS ON WELL-SEPARATED FLOWS

8.14.1 Pressure distribution

The pressure distributions of figure 8-39 show the flap pressure ratio for the blunt configuration to be well below that for the sharp configuration.

The hingeline Mach number for the blunt configuration is 3.4 (see section 6.5). Assuming the flap on the blunt configuration to be submerged in an "effective supersonic freestream" at the hingeline Mach number, the oblique shock theory method described in section 8.12.2 gives the flap pressure ratio to be $p_3/p_\infty = 9.1$. This is shown in figure 8-39.

The agreement between the predictions of the "effective supersonic freestream" model with the measured pressure distribution immediately downstream of reattachment confirms the reduction in flap pressure ratio on the blunt configuration to be the result of the reduction in hingeline Mach number. The latter arises due to the loss of reservoir pressure at the leading edge shock.

The pressure distribution on the blunt leading edge configuration (see figure 8-39) shows a secondary increase in pressure following reattachment. This is due to the Mach shear interaction effect and is further discussed in section 8.16.

8.14.2 Heat transfer distribution and flap boundary layer transition

In the heat transfer distributions for the sharp and the blunt leading edge $\beta = 25°$ configurations, shown in figure 8-39, the laminar structure of the corresponding flat plate boundary layers (see laminar heat transfer distributions in figure 8-27) results in a decrease in heat transfer at the start of the interaction region.

In figure 8-6, the agreement of the measured flap heat transfer rates on the sharp $\beta = 25°$ configuration with predictions from turbulent theory confirm the flap boundary layer as turbulent. Similar agreement for the blunt configuration between the measured flap heat transfer rates and the predictions of turbulent theory (see figure 8-34) means that flap boundary layer transition on the blunt configuration is also complete.

In summary, for both the sharp and the blunt $\beta = 25°$ configurations, the onset of transition occurs following separation. In both cases, the transition process is complete prior to, or at, reattachment after which the flap boundary layer is fully turbulent. Since both flap boundary layers are fully turbulent, the significant decrease in flap heat transfer due to bluntness (see figure 8-39) must be due to the reduction in the flap pressure ratio.

8.14.3 Effect of leading edge bluntness on separation

Schlieren photographs of the $\alpha = 0°$, $\beta = 25°$ sharp leading edge configuration, shown in figure 8-38, show a dual shock well-separated flow structure in the interaction region. An increase in leading edge diameter to d = 2 mm delays separation and causes earlier reattachment. These changes combine to decrease the extent of the separated flow region. Further increases in the leading edge diameter delays separation and promotes early reattachment.

Thus, the net effect of increasing leading edge diameter is a dramatic reduction in the size of the separated region.

Pressure distributions for various leading edge geometries from the study by Holden and Moselle (1992) are shown in figure 8-40. The relatively high Mach number and the low unit Reynolds number of these tests produce entirely laminar interaction regions.

The distributions show that for "small" bluntness, an increase in the leading edge diameter causes a progressive increase in the length of separated flow. This is characterised by an upstream movement of separation and a downstream movement of reattachment. The reattachment pressure rise remains similar for the "small" bluntness geometries tested.

For "large" bluntness, an increase in the leading edge diameter causes a progressive delay in separation and an upstream movement in reattachment. The net effect is a substantial reduction in the extent of the separated flow region. For "large" bluntness, there is a significant reduction in the reattachment pressure rise with leading edge diameter.

In a classical theoretical study, Cheng et al (1961) found that the relative effects of leading edge bluntness and the viscous displacement effect are measured by the bluntness-viscous interaction parameter $\chi_\varepsilon/\kappa_\varepsilon^{2/3}$. The separation lengths and reattachment pressure ratio from the present study and from that of Holden & Moselle (1992) are correlated with Cheng's parameter in figure 8-41.

The figure clearly shows two branches - one associated with "small" bluntness and the other associated with "large" bluntness. For the former, changes in the separated flow length occur due to the changes in boundary layer edge conditions arising from the entropy layer generated by leading edge bluntness.

For "large" bluntness, the correlation shows a substantial decrease in the reattachment pressure ratio with bluntness. This decreases the length of separated flow.

In the present tests, even the d = 2 mm leading edge configuration acts as a "large" bluntness and although pressure tests were not conducted for the d = 2 and 4 mm leading edges, the correlation of figure 8-41 means that the decrease in the extent of the separated flow with leading edge bluntness, observed in figure 8-38 occurs due to a progressive reduction in the flap pressure ratio.

The correlation of figure 8-41 shows that the onset of the "small" bluntness condition in the present tests occurs at a lower value of $\chi_\varepsilon/\kappa_\varepsilon^{2/3}$, as compared with the data of Holden. This may be associated with the transitional nature of the present study.

8.14.4 Three-dimensionality of the separation interaction region

In figure 8-38, the separation shock for the d = 6 mm $\alpha = 0°$, $\beta = 25°$ configuration is diffuse and axially spread out. In figure 8-35, the schlieren photograph of this configuration is shown alongside its liquid crystal thermograph.

The thermograph shows a symmetrical three-dimensional separation front. The locations of the leading and trailing edges of the diffuse separation shock in the schlieren photograph correlate well with the leading and trailing edges of the start of the separation interaction region in the thermograph.

Thus the three-dimensionality of the separation interaction region is responsible for the diffuse structure of the separation shock. The three-dimensionality of the separation front is possibly due to the wider Mach cones on the blunt configuration. It is noted that the Mach cones do not affect the flow at the centreline.

8.15 THE EFFECT OF LEADING EDGE GEOMETRY ON INCIPIENT SEPARATION

The incipient separation condition for laminar and turbulent flows represents the limit of attached flow and an accurate diagnosis of the incipient separation flap angle is critical to the efficient aerodynamic performance of control surfaces.

In figure 8-36, the introduction of "large" bluntness reduced the well-separated flow of the sharp leading edge configuration to an attached flow for the d = 6 mm blunt configuration. Therefore, bluntness must influence the incipient separation behaviour of control surfaces submerged within the entropy layer flow field.

In figure 8-42, the separated flow lengths for various bluntness are plotted. The incipient separation flap angle is defined as the greatest flap deflection angle for which separated flow length is zero. This is derived from the separated flow length curves by extrapolation to the x-axis, as shown in figure 8-42.

The extrapolation shows that, for "large" bluntness, the incipient separation flap angle increases with leading edge diameter. It is conjectured that than this is due to the progressive reduction in flap pressure ratio (and hence in the adverse pressure gradient) with leading edge bluntness.

8.16 THE MACH SHEAR INTERACTION EFFECT

8.16.1 The effect of Mach shear on flap pressure distribution

The pressure distribution for the 6 mm, $\beta = 25°$ configuration, shown in figure 8-39, shows a secondary increase in pressure following reattachment. A similar effect is observed in the large bluntness measurements of Holden and Moselle (1992), shown in figure 8-40.

Hayes and Probstein(1959) demonstrated that the interaction between a Mach shear and a shock produces a reflected and a transmitted compression wave (see section 6.6.2). The former is responsible for the secondary increase in pressure following reattachment.

The predicted pressure distribution from the Mach shear interaction model described in section 6.6.2.1 is shown in figure 8-43. The Mach shear profile at the hingeline has been estimated by using the experimental pitot pressure derived Mach number profile correlation of figure 6-10.

The inviscid nature of the model results in its inability to predict the pressure rise due to separation. However, the predicted pressure distribution following reattachment agrees with the measured pressure to within ± 10% along the length of the flap. The agreement confirms the Mach shear interaction effect as the cause of the secondary pressure rise on the flap.

8.16.2 The effect of flap deflection on Mach shear interaction.

Pressure distributions for d = 6.0 mm with various flap angles are shown in figure 8-36. Qualitative comparisons of these distributions shows that the secondary rise in pressure following reattachment increases with flap deflection angle.

The measured pressure level at x/L = 1.06 (immediately downstream of reattachment) and at x/L = 1.22 (close to the trailing edge) are shown in figure 8-44 for various flap deflection angles. This shows that the pressure difference between the front and the rear of the flap increases as the flap deflection angle is increased.

The Mach shear interaction model described in section 6.6.2.1 predicts the pressure distribution at x/L = 1.06 to within ± 5%. The pressure at the end of the flap (x/L = 1.22) is determined by the Mach shear interaction effect of the entropy layer.

Using an entropy layer Mach shear profile derived from the correlation of figure 6-10, the pressure distribution at the end of the flap was predicted using the model described in section 6.6.2.1.

The predictions agree with the measurements to an accuracy of ± 10%. This is sufficiently accurate to allow engineering predictions of the effects of entropy layer Mach shear. Therefore, the Mach shear interaction model may also be used as an engineering tool to estimate the effectiveness of controls in bluntness dominated flows.

8.17 THE EFFECTS OF INCIDENCE ON BLUNT FLAT PLATE FLOWS

8.17.1 Leading edge shock structure

The combined effects of incidence and bluntness on the leading edge shock structure are shown in figure 8-45. For all incidences, the blunt configuration shows a detached leading edge shockwave whilst equivalent sharp configuration retains an attached leading edge shock. Thus, the flow over the sharp plate at all incidences is characterised by a shock layer whilst that over the blunt plate is characterised by an entropy layer embedded within a shock layer.

8.17.2 Pressure distributions

Pressure distributions for the d = 6 mm blunt flat plate at various incidences are shown in figure 8-46. The measurements are compared with the predictions from Bade's (1975) analytic solution. This gives the pressure ratio on a blunt flat plate at incidence as

$$\frac{p}{p_\infty} = \frac{(\gamma+1)\gamma M_\infty{}^2\alpha^2}{2}\left[1+\frac{0.382}{\alpha^2}\left(\frac{2\varepsilon C_D d}{(\gamma+1)x}\right)^{2/3}\right] \qquad [8.17]$$

where α is in radians.

The analytic solution shows that the pressure distribution on a blunted body is a combination of the bluntness and the incidence effects. The former is governed by the blast analogy parameter $M_\infty{}^2(C_D d/x)^{2/3}$ whilst the latter is governed by the hypersonic similarity parameter $M\alpha$. Predictions from the analytic solution agree well with pressure measurements on the flat plate, as shown in figure 8-46.

At $\alpha = 0°$, the effects of leading edge bluntness dominate the pressure distribution along the entire body. However, at $\alpha = 5°$ and $\alpha = 10°$, the pressure distribution for the blunt configurations overexpand beyond the equivalent sharp leading edge pressure level.

The leading edge flow structure associated with a blunt flat plate at incidence is shown in the schematic diagram of figure 8-50. Following the deflection by the leading edge shock, the

streamlines in the vicinity of the leading edge are turned parallel to the flat plate by a Prandtl-Meyer expansion fan.

From the model described in section 6.5, the hingeline Mach number on the surface of the blunt flat plate at $\alpha = 0°$ was found to be 3.4. From the Ames tables, the associated Prandtl-Meyer function is

$$(M_{eL})_{\alpha=0°} = 3.4 \Rightarrow [\upsilon_L]_{\alpha=0°} = 57^{\circ} \qquad [8.18]$$

Therefore, at $\alpha = 5°$ and $\alpha = 10°$, the hingeline Mach number is

$$[\upsilon_L]_{\alpha=5°} = 57^{\circ} - 5^{\circ} \Rightarrow (M_{eL})_{\alpha=5°} = 3.12 \qquad [8.19]$$

$$[\upsilon_L]_{\alpha=10°} = 57^{\circ} - 10^{\circ} \Rightarrow (M_{eL})_{\alpha=10°} = 2.85 \qquad [8.20]$$

From the isentropic flow relations, the pressure ratio at x = L for the $\alpha = 5°$ can be written as

$$\left[\frac{P_o}{p_{eL}}\right]_{\alpha=0°}\left[\frac{p_{eL}}{P_o}\right]_{\alpha=5°} = \left[\frac{1+\frac{\gamma-1}{2}(M_{eL})_{\alpha=0°}}{1+\frac{\gamma-1}{2}(M_{eL})_{\alpha=5°}}\right]^{\frac{\gamma}{\gamma-1}} \qquad [8.21]$$

Since the flow at the edge of the entropy layer passes through the normal leading edge shock, the reservoir pressure along the boundary layer edge streamlines on a blunt configuration at $\alpha > 0°$ is equal to that downstream of a normal shockwave.

This is the same as the boundary layer edge reservoir pressure at $\alpha = 0°$. Therefore, the pressure relationship in equation 8.21 can be reduced to

$$\frac{[p_{eL}]_{\alpha=5°}}{[p_{eL}]_{\alpha=0°}} = \left[\frac{1+\frac{\gamma-1}{2}(M_{eL})_{\alpha=0°}}{1+\frac{\gamma-1}{2}(M_{eL})_{\alpha=5°}}\right]^{\frac{\gamma}{\gamma-1}} \qquad [8.22]$$

The hingeline pressure ratio at $\alpha = 0°$ can be determined from the quasi-similarity blast analogy of equation 6.09. Substitution of the Mach numbers derived by the Prandtl-Meyer expansion method of equations 8.19 and 8.20 a gives a hingeline pressure ratio of

$$(p_{eL}/p_{\infty})_{\alpha = 5°} = 2.3 \text{ and } (p_{eL}/p_{\infty})_{\alpha = 10°} = 3.9 \qquad [8.23]$$

These predictions at within ±10% agreement with the measurements shown in figure 8-46. Thus, the overexpansion of the flow on a blunt flat plate at incidence is due to the Prandtl-Meyer expansion fan. Eventually, the pressure level returns to its oblique shock value. However, as these and other tests show, the distance to recovery can be very large and depends on ($C_D d/x$)

8.17.3 Heat transfer distribution and boundary layer transition

Heat transfer distributions over the 6 mm blunt flat plate at various incidences are shown in figure 8-47. The measurements are compared against predictions from Bade's (1975) analytic solution. This is derived from Cheng et al's (1961) zero order theory and gives the laminar heat transfer on a blunt configuration at incidence as

$$\frac{2}{\gamma+1}\frac{1}{\gamma^{1/2}}\frac{M_\infty{}^2}{\bar{\chi}_d}\cdot\left(\frac{\varepsilon C_D}{\alpha^5}\right)^{1/2} C_H = \frac{0.332(1+0.382/\varphi)}{\varphi^{1/4}(1.145+\varphi)^{1/2}} \qquad [8.24]$$

where

$$\varphi = \alpha^2\left(\frac{\gamma+1}{2}\cdot\frac{x}{\varepsilon C_D d}\right)^{2/3} \qquad [8.25]$$

and α is in radians.

In figure 8-47, the heat transfer fluctuation distribution for the blunt flat plate at $\alpha = 5°$ shows no increase in fluctuations. Therefore, the boundary layer on this configuration is entirely laminar. In section 8.7.3, the boundary layer on the equivalent sharp flat plate was diagnosed as transitional. Therefore, for a flat plate at $\alpha = 5°$, bluntness delays transition.

In section 8.7.3, the boundary layer on the $\alpha = 10°$ sharp flat plate was diagnosed as transitional from x/L = 0.63. The fluctuation distributions for the blunt plate at $\alpha = 10°$, shown are shown in figure 8-47. This shows an increase in heat transfer and fluctuation amplitude from x/L = 0.50. Therefore, the boundary layer on the blunt flat plate at $\alpha = 10°$ is also transitional. In summary, bluntness delays transition of the flat plate boundary layer at $\alpha = 5°$ but has little effect on transition at $\alpha = 10°$.

At $\alpha = 0°$, the measured heat transfer rates agree with the laminar predictions of Bade's solution upto x/L = 0.62 after which all the measurements are somewhat above the theoretical laminar level. There are similar differences between the measured and predicted heat transfer distributions for the $\alpha = 5°$ configuration. The fluctuation distributions on both of these configurations remain constant.

Therefore, the differences between the measured and predicted heat transfer distribution arise not due to transition but due to the approximate nature of the curve fitted by Bade (1975) and caution must be exercised in diagnosing boundary layer transition on blunt plates at incidence using departures from the laminar heat transfer solution of Bade (1975). The ideal diagnostic for this purpose is the heat transfer fluctuation parameter.

8.17.4 Downstream limit of bluntness

The interplay between bluntness and incidence dominated flows can be judged by using Bade's (1975) incidence parameters, as shown in figure 8-48.

At $\alpha = 5°$, the pressure distribution near the leading edge of the plate is dominated by the leading edge bluntness effect. Further downstream, the incidence effect starts to affect the pressure distribution. At $\alpha = 10°$, the pressure distribution along almost the entire length of the flat plate is primarily influenced by the incidence effect. Therefore, in the vicinity of the leading edge, the surface flow properties are dominated by the bluntness whilst far away from the leading edge, the properties are dominated by the incidence.

8.17.5 The effect of incidence on entropy layer Mach shear

Deveikis et al (1973) studied the effects of incidence on entropy layer Mach shear using pitot pressure measurements along an axis normal to the surface of a blunt flat plate. The Mach number profiles derived from these measurements are shown in figure 8-49.

At $\alpha = 0°$ and $\alpha = 5°$, Mach shear extends from the edge of the boundary layer to the upper limit of the measurement domain. Thus the upper limit of the entropy layer is beyond the measurement domain at these incidences. At $\alpha = 10°$, the Mach number gradient decreases rapidly to zero at y = 6.2 cm. Above this, the local Mach number is equal to that predicted by oblique shock theory for a sharp flat plate. Thus, the upper limit of the entropy layer at

this incidence is at y = 6.2 cm. At α = 15°, the entropy layer Mach number gradient is reduced to zero at y = 5.0 cm. Again, the local Mach number for y > 5.0 cm agrees with the predictions of oblique shock theory for the corresponding sharp plate. Therefore, entropy layer thickness is reduced by incidence.

The entropy layer Mach number profiles of figure 8-49 show that both the Mach number and the Mach number gradient at a given height within the entropy layer increases with incidence. The effects of bluntness and incidence on the flowfield are shown schematically in figure 8-50.

8.18 THE EFFECT OF INCIDENCE ON BLUNT CONTROL FLAP FLOWS

8.18.1 Shock structure

The effect of incidence on the d = 6.0 mm blunt leading edge, β = 5° configuration is shown in figure 8-51. The presence of a single flap shockwave means that the flow is attached. This was also the case with the equivalent sharp leading edge configuration, shown in figure 8-15.

In section 8.17.5, it was shown that the Mach number gradient within the entropy layer increases with incidence. This increases the curvature of the flap shock, as shown in figure 8-51.

8.18.2 Pressure distribution

The flap pressure distributions for the β = 5° sharp and d = 6 mm blunt leading edge configurations are shown in figure 8-52. The absence of plateau pressures in these distributions confirms all the flows to be attached. A comparison between the sharp and the blunt distributions shows an increasing loss of control power with incidence.

For the blunt configuration, the pressure distributions in figure 8-52 at incidences of 0° and 5° show negligible pressure gradient on the flap. Thus, at these incidences, the effects of entropy layer Mach shear interaction are small. However, at an incidence

of $\alpha = 10°$, there is a 30% increase in pressure between the hingeline and the trailing edge of the flap.

The entropy layer Mach number profiles of Deveikis (1973), shown in figure 8-49, show an increase in the Mach number gradient within the entropy layer with incidence. From their method of characteristics analysis, Hayes and Probstein (1959) concluded that an increase in Mach shear increases the strength of the reflected compression waves.

Therefore, the increase in entropy layer Mach shear gradient with incidence increases the strength of the reflected compression waves. This increases in pressure gradient on the flap of the $\alpha = 10°$ $\beta = 5°$ configuration.

8.18.3 Theoretical estimation of flap pressure for blunt configurations at incidence

As the entropy layer Mach shear profiles of figure 8-49 demonstrate that the boundary layer edge Mach number is unaffected by incidence. Therefore, for a given flap deflection, the pressure ratio across the flap shock p_3/p_2 is unaffected by incidence. This ratio can be determined by the method described in section 8.12.2.

The hingeline pressure ratio on a blunt configuration at incidence can be estimated from Bade's equation (given in section 8.17.2). By combining the flap pressure ratio with the flat plate pressure ratio, the overall flap pressure ratio p_3/p_∞ can be determined.

Predictions from this method for the blunt $\beta = 5°$ configuration are shown in figure 8-52. For low incidences, the predicted flap pressure levels are in agreement with the measured flap pressure distributions. At $\alpha = 10°$, the pressure ratio at the start of the flap shows agreement with the above method.

However, further downstream, the measured pressure level increases above the predicted value. This is due to the interaction of the flap shock with entropy layer Mach shear. With knowledge of the Mach number distribution within the entropy layer, the estimated pressure level can be refined to account for the Mach shear interaction effect using the model described outlined in section 6.6.2.

8.18.4 Heat transfer

The heat transfer distributions at various incidences for the $\beta = 5°$ configuration with the sharp and the d = 6 mm blunt configuration are shown in figure 8-53. The measured heat transfer levels are compared against corresponding theoretical predictions for fully laminar and fully turbulent flap conditions.

The predictions for the sharp configurations are based on reference temperature theory as described in section 6.9.1. The predictions for the blunt configurations are based on the method described in section 6.9.3.

For the $\alpha = 0°$, $\beta = 5°$ configuration, the flap heat transfer distributions for both the sharp and the blunt configurations agree with corresponding laminar theoretical levels. Thus the flap boundary layers for both configurations are laminar.

For the $\alpha = 5°$, $\beta = 5°$ configuration, the heat transfer levels realised on the flap of the sharp configuration are well above the theoretical laminar values. Therefore, the flap boundary layer for this configuration is transitional. The measured flap heat transfer rates for the corresponding blunt leading edge configuration agree with predicted laminar values. Therefore, the flap boundary layer for this configuration is laminar.

For the $\alpha = 10°$, $\beta = 5°$ configuration, the agreement of the measured flap heat transfer levels with theoretical turbulent values for both the sharp and the blunt configuration means that the flap boundary layer is turbulent on both configurations..

In summary, the effect of leading edge bluntness on transition of the flap boundary layer for a configuration at incidence is complex. At low incidences (upto $\alpha = 5°$) , bluntness delays the onset of flap boundary layer transition. However, at high incidence ($\alpha = 10°$), bluntness does not affect transition of the flap boundary layer.

8.19 THE EFFECT OF INCIDENCE ON SEPARATION - BLUNT LEADING EDGE CONFIGURATIONS

Figure 8-54 shows all six flows to be separated in the vicinity of the hingeline. Clearly, bluntness reduces the length of the separated flow region. The effect becomes less

pronounced at high incidences where the effects of flat plate boundary layer transition cause substantial reduction of the separated flow length on the sharp configuration.

The other feature, shown in figure 8-55 is the dramatic reduction in control power caused by bluntness. This is due to the flap being enveloped by the low reservoir pressure flow associated with the entropy layer.

Chapter 9

CONTROL EFFECTIVENESS OF REACTION CONTROL JETS

In chapter 8, the effects of various parameters on the control effectiveness of mechanical flaps were studied. In free-flight conditions, these flaps are employed under continuum flow conditions provided the dynamic pressure ($\frac{1}{2}\rho u^2$) is adequate. Due to the low freestream dynamic pressure, the control effectiveness of mechanical flaps is poor at high altitudes.

Under these conditions, it becomes necessary to either augment the mechanical flap control system or to deploy an independent aerodynamic control using reaction control jets. The interaction of a modest control jet with the local crossflow creates a significant surface pressure field. The lateral force generated by this pressure field augments the jet thrust and thus increases the effectiveness of the jet.

The following study is aimed at diagnosing the flow structure generated on a blunt cone by a reaction control system and measuring its effect on control effectiveness.

9.1 GENERAL STRUCTURE OF THE JET INTERACTION REGION

The flow structure created by the interaction of an underexpanded sonic jet with the cone freestream is shown in figure 9-1. The test was conducted at $M_\infty = 12.3$, $Re_\infty/cm = 3.3 \times 10^4$ with a jet reservoir pressure of $P_{oj} = 29.7$ psia. Due to the relatively high Mach number and the low Reynolds number of this test, the interaction region is fully laminar.

The blunt leading edge of the body generates a highly curved bow shock. The curvature of this shock generates an entropy layer. Density gradients in the entropy layer mask the density gradients in the boundary layer and hence make it is difficult to identify the edge of the cone boundary layer.

The presence of a transverse underexpanded jet is somewhat analogous to a finite circular cylinder projecting from the cone surface. This generates a bow shock around the jet (called the jet bow shock). The jet bow shock and the expansion fan structure within it (assuming a hypothetical "inviscid" flow) is shown in diagram 9-1.

In real viscous flows, the jet bow shock interacts with the cone boundary layer to produce a complex three-dimensional adverse pressure gradient. This feeds out radially through the subsonic portion of the cone boundary layer (sublayer), causing a loss of momentum and a subsequent separation of the boundary layer some distance upstream of the jet.

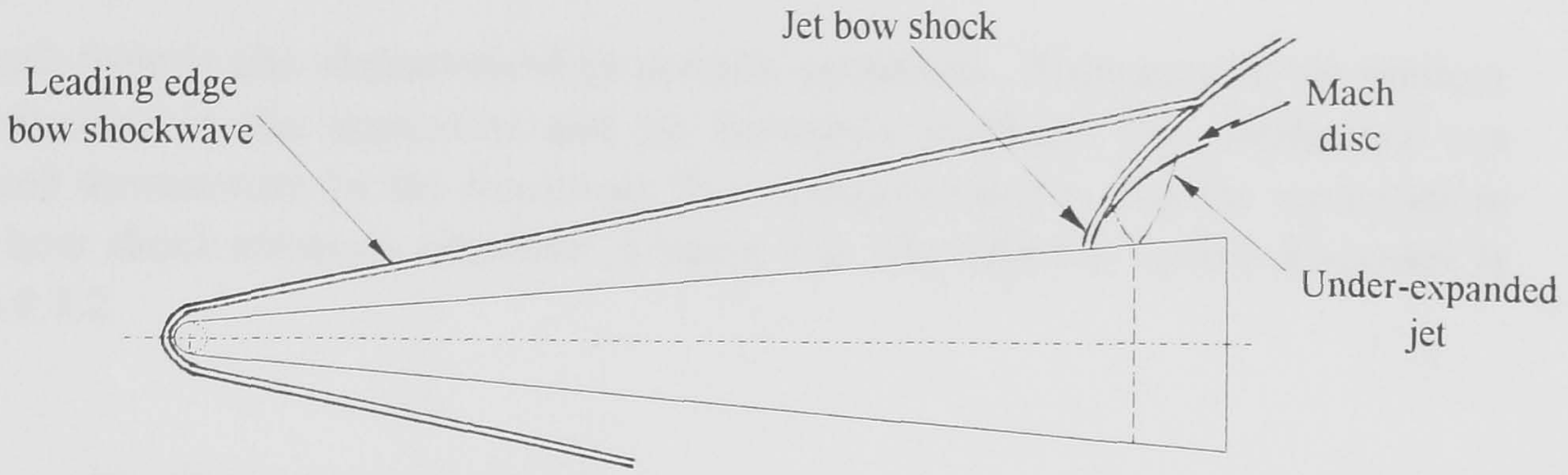

(a) side view

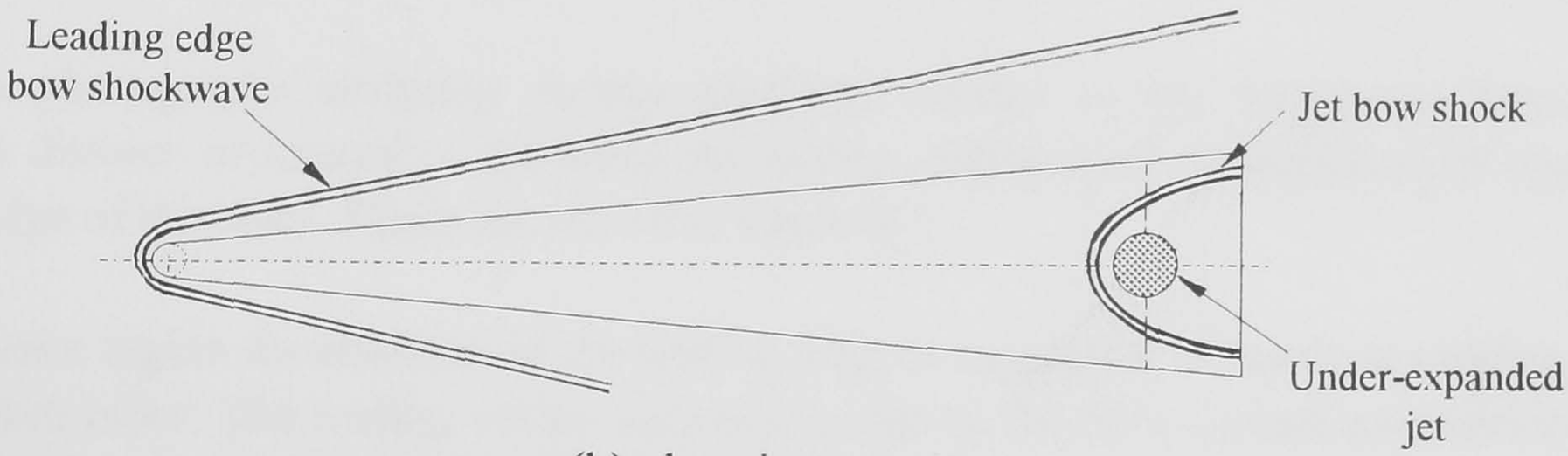

(b) plan view

Diagram 9-1 Interaction structure around an underexpanded jet in an "inviscid" hypersonic crossflow

In the vicinity of the separation point, the thickening of the sublayer rapidly increases the local thickness of the displacement body. This results in the formation of a separation shockwave.

The separated flow region is characterised by the separation vortex whilst immediately upstream of the jet, a horseshoe vortex is formed. As will be discussed in section 9.4.1, the latter vortex is located within the jet bow shock. Downstream of the jet, a wake region consisting of a recompression vortex / shock system is formed. The general flow structure in the interaction region of the blunt cone is shown in figure 9-1.

If the strength of the adverse pressure gradient arising from the jet bow shock structure is sufficient, the primary separation region extends right round to the 180° meridian. The resulting thickening of the boundary layer along this meridian generates a separation shockwave. This is evident in the schlieren photograph shown in figure 9-1.

The jet interaction region is characterised by strong normal and axial density gradients. Separate schlieren photographs with horizontal and vertical cut-off to emphasise normal and axial density gradients respectively are shown in figure 9-2. The photograph showing axial density gradients (figure 9-2, b) shows strong axial density gradients at the front of the jet bow shock.

The shock front is also characterised by periodic pulsations. These may be the product of fluctuations in the separation and jet horseshoe vortices. The oscillations are convected downstream by the freestream flow and produce the periodic variations in the jet bow shock structure observed in figure 9-2. The effect is further discussed in section 9.4.2.

9.1.1 Trailing vortex structures

Schlieren photographs analysing density gradients normal to the freestream have identified distinct structures in the wake interaction region well downstream of the trailing edge of the body. These are shown in figure 9-3.

The jet-wake region downstream of the trailing edge is suggestive of vortices rotating around each other. The trailing vortex structure is due to the downstream convection of separation and jet horse-shoe vortices by the freestream.

9.2 PARAMETRIC STUDIES OF THE JET INTERACTION REGION

9.2.1 Jet pressure ratio

The effect of jet reservoir pressure on the extent of the separated flow at $M_\infty = 8.2$, $Re_\infty/cm = 9.0 \times 10^4$ is shown in figure 9-4. Under given freestream conditions, an increase in jet reservoir pressure promotes separation along the jet meridian ($\theta_m = 0°$). This agrees with the observations of Zoukowski et al. (1964) and of Hefner et al. (1972).

The mass flow rate through a choked jet nozzle is given by

$$\frac{m\sqrt{c_p T_{oj}}}{A_j P_{oj}} = 0.393 \qquad [9.01]$$

For a given jet geometry and reservoir temperature, the jet mass flow rate increases with reservoir pressure. As is evident in figure 9-4, an increase in jet reservoir pressure increases the diameter and the penetration of the jet. This is due to the increase in the jet mass flow.

Using the circular cylinder analogy of the jet (described in section 9.1) and a blast wave type approach to model the shock around the blunt cylinder, Karamcheti et al. (1963) found that, for an inviscid flowfield on a flat plate, the shape of the trace of the jet bow shock is given by

$$\frac{R_s}{d_j} = C\left(\frac{P_{oj}}{p_\infty}\right)^{1/4}\left[\frac{\psi}{d_j}\right]^{1/2} \qquad [9.02]$$

where ψ is the jet bow shock stand-off distance and C is a constant based on the freestream Mach number and specific heat ratio. This is given by Karamcheti (1963) as

$$C = \left[\frac{1.14\gamma}{M_\infty}\left(\frac{2}{\gamma+1}\right)^{\frac{\gamma+1}{2(\gamma-1)}}\left(1+\frac{\gamma-1}{2}M_\infty{}^2\right)^{\left(\frac{\gamma-1}{\gamma}\right)+\left(\frac{\gamma+1}{2(\gamma-1)}\right)}\right]^{1/4} \qquad [9.03]$$

Equation 9.02 shows that an increase in jet reservoir pressure increases the lateral spreading of the jet bow shock. This, together with the increase in jet penetration promotes separation.

9.2.2 Gun tunnel driver pressure

The schlieren photographs of figure 9-5 show the effect of gun tunnel driver pressure on the extent of the interaction region. The tests were conducted at $M_\infty = 8.2$ with a constant jet reservoir pressure of $P_{oj} = 120$ psig.

For a given Mach number, a change in driver pressure is accompanied by a change in the freestream unit Reynolds number. In the tests shown in figure 9-5, freestream Reynolds number changes are small and thus do not affect the location of the separation front. This is further discussed in section 9.3.

By decreasing the gun tunnel driver pressure, the effective freestream reservoir pressure and hence the freestream static pressure is decreased. The decrease in the ambient pressure into which the jet exhausts increases the expansion of the jet.

This increases the diameter and the penetration of the jet, as evidenced from the schlieren photographs in figure 9-5. The combination of these effects increases the

adverse pressure gradient associated with the jet bow shock and thus promotes separation.

9.2.3 Jet-to-freestream pressure ratio

Schlieren photographs of the interaction region for two conditions with similar jet to freestream pressure ratio P_{oj}/p_∞ are shown in figure 9-6. The similar pressure ratios were simulated by varying the jet and freestream reservoir pressure. The latter was achieved through changes in the gun tunnel driver pressure.

The test Mach number was maintained at $M_\infty = 8.2$ whilst the test Reynolds number varied from $Re_\infty/cm = 4.5 \times 10^4$ for the $P_4 = 500$ psig test to $Re_\infty/cm = 7.0 \times 10^4$ for the $P_4 = 1000$ psig test. As discussed in section 9.3, the small difference in the freestream unit Reynolds number between these tests does not affect separation. In both tests, the cone boundary layer was laminar upto separation.

The similar locations of the separation shockwave along the $\theta_m = 0°$ and the $\theta_m = 180°$ meridian means that the lateral spreading of the separation front between these meridians is similar in both cases. The similarity in the shape of the separation front for these cases suggests that the extent of the jet interaction region is determined by neither P_{oj} (see section 9.2.1) nor P_4 (see section 9.2.2) but by the non-dimensional parameter P_{oj}/p_∞. The influence of this parameter arises primarily through its effect on the diameter and penetration of the jet.

9.3 SEPARATION LENGTH CORRELATION

A correlation of the length of separated flow along the jet meridian for various freestream conditions is shown in figure 9-7(a). The tests at Mach 8.2 on the cone encompass data from tests conducted in the freestream unit Reynolds number range $Re_\infty/cm = 4.5 \times 10^4$ to $Re_\infty/cm = 9.0 \times 10^4$. The correlation of the data in the absence of any Reynolds number factors suggests that small (factor of 2) changes in unit Reynolds number do not affect length of the separated flow. This argument is reinforced by the correlation of separation lengths on a 50% reduced scale model with that on the full scale model.

For a given jet to freestream pressure ratio, the length of separated flow at $M_\infty = 12.3$, $Re_\infty/cm = 3.3 \times 10^4$ is considerably reduced as compared to tests at Mach 8.2. This agrees with the effect of M_∞ on flap induced laminar separation interactions observed by Needham (1965) and Miller et al (1964).

A scaling of the separation length based on the freestream Mach number, jet diameter and the jet to freestream pressure ratio is shown in figure 9-7(b). Our data correlates as

$$\frac{L_{sep} M_\infty^{5/2}}{d_j} = 2 \left[\frac{P_{oj}}{p_\infty} \right]^{3/4} \qquad [9.04]$$

The correlation suggests that the length of the separated flow region increases with an increase in the jet to freestream pressure ratio. This agrees with the observations of the present study as described in section 9.2. The absence of a Reynolds number parameter from the scaling is supported by the observations described in section 9.2.4.

9.4 THREE-DIMENSIONALITY OF THE INTERACTION REGION

9.4.1 Correlation between the jet bow shock and the horseshoe vortex

As was described in section 9.2.1, the jet bow shock is highly curved. The curvature imposes a variable adverse pressure gradient on the cone surface boundary layer and produces a curved separation front some distance upstream of the jet.

The curvature of the jet bow shock and of the separation front was studied using liquid crystal thermography and schlieren flow visualisation techniques. The results are shown in figure 9-8. The tests were conducted under the freestream conditions of $M_\infty = 8.2$, $Re_\infty/cm = 9.0 \times 10^4$ with a jet reservoir pressure $P_{oj} = 60$ psig. In the schlieren tests shown in figure 9-8, selected meridians were placed normal to the schlieren beam by a rotation of the model.

In the thermograph shown in figure 9-8, the horseshoe shaped high temperature region immediately upstream of the jet is due to the jet horseshoe vortex. Along the jet meridian $\theta_m = 0°$, the leading edge of the vortex is located at x/d = -2.22. This correlates with the location of the leading edge of the jet bow shock in the schlieren photograph along this meridian.

Along the $\theta_m = 30°$ meridian, the thermograph (figure 9-8) shows the leading edge of the horseshoe vortex at x/d = 0.16 whilst the corresponding schlieren photograph shows the bow shock located at x/d = -1.43. On the $\theta_m = 60°$ meridian, the leading edge of the bow shock is at x/d = 2.54 (see schlieren photograph of figure 9-8) whilst on the $\theta_m = 75°$ meridian, the bow shock is absent. Thus the jet bow shock intersects the trailing edge of the body between the $\theta_m = 60°$ and the $\theta_m = 75°$ meridians.

The thermograph shows the leading edge of the jet horseshoe vortex to intersect the trailing edge of the body at the $\theta_m = 50°$ meridian. The correlation between the location of the leading edge of the horseshoe vortex and the jet bow shock demonstrates that the latter envelops the former.

9.4.2 Periodic fluctuations of the jet bow shock

In the schlieren photograph along the $\theta_m = 30°$ meridian (see figure 9-8), a disturbed flow region with strong density gradients is evident immediately behind the jet bow shock. The location of this disturbance correlates with the location of the leading and edge of the jet horseshoe vortex. Periodic oscillations in the jet bow shock along the $\theta_m = 30°$ meridian originate from the base of the shock.

The correlation of these oscillations with the location of the bow shock suggests that the fluctuations in the jet bow shock (see figure 9-2) arise due to variations in the structure of the jet horseshoe vortex.

9.5 LATERAL SPREADING OF THE SEPARATION FRONT

As was described in section 9.2.1, the interaction region around the underexpanded jet is characterised by a highly three-dimensional bow shock. The variable adverse pressure gradient associated with this shock produces a highly three-dimensional separation front upstream of the jet.

In the thermograph of figure 9-8, the separation front is characterised as a low temperature (red) region ahead of the jet. The three-dimensionality of the separation front is evident from the sweep of the red region and from the progressive delay of the separation shock in the corresponding schlieren photographs.

9.5.1 Algorithm for predicting the lateral spreading of the separation interaction region

In order to maximise the augmentation of the jet reaction force by the interaction force, the upstream extent of the separation front along the $\theta_m = 0°$ jet meridian must be maximised whilst the flow along the $\theta_m = 180°$ meridian must be maintained as attached.

In section 9.2, it was shown that the upstream extent of the separation interaction region on the jet meridian ($\theta_m = 0°$) and its lateral spreading is affected by the jet reservoir pressure, freestream pressure and the freestream Mach number. During the flight of a vehicle, these parameters vary due to changes in altitude and speed. This will produce changes in the extent of the separation interaction region and hence in the effectiveness of the control jet.

Nunn (1970) suggests that the shape of the separation front around a circular jet on a flat plate is a function of the shape of the bow shock. The latter is given by equation 9.02. Using this, the shape of the associated separation front can be written as

$$\frac{R_{sep}}{d_j} = C\left(\frac{P_{oj}}{p_\infty}\right)^{1/4}\left[\frac{(x - x_{sep})}{d_j}\right]^{1/2} \qquad [9.06]$$

For interactions on axisymmetric bodies with lateral curvature, the flat plate separation front generated around a circular sonic jet can be wrapped around the curved surface using the transformation

$$\theta_{m,sep} = k_1 C\left(\frac{P_{oj}}{p_\infty}\right)^{1/4}\left[\frac{x}{d_j} - \frac{x_{sep}}{d_j}\right]^{1/2}\frac{d_j}{d_b} \qquad [9.07]$$

where k_1 is a constant and d_b is the local body diameter at x. The co-ordinates of the transformation are shown in diagram 9-2.

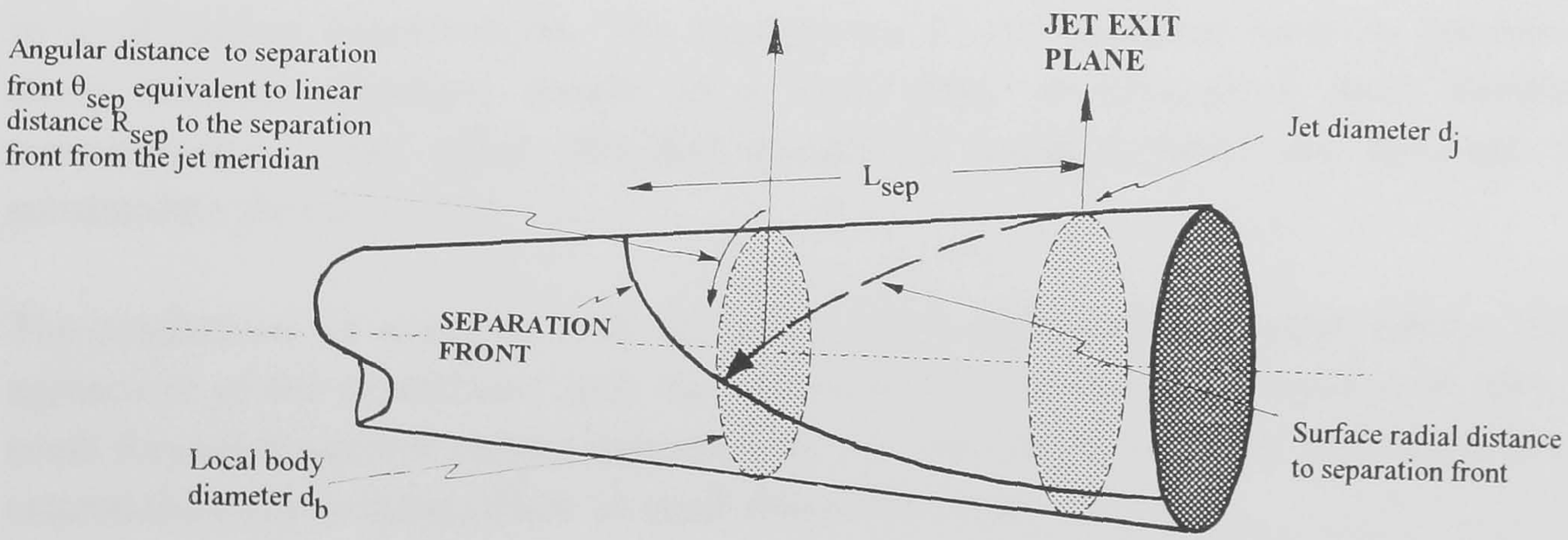

Diagram 9-2 Co-ordinate transformation for estimating the wrap around of the separation interaction region associated with the jet (Nunn, 1970)

For the present tests, the separation length directly upstream of a jet was correlated in section 9.3 in the Mach number range $8.2 \leq M_\infty \leq 12.3$. This gave the axial location of separation along the jet meridian as

$$\frac{x_{sep}}{d_j} = \frac{L_j}{d_j} - \frac{21}{M_\infty^{5/2}}\left(\frac{P_{oj}}{p_\infty}\right)^{3/4} \qquad [9.08]$$

Substituting for x_{sep}/d_j and the local diameter on the cone gives the angular location of separation on a blunt conical configuration as

$$\theta_{m,sep} = k_1 CQ\left(\frac{P_{oj}}{p_\infty}\right)^{1/4}\left[\frac{x}{d_j} - \left(\frac{L_j}{d_j} - \frac{21}{M_\infty^{5/2}}\left(\frac{P_{oj}}{p_\infty}\right)^{3/4}\right)\right]^{1/2} \qquad [9.09]$$

where

$$Q = \frac{d_j}{d_N(1-\tan\delta_c) + 2x\tan\delta_c} \qquad [9.10]$$

In figure 9-9, the predictions from the algorithm of equation 9.09 are compared with experimental observations of the location of the separation front. The latter was obtained from schlieren photographs using the method described in section 9.3.1. The predictions were made for $k_1 = 6.0$ whilst Nunn (1970) found agreement with $k_1 = 2.0$. The difference in this parameter is probably due to the hypersonic Mach number of the present study whilst the tests of Nunn (1970) were conducted at supersonic speeds.

The agreement between the experimental and predicted locations of the separation front (see figure 9-9) is within $\pm$ 5%. The difference between the two results for the $P_4 = 500$ psig test is conjectured to be the result of transition, generated possibly due to local surface imperfections. The energisation of the boundary layer by transition along selected meridians results in a local delay in separation. Heat transfer measurements using either thin-film gauges or liquid crystals are required to substantiate the conjecture.

The predictions of equation 9.09 are independent of Reynolds number effects. The agreement of the predictions with the experimental measurements (conducted over a small Reynolds number range) suggests that the location of a laminar separation front around the body is independent of small Reynolds number changes.

9.6 PRESSURE DISTRIBUTIONS IN THE JET INTERACTION REGION

Pressure measurements along selected meridians for $P_{oj} = 60$ psig are shown in figure 9-10. The tests were conducted at $M_\infty = 8.2$ with $Re_\infty/cm = 9.0 \times 10^4$. The distributions in the interaction region show a repeatability of $\pm$ 5%.

Along the jet meridian $\theta_m = 0°$, the flow separates at x/d = -10.97. Separation was identified to be at the location corresponding to the mid-point between the cone pressure and the plateau pressure levels.

The location correlates well with schlieren observations of the location of the separation shock (see figure 9-8). A second increase in pressure from x/d = -3.82 (see figure 9-10, $\theta_m = 0°$) is due to the jet bow shock.

Following its expansion around the jet, the flow separates due to the adverse pressure gradient generated by an oblique lip shock. The location of this shock is shown schematically in figure 9-1.

The separation generates a jet wake with a pair of contra-rotating recompression vortices (shown in figure 9-11). Since the lip shock is weak and the pressure gradient in a separated flow region is small, the centreline pressure immediately downstream of the jet is equal to the pressure at the separation point S (shown in figure 9-11). Thus the pressure along the centreline downstream of the jet (figure 9-10, $\theta_m = 0°$) is lower than the cone pressure.

The centreline pitot pressure distribution in the wake of a cylinder is shown in figure 9-11(b). Given the analogy between the interaction structure associated with a jet to that associated with a cylinder, the centreline pitot pressure distribution in the near wake of the jet interaction region is similar to that downstream of a circular cylinder. The rapid recovery of static pressure back to the cone pressure is due to the recovery in pitot pressure in the wake region.

The pressure distributions of figure 9-10 show little movement in the location of the separation point along the $\theta_m = 0°$, $\theta_m = 15°$ and $\theta_m = 30°$ meridians. This is confirmed by the thermograph and schlieren photographs shown in figure 9-8.

Using the separation front algorithm (section 9.5.1), it was shown that the shape of the separation front reflects that of the jet bow shock. Along meridians close to the jet, the jet bow shock is relatively two-dimensional. Thus the separation front along meridians close to the jet meridian is also two-dimensional.

The pressure distributions along the $\theta_m = 15°$, $\theta_m = 30°$ and the $\theta_m = 60°$ meridians show a small expansion following the separation plateau. The expansion starts from upstream of the jet exit plane and thus is not due to the expansion fans located within the jet bow shock.

It is conjectured that the presence of a small vortex is located between the separation and jet horseshoe vortices deflects the separation streamline towards the body surface. The deflection is achieved by Prandtl-Meyer fans located upstream of the jet bow

shock, as shown in diagram 9-3. The fans are responsible for the expansion upstream of the jet bow shock.

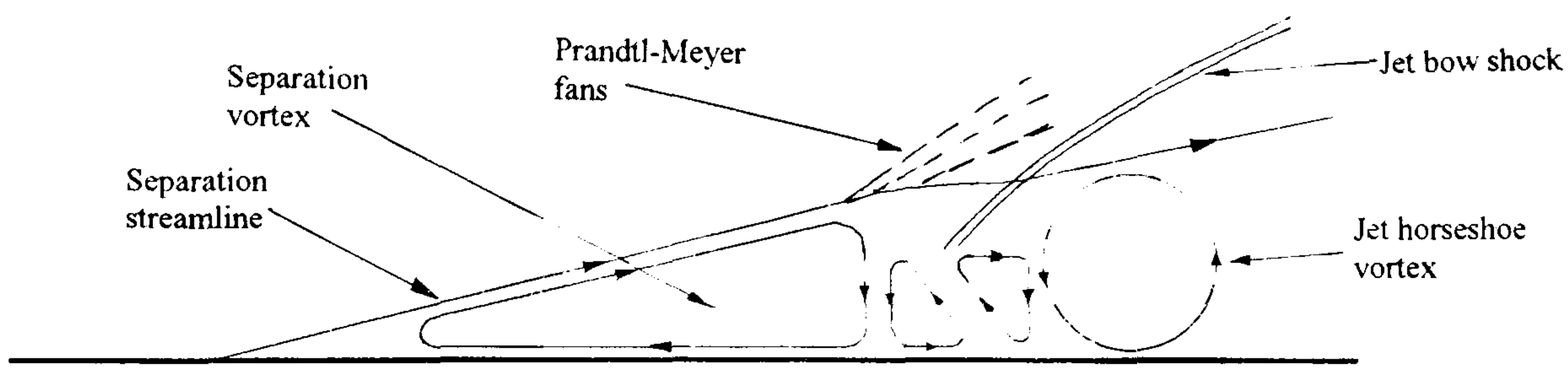

Diagram 9-3 Flow structure along meridians away from the jet meridian

At the jet exit plane, the pressure distributions of figure 9-10 show a complex highly three-dimensional pressure variation. The compressions in this plane observed along the $\theta_m = 0°$ and $\theta_m = 15°$ meridians occur due to the three-dimensional jet bow shock.

The schlieren photograph along the $\theta_m = 30°$ meridian (see figure 9-8) shows the jet bow shock to be located at x/d = -1.43 whilst the pressure distribution along this meridian (see figure 9-10) does not show the associated compression in the region of the jet exit plane (jet axis). This absence of the shock compression along this meridian is due to the low resolution of pressure tappings in the jet exit plane. The effect of the conjectured shock compression is thus shown as a dotted line. The expansion downstream of the jet axis along this meridian is due to Prandtl-Meyer fans located within the jet bow shock region.

The absence of a pressure rise along the 180° meridian (see figure 9-10) means that the flow remains attached along this meridian. This is also evidenced from the absence of shockwaves in the corresponding schlieren photographs along this meridian (see figure 9-4).

9.7 THE EFFECTS OF INCIDENCE ON THE FLOW STRUCTURE OVER A BLUNT CONE

Schlieren photographs and liquid crystal thermographs (plan view) of the flow at $M_\infty = 8.2$ on a blunt cone at various incidences are shown in figure 9-12.

The schlieren photograph at $\alpha = 3°$ shows a thickening of the boundary layer along the leeward meridian. The corresponding thermograph shows a decrease in heat transfer, seen as a localised reduction in temperature, along the leeward meridian. The decrease in heat transfer extends from the leeward meridian $\theta_m = 0°$ to meridians $\theta_m = 60°$ either side. As will be discussed later in this section, the decrease in heat transfer is due to a decrease in pressure in the leeward region of the body.

At incidences of $\alpha = 6°$ and $\alpha = 9.5°$, schlieren photographs (see figure 9-12) show the establishment of a disturbed flow region over the leeward meridian. This is due to separation of the crossflow resulting in the establishment of a pair of crossflow vortices over the leeward region of the body. A schematic cross-section drawing of crossflow separation is shown in figure 9-13.

The thermographs at $\alpha = 6°$ and $\alpha = 9.5°$ (see figure 9-12) show localised decreases in heat transfer either side of the leeward meridian but an increase in heat transfer along the leeward meridian itself. This is due to a reattachment of the separated crossflow along the leeward meridian (shown schematically in figure 9-13).

Circumferential heat transfer distributions on a blunt cone at incidence are shown in figure 9-13(a). At low incidence ($\alpha = 5°$), the heat transfer attains its minimum along the leeward meridian. This is due to a local thickening of the boundary layer along this meridian. At high incidence ($\alpha = 10°$), the heat transfer along the leeward meridian is greater than along surrounding meridians. This is due to the reattachment of separated crossflow vortices along the leeward meridian. The circumferential pressure distribution on a blunt cone at incidence is shown in figure 9-14(a). Given the qualitative similarity in the circumferential pressure and heat transfer distributions, it is conjectured that the variations in heat transfer in separated crossflows occur due to the pressure variations.

The results of the present study and that of Wrisdale (1992) show that on spherically blunt cones, crossflow separation effects are absent for $\alpha < \delta_c$. At these incidences, a thickening of the leeward boundary layer results in a minima in heat transfer along the leeward meridian. For $\alpha > \delta_c$, crossflow separation occurs. At moderate incidences, this results in the formation of a symmetrical pair of vortices over the leeward surface of the vehicle. The reattachment of the separated flow along the leeward meridian increases the local heat transfer.

9.8 THE EFFECT OF INCIDENCE ON JET INTERACTION

9.8.1 Attached crossflow [$\alpha < \delta_c$]

Schlieren photographs (see figure 9-15) show that an increase in incidence from $\alpha = 0°$ to $\alpha = 3°$ increases the diameter and penetration of the jet. Separation along the leeward meridian is promoted from x/d = -10.97 at $\alpha = 0°$ to x/d = -34.03 at $\alpha = 3°$.

Stetson (1972) measured a progressive decrease in cone pressure along the leeward meridian with incidence. This is shown in figure 9-14. Since the pressure on the leeward meridian of the sharp cone correlates with the frustum pressures a slender

blunt cone (downstream of the leading edge overexpansion) a similar decrease in leeward pressure with incidence is expected on a blunt cone.

The decrease in the local cone pressure along the leeward meridian with incidence effectively increases the local jet pressure ratio P_{oj}/p_e. The increased jet pressure ratio increases the diameter and penetration of the jet. This strengthens the interaction and promotes separation along the leeward meridian.

The increase in jet diameter also increases the jet bow shock stand-off distance and the diameter of the jet horseshoe vortex. This is evident in the thermographs of figure 9-16. As with the $\alpha = 0°$ configuration (see section 9.4.1), the leading edge of jet horseshoe vortex in the $\alpha = 3°$ configuration correlates with the leading edge of the jet bow shock. It is thus conjectured that the jet bow shock envelops the jet horseshoe vortex.

9.8.2 Separated crossflow [$\alpha > \delta_c$]

As was described in section 9.5, an increase in incidence beyond the cone semi-vertex angle δ_c causes crossflow separation on blunt cones. Therefore at these incidences, the under-expanded leeward jet exhausts into a multi-vortex separated crossflow structure. The crossflow on the present configuration became separated at incidences of $\alpha = 6°$ and $\alpha = 9.5°$.

Schlieren photographs of the jet interaction region at $\alpha = 6°$ and $\alpha = 9.5°$ are shown in figure 9-15. The density gradients associated with the crossflow vortices mask the gradients associated with the jet interaction region and thus make it difficult to observe the effects of the jet on the local flowfield. Thermographs of the jet interaction region (see figure 9-16) show horseshoe shaped high temperature regions around the jet at $\alpha = 6°$ and $\alpha = 9.5°$. This confirms the flow at these incidences to be separated.

At $\alpha = 6°$, the absence of the crossflow reattachment line (see figure 9-16) along the leeward meridian suggests that the jet changes the structure of the crossflow vortices. It is conjectured that the jet induced separation introduces separation and horseshoe vortices underneath the crossflow vortices (see figure 9-17a). The resulting displacement body effectively moves the crossflow reattachment off the surface of the cone. Peake et al (1982) showed the existence of this type of a flow structure on a cone-cylinder-flare body at incidence.

Pagan et al (1992) showed that an increase in incidence increases the strength of the crossflow vortices on a tangent ogive / cylinder configuration. A similar increase in the strength of the crossflow vortices occurs as the incidence of the blunt cone increases from $\alpha = 6°$ to $\alpha = 9.5°$. This strengths the crossflow reattachment and 'squashes' the

jet induced separation vortex along the leeward meridian to produces a local streak of high heat transfer. The conjectured crossflow patterns for the $\alpha = 9.5°$ configuration are shown in figure 9-18(b).

The experimental validation of these flow patterns requires laser sheet and surface oil-flow visualisations. These tests are required on the cone at incidence to establish the presence of crossflow vortices and on the cone / underexpanded jet configuration to show the effects of the jet on the crossflow vortex structure. The tests were beyond the scope of the current study.

9.9 AUGMENTATION OF NORMAL FORCE AND PITCHING MOMENT

The sign convention used for the normal force and moment measurements are shown in diagram 9-4. An upward force (normal to the axis of the model) and a nose up pitching moment were taken as positive.

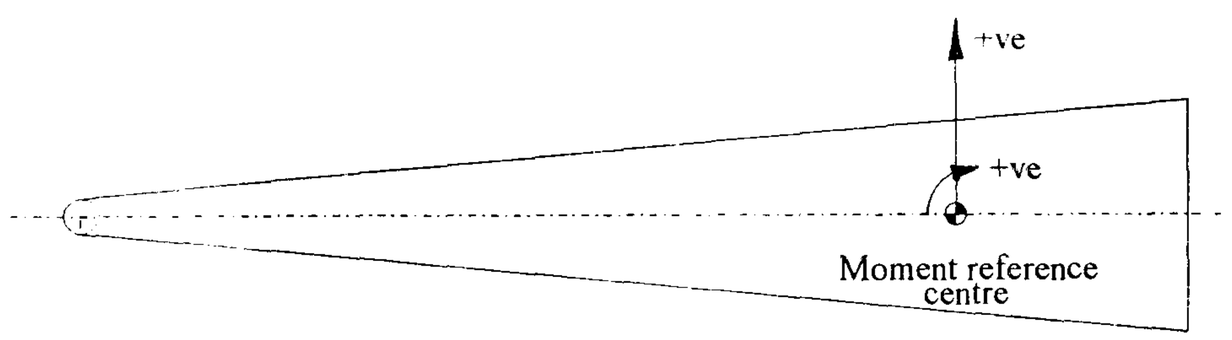

Diagram 9-4 Sign convention used for normal force and moment tests

The normal force measurements were non-dimensionalised using the freestream dynamic head and the base area of the blunt cone. The pitching moments were non-dimensionalised using the freestream dynamic head, base area and the length of the cone. The pitching moments were measured at the moment reference point located at x/d = -10.18 along the body axis.

9.9.1 Jet only

The jet only normal force and moment coefficient (measured under evacuated tunnel conditions, $P_{oj}/p_{am} = 700$) were $C_{N(j)} = -25 \times 10^{-3}$ and $C_{M(j)} = 3.4 \times 10^{-3}$ respectively. The negative reaction force was generated due to the upward exhaust of the jet. The pitching moment generated by the jet was nose-up due to the jet axis being aft of the moment reference centre.

9.9.2 Jet and freestream

9.9.2.1 $\alpha = 0°$

The effect of incidence on the normal force and pitching moment generated by the interaction was studied for the P_{oj} = 60 psig jet. The tests were conducted at $M_\infty = 8.2$, $Re_\infty/cm = 9.0 \times 10^4$ and $p_\infty = 0.13$ psia. The blunt cone model was located along the nozzle centreline with its leading edge located 2.0 cm upstream of the nozzle exit plane.

At $\alpha = 0°$, a small normal force $C_{N(c)} = -13 \times 10^{-3}$ and a pitching moment $C_{M(c)} = -1 \times 10^{-3}$ were measured on the blunt cone. These are shown in figure 9-18. The forces and moments observed are due to the centreline focusing effect (described in section 8.1.1) associated with the Mach 8.2 nozzle. The forces and moments were absent in similar tests at $\alpha = 0°$ conducted with the Mach 12.3 nozzle.

In the absence of any interaction between the jet and the crossflow, the total normal force realised is the algebraic sum of the normal force from the cone and from the jet. Therefore, the presence on a reaction jet (in the absence of any interaction effects) decreases the normal force by a magnitude equal to the jet force. Thus the negative normal force on the cone changes from $C_{N(c)} = -13 \times 10^{-3}$ in the absence of the jet to $C_{N(j+c)} = -38 \times 10^{-3}$ with the jet.

In figure 9-10, it was shown that the interaction of the jet with the cone freestream generates a pressure field. The interaction pressure field also generates an normal force and a pitching moment on the cone. This augments the normal force generated by the reaction jet. A positive augmentation is defined as the case where the forces generated by the interaction favourably assist the normal force and pitching moment of the jet

At $\alpha = 0°$, the absolute normal force in the presence of the jet was $C_{N(j+i+c)} = -55 \times 10^{-3}$ (including the normal force on the cone). The combined jet and interaction normal force was $C_{N(j+i)} = C_{N(j+i+c)} - C_{N(c)} = -42 \times 10^{-3}$. Thus, the interaction increases the total force generated by the jet by 70%.

At $\alpha = 0°$, the normal of the jet (in the absence of an interaction) increases and the nose-up moment on the cone from $C_{M(c)} = -0.87 \times 10^{-3}$ to $C_{M(j+i+c)} = 2.98 \times 10^{-3}$. This is shown in figure 9-18. The combined jet and interaction pitching moment was $C_{M(j+i)} = C_{M(j+i+c)} - C_{M(c)} = 3.85 \times 10^{-3}$. Thus, the interaction increases the pitching moment generated by the jet by 13%.

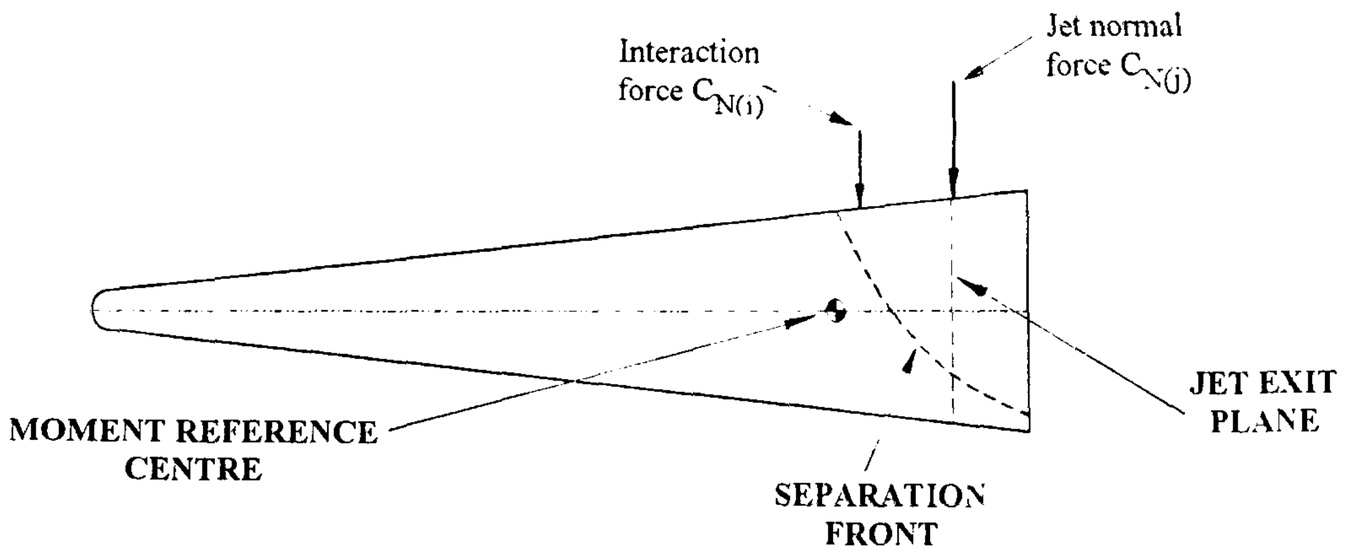

Diagram 9-5 The relative locations of the centre of pressures of the jet and the interaction force ($M_\infty = 8.2$, $Re_\infty/cm = 9.0 \times 10^4$, $P_{oj} = 60$ psig, $\alpha = 0°$)

The relative locations of the centre of pressure of the jet alone and of the interaction force are shown in diagram 9-5. The centre of pressure of the jet force is located at x/d = 0.16. This is within 1% of the location of the jet exit plane. The centre of pressure of the jet interaction force is located within the separation interaction region. The latter is mapped by the separation front calculated using the algorithm given in section 9.3.3.1.

The increase in pressure upstream of the jet on meridians in the region $\theta_m < 90°$ favourably assists the normal force and pitching moment of the jet. The over-expansion behind the jet and the increase in pressure along meridians in the region $\theta_m > 90°$ adversely affect the forces and moments generated by the jet. The centre of pressure of the interaction, shown in diagram 9-3 is effectively an integration of the elemental forces and moments generated in the interaction region.

9.9.2.2 Small incidence $\alpha < \delta_c$

The study of the effects of incidence on the augmentation of the force was limited to $\alpha = 3°$. At this incidence, the liquid crystal thermographs (shown in figure 9-12) show the crossflow on the blunt cone to be attached.

As described in section 9.5, incidence increases the pressure along windward meridians and decreases the pressure along leeward meridians. The pressure difference between the leeward and windward meridians generates a positive normal force $C_{N(c)} = 83 \times 10^{-3}$. This is shown in figure 9-18.

Stetson (1972) has shown that incidence generates axial pressure gradients along the windward and leeward meridians of a cone at incidence. These axial pressure gradients together with the pressure differences between the leeward and windward meridians creates a positive pitching moment $C_{M(c)} = 10 \times 10^{-3}$.

The firing of a reaction jet and the associated interaction region generates a negative normal force. Since the normal forces from the reaction jet and its interaction oppose the cone force, the total force on the cone & jet configuration decreases from $C_{N(c)} = 83 \times 10^{-3}$ to $C_{N(j+i+c)} = 29 \times 10^{-3}$. Thus, the normal force generated by the jet and interaction is $C_{N(j+i)} = C_{N(j+i+c)} - C_{N(c)} = -54 \times 10^{-3}$. Thus, at $\alpha = 3°$, the interaction augments the jet force by 112%.

An increase in incidence from $\alpha = 0°$ to $\alpha = 3°$ promotes separation along the leeward meridian (see figure 9-15). Incidence also limits the lateral extent of the separation region. The shape of the separation front on the cone at $\alpha = 0°$ and $\alpha = 3°$ are shown in diagram 9-6. The increase in the area of the interaction region together with the limitation of its effect to the leeward meridians results in an increased augmentation of the normal force with incidence.

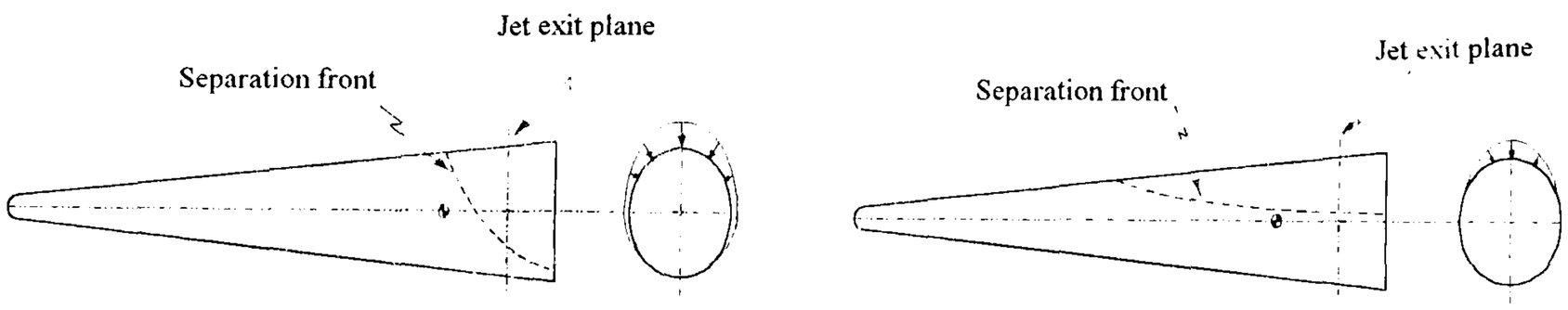

$\alpha = 0°$ $\alpha = 3°$

Diagram 9-6 The effect of incidence on the shape of the separation front

At $\alpha = 3°$, the firing of a trailing edge jet (in the absence of any interaction) increases the nose up moment from $C_{M(c)} = 10 \times 10^{-3}$ in the absence of the jet to $C_{M(c+j+i)} = 13.1 \times 10^{-3}$. This is shown in figure 9-18. The moment generated by the jet & interaction is $C_{M(j+i)} = C_{M(c+j+i)} - C_{M(c)} = 3.1 \times 10^{-3}$. Therefore, at $\alpha = 3°$, the total nose up moment associated with the jet & interaction is lower than the moment due to the jet. The latter was shown in section 9.9.1 to be $C_{M(j)} = 3.4 \times 10^{-3}$.

At $\alpha = 3°$, the schlieren photograph of figure 9-15 shows the upstream limit of the separation front to be located well upstream of the moment reference point. The conjectured separation front at $\alpha = 3°$ is mapped in diagram 9-7.

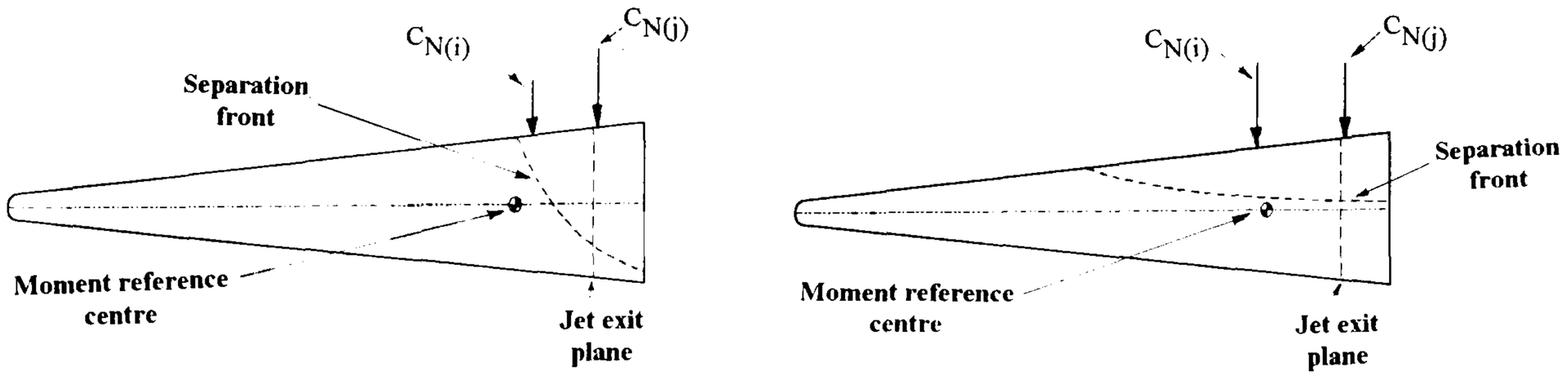

$\alpha = 0°$ $\alpha = 3°$

Diagram 9-7 Schematic diagram of the effect of incidence on the location of the centre of pressure

The increase in the upstream extent of the separation moves the centre of pressure of the interaction from downstream of the moment reference point at $\alpha = 0°$ to upstream of the reference point at $\alpha = 3°$. This increases the nose down pitching moment associated with the interaction region and causes the jet moment to be reduced.

9.10 THE EFFECT OF JET NOZZLE GEOMETRY ON SEPARATION

9.10.1 Slot jet

The effect of a change in the jet nozzle geometry from a sonic circular jet to a sonic 3:1 transverse slot jet was studied using schlieren flow visualisation and surface pressure measurements. The jet exit area was maintained at π mm^2. Similar jet reservoir conditions were used to eliminate any effects associated with changes of the jet mass flow.

The schlieren photograph of figure 9-19 shows that the slot jet promotes separation a along the $\theta_m = 0°$ meridian from x/d = -10.97 for the circular jet to x/d = -14.15 for the slot jet. Pressure measurements along the jet meridian $\theta_m = 0°$ (see figure 9-20) confirm the promotion of separation by the slot jet.

The slot jet also promotes separation along all meridians. This is shown for the $\theta_m = 30°$, $\theta_m = 60°$ and $\theta_m = 90°$ meridians in figure 9-20. The greater span of the slot jet nozzle increases the lateral extent of the under-expanded jet. Effectively the slot jet presents a greater disturbance to the freestream flow over the cone and leads to a greater augmentation of the jet force.

9.10.2 Mach 3 jet

9.10.2.1 Jet structure

A Mach 3 jet was established using the nozzle flow area / Mach number relationship assuming isentropic flow between the throat and the nozzle exit plane i.e.

$$\frac{A}{A^*} = \frac{1}{M^2}\left[\frac{2}{\gamma+1}\left(1+\frac{\gamma-1}{2}M^2\right)\right]^{\frac{\gamma+1}{2(\gamma-1)}} \qquad [9.10]$$

Schlieren photographs of the underexpanded [P_{oj}/p_{am} = 1000] sonic and Mach 3 jets are shown in figure 9-21. This shows that the Mach 3 jet to be more slender than the

sonic jet. The pressure in the exit plane of the jet (assuming isentropic flow between the throat and the exit plane) is given by the isentropic pressure relationship as

$$p_{exit} = \frac{P_{oj}}{\left[1 + \frac{\gamma - 1}{2} M_{exit}{}^2\right]^{\frac{\gamma}{\gamma - 1}}} \qquad [9.11]$$

An increase in the jet exit plane Mach number decreases the exit plane pressure ratio. Thus, the local diameter of the Mach 3 jet is lower than that of the sonic jet.

9.10.2.2 The effect of Jet Mach number on jet/crossflow interaction scales

Schlieren photographs of the separation scales along the jet meridian of a sonic and a Mach 3 jet are shown in figure 9-22. The jet throat area was maintained at π mm^2. This, together with similar jet reservoir conditions ensured the jet mass flux to be constant.

The schlieren photographs of figure 9-22 show that the increase in jet Mach number delays separation along the $\theta_m = 0°$ meridian. This is also confirmed by the pressure distributions shown in figure 9-23. The delay in separation for the Mach 3 jet is due to its more slender structure (compared to the corresponding sonic jet). This also delays separation along all meridians, as shown by the pressure distributions of figure 9-23 and the thermographs of figure 9-24 show separation.

The plan view of the jet interaction region, shown in the thermographs of figure 9-24 shows the jet bow shock around the Mach 3 jet to be located at x/d = 0.64. This correlates with its location in the corresponding schlieren photograph, shown in figure 9-22. The jet bow shock for the sonic jet configuration is located at x/d = -2.23. The downstream movement of the leading edge of the jet bow shock is also due to the reduction in jet diameter with jet Mach number.

The reduced diameter of the Mach 3 jet decreases the downstream extent of the wake. This is evident by the rapid closure of the wake in the thermograph (see in figure 9-24). The change in wake structure prevents the over-expansion of the flow behind the jet (see figure 9-23).

As the extent of the interaction region is smaller for the Mach 3 jet, less augmentation is expected from this jet. However, it must be noted that the total jet thrust is greater for the Mach 3 jet in comparison to a sonic jet. Thus, the total normal force associated with the jet + interaction may increase with jet Mach number.

Chapter 10

CONCLUSIONS & RECOMMENDATIONS FOR FURTHER WORK

A FLAP DEFLECTION

1. Flap deflection promotes separation and delays reattachment of a laminar boundary layer.

2. In contrast to fully laminar interactions, the location of reattachment in transitional interactions exhibits a small upstream movement with flap deflection.

3. In transitional interactions, the separated shear layer rapidly becomes transitional following separation. For well separated flows, transition of the separated shear layer causes a boundary layer which is initially laminar at separation to become fully turbulent at reattachment.

4. The acceleration of transition within the shear layer leads to a severe increase in the aerothermal load on the flap.

5. In cases where transition occurs close to the hingeline, the turbulent heat transfer rates on the flap are satisfactorily predicted by reference temperature theory. Further work at various freestream conditions is required to extend and define the accuracy of this method.

6. For transitional interactions, the increased energisation of the shear layer by transition causes early reattachment. This leads to a significant reduction in the extent of the separated flow lengthscale.

B INCIDENCE

1. Incidence promotes transition of a sharp flat plate boundary layer. This is due to a reduction in the local Mach number and an increase in the boundary layer edge unit Reynolds number.

2. For both attached and separated flows, the combination of incidence and flap deflection accelerates flap boundary layer transition.

3. For a given flap deflection, the flap boundary layer which is laminar at zero incidence can become transitional/turbulent at incidence. This significantly increases the aerothermal loads on the flap.

4. For sharp leading edge configurations, incidence reduces the length of the separated flow region. For laminar interactions, this is due to changes in the flat plate boundary layer thickness. Further work under fully laminar conditions is required to extend the proposed correlation.

5. The promotion of transition by incidence significantly decreases the separated flow lengthscales. As with laminar interactions, the reduction in separated flow length scales by incidence for transitional interactions occurs due to a decrease in flat plate boundary layer thickness. Further work under transitional conditions is required to extend the proposed correlation.

C BLUNTNESS

1 Leading edge bluntness reduces the Mach number on a flat plate from hypersonic to supersonic speeds. This is due to reservoir pressure losses sustained across the leading edge shock.

2. The pressure recovered on the flap embedded within the flowfield on a blunt body is an order of magnitude lower than on a corresponding sharp body. Thus bluntness reduces control flap effectiveness.

3. The entropy layer Mach shear interaction method (based on oblique shock theory and wave interactions) satisfactorily predicts the flap pressure distribution in strongly blunted flows. This shows that the pressure distribution on a control flap embedded within an entropy layer is determined by the hingeline Mach shear profile. Further studies are required to extend the model to higher Mach numbers.

4. The reduction in flap pressure for blunt configurations reduces laminar and turbulent heat transfer rates on the flap. The reduction in flap pressure also reduces separated flow length scales.

5. For transitional interactions (with transition close to the hingeline), a modified version of reference temperature theory accurately predicts the flap heat transfer

rates on blunt configurations. Further transitional studies are required to extend this model.

D JET CONTROL EFFECTIVENESS

1. The upstream length of the interaction region (along the jet meridian) increases with incidence but its lateral spreading decreases with incidence.

2. The extent of the separation interaction region is reduced by increasing Mach number.

3. Small (factor of 2) changes in the freestream unit Reynolds number do not affect the shape of the separation interaction region. Further work is required to extend the Reynolds number range of the jet interaction database.

4. At zero incidence, the shape of the separation interaction region is a direct function of the shape of the jet bow shock.

5. A close-loop engineering algorithm developed in the present study accurately predicts the shape of the separation front. This allows accurate prediction of the jet augmentation force. Further studies are required to extend the model to higher Mach numbers.

6. For small incidences, the augmentation of the jet normal force increases with incidence. At high incidence, the augmentation is affected by interaction of the jet with body vortices. Further work using laser sheet visualisation is required to study the interaction of the jet with the body vortices.

7. At zero incidence, the interaction favourably augments the pitching moment of the jet. However, at small incidence, the interaction adversely affects the pitching moment of the jet.

E TRANSITION DIAGNOSTICS

1. Relative heat transfer fluctuation measurements allow early detection boundary layer transition on flat plates and compression corner configurations.

2. For complex hypersonic flow regimes, the detection of an increase in relative heat transfer fluctuations forms a new and accurate tool for the diagnosis of the onset of transition. Further studies in other transitional flow regimes and in free-flight conditions are required to extend the method.

APPENDIX 1

Skin friction distribution for compressible flows with local similarity using the reference temperature approximation

From the incompressible Blasius solution at the reference temperature, the shear stress is given by

$$\tau_w = c_{fe}\frac{\rho_e u_e^2}{2} = A\rho^* u_e^2\left[\frac{\mu^*}{\rho^* u_e x}\right]^n$$

Therefore, the skin friction coefficient (based on local conditions) is given by

$$\frac{c_{fe}}{2} = A\frac{\rho^*}{\rho_e}\left[\frac{\mu^*}{\rho^* u_e x}\right]^n$$

Assuming negligible pressure gradient across the boundary layer, this can be written as

$$\frac{c_{fe}}{2} = A\frac{Te}{T^*}\left[\frac{\mu_e}{\rho_e u_e x}\cdot\frac{\rho_e \mu^*}{\rho^* \mu_e}\right]^n$$

and assuming a linear viscosity-temperature relationship

$$\frac{c_{fe}}{2} = A\frac{Te}{T^*}\left[\frac{1}{Re_{ex}}\cdot\left(\frac{T^*}{T_e}\right)^2\right]^n$$

The skin-friction coefficient can be referenced to freestream conditions to give

$$\frac{c_{f\infty}}{2} = A\cdot\frac{\rho_e u_e^2}{\rho_\infty u_\infty^2}\cdot\left(\frac{T_e}{T^*}\right)^{(1-2n)}\left[\frac{1}{Re_{ex}}\right]^n$$

which can be rewritten as

$$\frac{c_{f\infty}}{2} = A\cdot\frac{p_e T_\infty u_e^2}{p_\infty T_e u_\infty^2}\cdot\left(\frac{T_\infty}{T^*}\right)^{(1-2n)}\left(\frac{T_e}{T_\infty}\right)^{(1-2n)}\left[\frac{1}{Re_{\infty x}}\frac{p_\infty T_e u_\infty}{p_e T_\infty u_e}\frac{T_e}{T_\infty}\right]^n$$

Simplifying this expression gives

$$\frac{c_{f\infty}}{2}Re_{\infty x}^{\,n} = A\left(\frac{p_e}{p_\infty}\right)^{(1-n)}\left(\frac{u_e}{u_\infty}\right)^{(2-n)}\left[\frac{T_\infty}{T^*}\right]^{(1-2n)}$$

APPENDIX 2

Heat transfer distribution for compressible flows with local similarity using the reference temperature approximation

It has been demonstrated in appendix 1 that the skin friction coefficient (based on local conditions) in compressible flows can be described by

$$\frac{c_{fe}}{2} = A\left(\frac{Te}{T^*}\right)^{1-2n}\left[\frac{1}{Re_{ex}}\right]^n$$

The local Stanton number is related to the local skin friction coefficient through Reynolds analogy. This is given by Simeonides[43] as

$$St_e = \frac{c_{fe}}{s}$$

where for laminar boundary layers, $s = Pr^{2/3}$ and for turbulent boundary layers $s = 1$. Thus by substitution,

$$St_e = \frac{A}{s}\left(\frac{Te}{T^*}\right)^{1-2n}\left[\frac{1}{Re_{ex}}\right]^n$$

The Stanton number can be referenced to freestream conditions by

$$St_\infty = \frac{A}{s}\frac{\rho_e u_e}{\rho_\infty u_\infty}\left(\frac{Te}{T^*}\right)^{1-2n}\left[\frac{1}{Re_{ex}}\right]^n$$

This can be further simplified and referred to the freestream conditions to give the heat transfer coefficient with respect to freestream conditions as

$$C_{H\infty}(Re_{\infty x})^n = \frac{A}{s}\left(\frac{p_e u_e}{p_\infty u_\infty}\right)^{(1-n)}\left(\frac{T_\infty}{T^*}\right)^{(1-2n)}\left[\frac{T_r - T_w}{T_o - T_w}\right]$$

REFERENCES

Ames Research Staff
Equations, tables and charts for compressible flows
NACA Report 1135 [1953]

Anderson, J D Jr.
Fundamentals of Aerodynamics
McGraw-Hill International Editions (1985)

Anderson, J D Jr.
Hypersonic and high temperature gas dynamics
McGraw Hill (1989)

Anonymous
Space Commerce - An industrial overview

Arianespace
Marketing Survey Abstract
Marketing Service, Commercial Department, Arianespace (Dec.1990)

Arnal, D
Laminar-Turbulent transition in supersonic and hypersonic flows
Special course on Aerothermodynamics of hypersonic vehicles AGARD R-761, Paper no.8 (1989)

Bade, W L
Analytic formulas for conditions on blunt wedges in hypersonic flows
AIAA Journal, vol. 13, no. 9, pp 1245 - 1247 (Sep. 1975)

Benton, D L
Supply and demand in the commercial space launch marketplace
AIAA-87-1799 (1987)

Bertram, M H
Blackstock, T A
Some simple solutions to the problems of predicting boundary layer self-induced pressures
NASA TN-D 798, (1961)

Beyer, U
Control effectiveness of flaps at hypersonic speeds
MSc Thesis, Cranfield Institute of Technology (1988)

Bradshaw, D
Trapped in a regulatory mire
International Telecommunications - Financial Times survey (April 1990)

Brinich, P F
Effect of leading edge geometry on boundary layer transition at $M_\infty = 3.1$
NACA TN 3659 (1956)

Brinich, P F
Sands, N
Effects of bluntness on transition for a cone and a hollow cylinder at Mach 3.1
NACA TN 3979 (1957)

British Broadcasting Corporation
World radio and television receivers
International broadcasting and Audience Research (June 1991)

Chapman, D R
Kuehn, D M
Larson H K
Investigation of separated flows in supersonic and subsonic streams with emphasis on the effect of transition
NACA TN 3869 (March 1957)

Chapman, D R
Kuehn, D M
Larson H K
Investigation of separated flows in supersonic and subsonic streams with emphasis on the effects of transition
NACA Report 1356 (1958)

Chen, F J
Wilkinson, S P
Gortler instability and hypersonic quiet nozzle design
AIAA-91-1648 (1991)

Chenard, S
Space insurers now fret about satellites
Interavia Space Markets, vol 2 (May/June 1989)

Chenard, S
Pegasus finds friends at the Pentagon
Interavia Spacemarkets (July 1989)

Chenard, S
The long march to launch regulation
Interavia Space Markets, vol 6, no. 4 (Jul/Aug 1990)

Cheng, H K
Pallone, A J
Inviscid leading edge effects in hypersonic flow
J. of the Aeronautical sciences, pp 700-702 (1956)

Cheng, H K
Hall, J G
Golian, T C
Hertzberg, A
Boundary layer displacement and leading edge bluntness effects in high temperature hypersonic flow
J. of the Aerospace Sciences, vol 28, no. 5 (May 1961)

Clarke, A C
Extraterrestrial relays
Wireless World (Oct.1945)

Coet, M C
Delery, J
Chanetz, B
Experiments on Shock Wave - Boundary Layer Interaction at High Mach number with Entropy Layer Effect
IUTAM Symposium, Marseille, France (1-4 Sep 1992)

Coleman, G T
Hypersonic boundary layer studies
PhD thesis, Univ. of London (1973)

Coles, D
Measurements in the boundary layer on a smooth flat plate in supersonic flow
ORDCIT Report no.20-71 (1953)

Committee on Earth Observations satellites
The relevance of satellite missions to the study of the global environment
UNCED Conference, Rio De Janeiro (1992)

Courtis, N
Private Communications
College of Aeronautics, Cranfield University (1994)

Creager, M O
The effects of leading edge bluntness on the local heat transfer and pressure distributions over flat plates in supersonic flows
NACA TN 4142 (December 1957)

Crist, S
Sherman, P M
Glass, D R
Study of the highly underexpanded sonic jet
AIAA J., vol 4, no.1, pp 68-71 (1966)

Crockett, B
The changing role of satellites in telecommunications
Telecommunications (North American ed.), vol 23, pp37-46 (June 1989)

Dandelot, M M
Promoting the modernisation and extension of telecommunications in Eastern Europe
World Telecommunications - Financial Times Conference (December 1991)

Deem, R E
Murphy, J S
Flat plate boundary layer transition at hypersonic speeds
AIAA-65-0128 (1965)

Delery, J
Marvin, J G
Shockwave boundary layer interactions
AGARD-AG-280 (1986)

Delery, J
Shock / Shock and Shockwave / Boundary Layer interactions in hypersonic flows
Special course on Aerothermodynamics of hypersonic vehicles AGARD R-761 (1989)

Derksen, W B G
Veldman, J
Measurements on model pistons for gun tunnel applications
42nd annual meeting of the Supersonic Tunnel Association, Calspan Corp., (1973)

Deveikis, W D
Roane Hunt, L
Loading and heating of a large flat plate at Mach 7 in the Langley 8-foot high-temperature structures tunnel
NASA TN D-7275 (1973)

Dixon, H
Cartel distorts World Economy
International Telecommunications - Financial Time Survey (April 1990)

Dixon, H
The sleeping giants awaken
World Telecommunications - Financial Times Survey (October 1990)

Eckert, E R G
Engineering relations of friction and heat transfer to surfaces in high velocity flow
J. of the Aeronautical Sciences, vol.22, no.8, pp 585-587 (August 1955)

Economist, The
The uses of heaven
The Economist (15th June 1991)

Edwards, C L W
Anders, J B
Low density, leading edge bluntness and ablation effects on wedge induced laminar boundary layer separation at moderate enthalpies in hypersonic flows
NASA TN-D 4829 (1968)

Edelson, B I
The Experimental Years
The Intelsat Global Satellite System (Ed. Alper, J and Pelton, J N), Progress in Aeronautics and Astronautics, American Institute of Aeronautics and Astronautics (1984)

Elfstrom, G M
Turbulent hypersonic flow at a wedge compression corner
J. of Fluid Meahcnics, vol. 53, part 1 pp 113-127 (1972)

Ericsson, L E
Effects of nose bluntness and cone angle on slender vehicle transition
AIAA J. vol.26, no.10, pp 1168-1174 (October 1988)

Fisher, M C
Weinstein, L M
Cone transitional boundary layer structure at Mach 14
AIAA J., vol.10 pp 699-701 (1972)

Furniss, T
Competing for the space stakes
Interavia Space markets (May-June 1990)

Gilhooly, D
Rewiring Europe - The global telecommunications traffic report
International Institute of Telecommunications (1991)

Ginoux, J J
On some properties of reattaching laminar and transitional high speed flows
VKI-TN-53 (1969)

Gran, R L
Lewis, J E
Kubota, T
The effect of wall cooling on a compressible turbulent boundary layer
Journal of Fluid Mechanics, vol 66, part 3, pp 507-528 (1974)

Groth, C P T
Gottlieb, J J
Sullivan, P A
Numerical investigation of high-temperature effects in the UTIAS-RPI hypersonic impulse tunnel
Canadian Journal of Physics, vol.69, no.7, pp 897-918 (1969)

Hakkinen R J
Greber, I
Trilling, L
Abarbanel S S
The interaction of an oblique shockwave with a laminar boundary layer
NASA MEMO 2-18-59W (March 1959)

Hankey, W L
Holden. M S
Experimental studies of shockwave / boundary layer interactions
AGARD-AG-203 (1975)

Harr, M
Kohli, R
Commercial utilisation of space - An international comparison of framework conditions
Battelle Press, Columbus, Ohio (1990)

Hay, T
Roberts, S
International directory of telecommunications - markets, trends, companies statistics and personnel, 3rd ed.,
Longman (1988)

Hayes, W D
Probstein, R F
Hypersonic flow theory vol. 1 - Inviscid flows (2nd Ed)
Academic Press (1966)

Hayes, W D
Probstein, R F
Hypersonic flow theory
Academic Press (1959)

Hefner, J N
Sterrett, J R
Secondary jet interaction with the emphasis on outflow and jet location
J. of Spacecraft and Rockets, vol.9, no.11, pp 845 - 847, November (1972)

Hilton, W F
Advances in Space Technology
Proc. of a Symposium held at Hatfield College, George Newnes Ltd., (1962)

Holden, M S
Moselle, J R
A Database of Aerothermal Measurements in Hypersonic Flow for CFD Validation
AIAA-92-4023 (1992)

Holden, M S
A review of Aerothermal problems associated with hypersonic flight
AIAA Paper 86-0267 (1986)

Holden, M S
A study of flow separation in regions of laminar shockwave boundary layer interactions in hypersonic flow
AIAA Paper 78-1169 (1978)

Inger, G R
Scaling of incipient separation in high speed laminar flows
AIAA 93-3435 (1993)

Inger, G R
Three-dimensional disturbances in reattaching separated flows
AGARD CP-168 (1975)

Isakowitz, S J
International reference guide to space launch systems
American Institute of Aeronautics and Astronautics (1991)

Jaques, B
The future of space insurance
Interavia space markets (Summer 1987)

Jillie, D W
Hopkins, E J
Effects of Mach number, leading edge bluntness and sweep on boundary layer transition on a flat plate
NASA TN-D 1071 (1961)

Karamcheti, K
Hsia, H T S
Integral approach to an approximate analysis of thrust vector control by secondary injection
AIAA J. vol.1, no.11, November 1963

Katzer, E
On the length scales of laminar shockwave boundary layer interactions
Journal of Fluid Mechanics, vol.206, pp 477-496 (1989)

Kaufman, L G
Meckler, L
Hartofilis, S A
An investigation of flow separation and aerodynamic controls at hypersonic speeds
Journal of Aircraft, vol.3, no.6, pp 555-561

Kelly, T
Performance indicators for public telecommunications operators
OECD report (1990)

Knight, I N
Neibert, M T
An overview of satellite transmission issues and the ISDN
Proceedings of the IEEE - International conference on communications pp1073-1076, Toronto Canada (Jun 1986)

Korkegi, R H
Transition studies and skin friction measurements on an insulated flat plate at a Mach number of 5.8
J. of the Aeronautical Sciences, vol.23, no.2, (Feb, 1956)

Kramer, H J
Earth Observation Remote Sensing - survey of missions and sensors
Springer-Verlag, Heidelberg (1992)

Kumar, D
Control effectiveness at hypersonic speeds
MSc thesis, Cranfield Institute of Technology (1991)

Laderman, A J
Demetriades, A
Detection of boundary layer transition with a Laser beam
AIAA Journal, vol.14, no.1, pp 102-104 (1976)

Ledford, O C
Hypersonic film cooling
PhD thesis, Univ. of London (1973)

Ledger, J D
Vas, I E
Bogdonoff, S M
Hypersonic studies of wakes behind cylinders - Part 1 [Pitot pressure measurements at M = 16 in helium]
Report 739 [1965], Dept. of Aeronautical Engineering, Princeton University

Legraff, J E
Observations of hypersonic boundary layer transition using hot wire anemometry
AIAA Journal, vol.10, no.6, pp 762 - 769 (June 1972)

Lewis, C H
The blast-hypersonic flow analogy based upon Oshima's quasi-similarity model
AEDC-TN-61-158 (1961)

Lewis, J E
Gran, R L
Kubota, T
An experiment on the adiabatic compressible boundary layer in adverse and favourable pressure gradients
Journal of Fluid Mechanics, vol 51, part 4, pp 657-672 (1972)

Lukasiewicz, J
Hypersonic flow blast analogy
AEDC-TR-61-4 (1961)

Lukasiewicz, J
Experimental methods in Hypersonics
Marcel Dekker, New York (1973)

Mahle, C
Hyde, G
Efficiency of communications satellites
AIAA-92-2053 (1992)

Mack, L M
Linear stability theory and the problem of supersonic boundary layer transition
AIAA Journal, vol.13, no.3, pp 278-289 (1975)

Malik, M R
Zang, T A
Bushnell, D M
Boundary layer transition in hypersonic flows
AIAA 90-5232 [1990]

Markovin, M V
Critical evaluation of transition from laminar to turbulent shear layers with emphasis on hypersonically travelling bodies
AFFDL-TR-68-149 (1969)

Mateer, G G
Larson, H K
Unusual boundary layer transition results on cones in hypersonic flow
AIAA J. vol.7, no.4, pp 660-664 (April 1969)

Miller, D S
Hijman, R
Childs, M E
Mach 8 to 22 studies of flow separation due to deflected control surfaces
AIAA J. vol.2, no.2, pp 312-321 (1964)

Moeckel, W E
Some effects of bluntness on boundary layer transition and heat transfer at supersonic speeds
NACA R-1312 (1957)

Mohammadian, S
Calibration of the Mach 12 contoured nozzle
ICST Report no.70-02 (1968)

Muir, J F
Trujillo, A A
Experimental investigation of the effects of nose bluntness, freestream unit Reynolds number and angle of attack on cone boundary layer transition at Mach number of 6
AIAA Paper 72-0216 (1972)

Nagamatsu, H T
Sheer, R E
Graber, B C
Hypersonic laminar boundary layer transition on 8-foot long, 10° cone, M_1 = 9.1 - 16
AIAA Journal vol.5, no.7, pp 1245 - 1252 (July 1967)

Neal, L
A study of pressure, heat transfer and skin friction on sharp and blunt flat plates at Mach 6.8
NASA TN D-3312 (1966)

Needham, D A
A note on hypersonic incipient separation
AIAA Journal, pp 2284 - 2285 (1967)

Needham, D A
Laminar separation in hypersonic flows
PhD thesis, Univ. of London (August 1965)

Needham, D A
Stollery, J L
Boundary layer separation in hypersonic flow
AIAA Paper 66-455 (1966)

Needham, D A
Progress Report on the Imperial College Hypersonic Gun Tunnel
ICST Report no.118 (1963)

Nunn, A
Jet Interaction Wrap-Around on Bodies of Revolution
J. Spacecraft vol.7, no.3,pp 334 - 337 (1970)

Oldfield, M L G
Private Communications
Dept. of Engineering, Univ. of Oxford, UK (1993)

Oldfield, M L G
Experimental techniques in unsteady flows
OUEL 1843/90
[see also VKI lectures on unsteady aerodynamics, 1988]

Oldfield, M L G
Burd, H J
Doe, N G
Design of wide-bandwidth analogue circuits for heat transfer instrumentation in transient tunnels - Heat and Mass transfer in Rotating Machinary
Proc. of the 16th symposium of the International centre for heat and mass transfer, Dubrovnik, September 1982 - Hemisphere Publ. Corp (1984)

Opatowski, T P S
An experimental study of the flow around and the forces developed by hypersonic lifting vehicles
PhD Thesis, Univ. of London (Sept. 1967)

Opatowski, T P S
A three-component gun tunnel balance designed for testing thin delta wings
ARC 31278 (1969)

Owen, F K
Horstman, C C
Stainback, P C
Wagner, R D
Comparison of wind tunnel transition and freestream disturbance measurements
AIAA Journal, vol.13, no.3, pp 266-269 (March 1975)

Owen, F K
Horstman, C C
Hypersonic transitional boundary layers
AIAA J., vol.10, no.6 (June 1972)

Owen, F K
Transition experiments on a flat plate at subsonic a supersonic speeds
AIAA J., vol.8, no.3, (March 1970)

Pagan, D
Molton, P
Delery, J
Basic experiments on a supersonic vortex flow around a missile body
J. Spacecraft and Rockets, vol.29, no.3, pp 373-378 (1992)

Parkinson, R C
Why space is expensive - Operational/economic aspects of space transport
(British Aerospace Space Systems, Stevenage)

Peake, D J
Tobak, M
Three-dimensional flows about simple components at angle of attack
High angle of attack aerodynamics, AGARD-LS-121(1982)

Pearce, F
The great debate - Cable Vs Satellite
Far Eastern Economic Review, vol 141, pp 59-61 (July 1988)

Pelton, J N
The satellite communications industry - new doors opening
Telecommunications (North American ed.), vol 23,pp 59-60 (June 1989)

Poisson-Quinton PH.
Ceresuela, R
Efficiency and kinetic heating of aerodynamic devices in devices in hypersonic flow
Aerospace Proceedings pp 439 - 482 [1966]

Popinski, Z
Ehrlich, C F
Development design methods for predicting hypersonic aerodynamic control characteristics
AFFDL-TR-66-85 (1966)

Potter, J L
Whitfield, J D
Effects of unit Reynolds number, nose bluntness and roughness on boundary layer transition
AEDC-TR-60-5 (March 1960)

Price, K M
Kwan, R K
White, L W
Garlow, R K
Henderson, T R
Technical and economic feasibility of integrated video service by satellite
AIAA-92-2054 (1992)

Putnam, L E
Investigation of effects of ramp span and deflection angle on laminar boundary layer separation at M = 10.03
NASA TN-D 2833 (1965)

Rae, W H
Pope, A
Low speed wind tunnel testing
John Wiley & Sons (1984)

Reshotko, E
Khan, M M S
Stability of the laminar boundary layer on a blunted flat plate in supersonic flow
Proceedings of IUTAM symposium on laminar-turbulent transition, pp 187-200, Stuttgart (September 16-22 1979)

Richards, B E
Film cooling in hypersonic flows
PhD thesis, Univ. of London (1967)

Richards, G
High speed flows over two-dimensional and axisymmetric bodies
PhD thesis, Cranfield Institute of Technology (1978)

Roberts, M L
Transitional flow separation upstream of a compression corner
AIAA Paper 70-764 (1970)

Russell, D
Wyatt, J
MSPECTE - Digital signal analysis package
Private Communications [CoA, Cranfield]

Sanator, R J
Boccio, J L
Shamshins, D
Effects of bluntness on hypersonic two-dimensional inlet type flows
NASA CR-1145 (1968)

Schultz, D L
Jones, T V
Heat Transfer Measurements in short duration hypersonic facilities
AGARD-AG-165 (1975)

Sema Group Management Consultants
Telecommunications services
Panorama of European Community Industry (1991-1992)

Simeonides, G
Hypersonic shockwave boundary layer interactions over compression corners
PhD thesis, Von Karman Institute / University of Bristol (April 1992)

Simeonides, G
Hasse, W
Manna, M
Experimental, Analytical and Computational Methods Applied to Hypersonic Compression Ramp Flows
AIAA Journal, Vol. 32, No. 2 (February 1994)

Singh, I B
New markets for satellite communications
Telecommunications (North American ed.), vol 22, pp 88-96 (1988)

Smith, A J D
The dynamic response of a wedge separated hypersonic flow and its effects on heat transfer
PhD Thesis, Univ. of Southampton (1993)

Smith, R J
Circuits, Devices and Systems, 4th ed.
John Wiley & Sons (1984)

Softley, E J
Graber, B C
Zempel, R C
Experimental observation of transition of the hypersonic boundary layer
AIAA J., vol.7, pp257-263 (1969)

Spall, R E
Malik, M R
Goertler vortices in supersonic and hypersonic boundary layers
Physics of Fluids A 1, vol.11, pp 1822-1835 (1989)

Staple, G
The year in review - The global telecommunications traffic report
International Institute of Telecommunications (1991)

Stetson, K F
Kimmel, R L
Unit Reynolds number effects on boundary layer transition
AIAA J. vol.31, no.1, pp 195-196 (1993)

Stetson, K F
Kimmel, R L
Thompson, E R
Donaldson, J C
Siler, L G
A comparison of planar and conical boundary layer stability and transition at a Mach number of 8
AIAA Paper 91-1639 (1991)

Stetson, K F (a)
On cone frustum pressure gradient effects on transition
AIAA J. vol.26, no.4. pp 500-502 (1988)

Stetson, K F (b)
On non-linear aspects of hypersonic boundary layer stability
AIAA J. vol.26, no.7. pp 883-885 (1988)

Stetson, K F
Thompson, E R
Donaldson, J C
Siler, L G

Laminar boundary layer stability experiments on a cone at Mach 8
AIAA 86-1087 (1986)

Stetson, K F
Thompson, E R
Donaldson, J C
Siler, L G

Laminar boundary layer stability experiments on a cone at Mach 8, Part 2 : Blunt Cone
AIAA Paper 84-0006 (1984)

Stetson, K F (a)

Nose bluntness effects on cone frustum boundary layer transition in hypersonic flow
AIAA Paper 83-1763 (1983)

Stetson, K F (b)
Thompson, E R
Donaldson, J C
Siler, L G

Laminar boundary layer stability experiments on a cone at Mach 8, Part 1 : Sharp cone
AIAA Paper 83-1761 (1983)

Stetson, K F

Effect of bluntness and angle of attack on boundary layer transition on cones and biconic configurations
AIAA Paper 79-0269 (1979)

Stetson, K F

Boundary layer separation on slender cones at angle of attack
AIAA Journal, vol.10, no.5, pp 642 - 648 (May 1972)

Stetson, K F
Rushton, A

Shock tunnel investigation of boundary layer transition at Mach 5.5
AIAA J. vol.5, no.5, pp 899-906, (May 1967)

Stollery, J L
Maull, D J
Belcher, B J

The Imperial College Hypersonic Gun Tunnel
Journal of the Royal Aerospace Society (1960)

Stollery, J L

Hypersonic viscous interactions on curved surfaces
Journal of Fluid Mechanics, vol. 43, part 3, pp 497-511 (1970)

Stollery, J L

Supersonic turbulent boundary layers : some comparisons between experiment and a simple theory
College of Aeronautics Aero Note 7510 (Aug.1975)

Stollery, J L
Coleman G T
A correlation between pressure and heat transfer distributions at supersonic and hypersonic speeds
Aeronautical Quarterly (Nov.1975)

Stollery, J L
An introduction to hypersonic aerodynamics
Project SPIN, CNRS, Ecole Centrale Paris (1990)

Stone, H W
The leading edge effects on the laminar flat plate boundary layer and the aerodymanuc heating at Mach 10.4
NASA TN D-5160 (May 1969)

Townsend, J C
The effects of leading edge bluntness and ramp deflection angle on laminar boundary layer separation in hypersonic flow
NASA TN-D 3290

Uehara, K
Nishida, H
Looking beyond the fax machine - The global telecommunications traffic report
International Institute of Telecommunications (1991)

Van Driest, E R
Investigation of Laminar boundary layer in compressible fluids using the Crocco method
NACA TN 2597 (1952)

Vermeulen, J P
Simeonides, G
Parametric studies of shockwave boundary layer interactions in two dimensional compression corners at Mach 6
VKI-TN-181 (Sept. 1992)

White, F M
Viscous fluid flow
McGraw Hill (1974)

Wilson, A (Ed.)
Interavia Space Directory 1991-92
Jane's information group (1991)

Wrisdale I E
Heat transfer measurements on axisymmetric bodies at high Mach numbers and incidence
RAE-TM-W4 (1992)

Zukowski, E E
Spaid, F W
Secondary injection of gases in a supersonic flow
AIAA J. vol 2, no.10, pp 1689-1696, October 1964

Zoby, E V
Thompson, R A

Flowfield and vehicle parameter influence on hypersonic heat transfer and drag
Journal of Spacecraft, vol .27, no.4, 1990

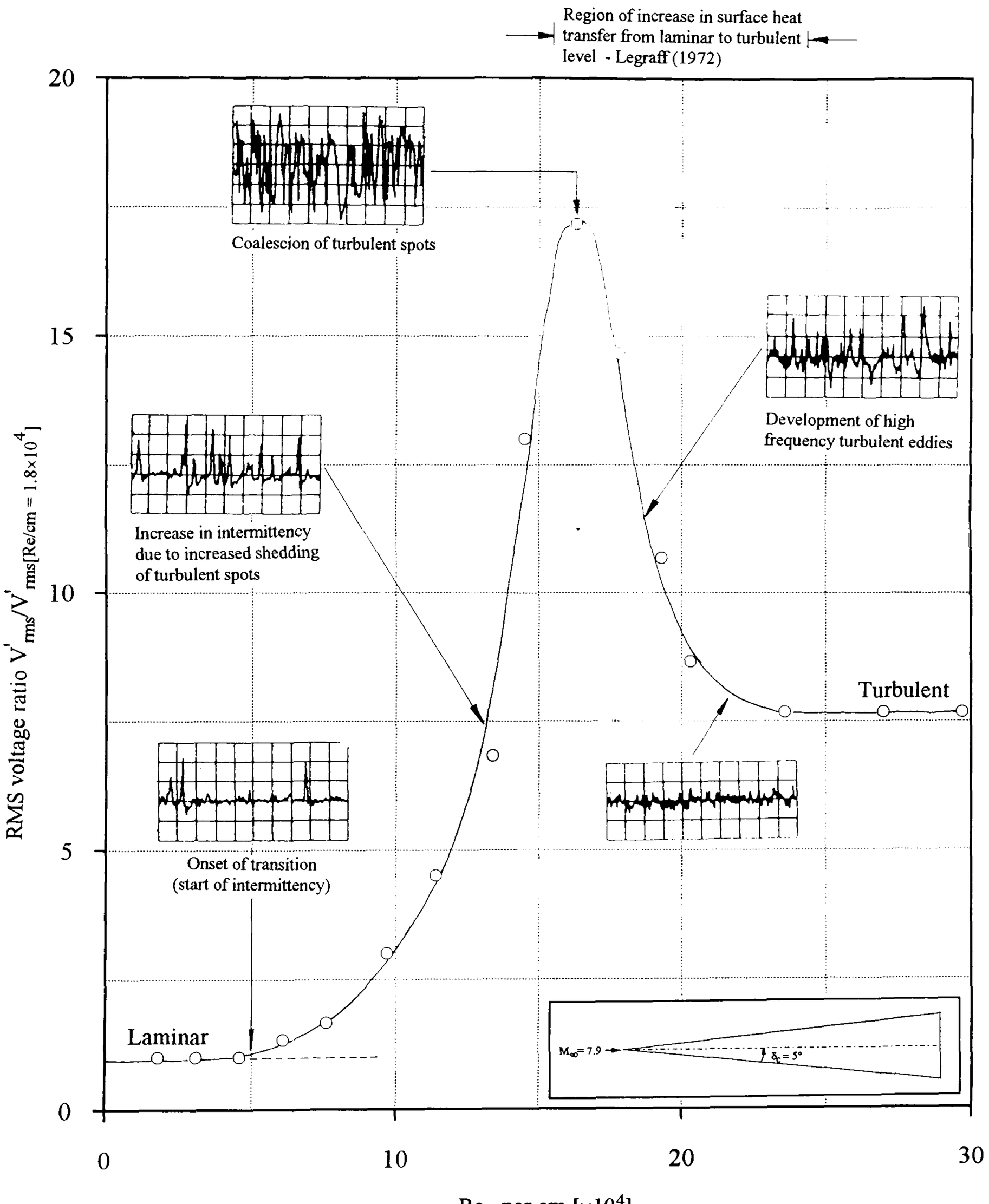

Figure 5-1 Development of intermittency at a given location on a 5° cone due to boundary layer transition - Owen et al. (1975)

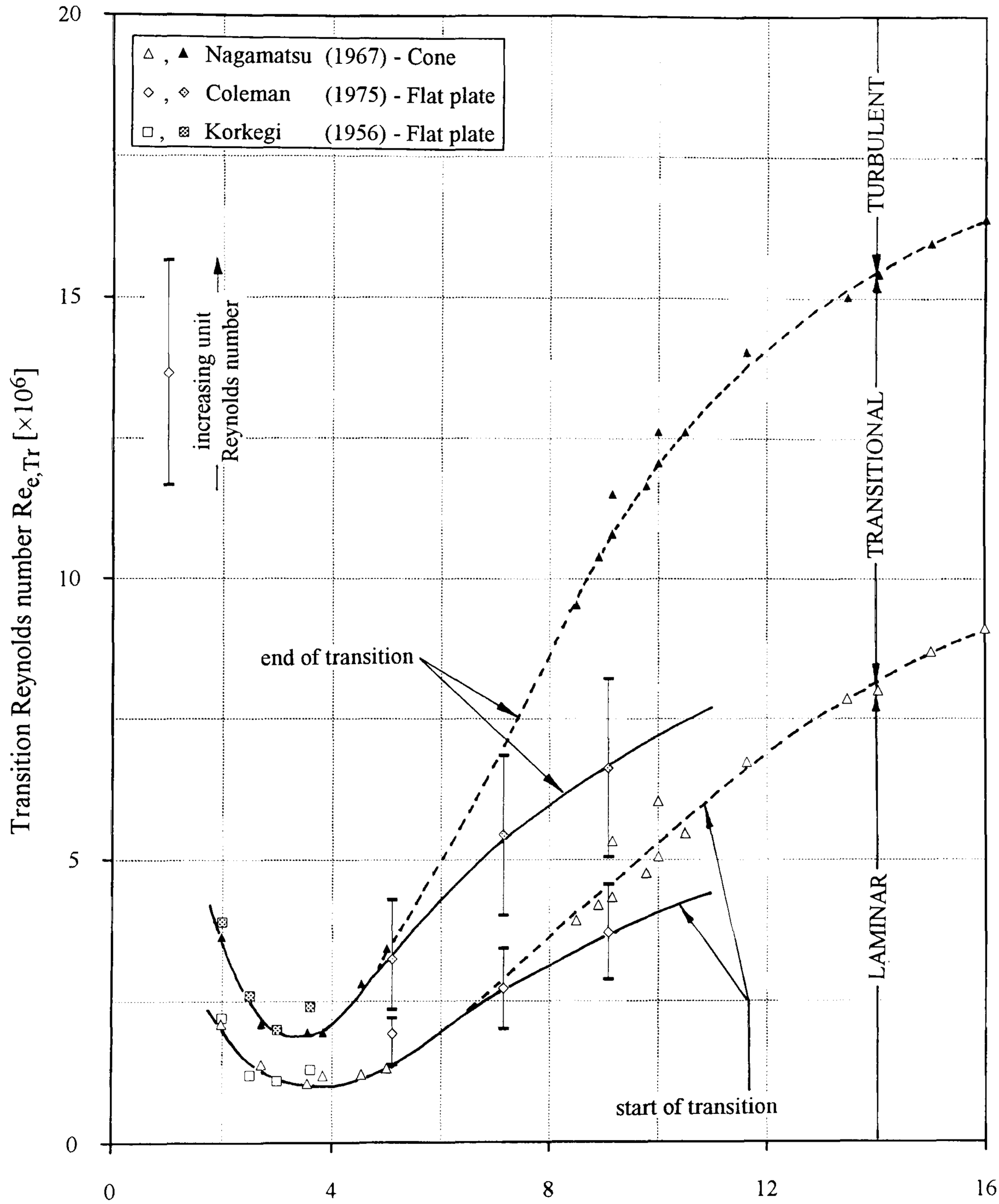

Figure 5-2 The effect of Mach number on the transition of conical and quasi two-dimensional boundary layers

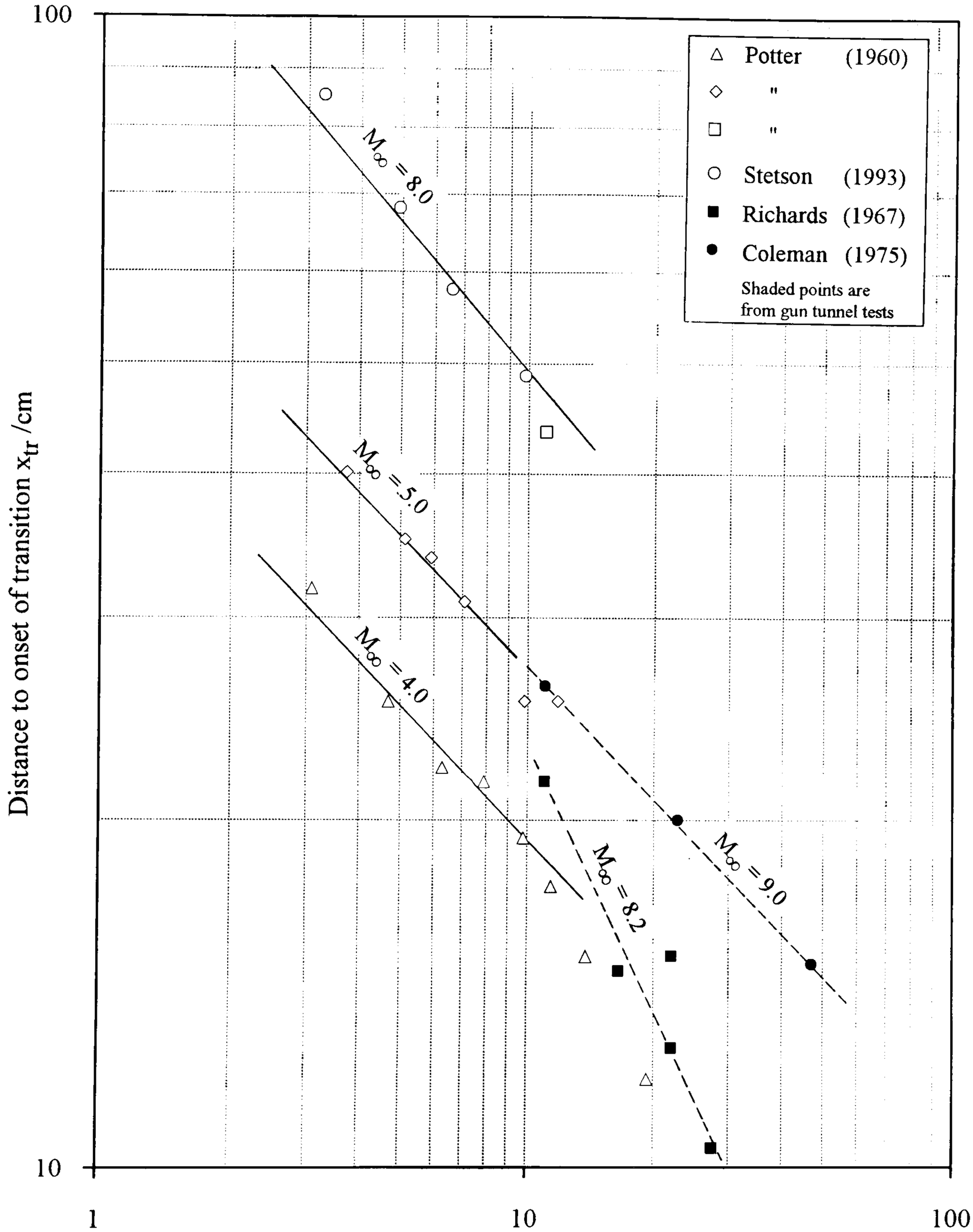

Figure 5-3 The effect of unit Reynolds number on the transition of quasi two-dimensional boundary layers

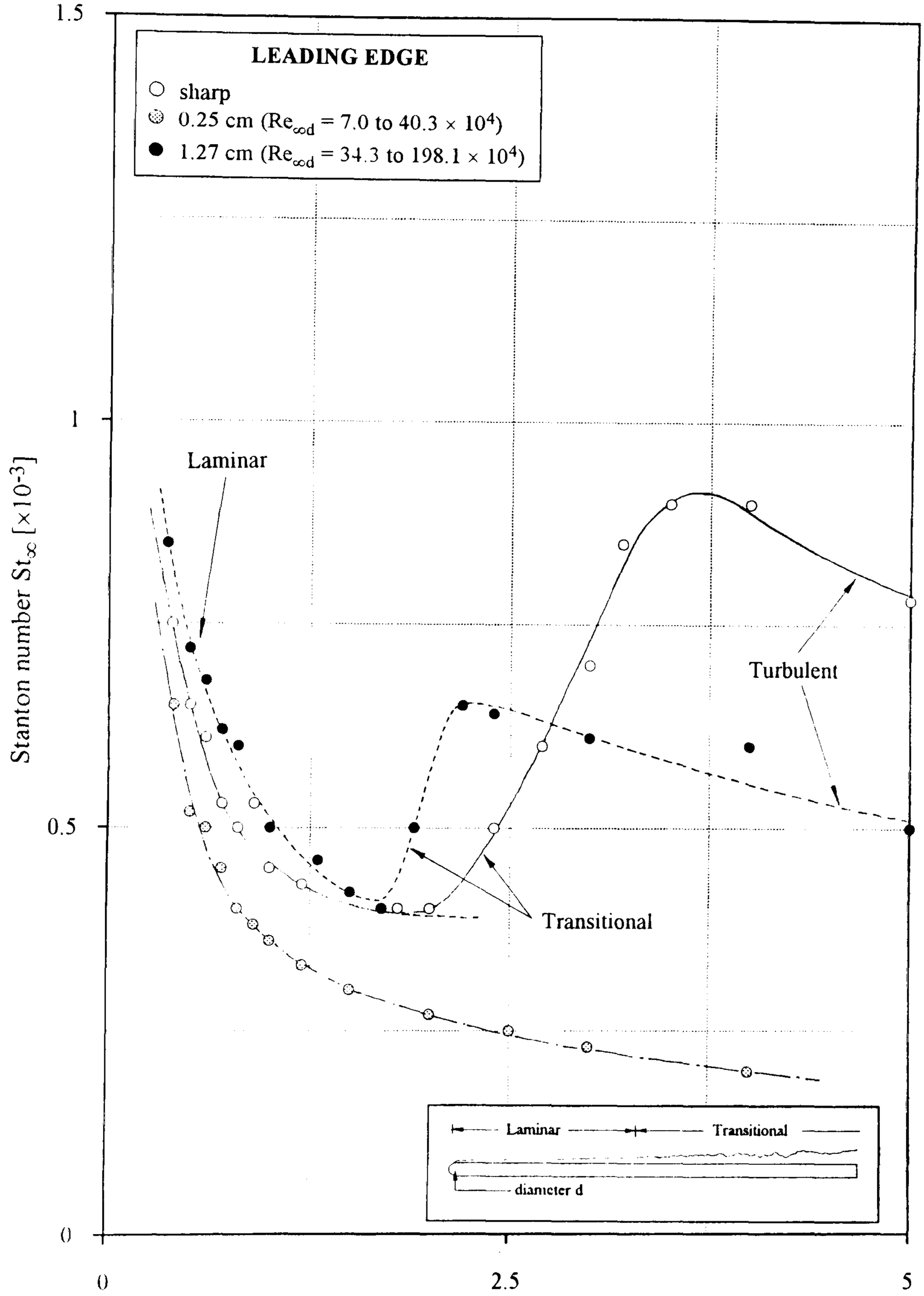

Figure 5-4 The effect of leading edge diameter on heat transfer distributions over a flat plate at M_∞ = 6.8 [Neal, 1966]

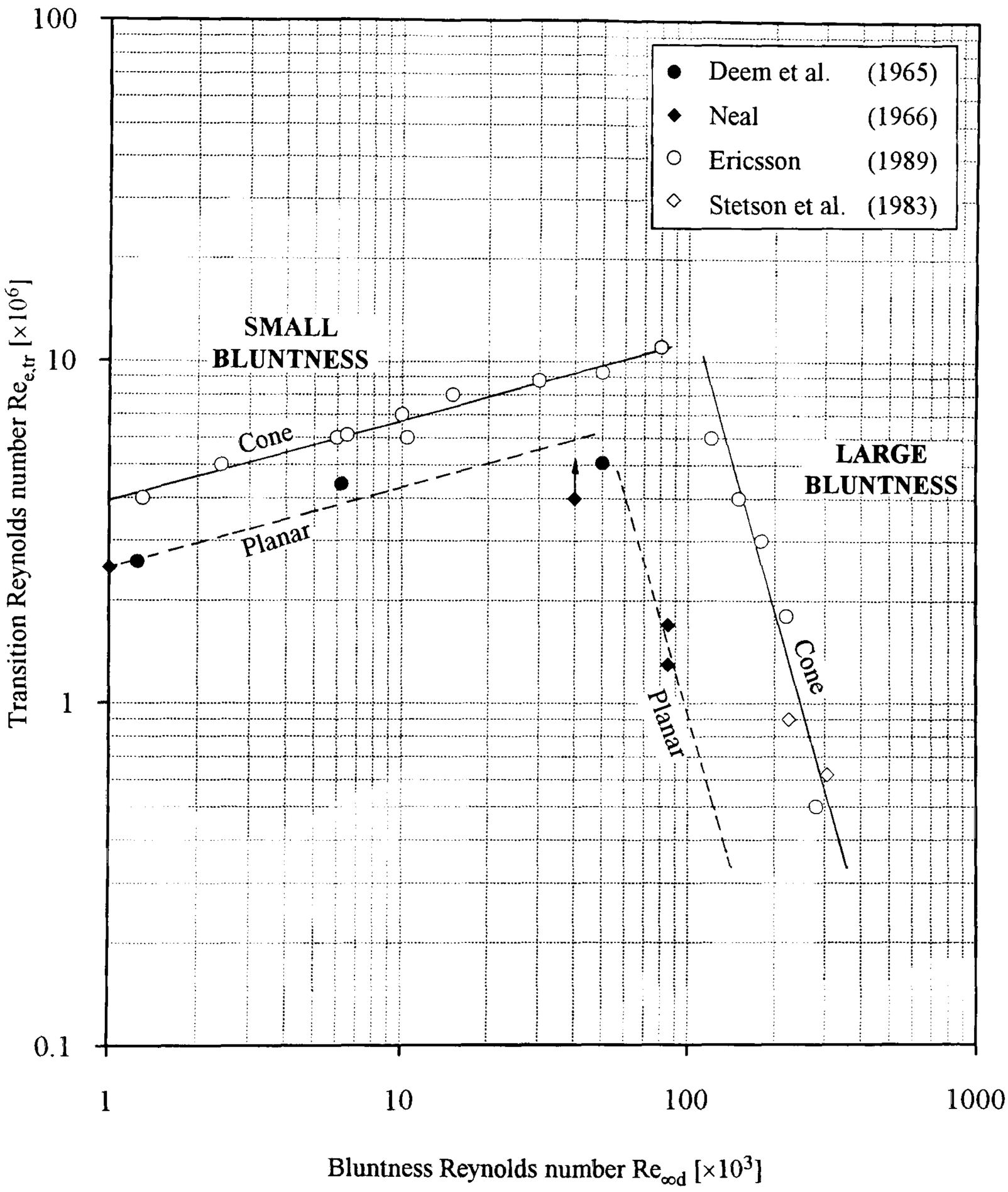

Figure 5-5 The effect of "small" and "large" bluntness on the onset of transition in planar and conical boundary layers

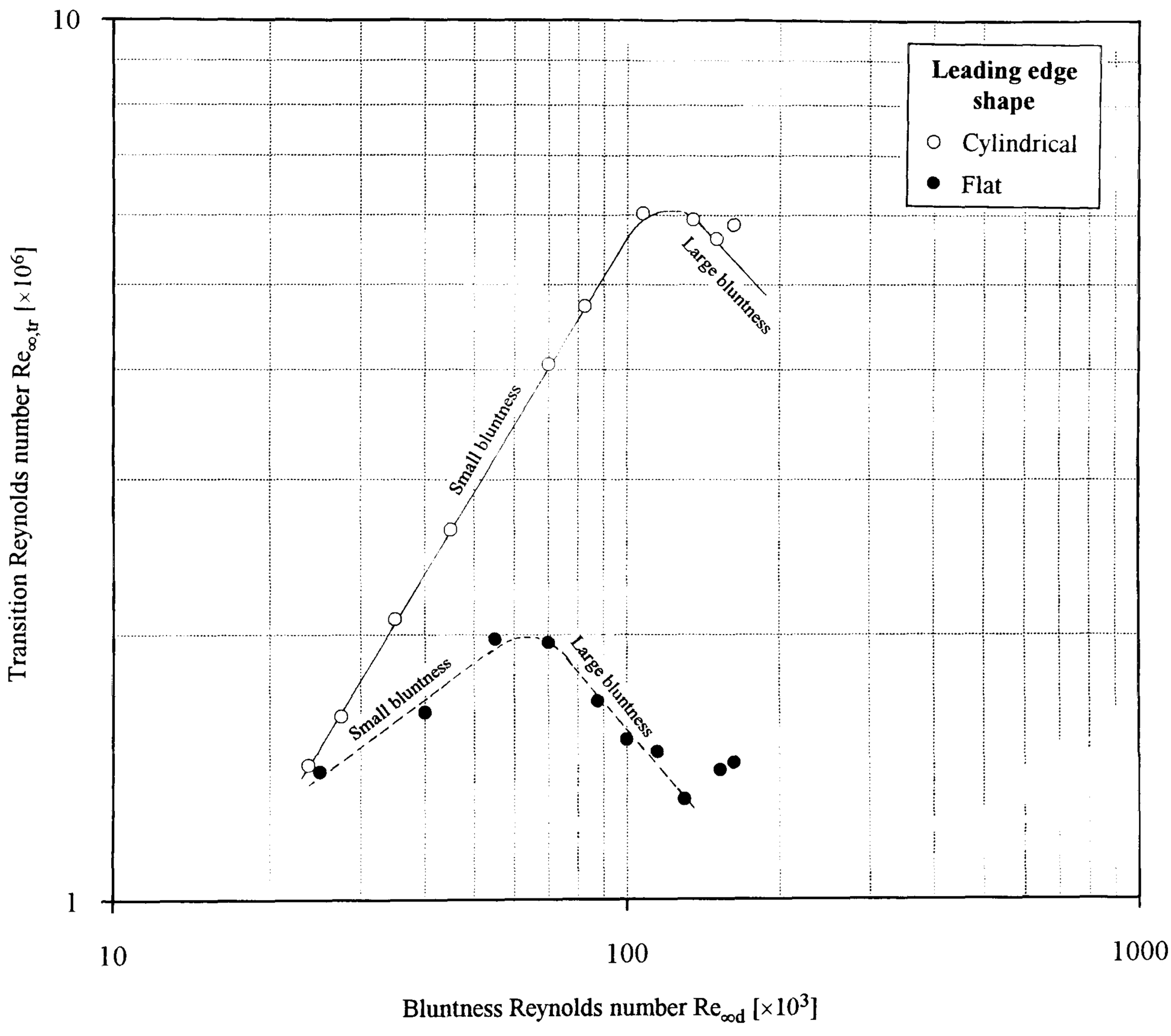

Figure 5-6 The effect of leading edge shape on the onset of transition in flat plate boundary layers - Brinich & Sands, 1957 ($M_\infty = 3.1$, d = 0.64 cm)

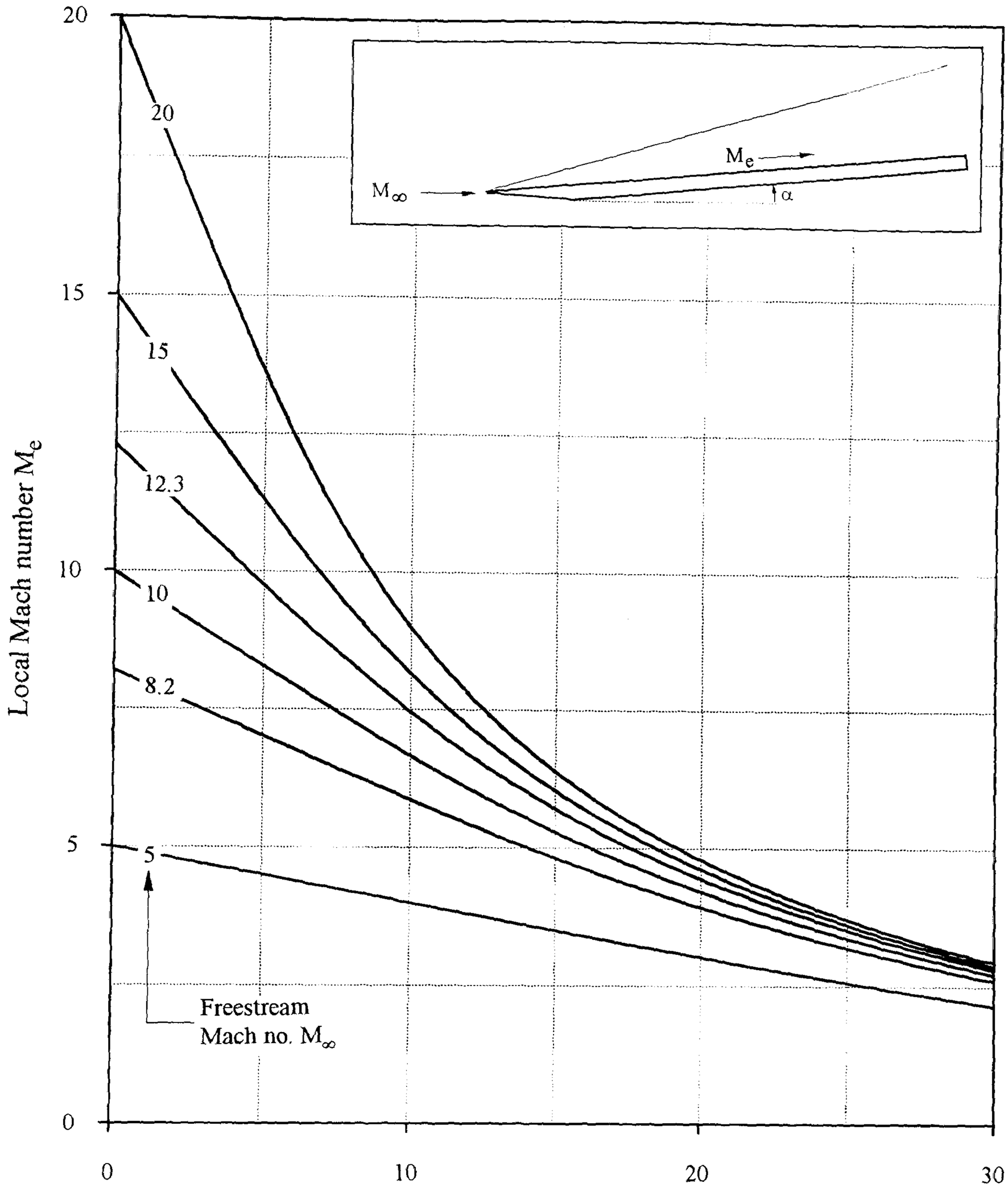

Figure 6-1 The effect of incidence on the local Mach number over a flat plate

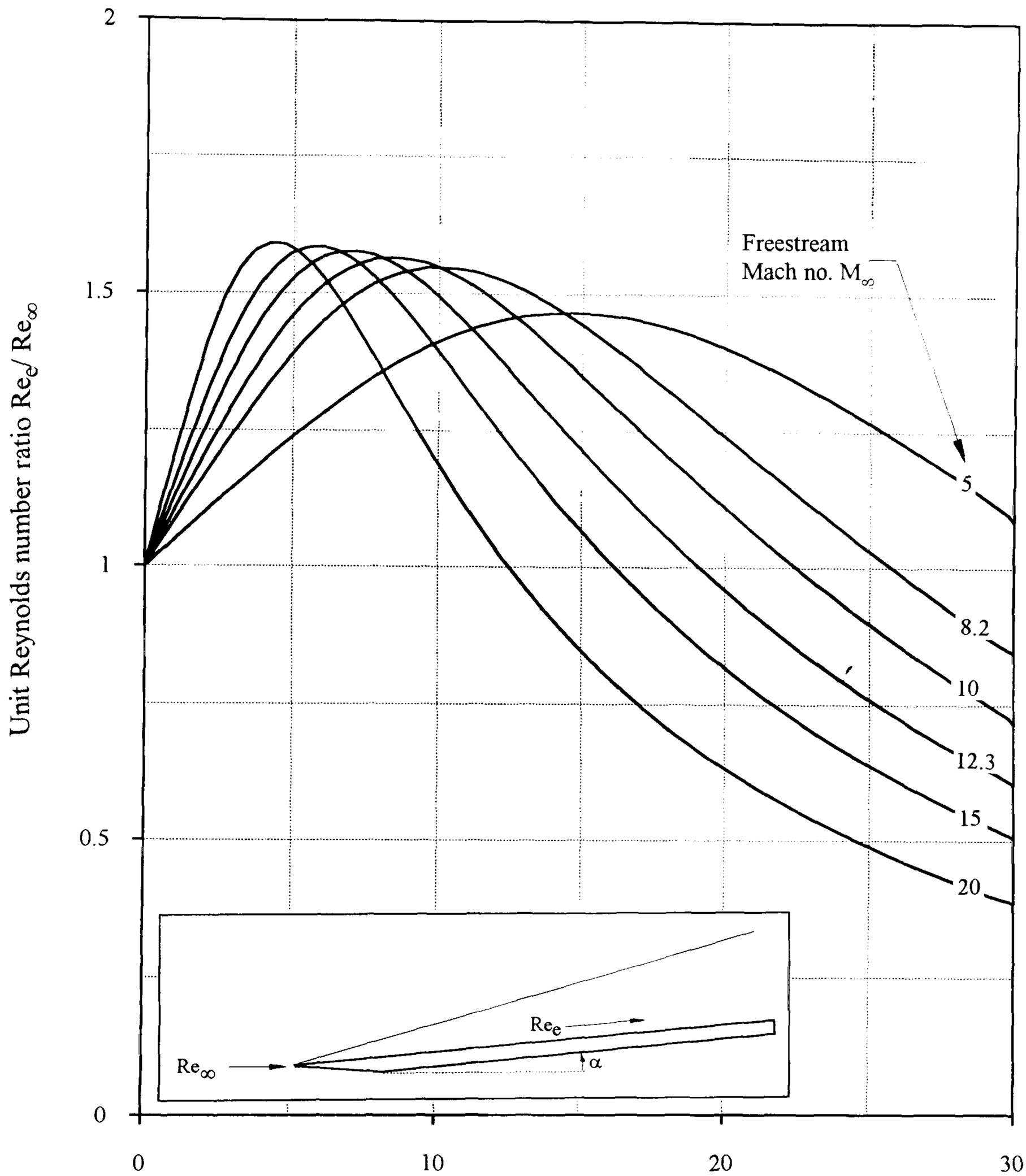

Figure 6-2 The effect of incidence on the local unit Reynolds number over a flat plate

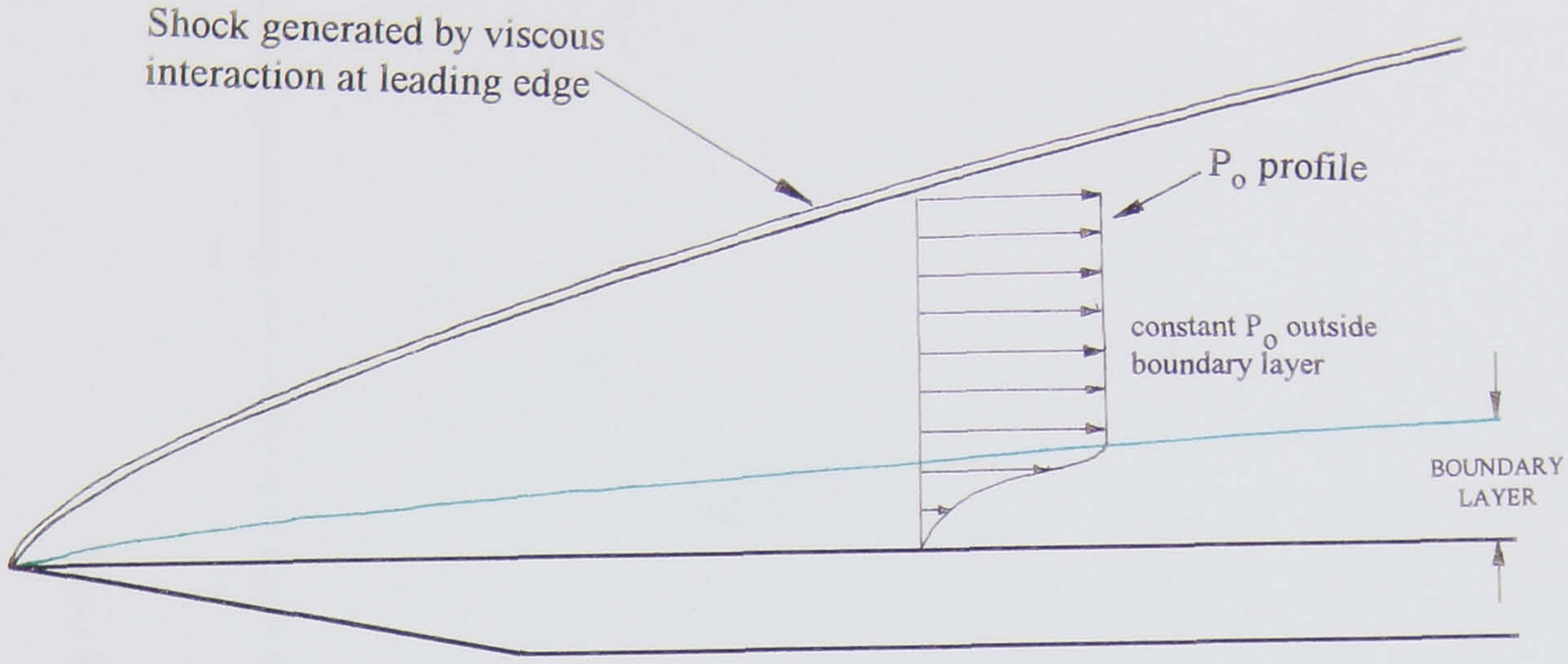

(a) sharp leading edge

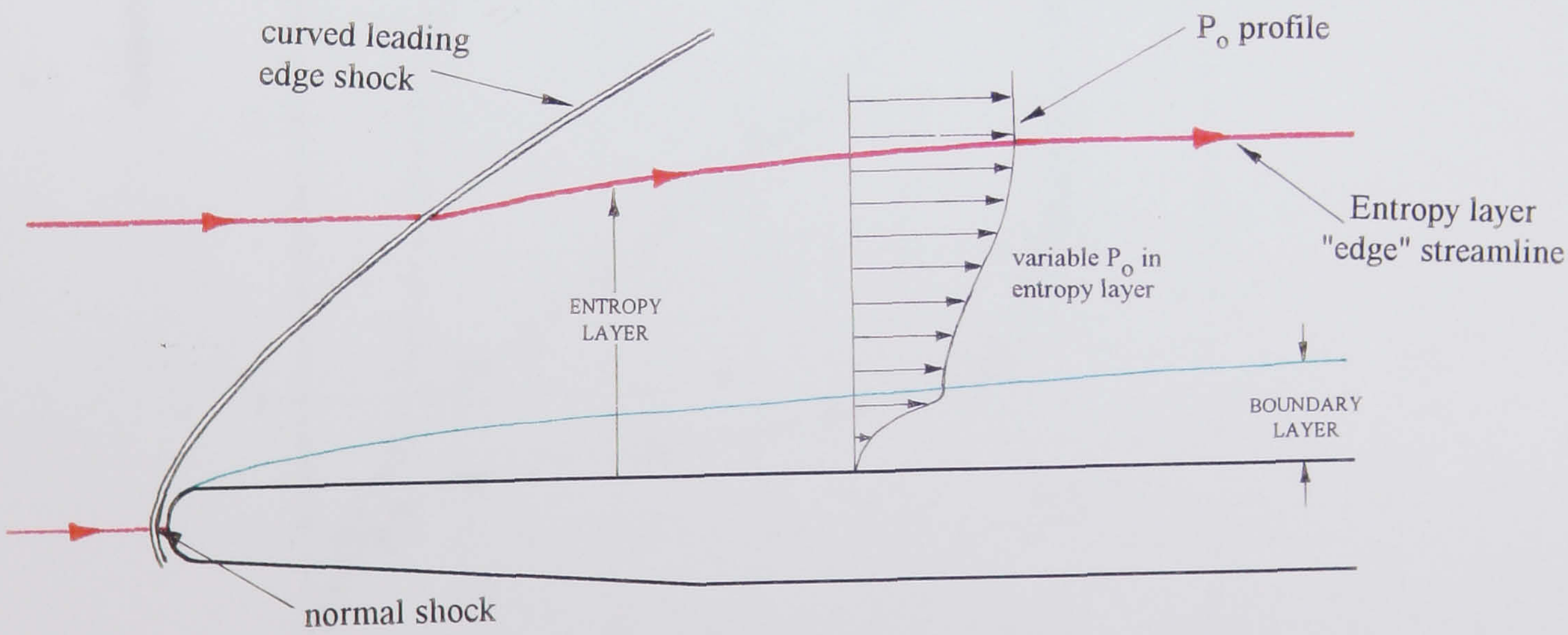

(b) blunt leading edge

Figure 6-3 The effect of leading edge bluntness on flat plate flow structure

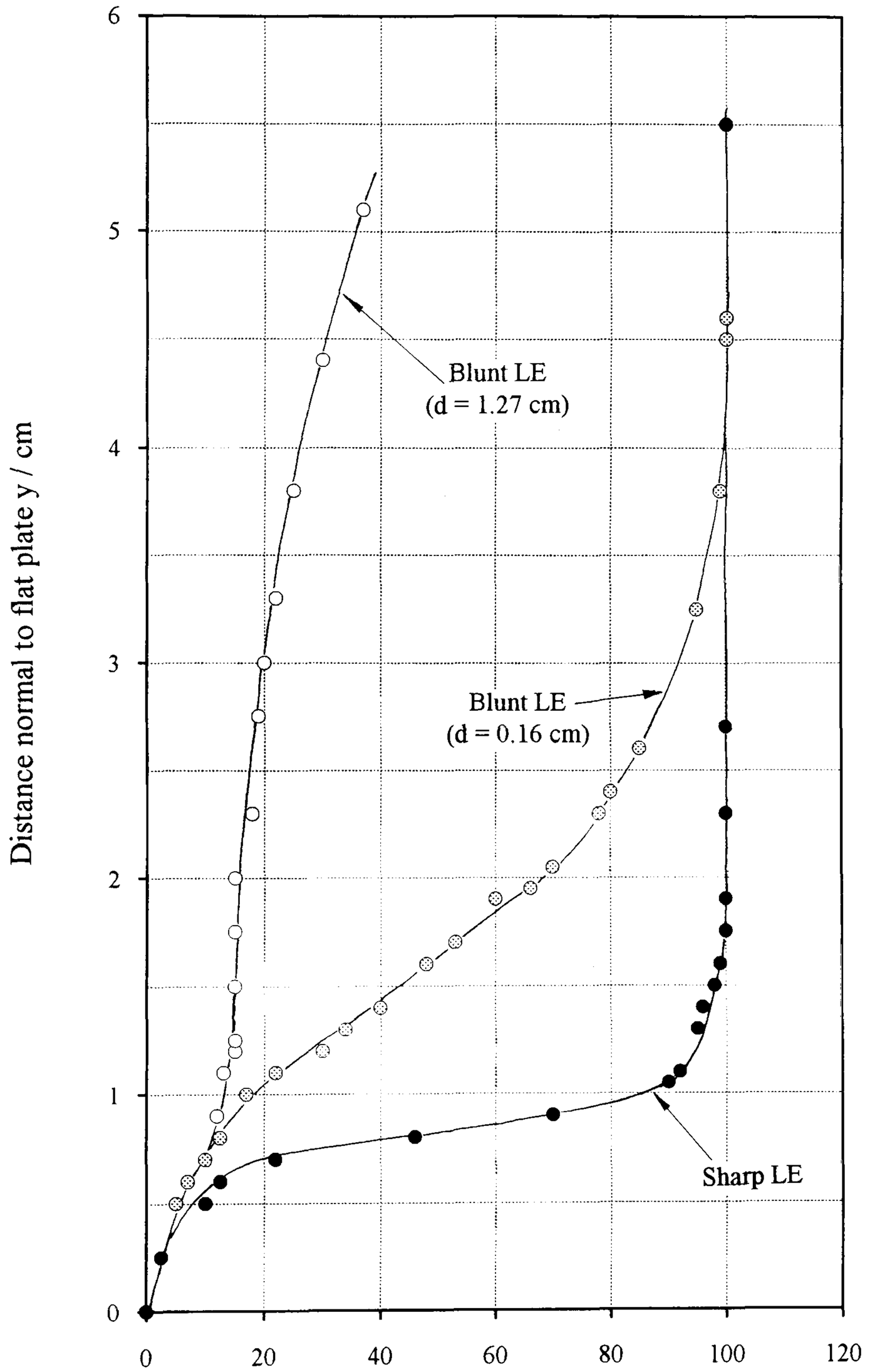

Figure 6-4 The effect of leading edge diameter on pitot pressure distributions in the entropy layer - Stone (1969)
(M_∞ = 10.4, Re_∞/ cm = 3.0×10^4, x = 38.1 cm, hemicylindrical LE)

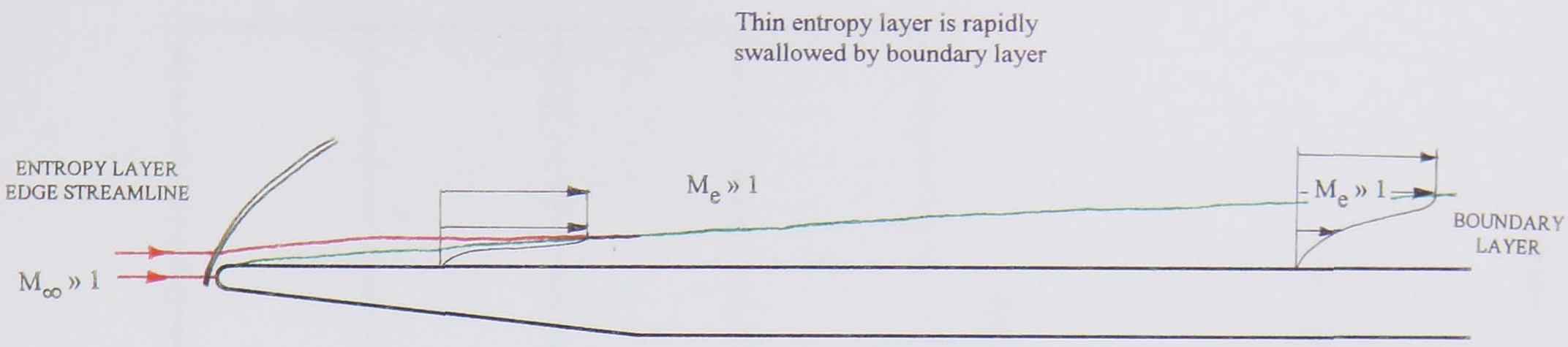

(a) small bluntness

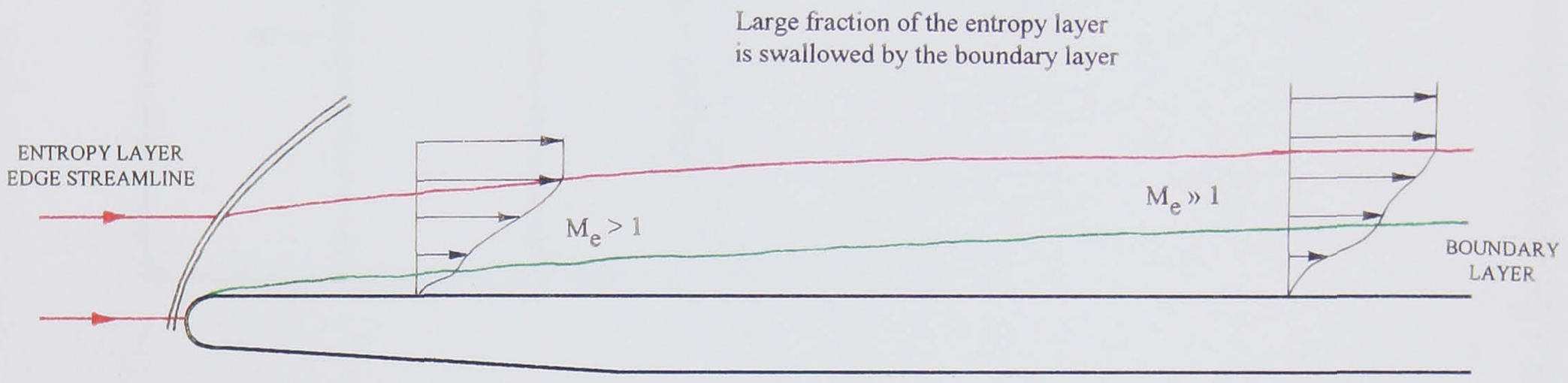

(b) moderate bluntness

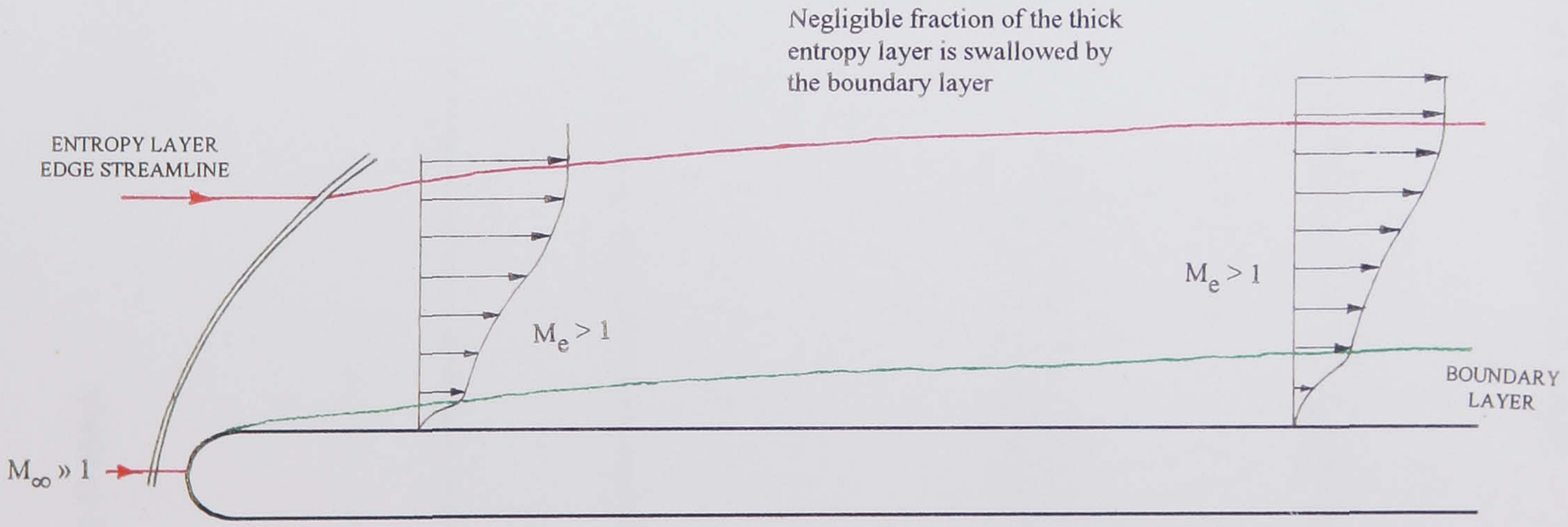

(c) large bluntness

Figure 6-5 The effect of leading edge diameter on the flow structure over a blunt flat plate

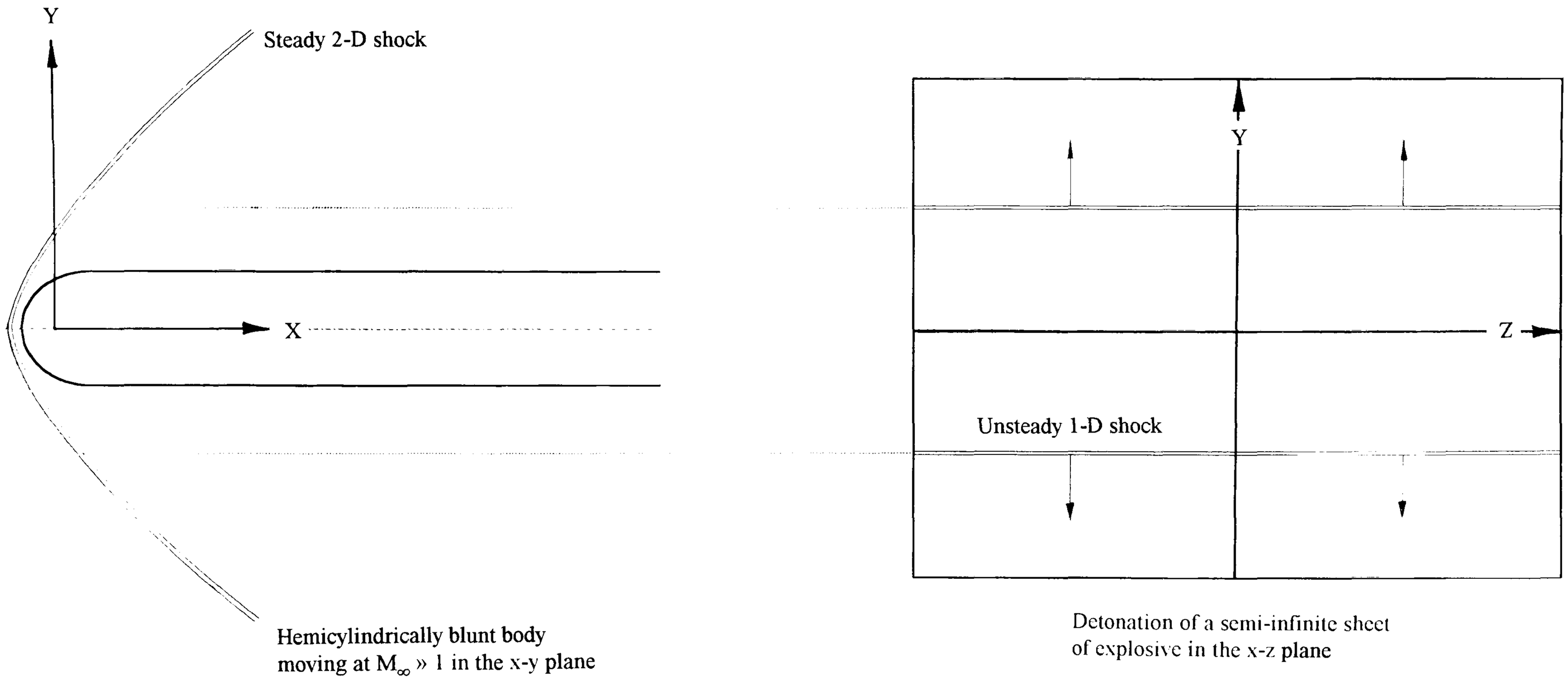

(a) hypersonic flow over a blunt 2-D body

(b) propagation of a 1-D blast wave

Figure 6-6 Blast wave analogy for hypersonic flow - the hypersonic equivalence principle (Anderson, 1989)

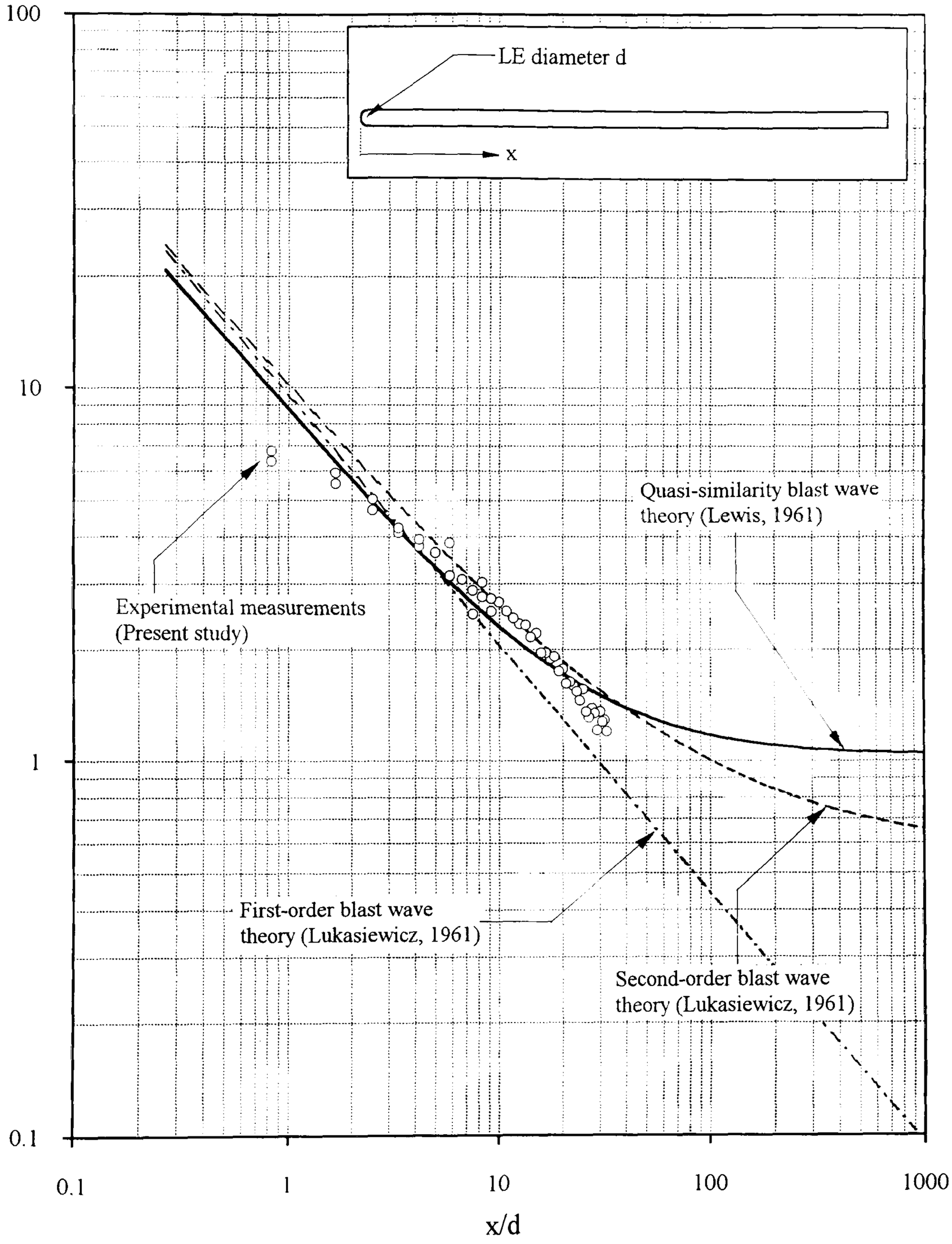

Figure 6-7 Correlation of the pressure measurements on a blunt flat plate with predictions from various approximations of blast wave theory
($M_\infty = 8.2$, $Re_\infty/cm = 9.0 \times 10^4$, $\alpha = 0°$, d = 6.0 mm, hemi-cylindrical LE $C_D = 1.27$)

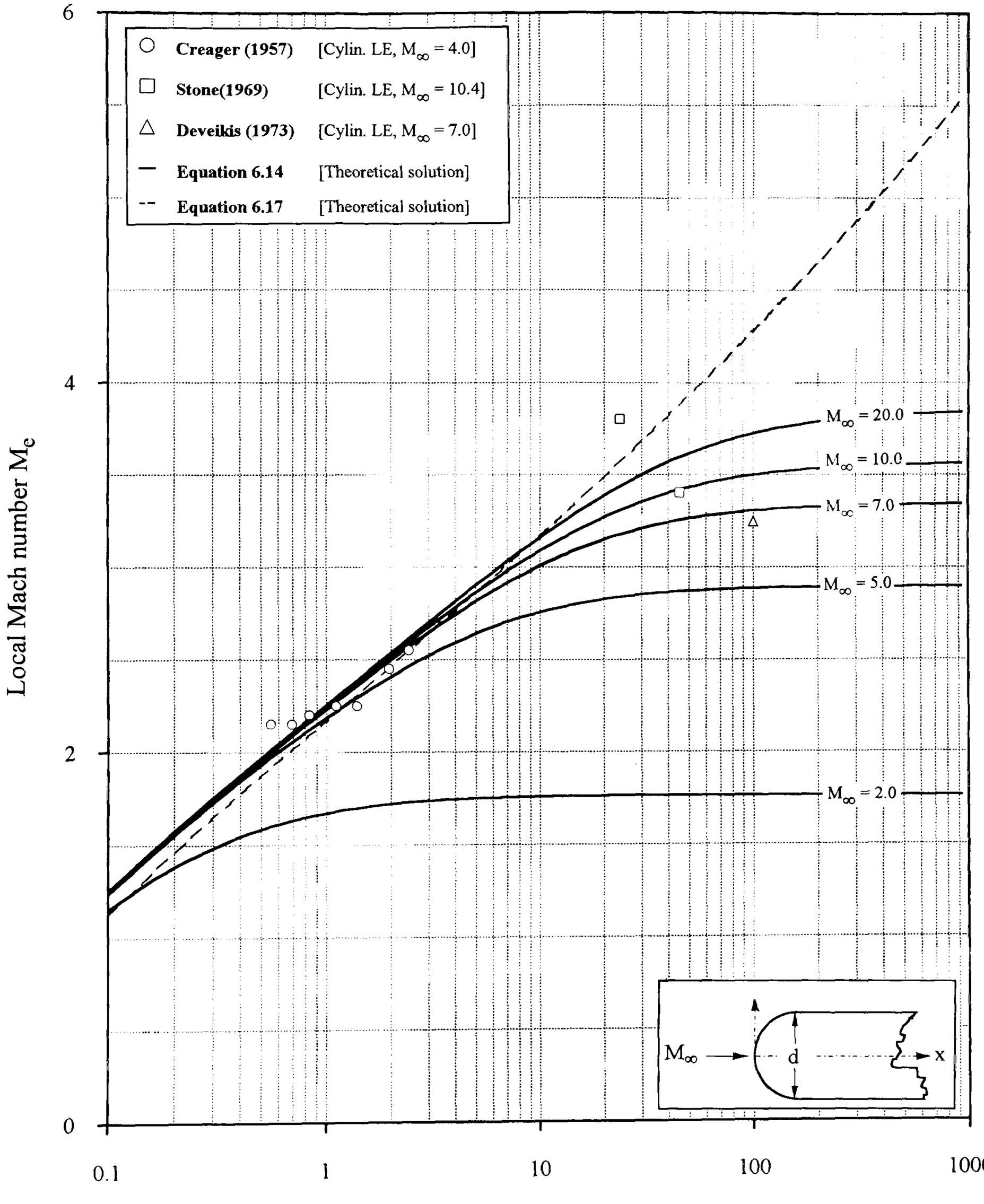

Figure 6-8 The effect of leading edge bluntness on the boundary layer edge Mach number over a blunt flat plate

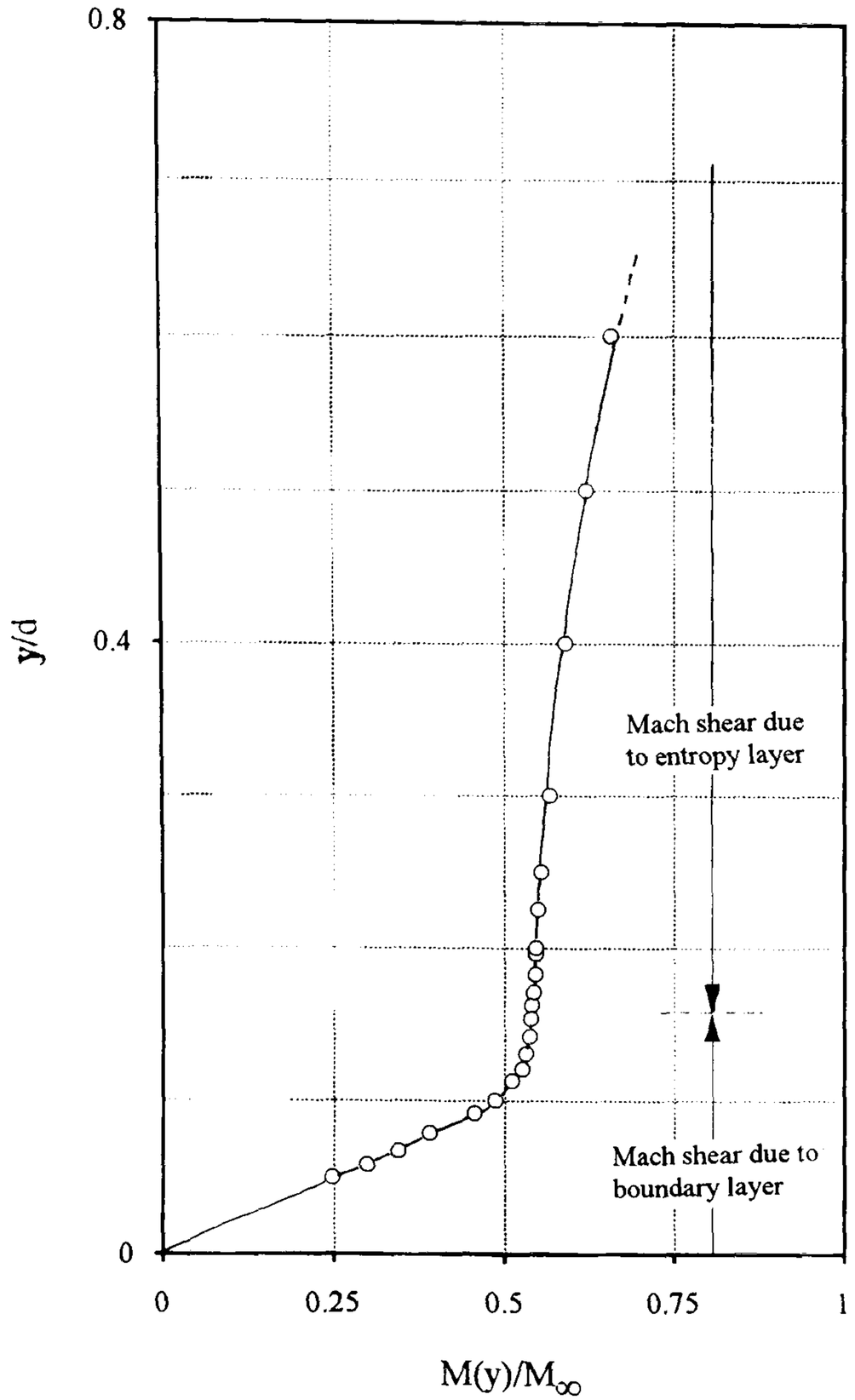

(i) Creager (1957), $M_\infty = 3.95$, x/d = 1.0

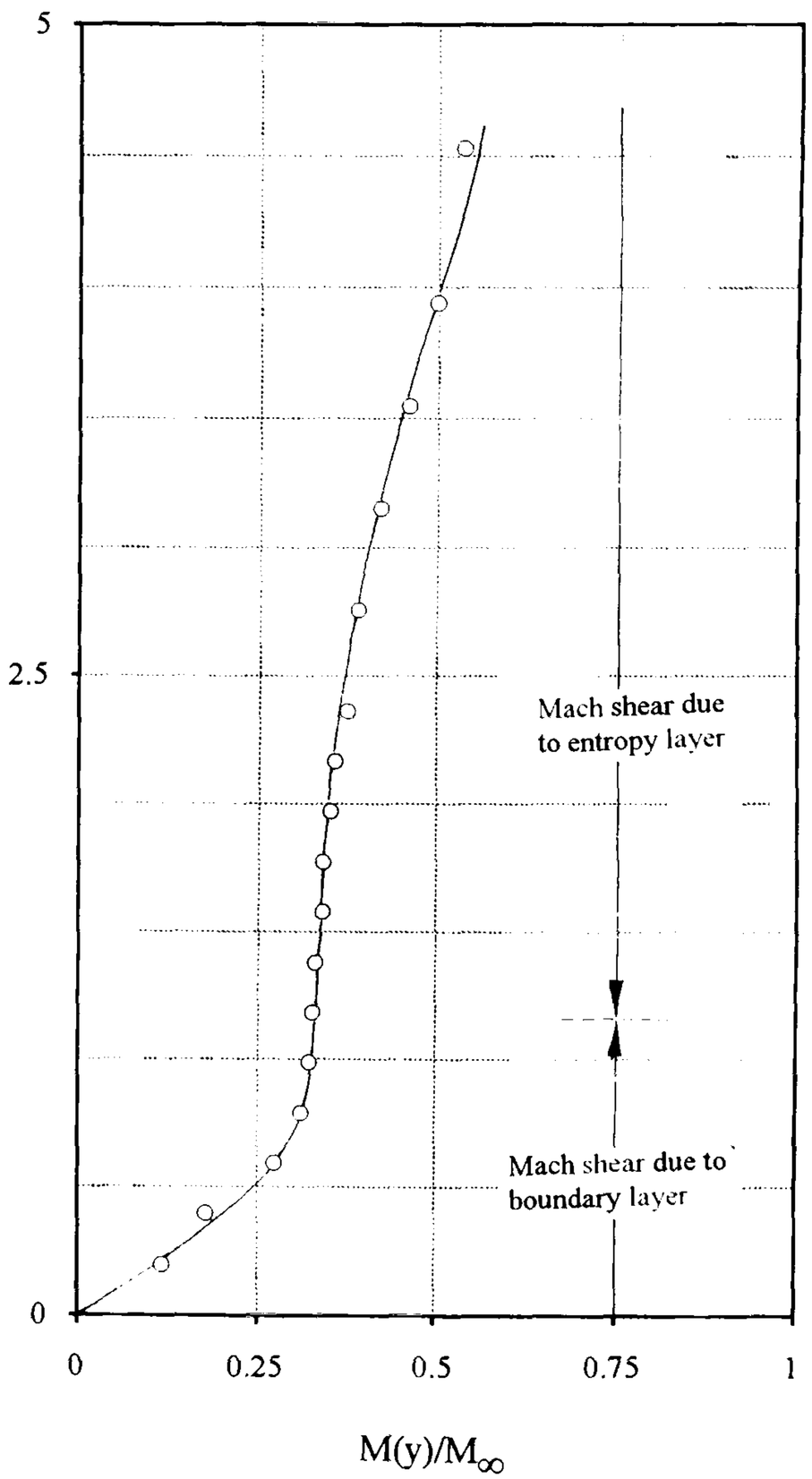

(ii) Stone (1969), $M_\infty = 10.4$, x/d = 40

Figure 6-9 Mach number distributions within the entropy layer on a blunt flat plate at zero incidence

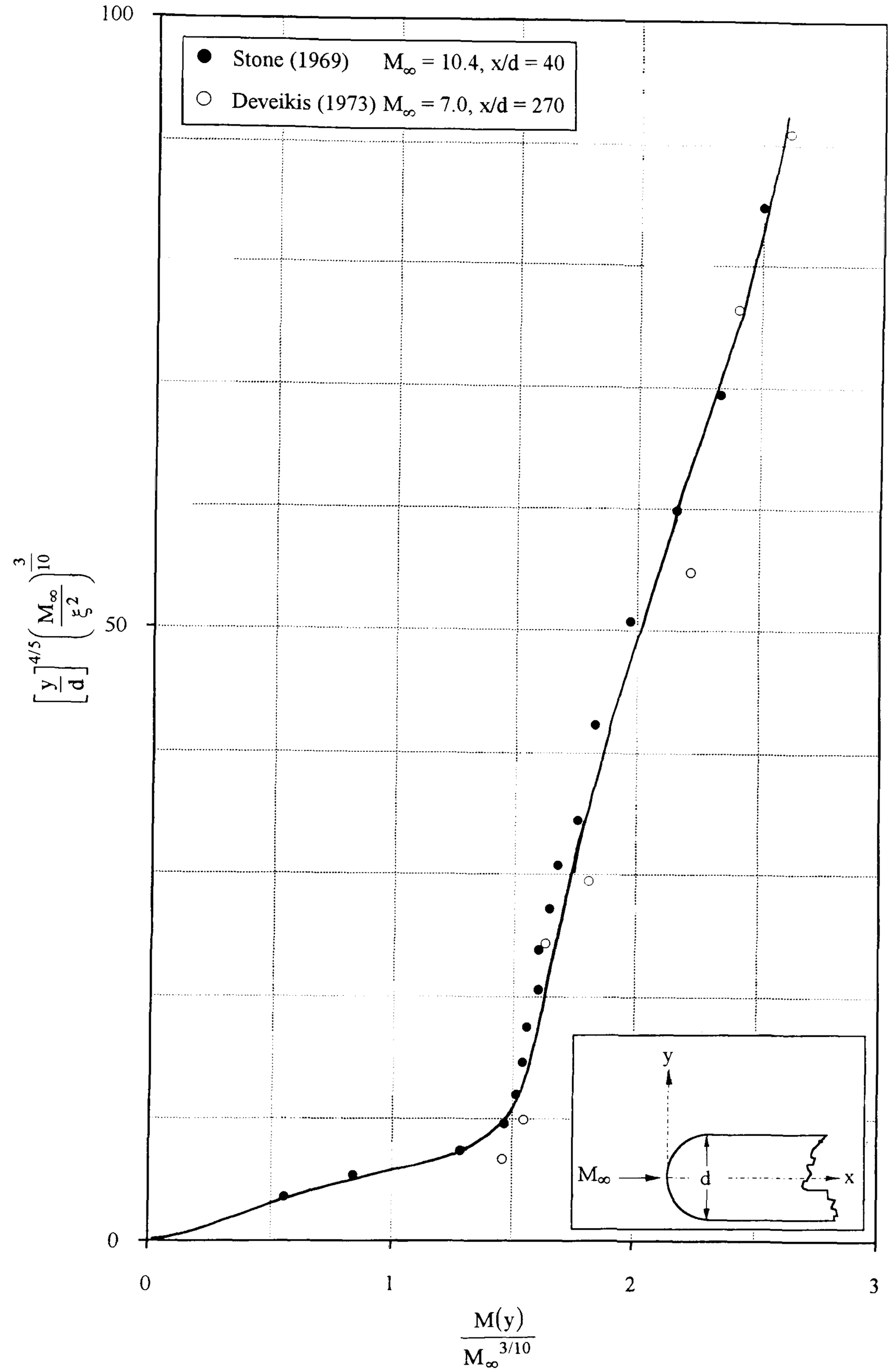

Figure 6-10 Correlation of entropy layer Mach number profiles in hypersonic flows

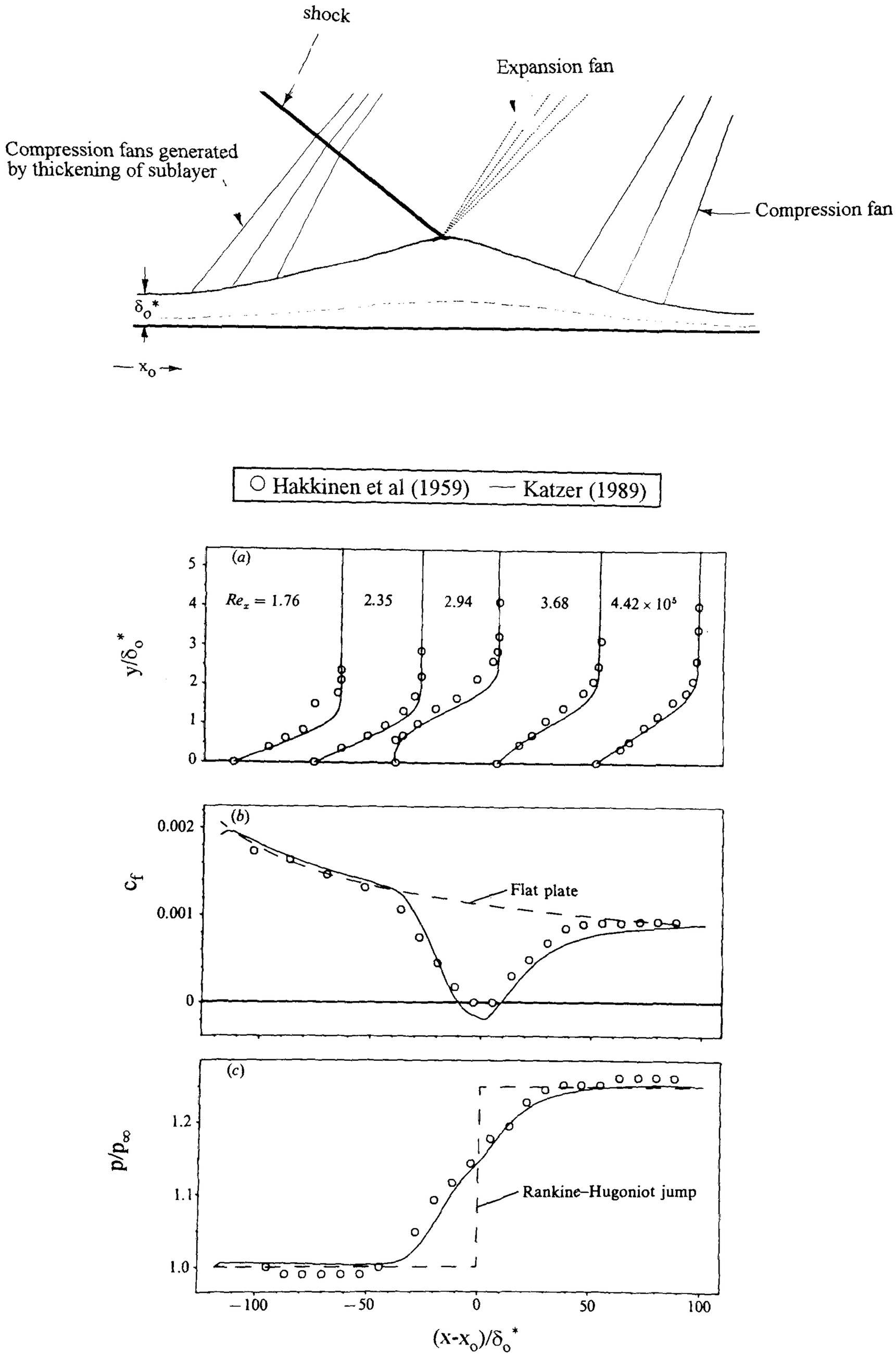

Figure 6-11 Pressure, skin-friction and velocity profiles in a laminar supersonic shockwave boundary layer interaction region ($M_\infty = 2.0$, $Re_{x_o} = 3.0 \times 10^{5)}$

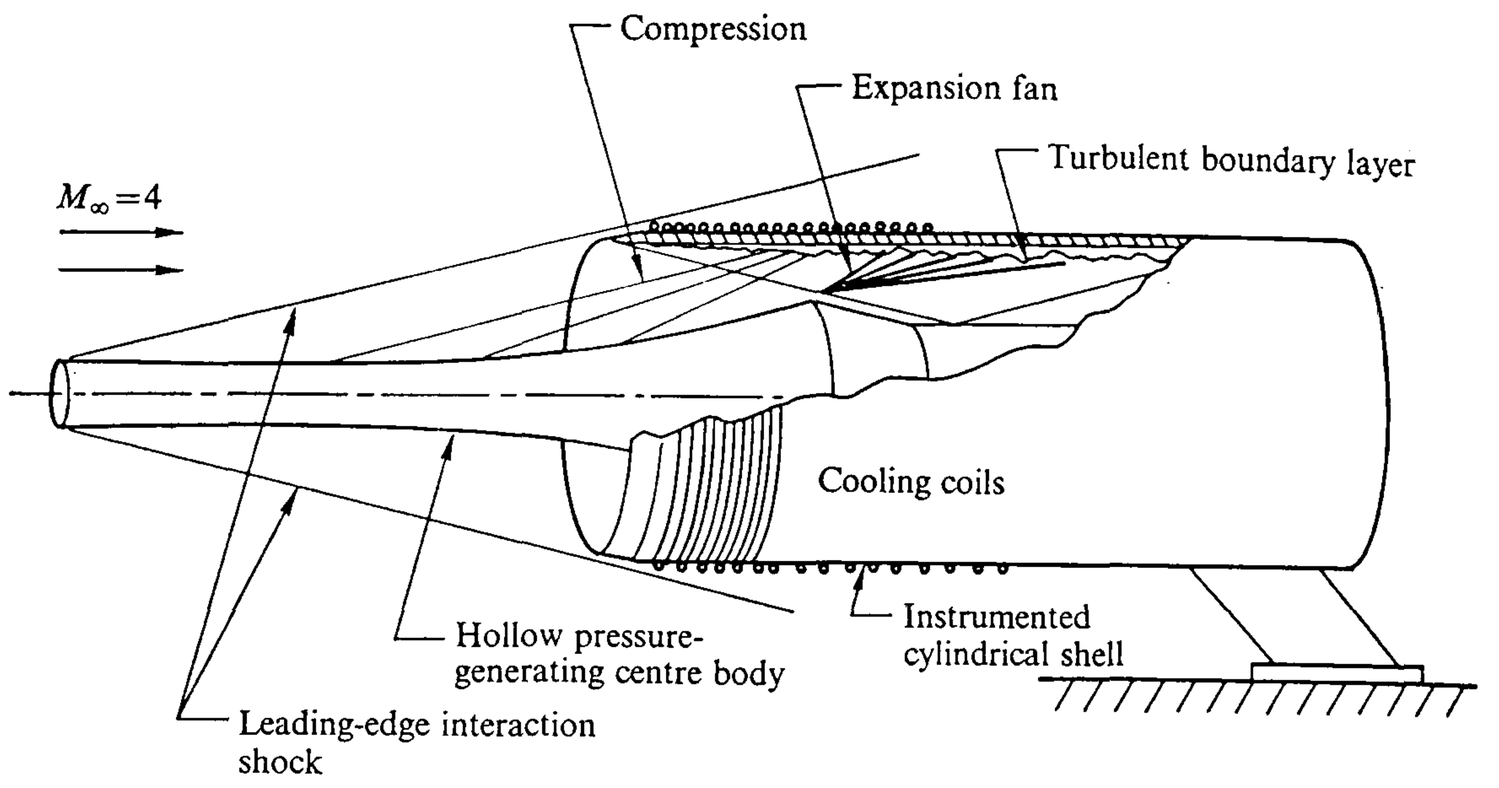

(a) wind tunnel set-up used

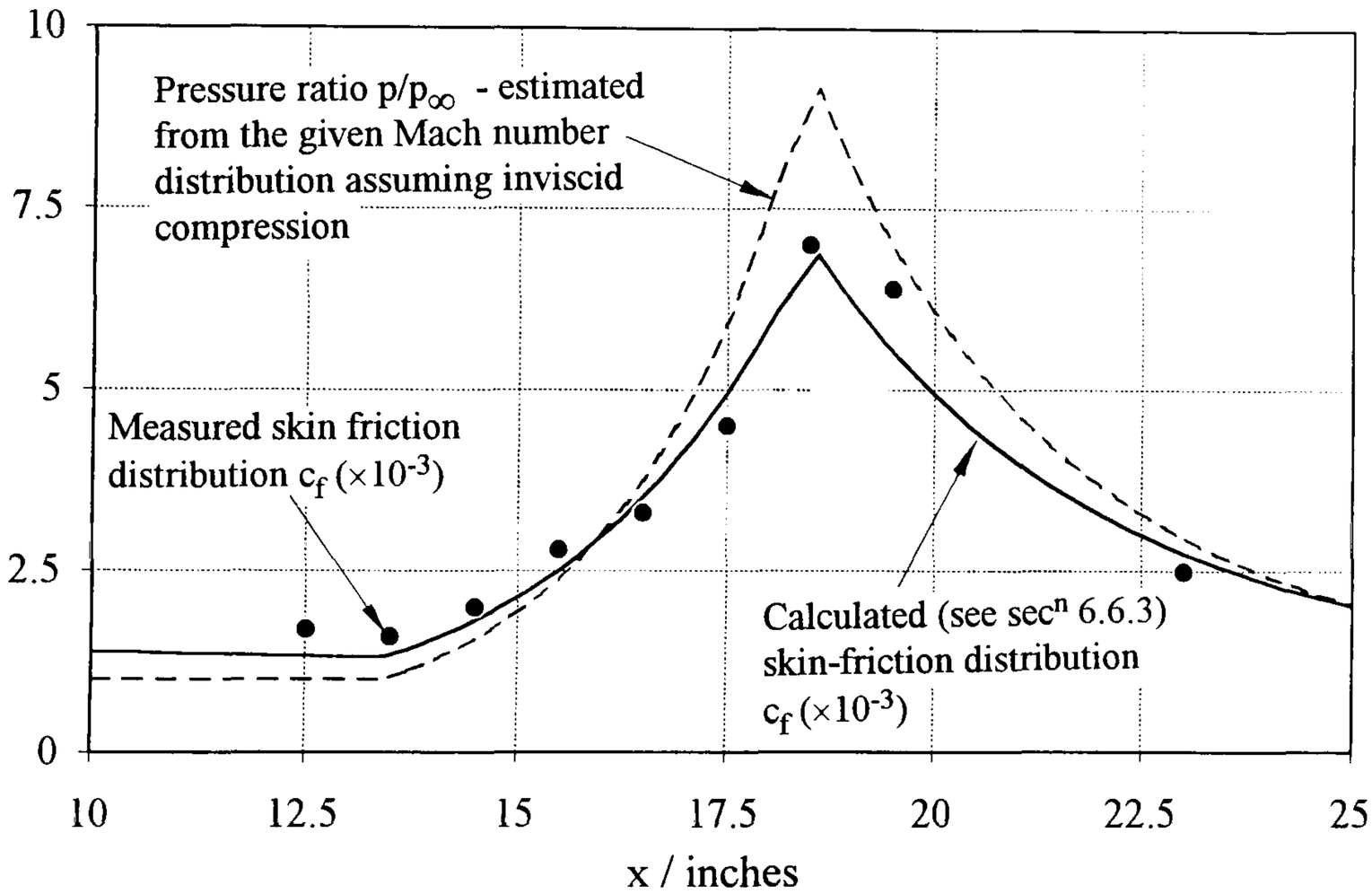

(b) pressure and skin-friction distributions

Figure 6-12 The effect of an axial pressure gradient on the local skin friction in a turbulent boundary layer - Gran et al., 1974
($M_\infty = 4.0$, $Re_\infty/in = 0.5 \times 10^6$, $T_w/T_\infty = 3.85$)

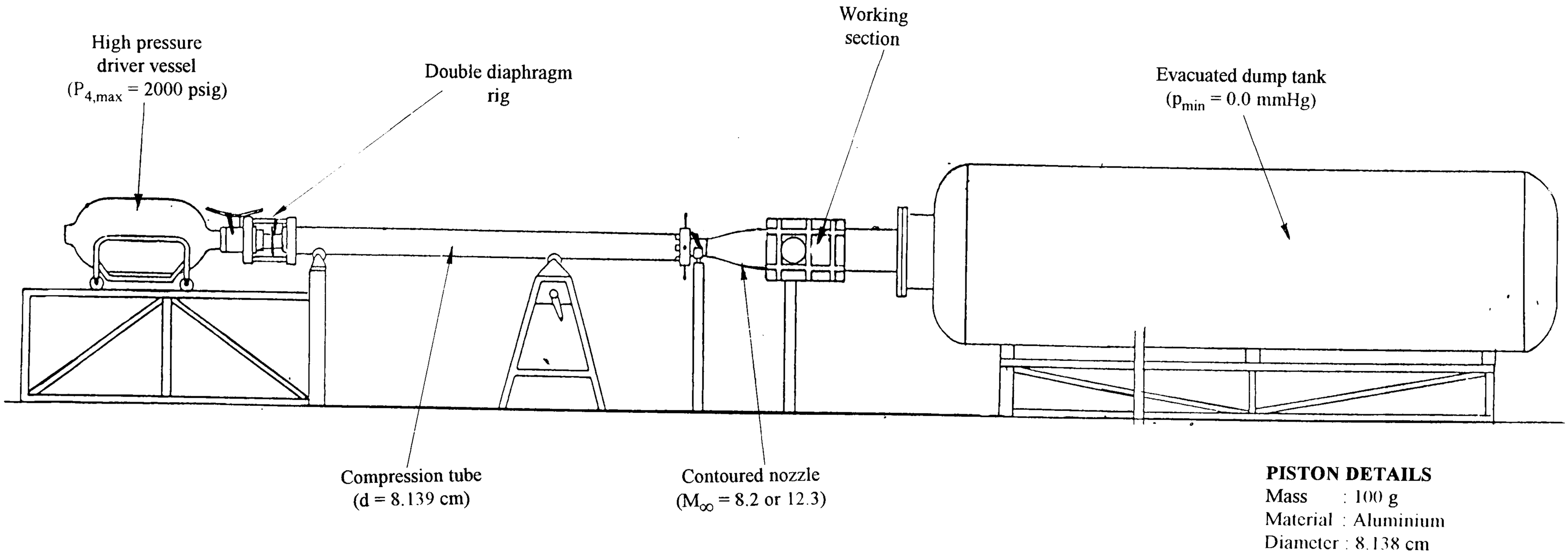

Figure 7-1 Schematic diagram of the Cranfield hypersonic gun tunnel facility

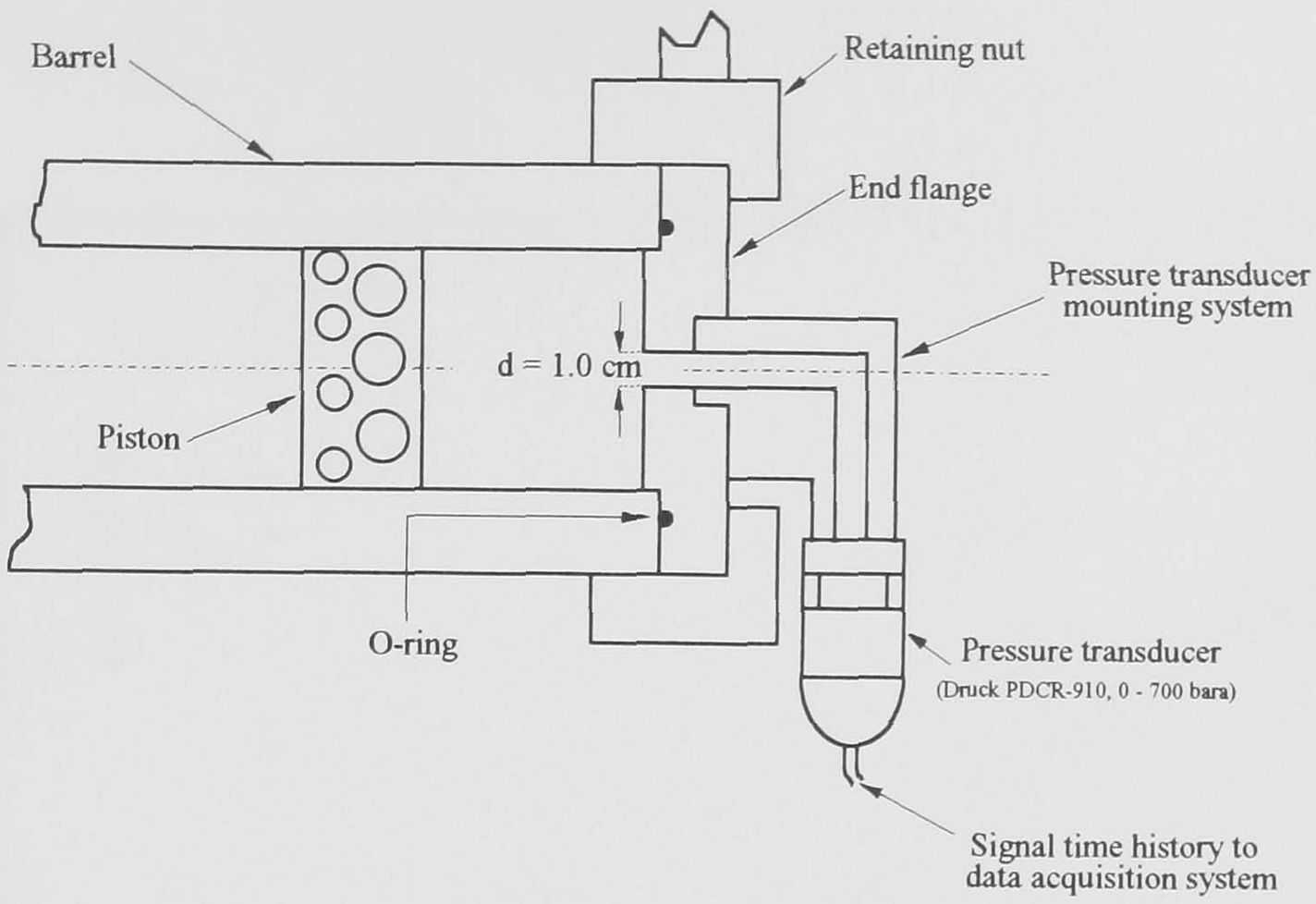

(a) setup employed for barrel end reservior pressure history

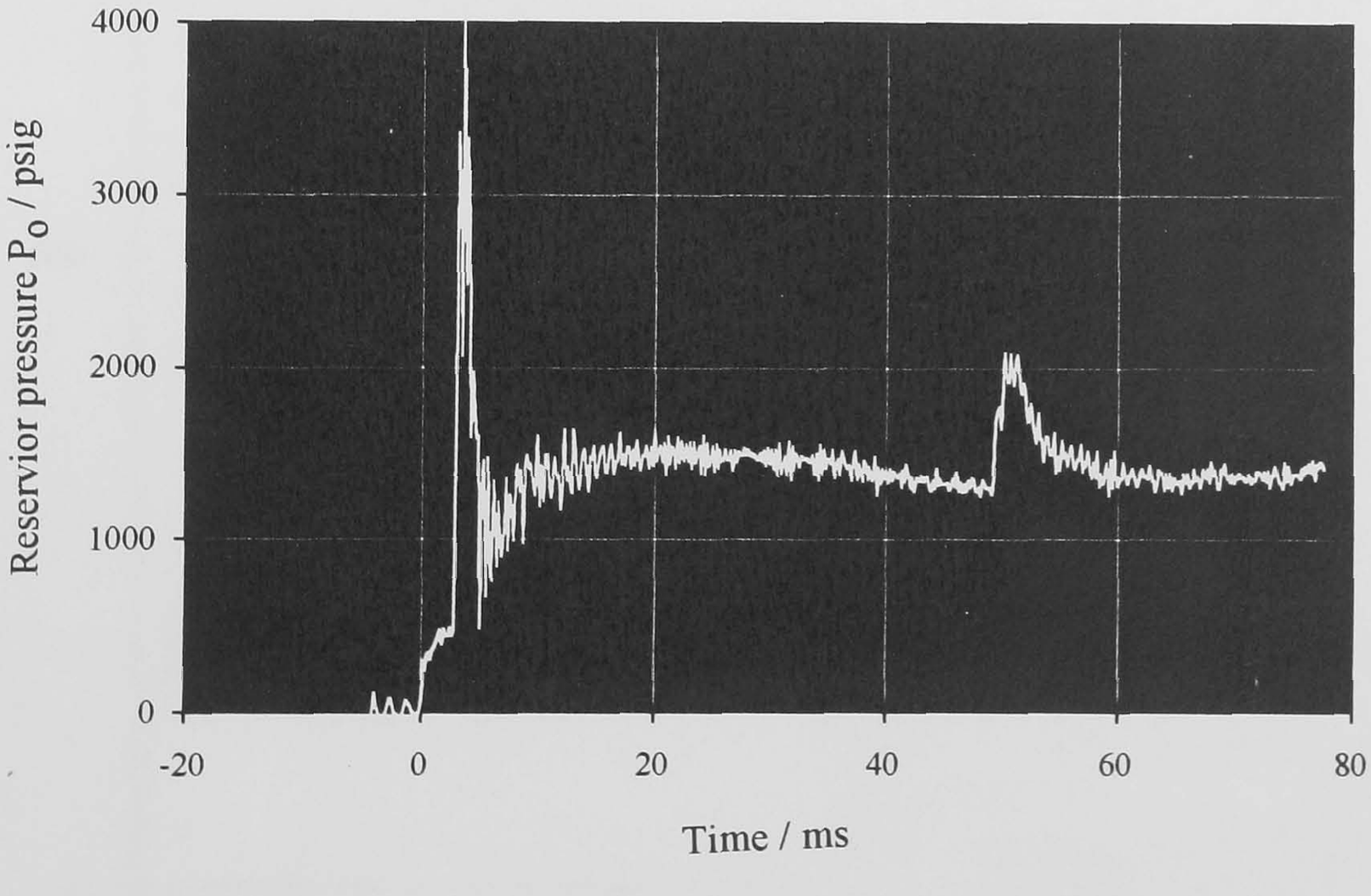

(b) reservior pressure time history

Figure 7-2 Barrel end reservoir pressure history in the Cranfield hypersonic facility (P_4 = 2000 psig, piston mass = 100.0 g)

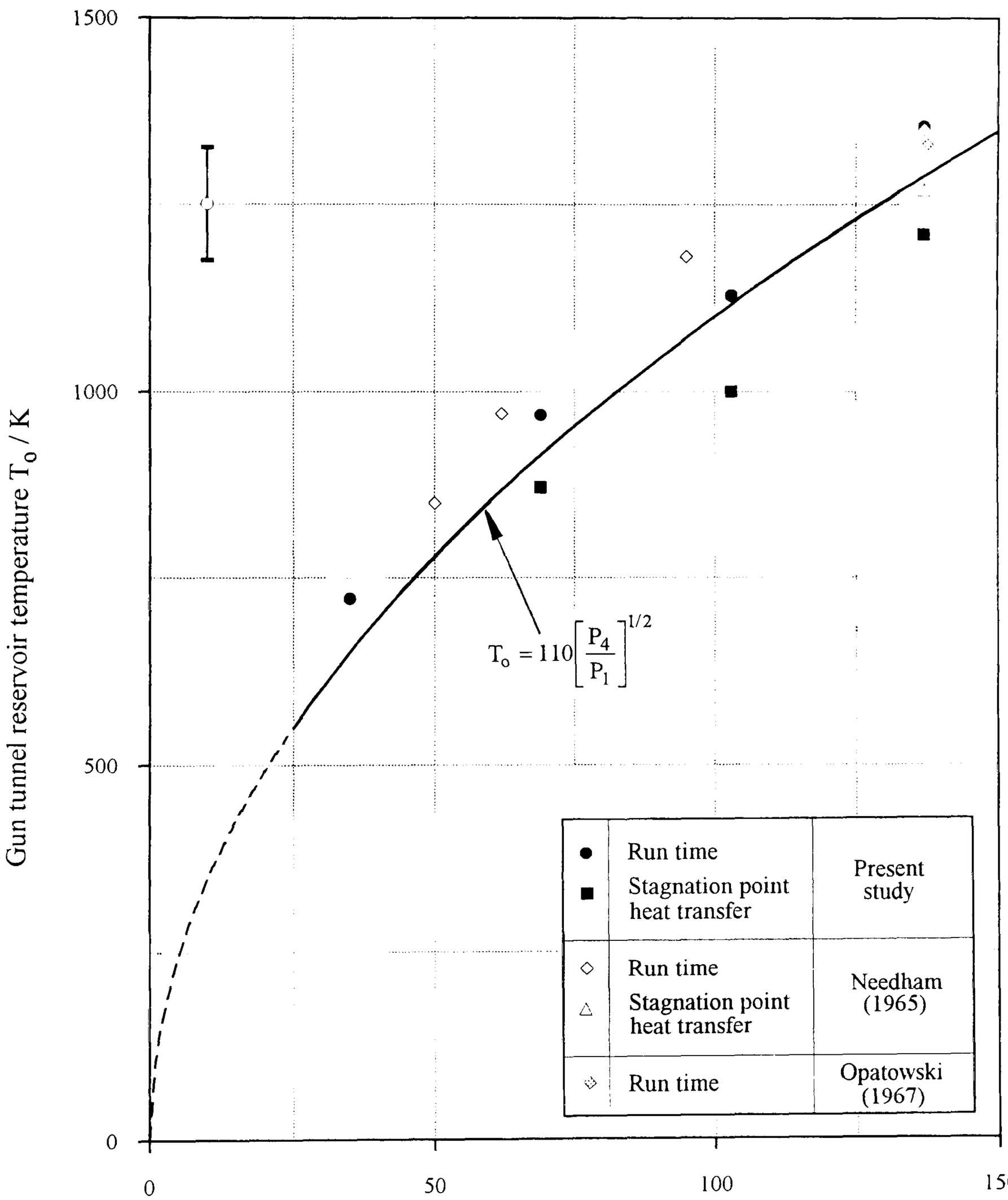

Figure 7-3 Variation of reservoir temperature in the Cranfield hypersonic facility

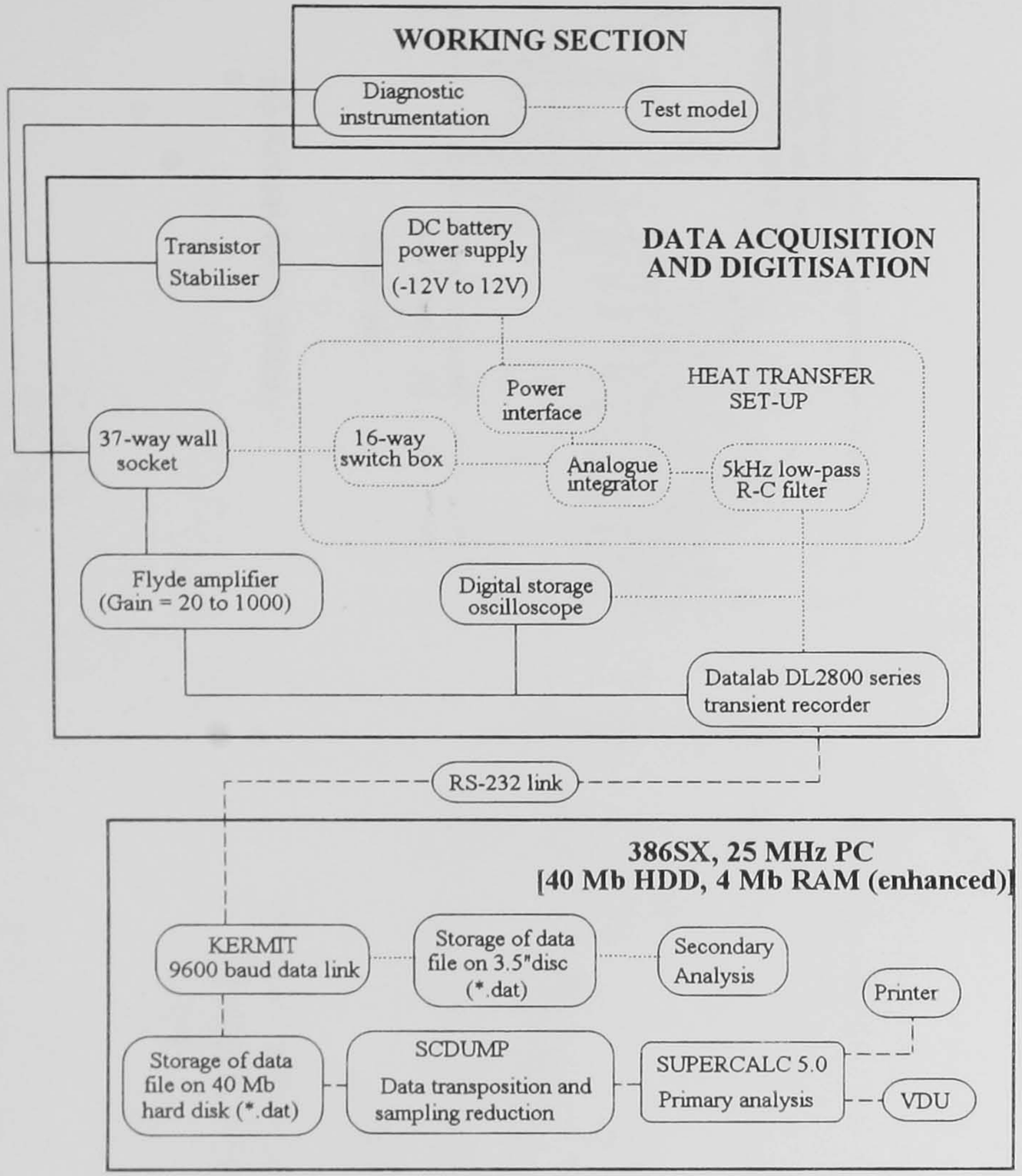

(a) schematic diagram of the overall instrumentation system

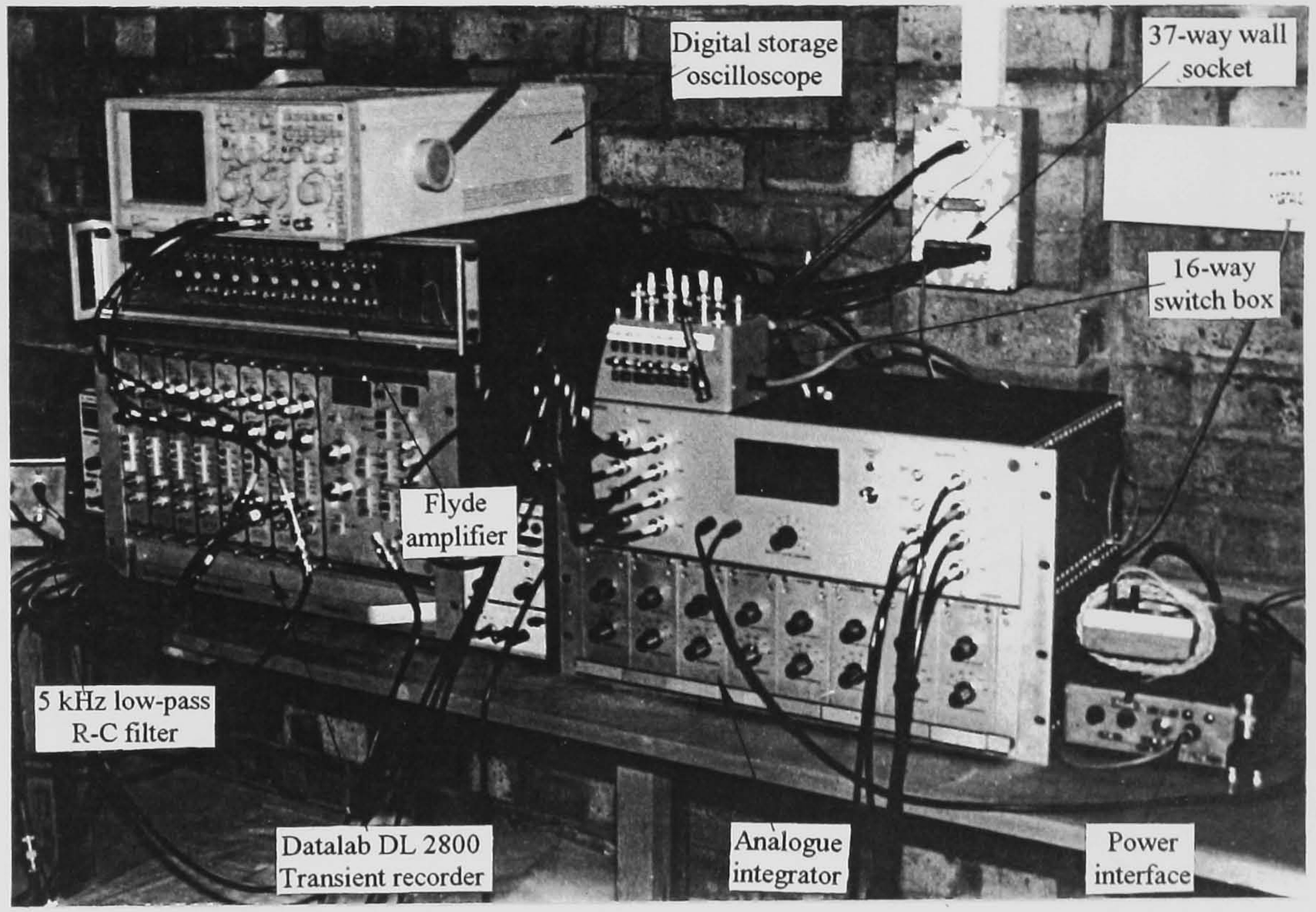

(b) instrumentation setup for data acquisition and digitisation

Figure 7-4 Digital data acquisition system established for signal measurement and anaylsis in the Cranfield hypersonic facility

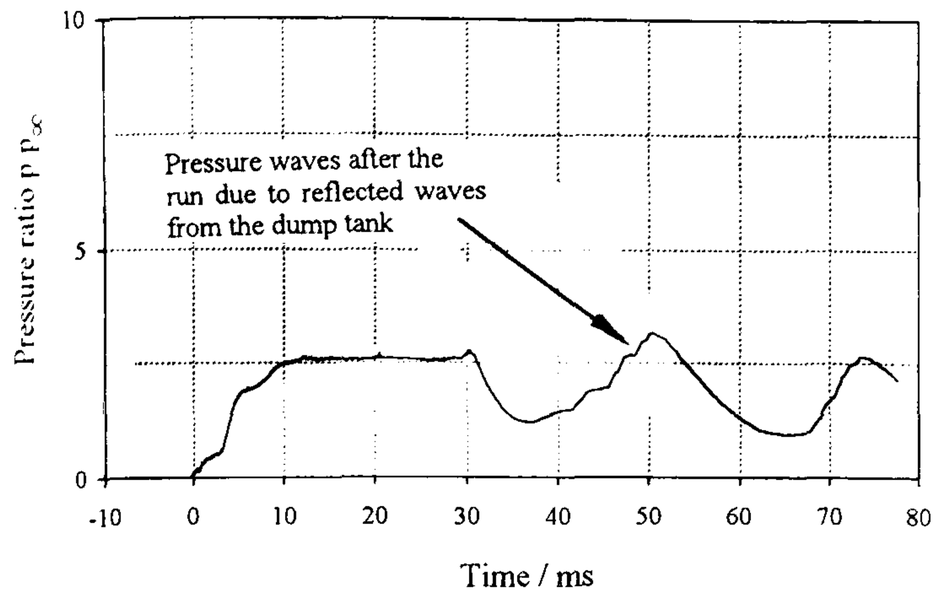

(a) Low pressure ratio

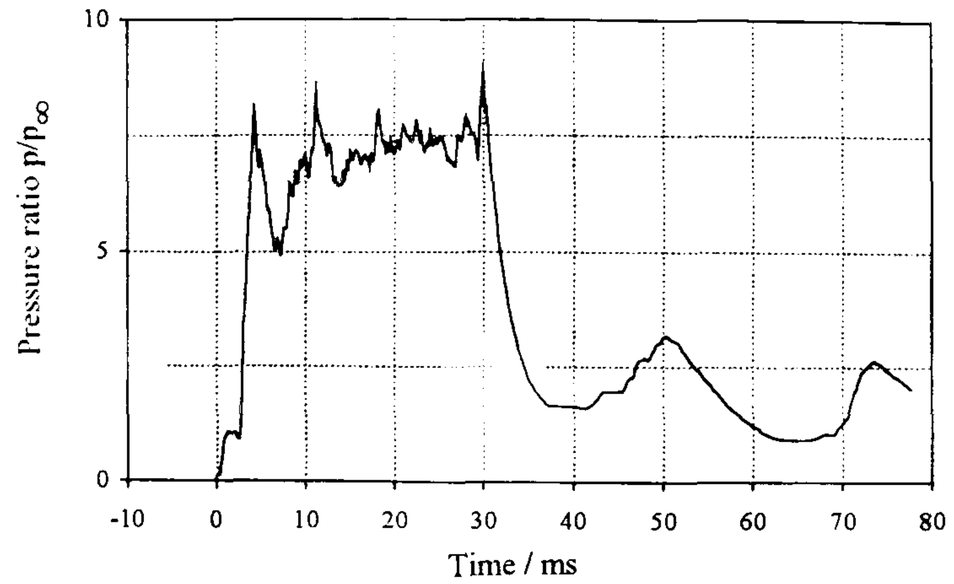

(b) High pressure ratio

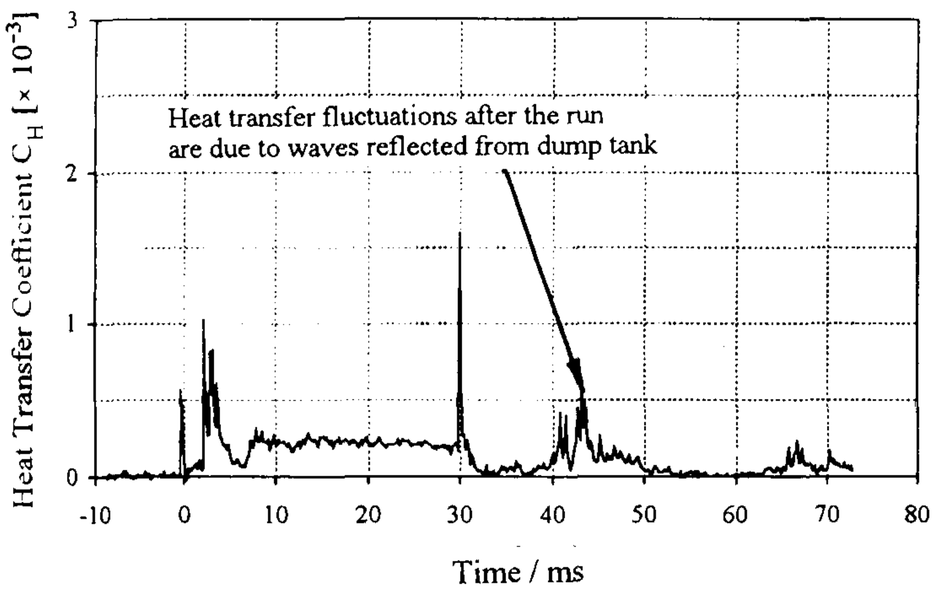

(c) Low heat transfer rate

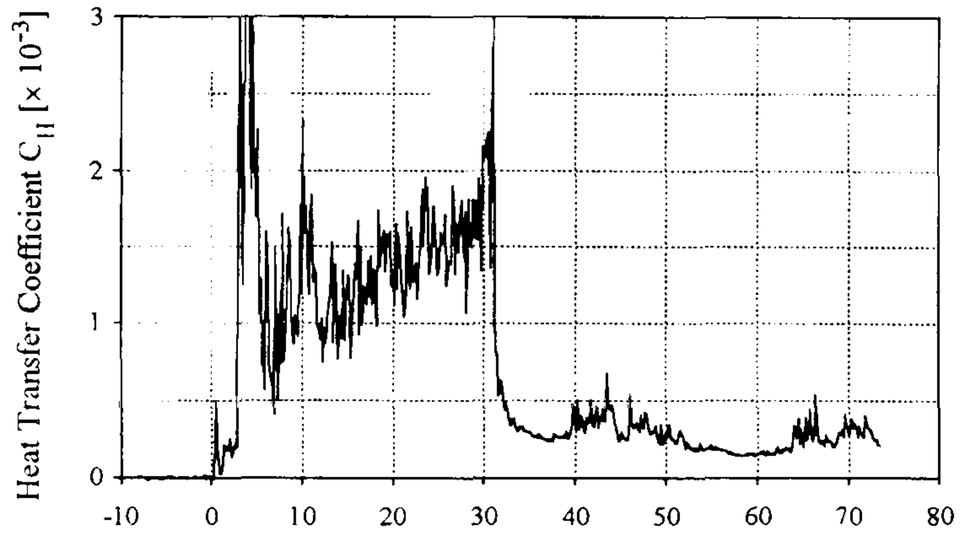

(d) High heat transfer rate

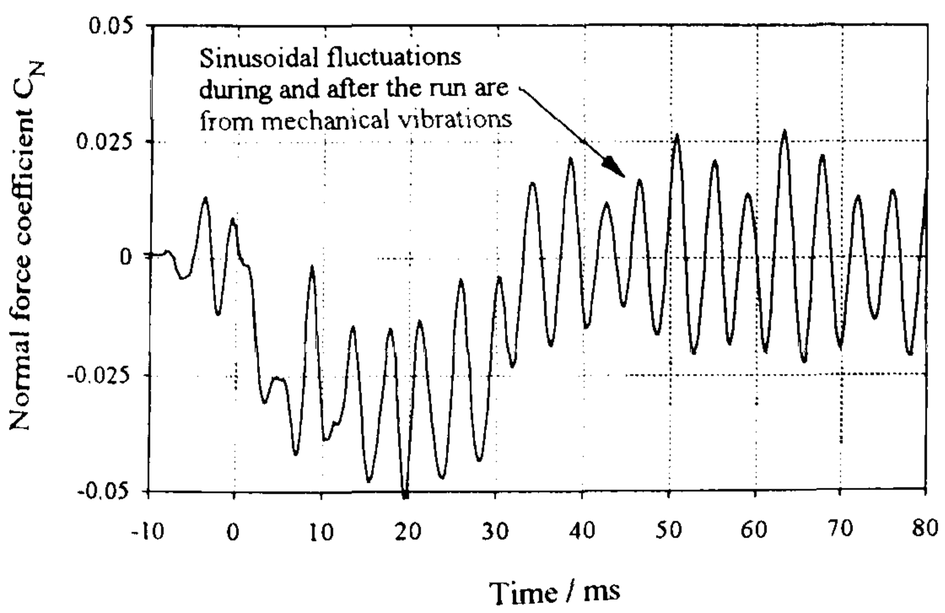

(e) Actual force history

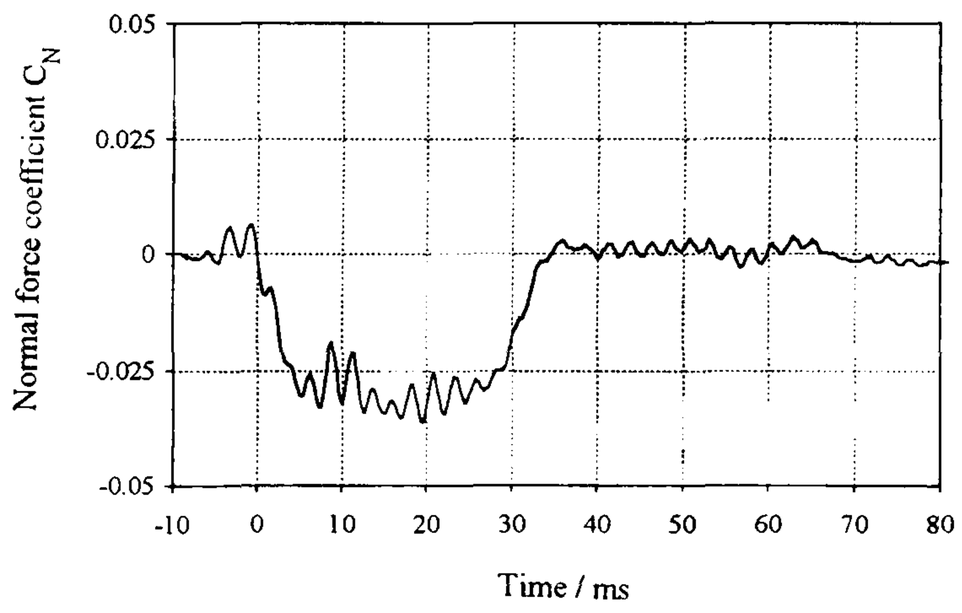

(f) Force history after digital filtering of sinusoidal component

Figure 7-5 Typical pressure, heat transfer and force time histories obtained in the Cranfield hypersonic facility ($M_\infty = 8.2$, $Re_\infty/cm = 9.0 \times 10^4$)

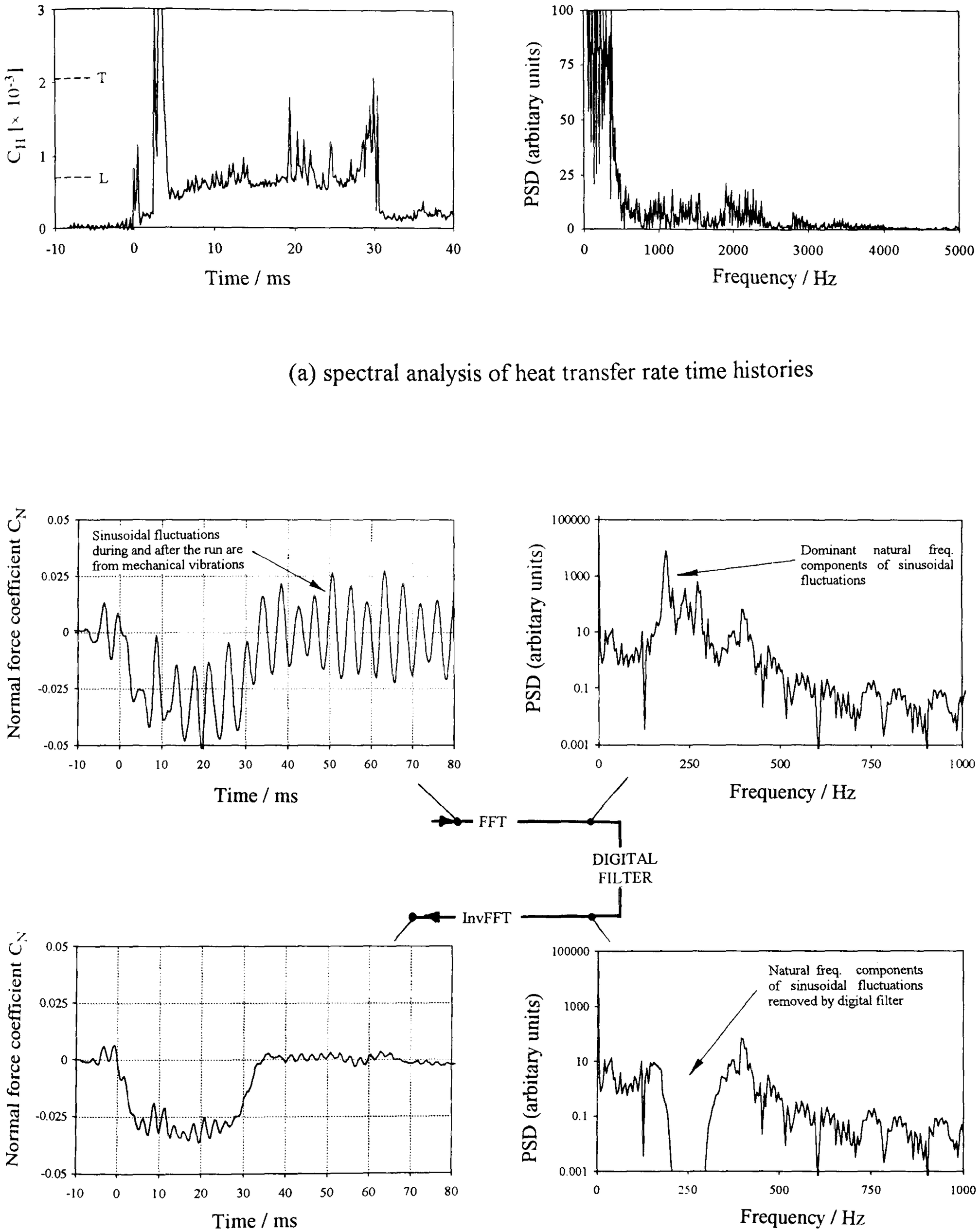

Figure 7-6 Methodology for spectral analysis and digital filtering of force and heat transfer time histories

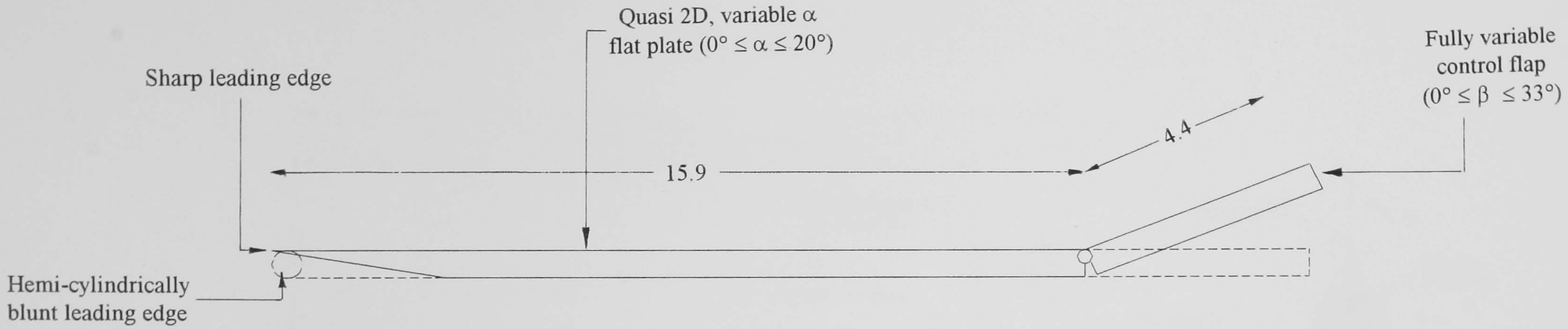

(a) general set-up

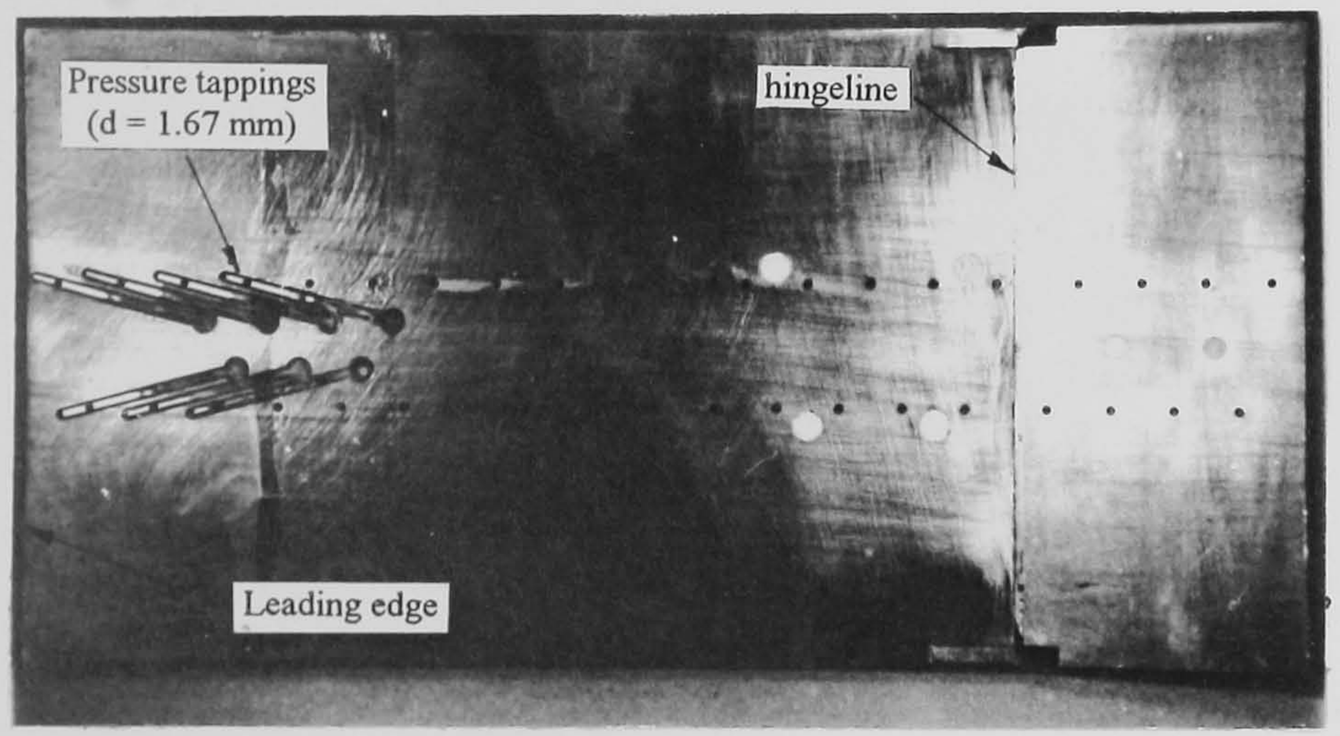

(b) plan view of overall configuration

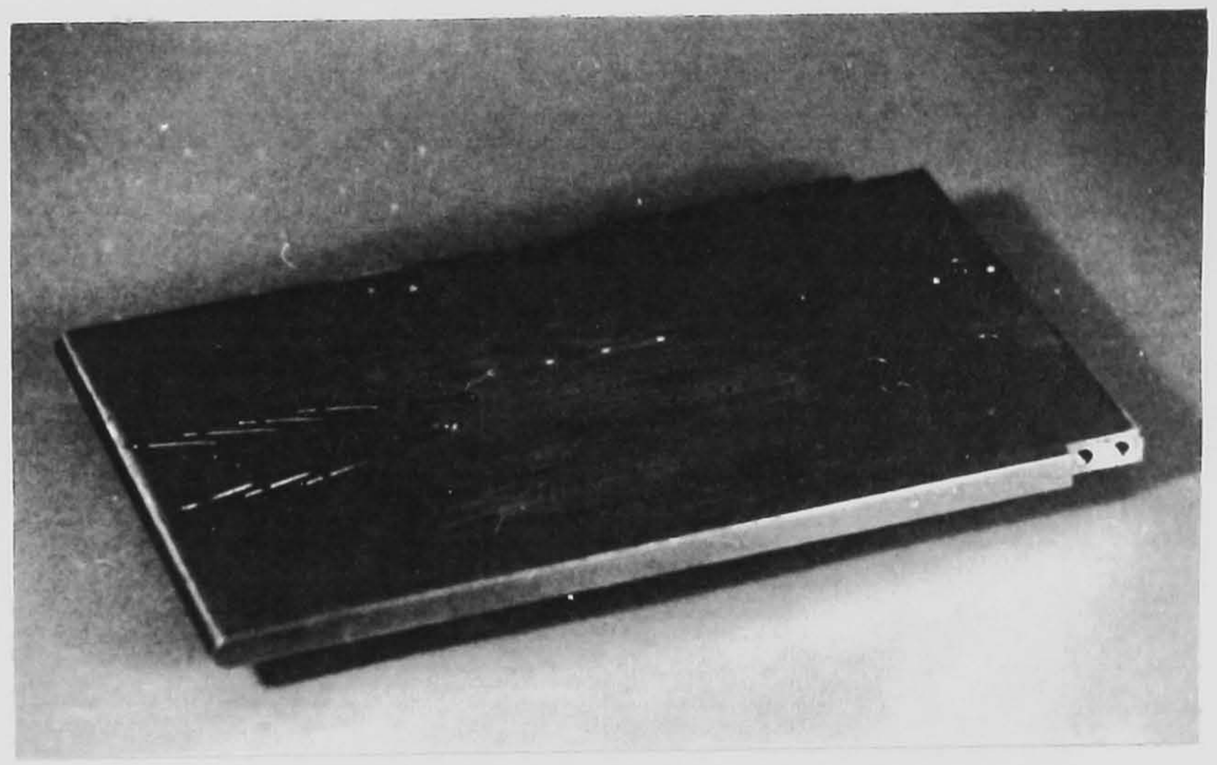

(c) blunt leading edge (flat plate section)

Figure 7-7 General set-up of mechanical control flap pressure model (all dimensions in cm unless stated otherwise)

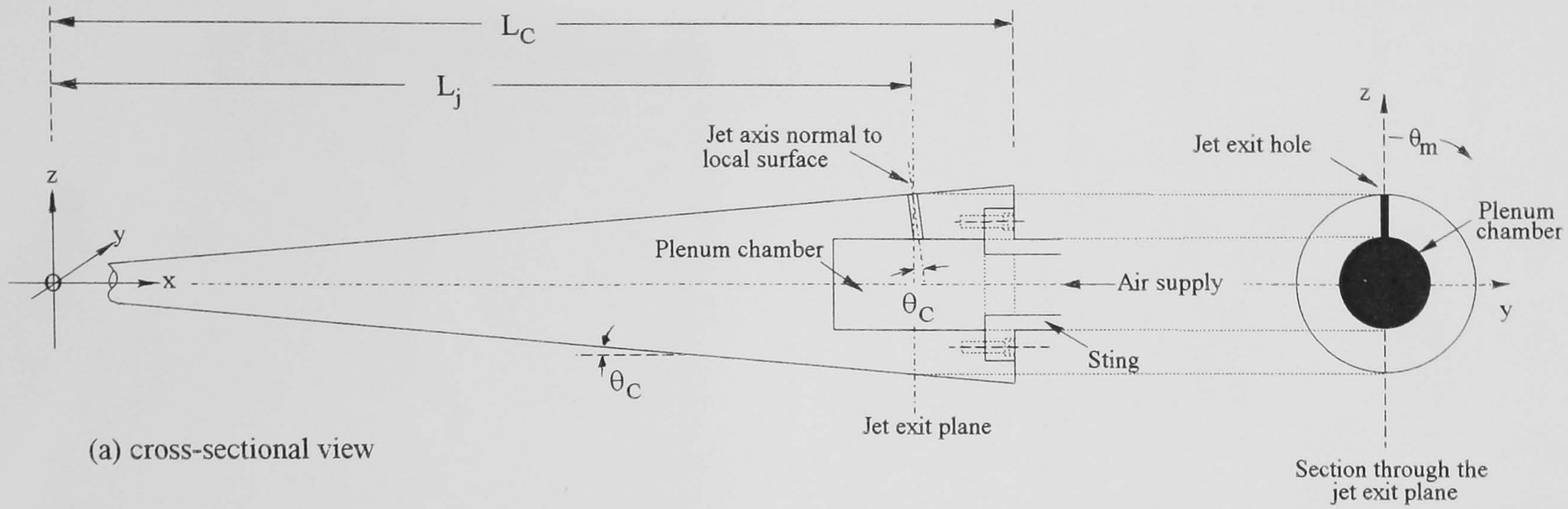

(a) cross-sectional view

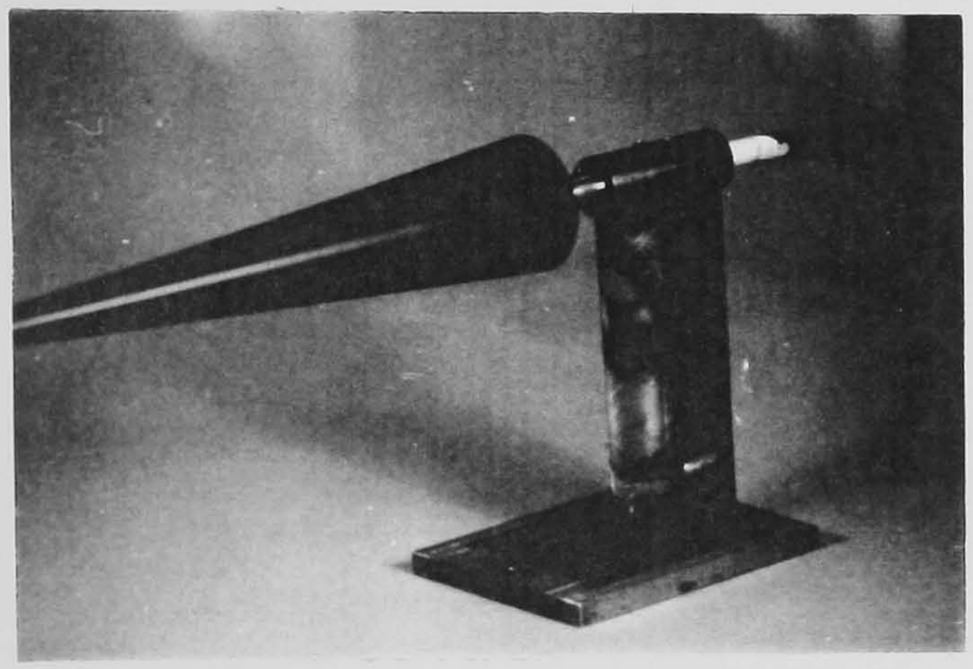

(b) general set-up

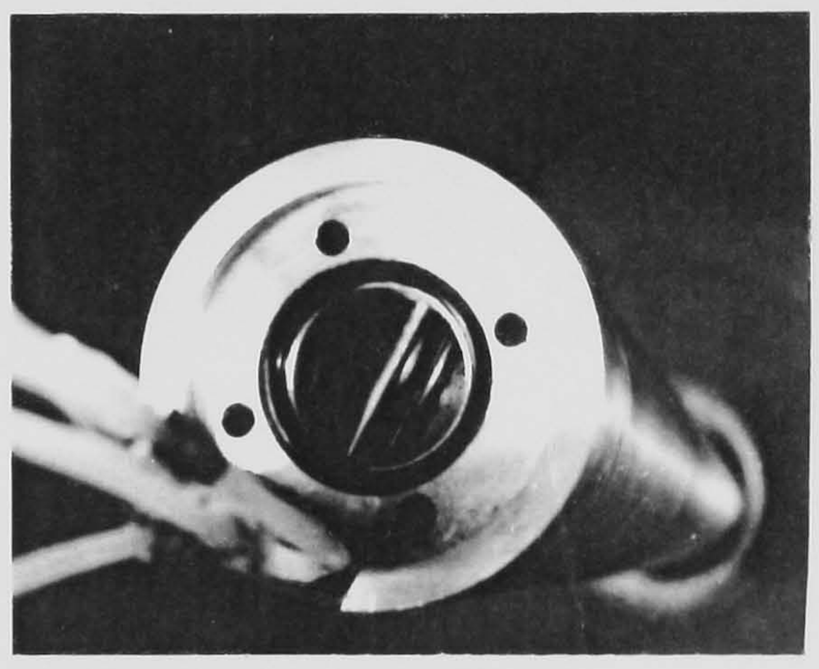

(c) plenum chamber

Figure 7-8 General set-up of the model used for jet interaction studies (all dimensions in mm unless stated otherwise)

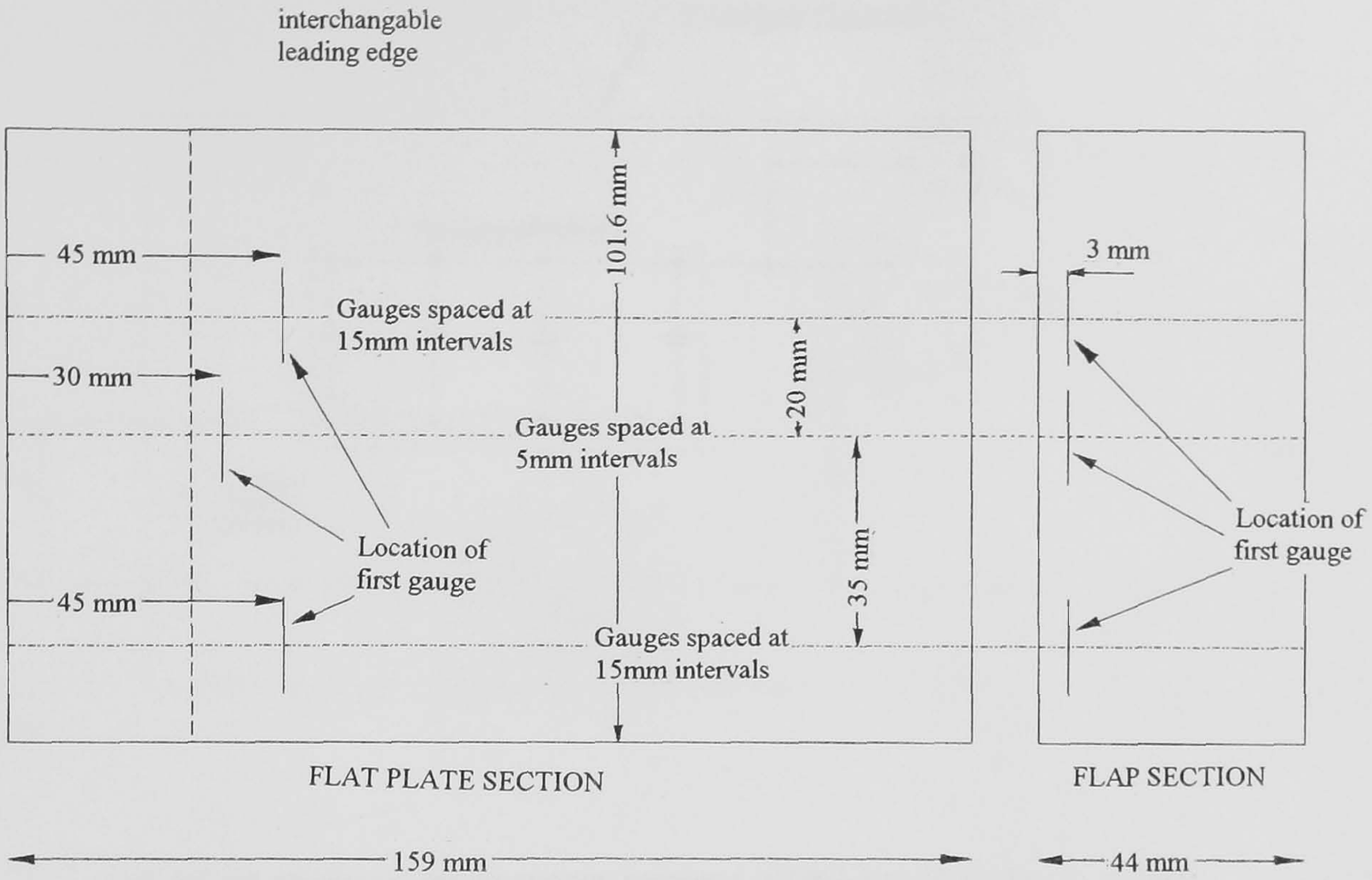

(a) plan view of gauge distributions

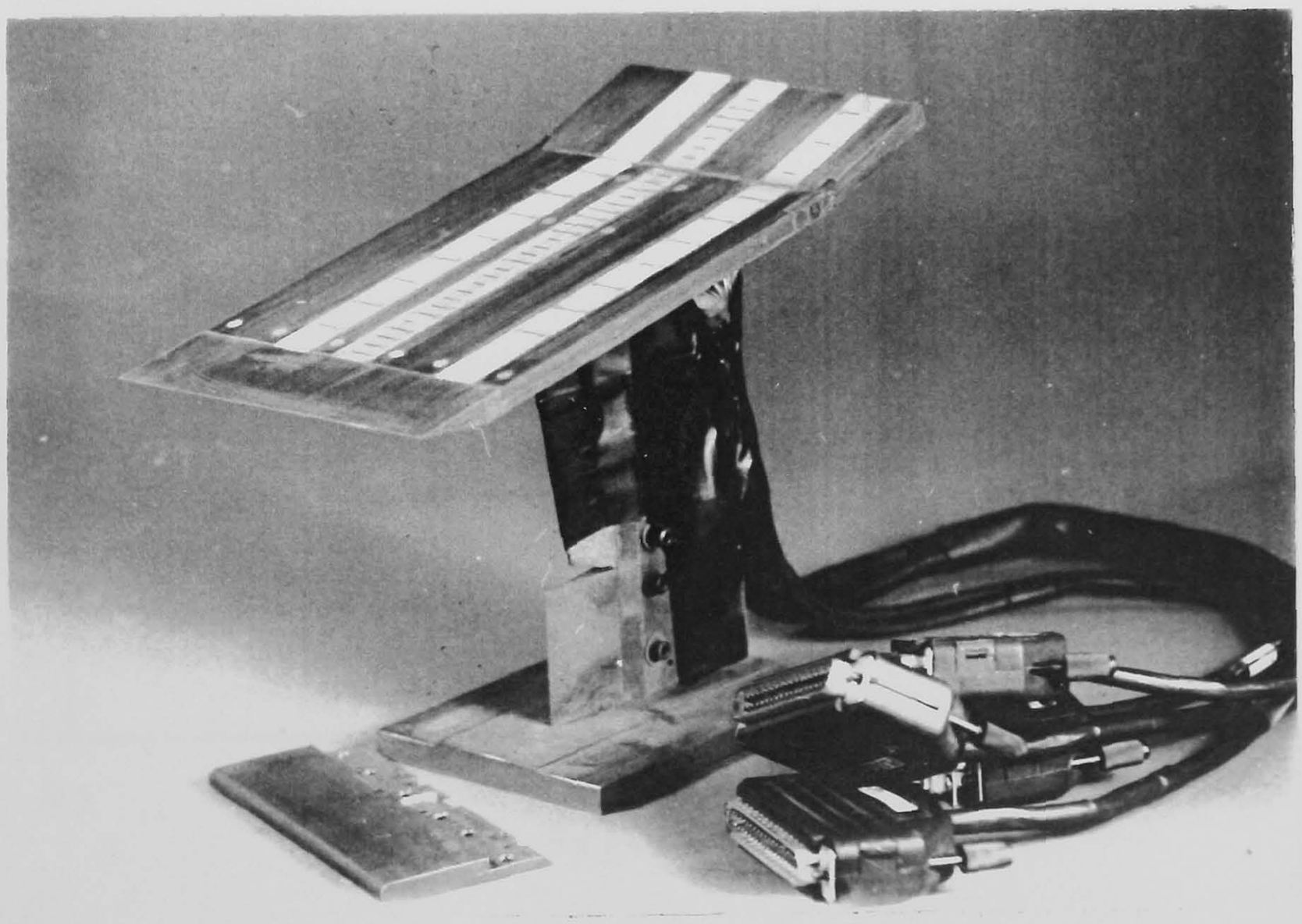

(ii) model

Figure 7-9 General set-up of the thin-film gauge model used for control flap heat transfer studies

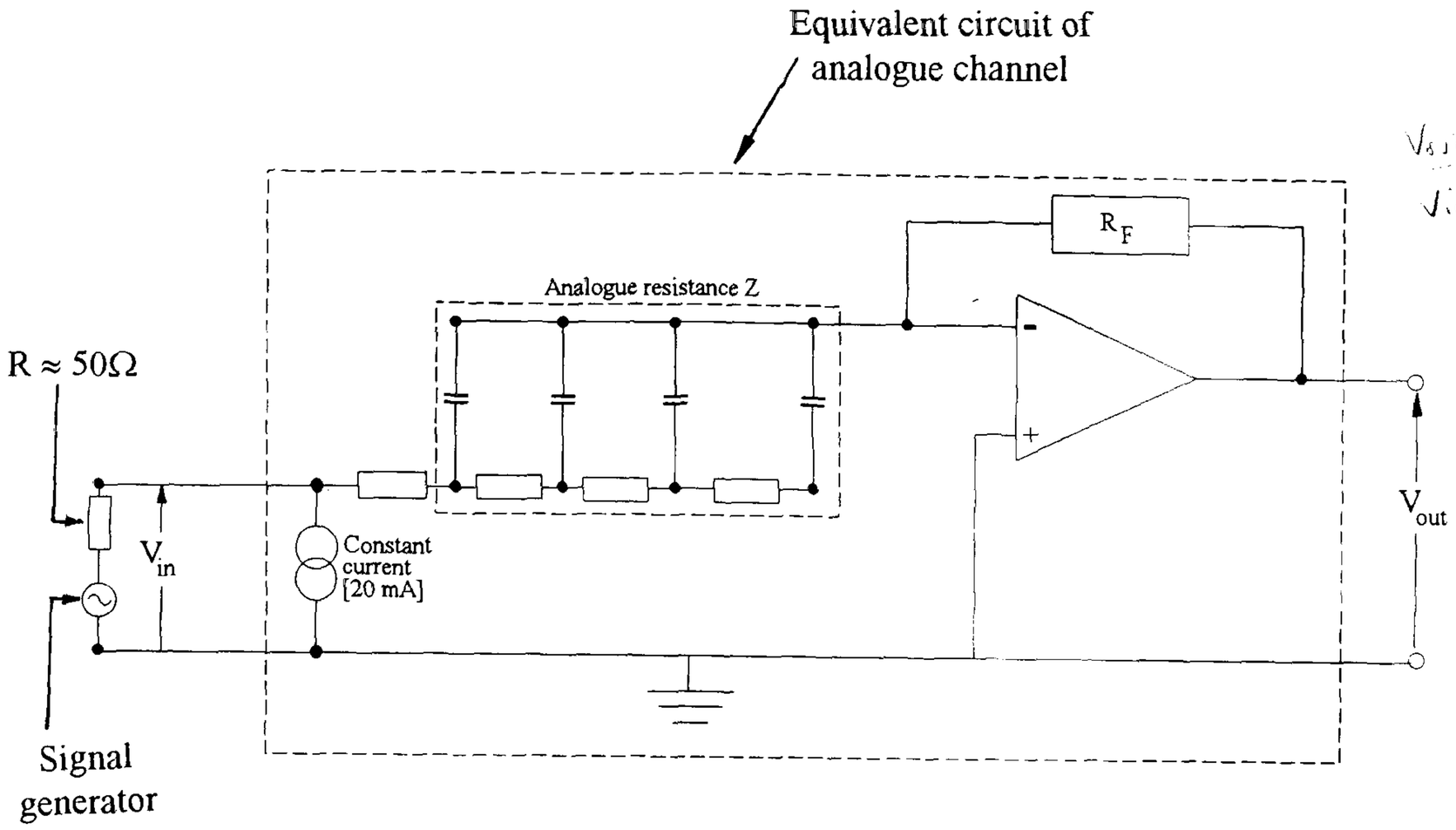

(a) set-up employed for frequency response calibration of analogue circuits

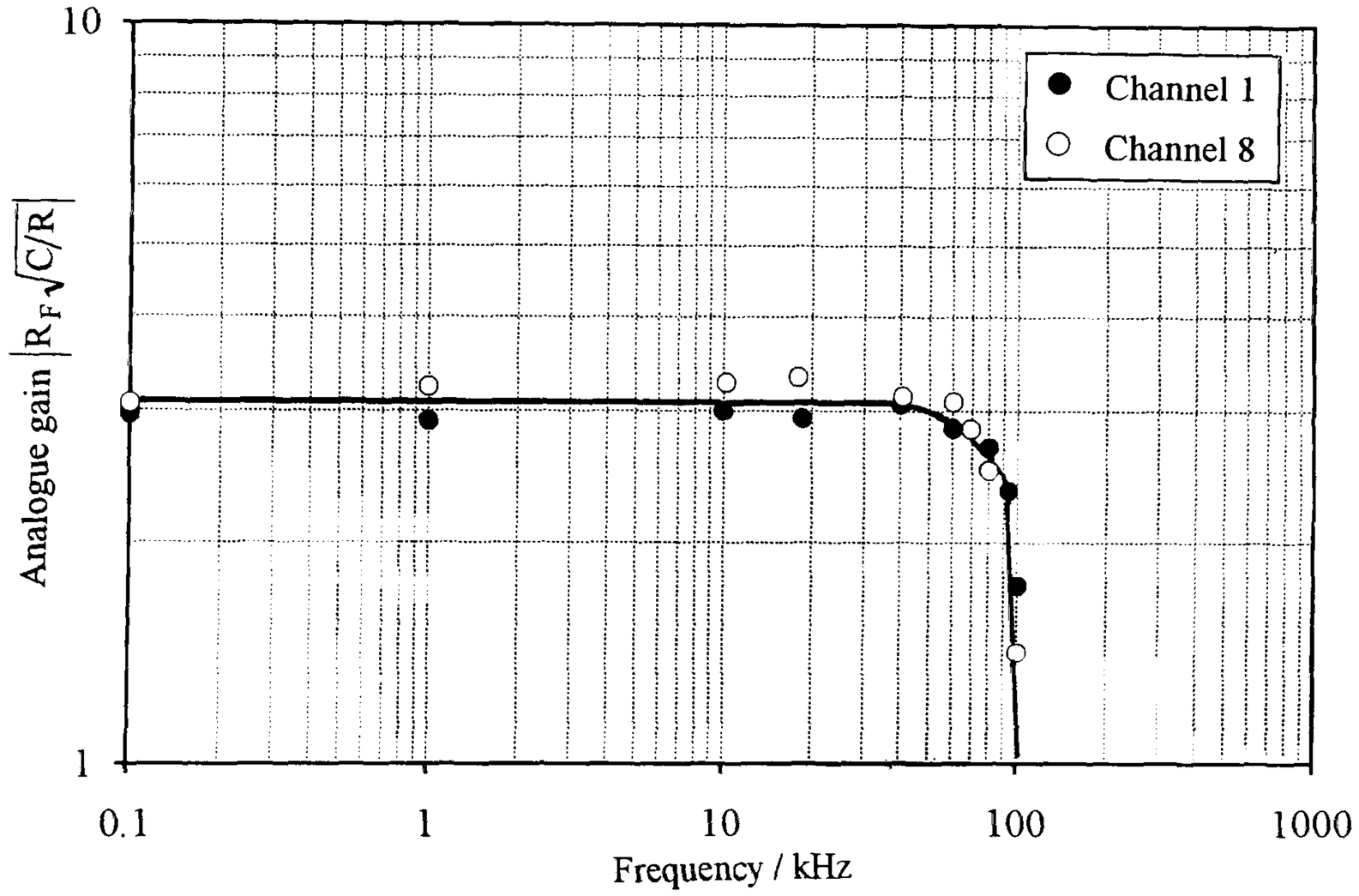

(b) frequency response of analogue circuits

Figure 7-10 Frequency response calibration setup used for the CONTECH analogue integrator circuits

(a) heat transfer rate time histories

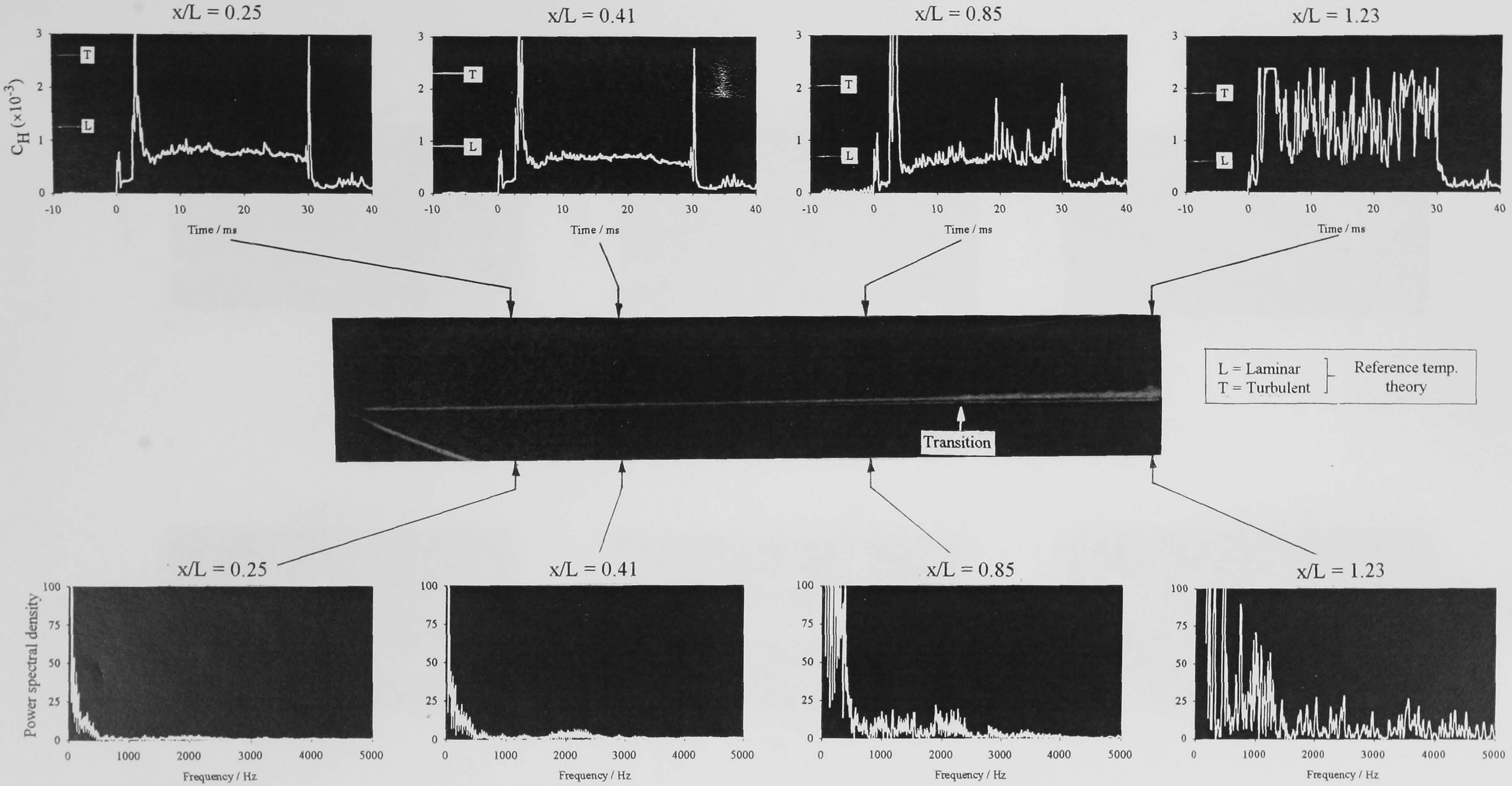

(b) frequency distributions

Figure 7-11 The development of disturbances in heat transfer during the transition of a hypersonic flat plate boundary layer ($M_\infty = 8.2$, $Re_\infty/cm = 9.0 \times 10^4$, $\alpha = 10°$, L = 15.9 cm)

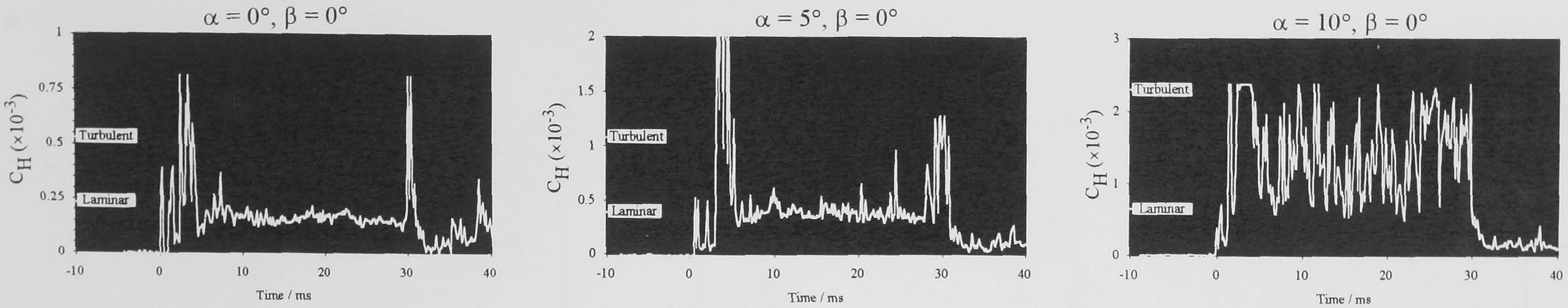

(a) flat plate time histories

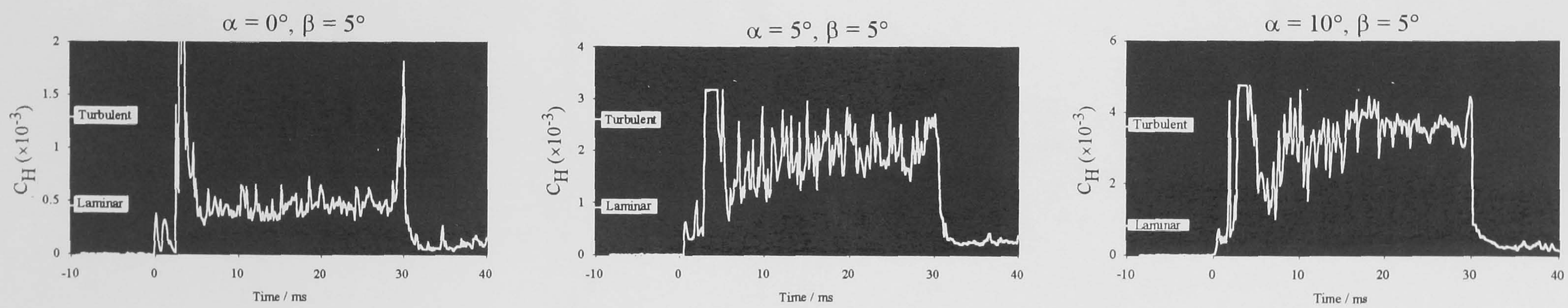

(b) deflected flap time histories (attached flow)

Figure 7-12 The effects of incidence and flap deflection on the development of disturbances in heat transfer during boundary layer transition ($M_\infty = 8.2$, $Re_\infty/cm = 9.0 \times 10^4$, L = 15.9 cm, x/L = 1.23, laminar and turbulent predictions from reference temp. theory (section 6.9.2))

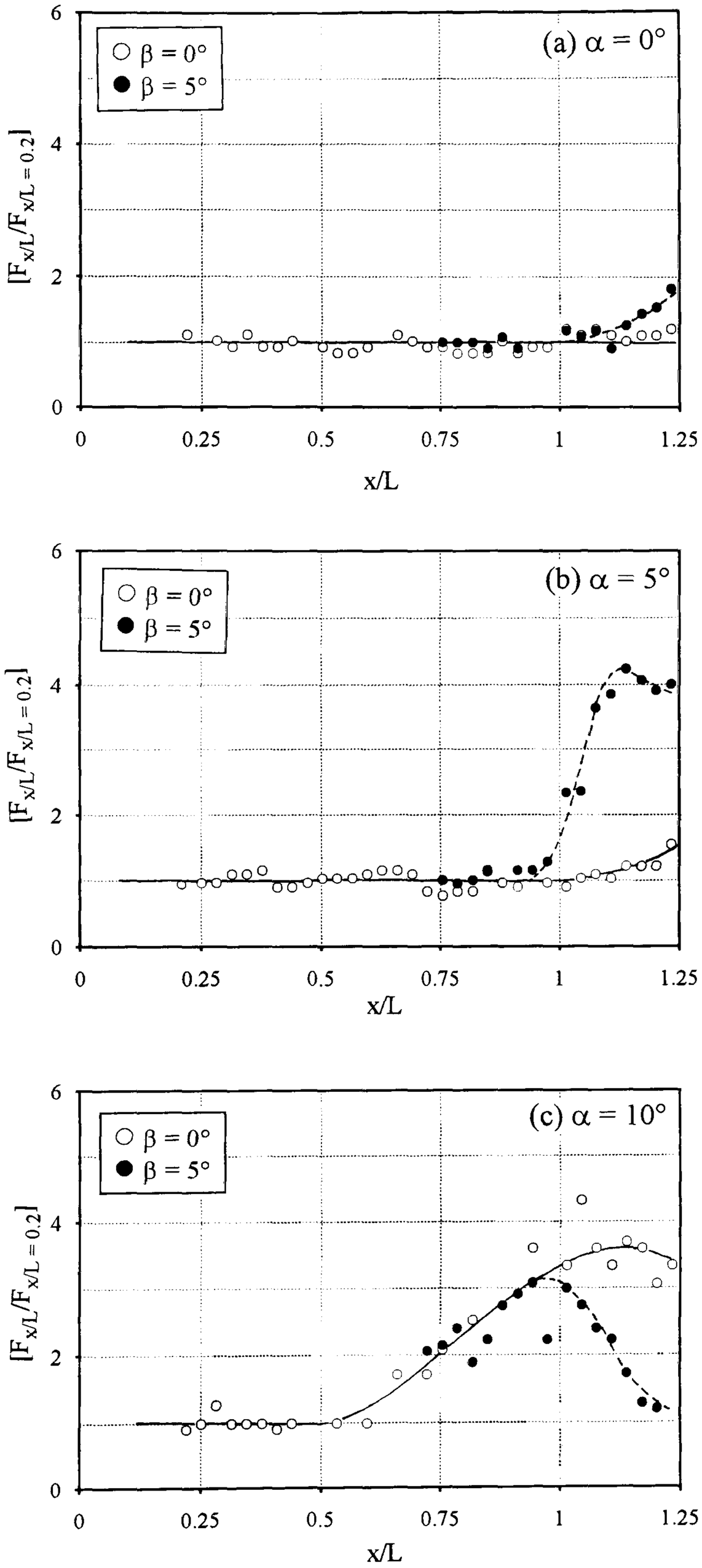

Figure 7-13 The effect of incidence and flap deflection on the relative amplitude of heat transfer fluctuations ($M_\infty = 8.2$, $Re_\infty/cm = 9.0 \times 10^4$, L = 15.9 cm)

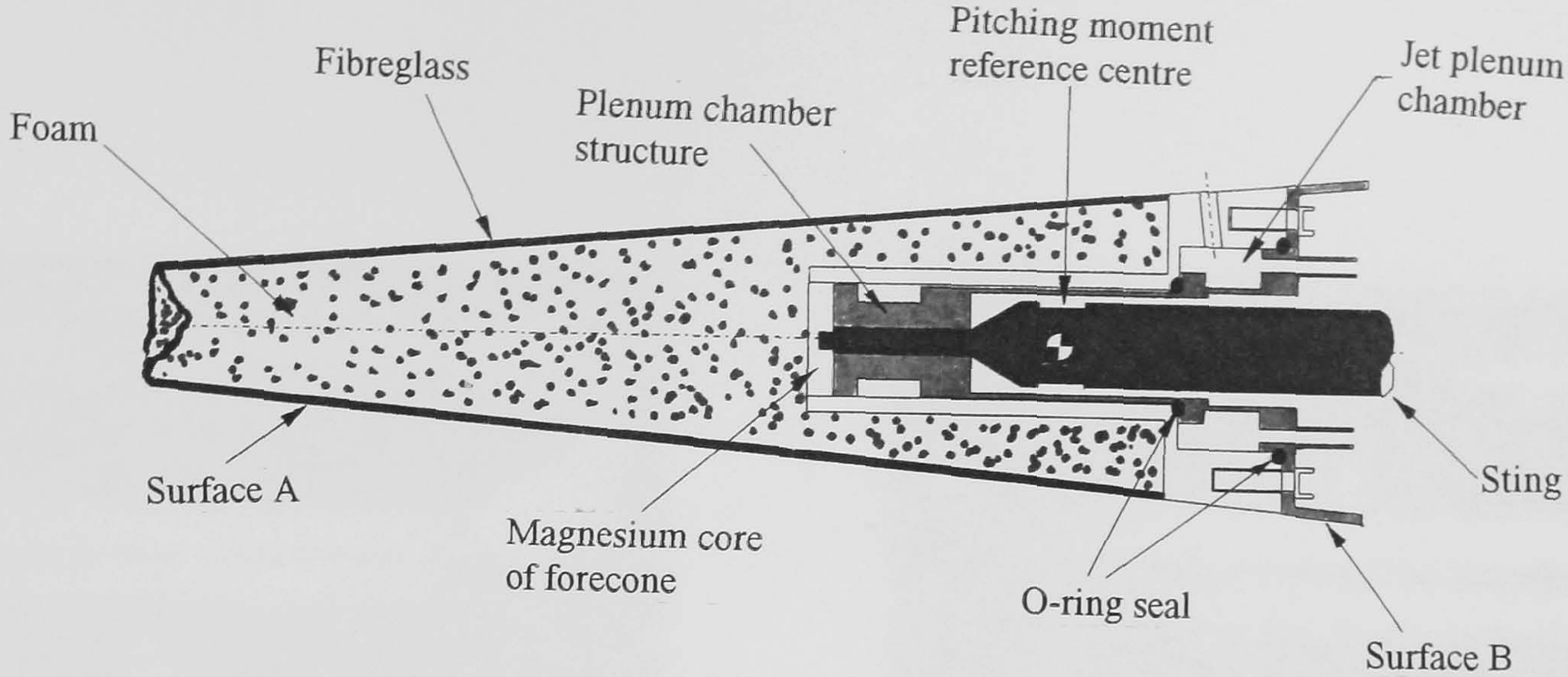

(a) general structure of the model used to study jet interaction force

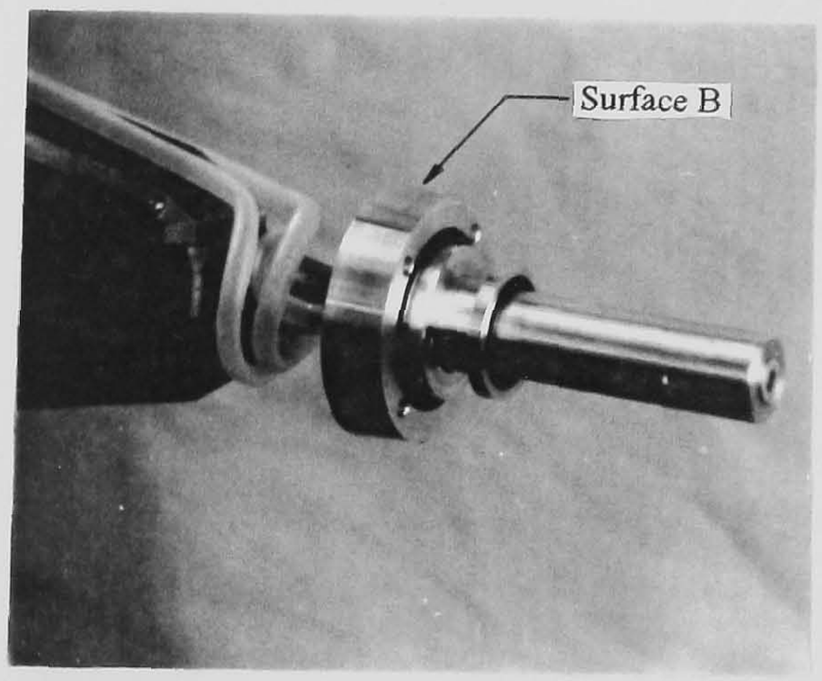

(b) model plenum chamber

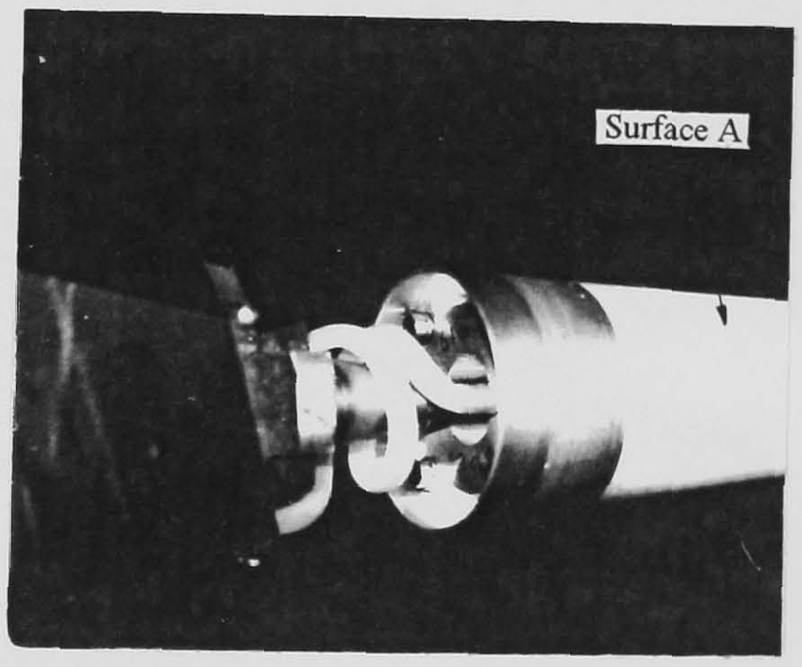

(c) coiled jet feed system

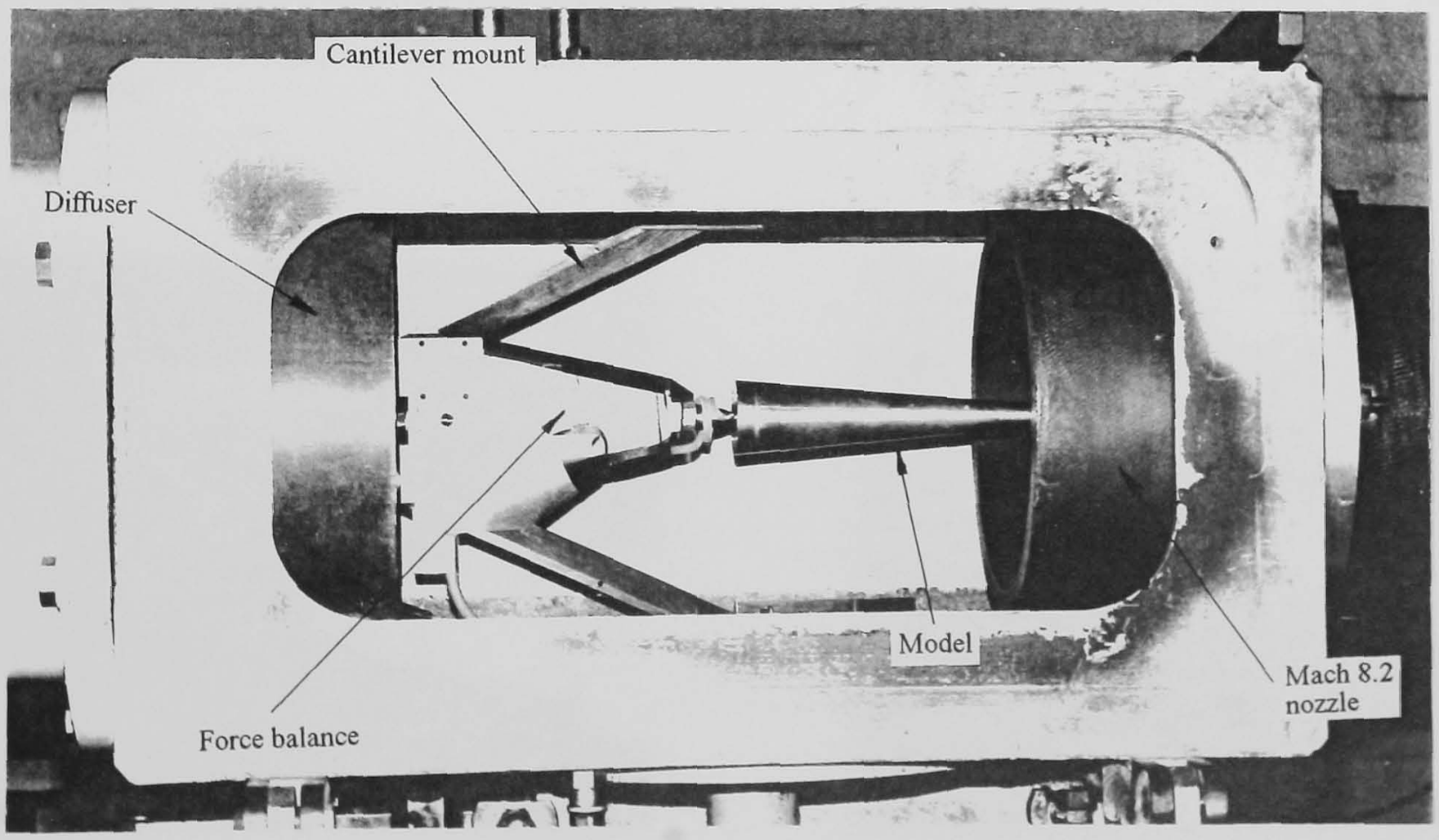

(d) general wind tunnel set-up used for jet interaction force study

Figure 7-14 General structure of the model and wind-tunnel setup used for studying jet interaction forces

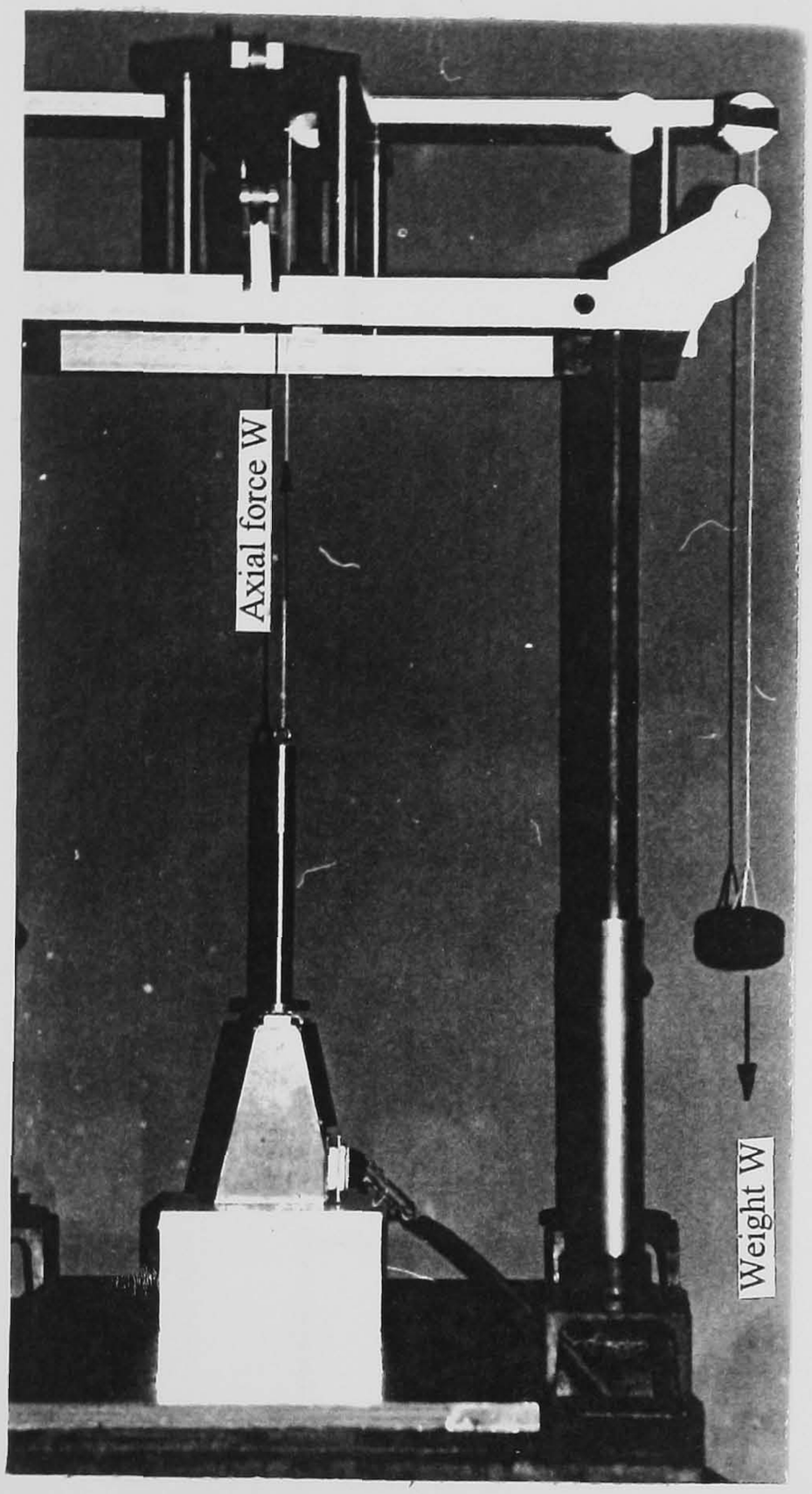

(a) vertical balance set-up used for axial force calibration

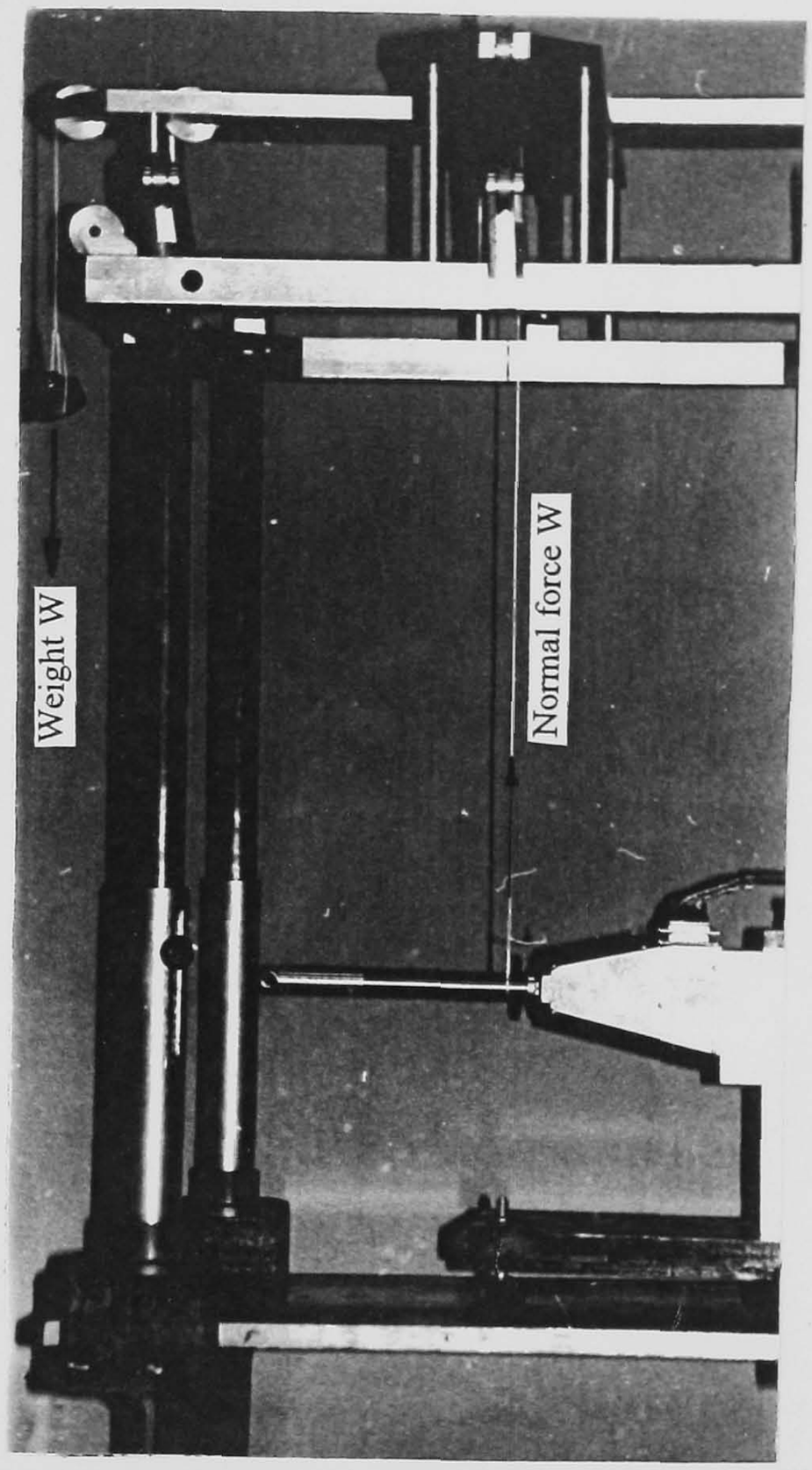

(b) horizontal balance set-up used for normal force and pitching moment calibration

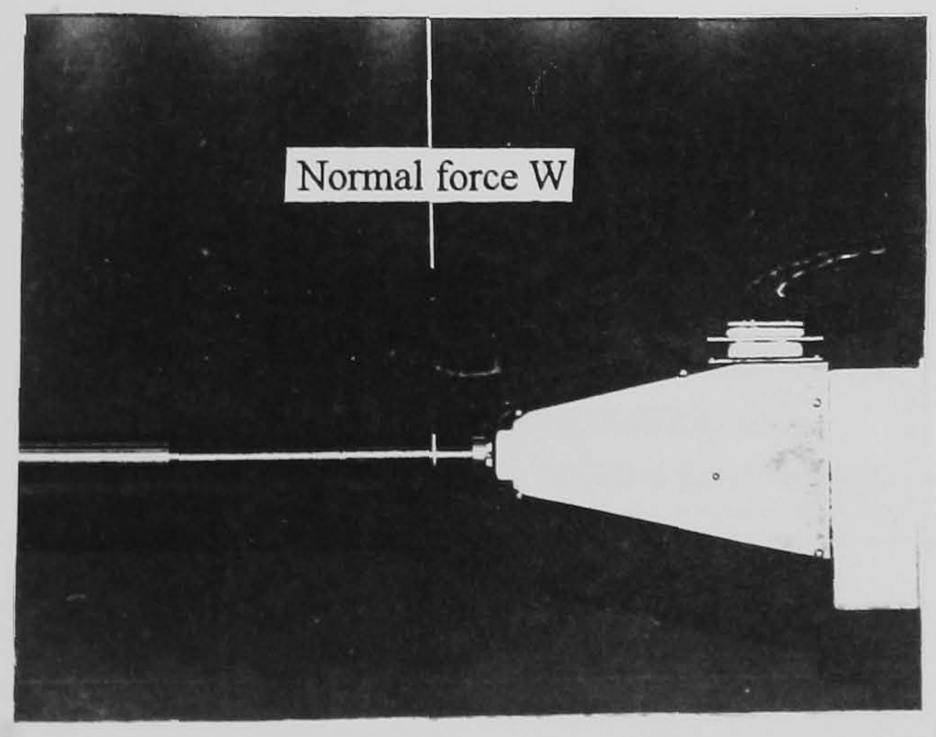

(c) load structure for normal force calibration

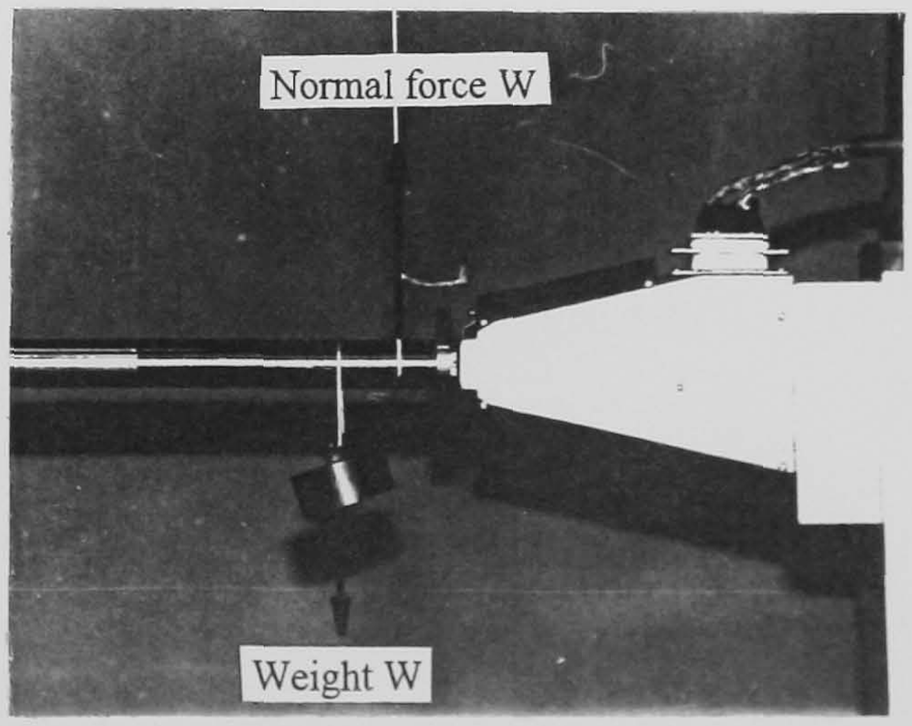

(d) load structure for pitching moment calibration

Figure 7-15 Set-up used for calibration of Gun tunnel 3-component force balance

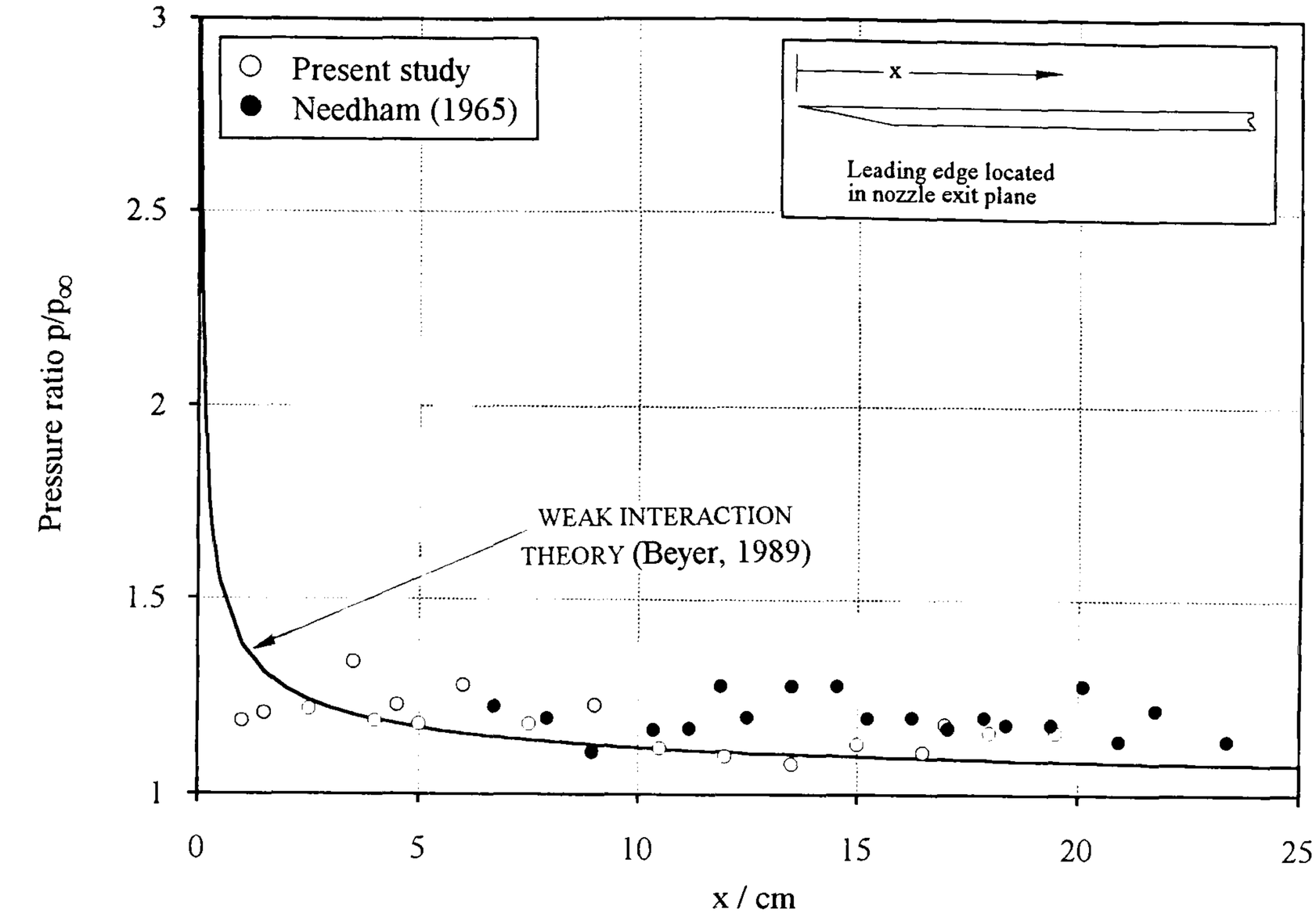

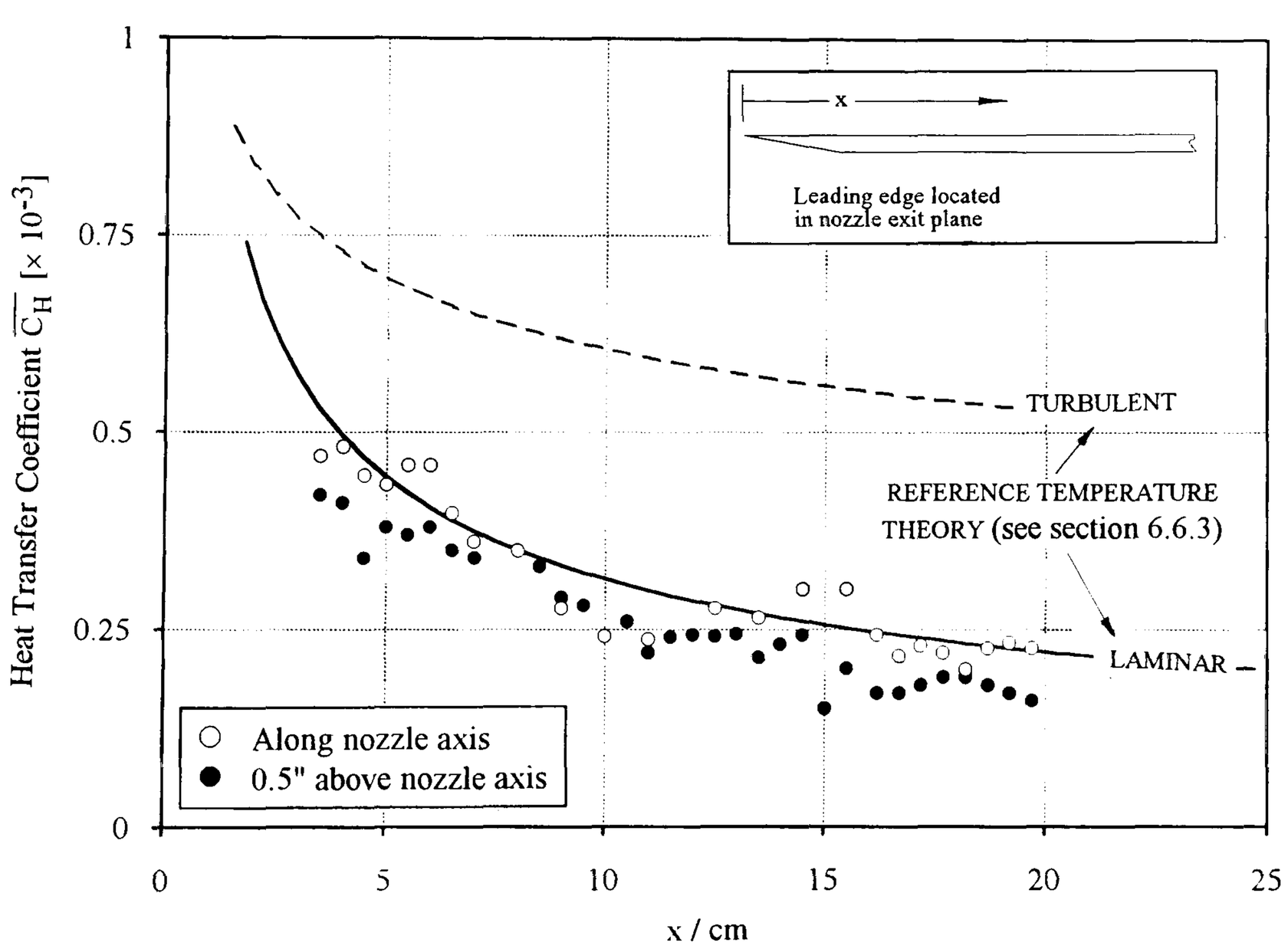

Figure 8-1 Pressure and heat transfer distributions on a sharp leading edge flat plate mounted along the nozzle axis ($M_\infty = 8.2$, $Re_\infty/cm = 9.0 \times 10^4$, $\alpha = 0°$)

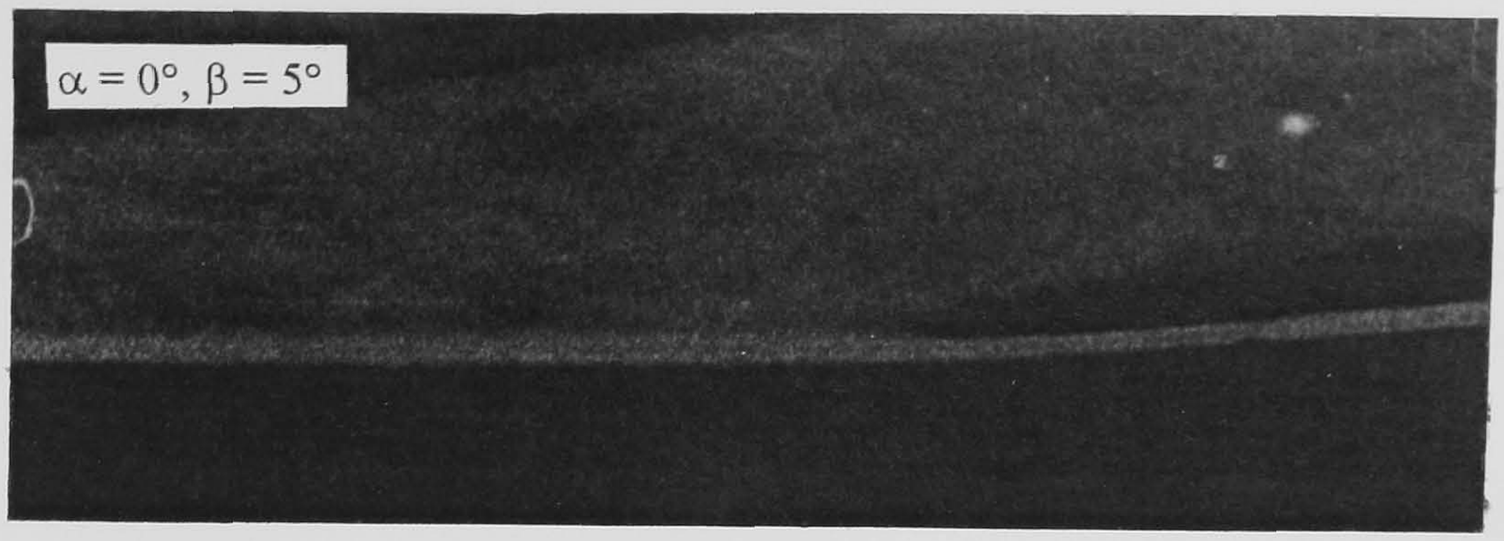

(a) schlieren photograph

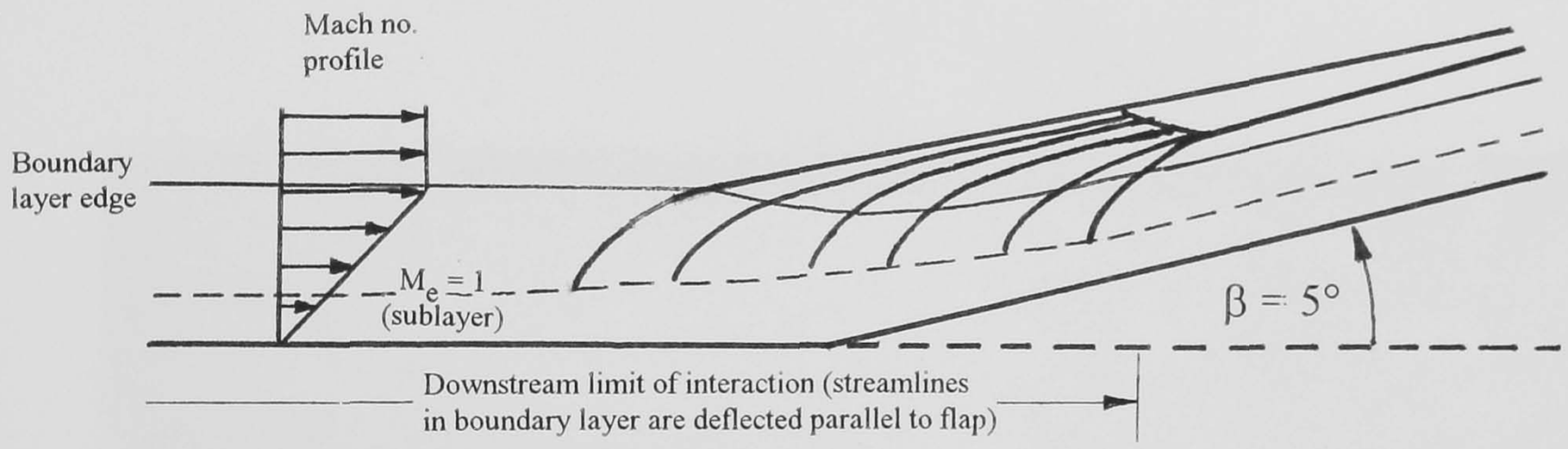

(b) schematic diagram

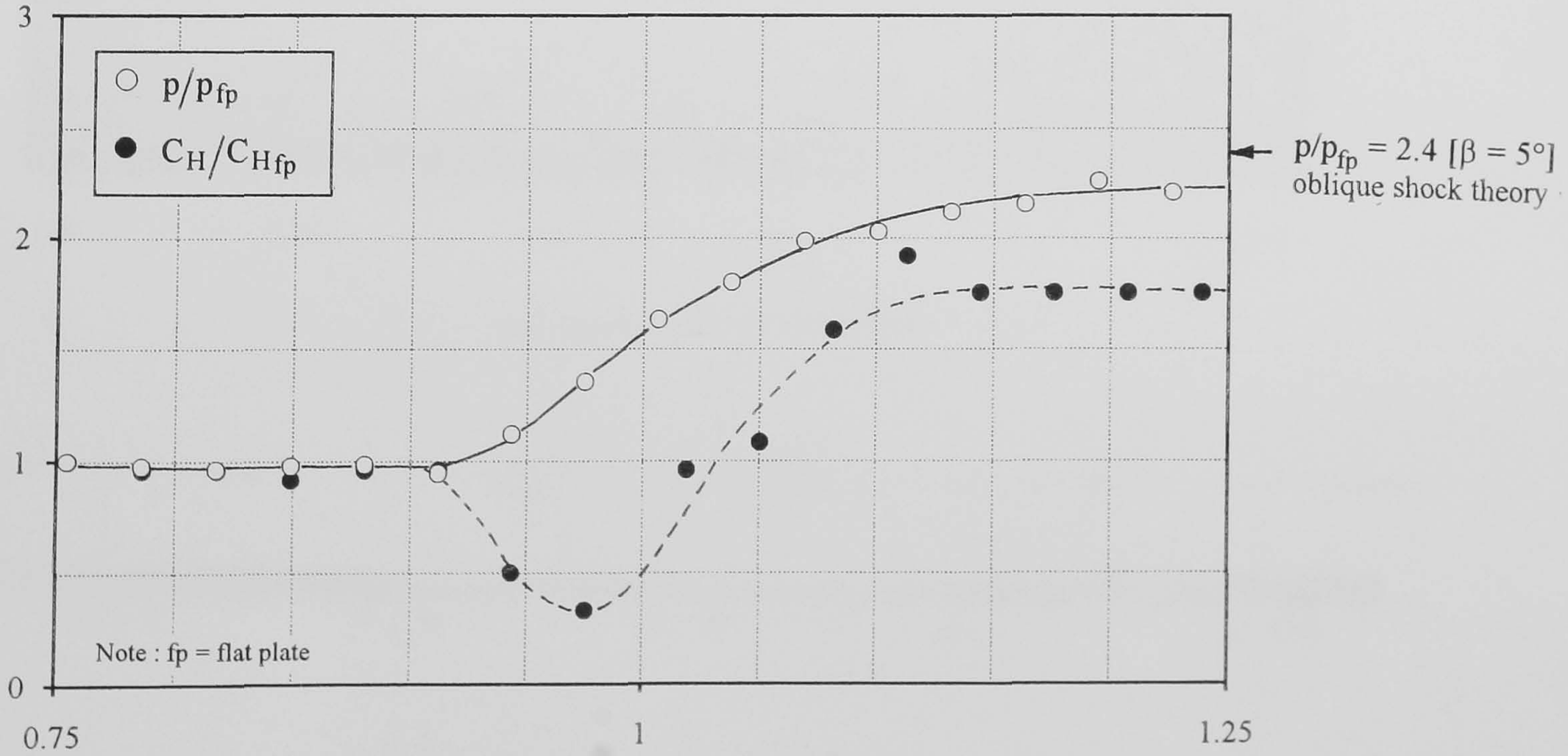

(c) surface properties

Figure 8-2 The effect of flap deflection on local flow properties in laminar unseparated flows ($M_\infty = 8.2$, $Re_\infty/cm = 9.0 \times 10^4$, L = 15.9 cm, $\alpha = 0°$, $\beta = 5°$)

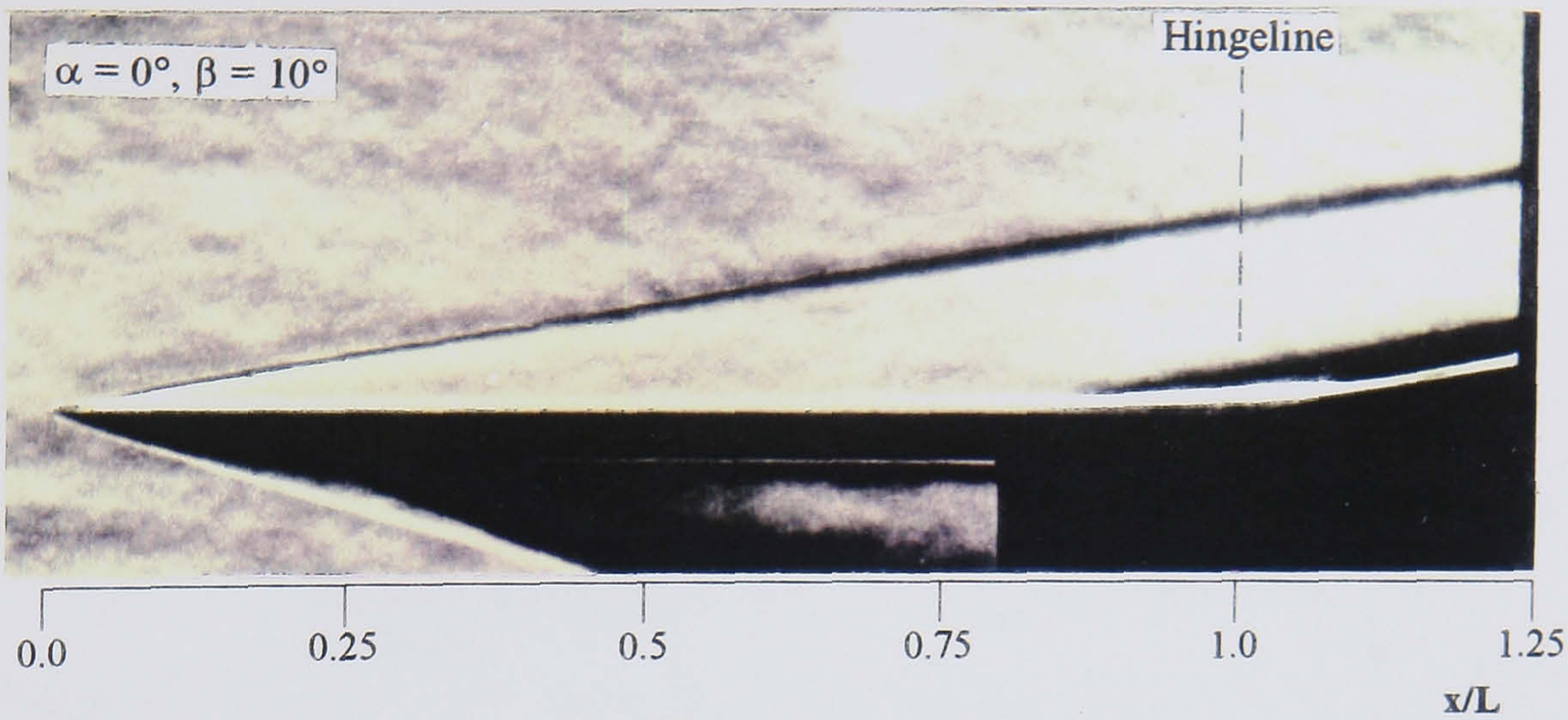

(i) schlieren flow visualisation

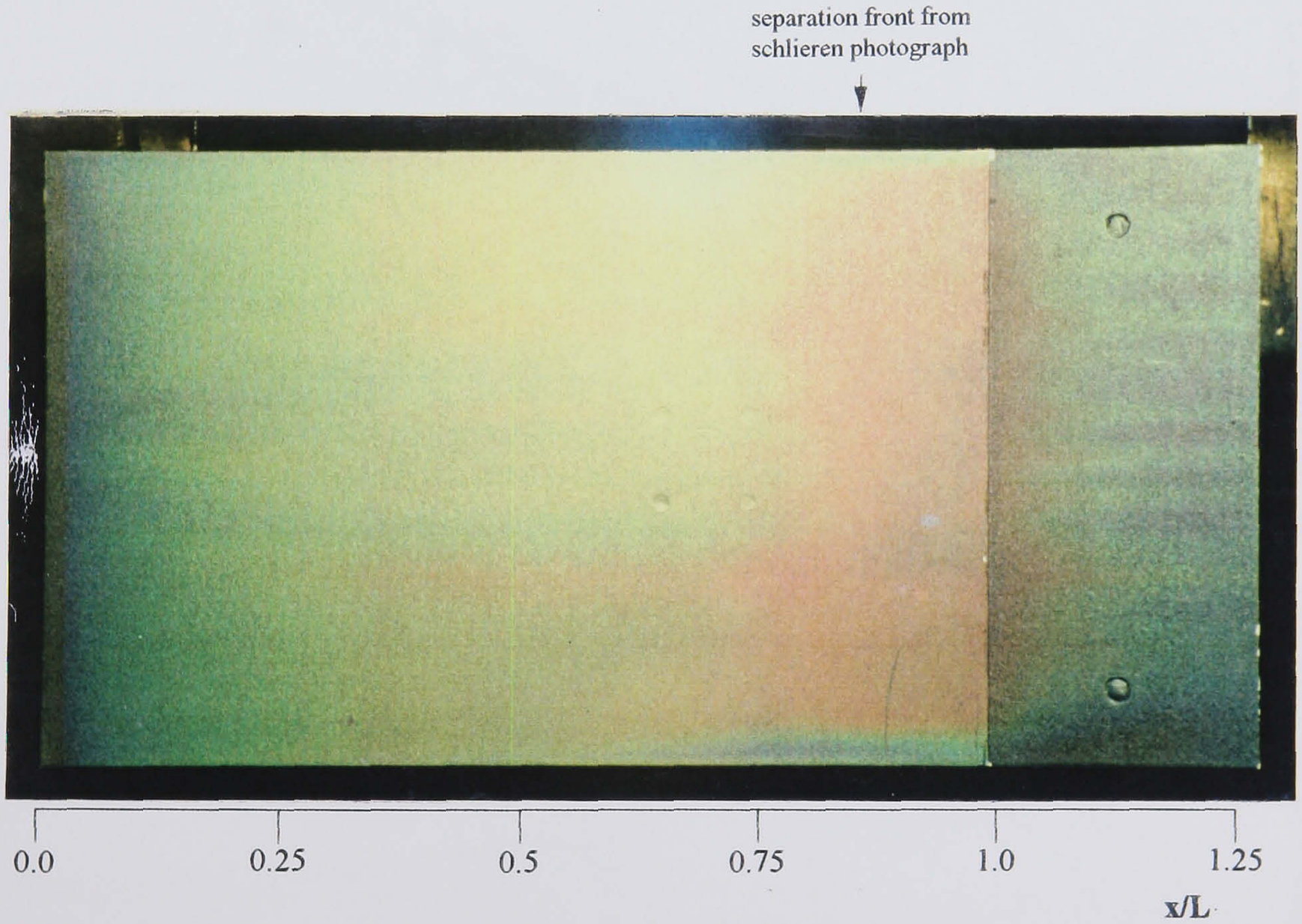

(ii) liquid crystal thermography

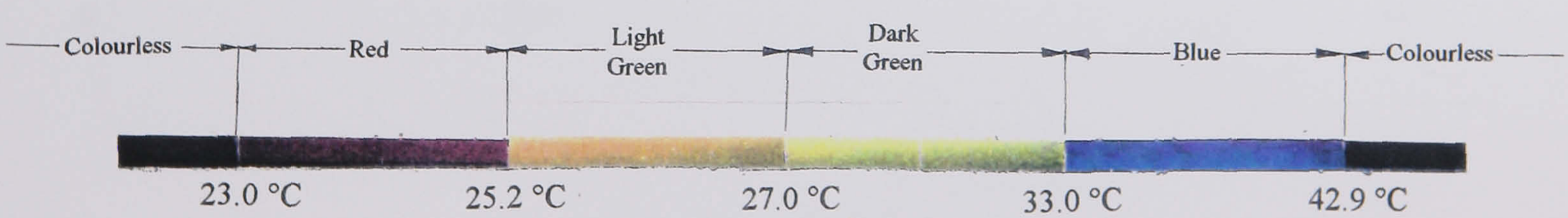

Figure 8-3 Schlieren photograph and liquid crystal thermograph of the flow structure on a control flap configuration - $\alpha = 0°$, $\beta = 10°$
($M_\infty = 8.2$, $Re_\infty/cm = 9.0 \times 10^4$, L = 15.9 cm, sharp leading edge)

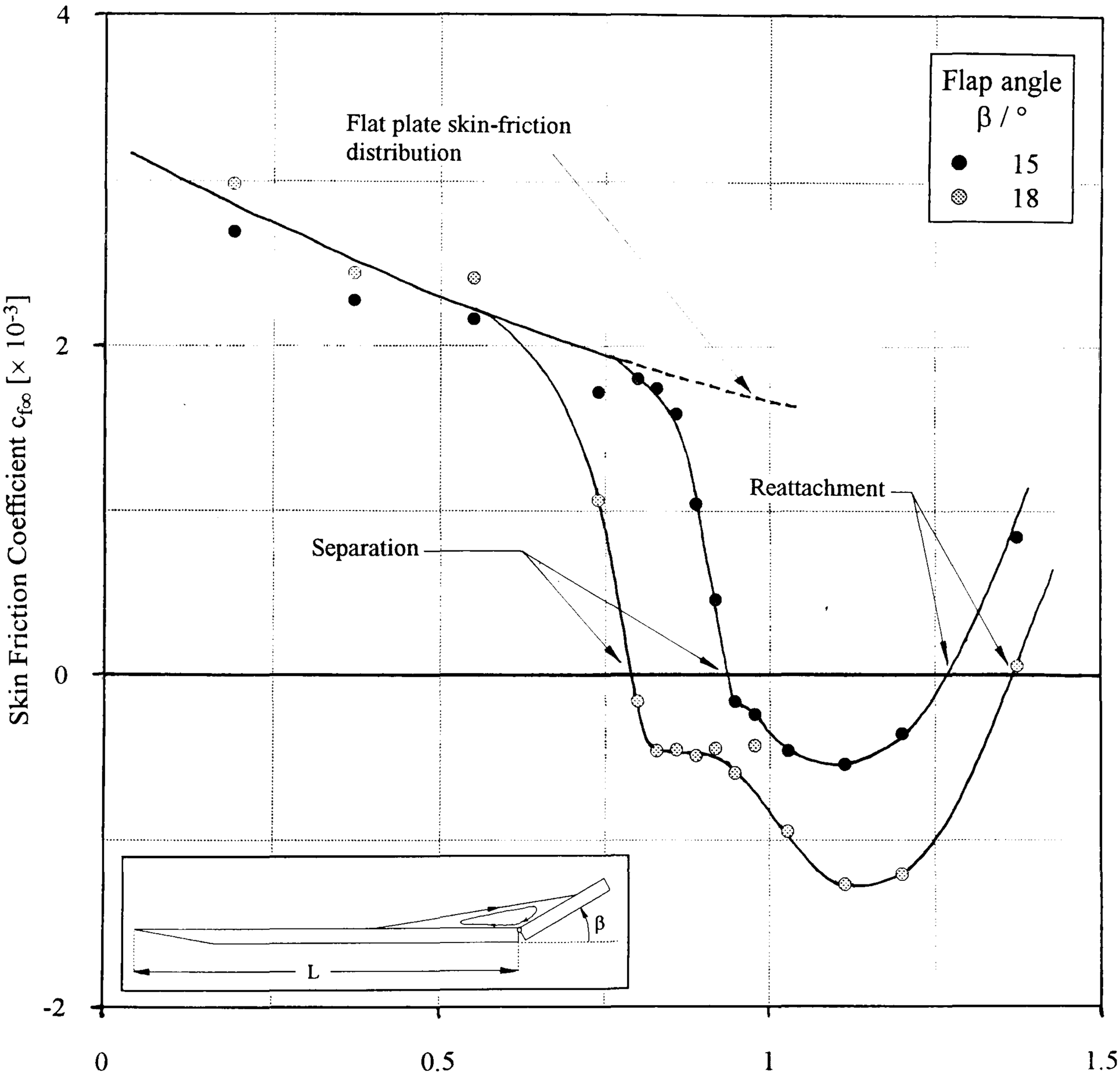

Figure 8-4 The effect of flap deflection on the relative location of separation and reattachment points in a fully laminar interaction - Holden et al (1992) (M_∞ = 18.9, Re_∞/cm = 0.6 × 10^4, α = 0°, L = 28.3 cm)

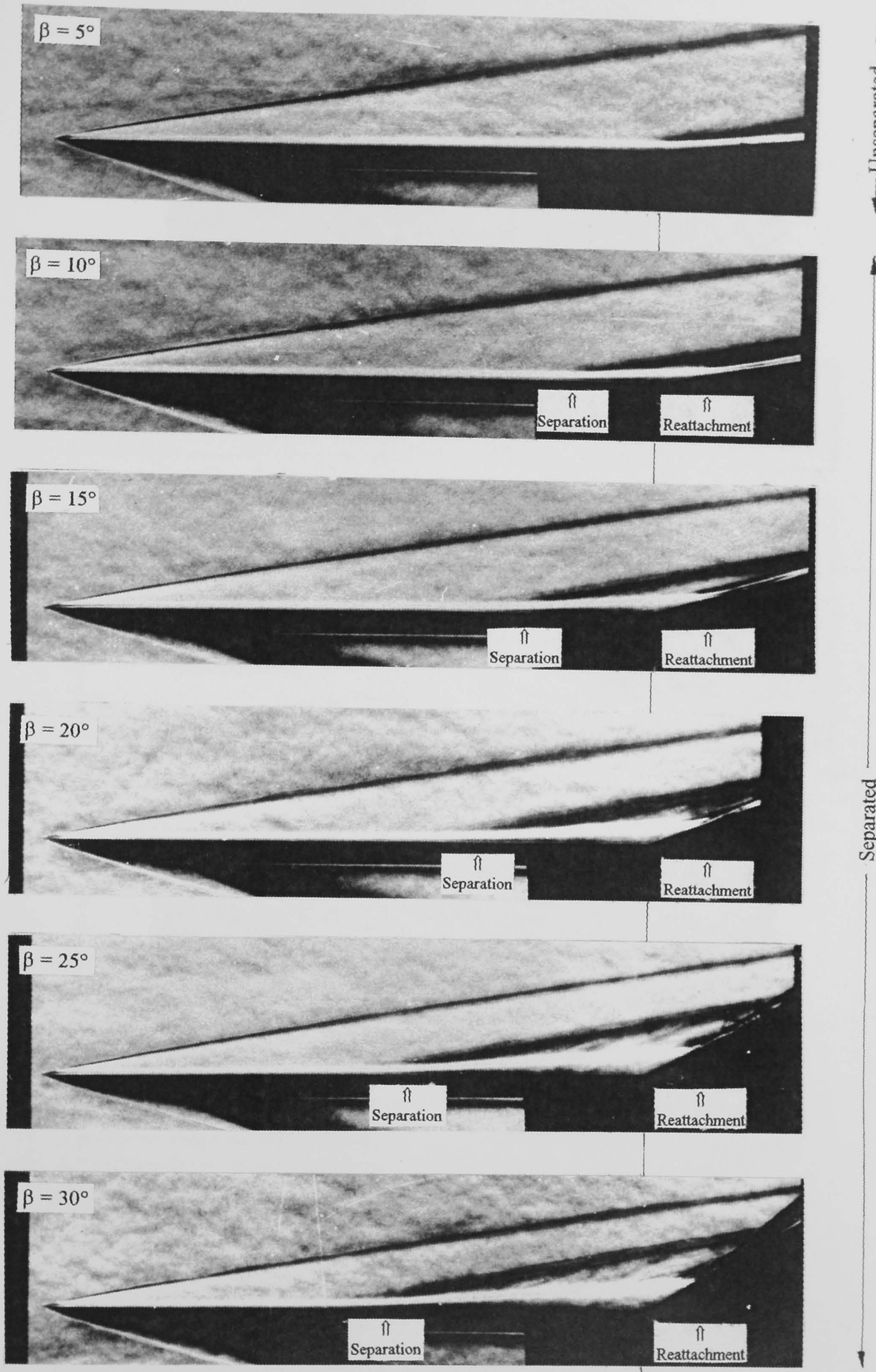

Figure 8-5 The effect of flap deflection on the location of separation and reattachment in transitional flows ($M_\infty = 8.2$, $Re_\infty/cm = 9.0 \times 10^4$, L = 15.9 cm, sharp LE)

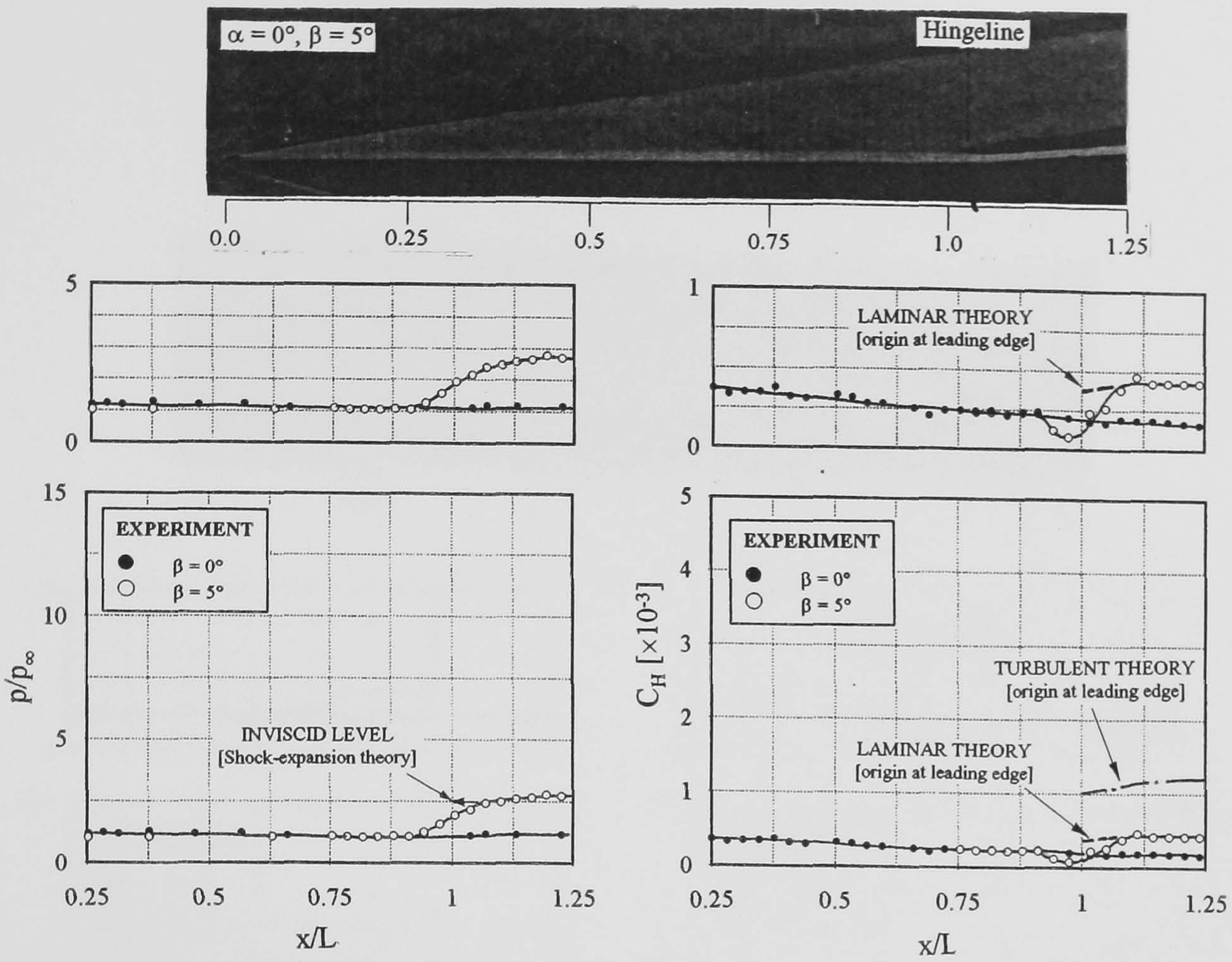

Figure 8-6 Pressure and heat transfer measurements on control flap configurations ($M_\infty = 8.2$, $Re_\infty/cm = 9.0 \times 10^4$, L = 15.9 cm)

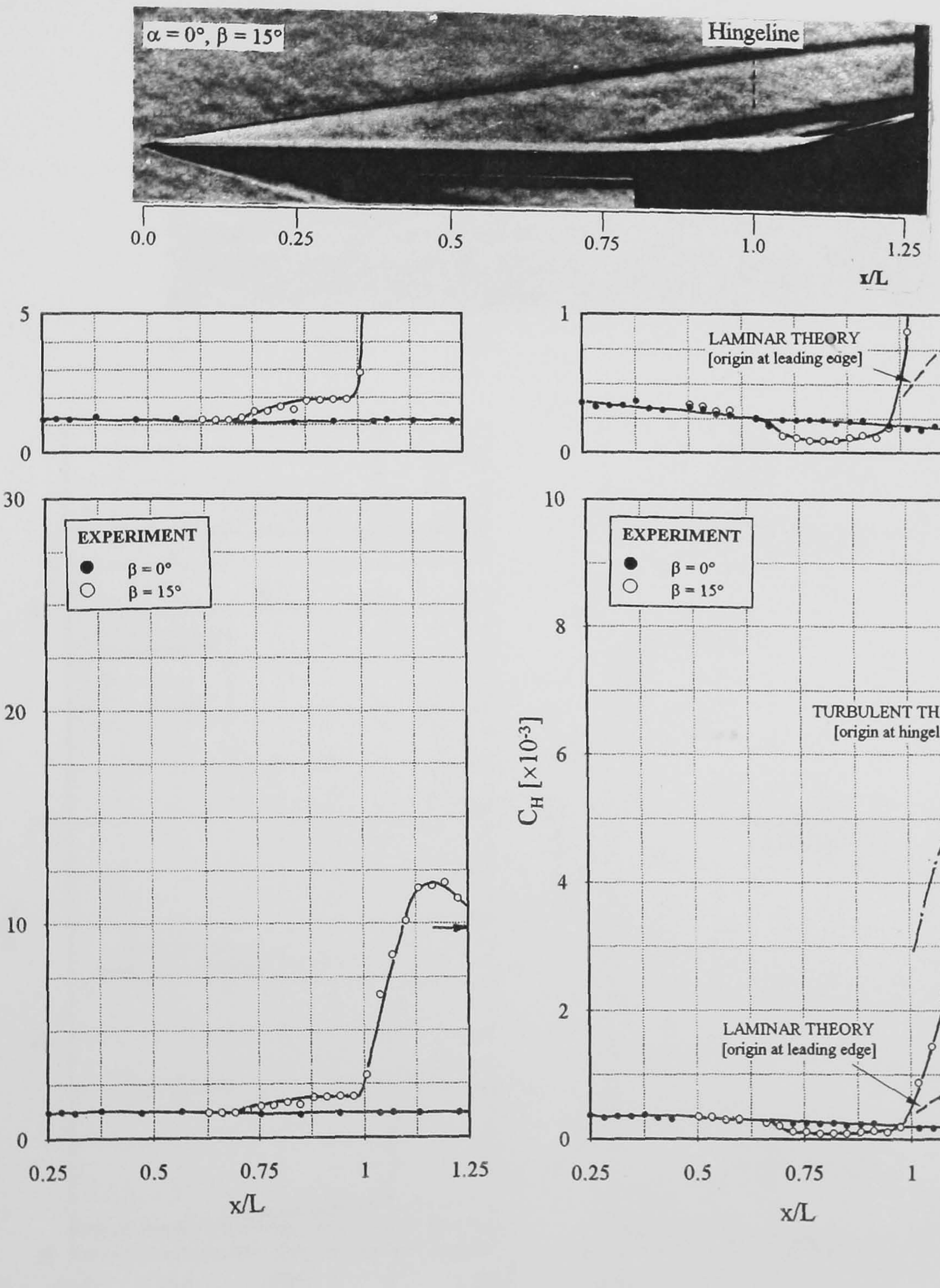

Figure 8-6 (cont'd) Pressure and heat transfer measurements on control flap configurations ($M_\infty = 8.2$, $Re_\infty/cm = 9.0 \times 10^4$, L = 15.9 cm)

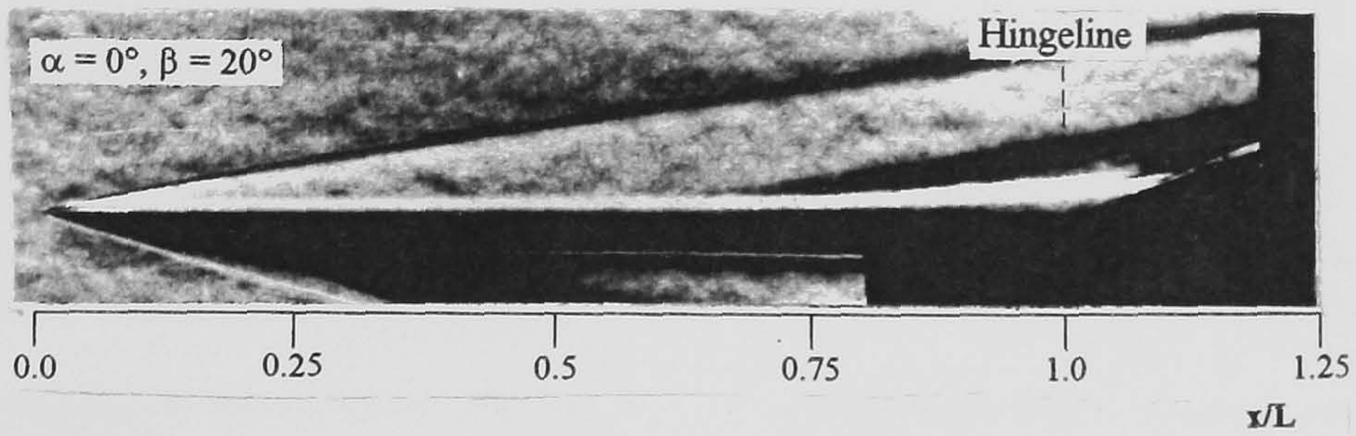

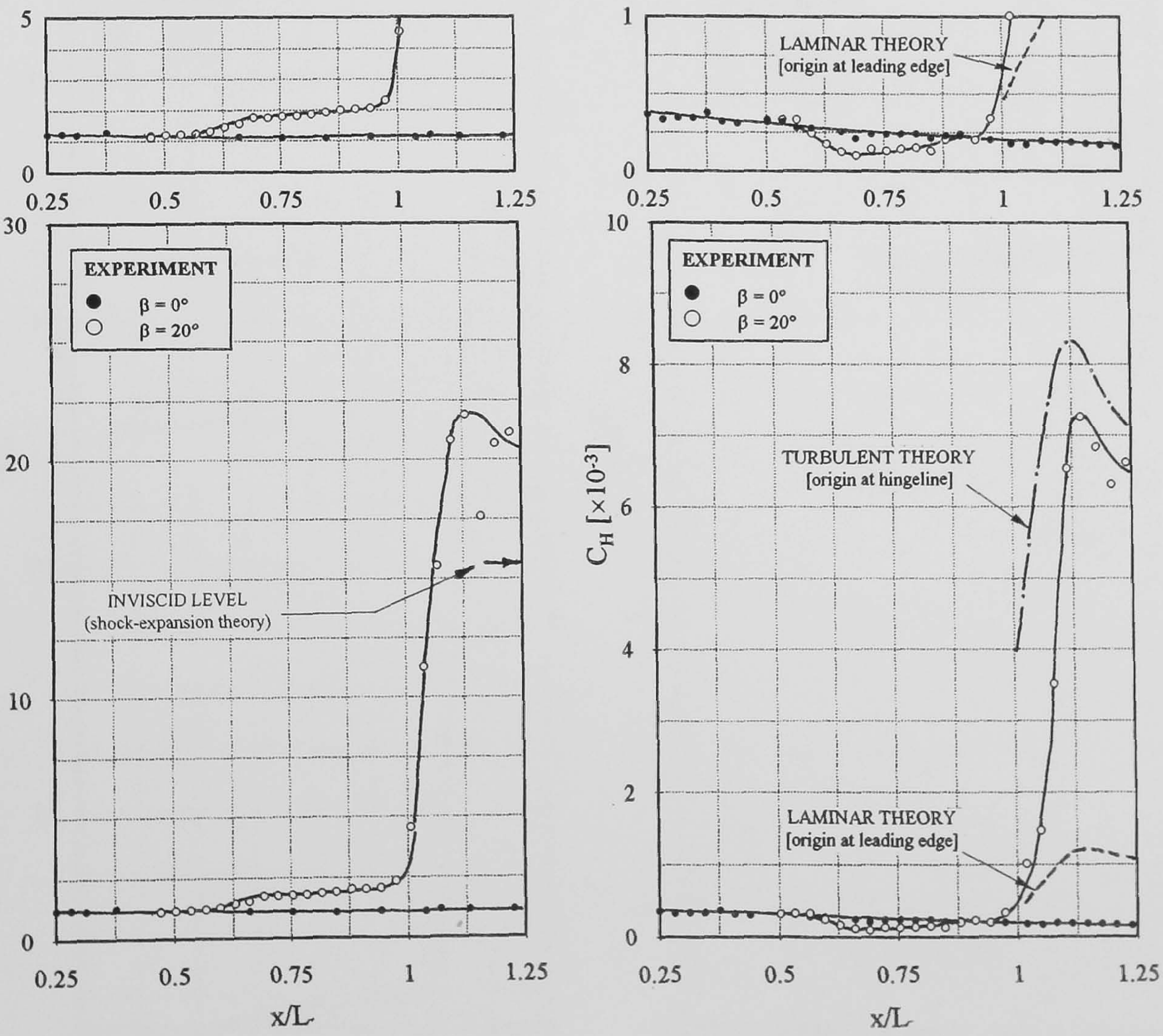

Figure 8-6 (cont'd) Pressure and heat transfer measurements on control flap configurations ($M_\infty = 8.2$, $Re_\infty/cm = 9.0 \times 10^4$, L = 15.9 cm)

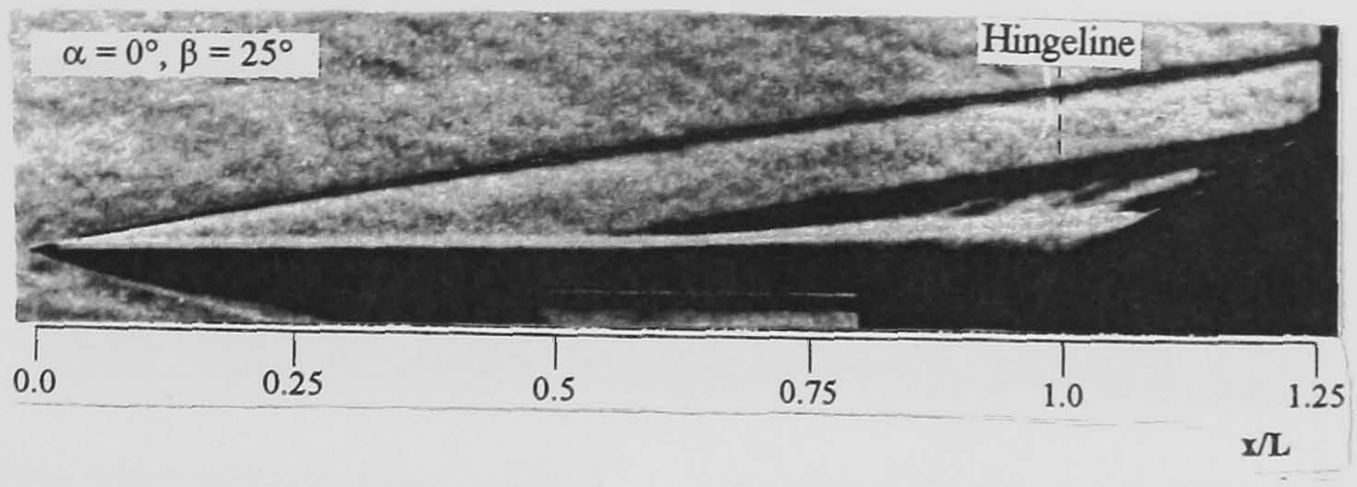

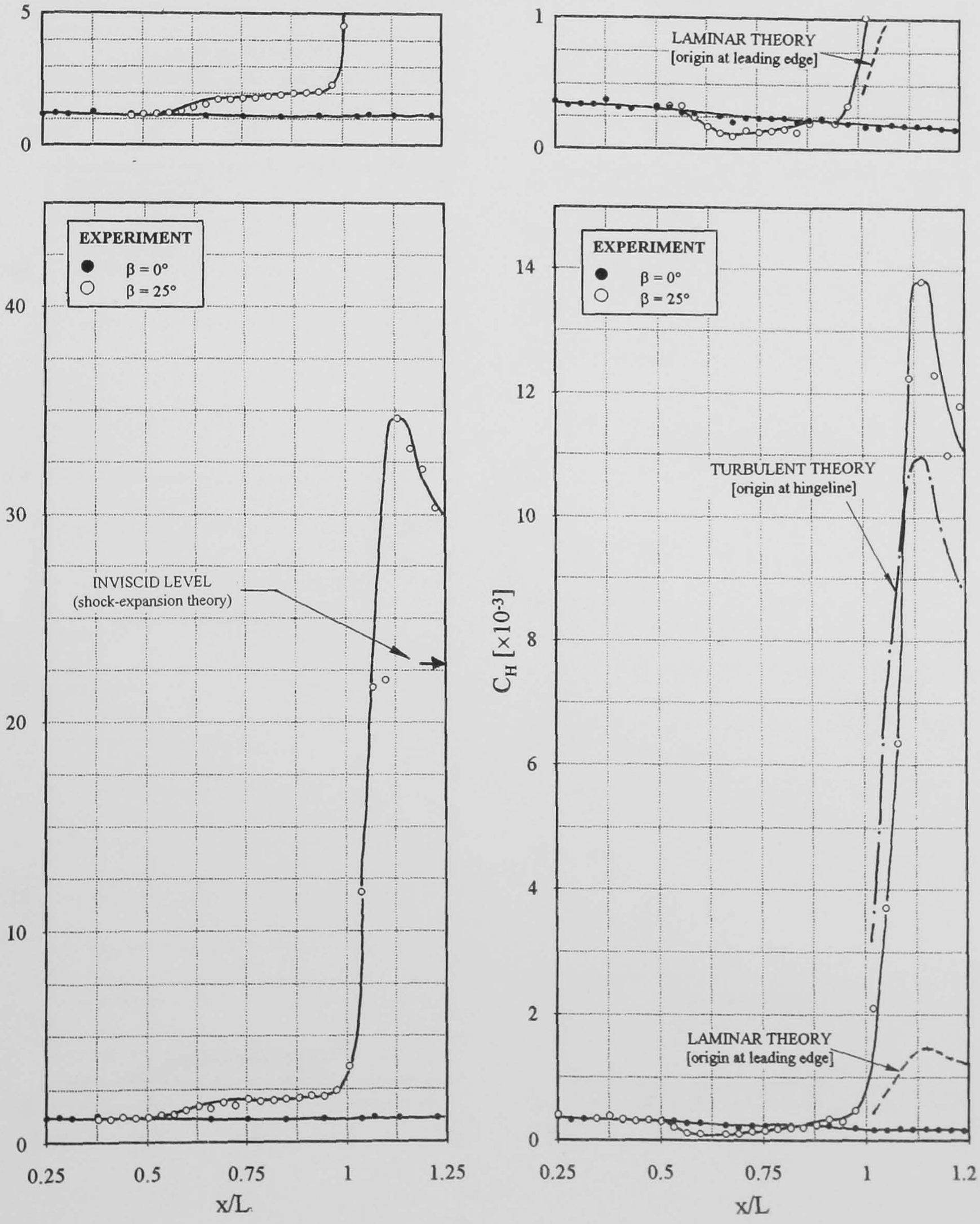

Figure 8-6 (cont'd) Pressure and heat transfer measurements on control flap configurations ($M_\infty = 8.2$, $Re_\infty/cm = 9.0 \times 10^4$, L = 15.9 cm)

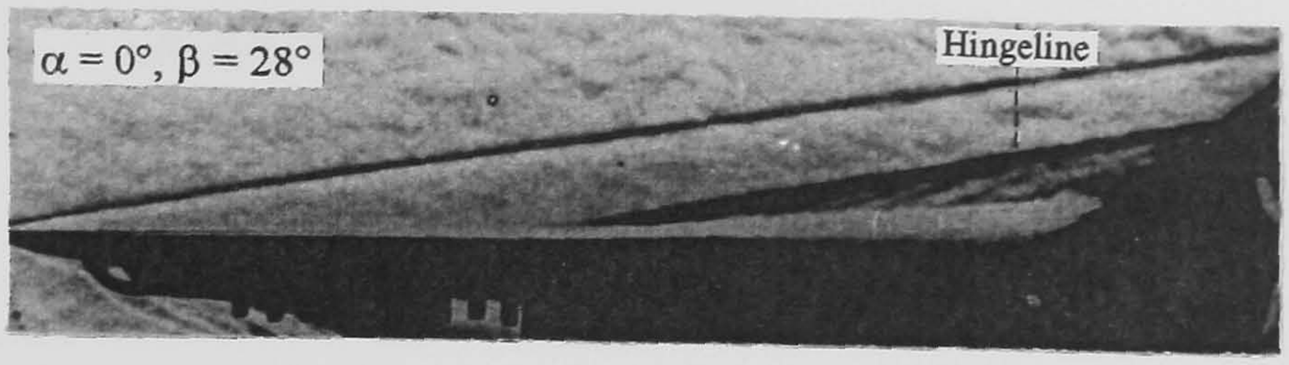

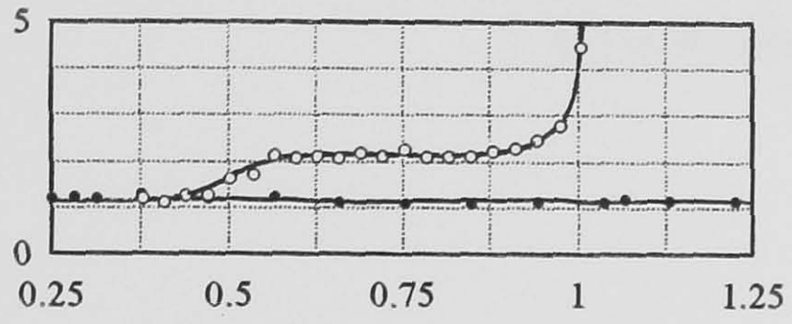

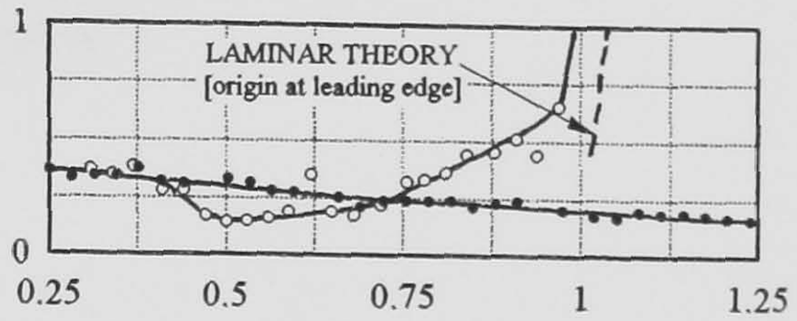

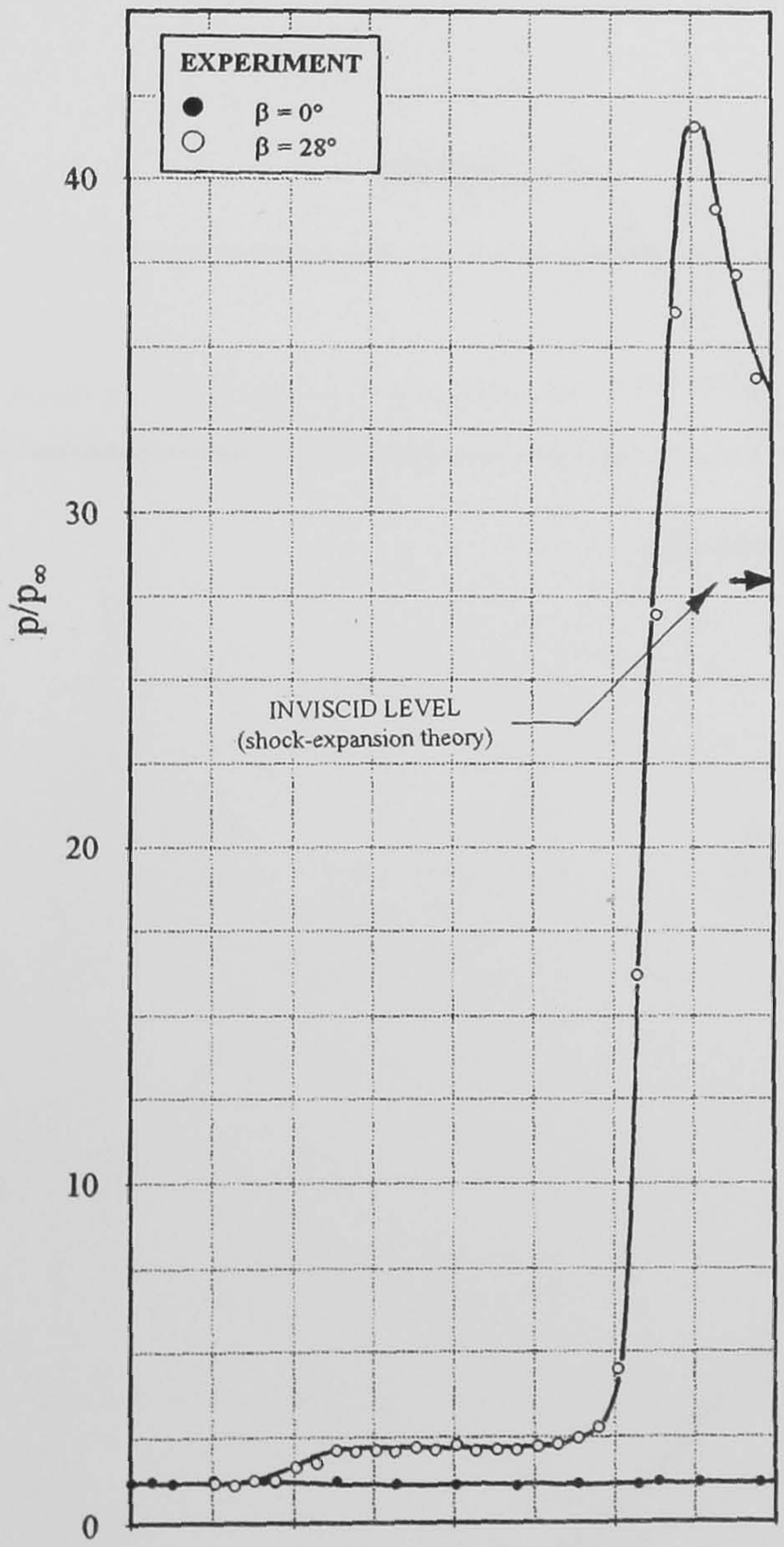

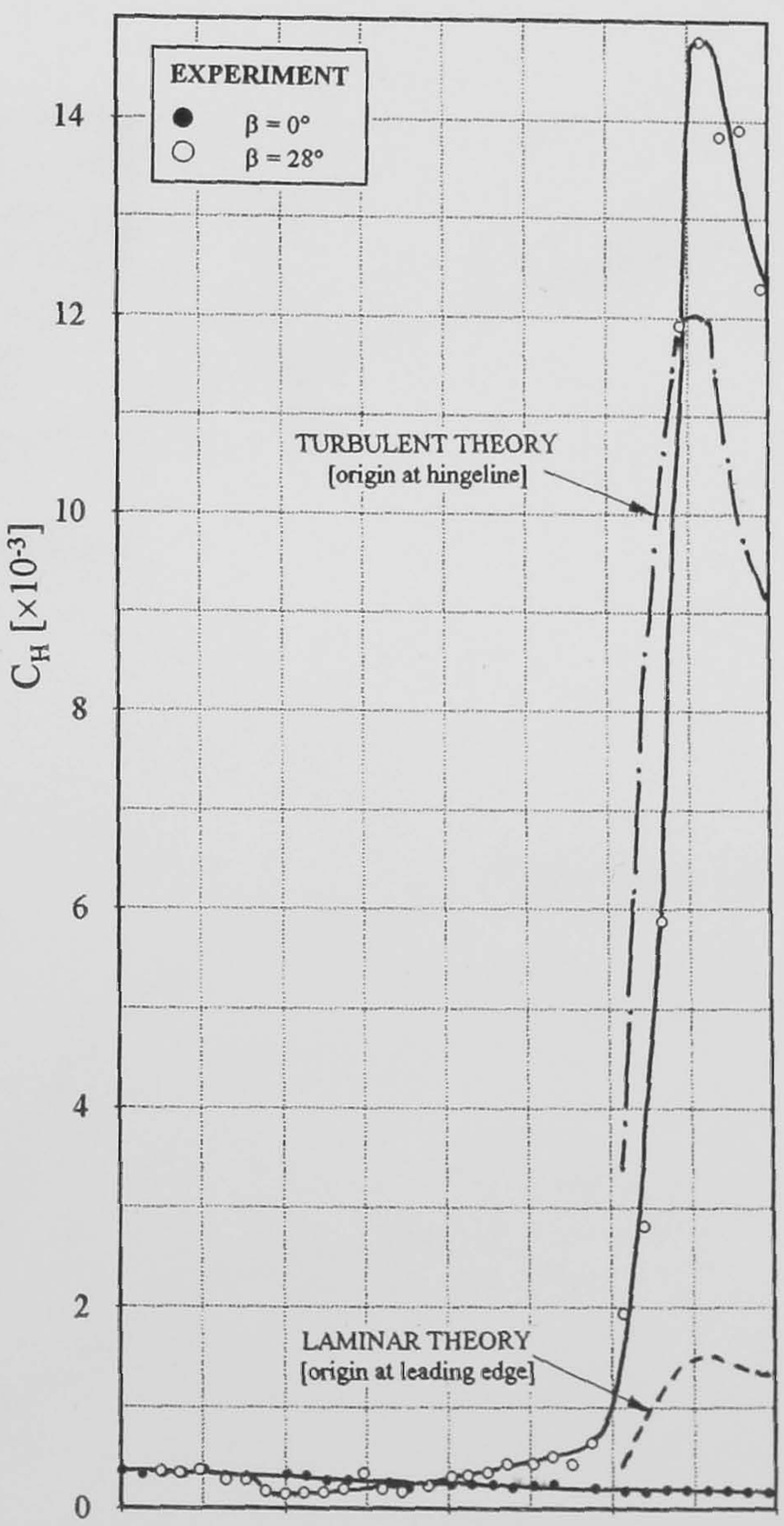

Figure 8-6 (cont'd) Pressure and heat transfer measurements on control flap configurations ($M_\infty = 8.2$, $Re_\infty/cm = 9.0 \times 10^4$, L = 15.9 cm)

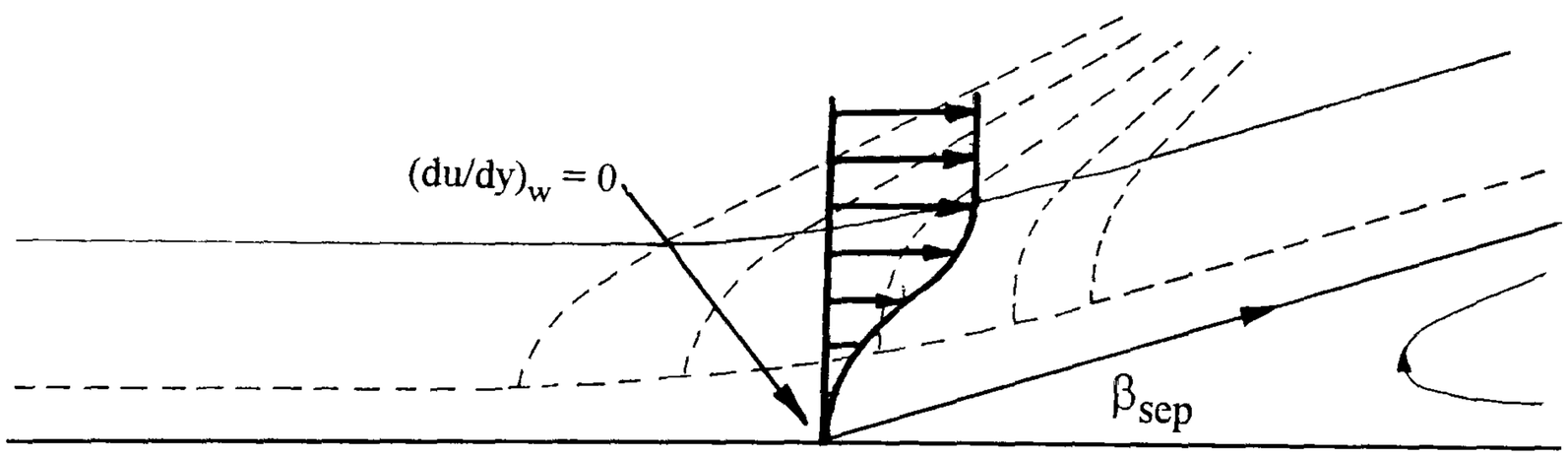

(a) well-separated flow

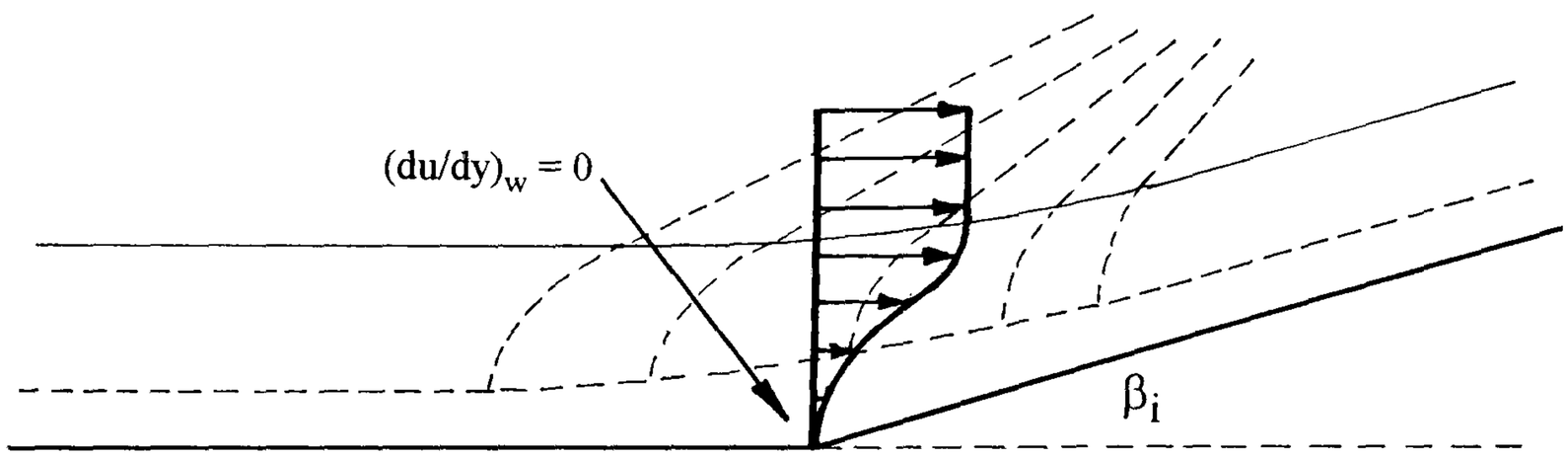

(b) incipient flow

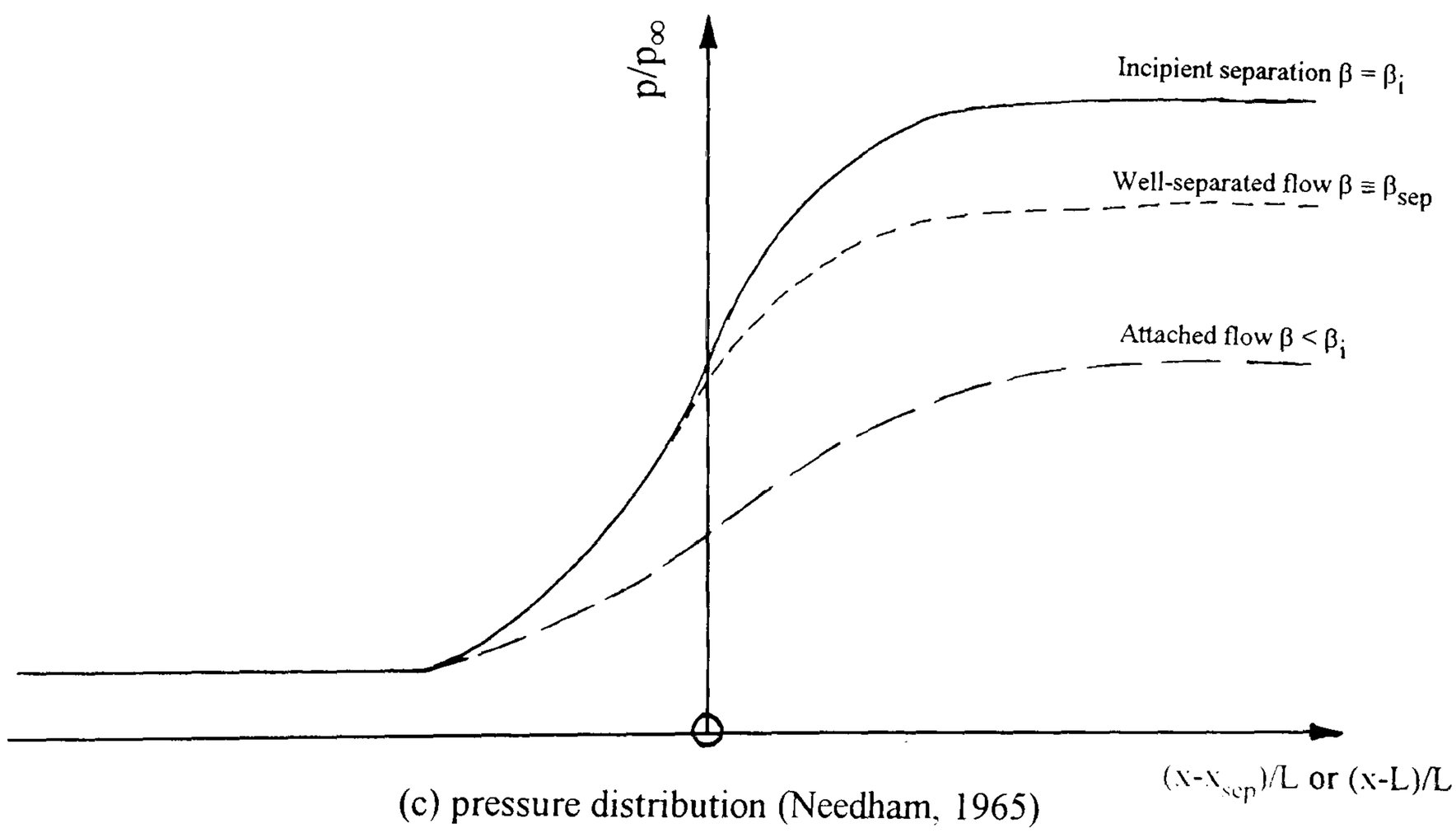

(c) pressure distribution (Needham, 1965)

Figure 8-7 Similarity of flow structures in the interaction region of incipient and well-separated laminar flows

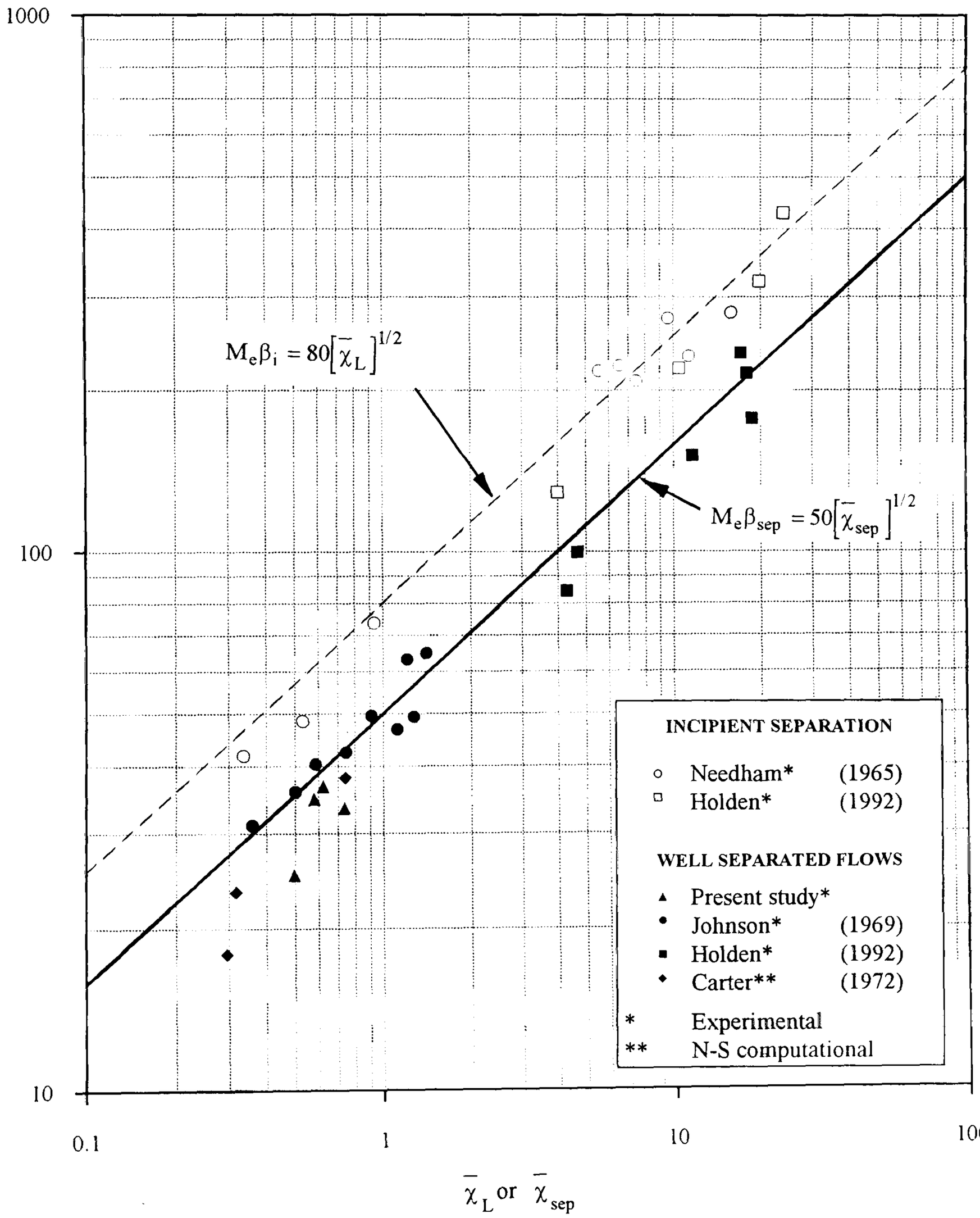

Figure 8-8 The similarity between flap deflection angle for laminar incipient separation and the separation streamline angle for well-separated laminar flows

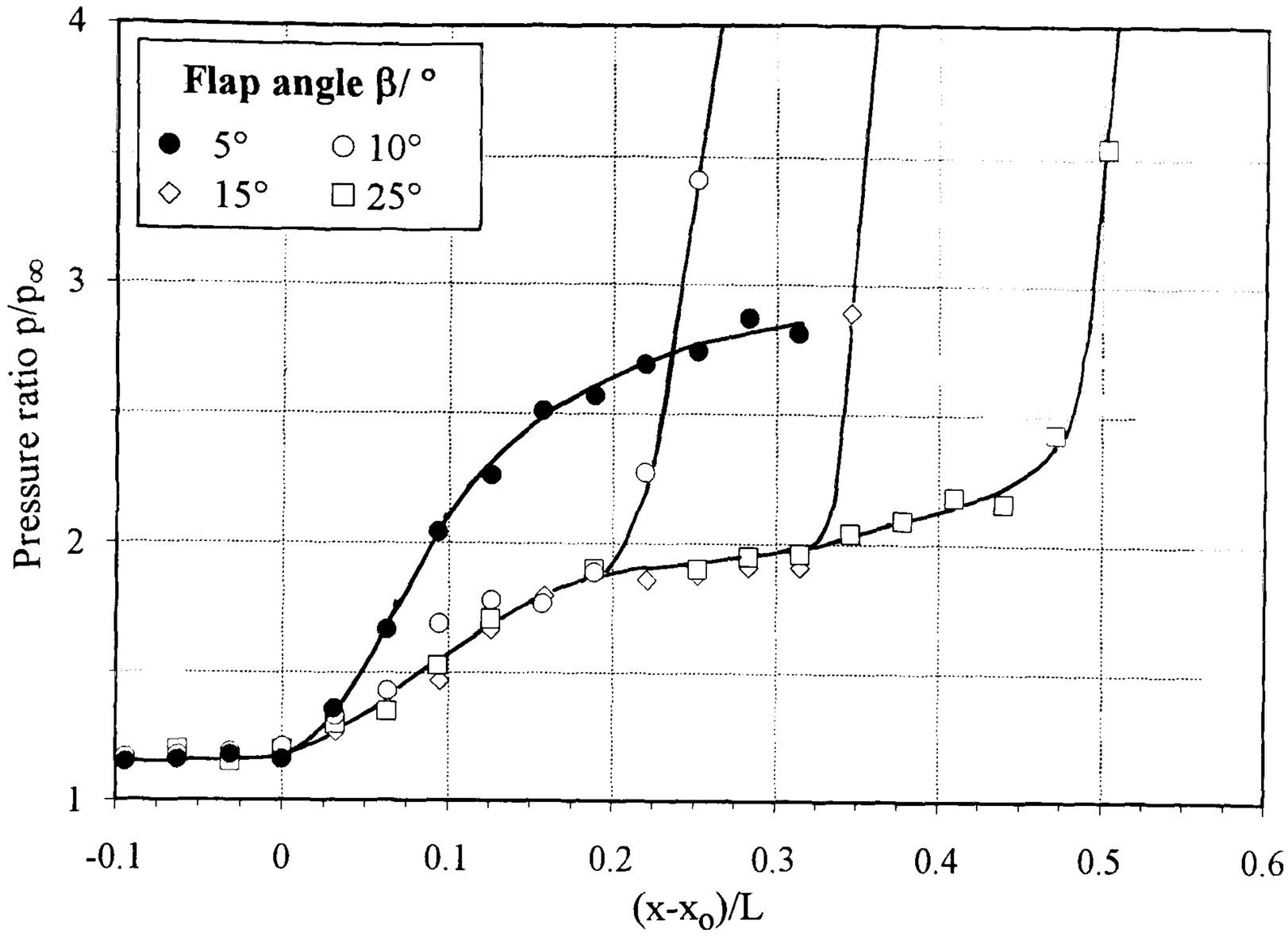

(a) pressure distribution

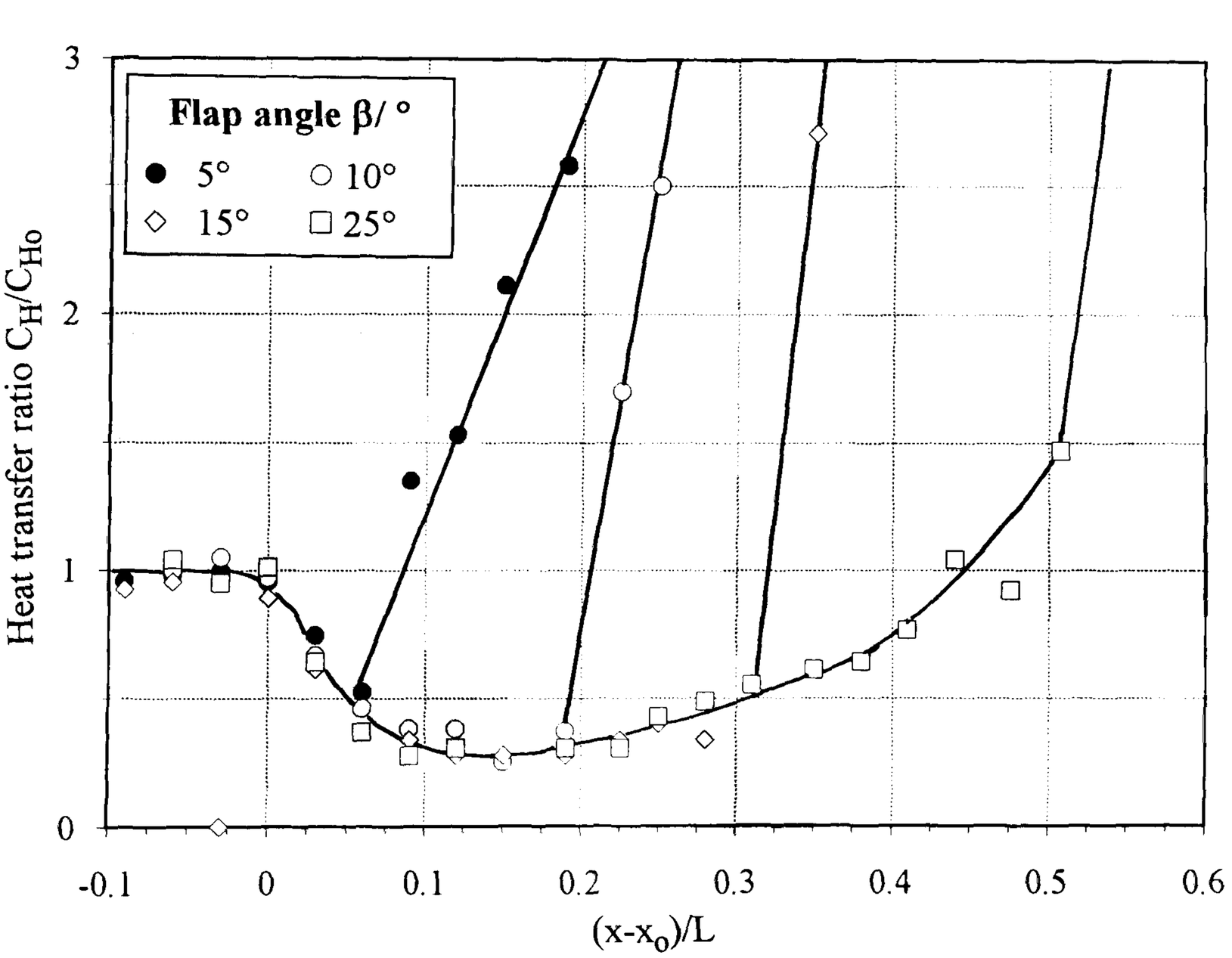

(b) heat transfer distribution

Figure 8-9 Similarity of pressure and heat transfer distributions in the interaction region of transitional flows (M_∞ = 8.2, Re_∞/cm = 9.0×10^4, L = 15.9 cm, Sharp LE)

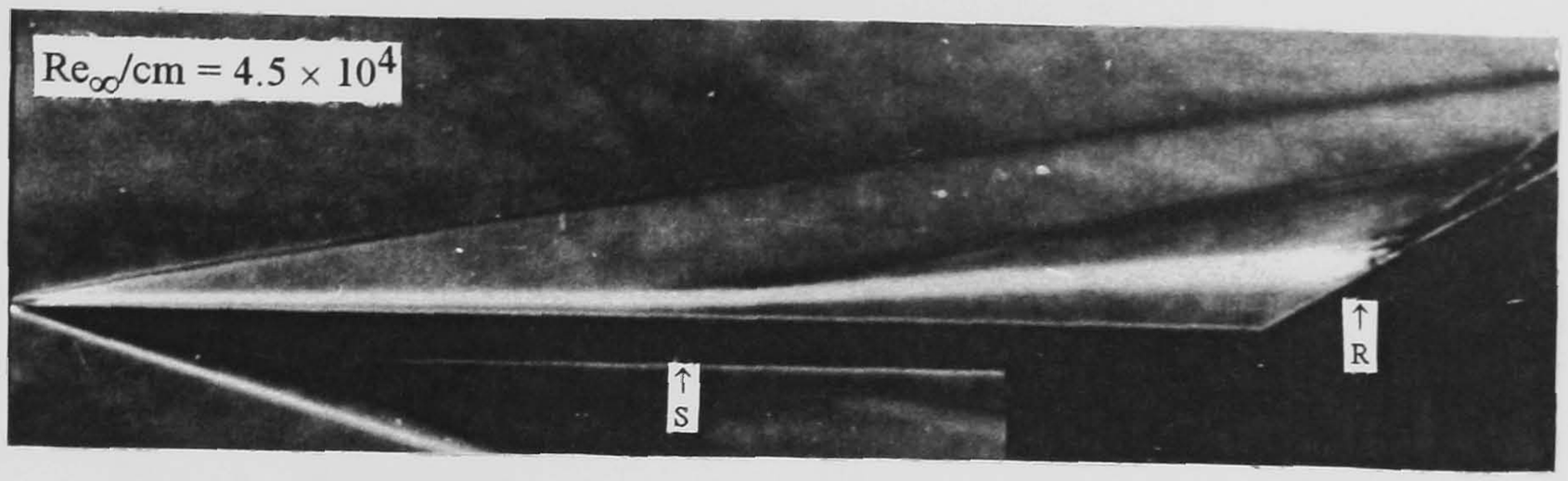

S : Separation R : Reattachment Tr : Transition

Figure 8-10 The promotion of shear layer transition in well separated transitional flows ($M_\infty = 8.2$, $\alpha = 0°$, $\beta = 30°$, L = 15.9 cm, Sharp LE)

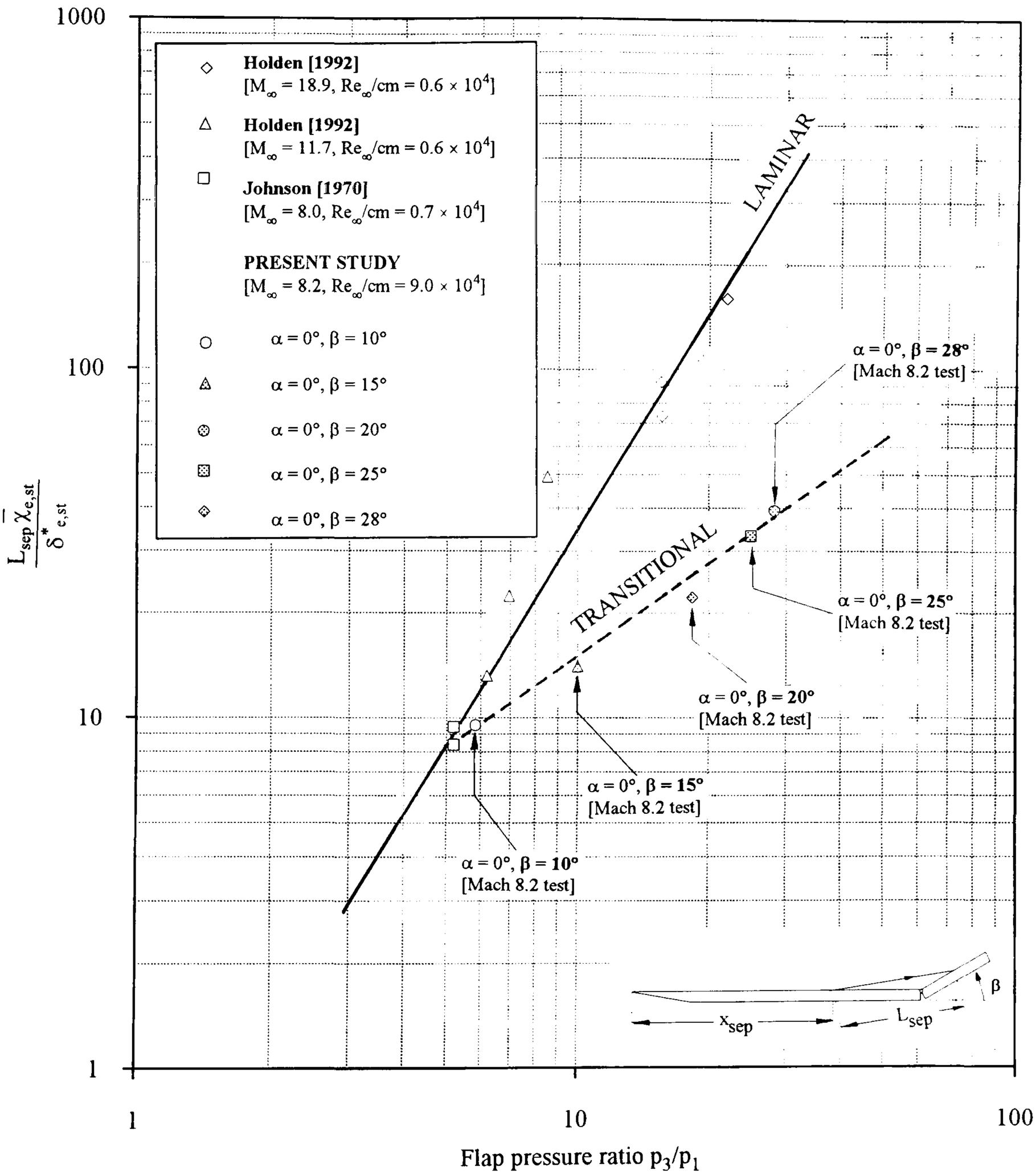

Figure 8-11 The effect of shear layer transition on the length of separated flow

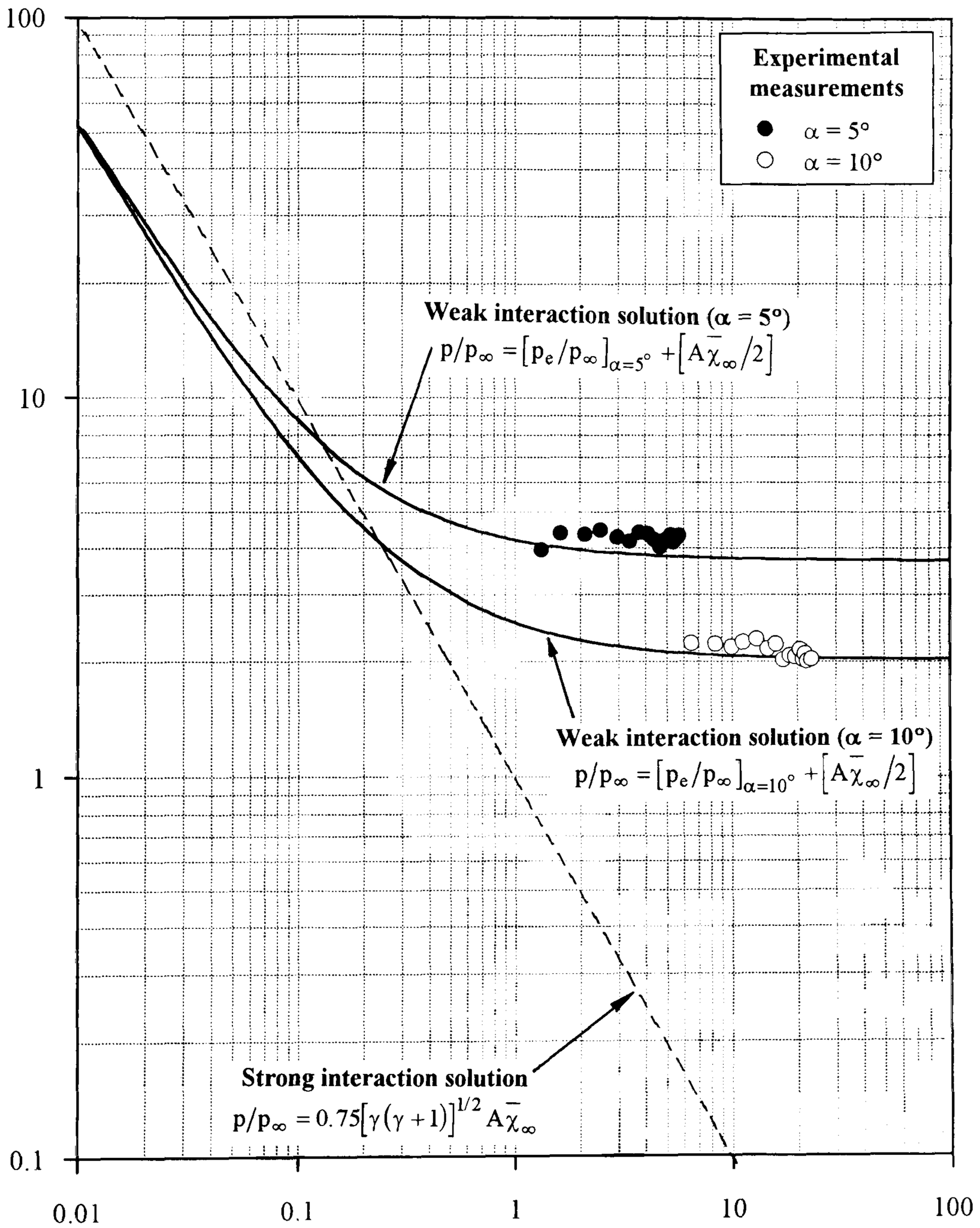

Figure 8-12 The effect of incidence on the pressure distribution for a sharp flat plate ($M_\infty = 8.2$, $Re_\infty/cm = 9.0 \times 10^4$, Sharp LE)

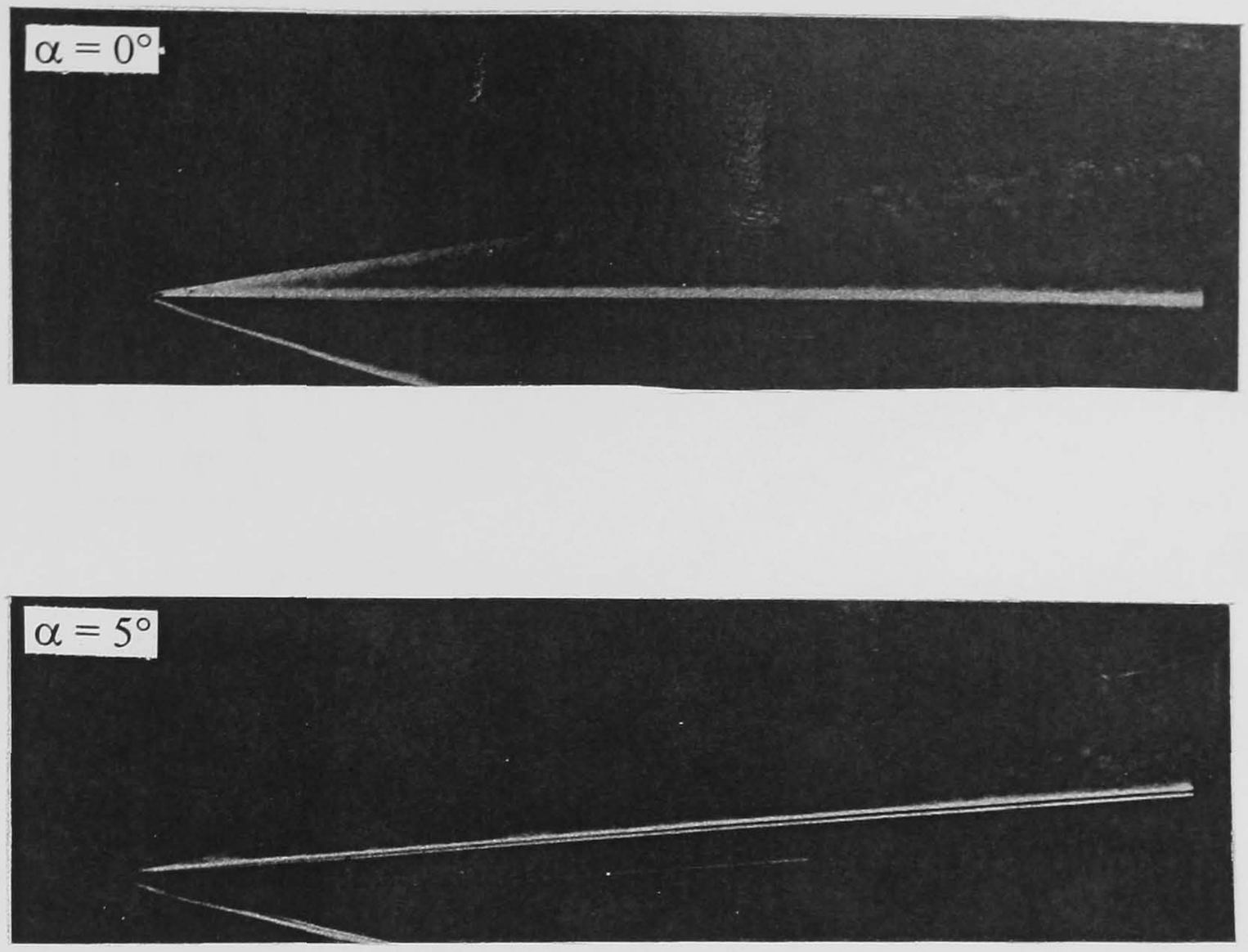

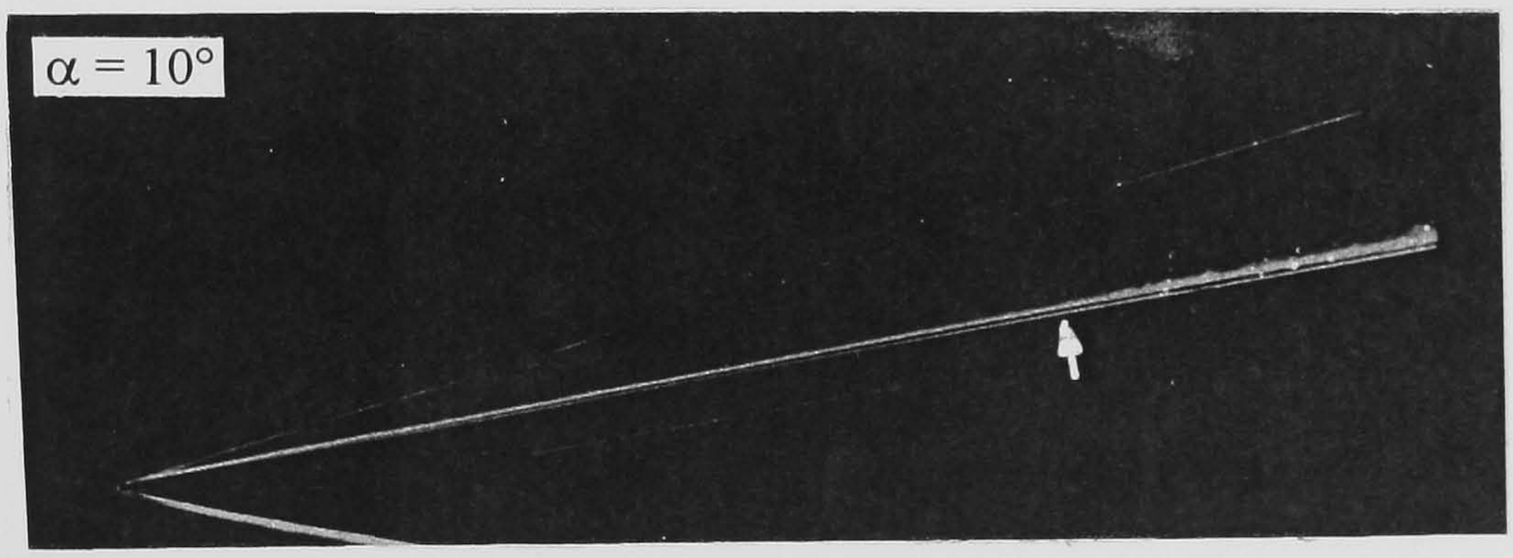

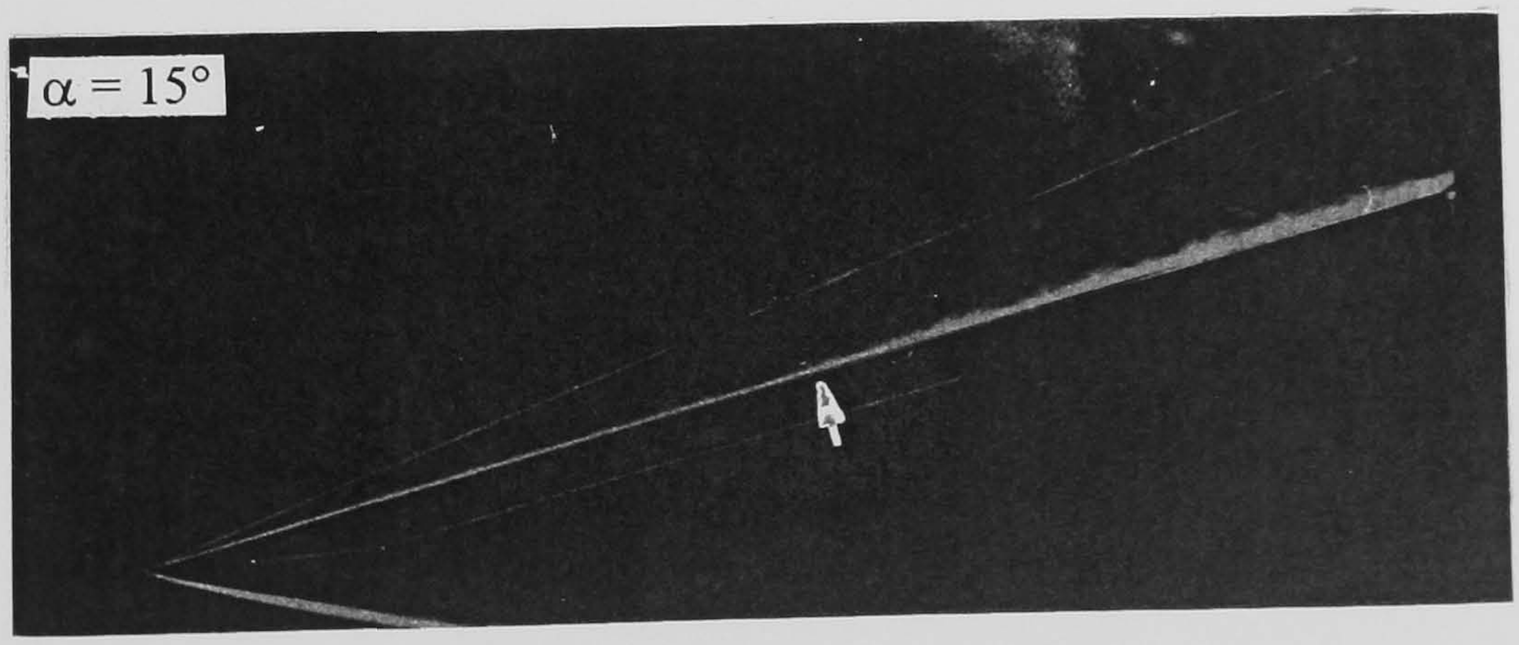

Figure 8-13 The effect of incidence on the transition of a flat plate boundary layer ($M_\infty = 8.2$, $Re_\infty/cm = 9.0 \times 10^4$, L = 15.9 cm, Sharp LE)

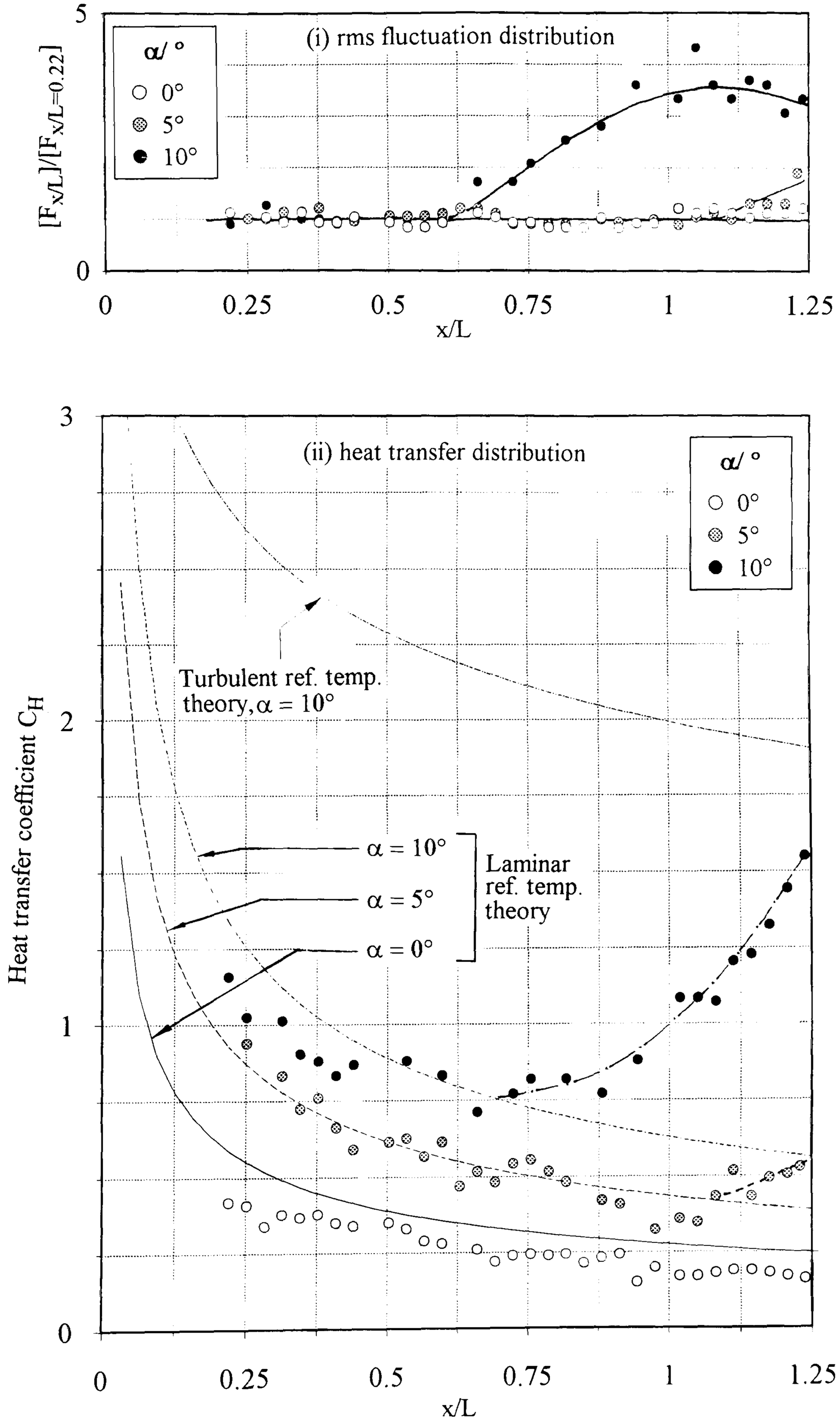

Figure 8-14 The effect of incidence on the heat transfer distribution over a flat plate ($M_\infty = 8.2$, $Re_\infty/cm = 9.0 \times 10^4$, L = 15.9 cm, Sharp LE)

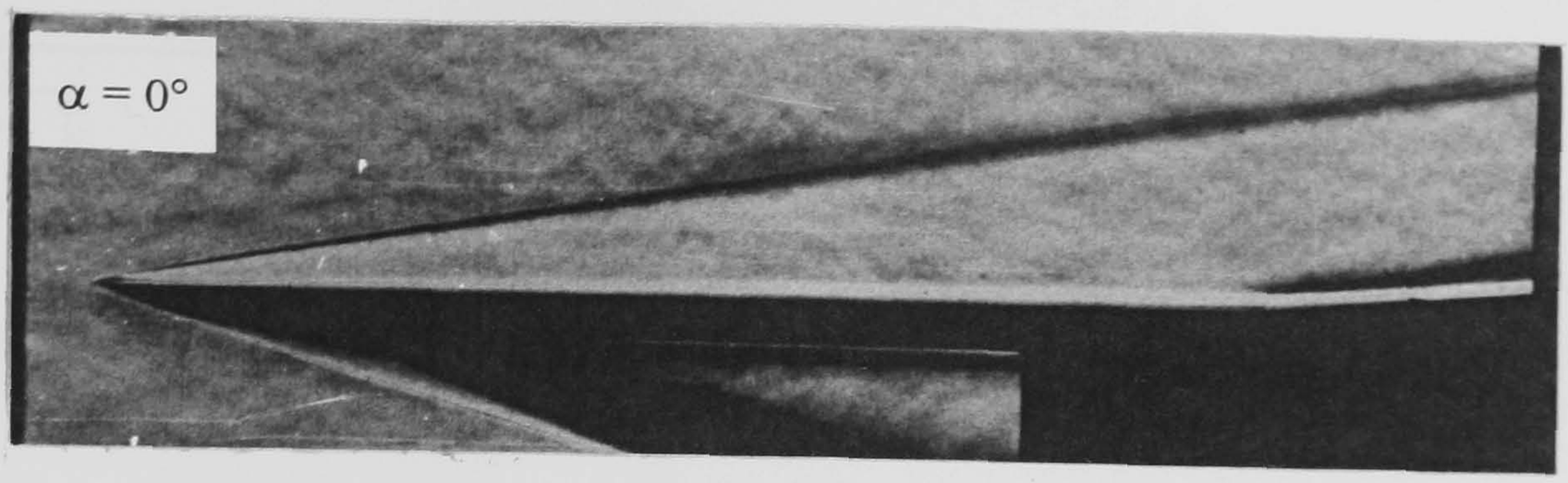

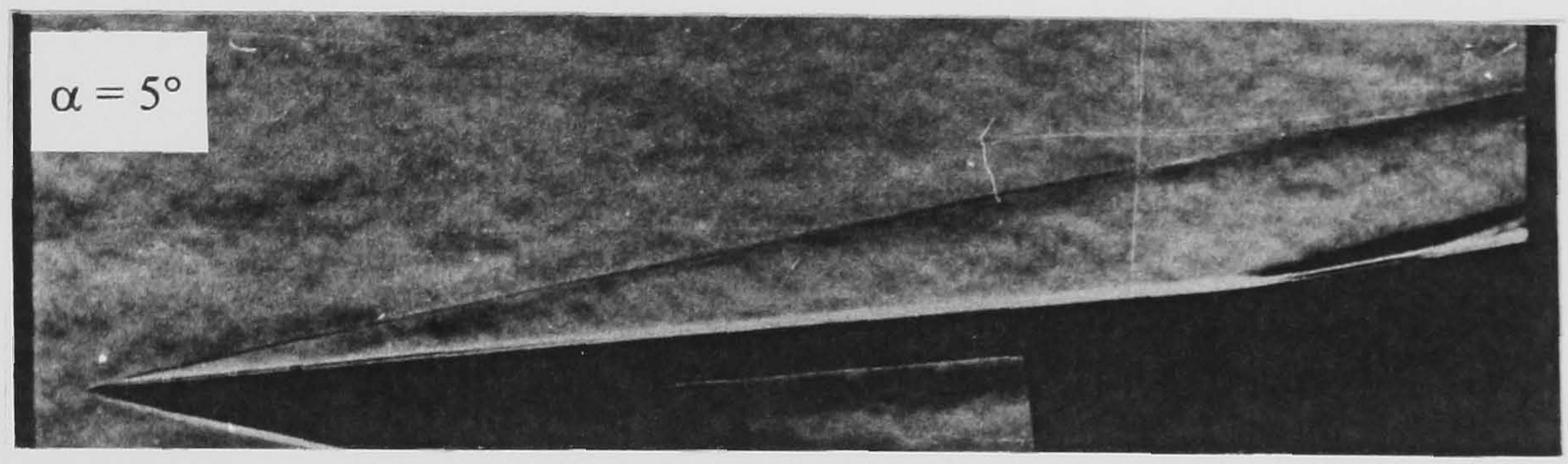

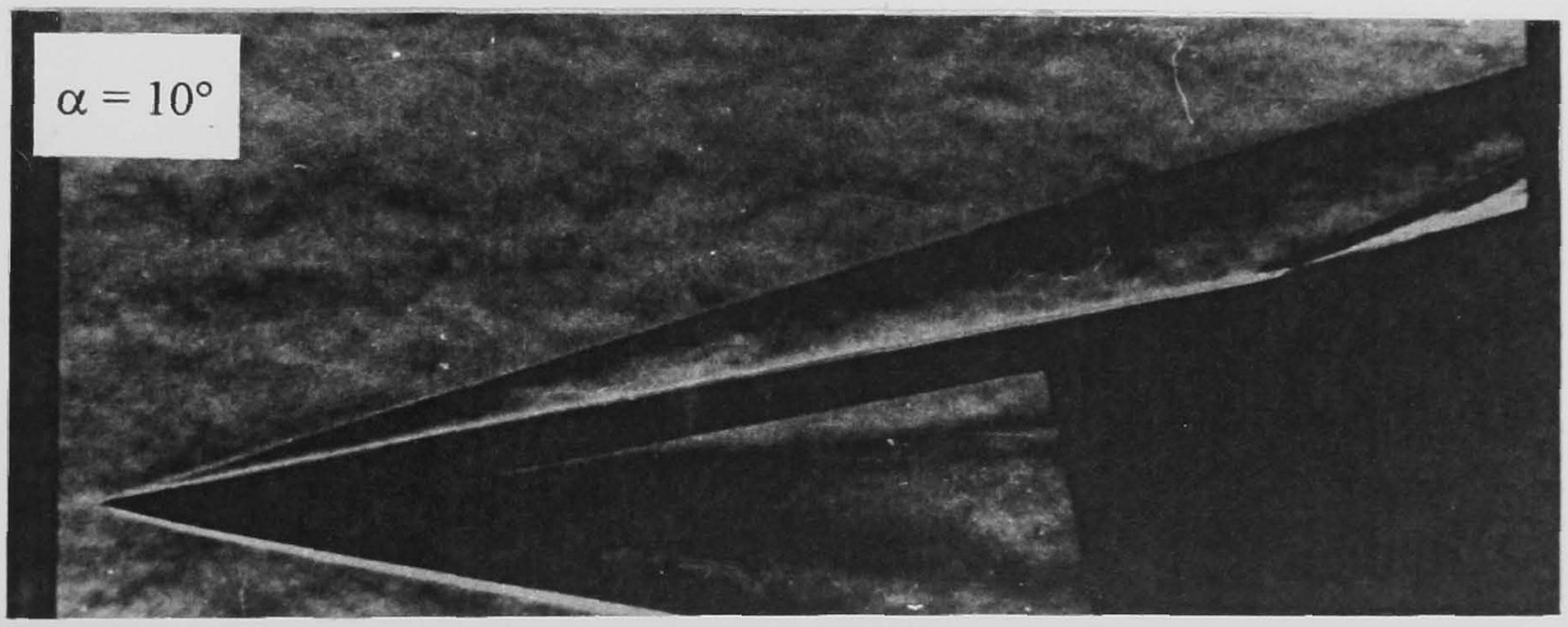

Figure 8-15 The effect of incidence on attached flows for sharp LE control flaps ($M_\infty = 8.2$, $Re_\infty/cm = 9.0 \times 10^4$, L 15.9 cm, $\beta = 5°$)

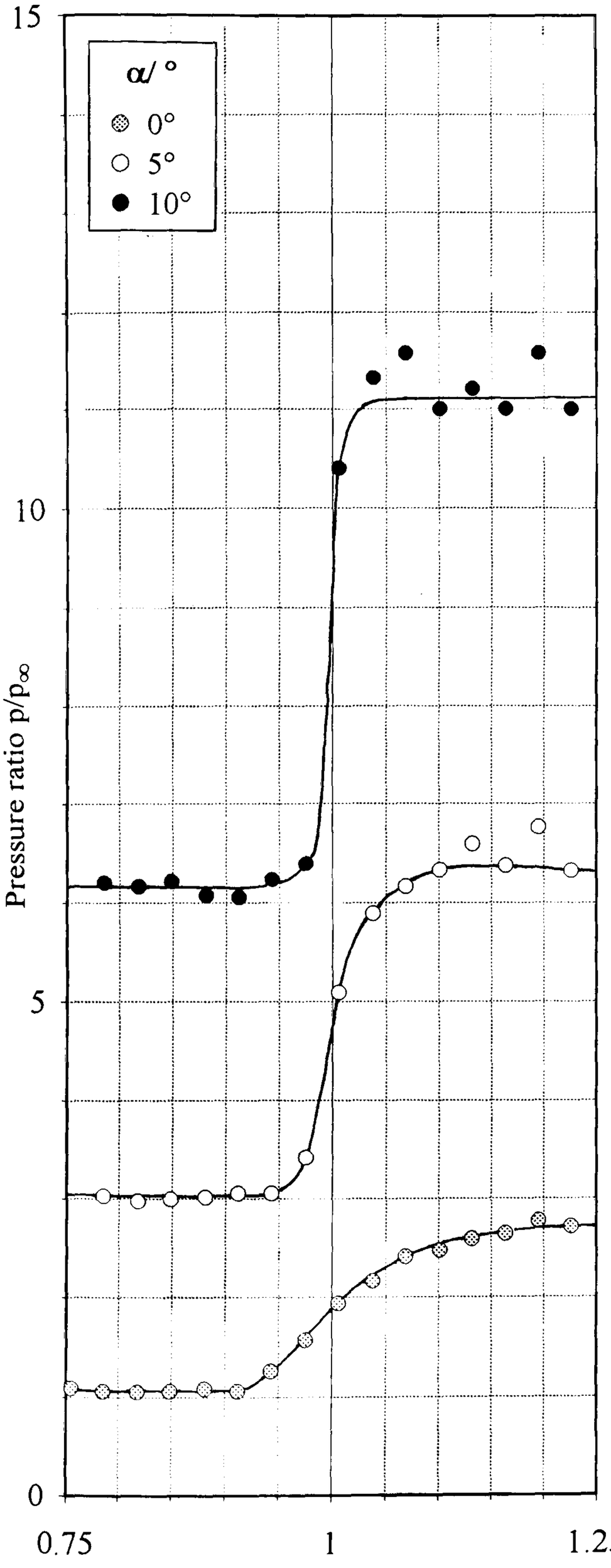

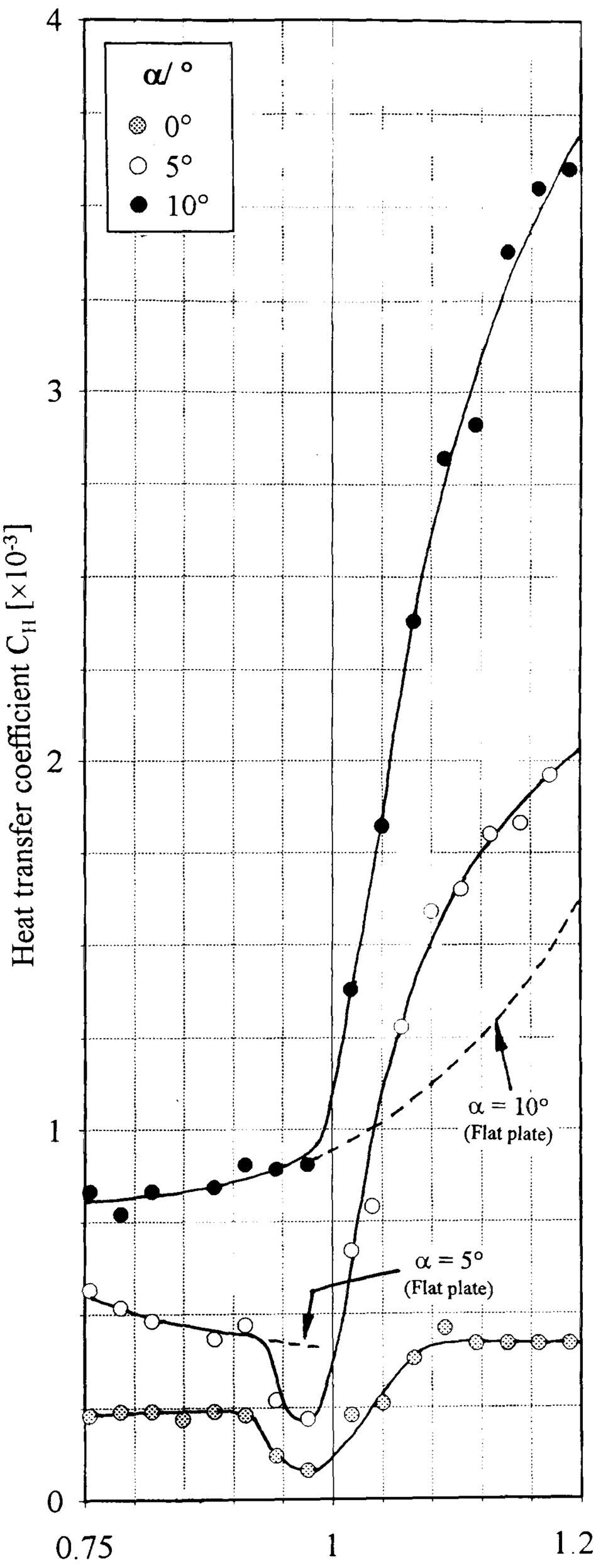

Figure 8-16 The effect of incidence on the pressure and heat transfer distribution in the interaction region of attached flows
($M_\infty = 8.2$, $Re_\infty/cm = 9.0 \times 10^4$, L = 15.9 cm, $\beta = 5°$, Sharp LE)

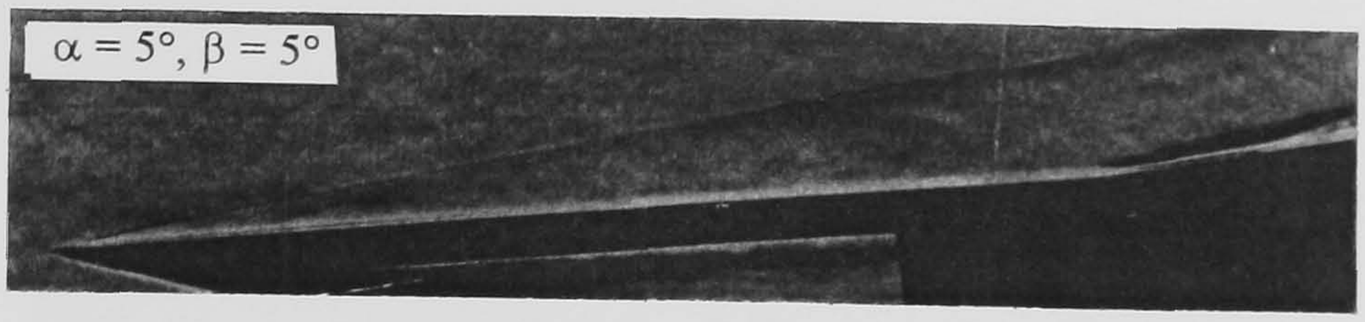

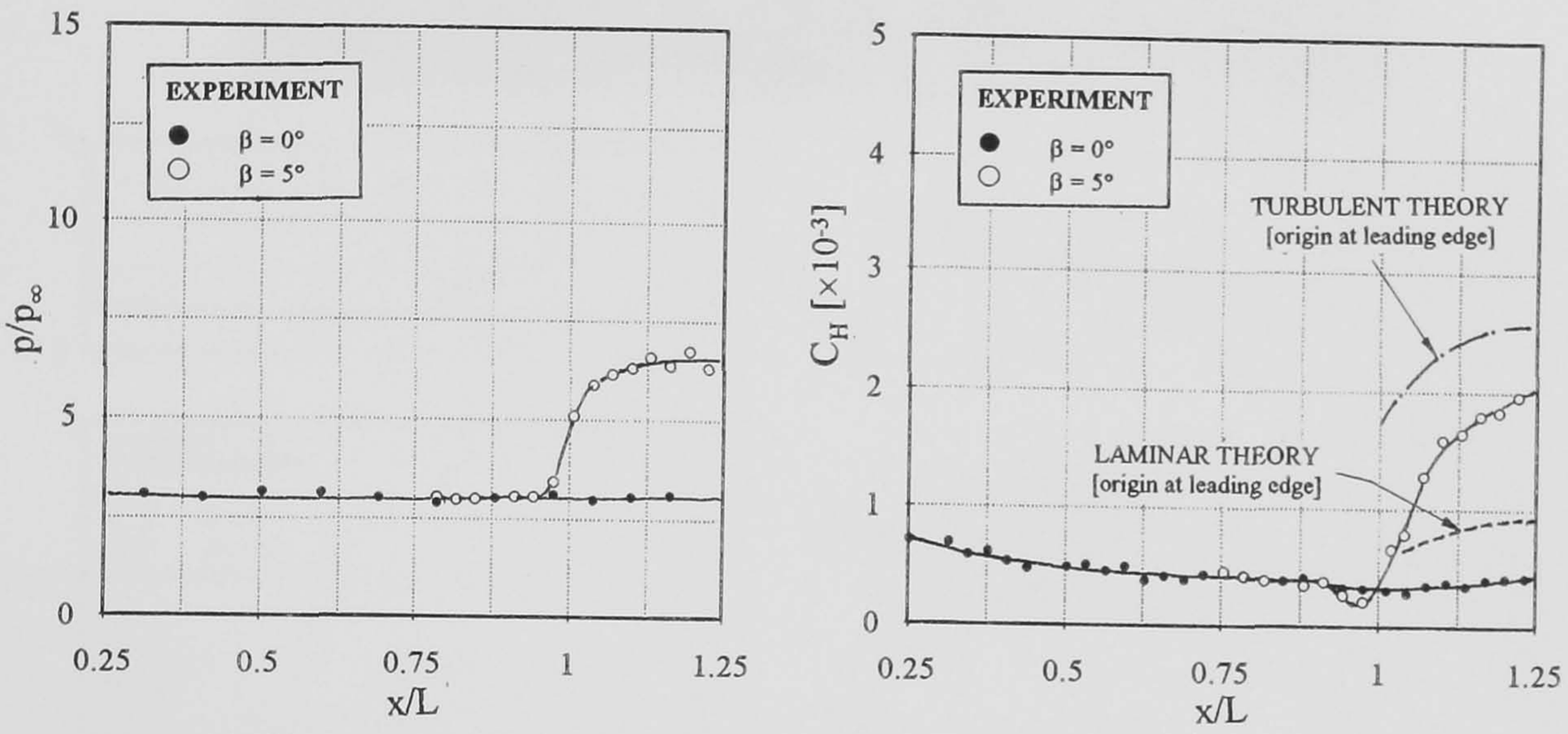

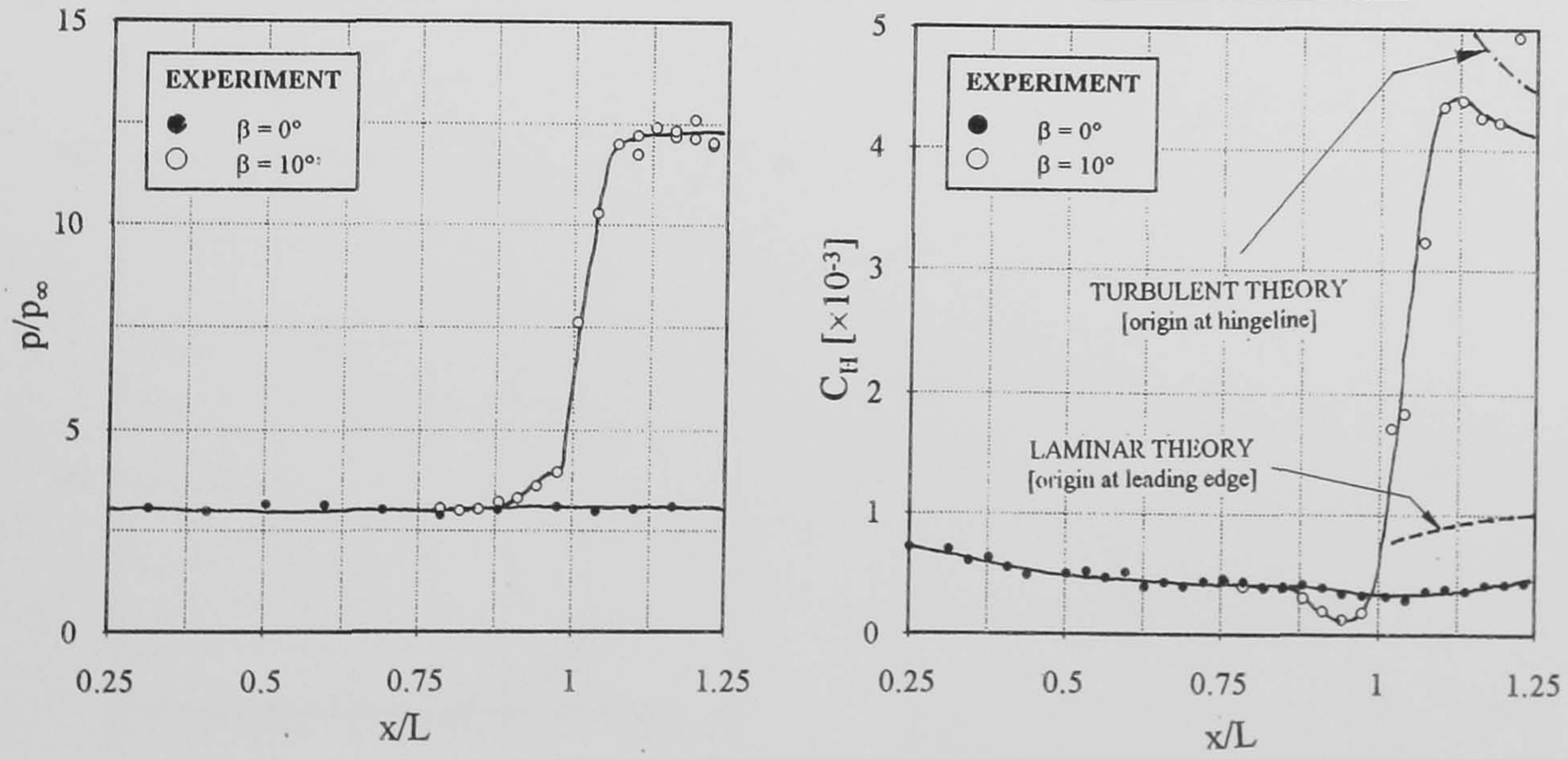

Figure 8-17 Pressure and heat transfer measurements on control flap configurations at incidence - $\alpha = 5°$
($M_\infty = 8.2$, $Re_\infty/cm = 9.0 \times 10^4$, $L = 15.9$ cm)

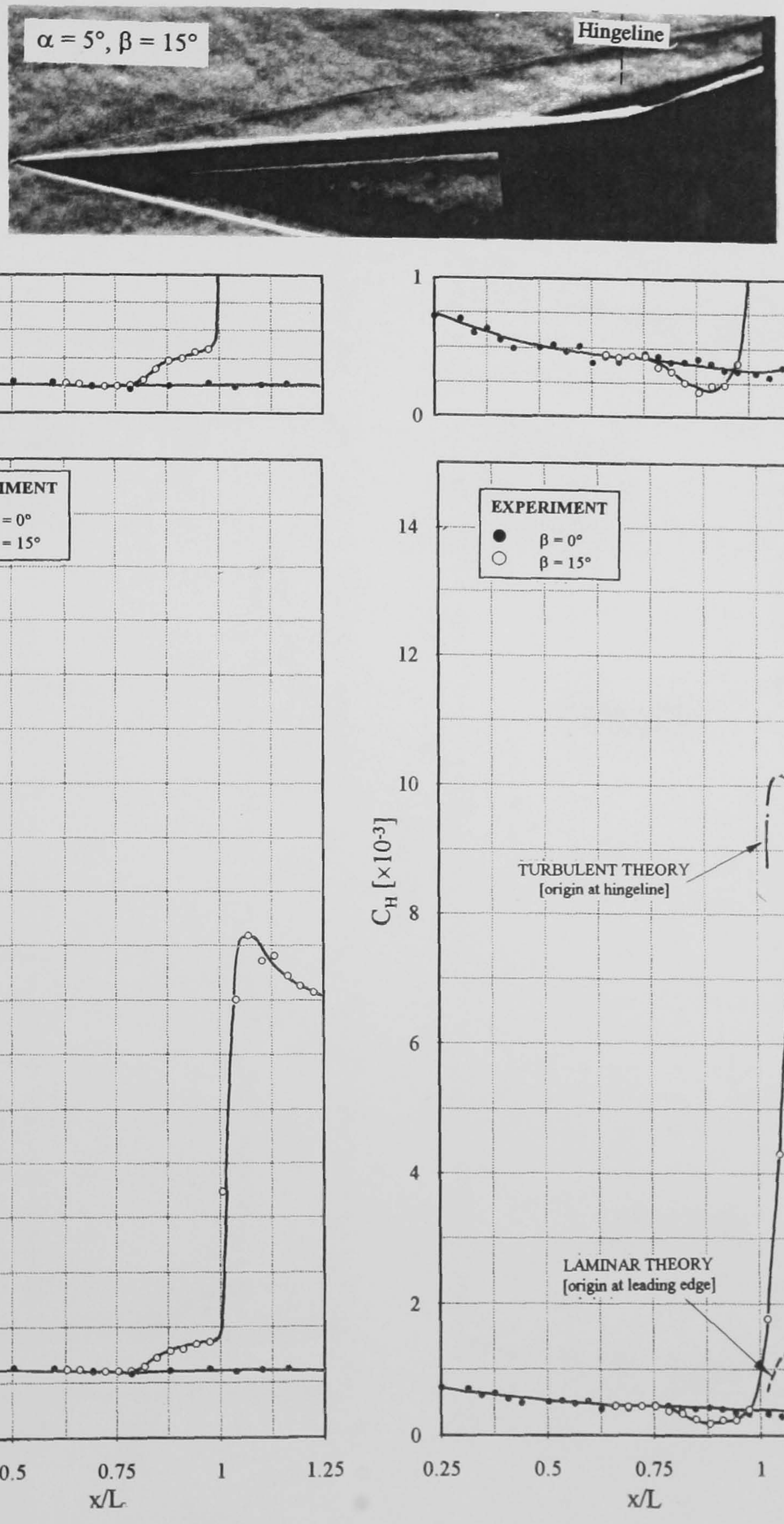

Figure 8-17 (cont'd) Pressure and heat transfer measurements on control flap configurations at incidence - $\alpha = 5°$
($M_\infty = 8.2$, $Re_\infty/cm = 9.0 \times 10^4$, $L = 15.9$ cm)

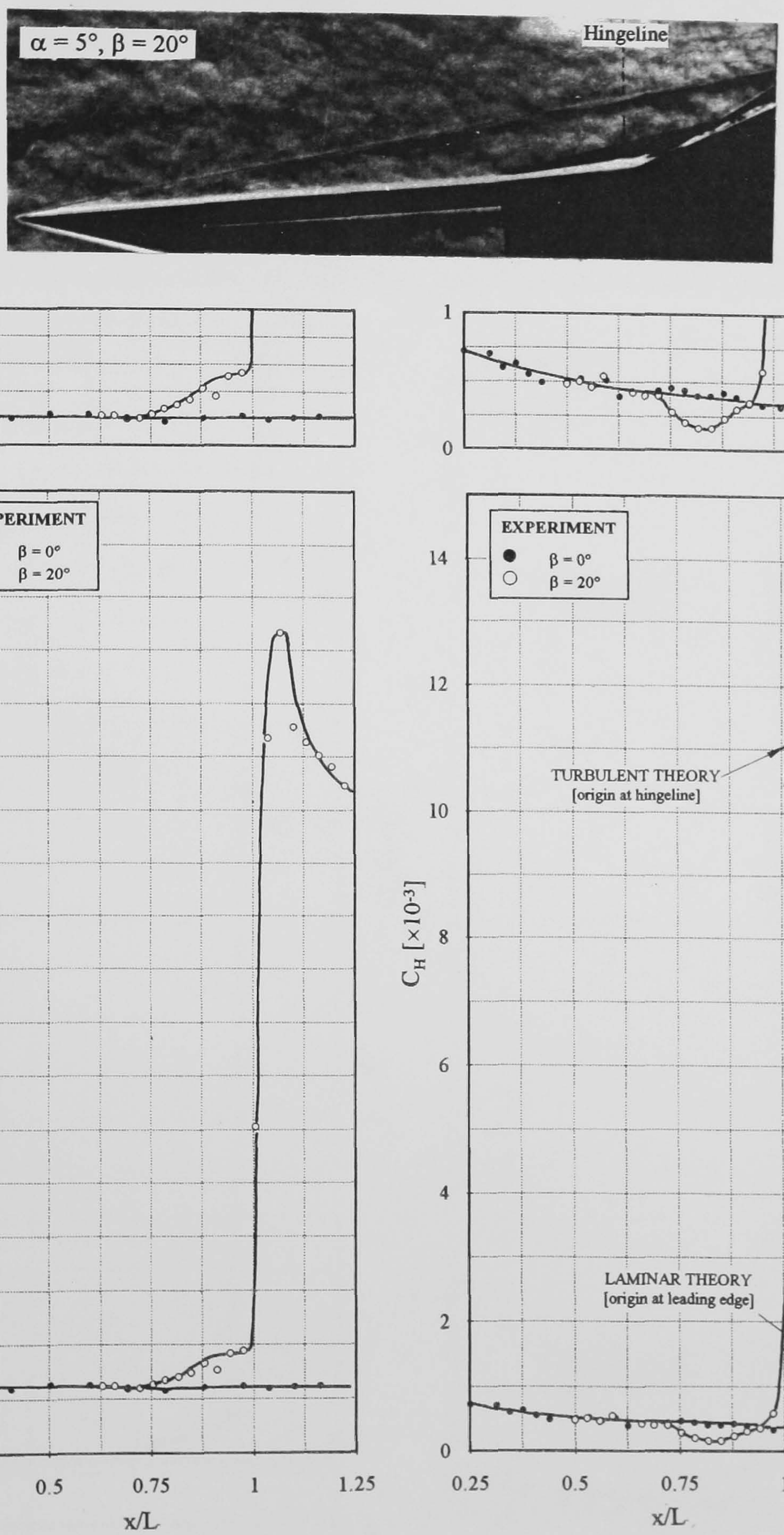

Figure 8-17 (cont'd) Pressure and heat transfer measurements on control flap configurations at incidence - $\alpha = 5°$
($M_\infty = 8.2$, $Re_\infty/cm = 9.0 \times 10^4$, $L = 15.9$ cm)

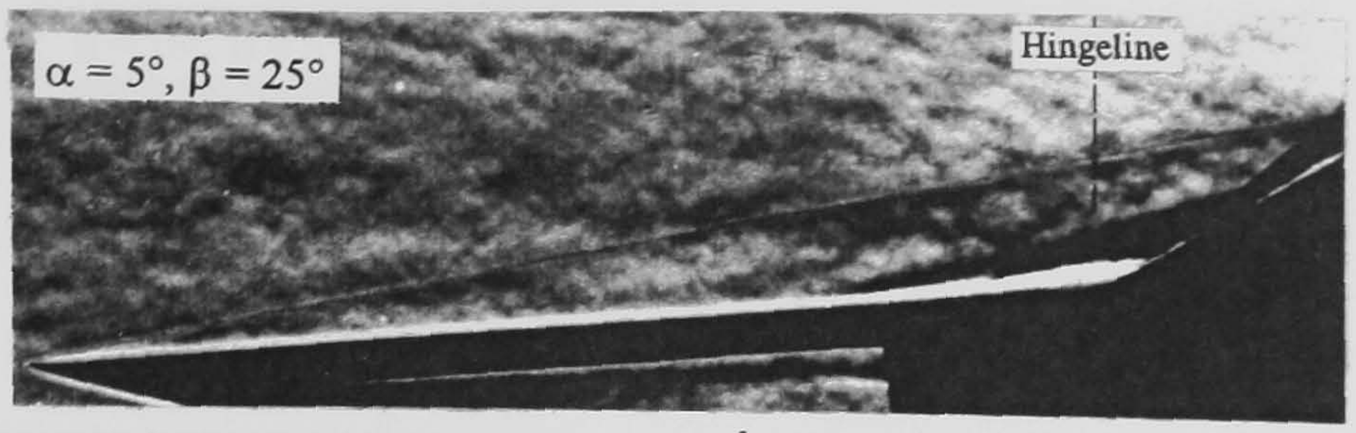

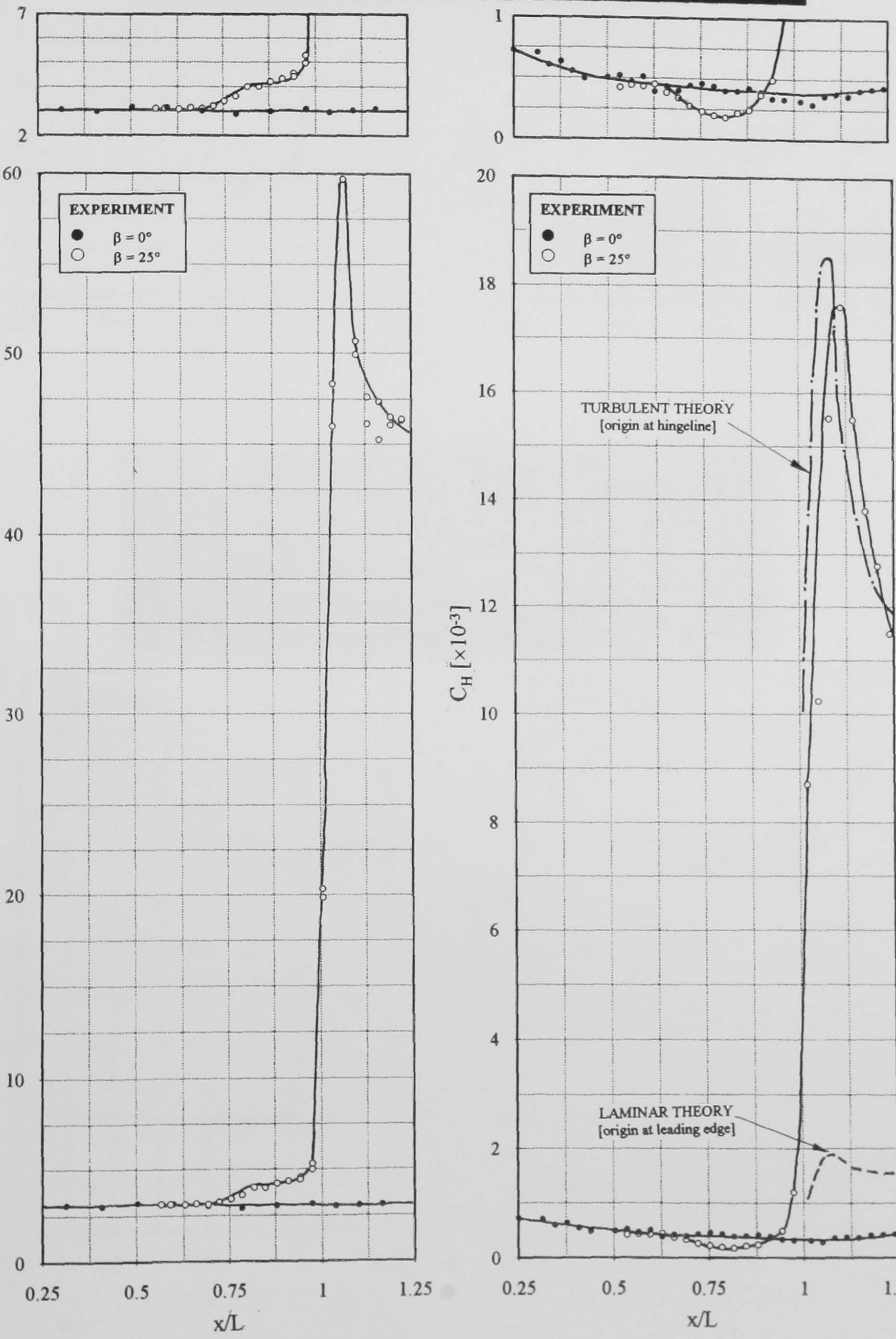

Figure 8-17 (cont'd) Pressure and heat transfer measurements on control flap configurations at incidence - $\alpha = 5°$
($M_\infty = 8.2$, $Re_\infty/cm = 9.0 \times 10^4$, L = 15.9 cm)

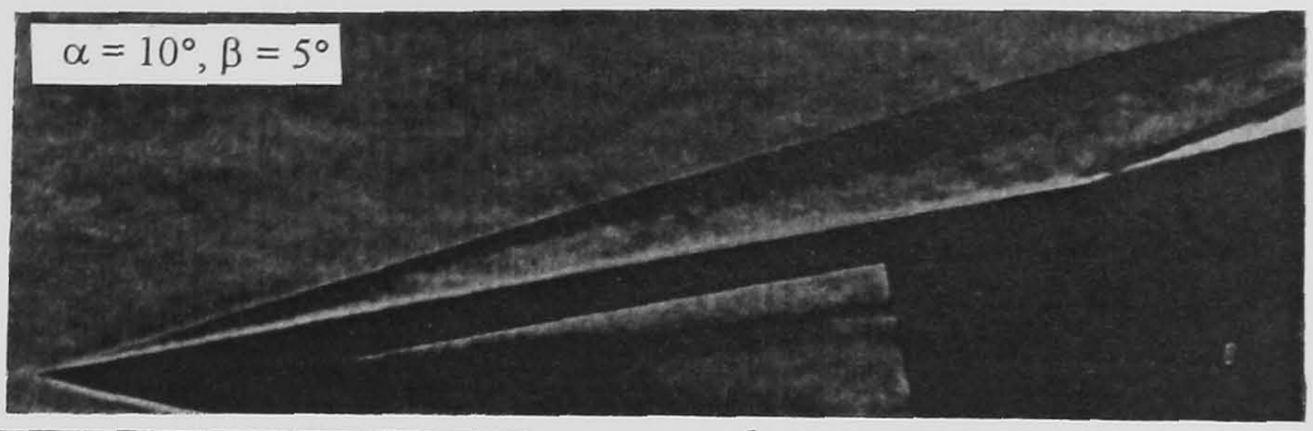

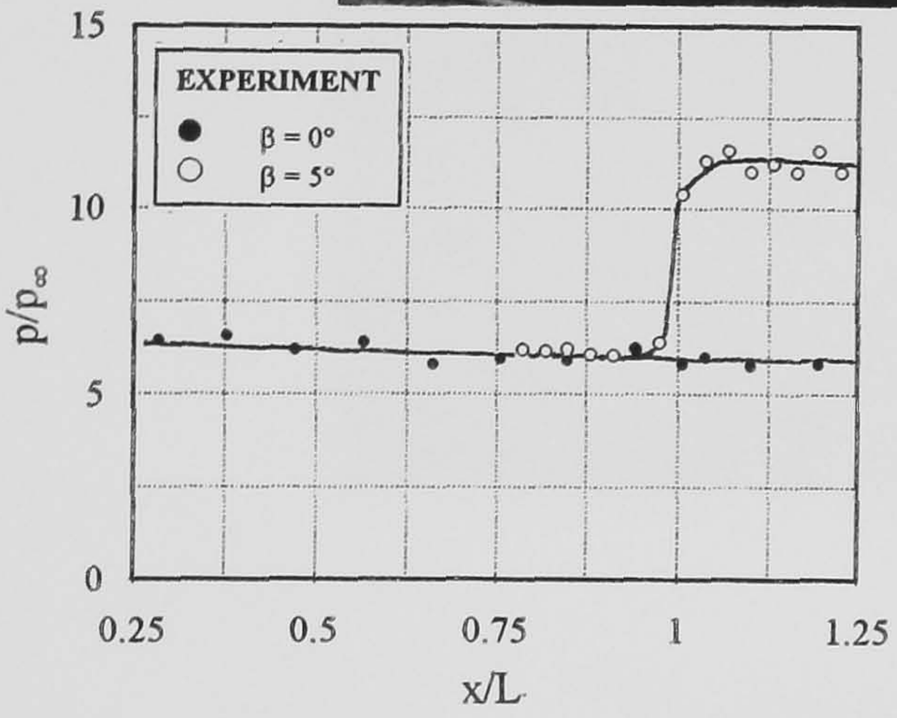

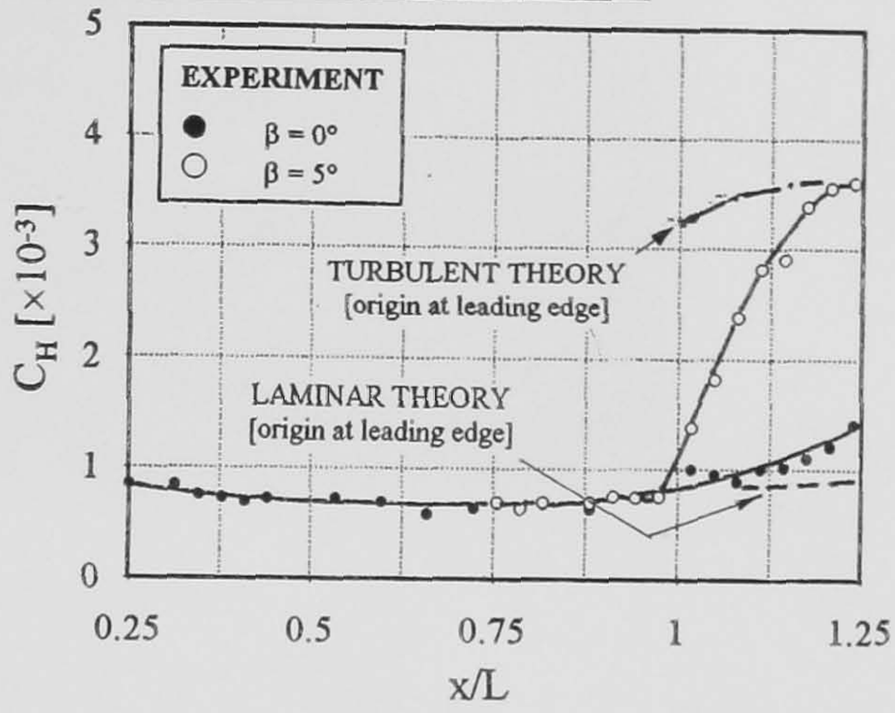

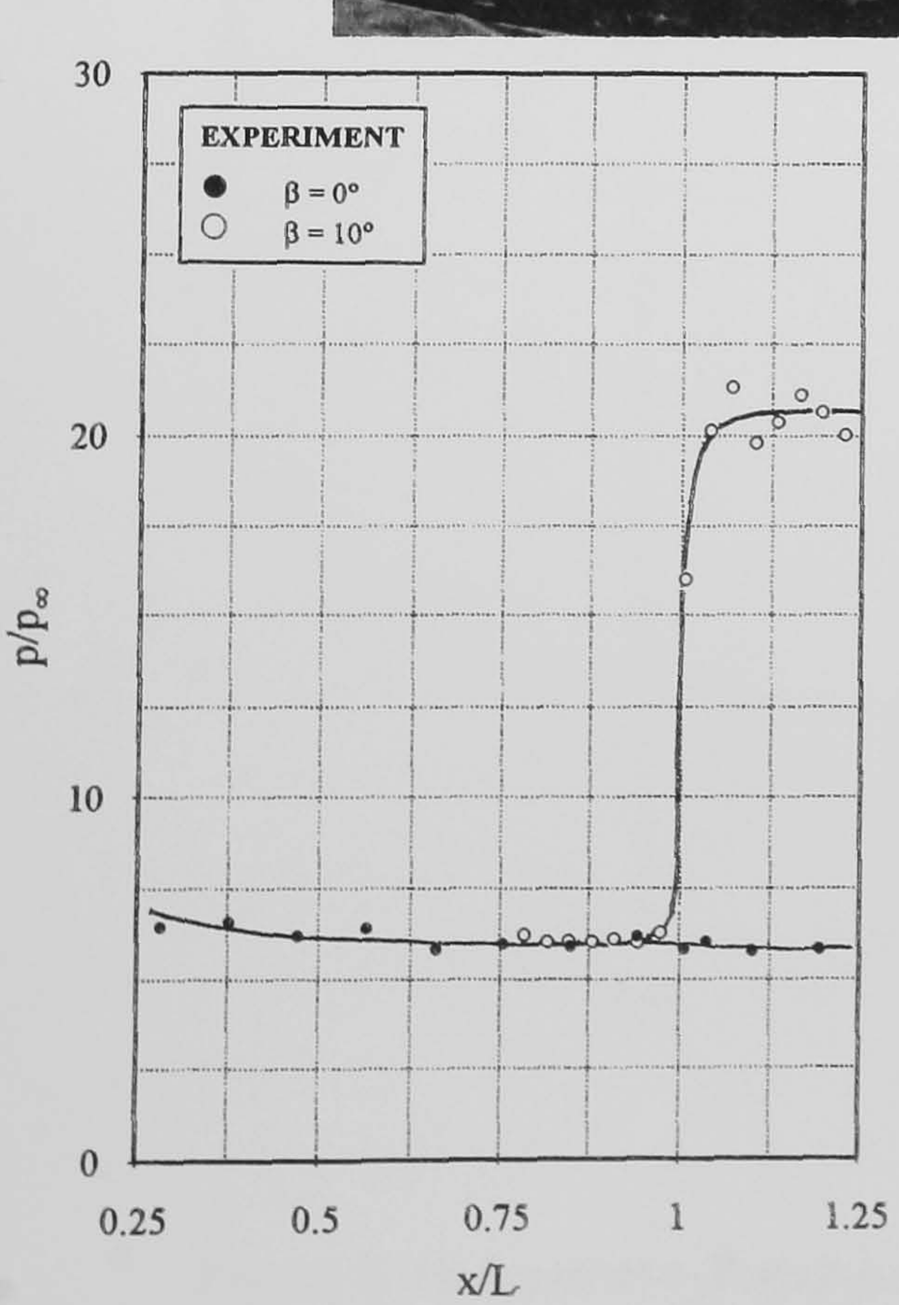

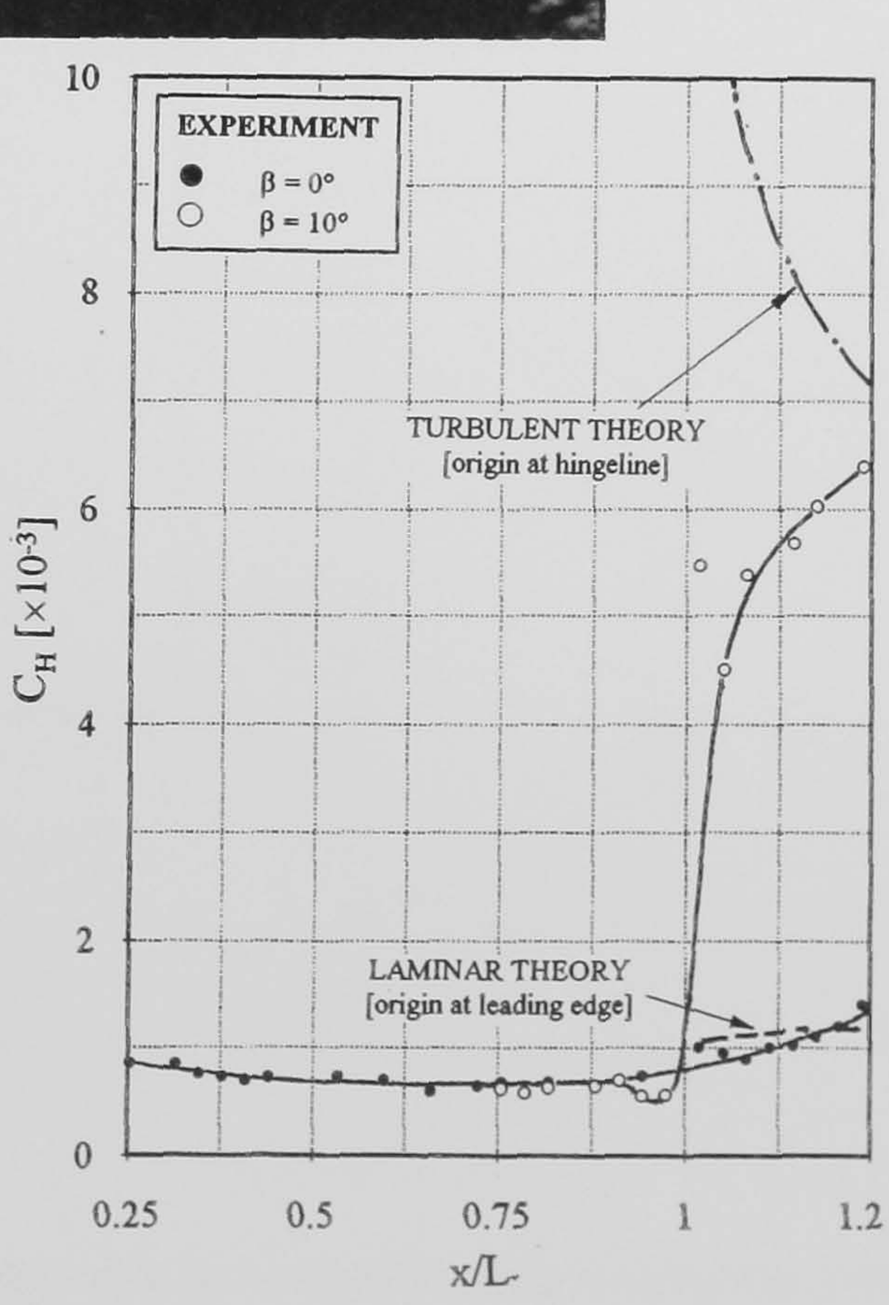

Figure 8-18 Pressure and heat transfer measurements on control flap configurations at incidence - $\alpha = 10°$
($M_\infty = 8.2$, $Re_\infty/cm = 9.0 \times 10^4$, L = 15.9 cm)

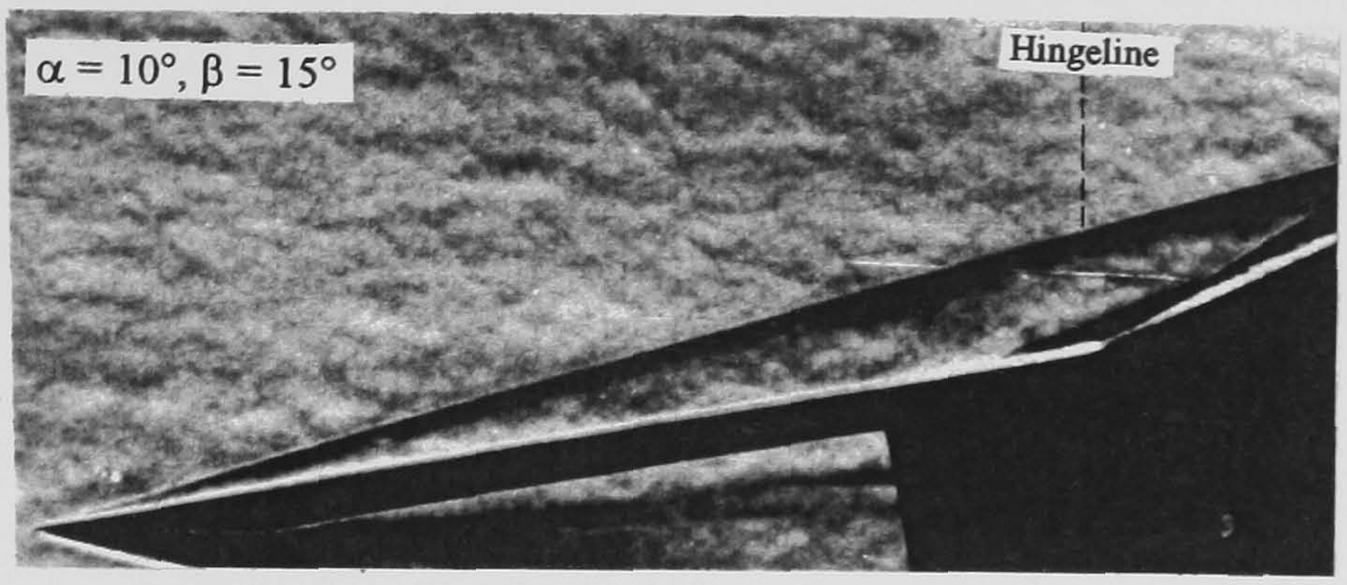

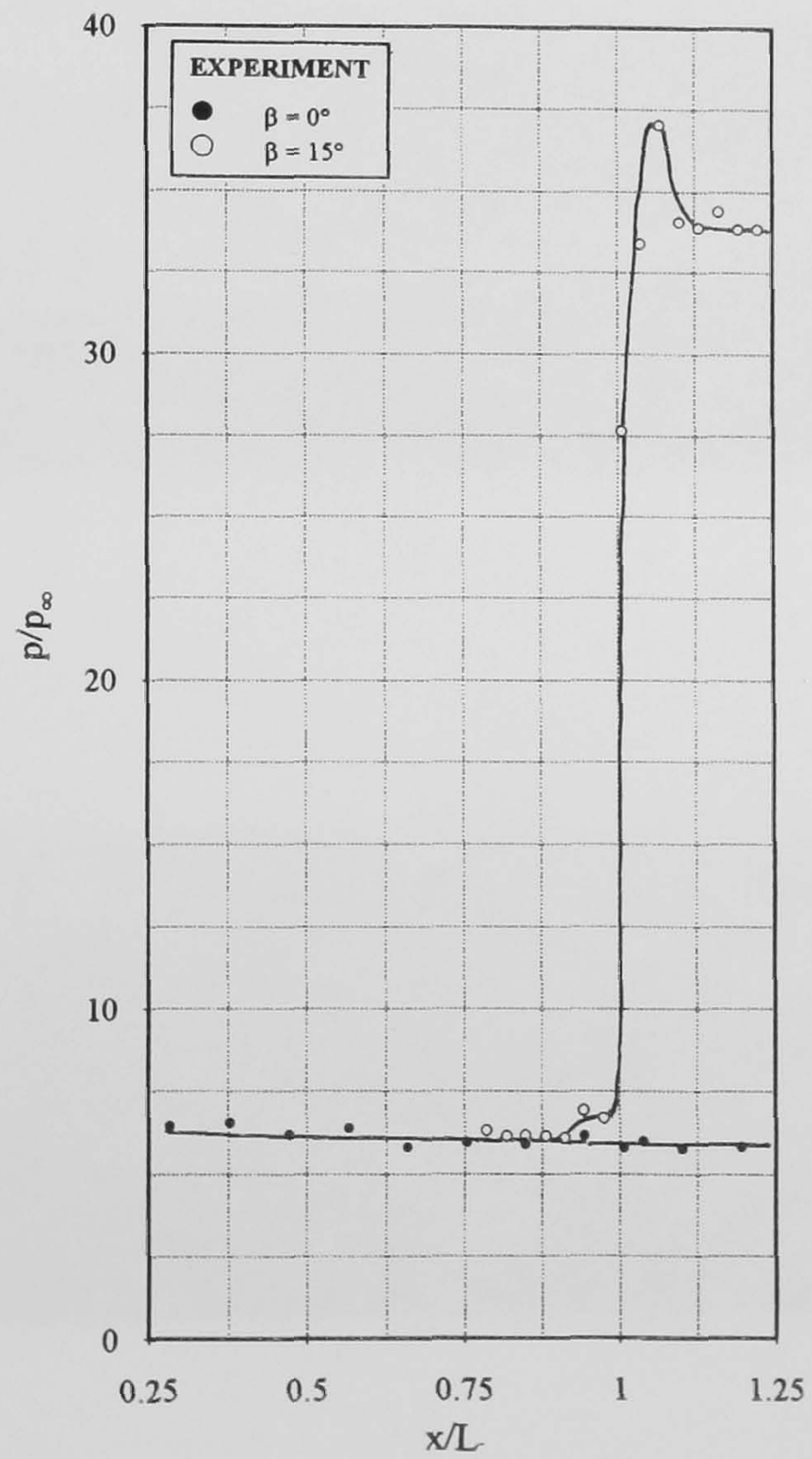

Figure 8-18 (cont'd) Pressure measurements on control flap configurations at incidence - $\alpha = 10°$
($M_\infty = 8.2$, $Re_\infty/cm = 9.0 \times 10^4$, L = 15.9 cm)

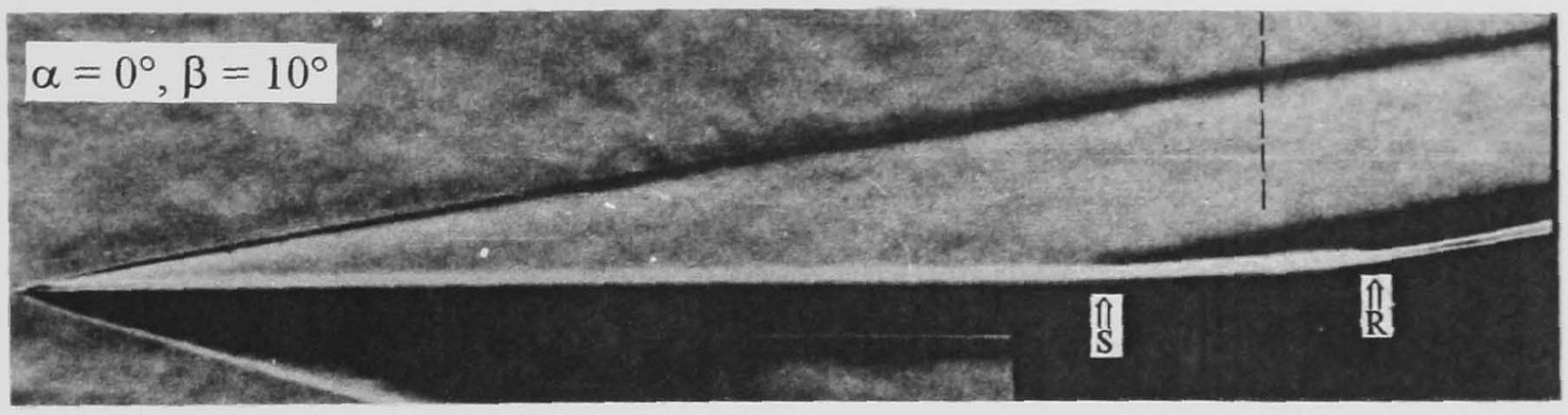

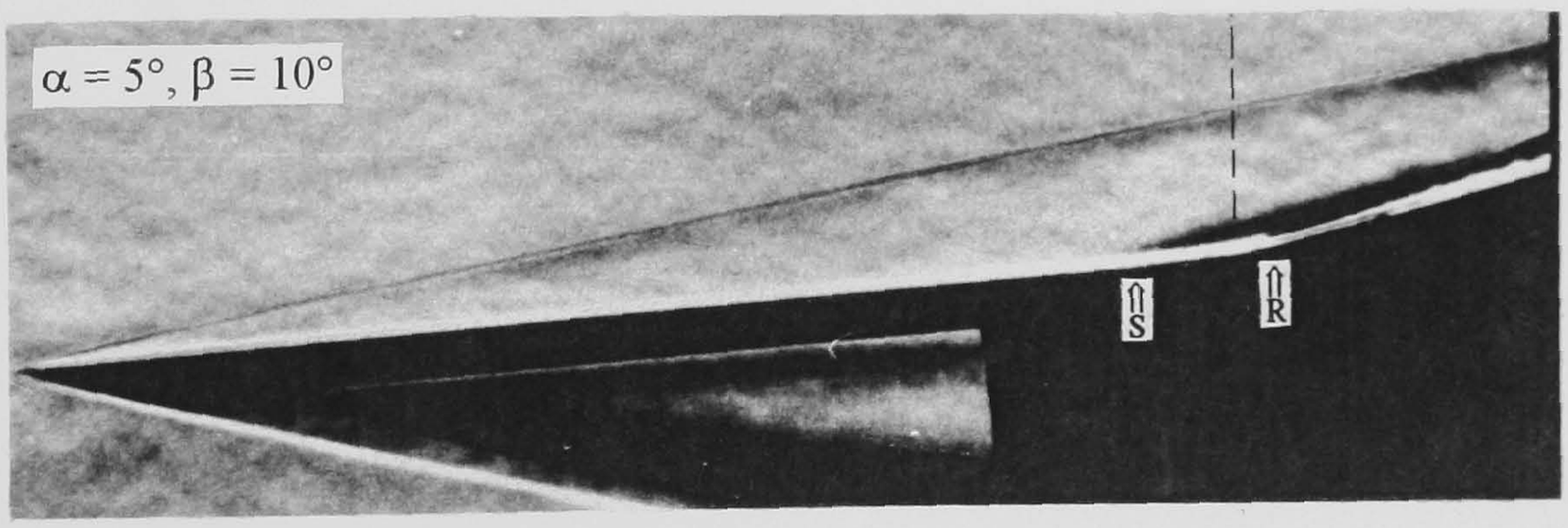

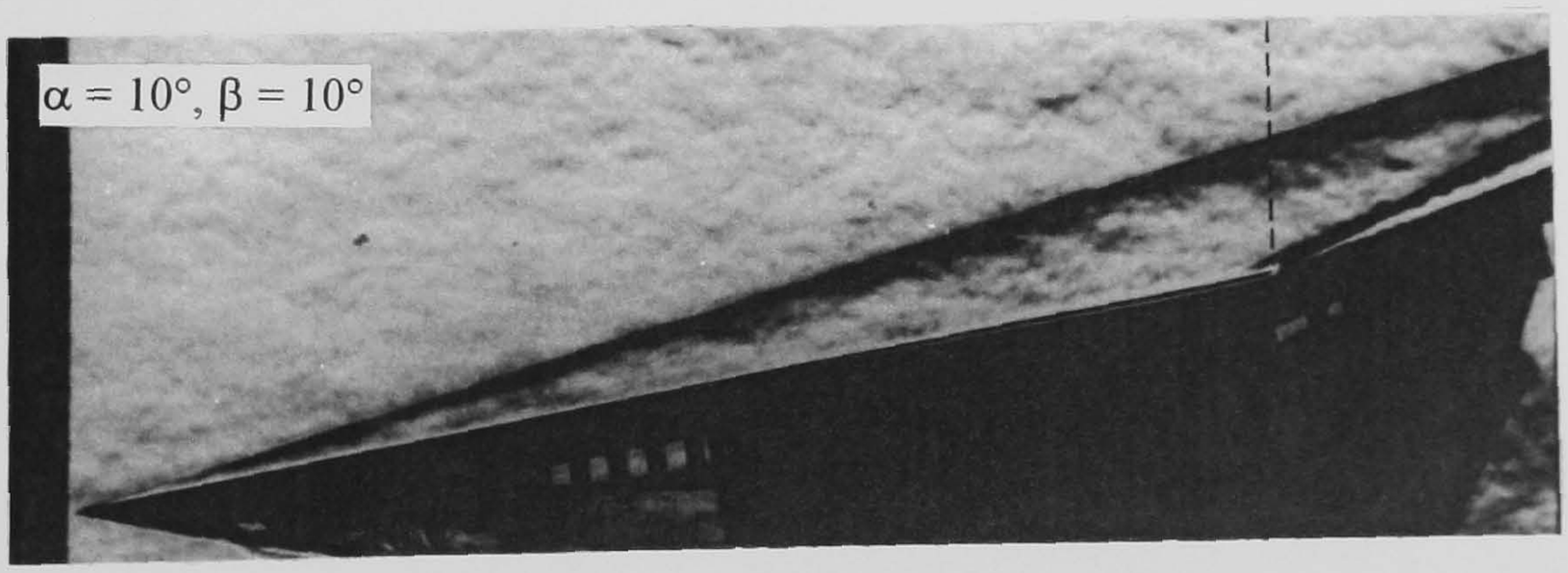

Figure 8-19 The effect of incidence on moderately separated flows ($M_\infty = 8.2$, $Re_\infty/cm = 9.0 \times 10^4$, L = 15.9 cm, Sharp LE)

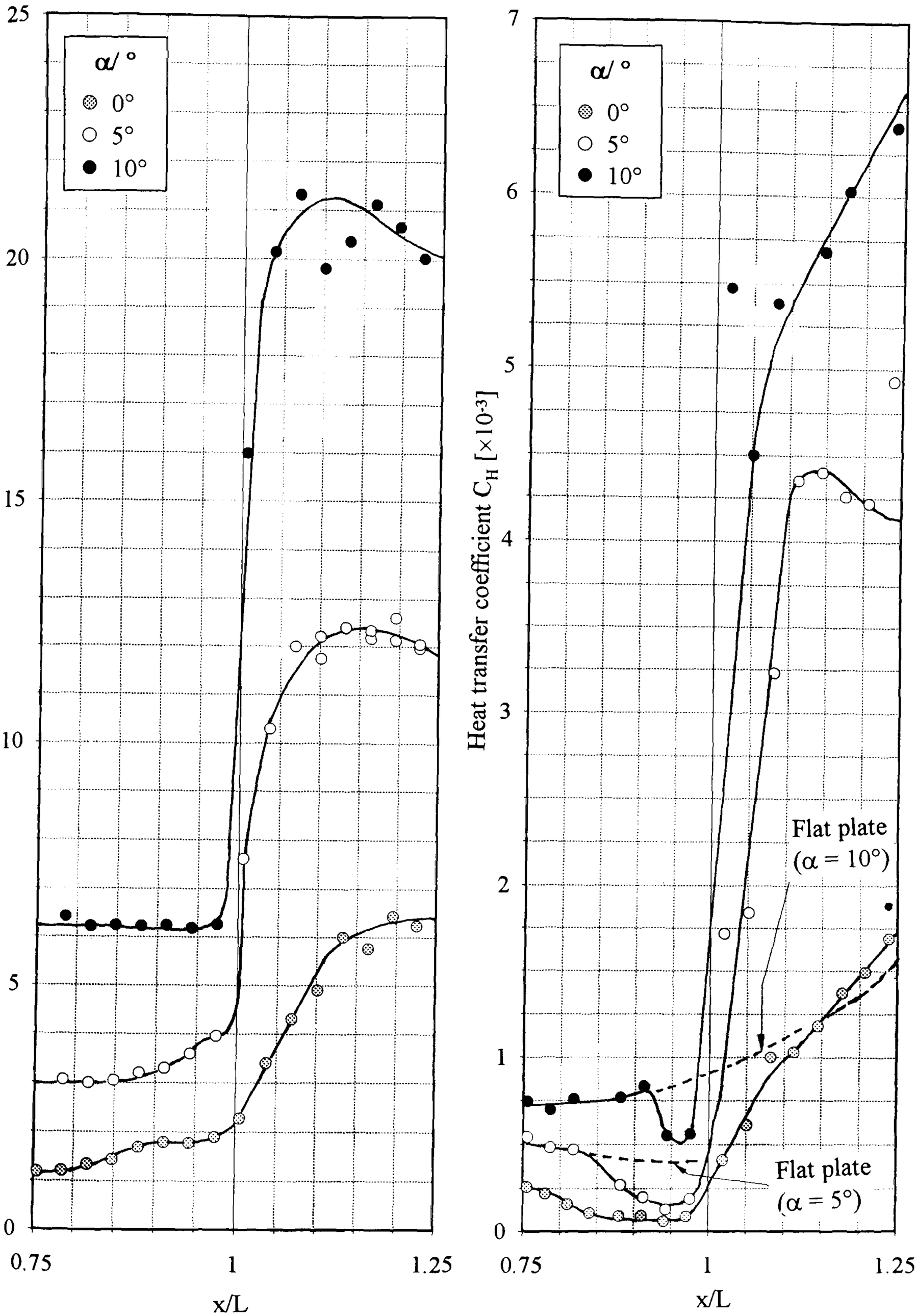

Figure 8-20 The effect of incidence on the pressure and heat transfer distribution in separated interaction regions
(M_∞ = 8.2, Re_∞/cm = 9.0 × 10^4, L = 15.9 cm, β = 10°, Sharp LE)

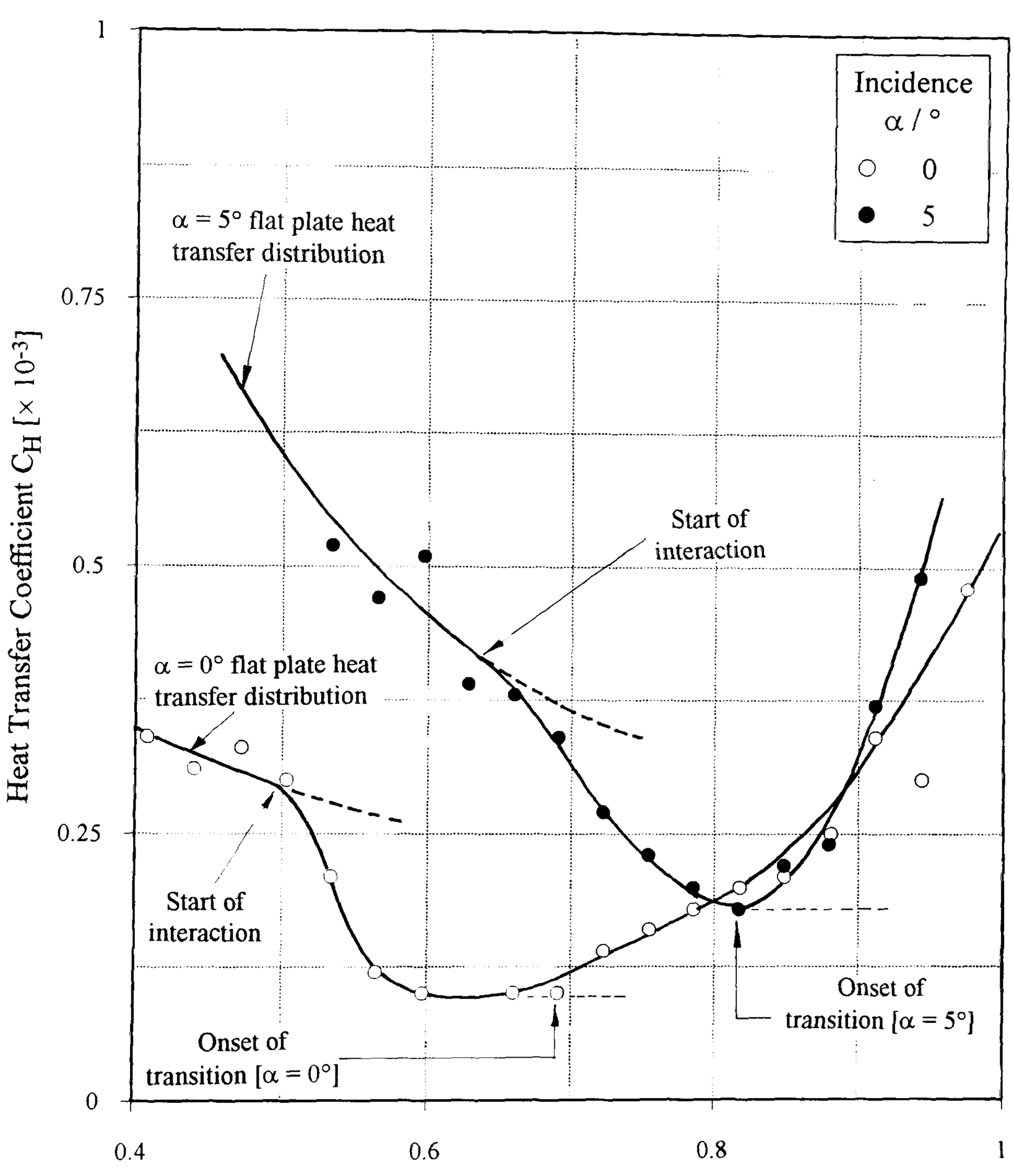

Figure 8-21 The effect of incidence on shear layer transition in well-separated flows ($M_\infty = 8.2$, $Re_\infty/cm = 9.0 \times 10^4$, $\beta = 25°$, $L = 15.9$ cm)

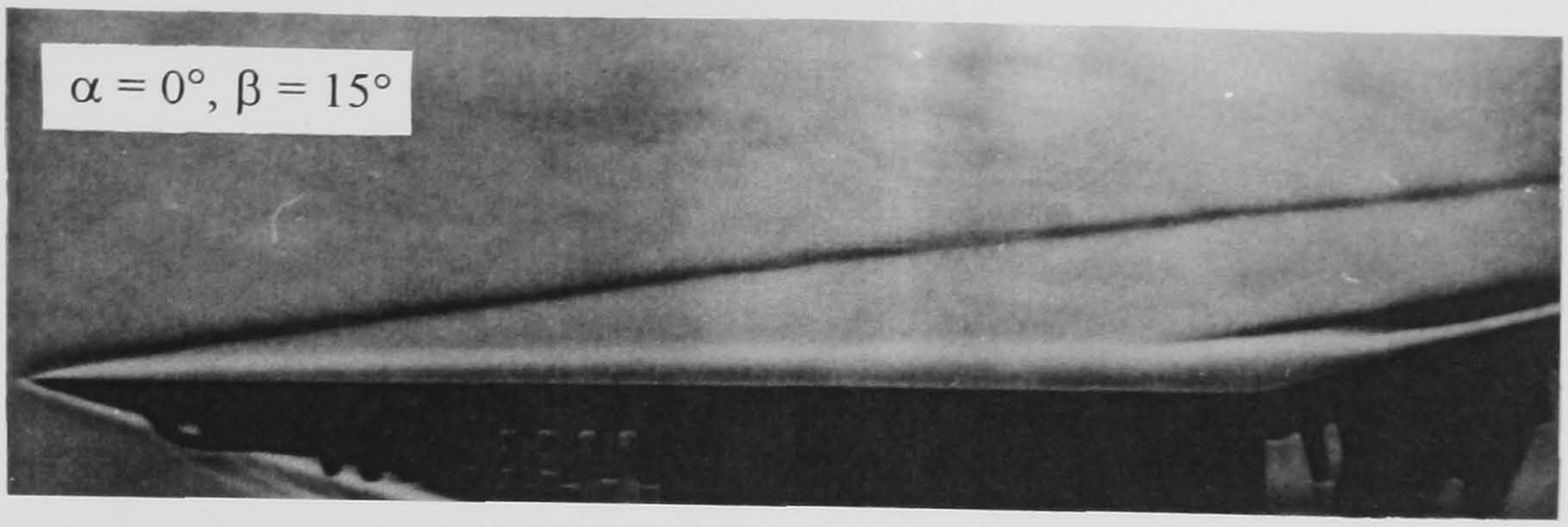

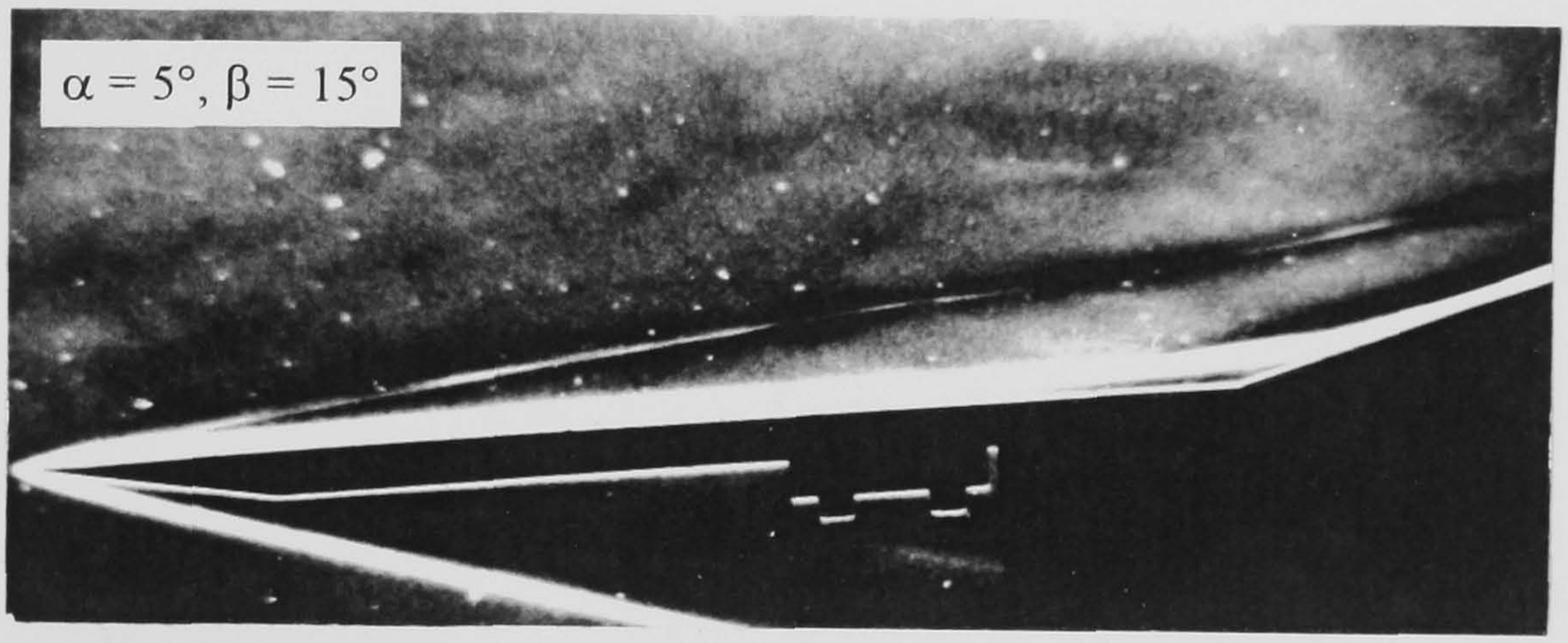

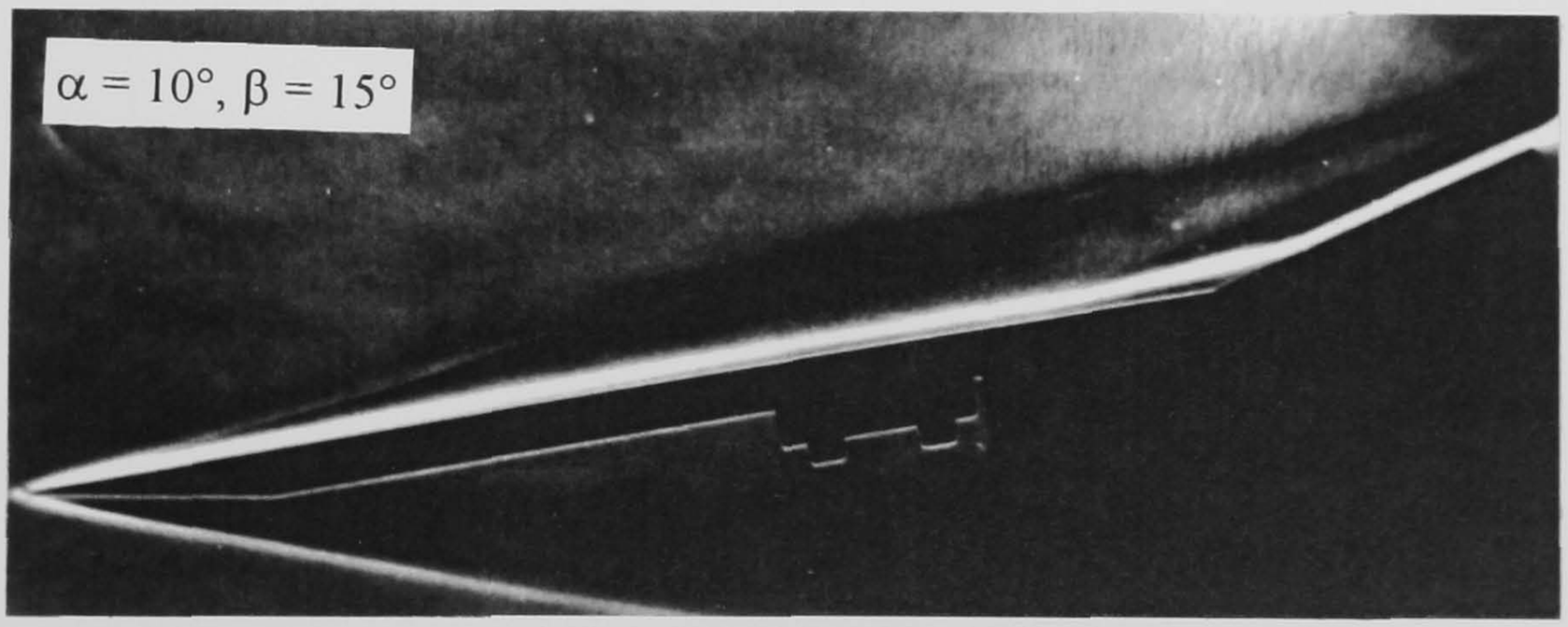

Figure 8-22 The effect of incidence on separation of a laminar boundary layer ($M_\infty = 12.3$, $Re_\infty/cm = 3.3 \times 10^4$, L 15.9 cm, $\beta = 15°$, Sharp LE)

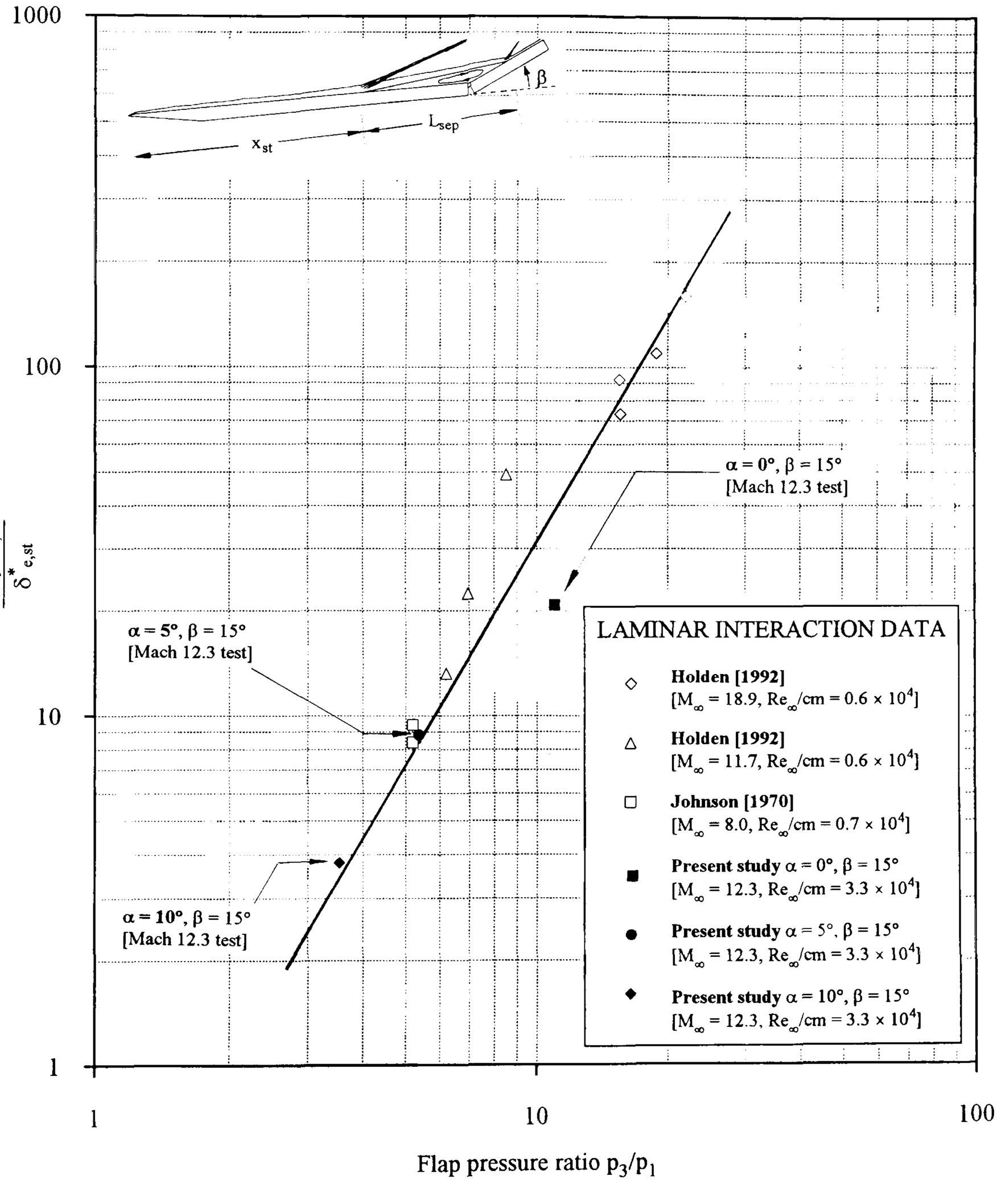

Figure 8-23 The effect of incidence on the length of separated flow for laminar interactions

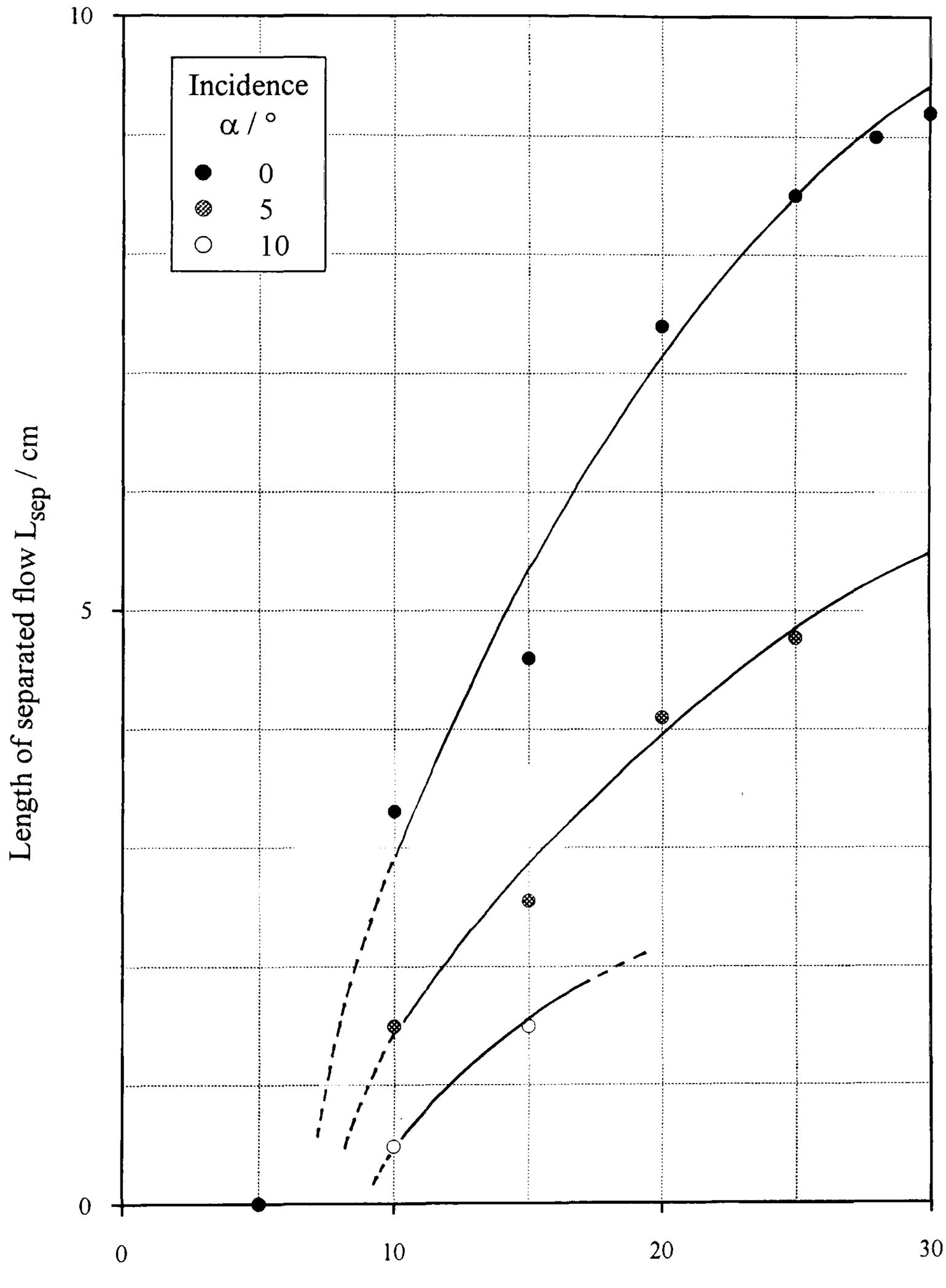

Figure 8-24 The effect of incidence on the length of separated flow (for sharp LE configurations) ($M_\infty = 8.2$, $Re_\infty/cm = 9.0 \times 10^4$)

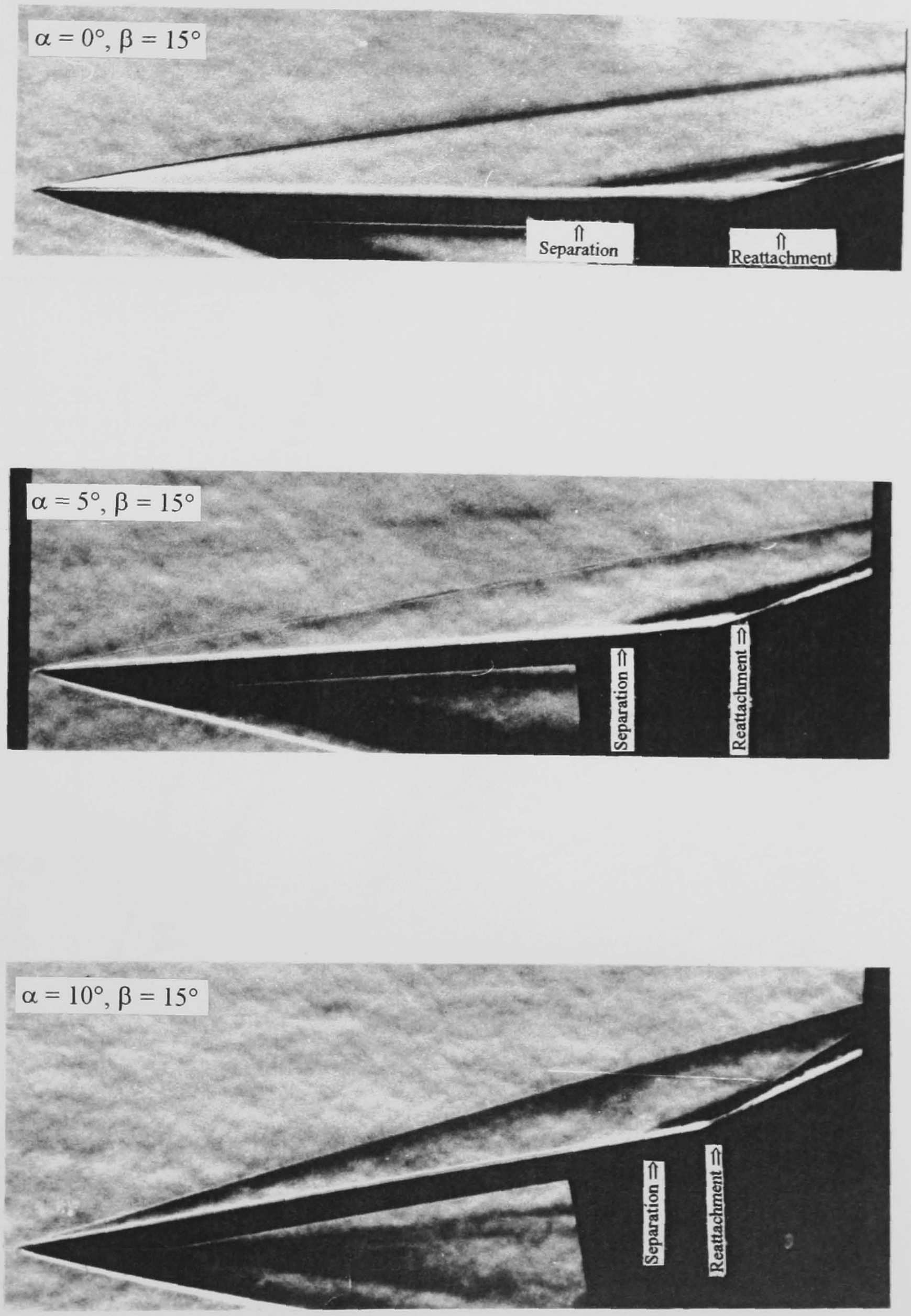

Figure 8-25 The effect of incidence on separation - for well separated flows ($M_\infty = 8.2$, $Re_\infty/cm = 9.0 \times 10^4$, L = 15.9 cm, Sharp LE)

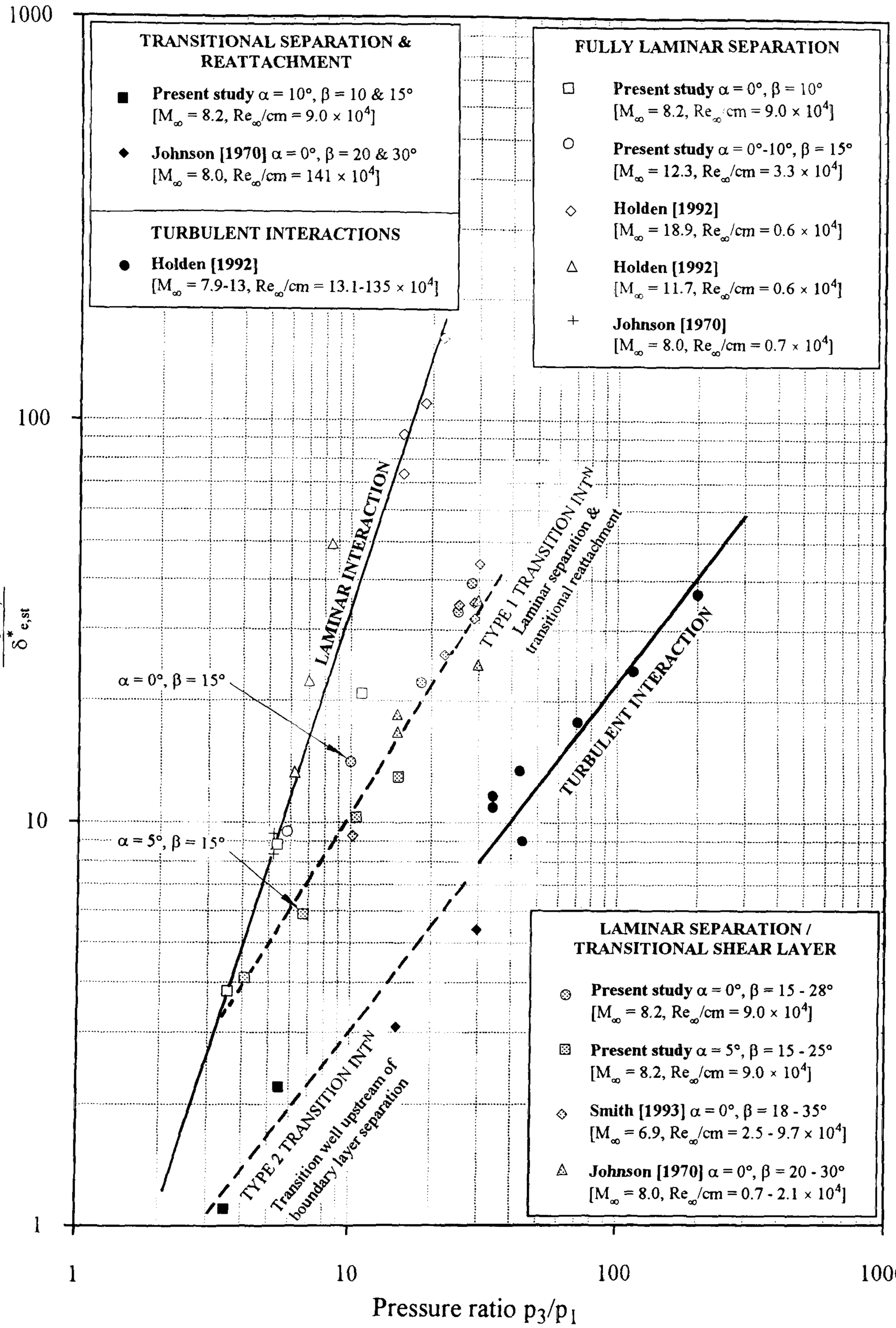

Figure 8-26 Separated flow length correlation for laminar, transitional and turbulent flows (including the effects of configuration incidence)

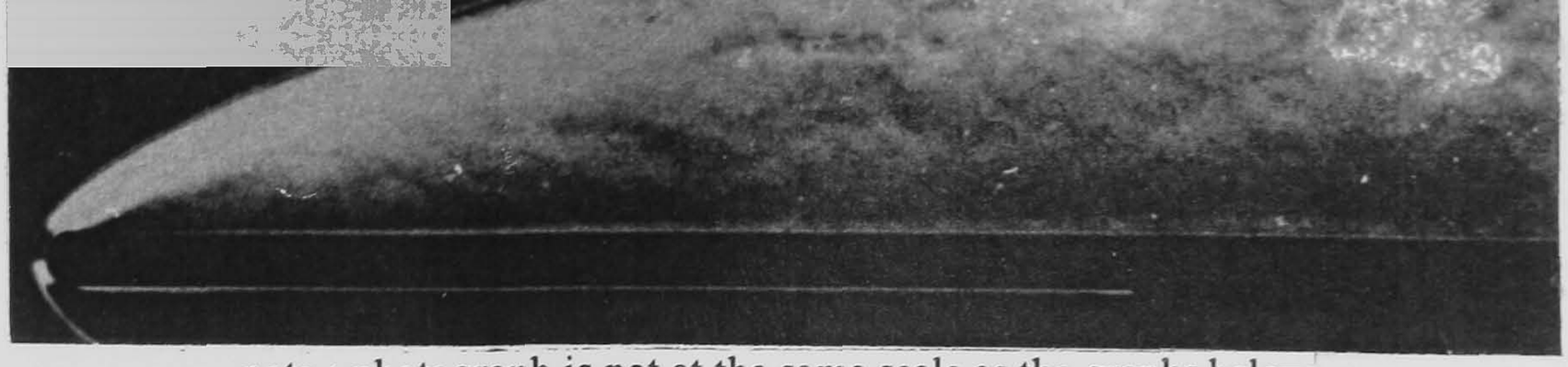

note : photograph is not at the same scale as the graphs below

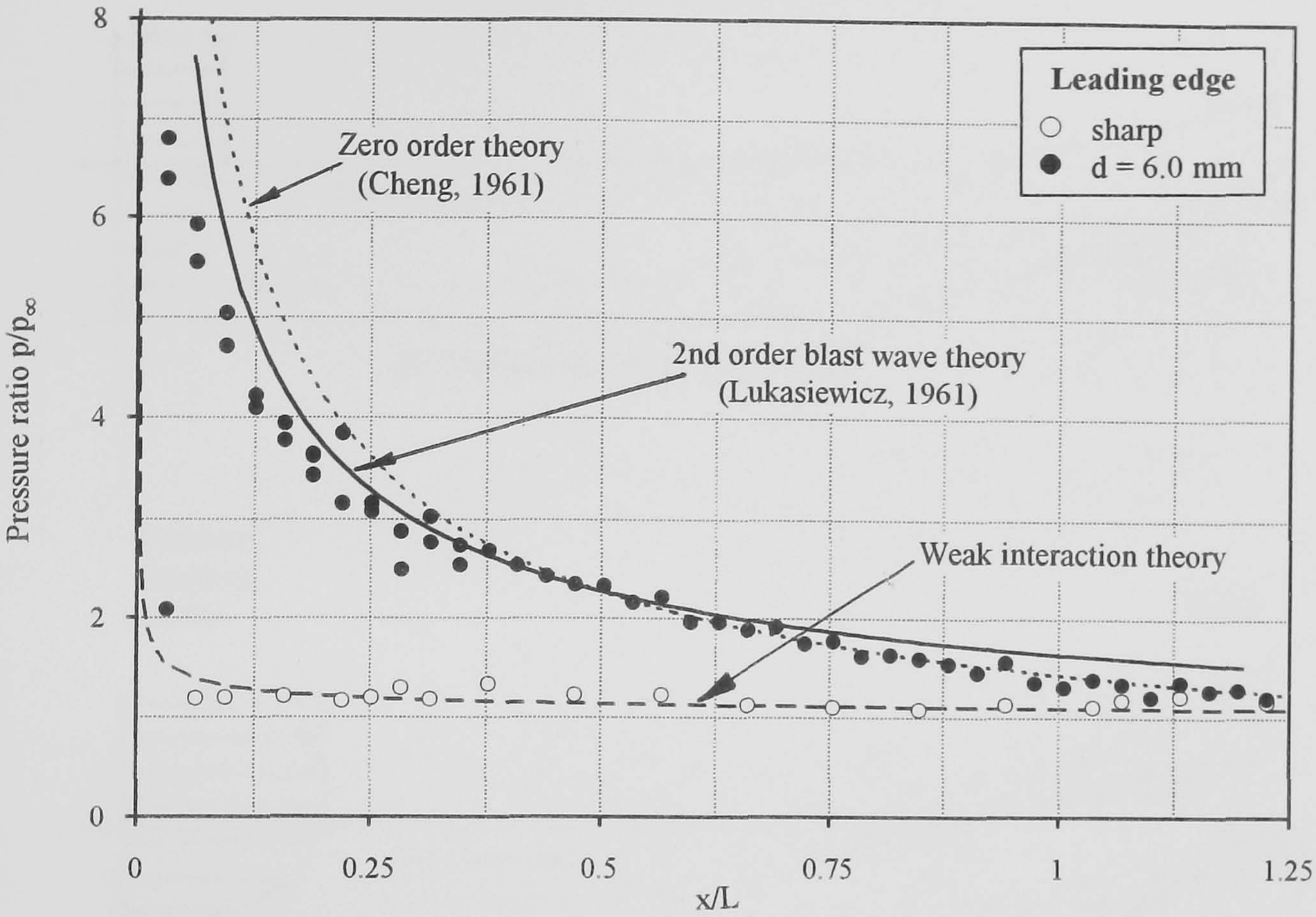

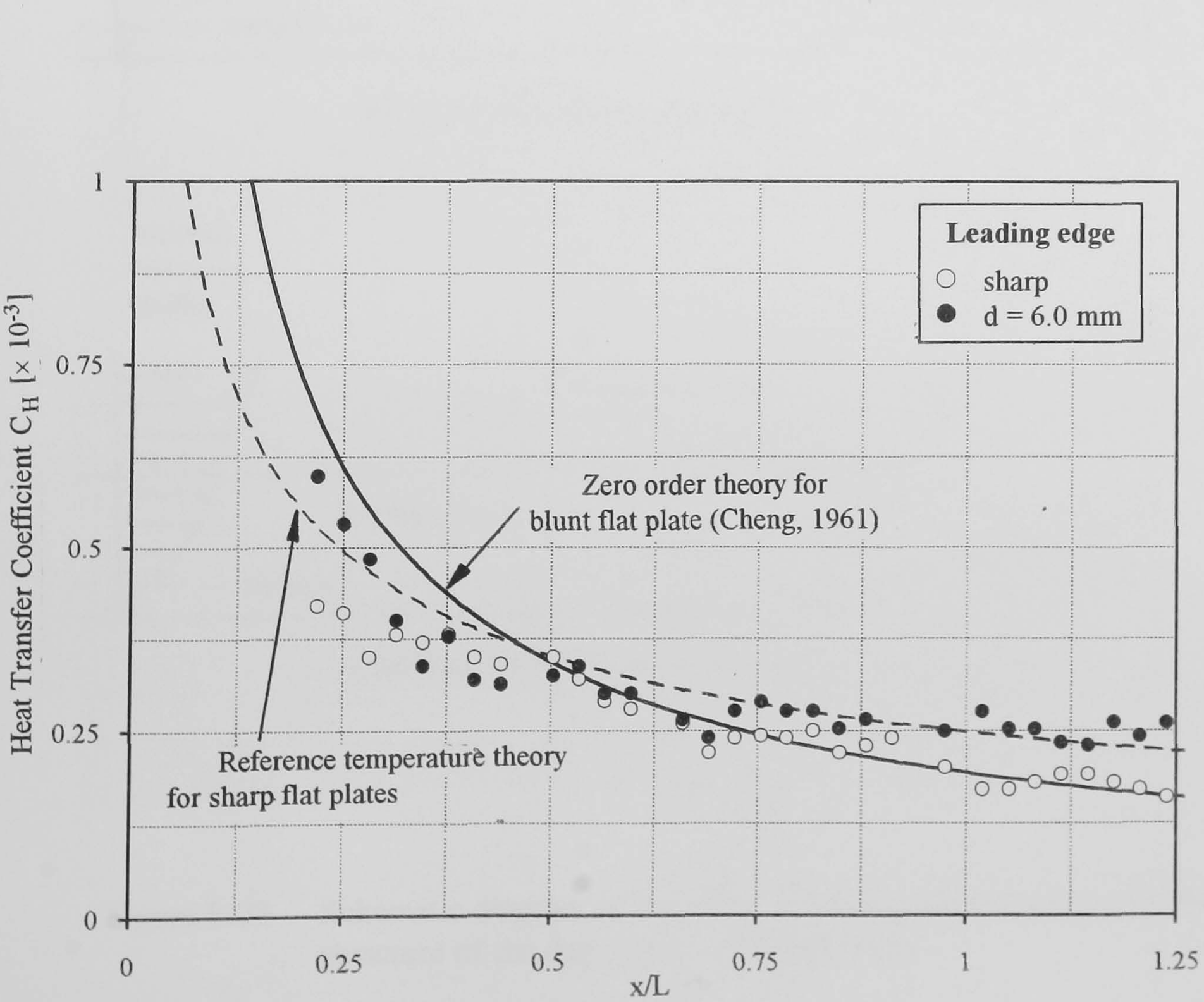

Figure 8-27 The effect of leading edge bluntness on flat plate pressure and heat transfer ($M_\infty = 8.2$, $Re_\infty/cm = 9.0 \times 10^4$, $\alpha = 0°$)

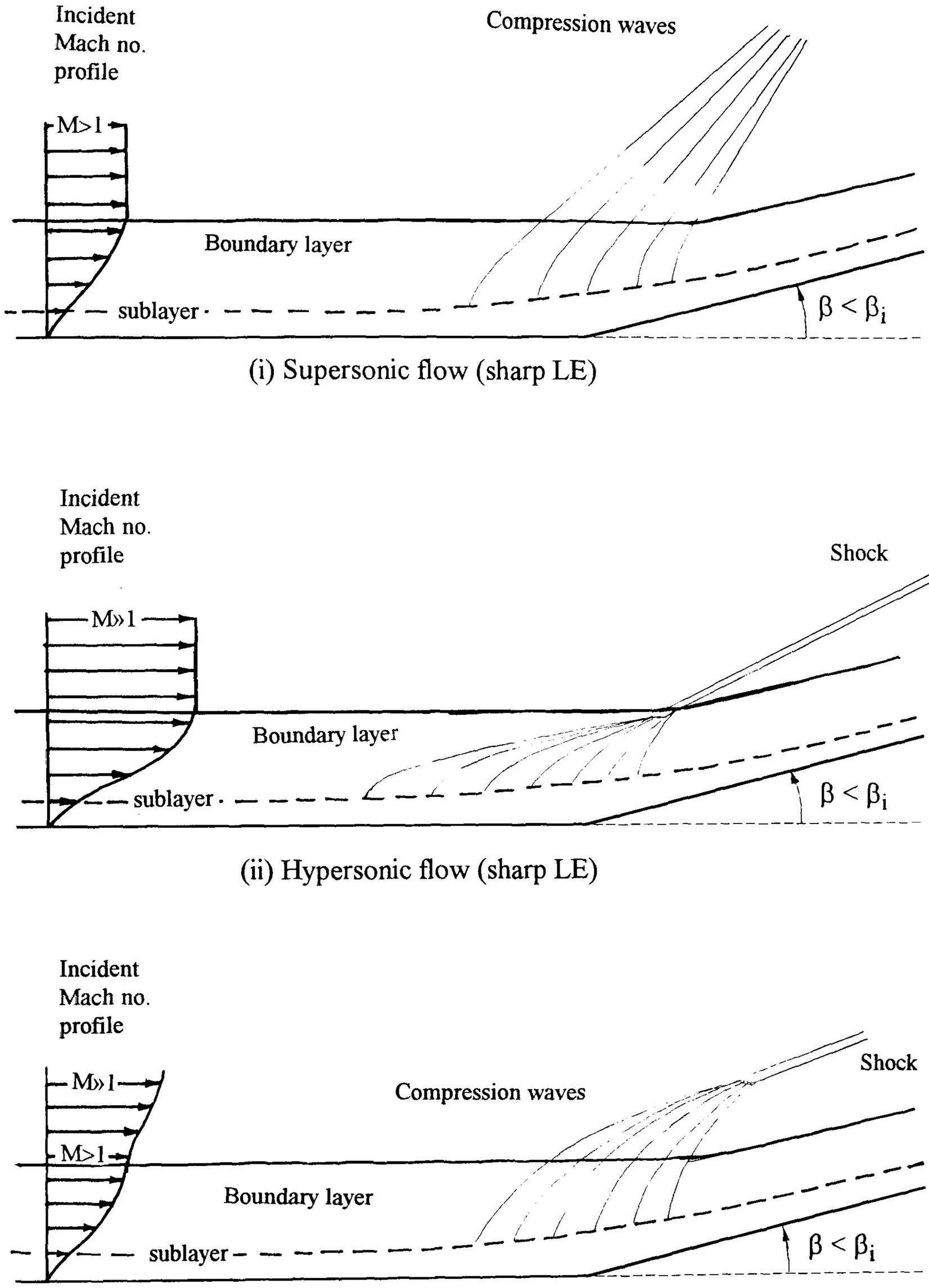

Figure 8-28 Schematic diagram of the effect of leading edge bluntness on the structure of the flap shock - attached flows

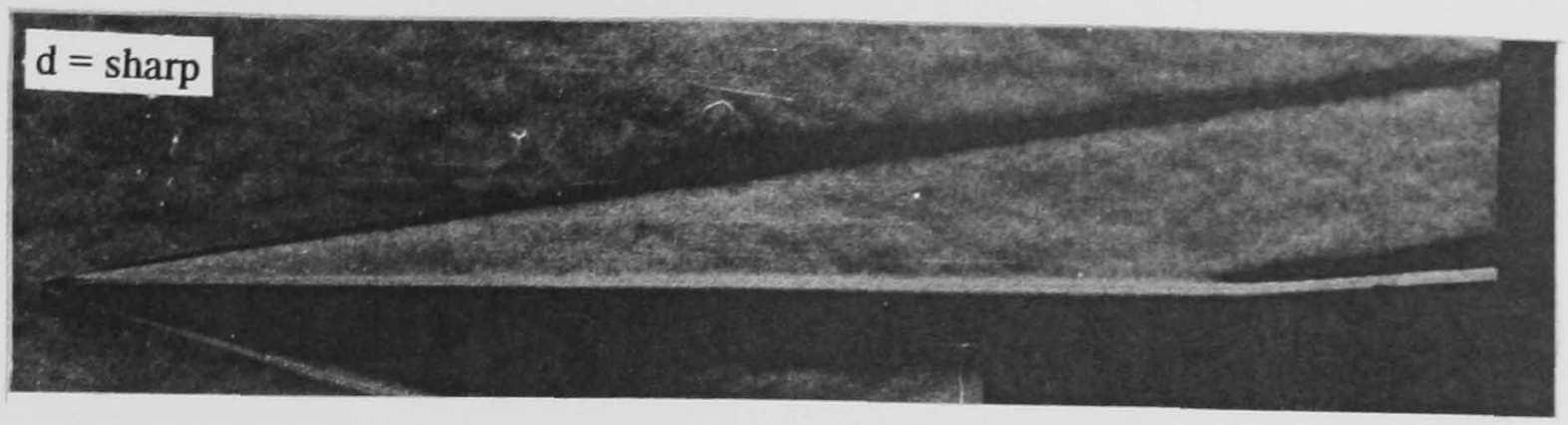

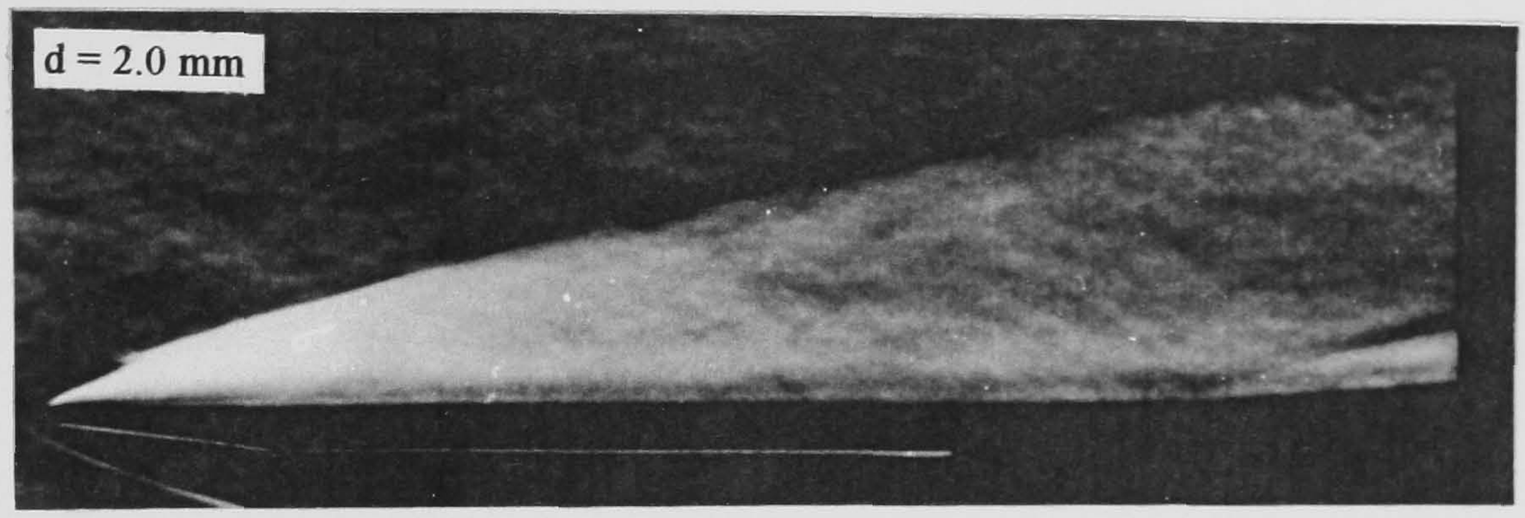

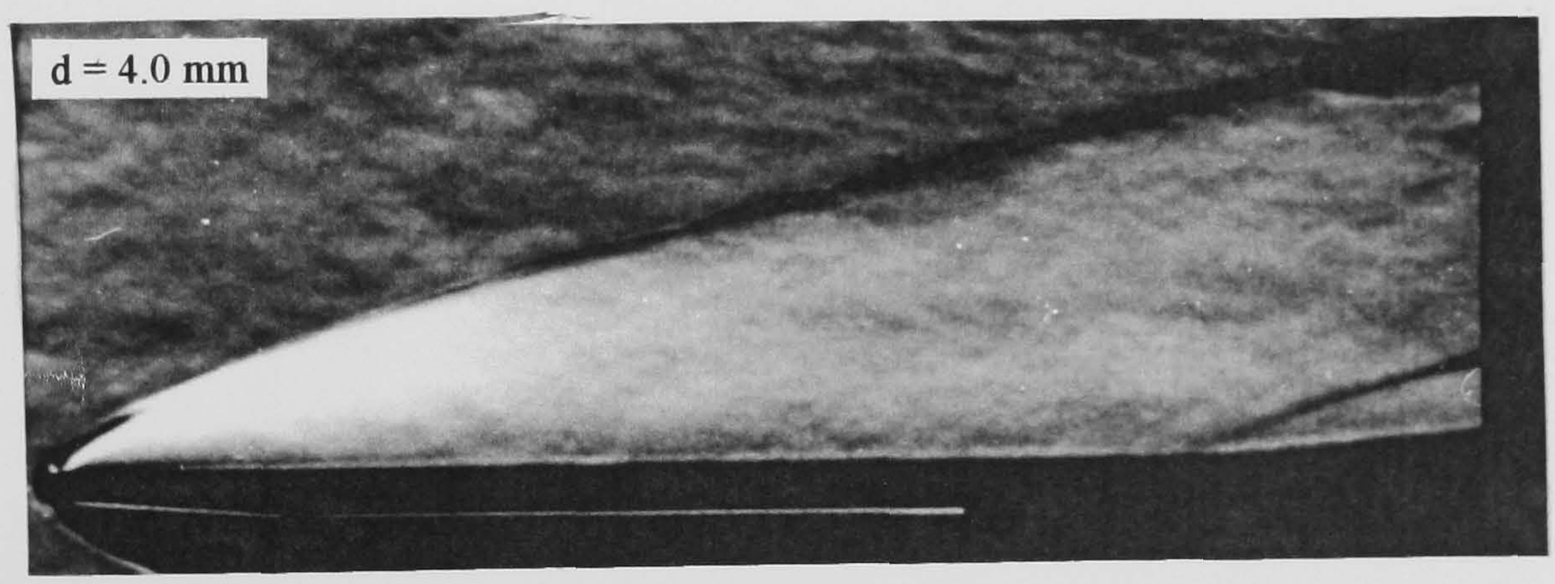

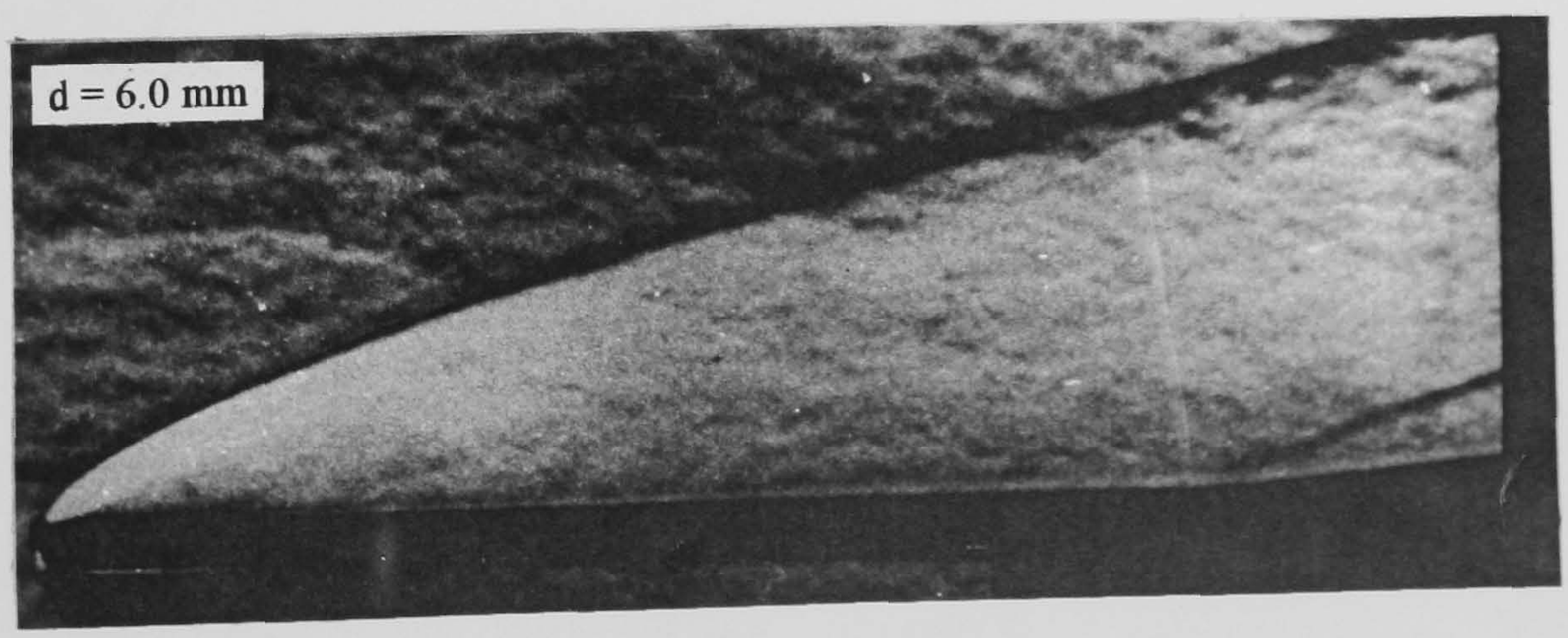

Figure 8-29 Schlieren photographs of the effect of leading edge bluntness on attached flows

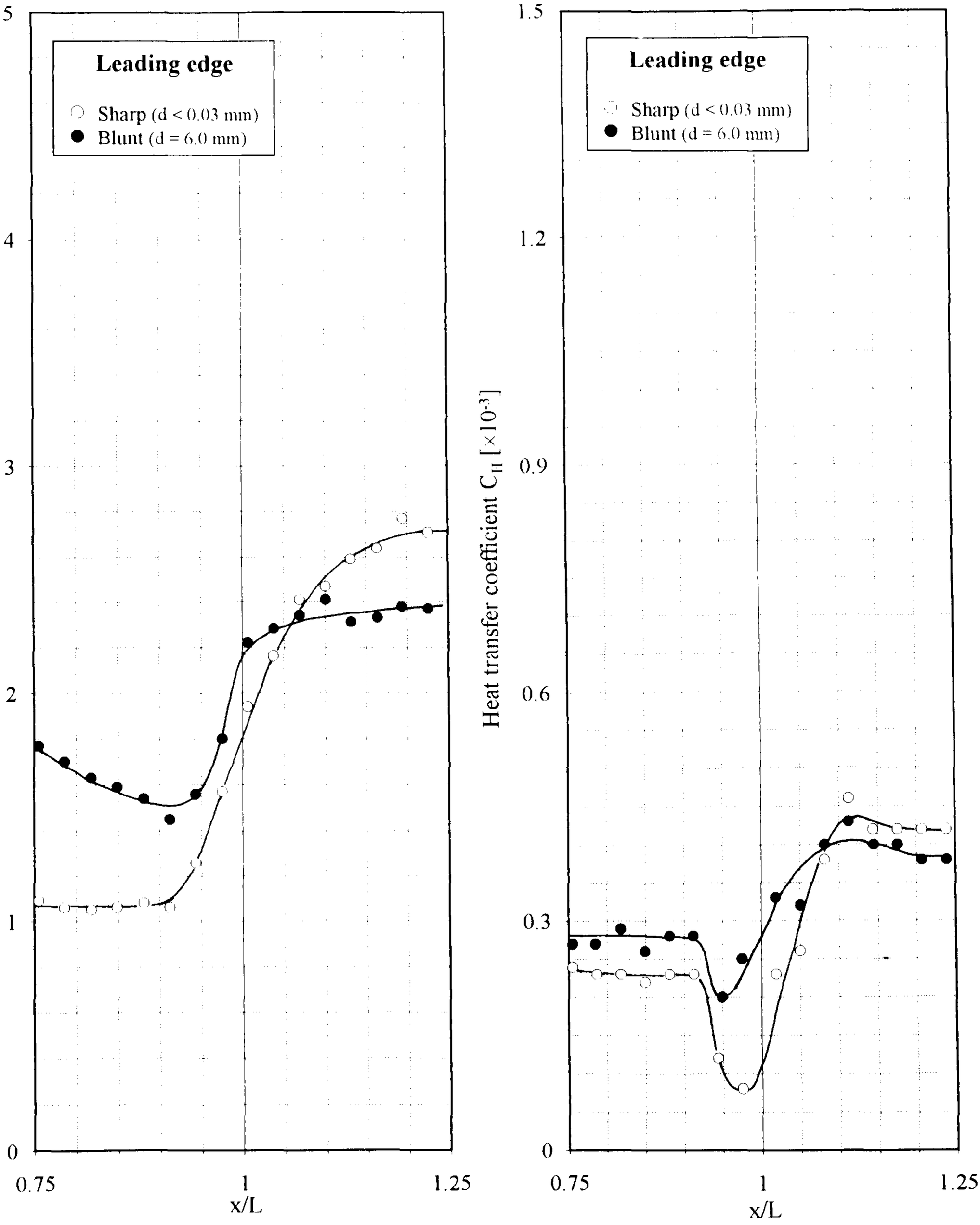

(i) pressure distribution

(ii) heat transfer distribution

Figure 8-30 The effect of leading edge bluntness on the pressure and heat transfer distribution in the flap interaction region - attached flow
($M_\infty = 8.2$, $Re_\infty/cm = 9.0 \times 10^4$, L = 15.9 cm, $\alpha = 0°$, $\beta = 5°$)

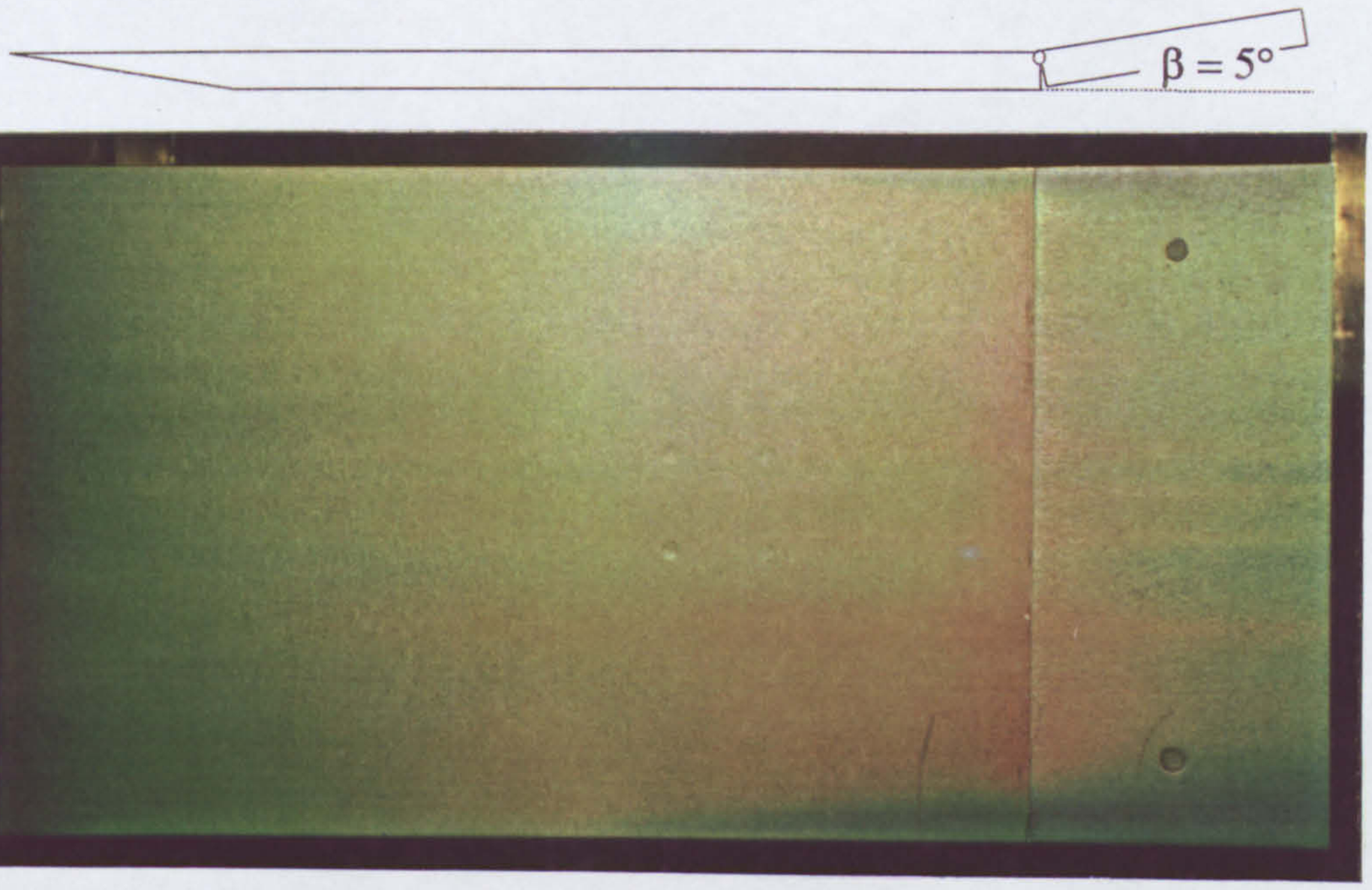

(i) sharp leading edge (d < 0.0025 mm)

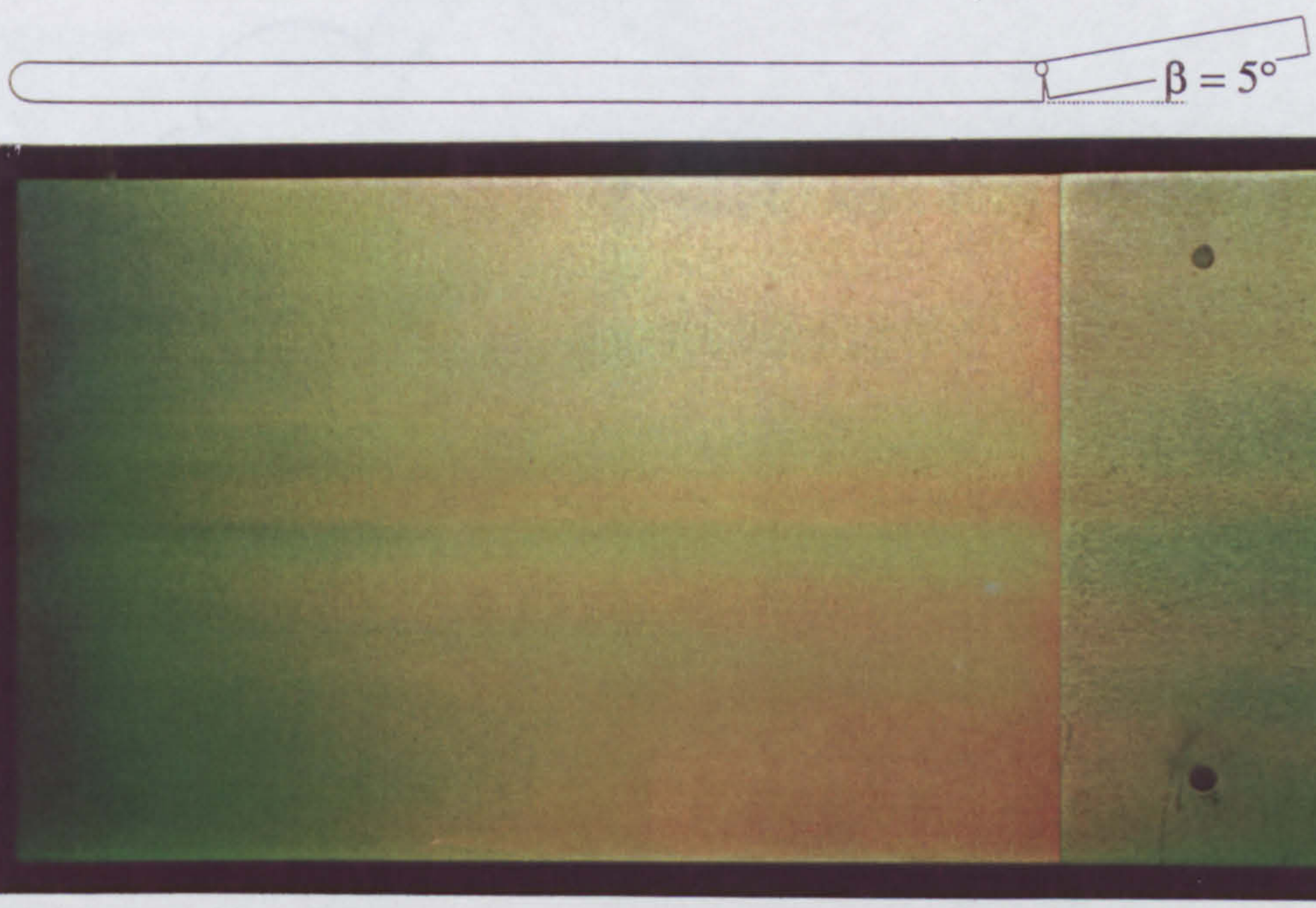

(ii) blunt leading edge (d = 6.0 mm, hemicylindrical)

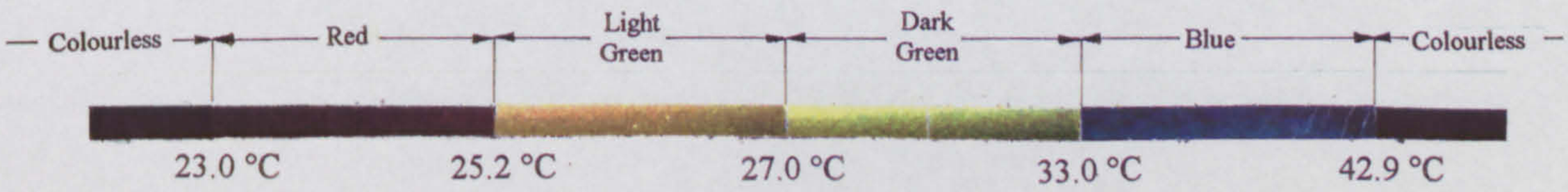

Figure 8-31 Liquid crystal thermographs of the effect of leading edge bluntness on the flow structure - attached flows
($M_\infty = 8.2$, $Re_\infty/cm = 9.0 \times 10^4$, L = 15.9 cm, $\alpha = 0°$, $\beta = 5°$)

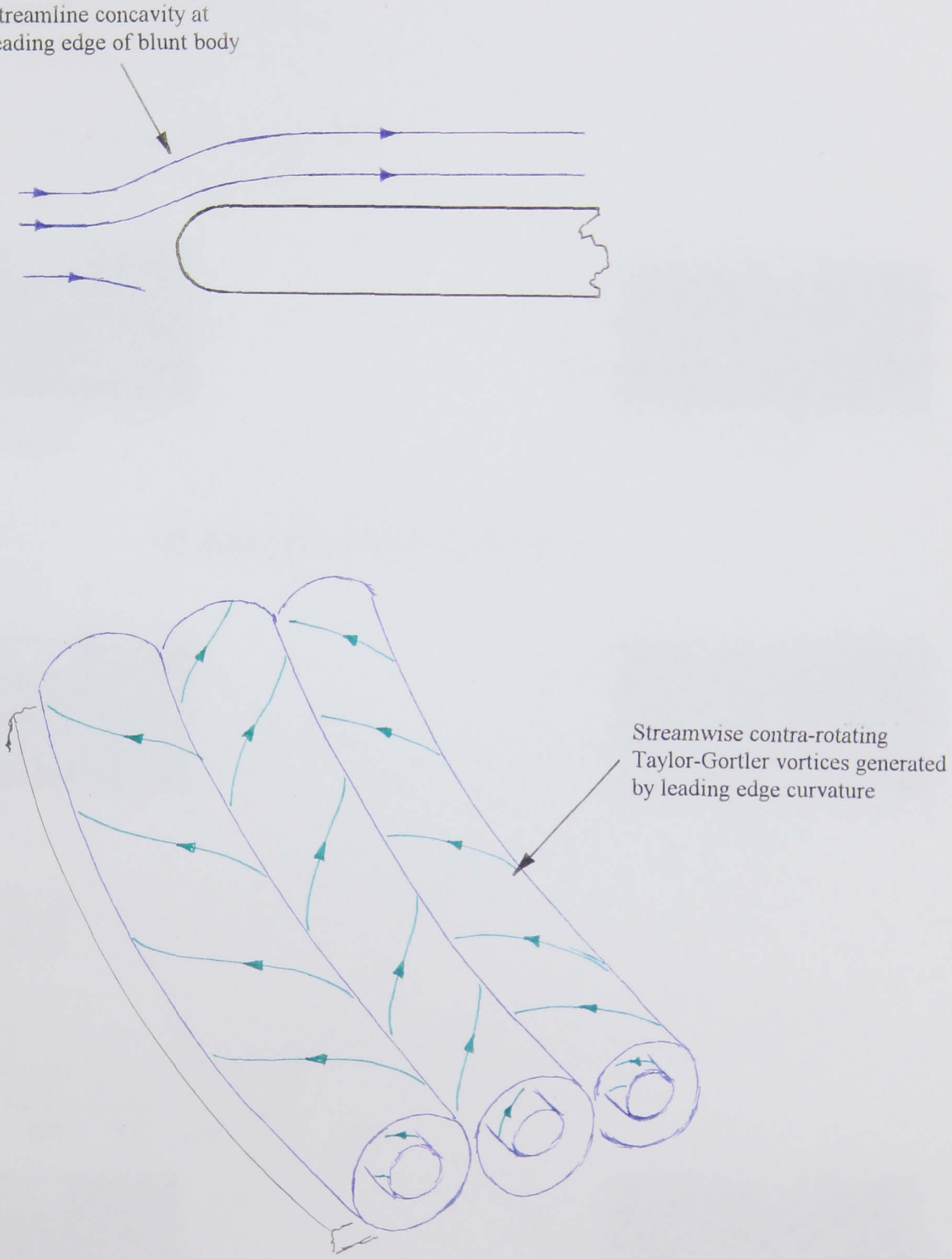

Figure 8-32 Streamwise structures generated at the leading edge of a blunt body

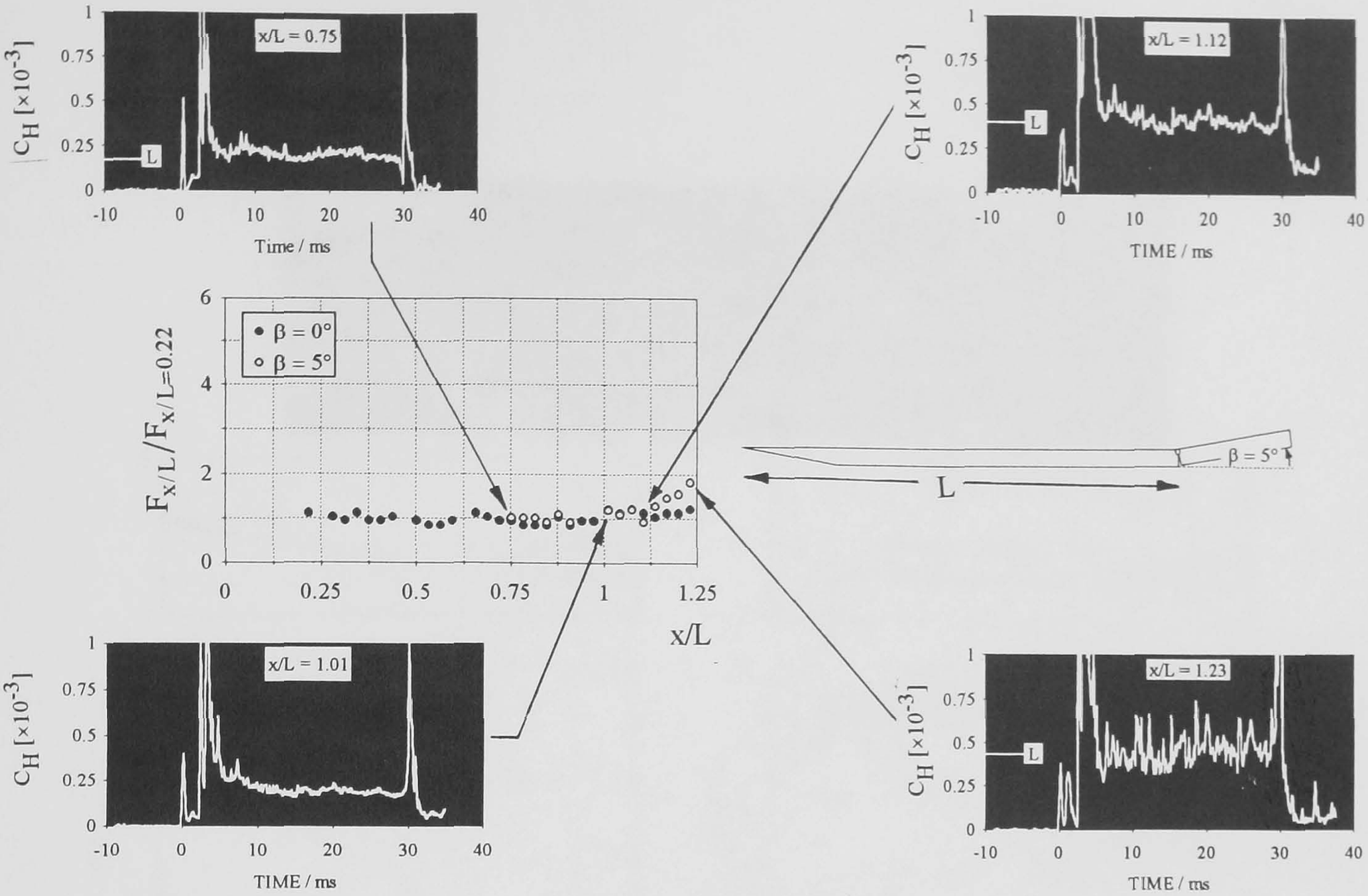

(a) sharp leading edge configuration

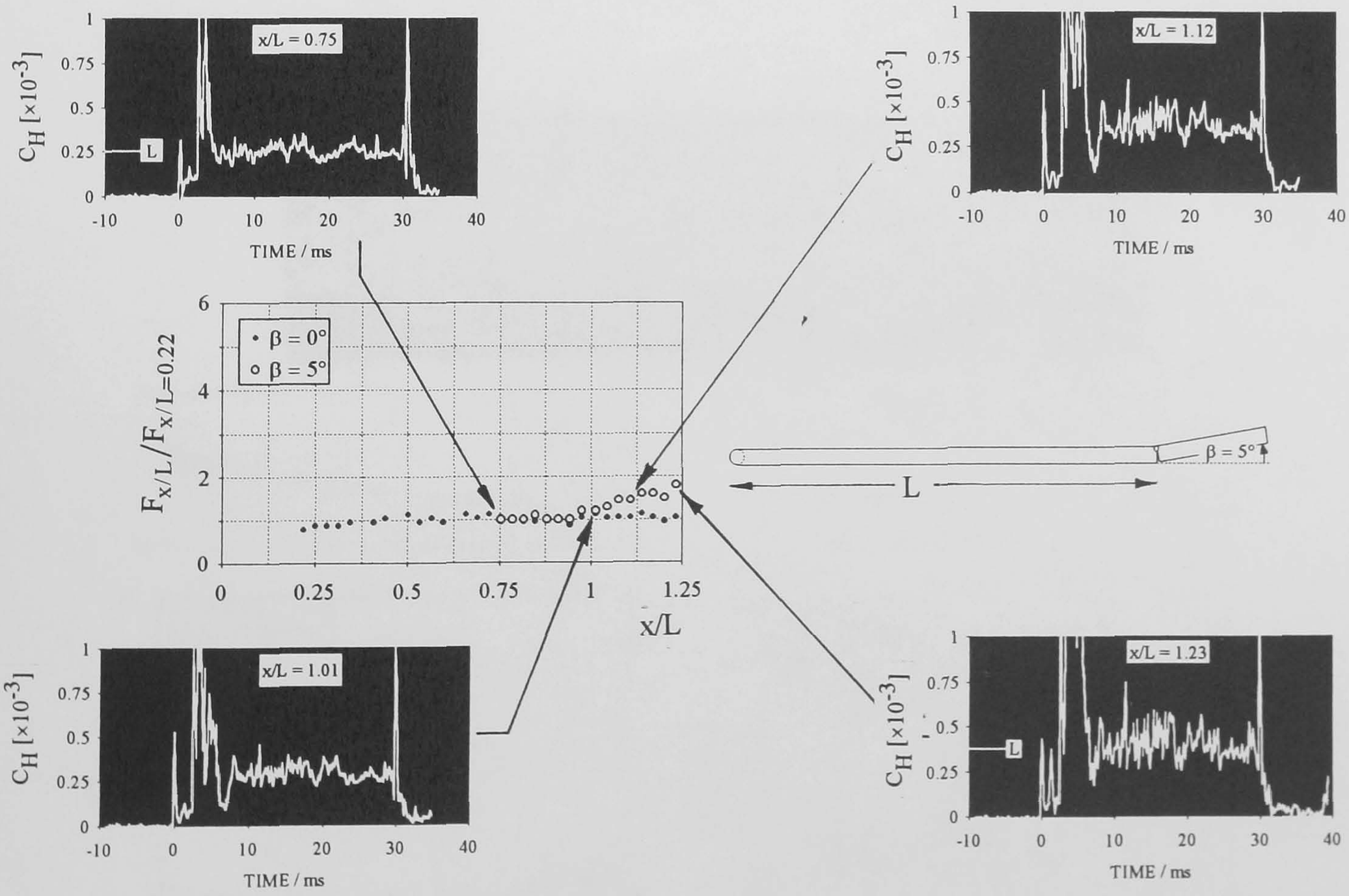

(b) d = 6.0 mm blunt leading edge configuration

Figure 8-33 The effect of leading edge bluntness on flap heat transfer fluctuations ($M_\infty = 8.2$, $Re_\infty/cm = 9.0 \times 10^4$, $\alpha = 0°$, $\beta = 5°$)

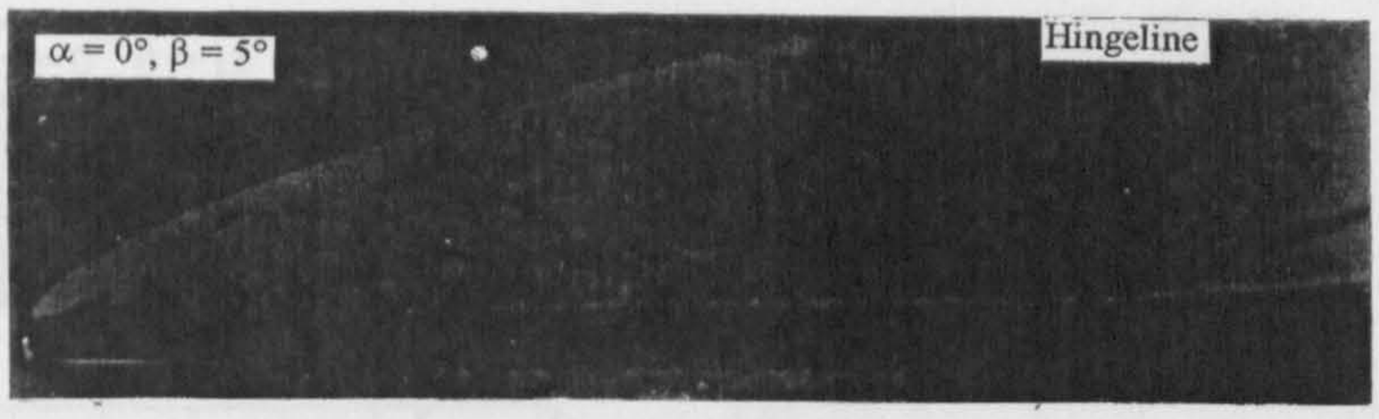

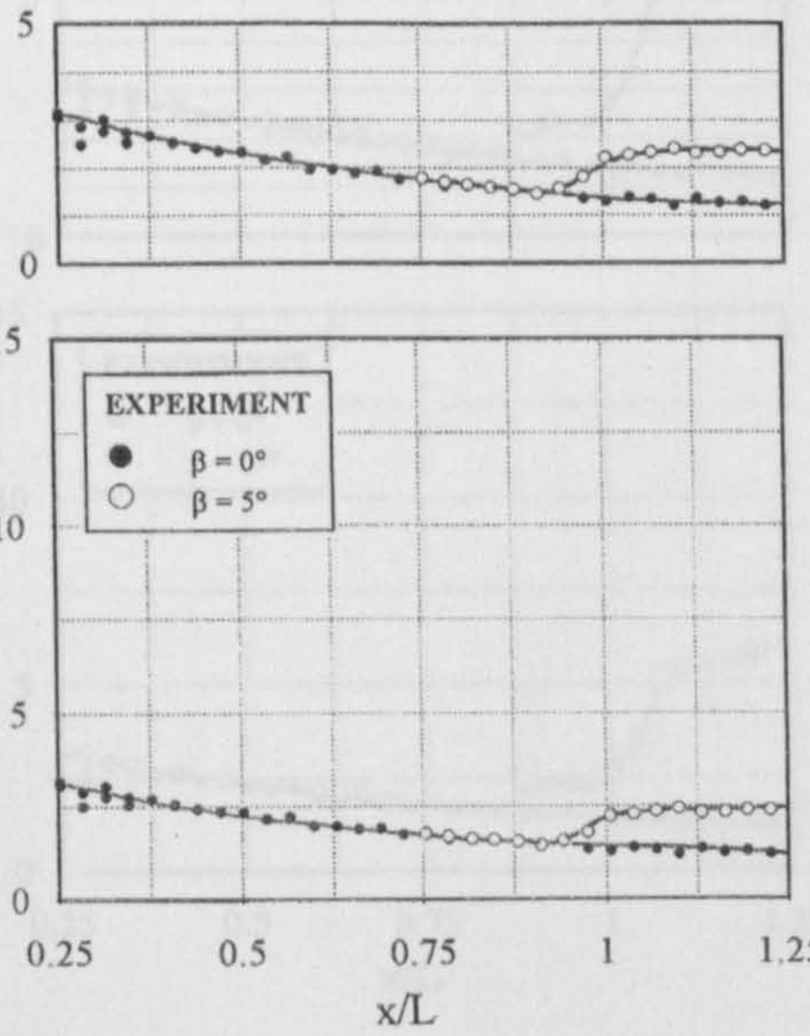

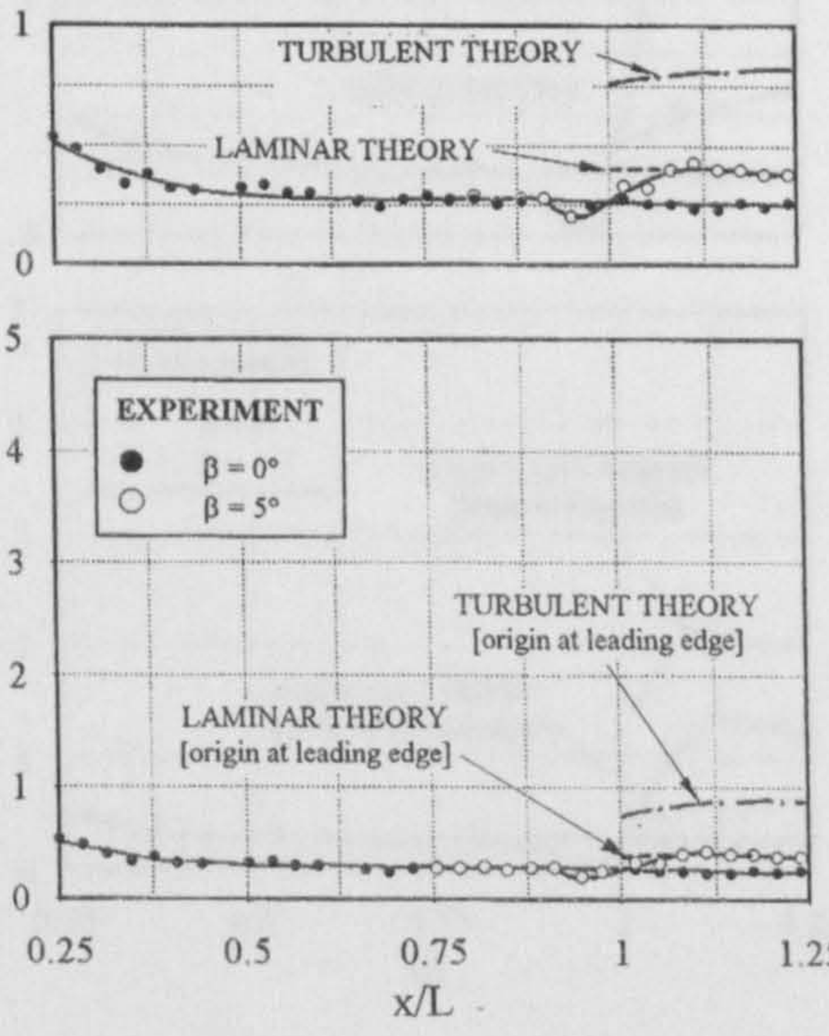

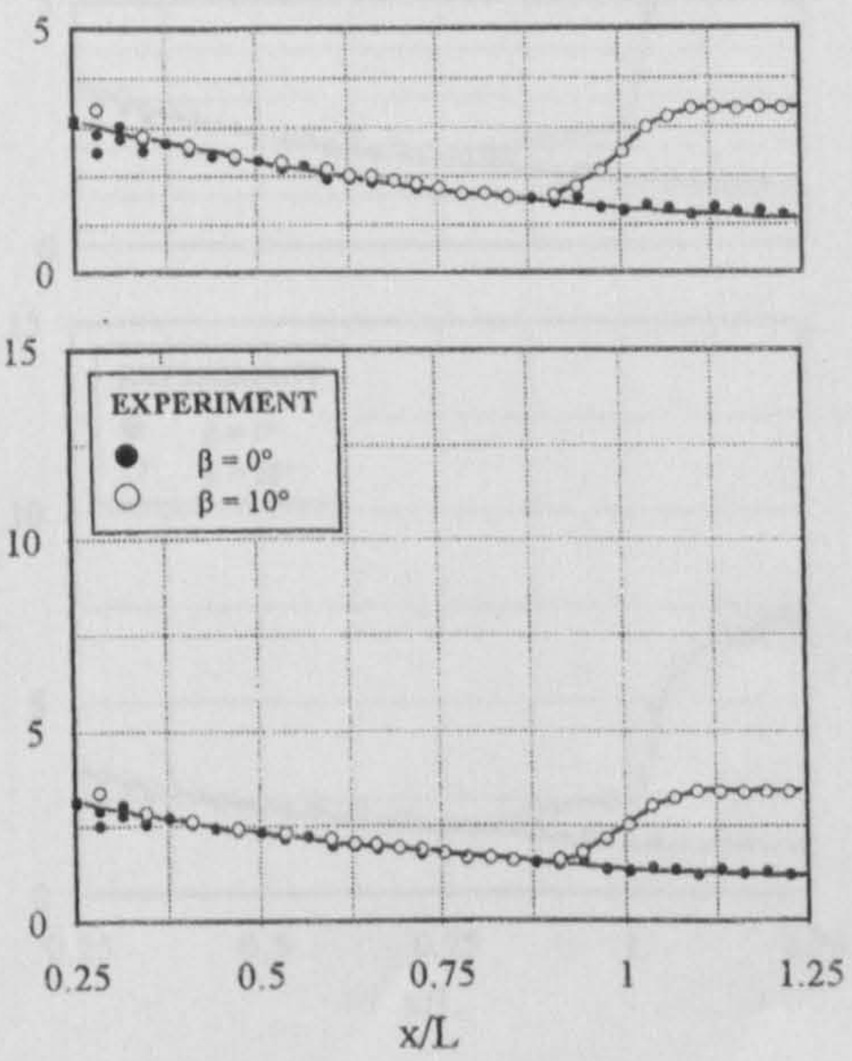

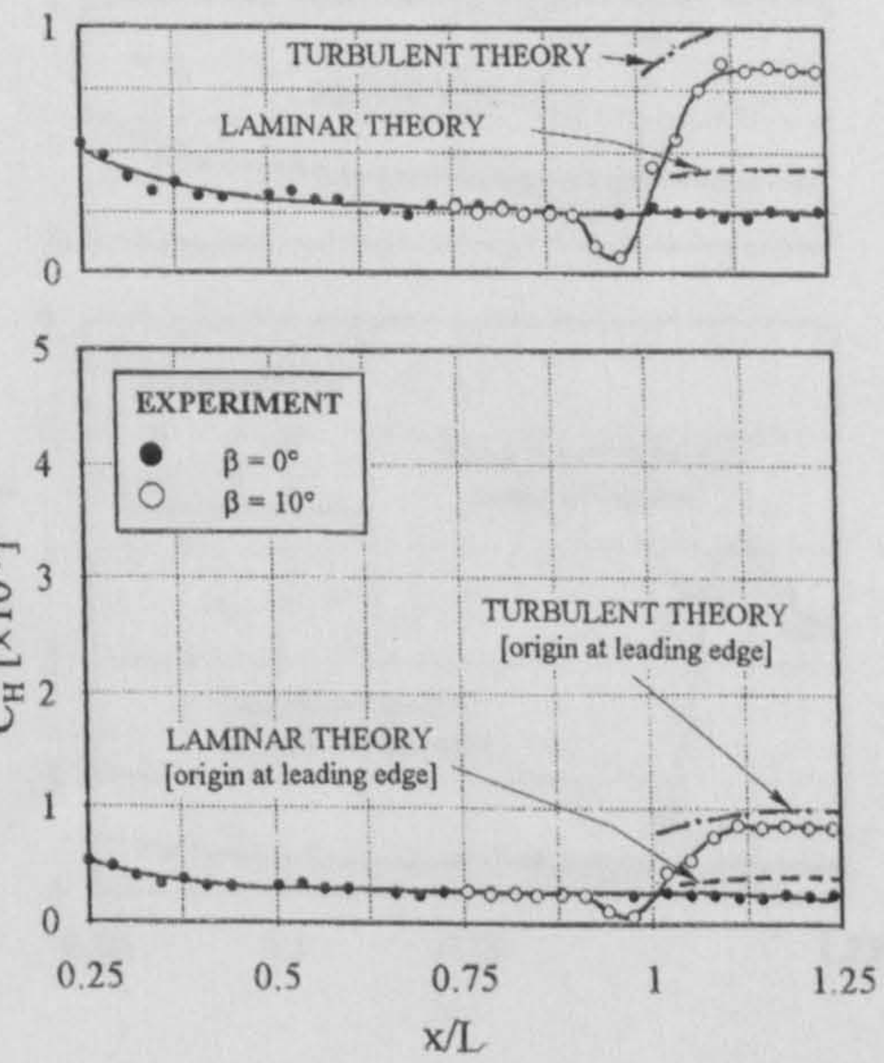

Figure 8-34 Pressure and heat transfer measurements on blunt leading edge control flap configurations
($M_\infty = 8.2$, $Re_\infty/cm = 9.0 \times 10^4$, L = 15.9 cm, d = 6.0 mm)

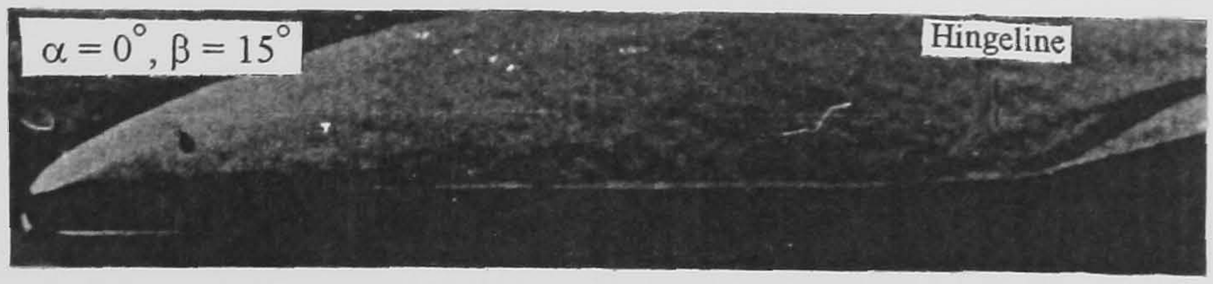

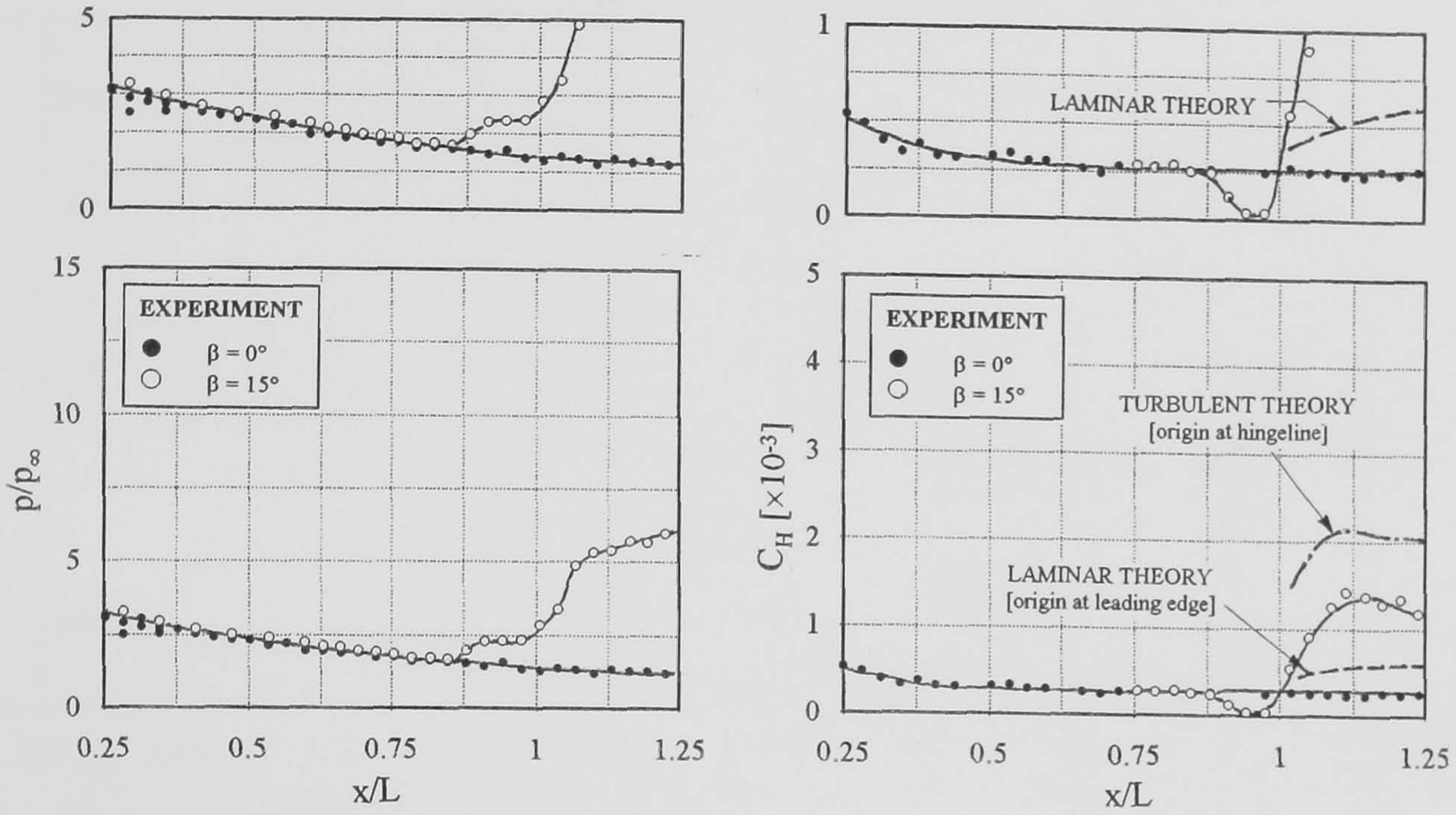

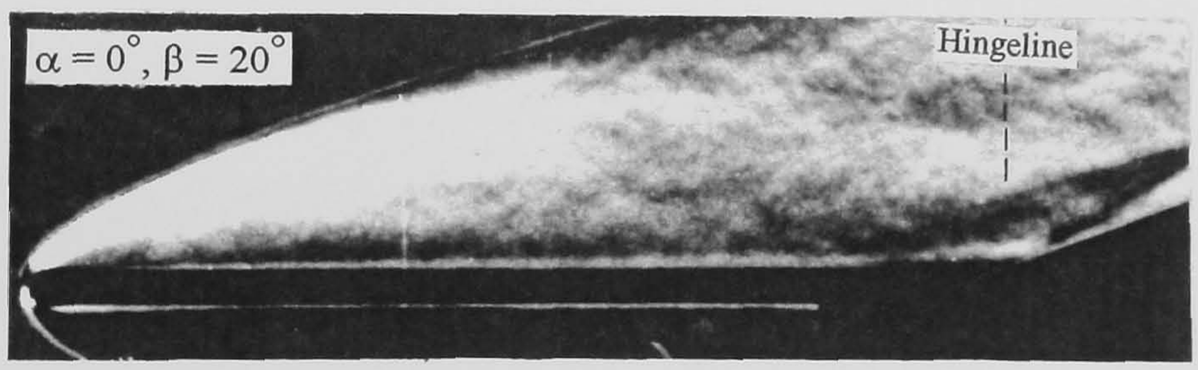

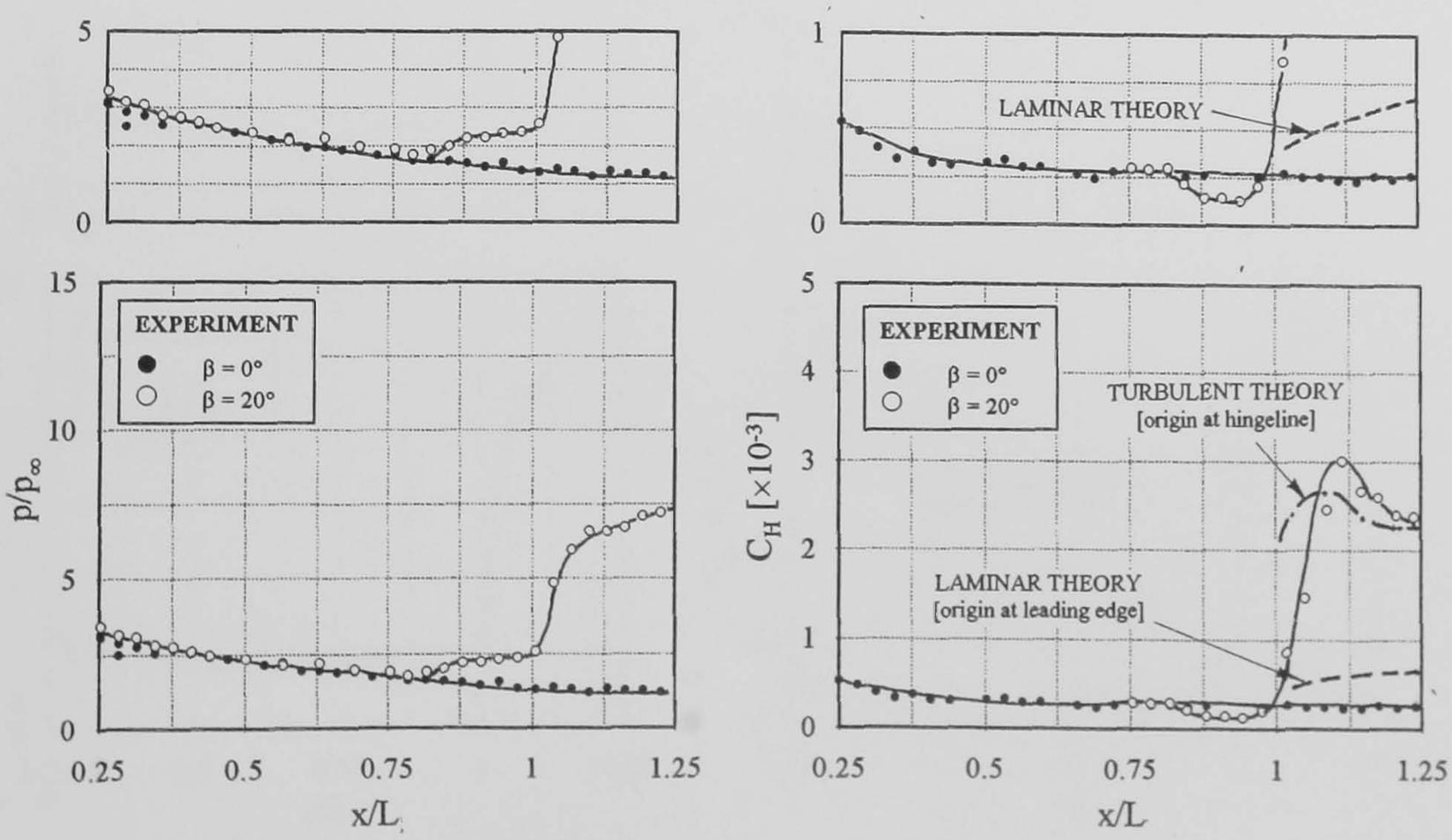

Figure 8-34 (cont'd) Pressure and heat transfer measurements on blunt leading edge control flap configurations
($M_\infty = 8.2$, $Re_\infty/cm = 9.0 \times 10^4$, L = 15.9 cm, d = 6.0 mm)

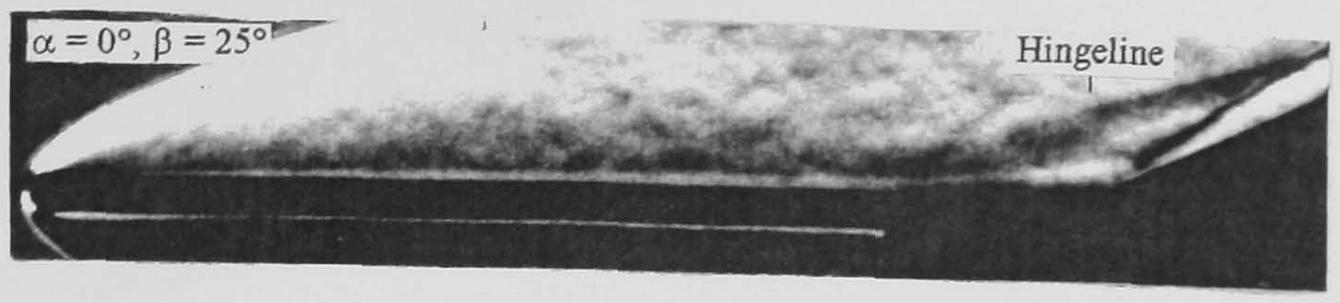

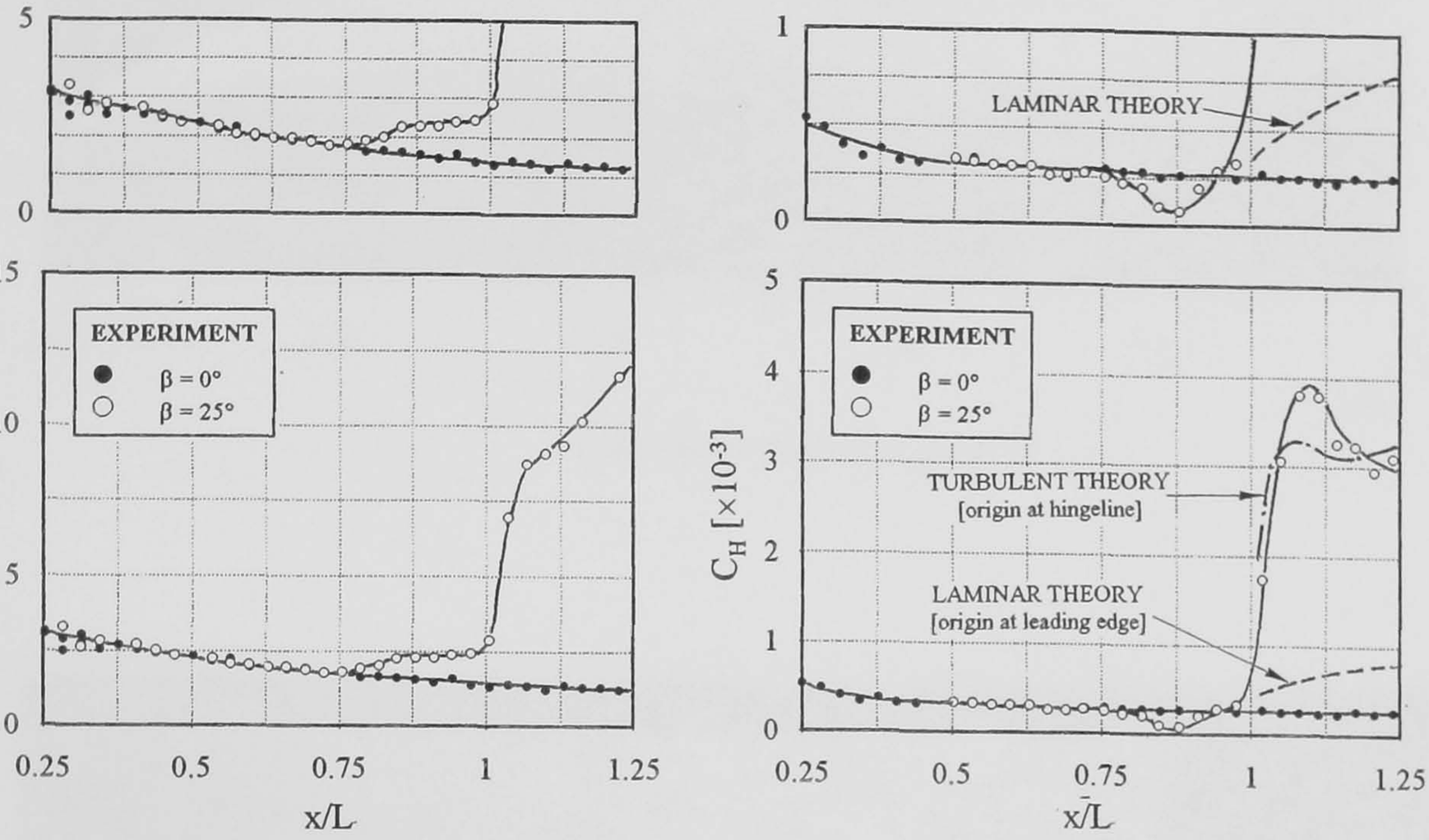

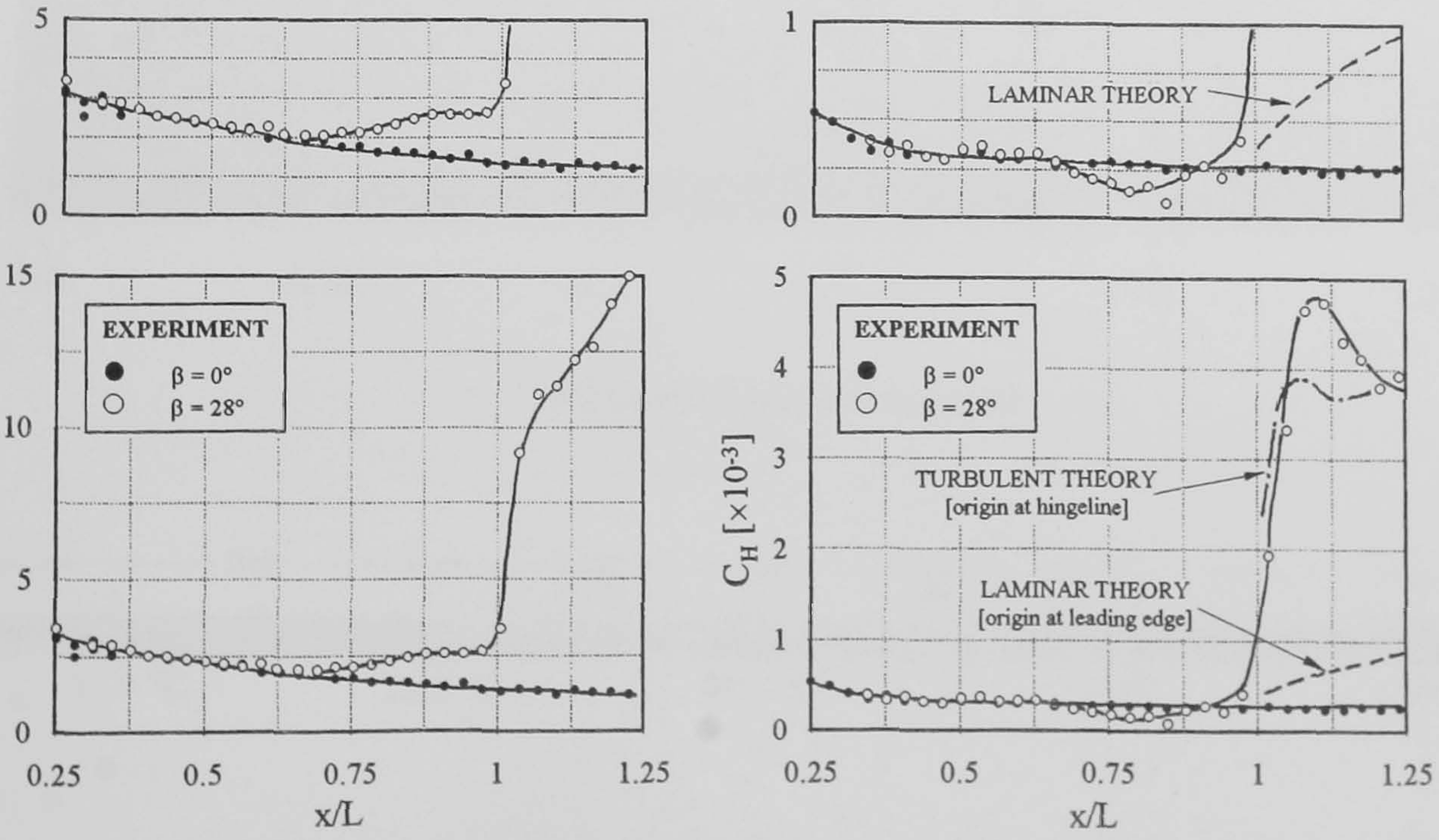

Figure 8-34 (cont'd) Pressure and heat transfer measurements on blunt leading edge control flap configurations
($M_\infty = 8.2$, $Re_\infty/cm = 9.0 \times 10^4$, L = 15.9 cm, d = 6.0 mm)

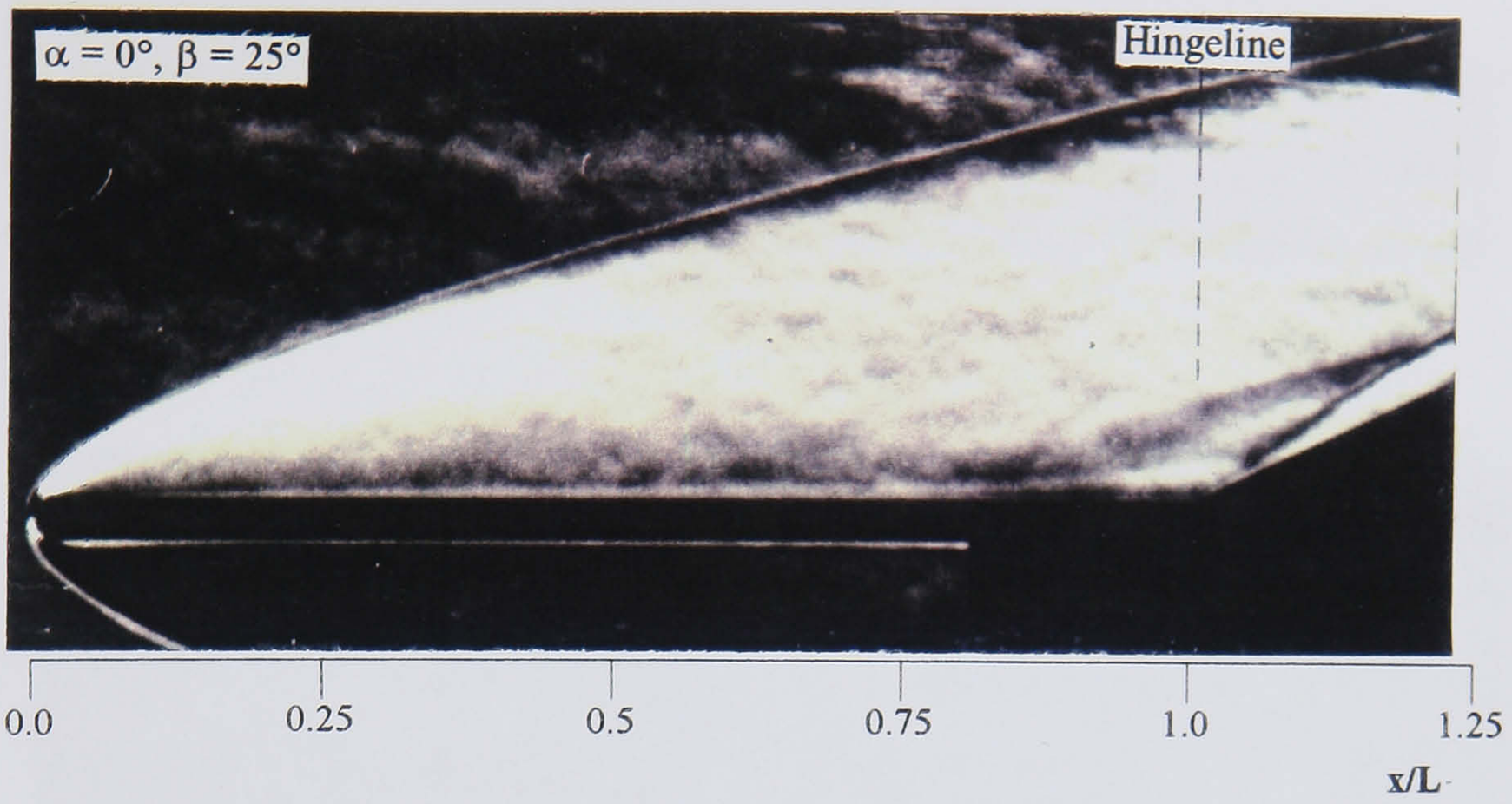

(i) schlieren flow visualisation

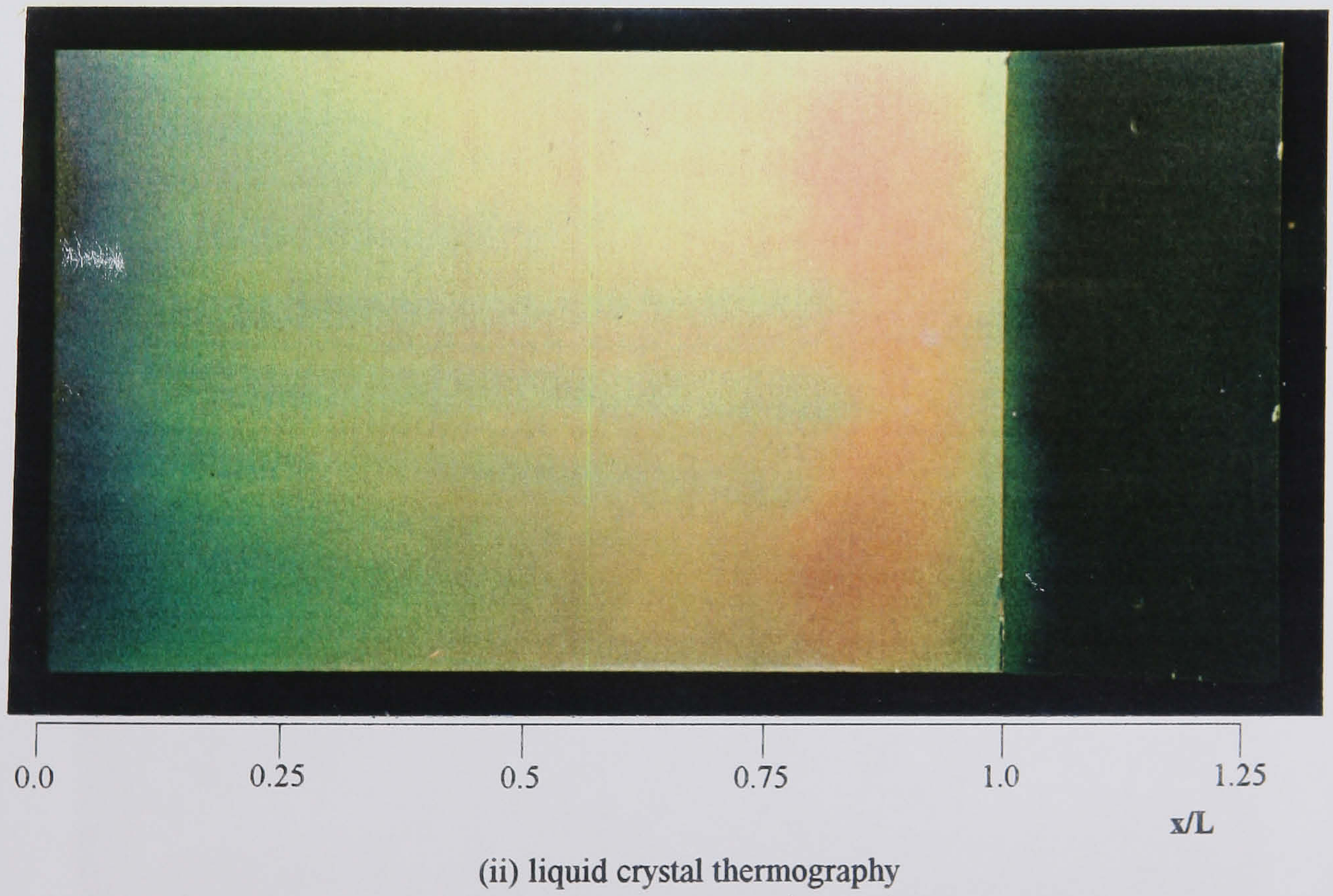

(ii) liquid crystal thermography

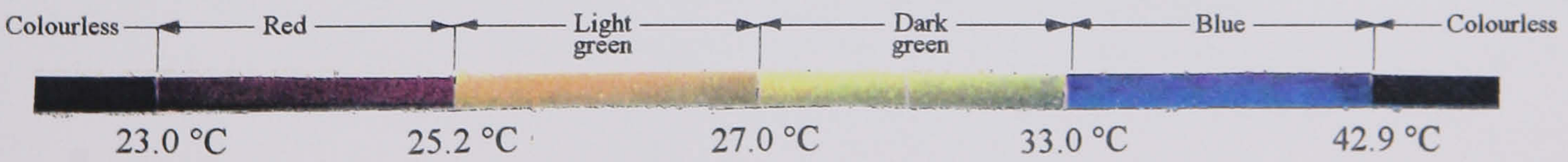

Figure 8-35 Schlieren photograph and liquid crystal thermograph of the flow structure over blunt leading edge configurations
($M_\infty = 8.2$, $Re_\infty/cm = 9.0 \times 10^4$, L = 15.9 cm, $\alpha = 0°$, $\beta = 25°$)

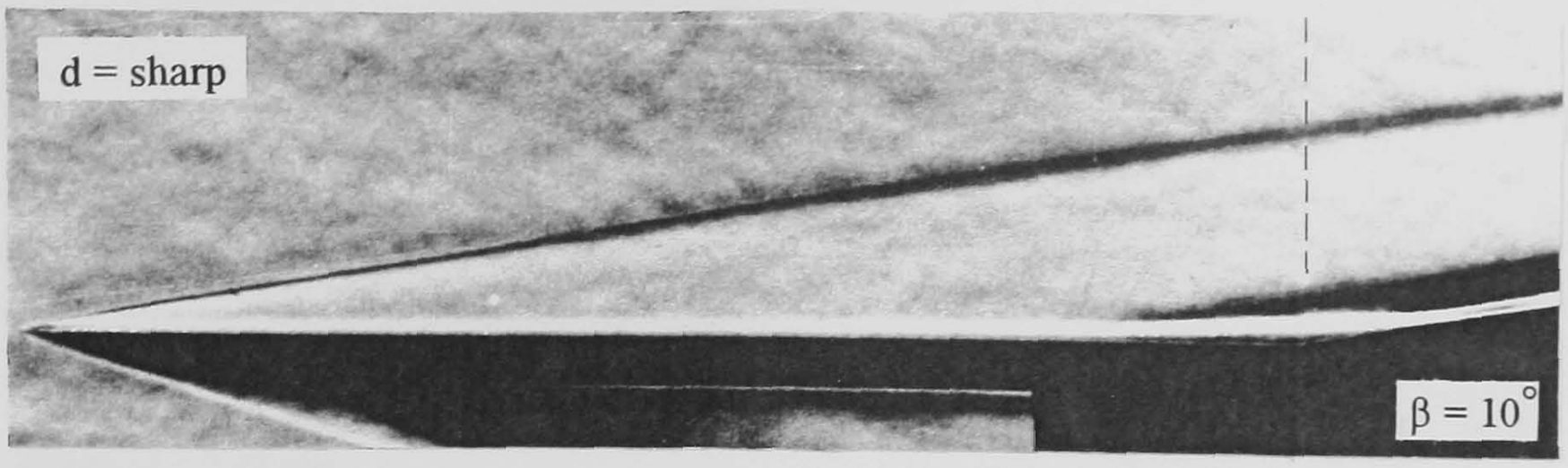

Figure 8-36 The effect of leading edge bluntness on separation ($M_\infty = 8.2$, $Re_\infty/cm = 9.0 \times 10^4$, L = 15.9 cm, $\alpha = 0°$)

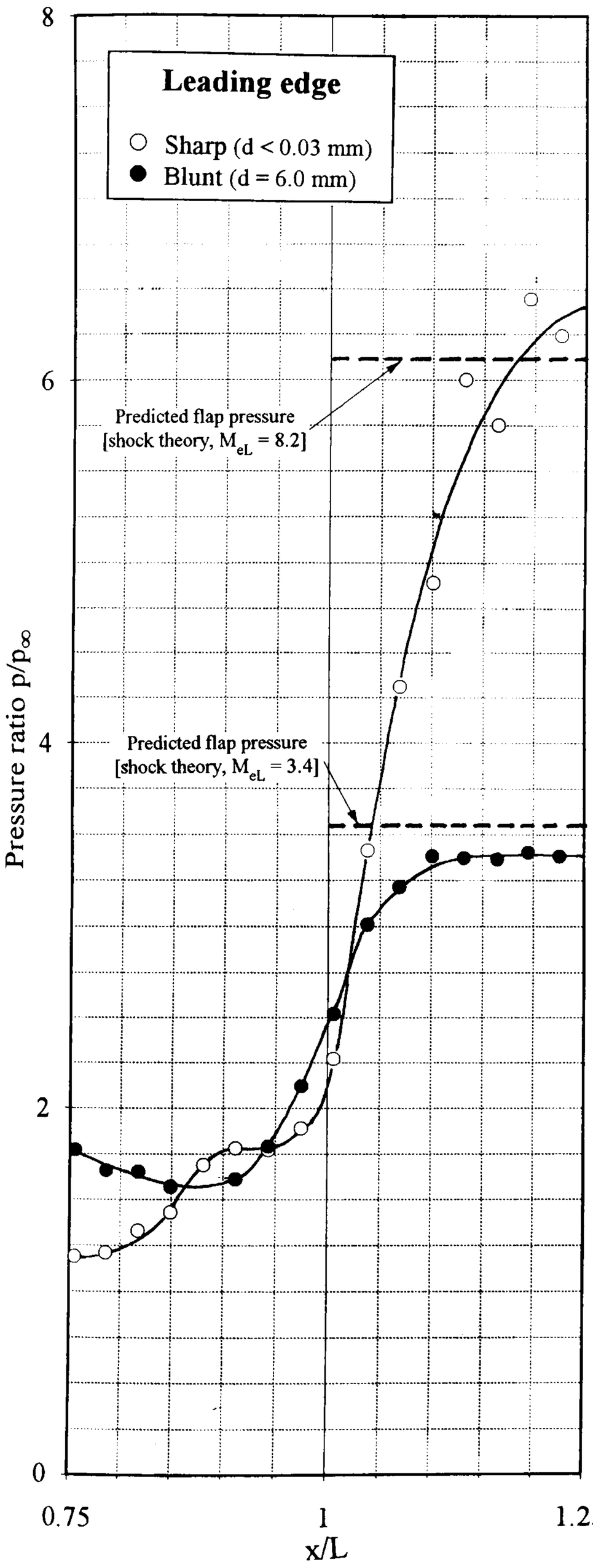

(i) pressure distribution

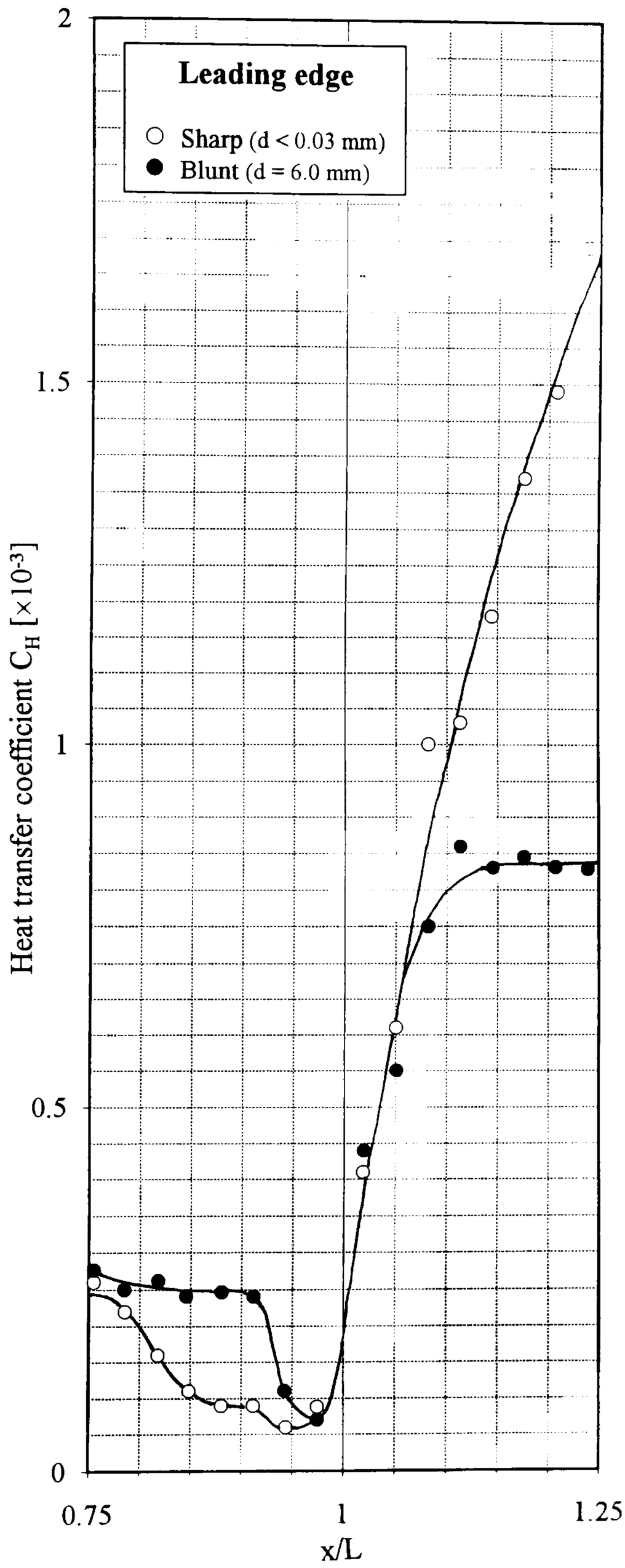

(ii) heat transfer distribution

Figure 8-37 The effect of leading edge bluntness on the pressure and heat transfer distribution in the flap interaction region
(M_∞ = 8.2, Re_∞/cm = 9.0 × 10^4, L = 15.9 cm, α = 0°, β = 10°)

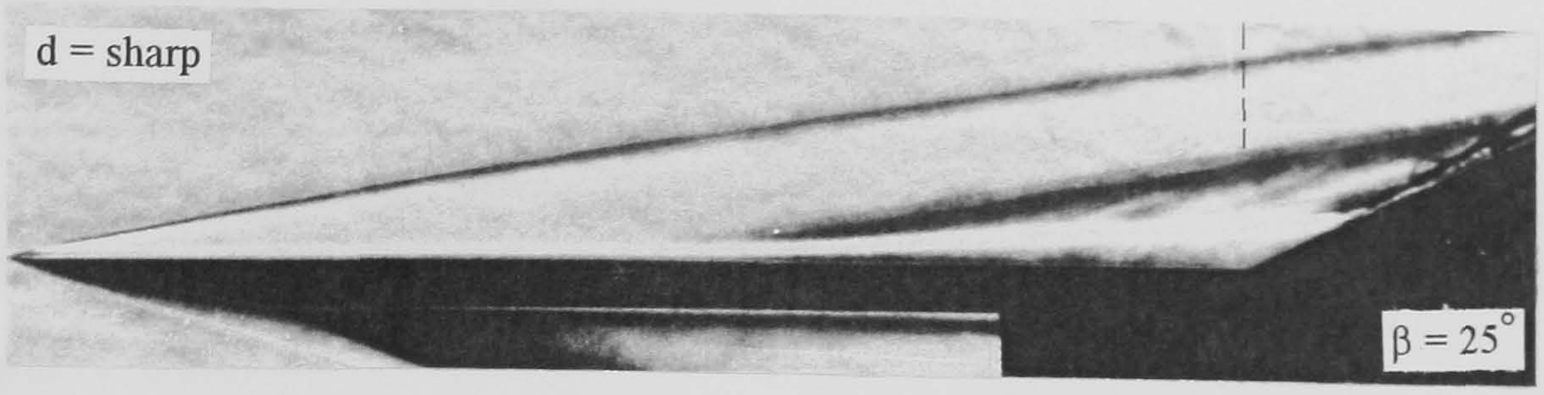

Figure 8-38 The effect of leading edge bluntness on well separated flows ($M_\infty = 8.2$, $Re_\infty/cm = 9.0 \times 10^4$, L = 15.9 cm, $\alpha = 0°$)

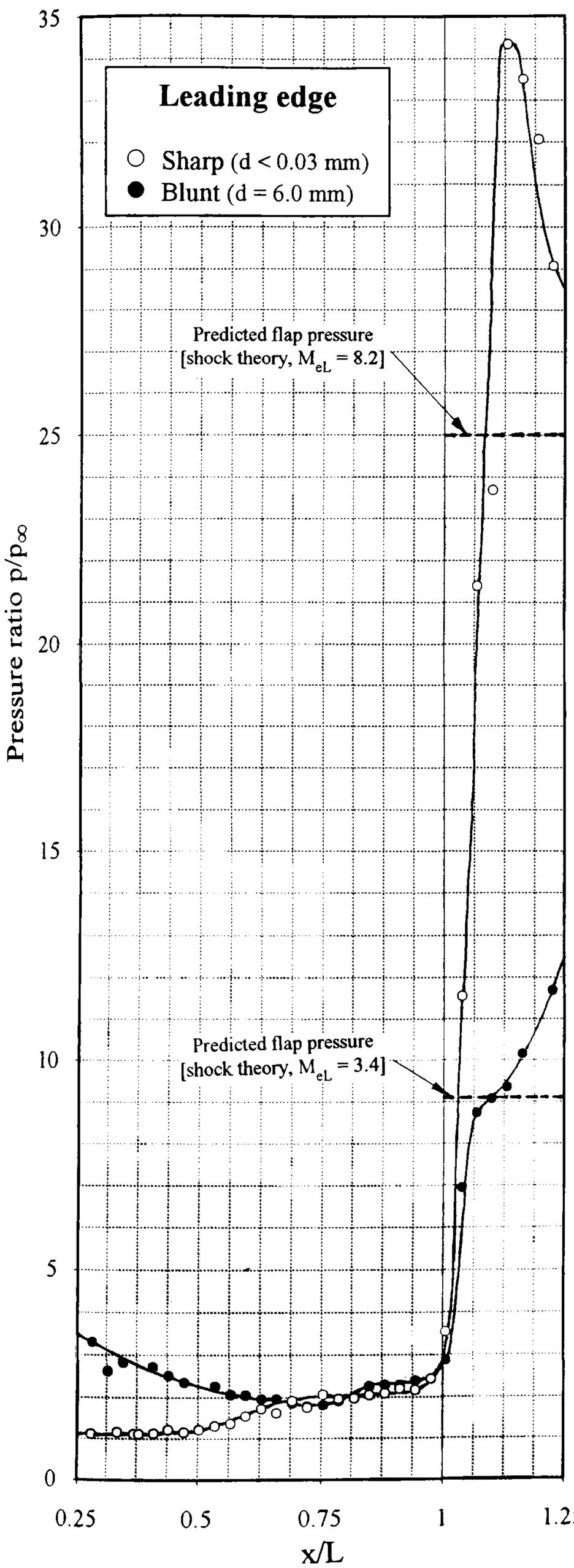

(i) pressure distribution

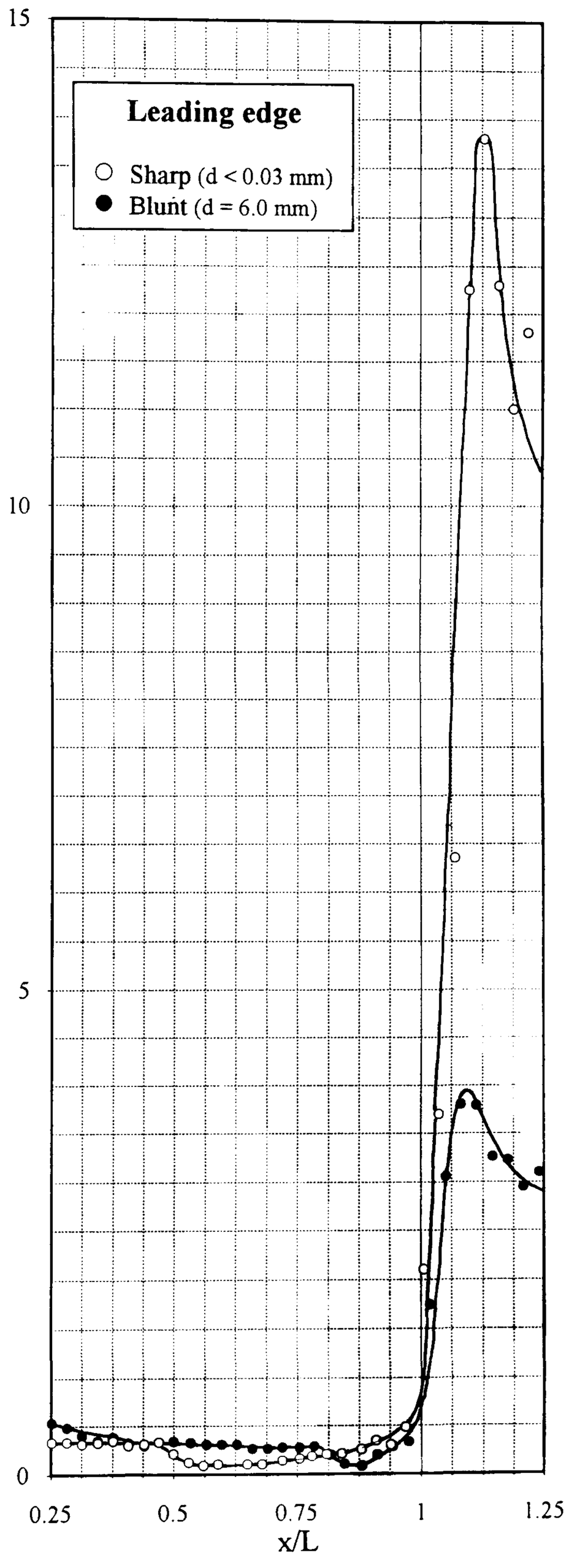

(ii) heat transfer distribution

Figure 8-39 The effect of leading edge bluntness on the pressure and heat transfer distribution in the flap interaction region of well separated flows
(M_∞ = 8.2, Re_∞/cm = 9.0 × 10^4, L = 15.9 cm, α = 0°, β = 25°)

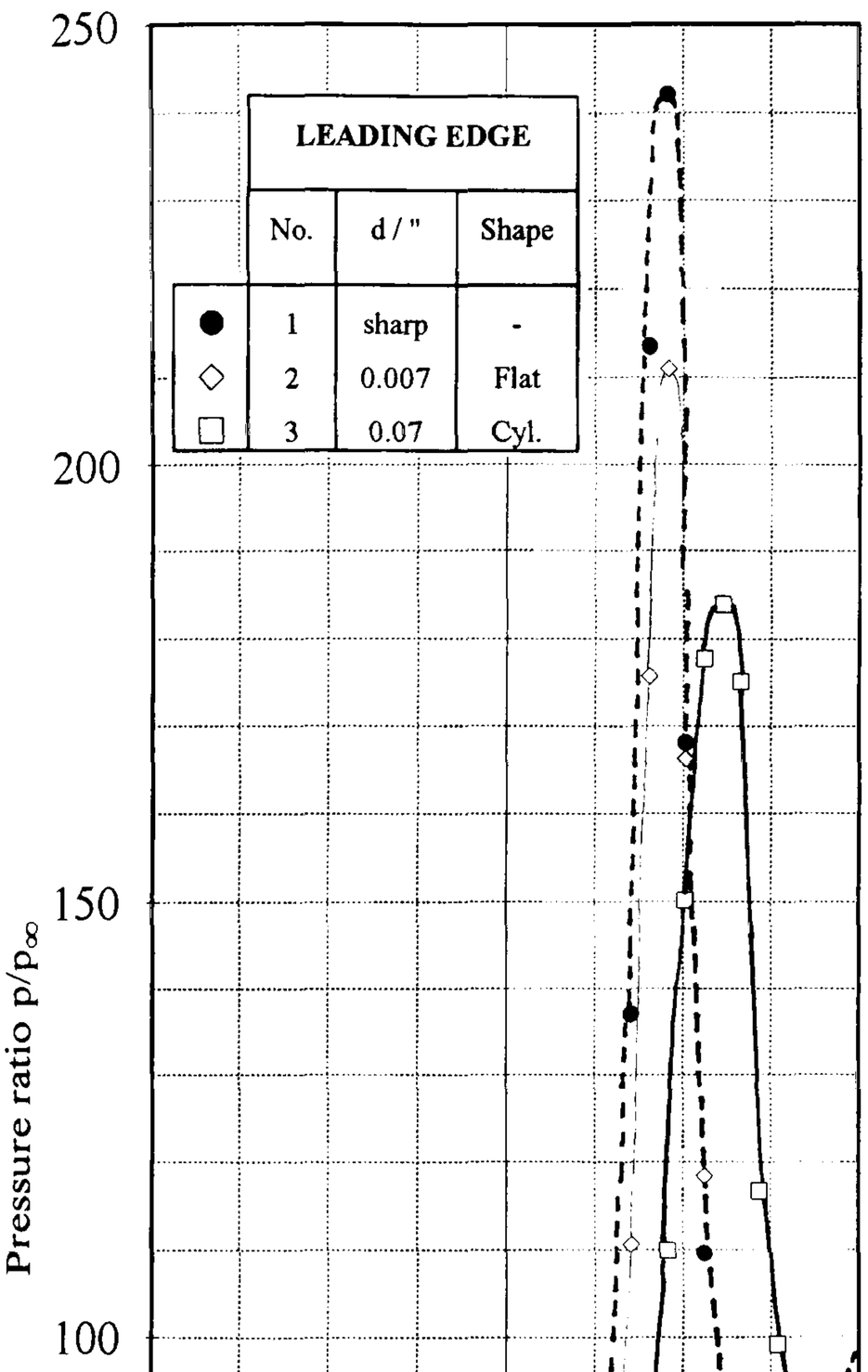

(i) small bluntness

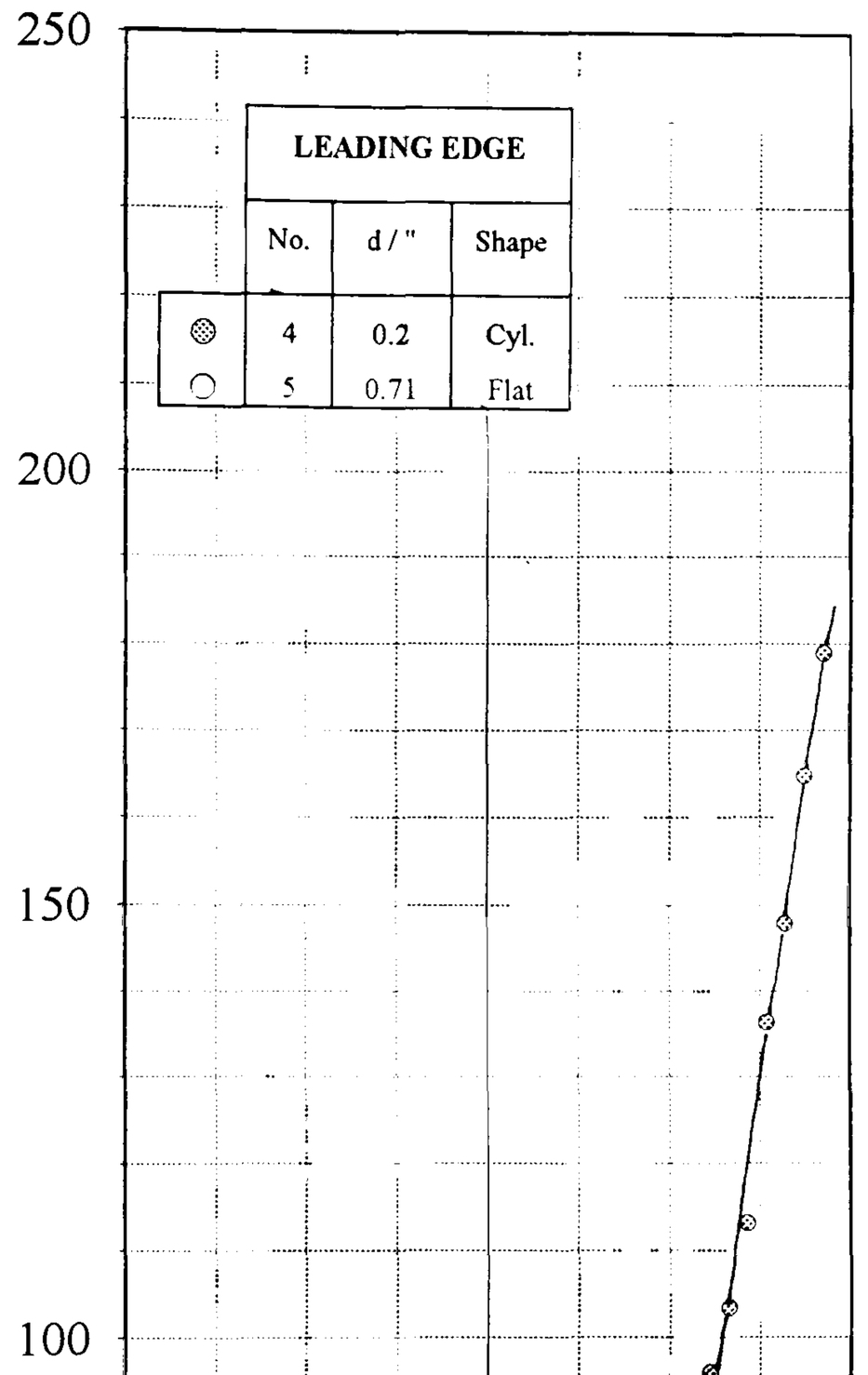

(ii) large bluntness

Figure 8-40 The effect of leading edge bluntness on the pressure distribution in well separated laminar flows - Holden and Moselle [1992]
(M_∞ = 19.8, Re_∞/cm = 0.34 × 10^4, L = 31.2 cm, $\alpha = 0°$, $\beta = 25°$)

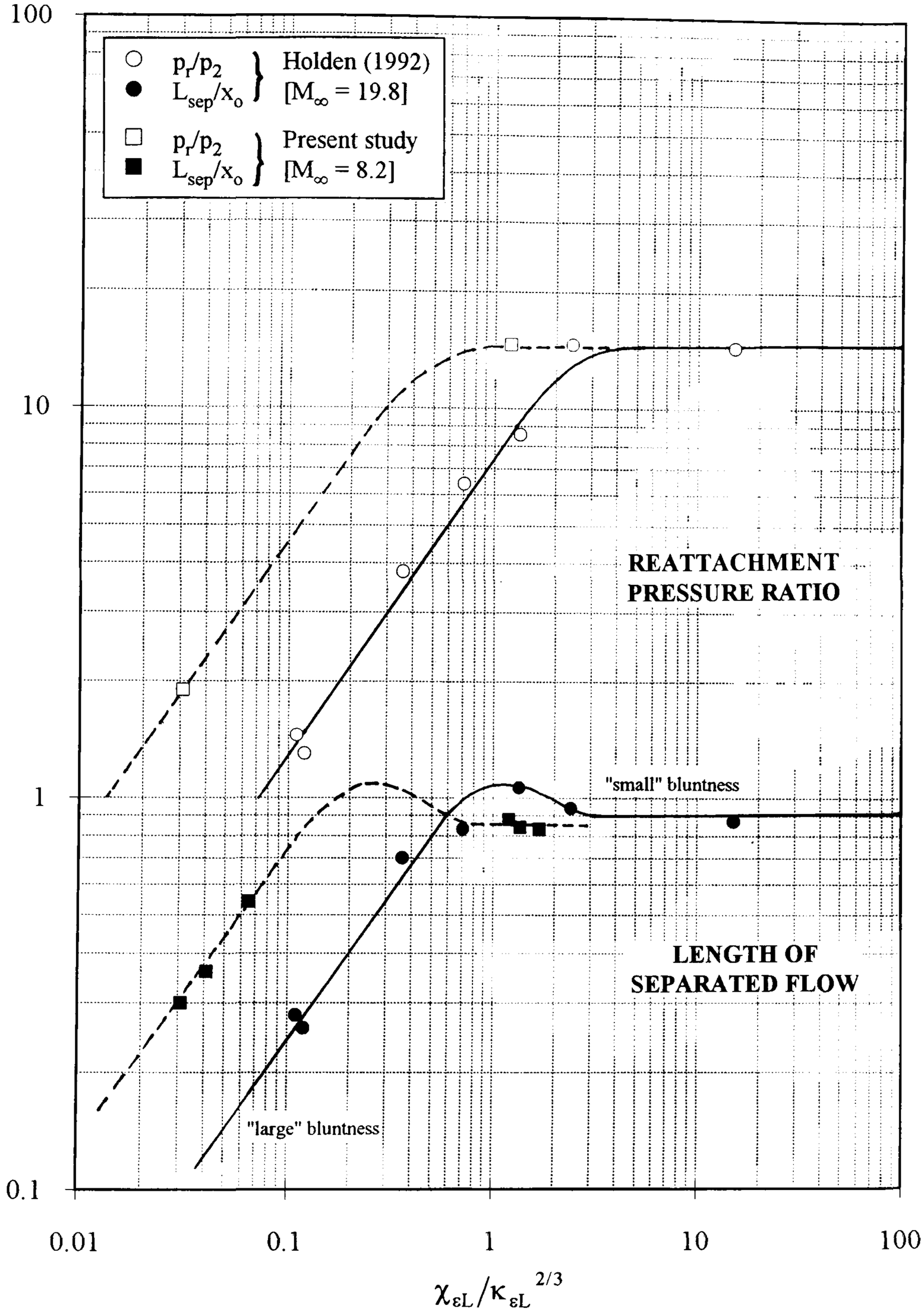

Figure 8-41 Correlation between the effect of leading edge bluntness on the length of separated flow and on the reattachment pressure ratio ($\alpha = 0°$, $\beta = 25°$)

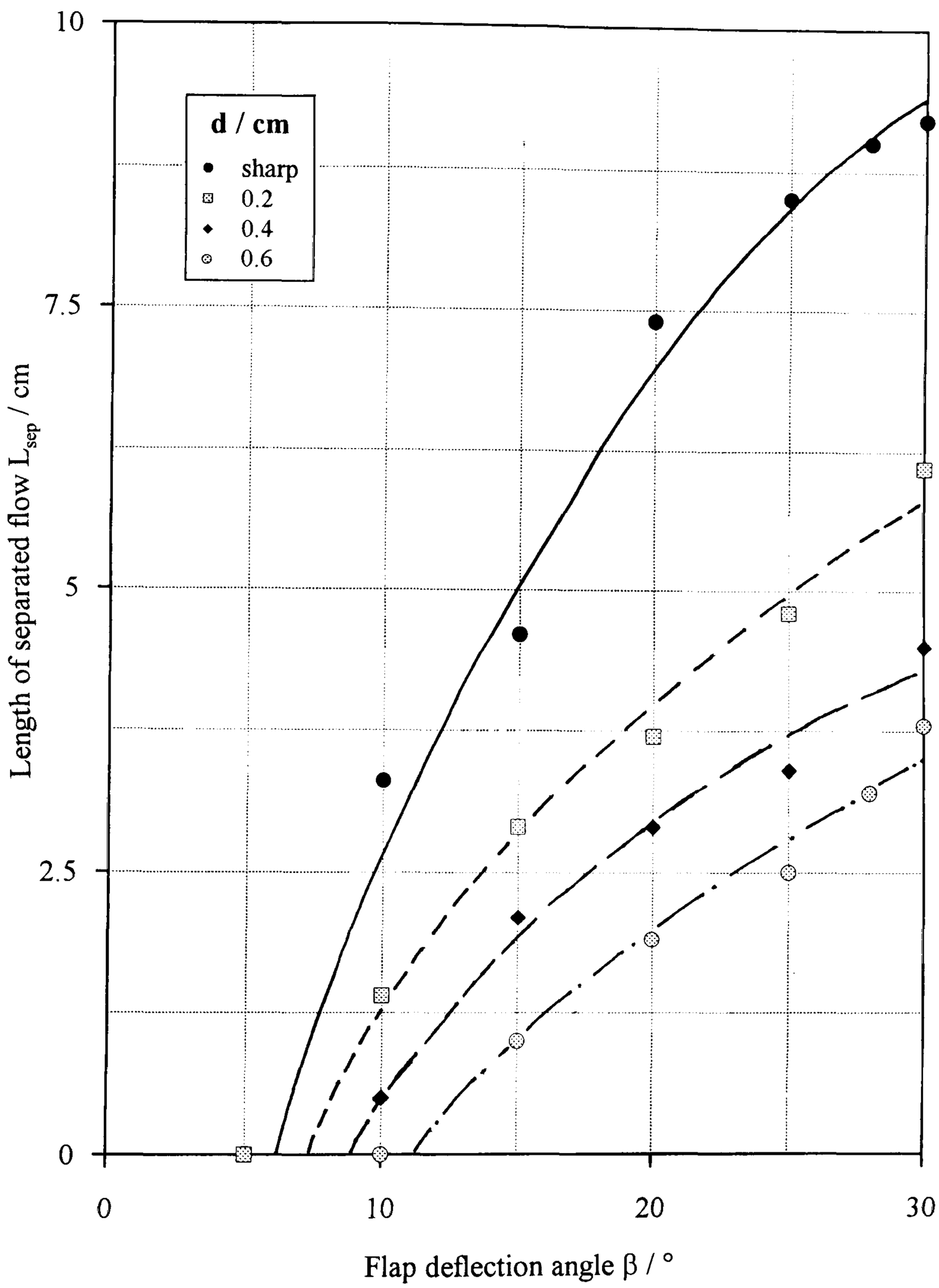

Figure 8-42 The effect of leading edge bluntness on the incipient separation flap angle ($M_\infty = 8.2$, $Re_\infty/cm = 9.0 \times 10^4$, L = 15.9 cm, $\alpha = 0°$)

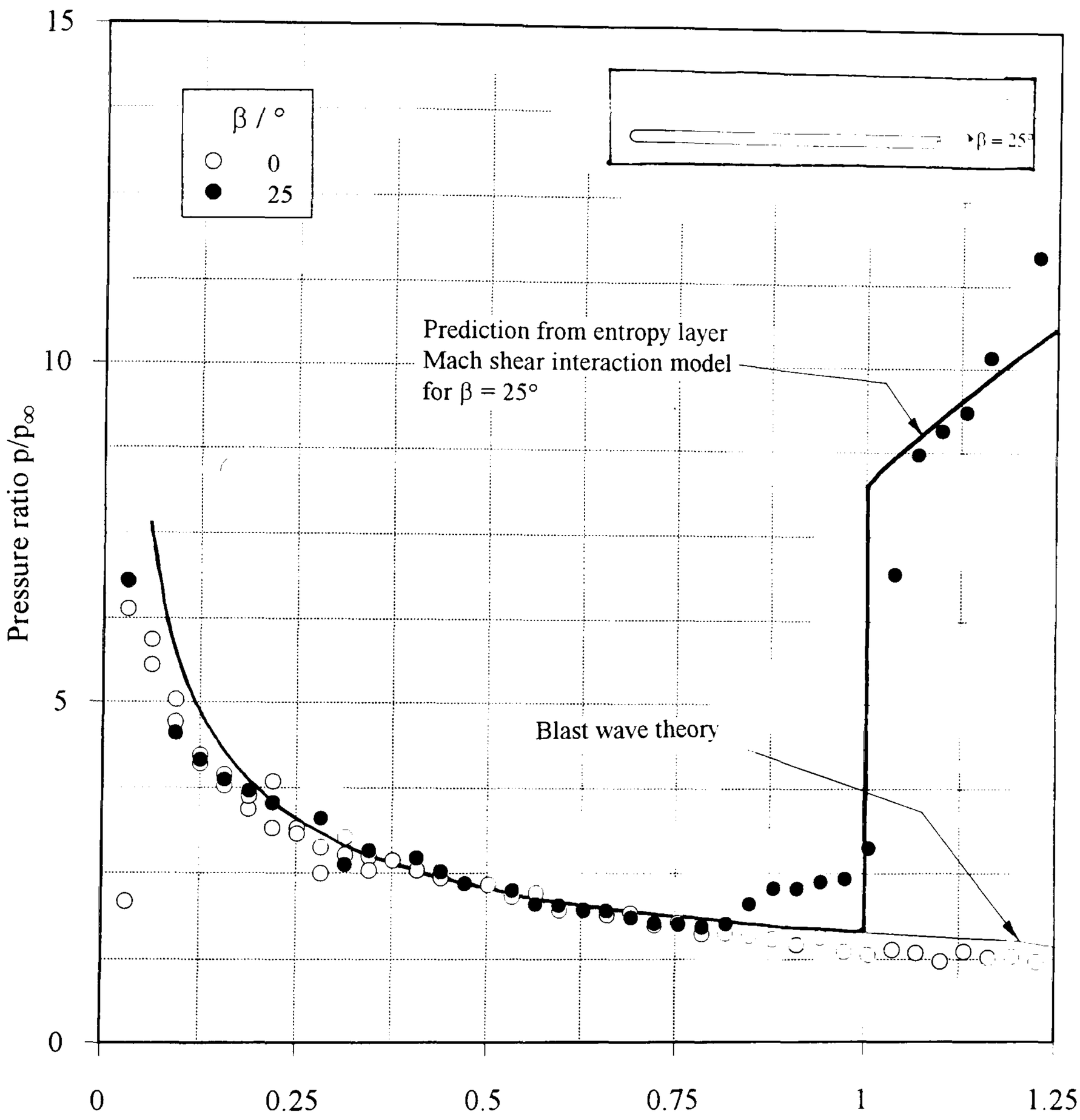

Figure 8-43 The effect of entropy layer Mach shear interaction on the flap pressure distribution
($M_\infty = 8.2$, $Re_\infty/cm = 9.0 \times 10^4$, L = 15.9 cm, $\alpha = 0°$, $\beta = 25°$, d = 6.0 mm, hemi-cylindrical LE)

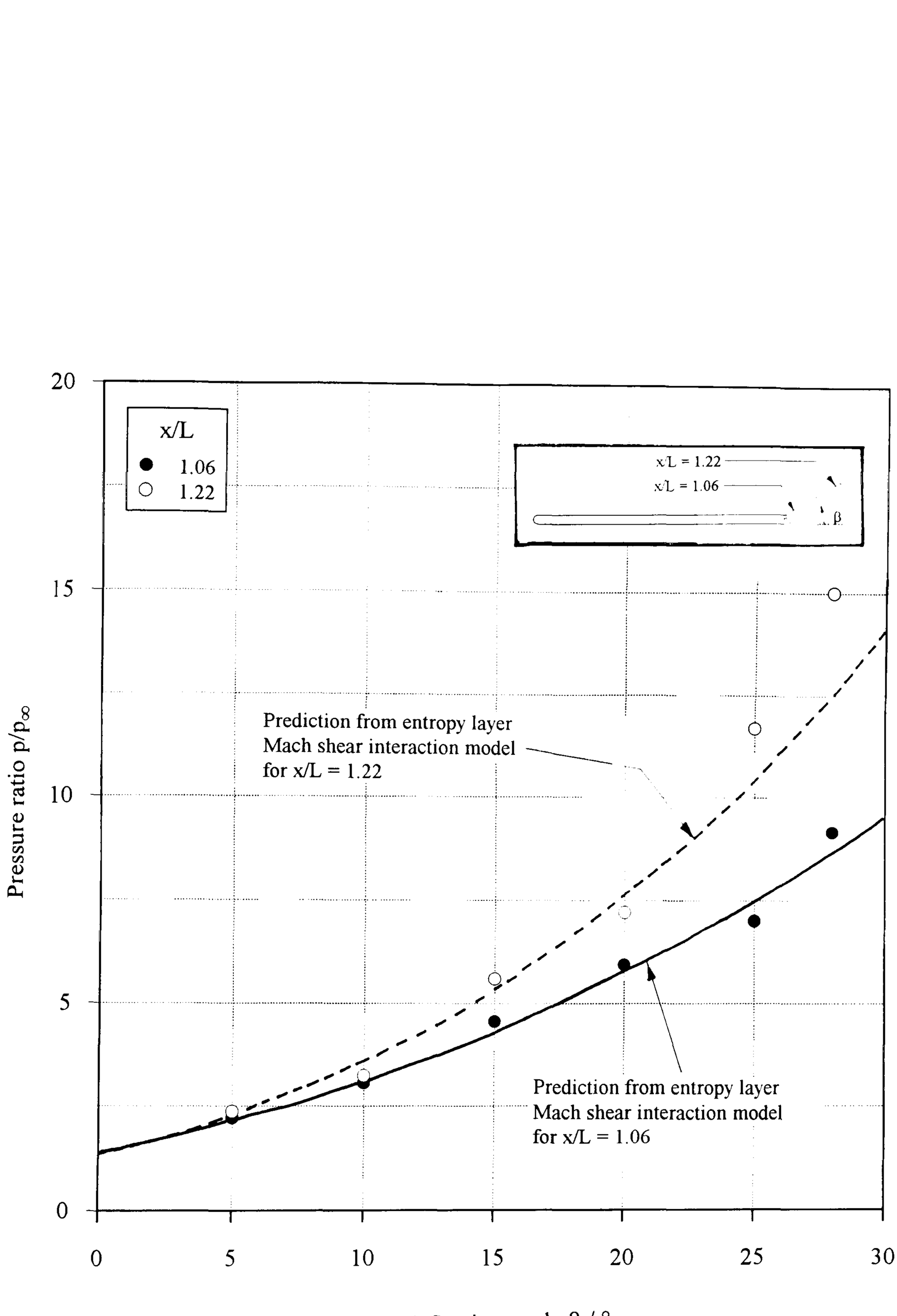

Figure 8-44 The effect of flap deflection on entropy layer Mach shear interaction
($M_\infty = 8.2$, $Re_\infty/cm = 9.0 \times 10^4$, L = 15.9 cm, $\alpha = 0°$, d = 6.0 mm, hemi-cylindrical LE)

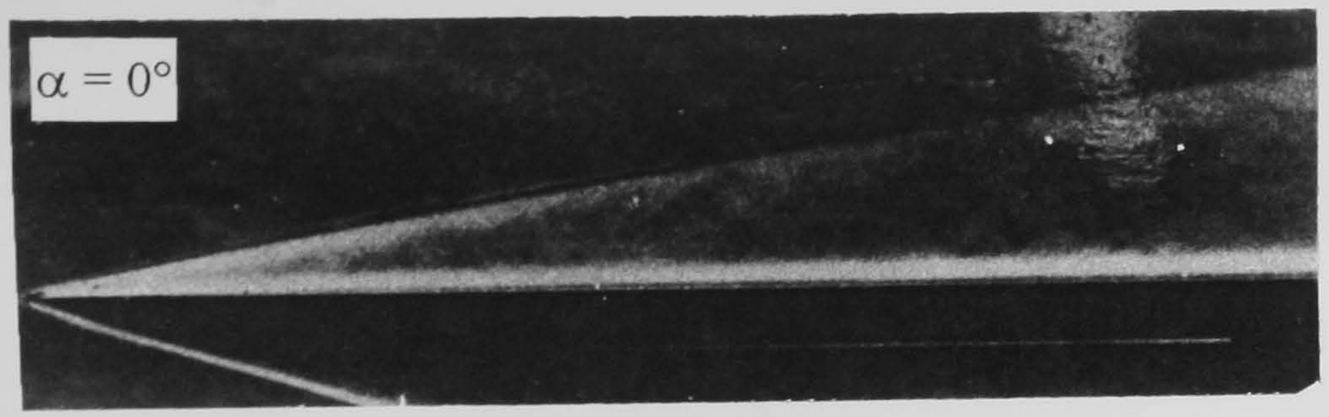

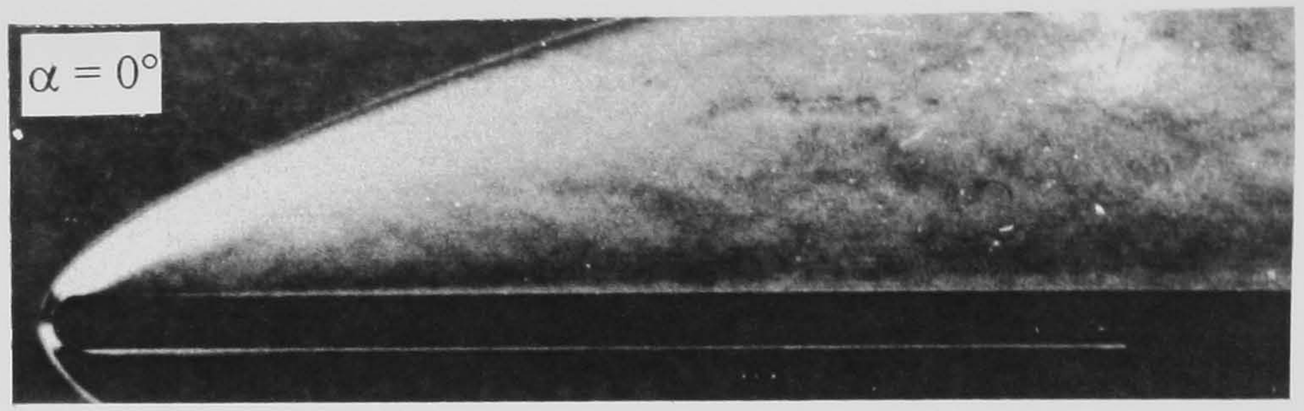

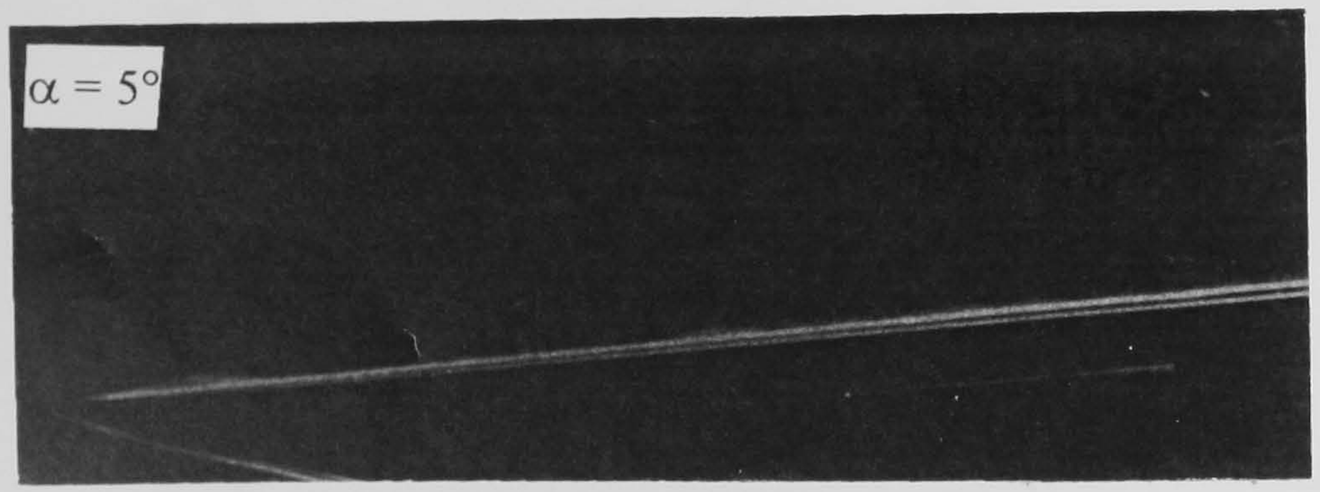

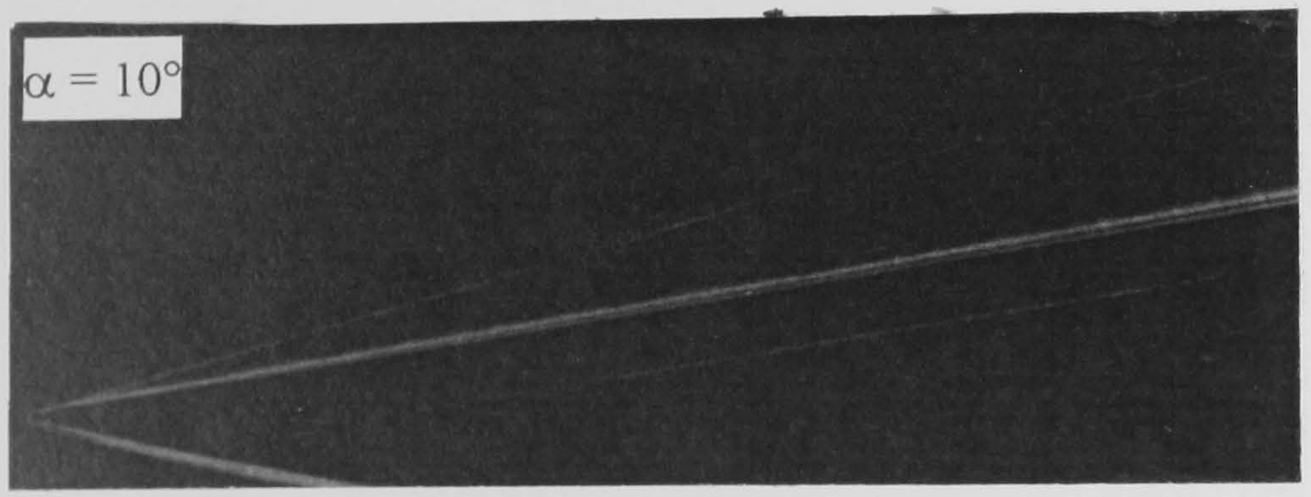

(i) sharp leading edge

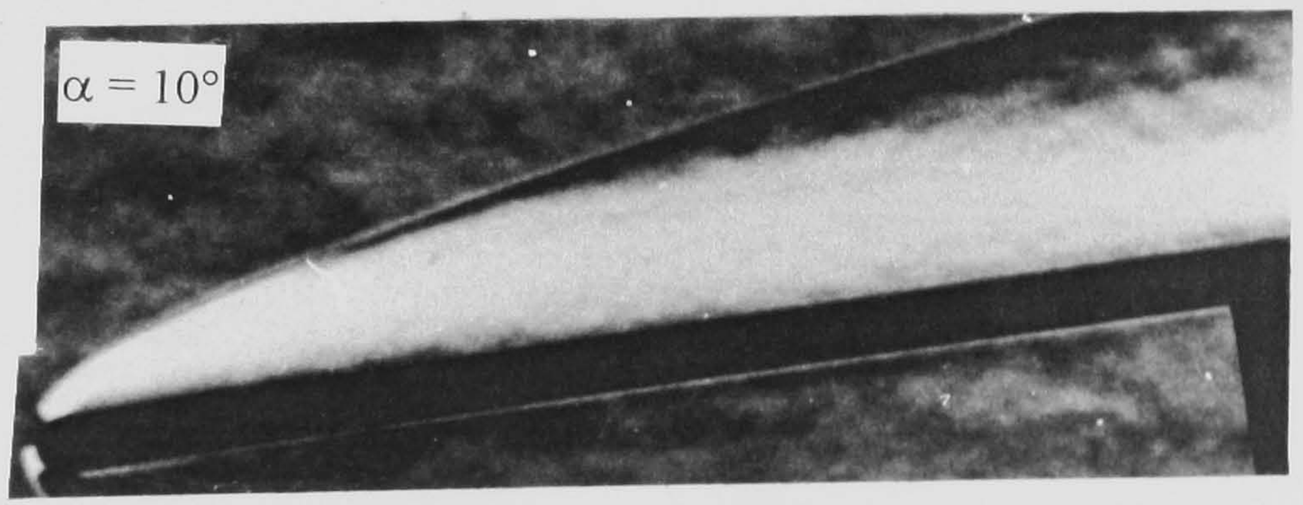

(ii) blunt leading edge
(d = 6.0 mm)

Figure 8-45 The combined effects of incidence and bluntness on the leading edge shock structure ($M_\infty = 8.2$, $Re_\infty/cm = 9.0 \times 10^4$)

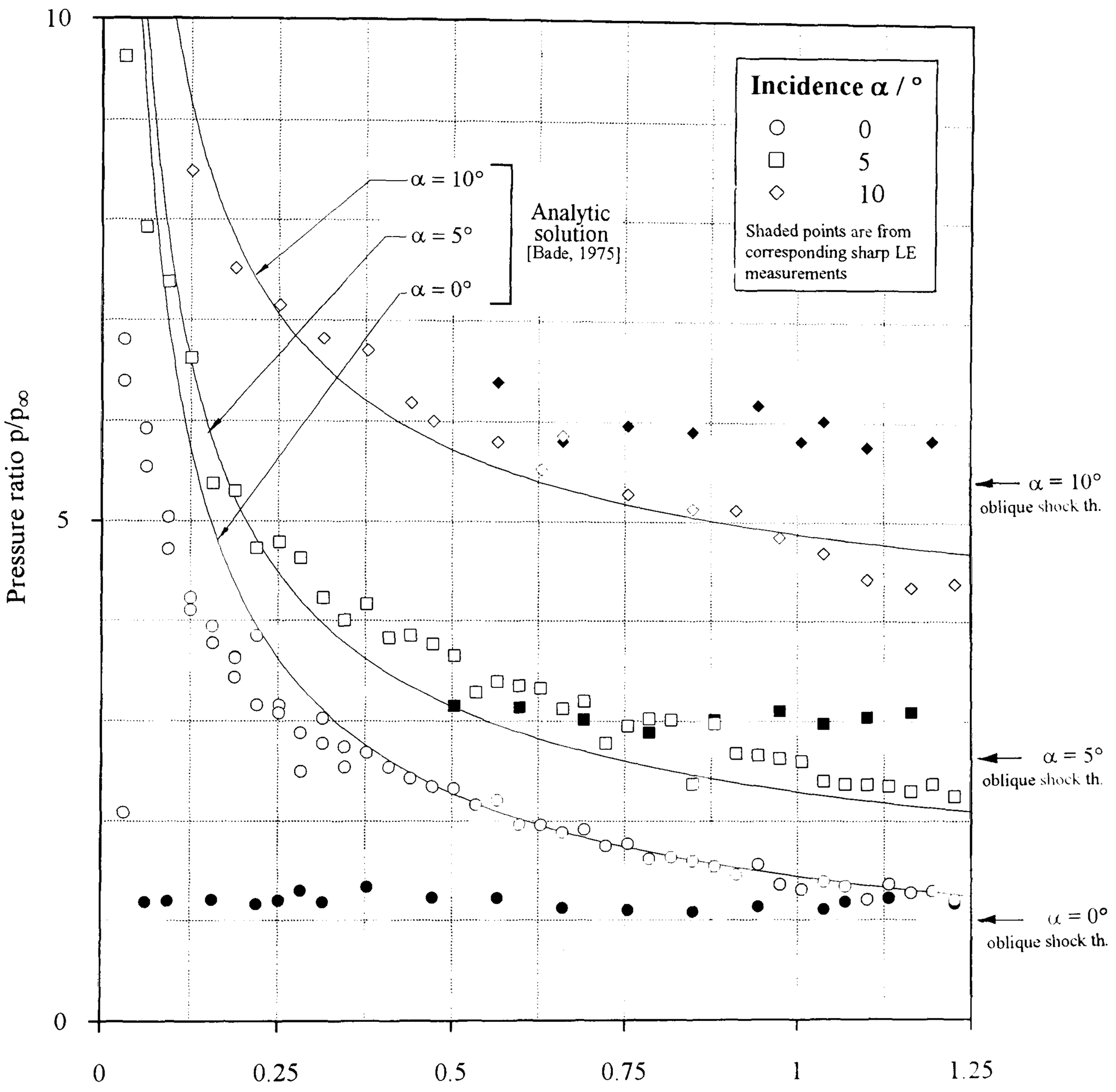

Figure 8-46 The combined effects of incidence and bluntness on flat plate pressure distribution ($M_\infty = 8.2$, $Re_\infty/cm = 9.0 \times 10^4$, d = 6.0 mm, hemi-cylindrical LE)

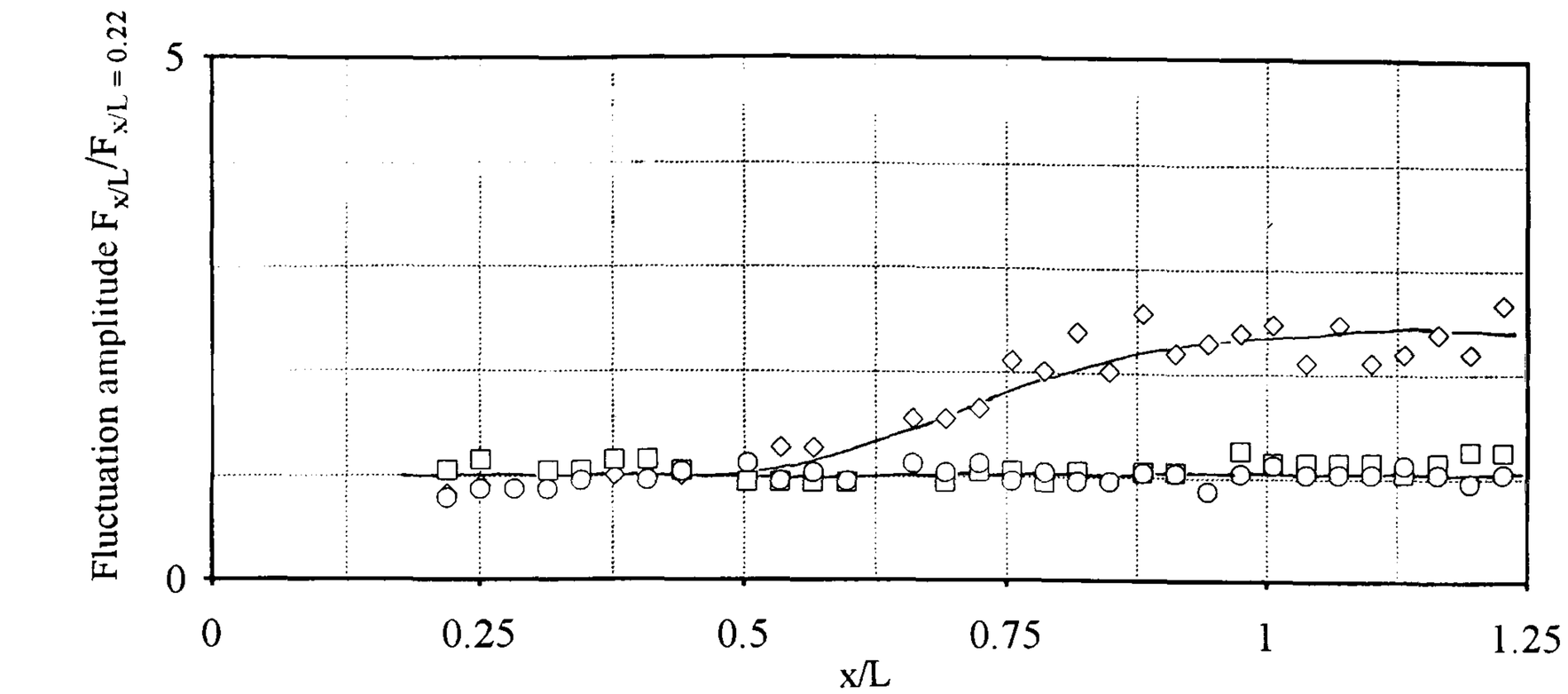

(i) fluctuation distribution

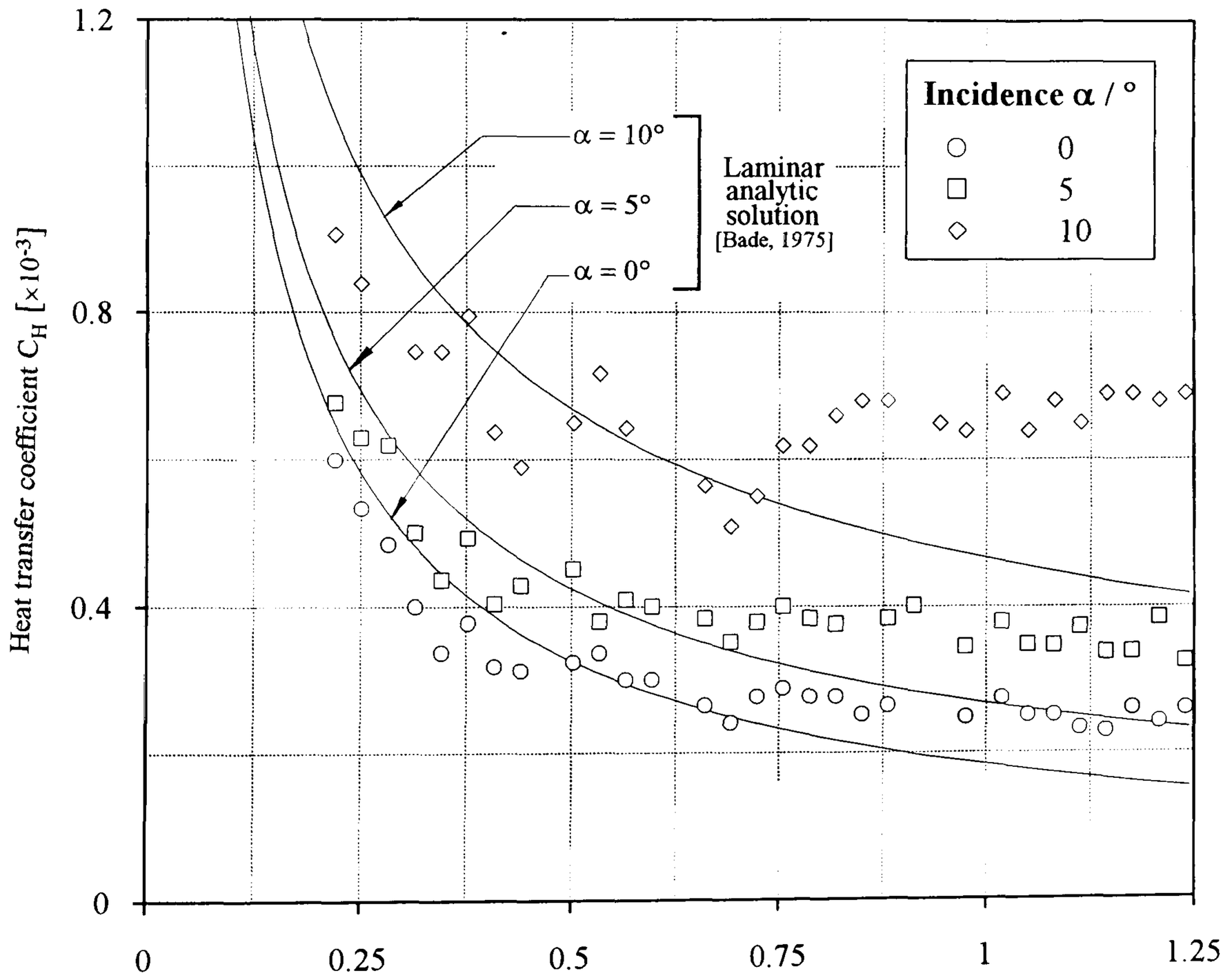

(ii) heat transfer distribution

Figure 8-47 The combined effects of incidence and bluntness on flat plate boundary layer transition ($M_\infty = 8.2$, $Re_\infty/cm = 9.0 \times 10^4$, d = 6.0 mm, hemi-cylindrical LE)

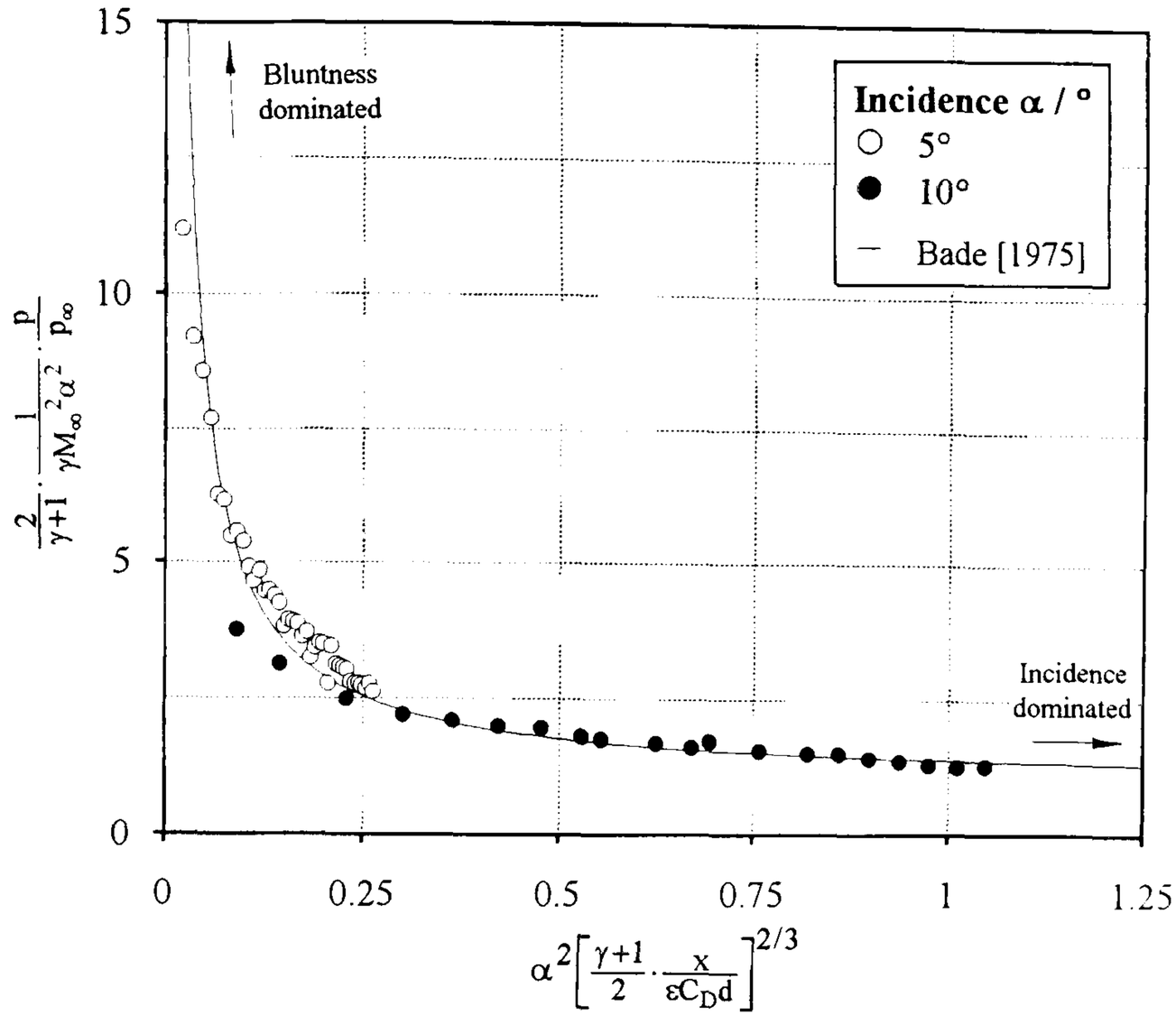

(i) pressure

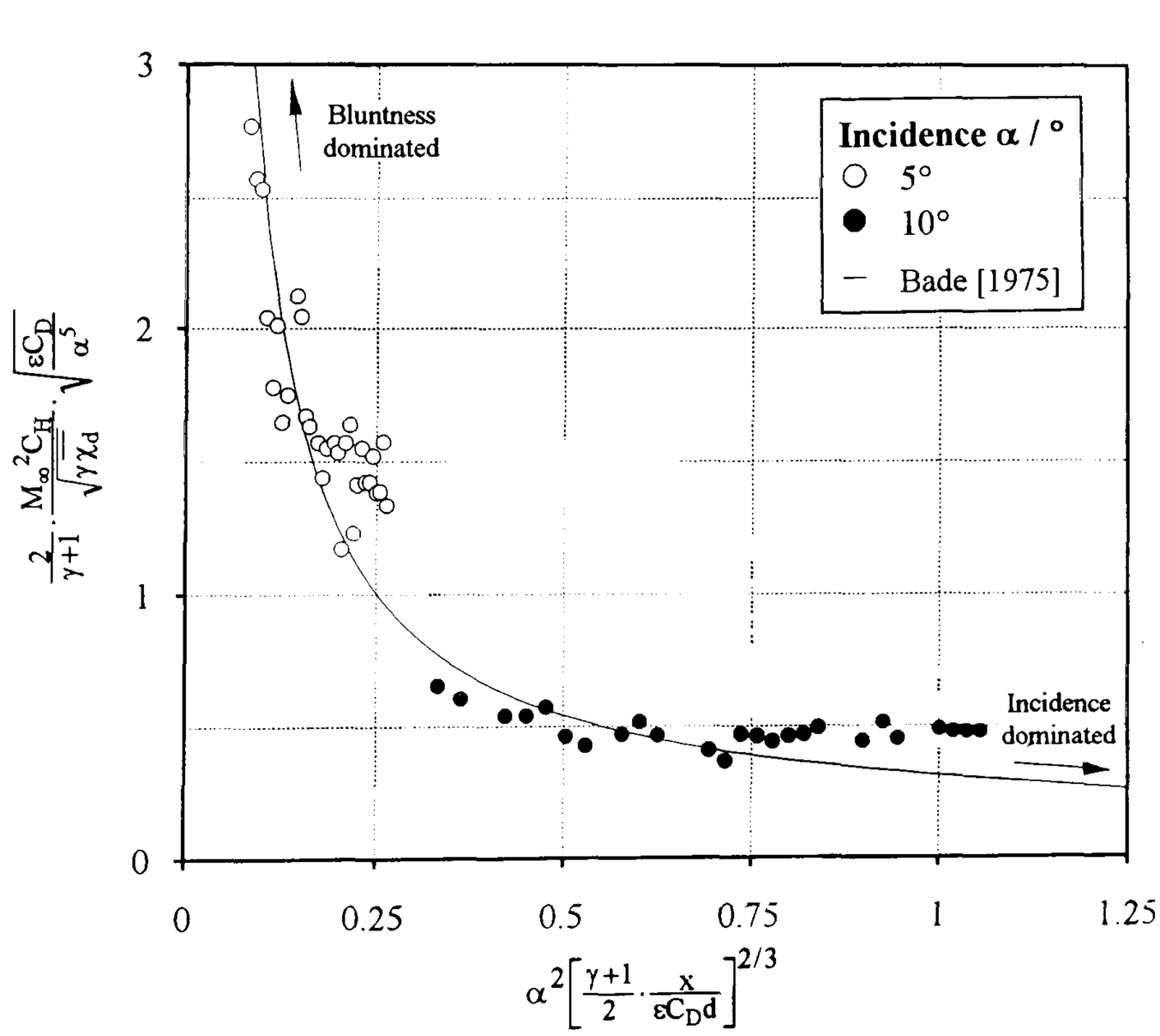

(ii) heat transfer

Figure 8-48 The effect of flat plate incidence on bluntness and incidence dominated regions of flow ($M_\infty = 8.2$, $Re_\infty/cm = 9.0 \times 10^4$, d = 6.0 mm, hemi-cylindrical LE)

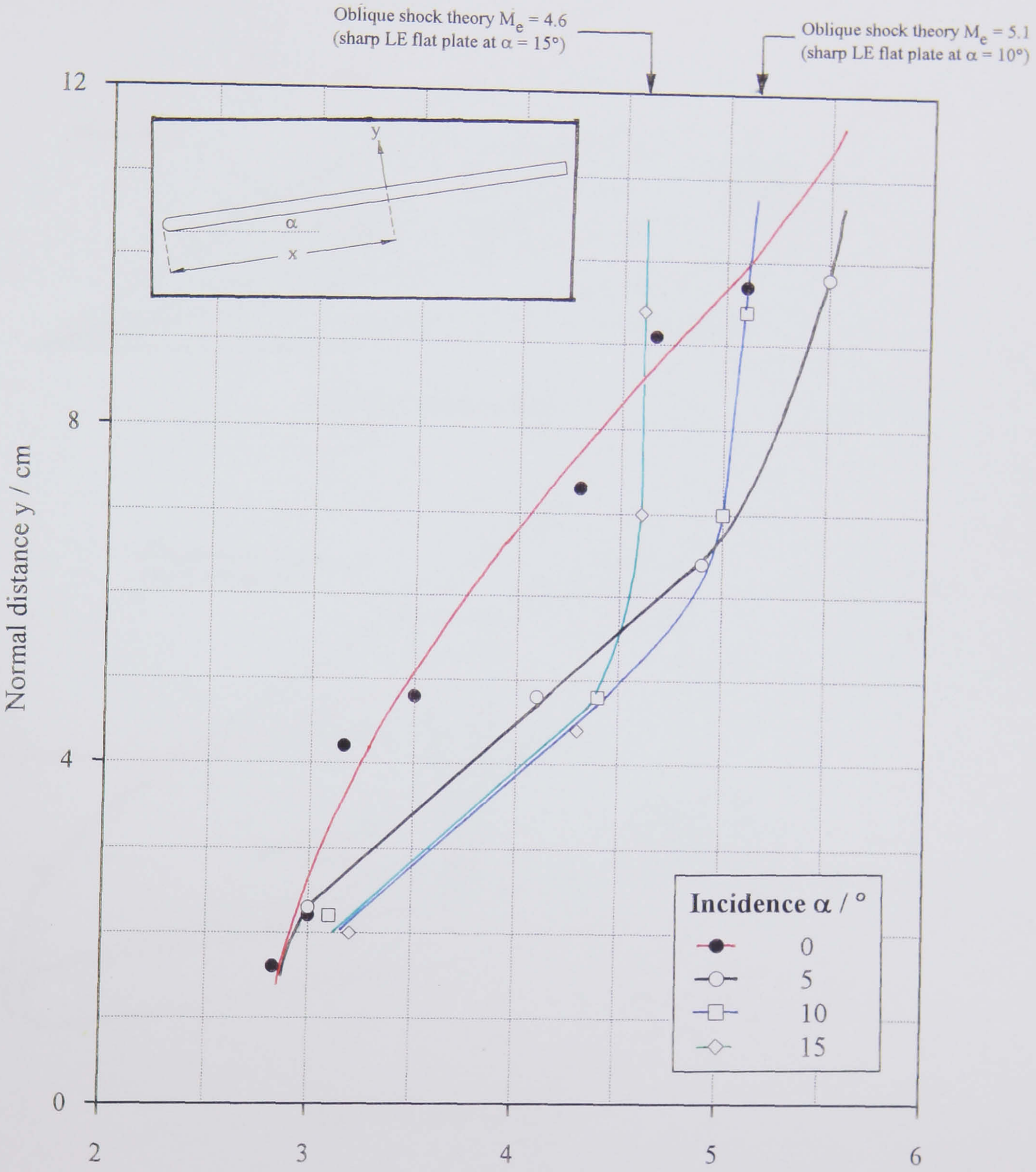

Figure 8-49 The effect of incidence on entropy layer Mach number profiles - Deveikis et al, 1973 (M_∞ = 7.0, Re_∞/cm = 1.3 × 10^4, d = 9.6 mm, x/d = 153.4, hemi-cylindrical LE)

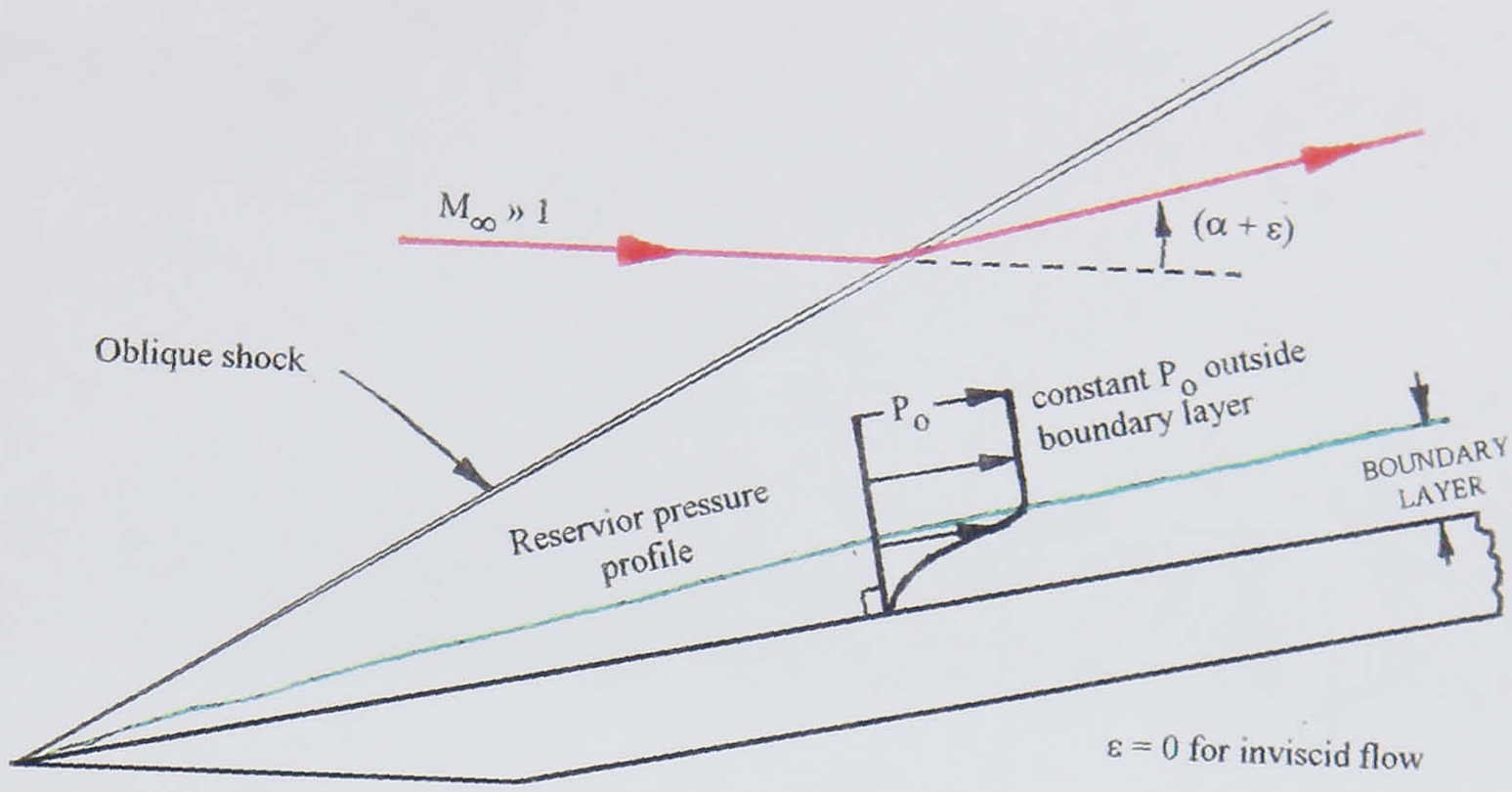

(a) sharp leading edge

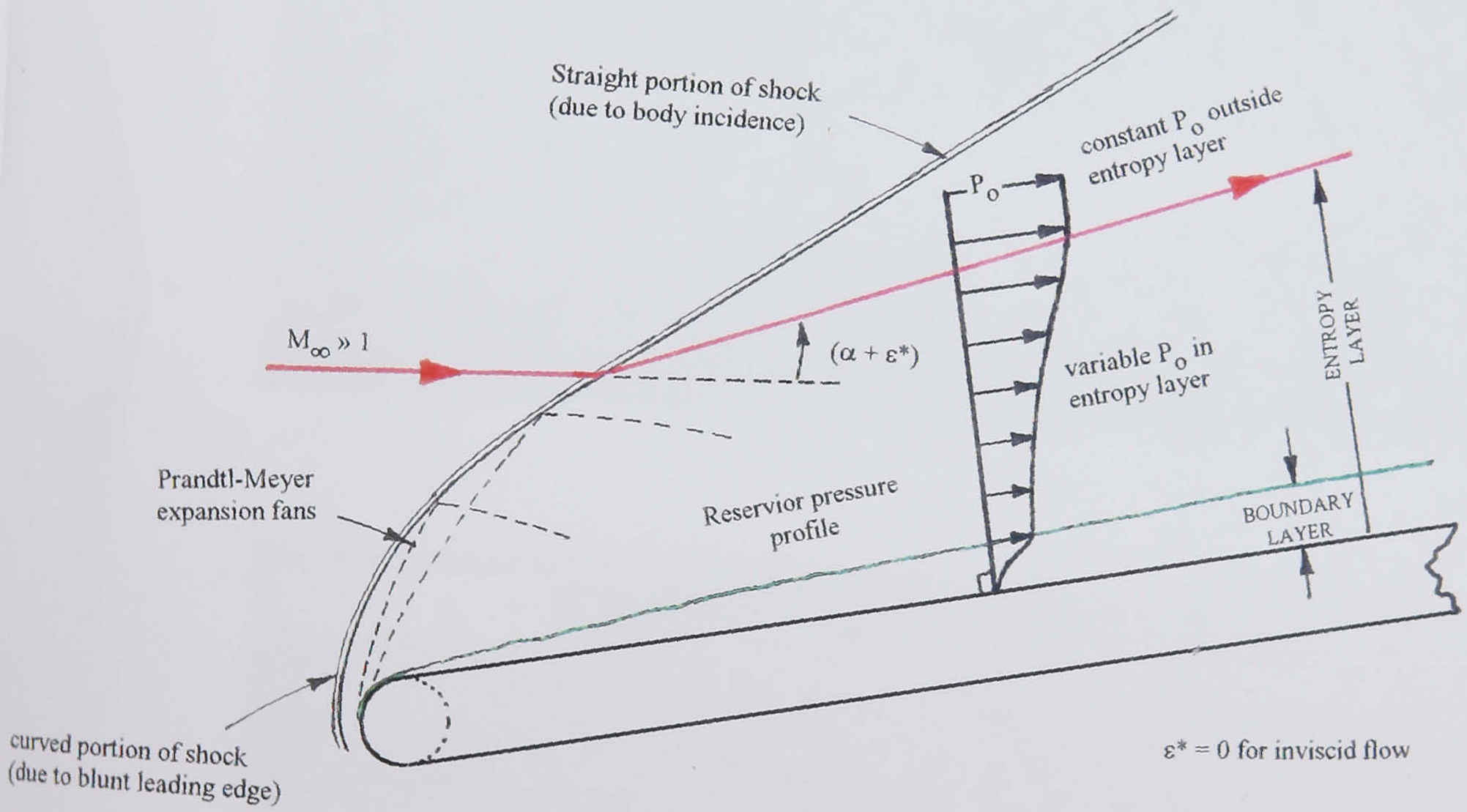

(b) blunt leading edge

Figure 8-50 The effect of leading edge bluntness on the flow structure over a flat plate at incidence

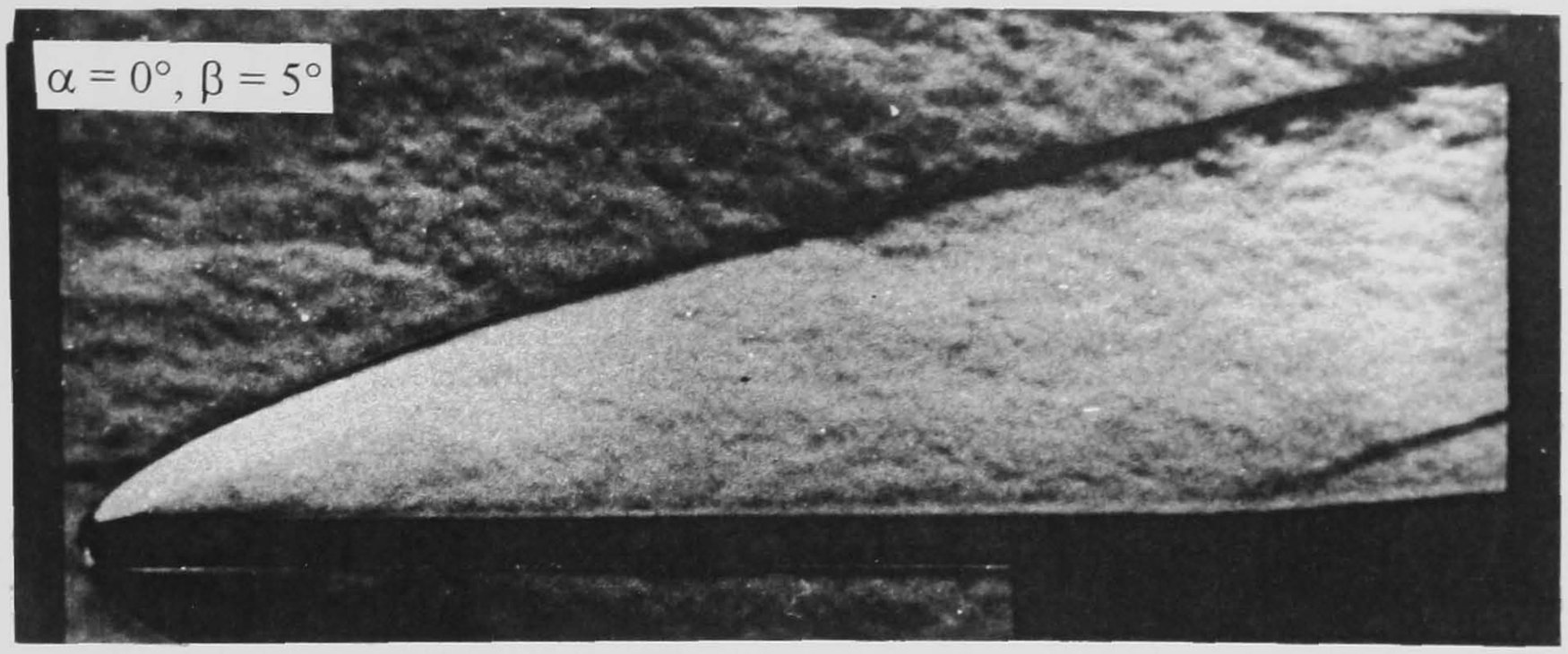

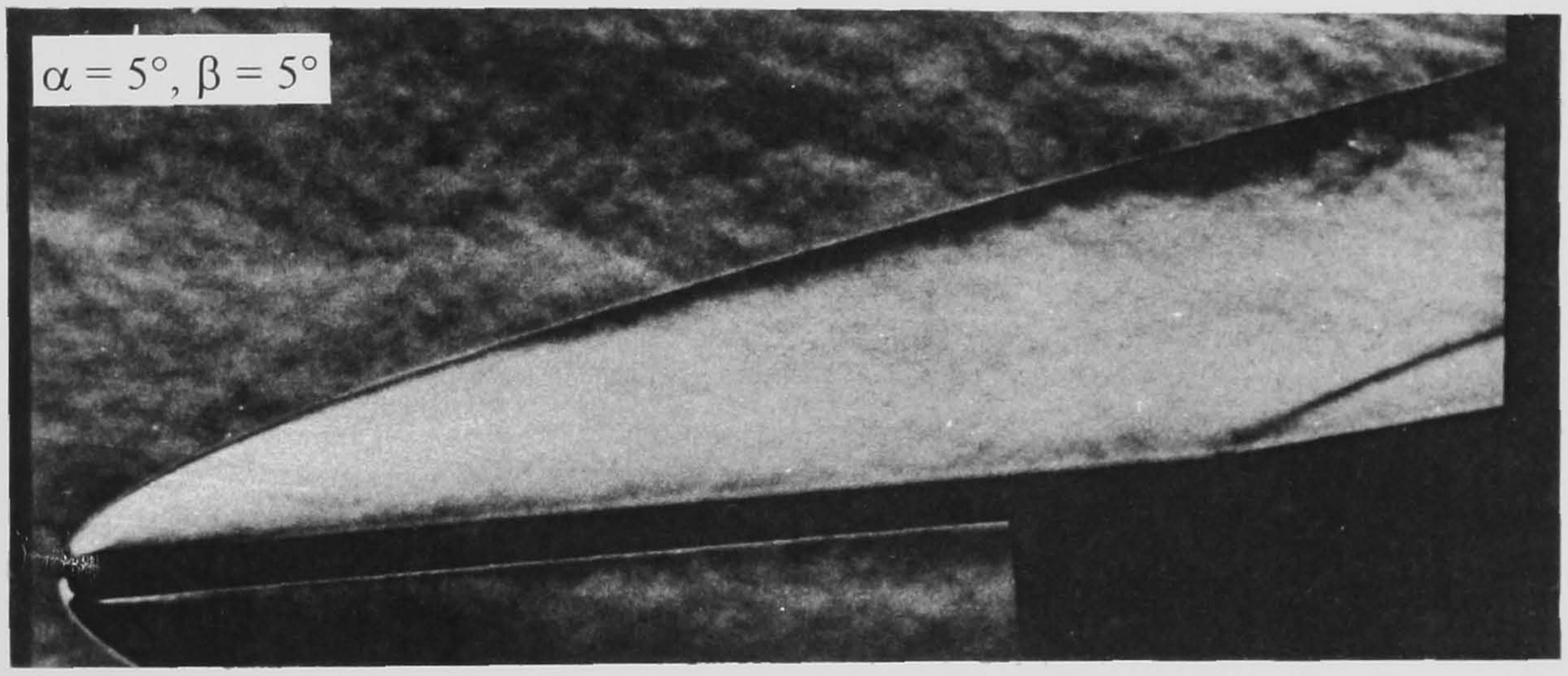

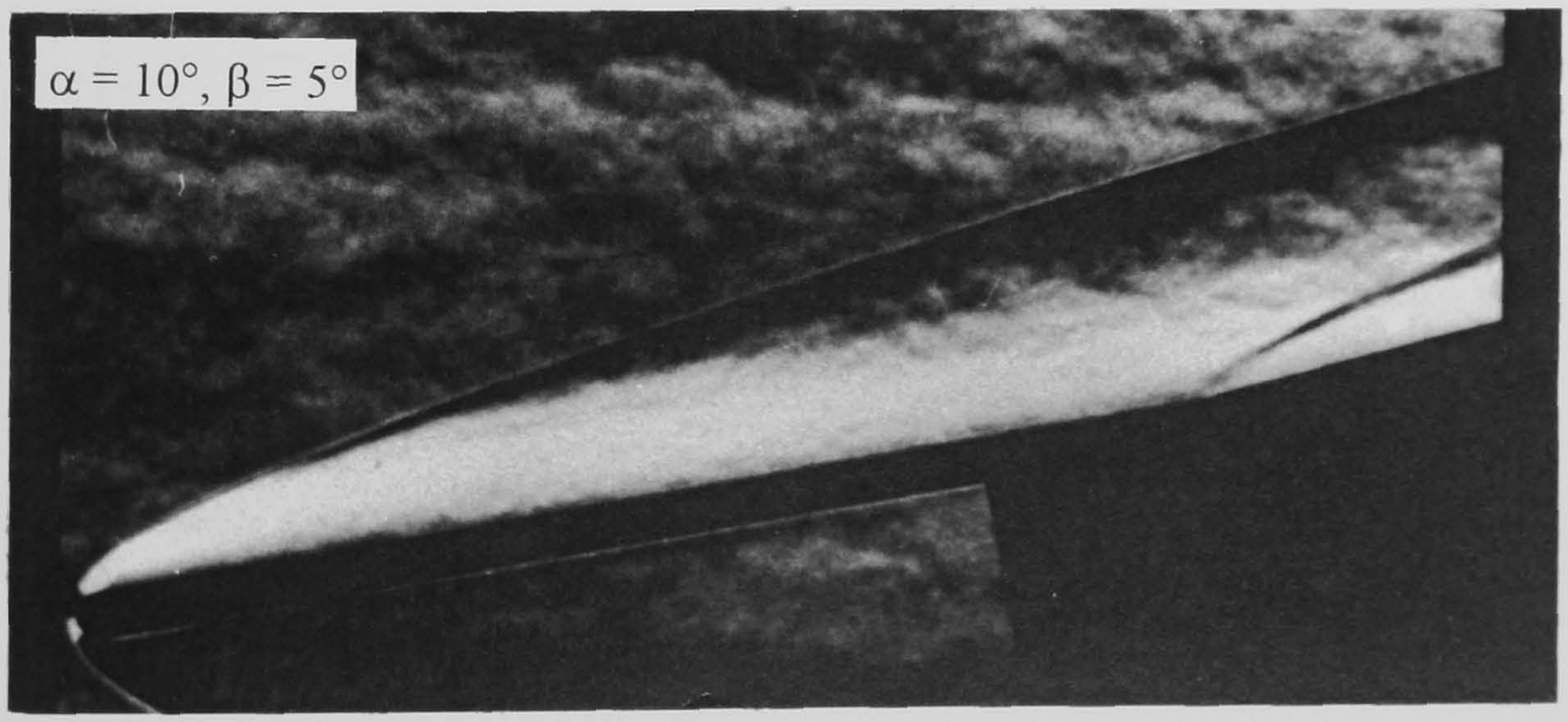

Figure 8-51 The combined effects of bluntness and incidence on attached flows ($M_\infty = 8.2$, $Re_\infty/cm = 9.0 \times 10^4$, L = 15.9 cm)

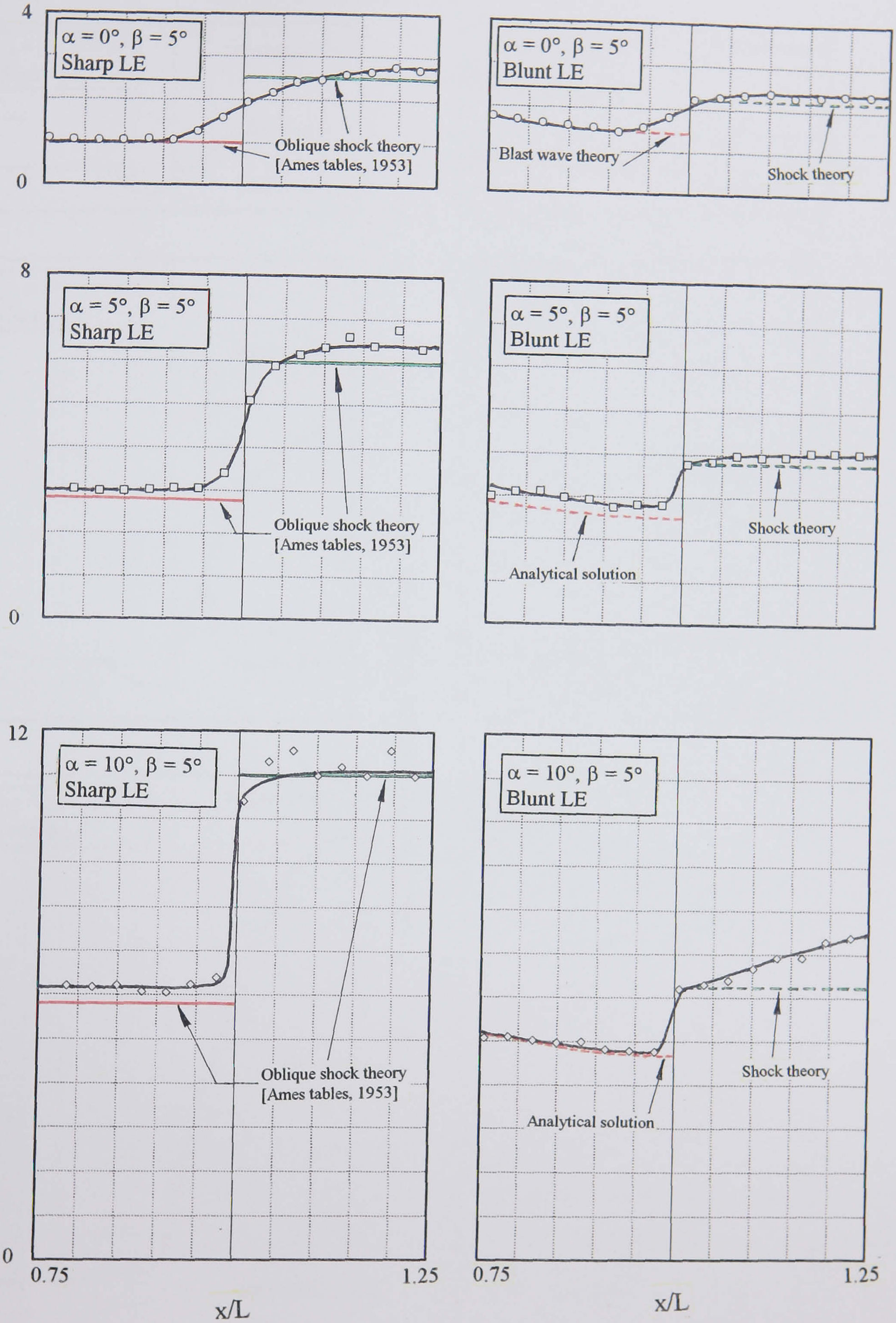

(i) sharp leading edge

(ii) blunt leading edge
[d = 6.0 mm, hemi-cylindrical LE]

Figure 8-52 The combined effects of bluntness and incidence on pressure distribution in attached flows ($M_\infty = 8.2$, $Re_\infty/cm = 9.0 \times 10^4$, $\beta = 5°$)

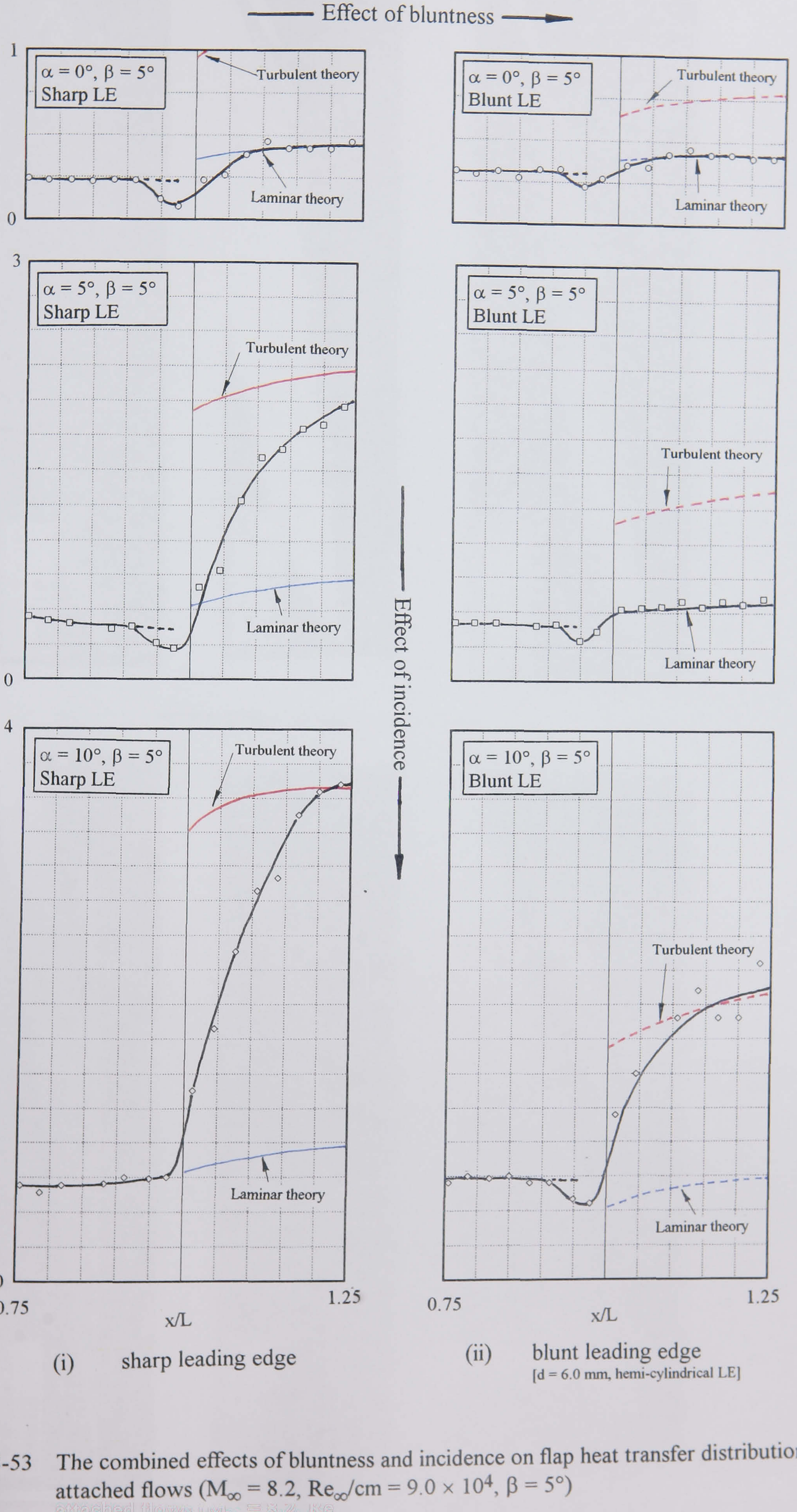

(i) sharp leading edge

(ii) blunt leading edge
[d = 6.0 mm, hemi-cylindrical LE]

Figure 8-53 The combined effects of bluntness and incidence on flap heat transfer distribution in attached flows ($M_\infty = 8.2$, $Re_\infty/cm = 9.0 \times 10^4$, $\beta = 5°$)

Effect of bluntness →

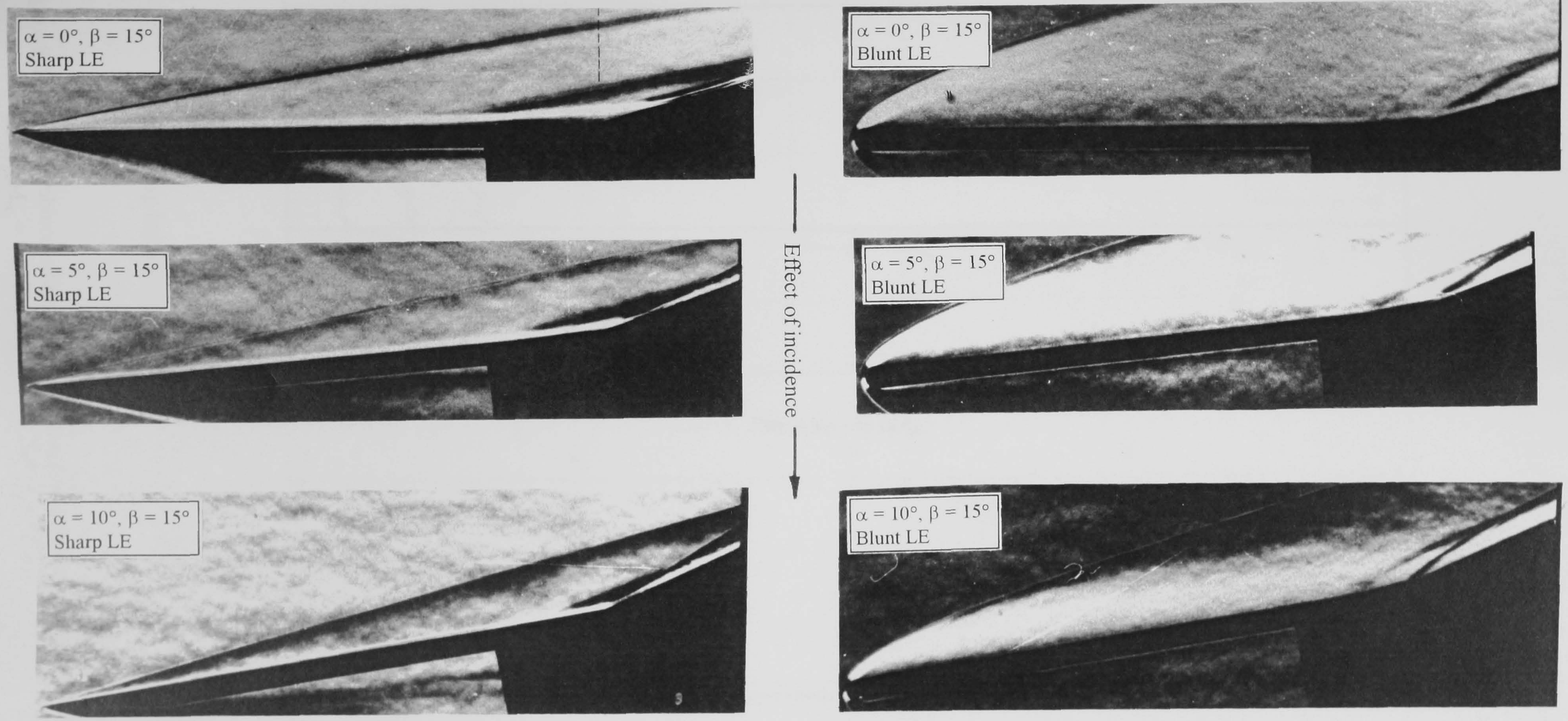

(i) sharp leading edge

(ii) blunt leading edge
[d = 6.0 mm, hemi-cylindrical LE]

Figure 8-54 The combined effects of bluntness and incidence on the flap shock structure in separated flows ($M_\infty = 8.2$, $Re_\infty/cm = 9.0 \times 10^4$, $\beta = 15°$)

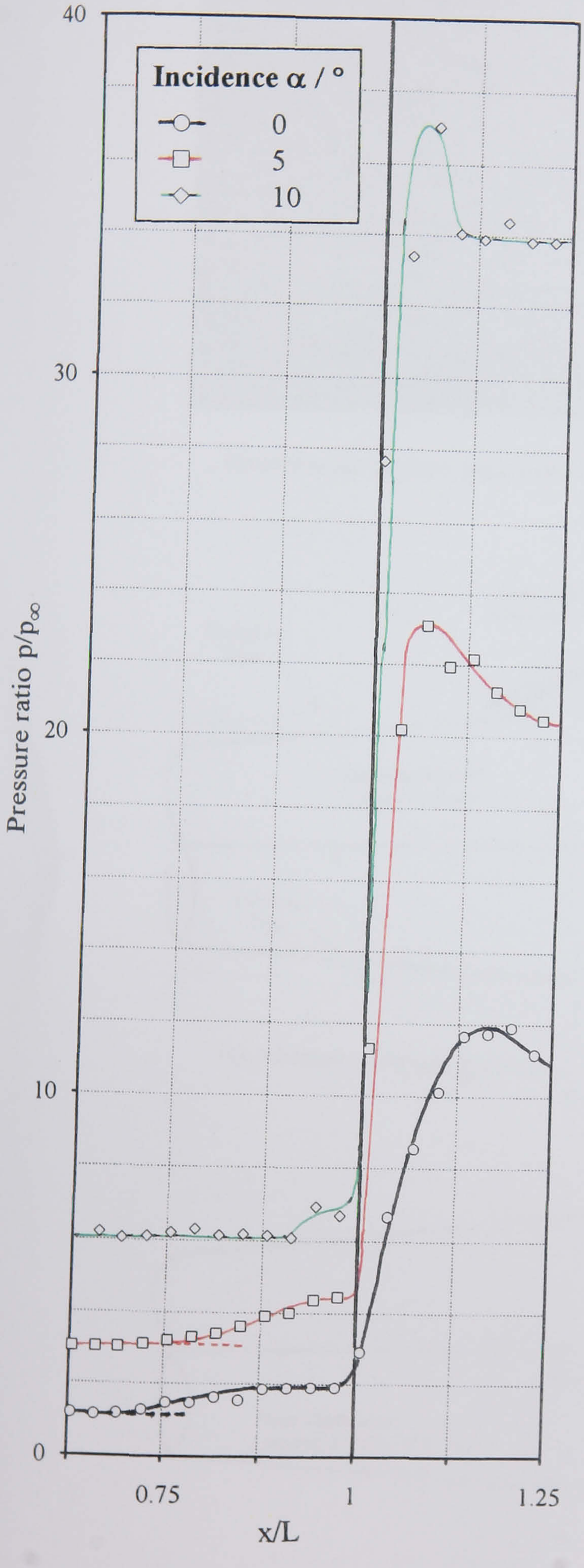

(i) sharp leading edge

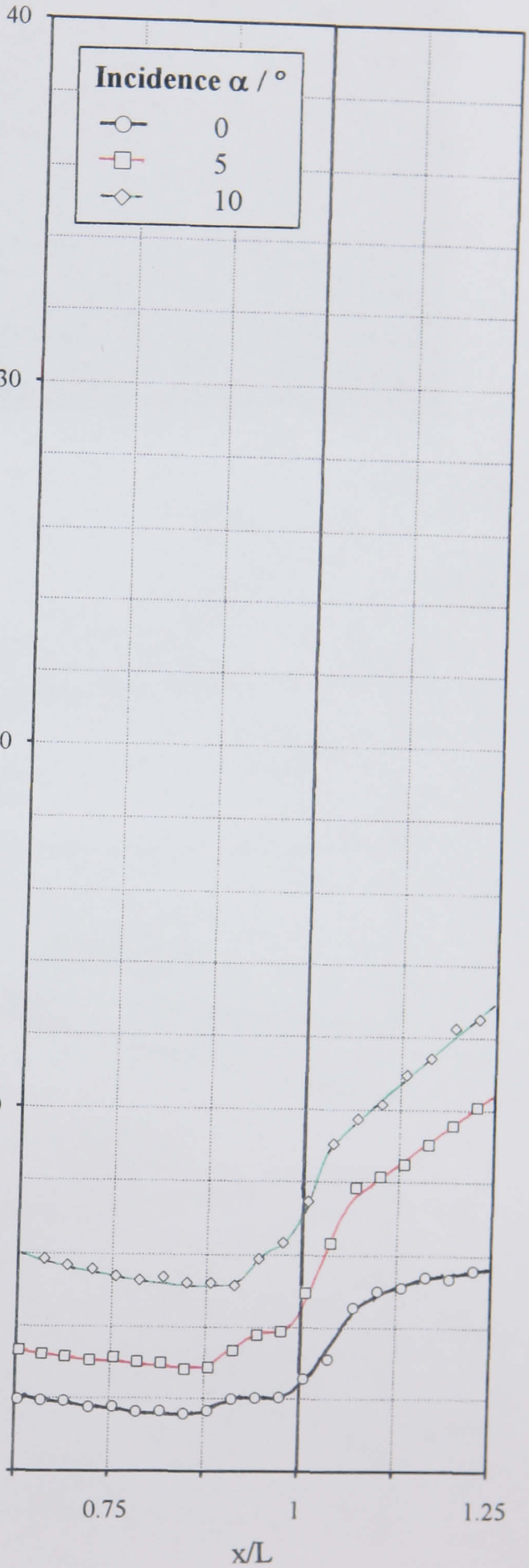

(ii) blunt leading edge
[d = 6.0 mm, hemi-cylindrical LE]

Figure 8-55 The combined effects of bluntness and incidence on pressure distribution in separated flows ($M_\infty = 8.2$, $Re_\infty/cm = 9.0 \times 10^4$, $\beta = 15°$)

(a) schlieren photograph

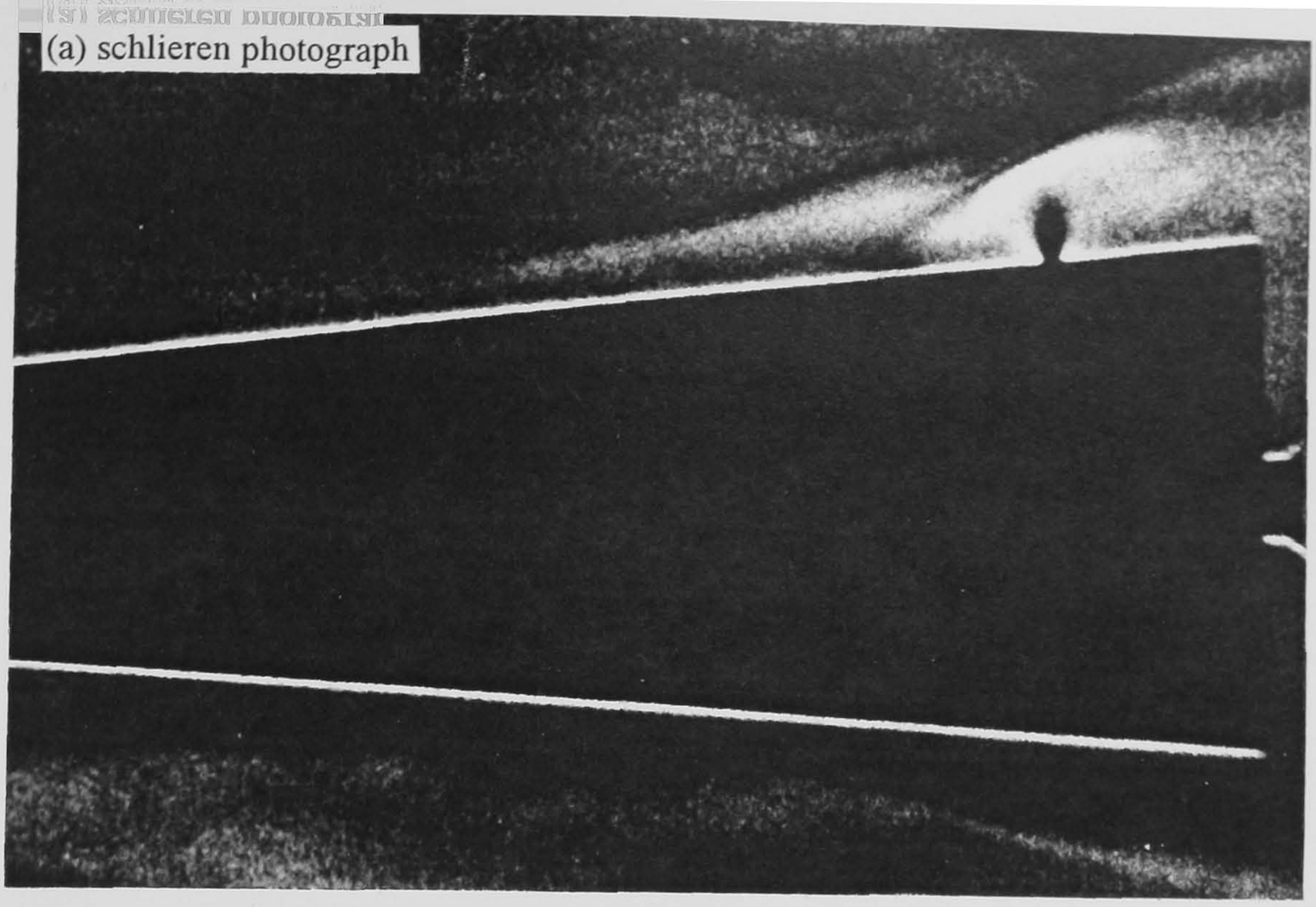

(b) schematic diagram (side view)

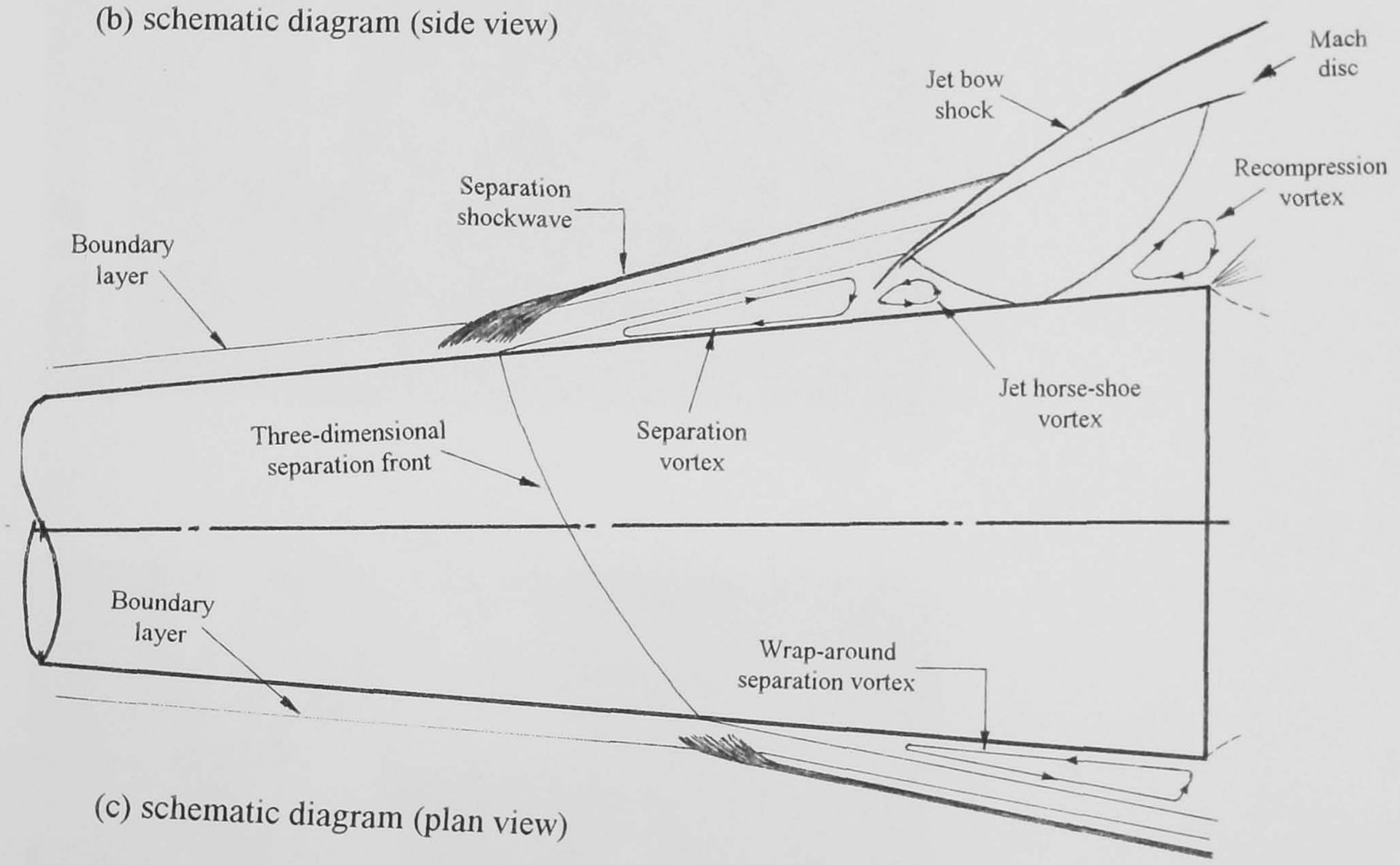

(c) schematic diagram (plan view)

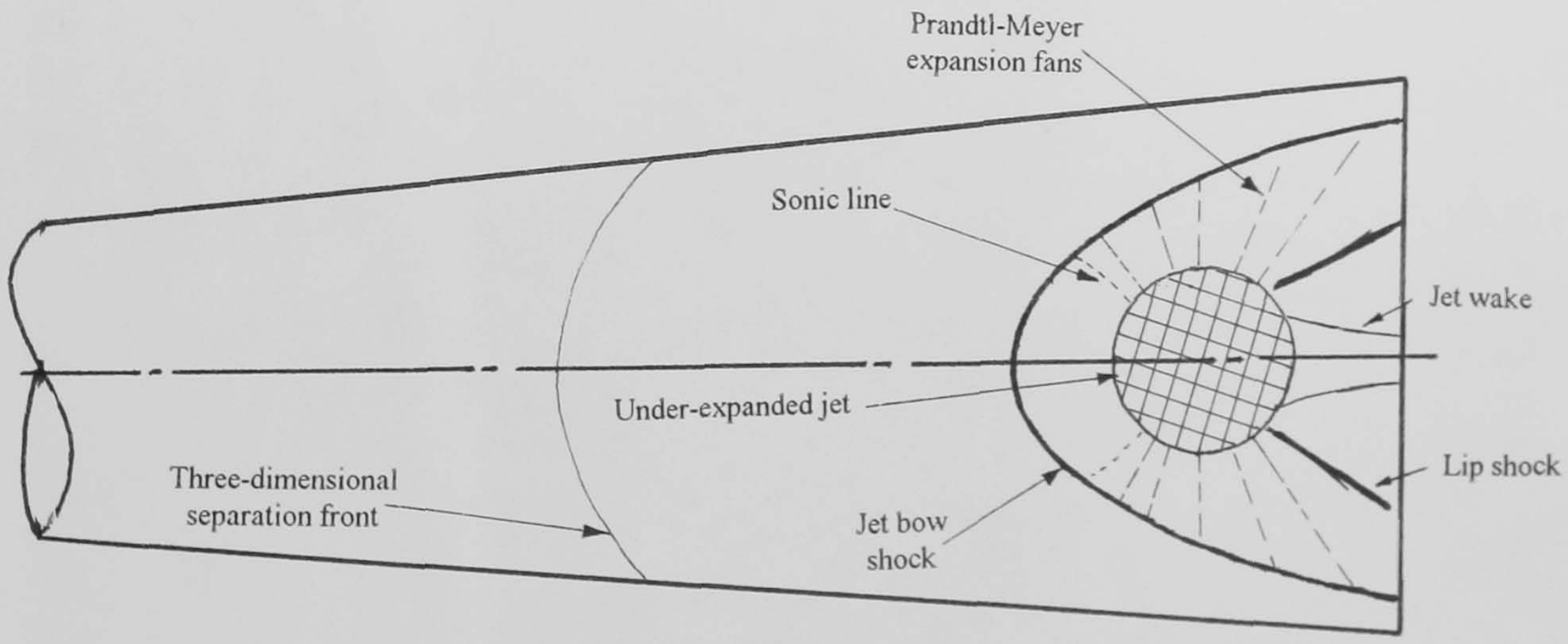

Figure 9-1 Flow structures associated with the interaction of a supersonic under-expanded jet with a hypersonic crossflow
($M_\infty = 12.3$, $Re_\infty/cm = 3.3 \times 10^4$, $P_{oj} = 29.7$ psia, $\alpha = 0°$)

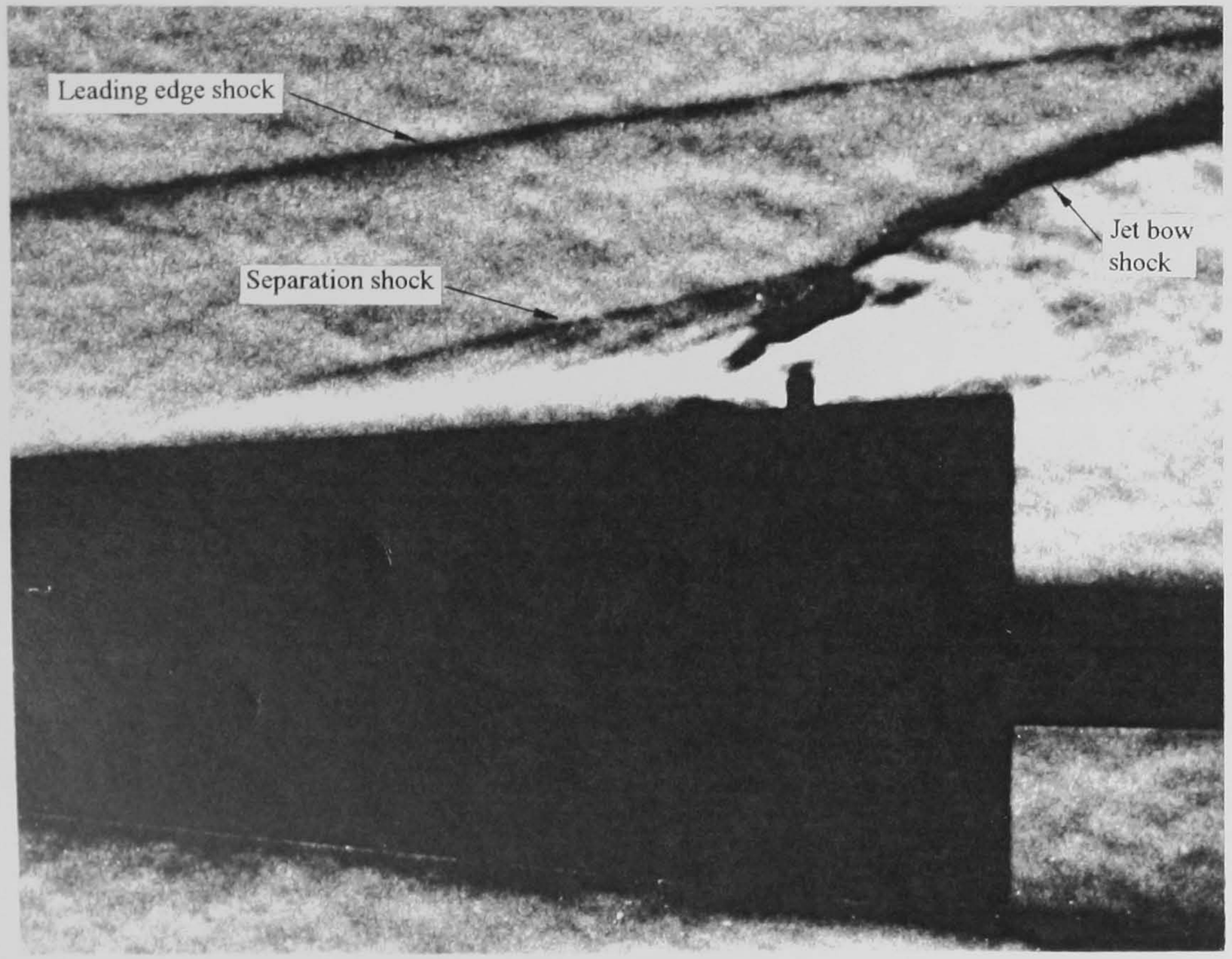

(a) density gradients normal to freestream (horizontal cut-off)

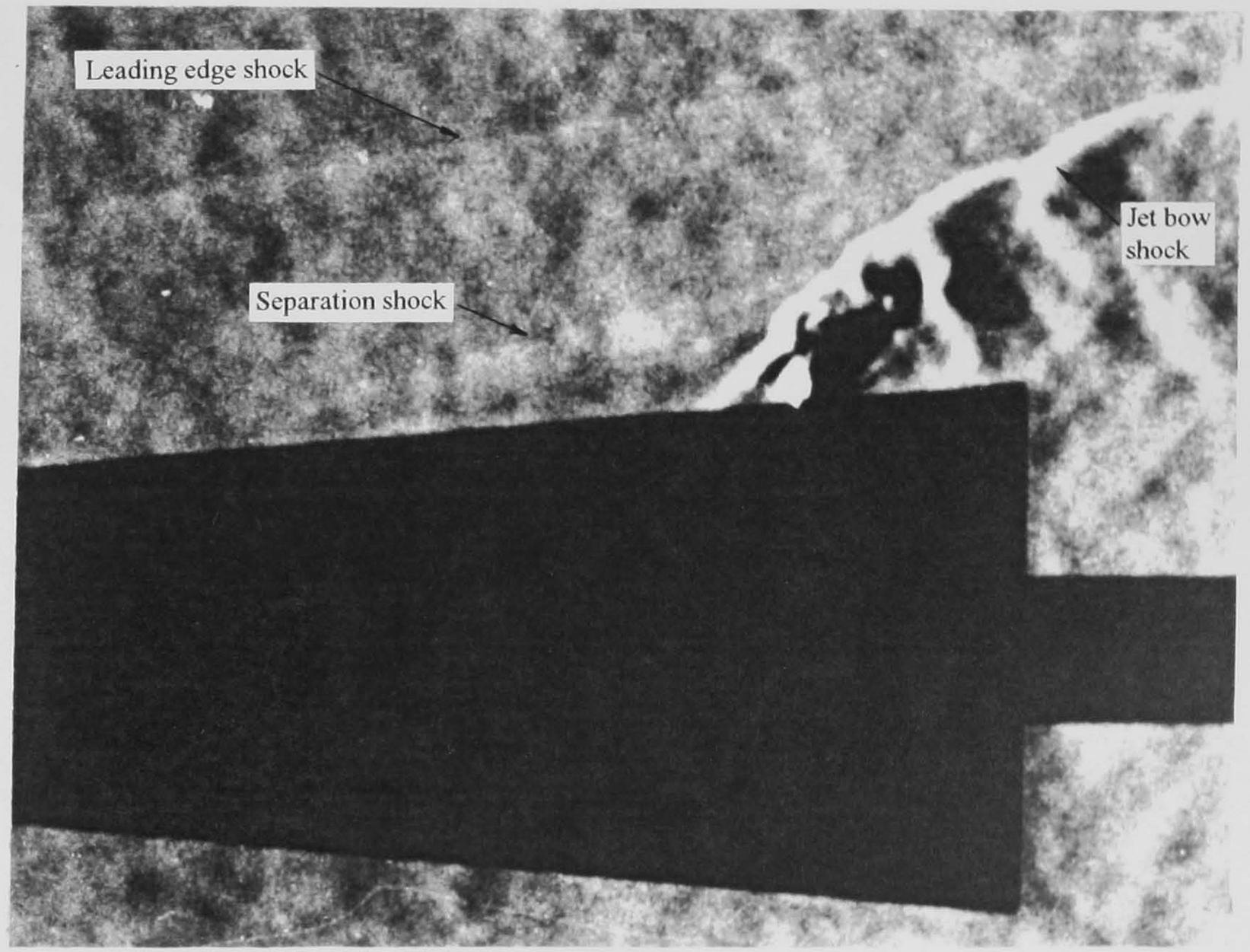

(b) density gradients parallel to freestream (vertical cut-off)

Figure 9-2 Axial and normal density gradients associated with the interaction of a supersonic under-expanded jet with a hypersonic crossflow ($M_\infty = 8.2$, $Re_\infty/cm = 9.0 \times 10^4$, $P_{oj} = 134.7$ psia, $\alpha = 0°$)

(a) schlieren photograph

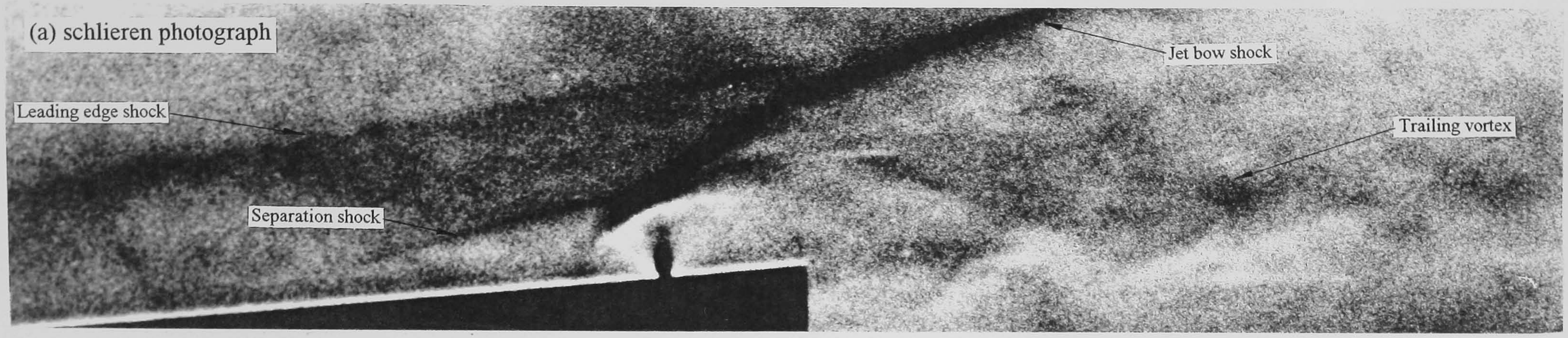

(b) schematic diagram

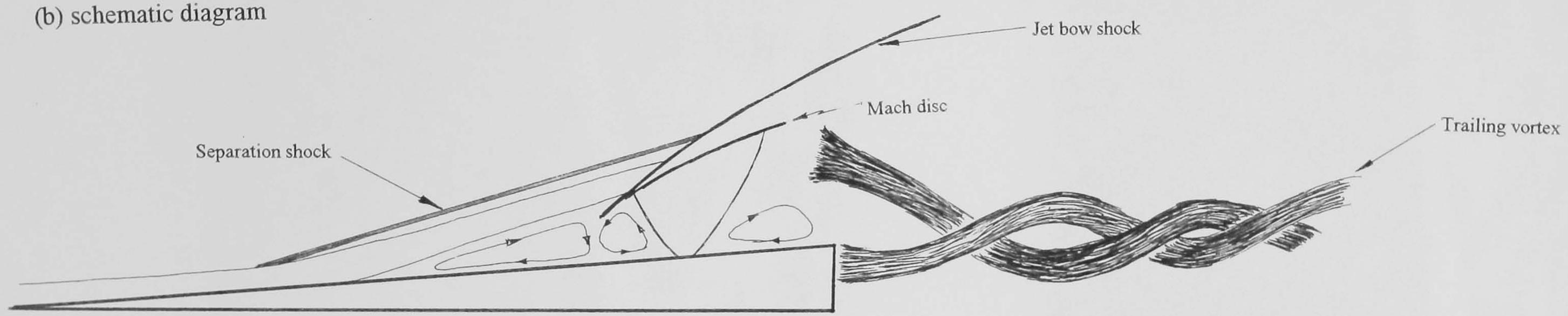

Figure 9-3 Trailing vortex structures associated with the interaction of a supersonic under-expanded jet with a hypersonic crossflow ($M_\infty = 12.3$, $Re_\infty/cm = 3.3 \times 10^4$, $P_{oj} = 29.7$ psia, $\alpha = 0°$)

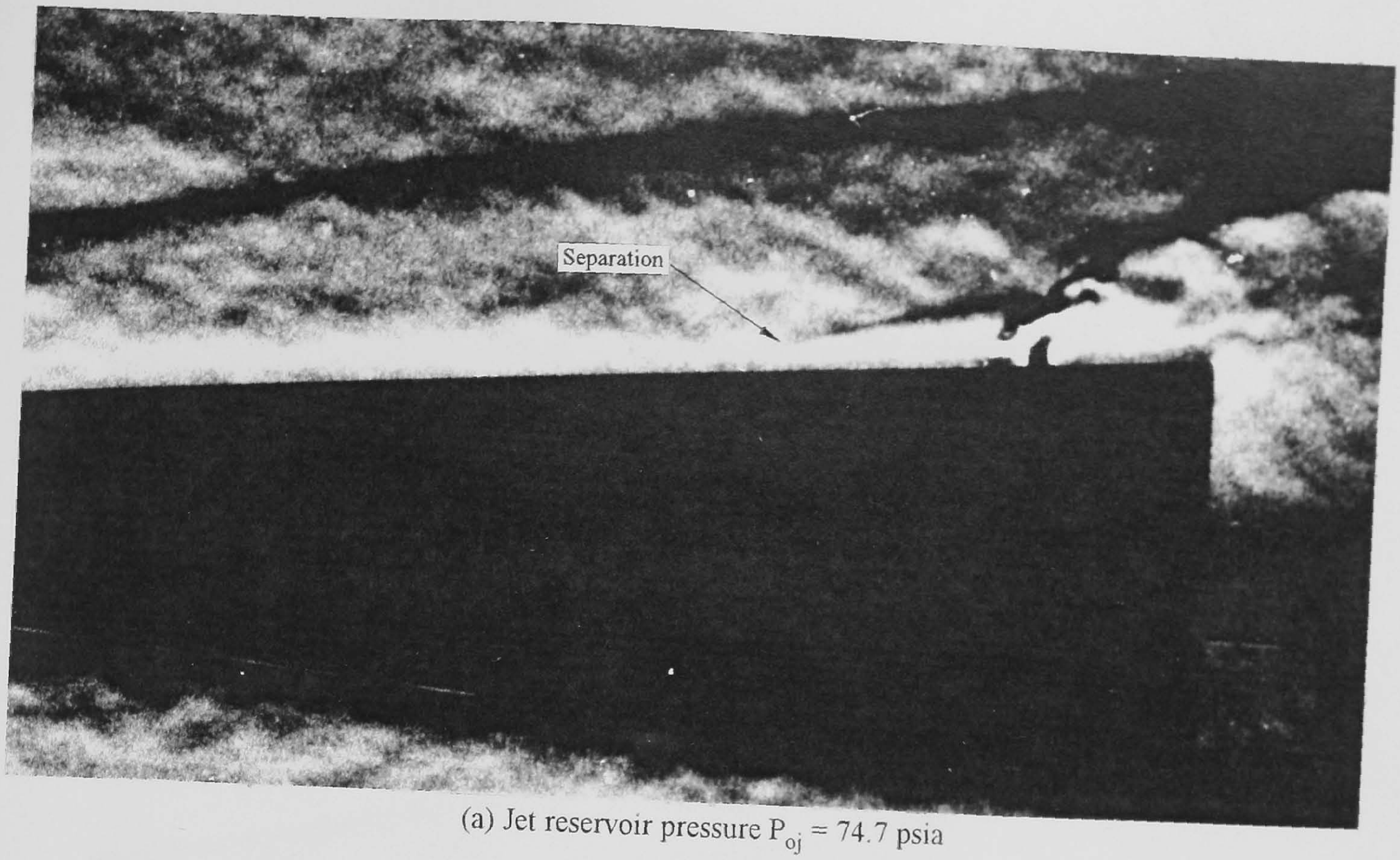

(a) Jet reservoir pressure P_{oj} = 74.7 psia

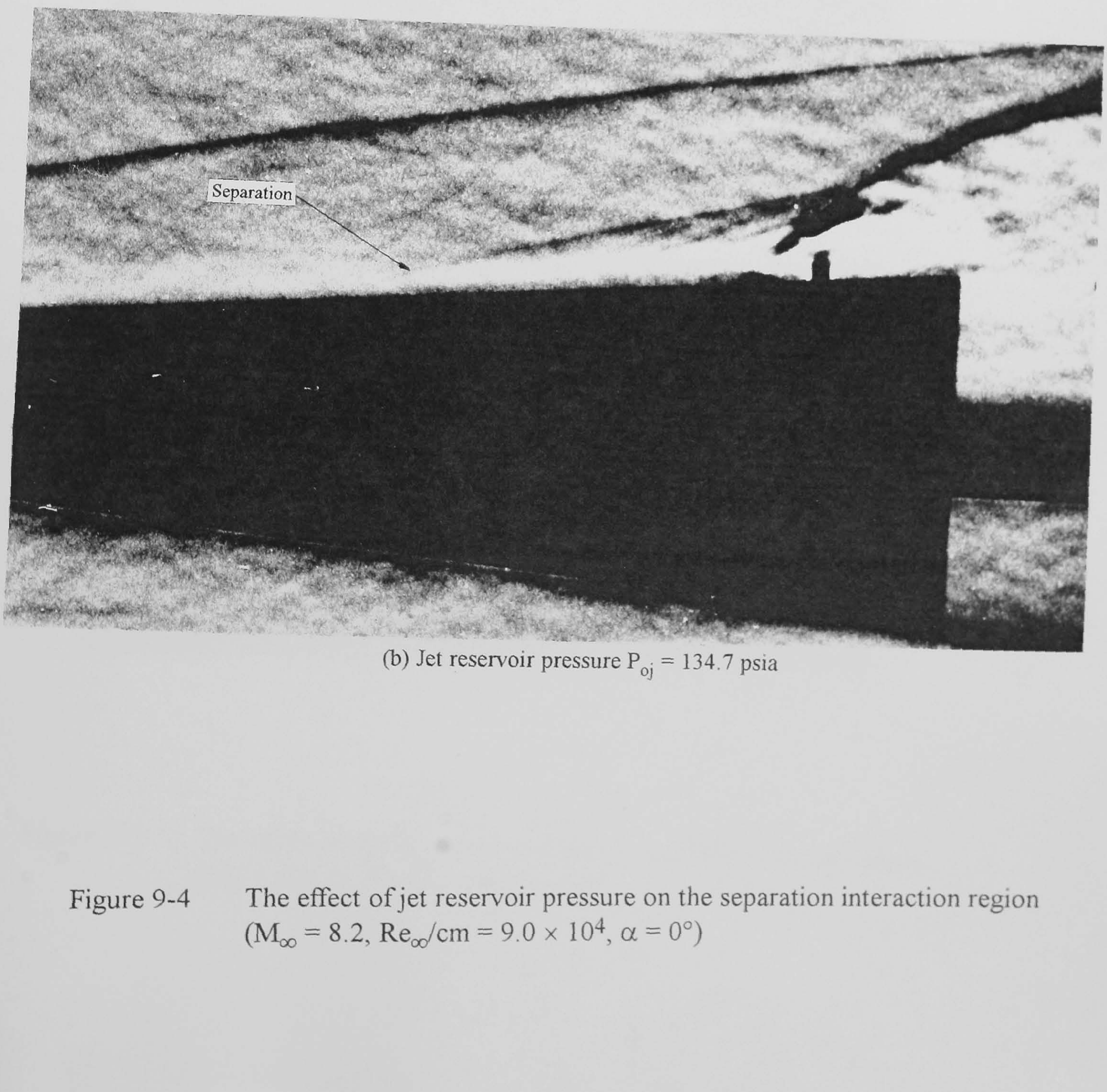

(b) Jet reservoir pressure P_{oj} = 134.7 psia

Figure 9-4 The effect of jet reservoir pressure on the separation interaction region ($M_\infty = 8.2$, $Re_\infty/cm = 9.0 \times 10^4$, $\alpha = 0°$)

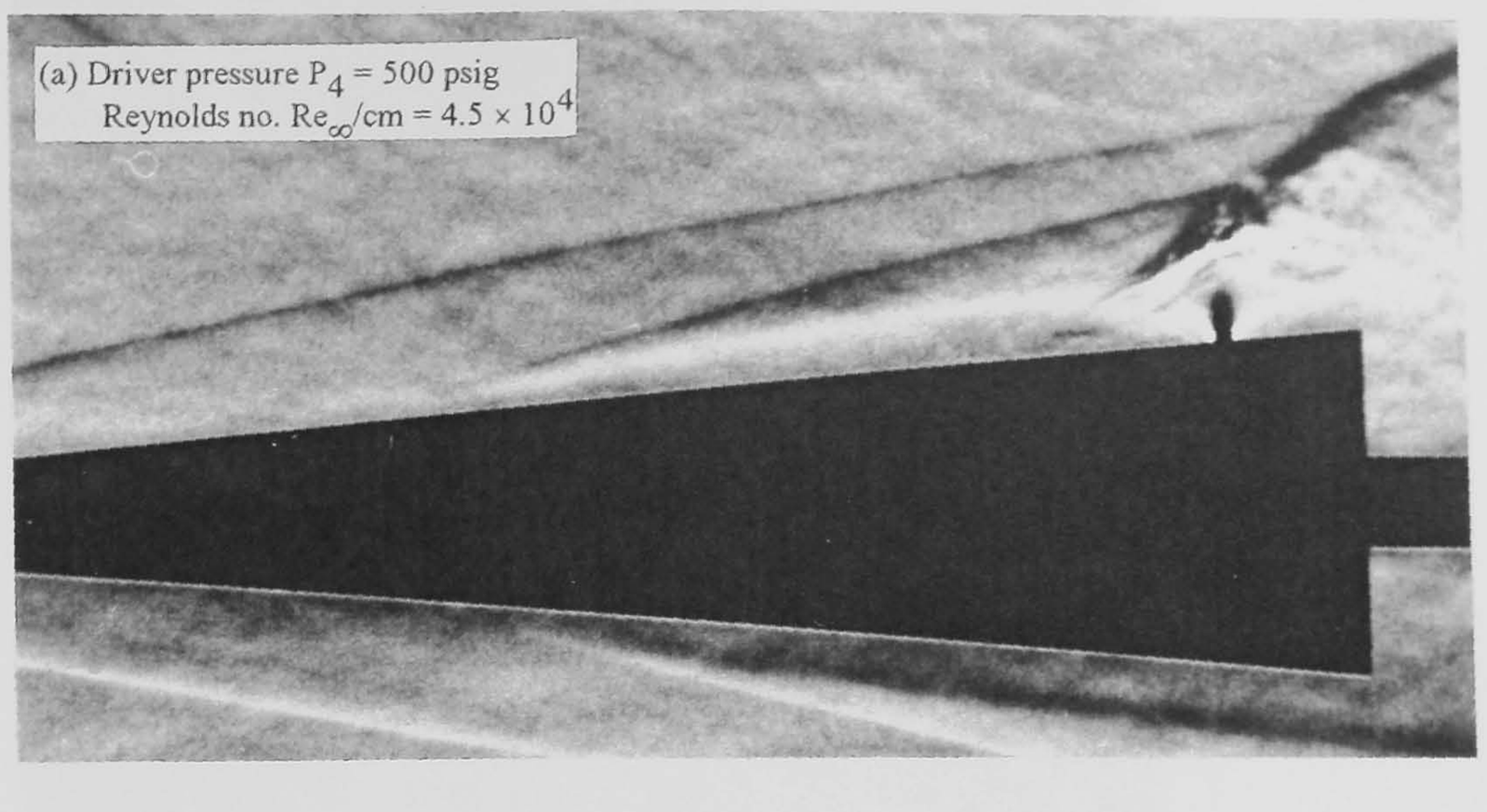

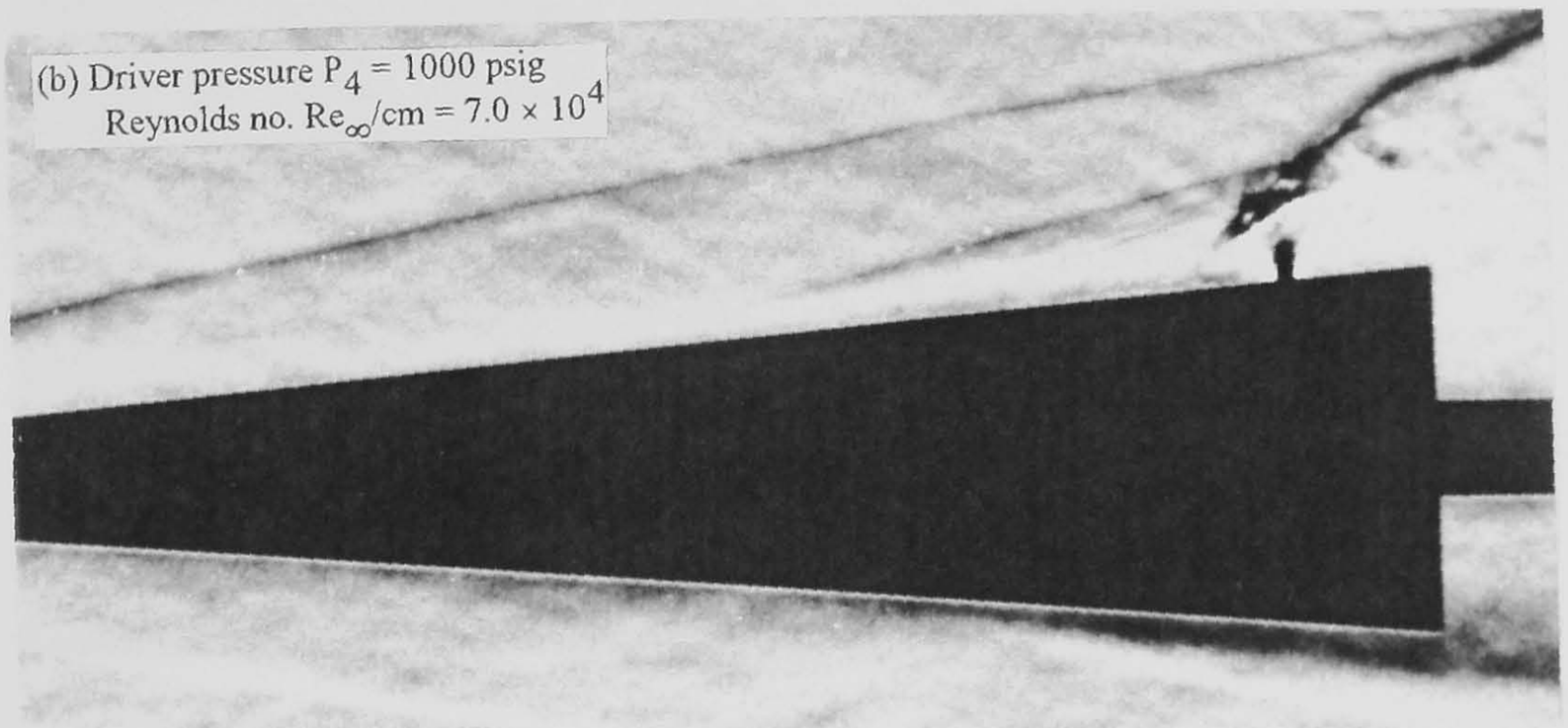

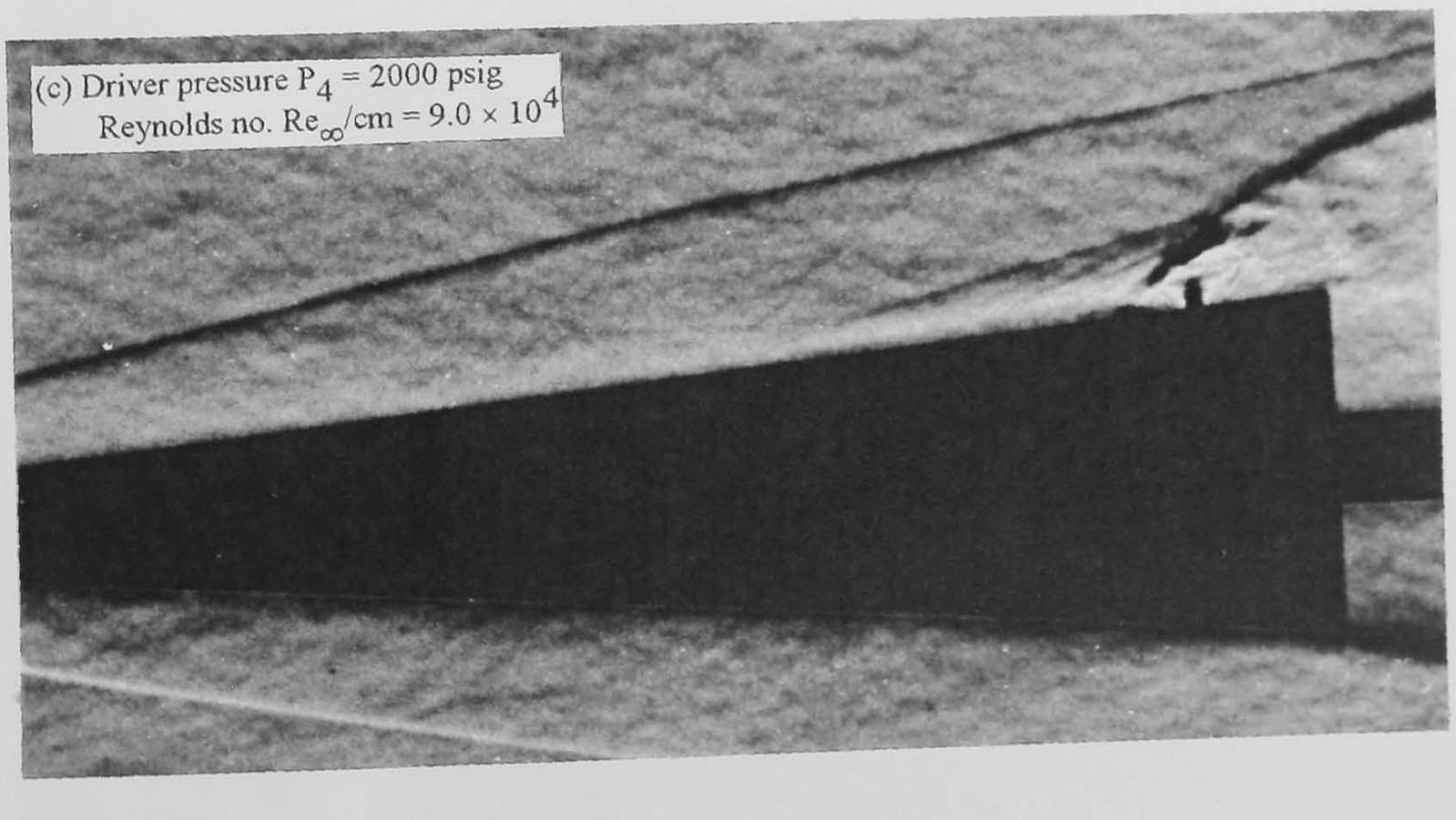

Figure 9-5 The effect of driver pressure on the separation interaction region ($M_\infty = 8.2$, $P_{oj} = 134.7$ psia, $\alpha = 0°$)

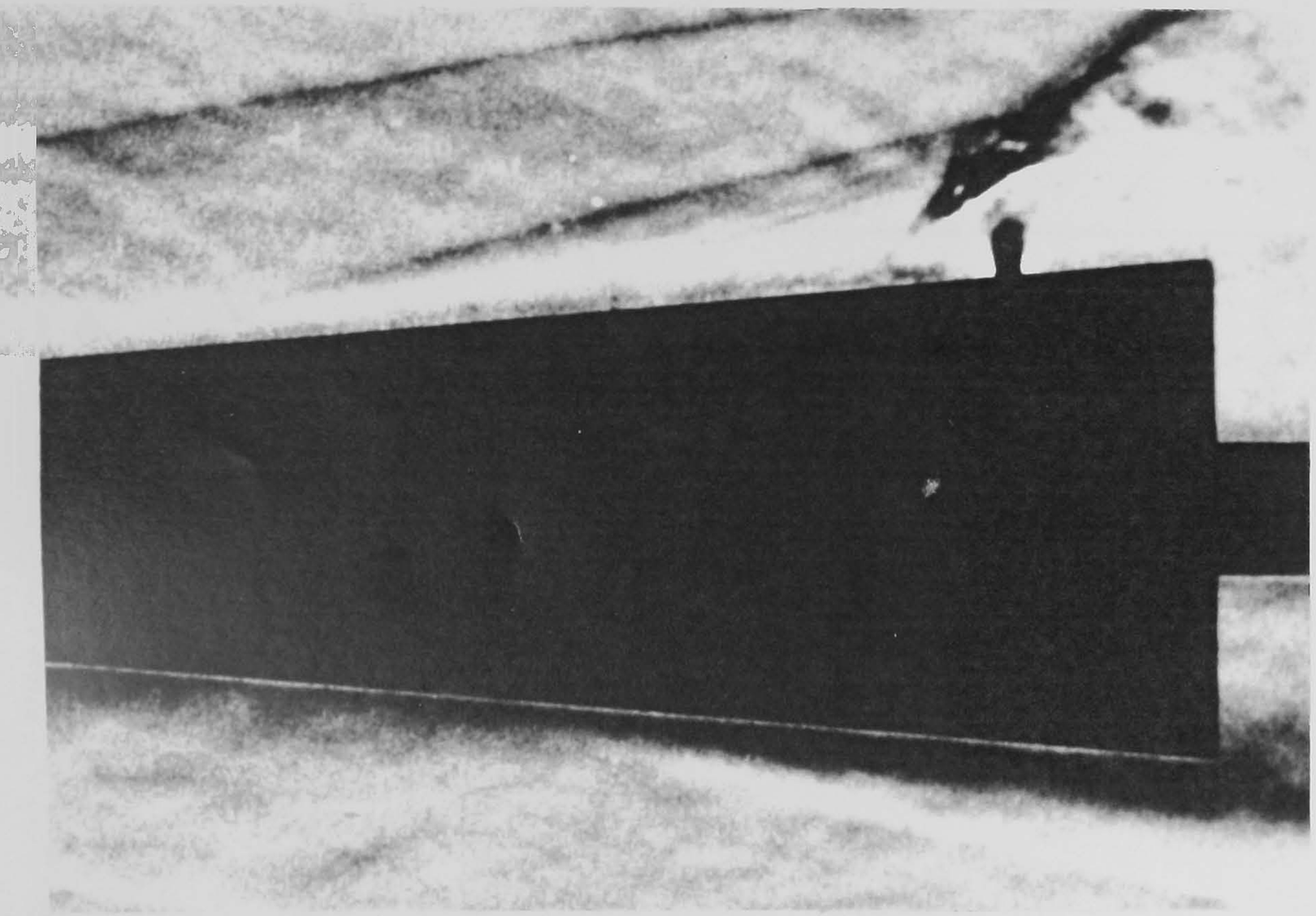

(a) P_4 = 1000 psig, P_{oj} = 134.7 psia, P_{oj}/p_∞ = 1950

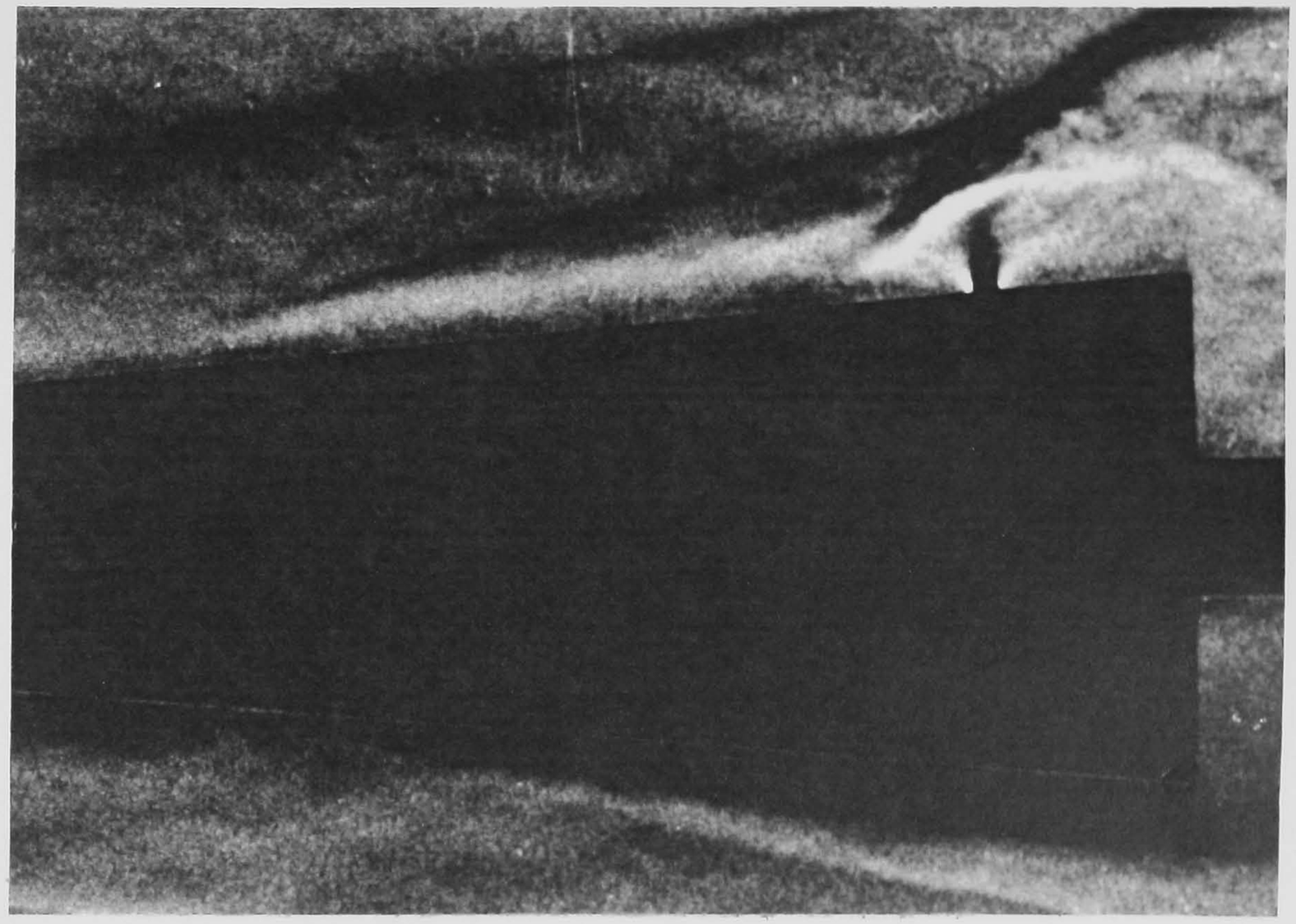

(b) P_4 = 500 psig, P_{oj} = 74.7 psia, P_{oj}/p_∞ = 2130

Figure 9-6 The effect of jet to freestream pressure ratio on the interaction of an under-expanded supersonic jet with a hypersonic crossflow (M_∞ = 8.2, α = 0°)

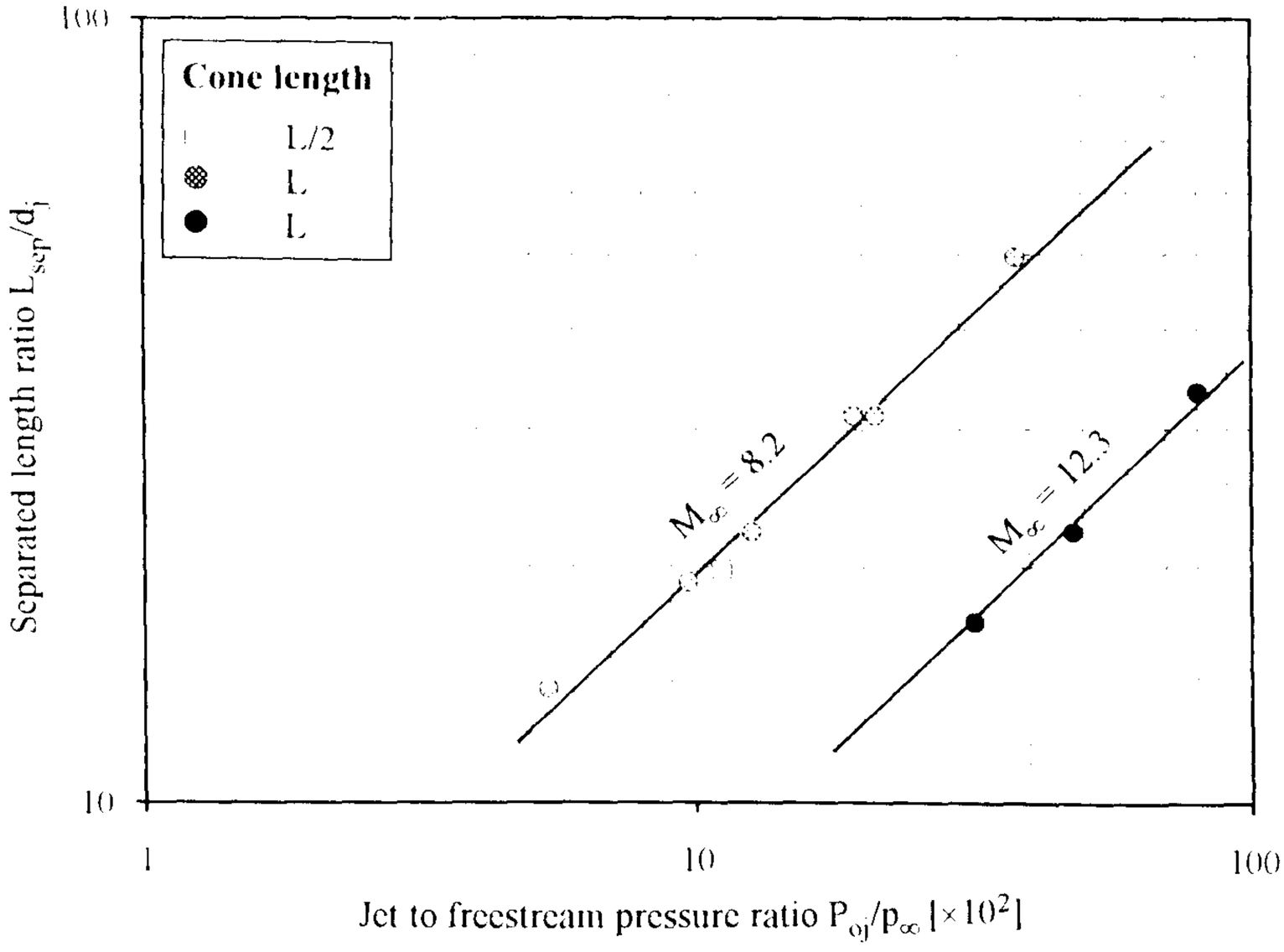

(a) data from present study

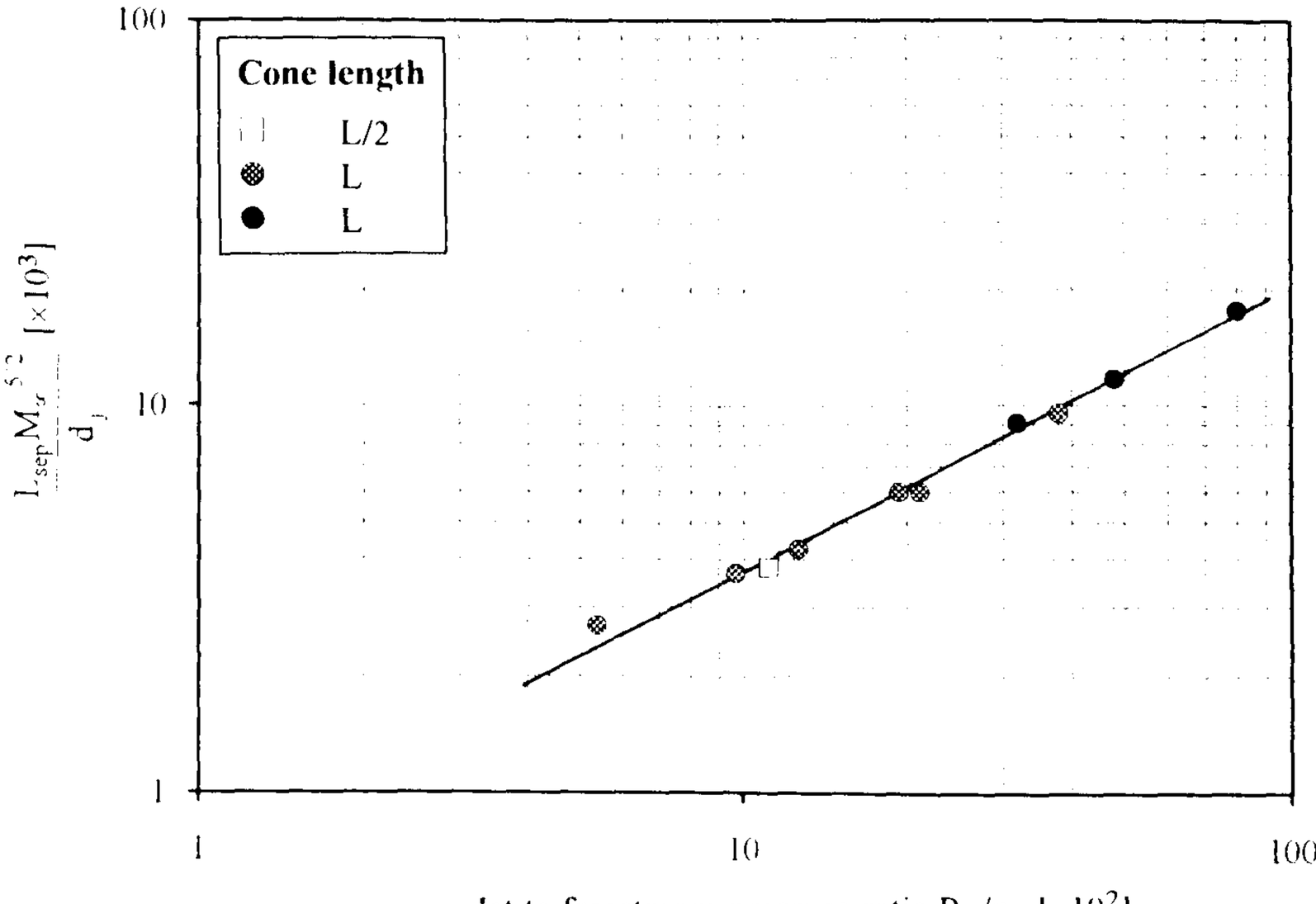

(b) correlation of data from present study

Figure 9-7 Correlation of the length of separated flow arising from the interaction of an underexpanded sonic jet with a hypersonic crossflow

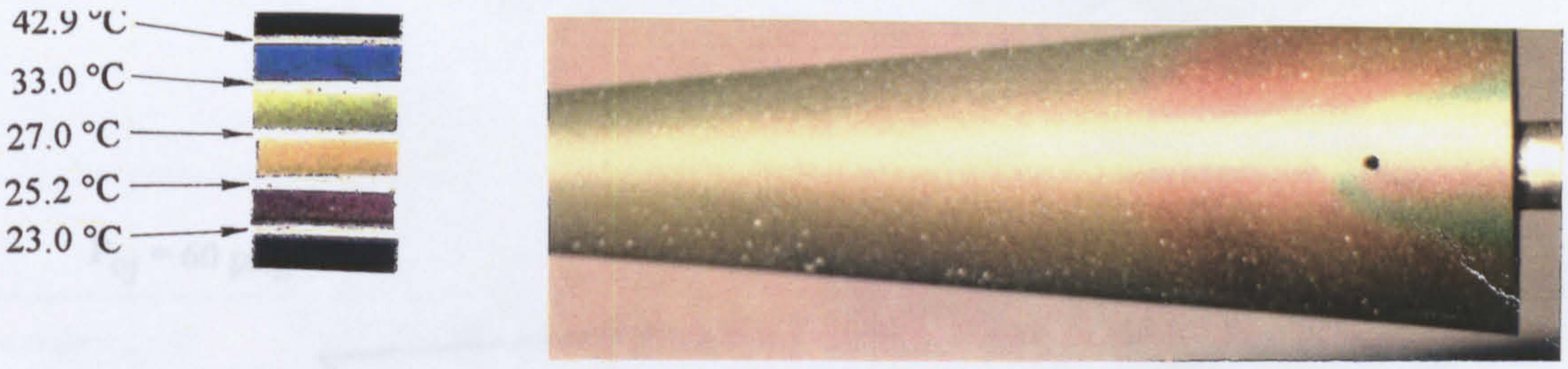

(a) liquid crystal thermograph

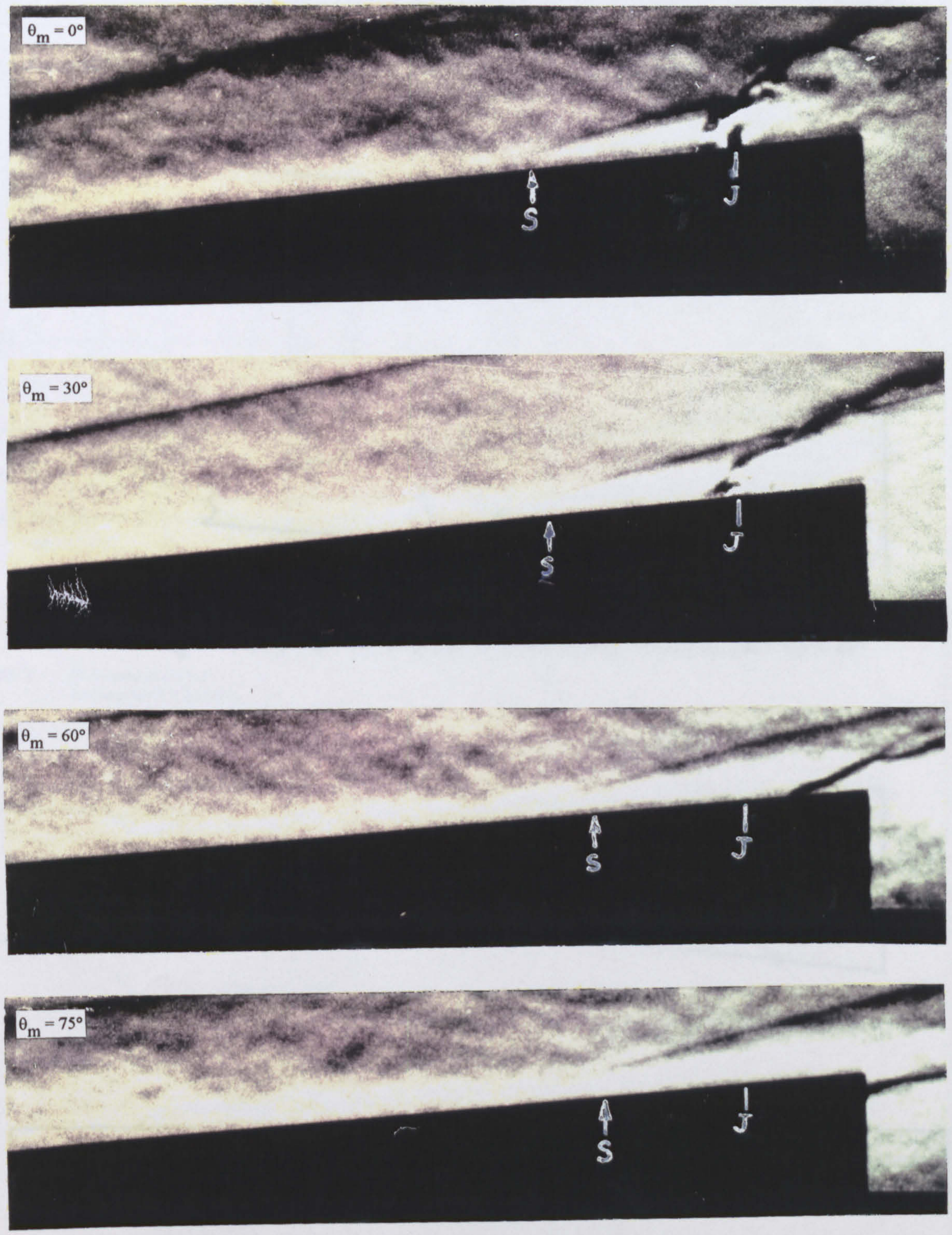

(b) schlieren flow visualisation photographs

Figure 9-8 Three-dimensionality of the separation interaction region ($M_\infty = 8.2$, $Re_\infty/cm = 9.0 \times 10^4$, $P_{oj} = 74.7$ psia, $\alpha = 0°$)

P_{oj} = 60 psig

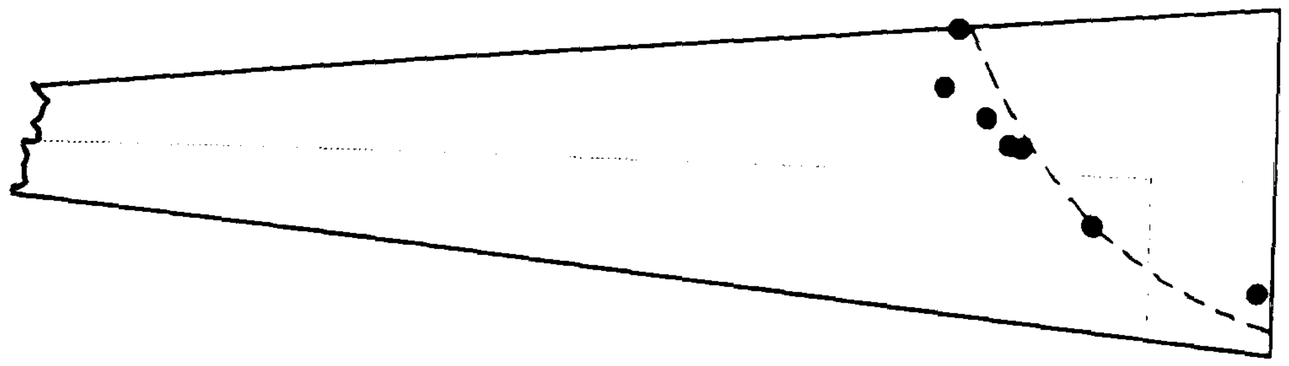

P_{oj} = 120 psig

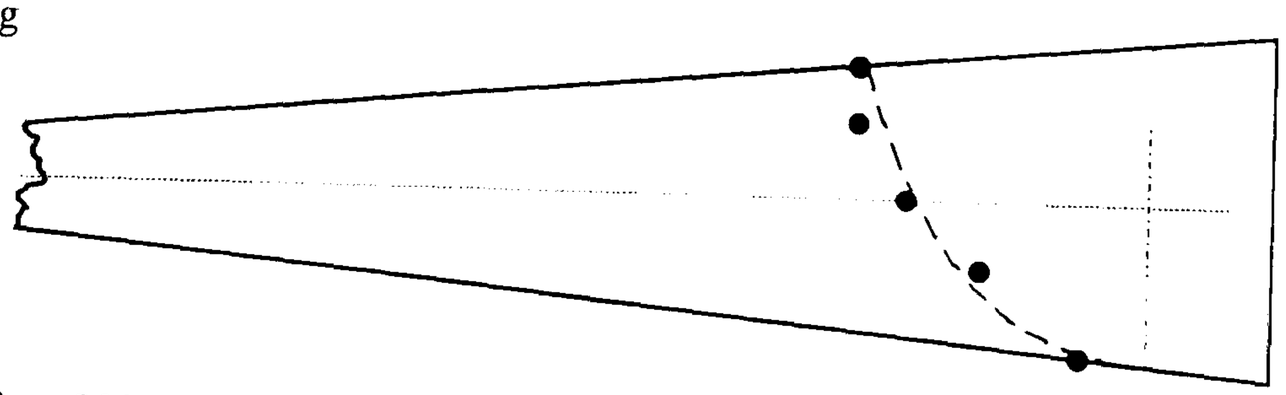

(a) P_4 = 2000 psig, p_∞ = 0.13 psia, M_∞ = 8.2, Re_∞/cm = 9.0×10^4

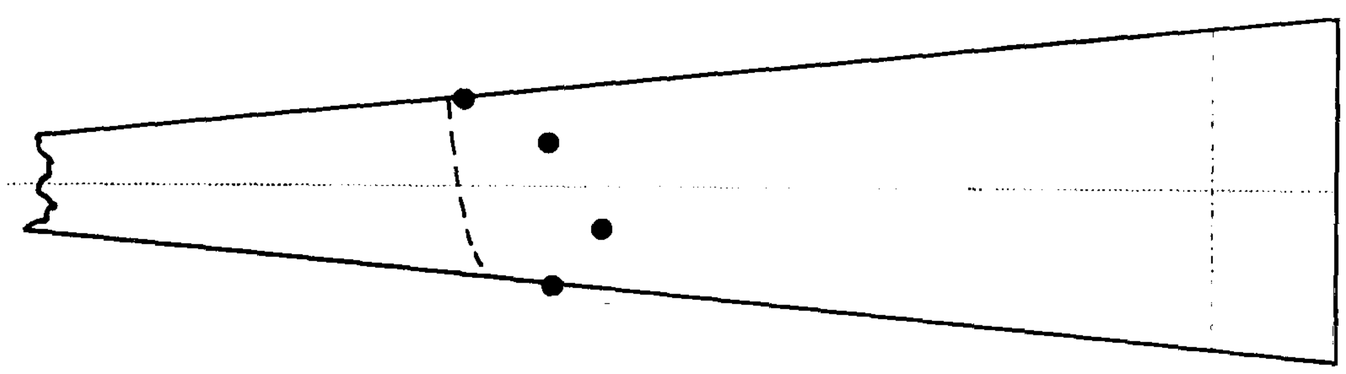

(b) P_{oj} = 120 psig, P_4 = 500 psig, p_∞ = 0.036 psia, M_∞ = 8.2, Re_∞/cm = 4.6×10^4

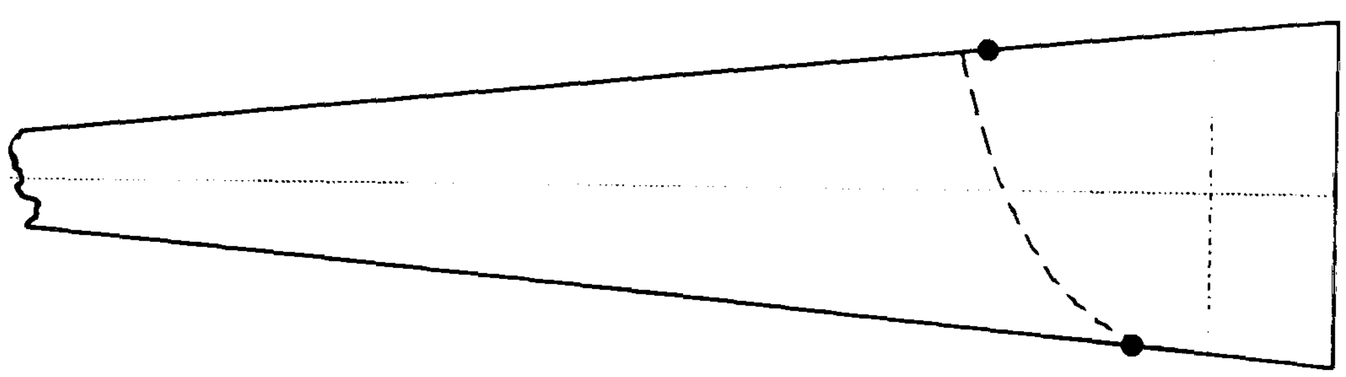

(c) P_{oj} = 15 psig, P_4 = 2000 psig, p_∞ = 0.0093 psia, M_∞ = 12.3, Re_∞/cm = 3.3×10^4

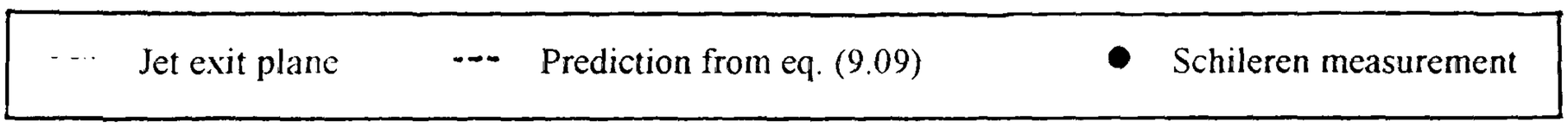

Figure 9-9 Comparison of the predicted location of the separation front with measurements from schlieren photographs

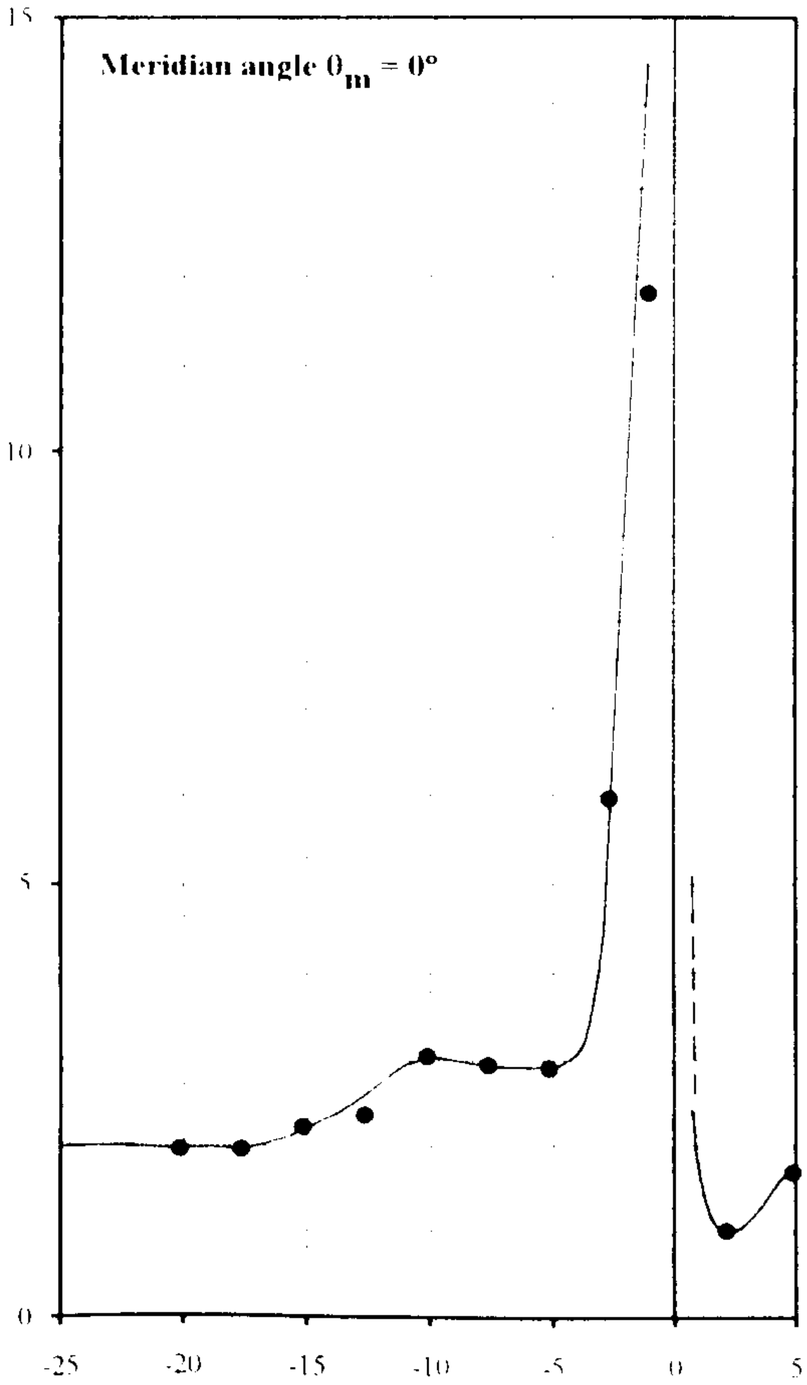

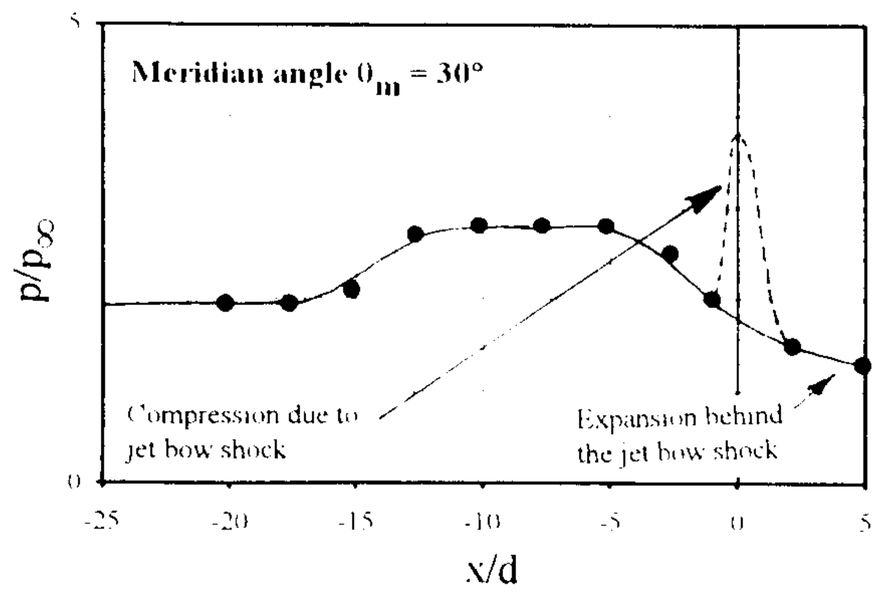

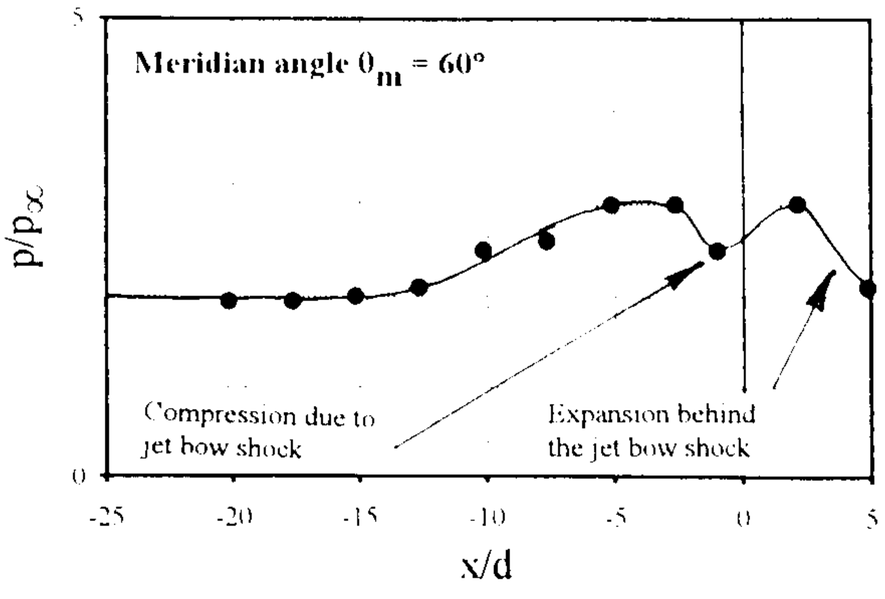

NOTE : Jet located at x/d 0
Jet diameter d 2.0 mm

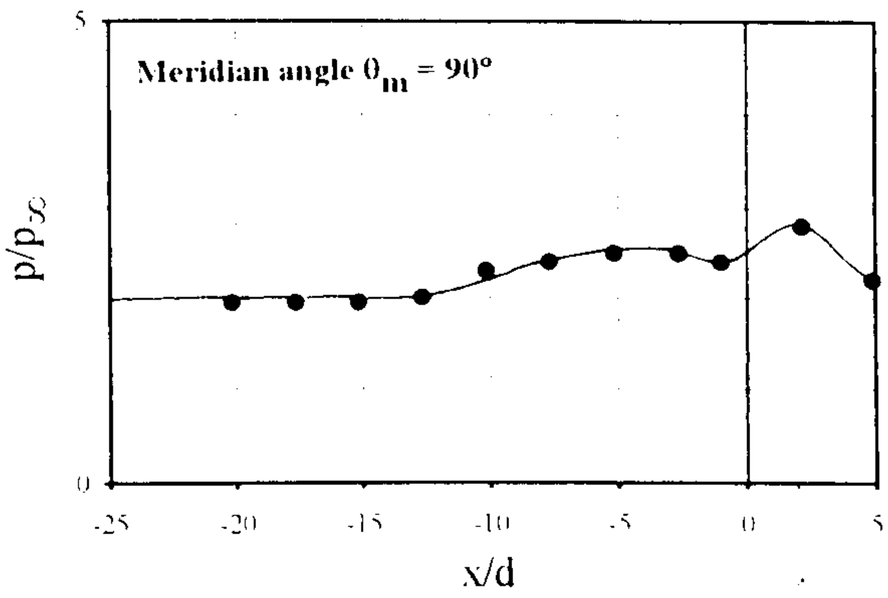

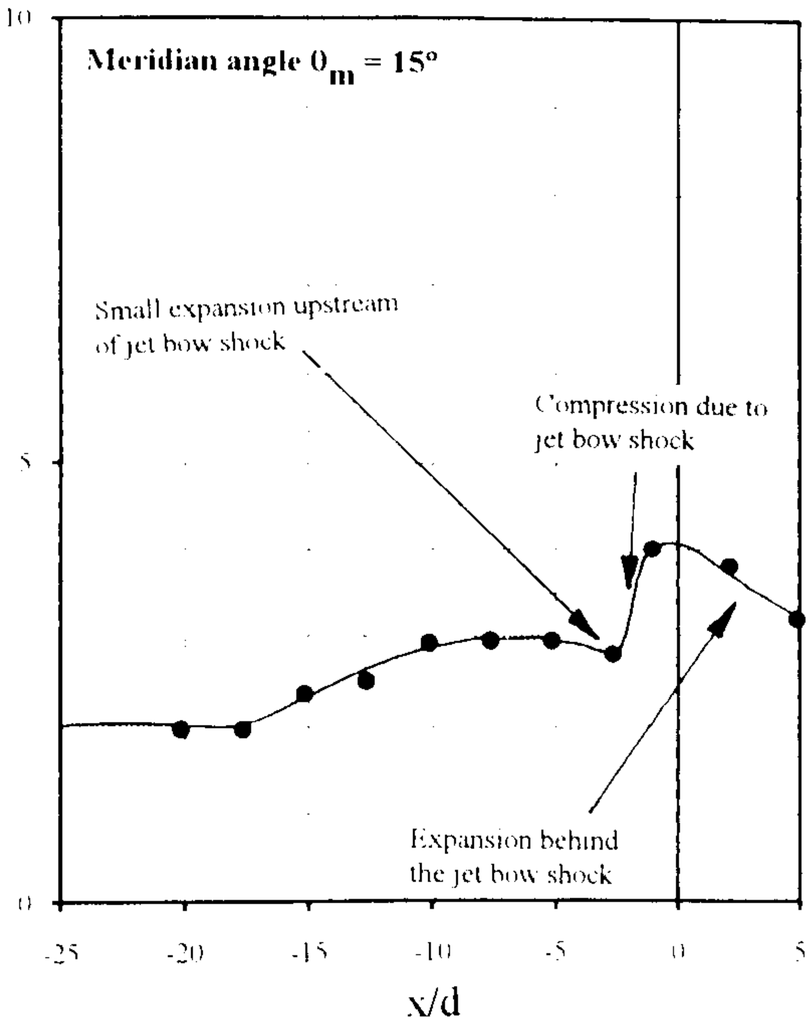

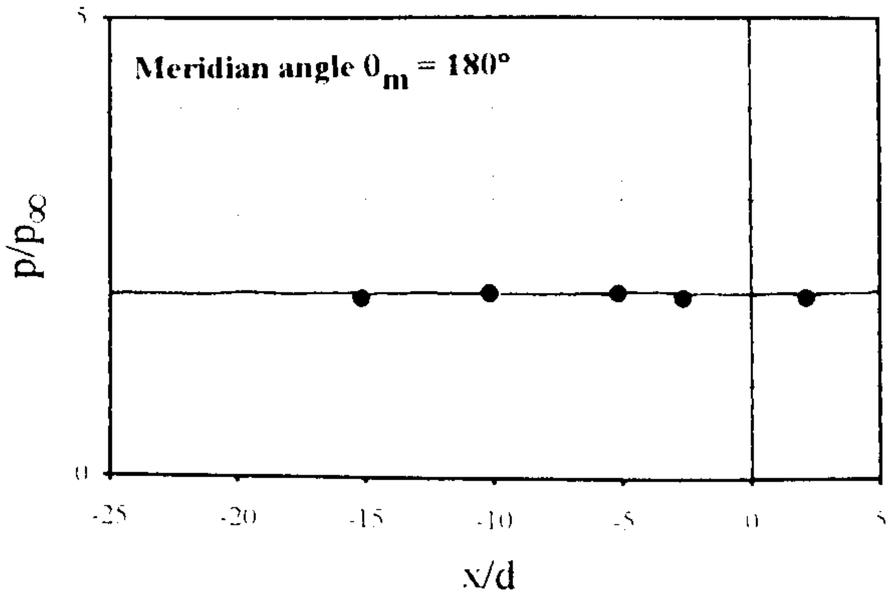

Figure 9-10 Pressure distributions along selected meridians in the jet interaction region (M_∞ = 8.2, Re_∞/cm = 9.0 × 10^4, P_{oj} = 74.7 psia, α = 0°, $A_{j,\,exit}$ = π mm^2)

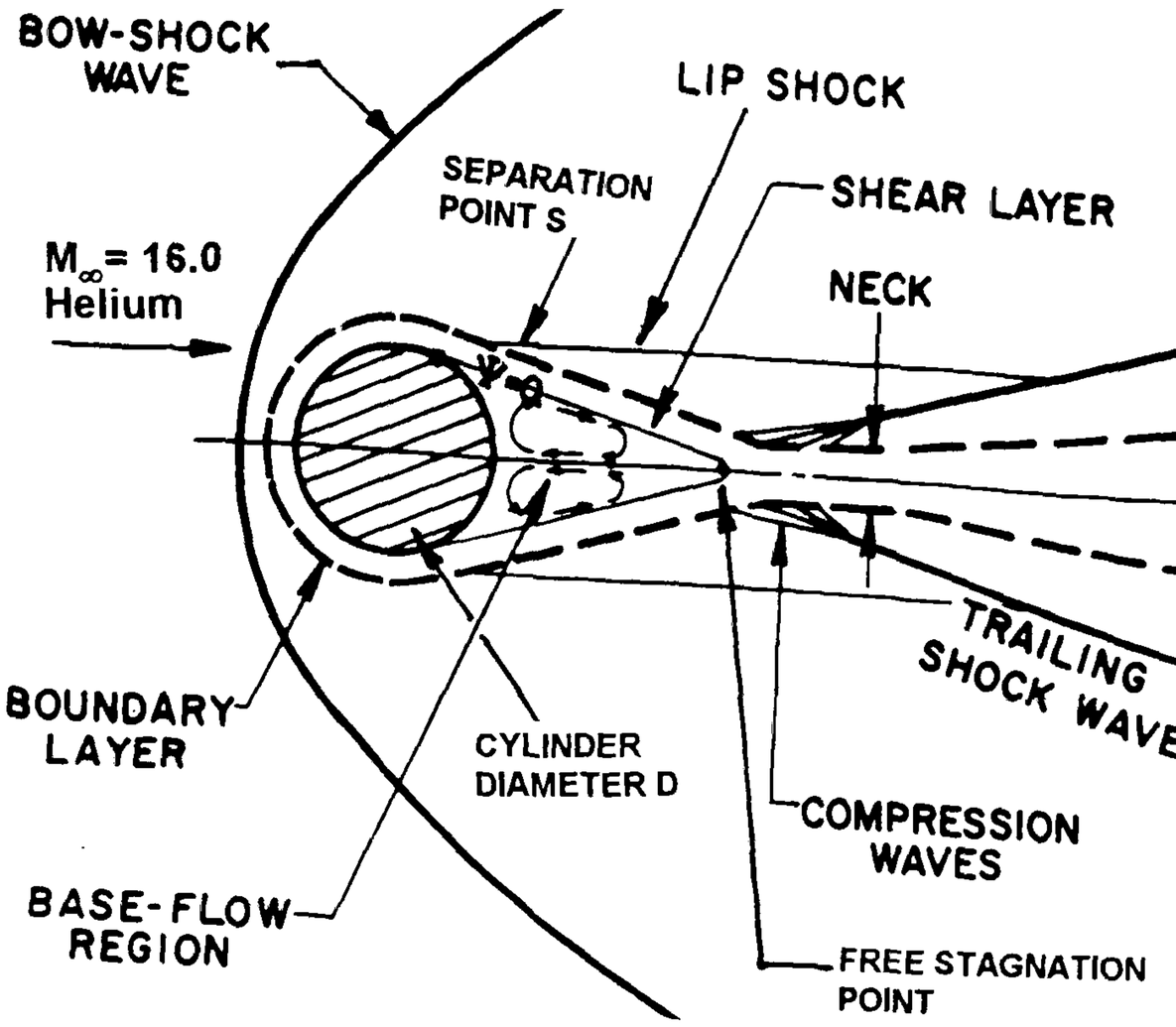

(a) schematic diagram of the local flow structure

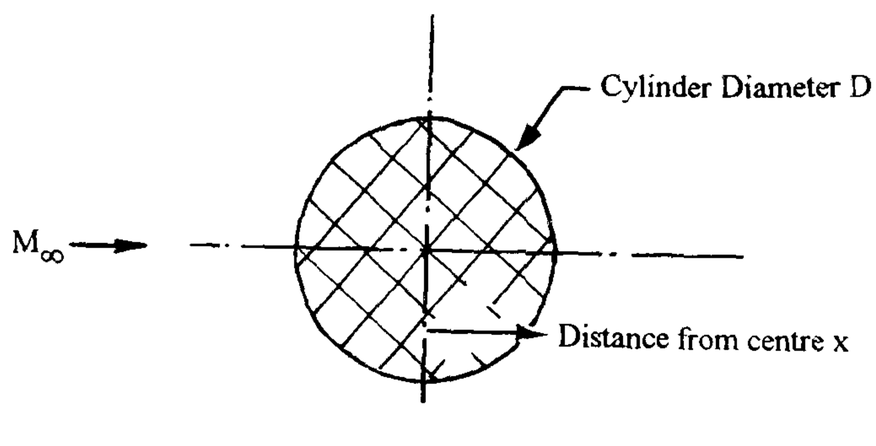

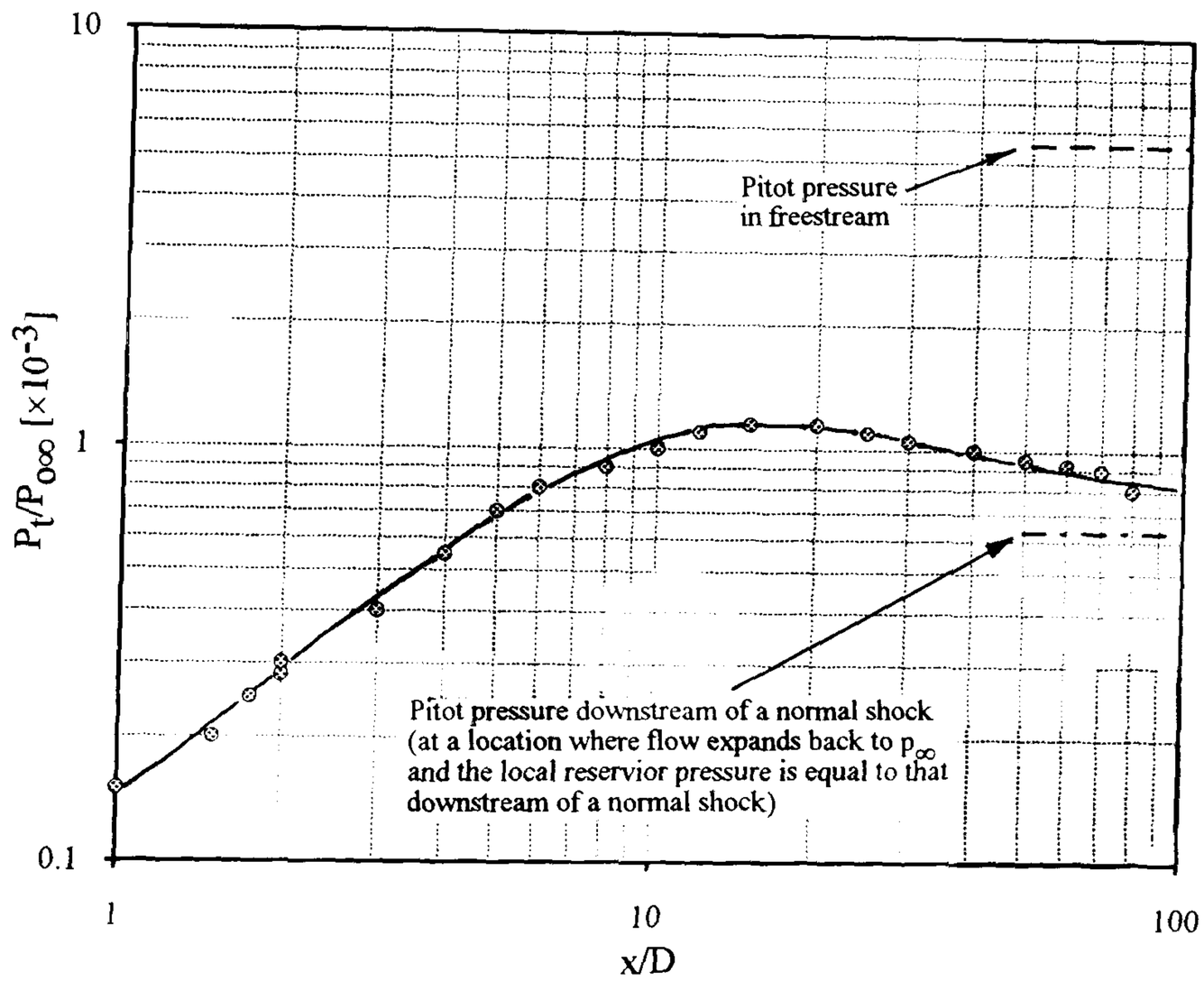

(b) pitot pressure distribution in the wake region

Figure 9-11 Axial pitot pressure along the wake centreline of a cylinder in hypersonic flow Ledger et al, 1965 (M_∞ = 16.0, Re_∞/cm = 5.3 × 10^4, D = 0.47 cm, helium test gas)

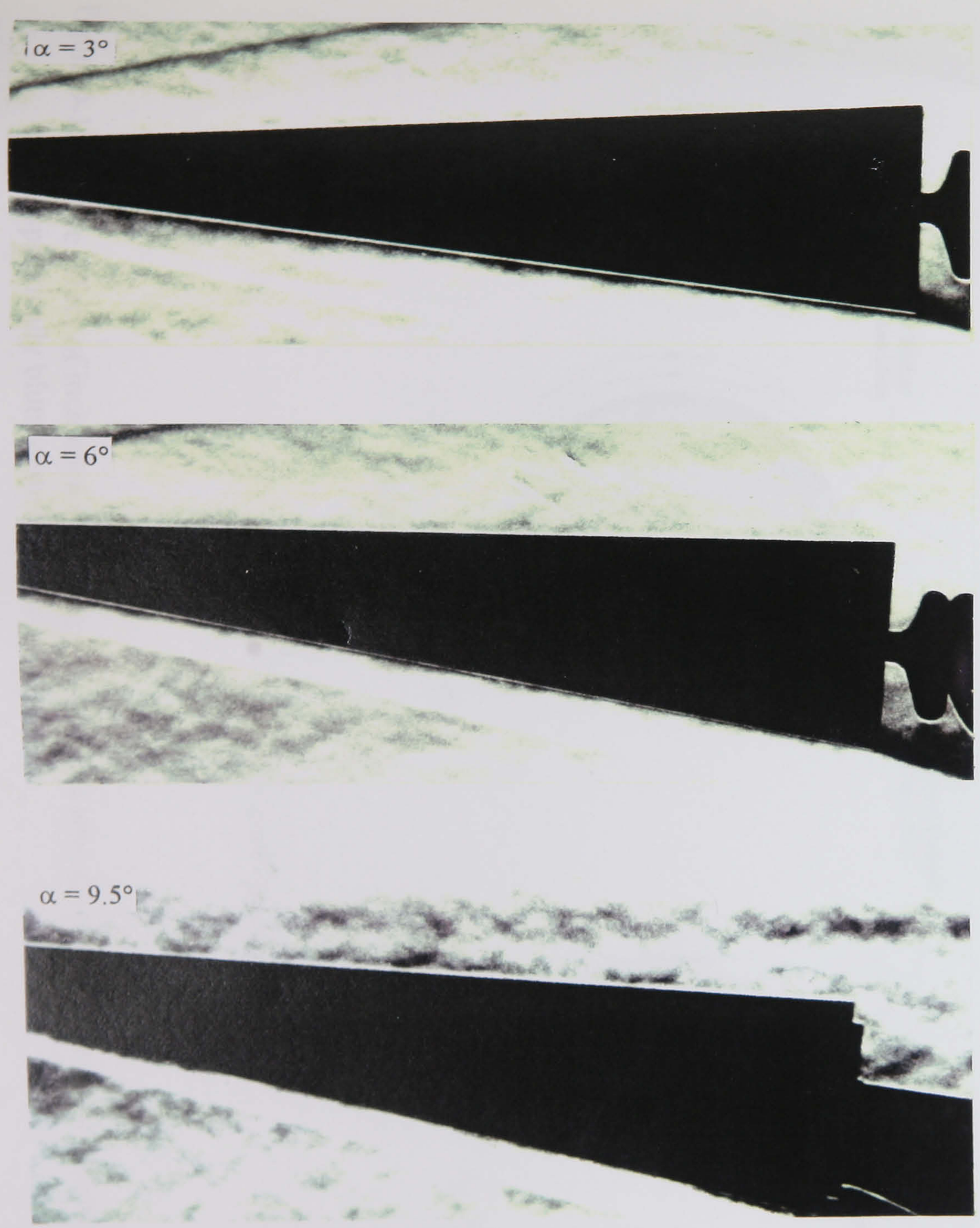

(a) schlieren photographs (side view)

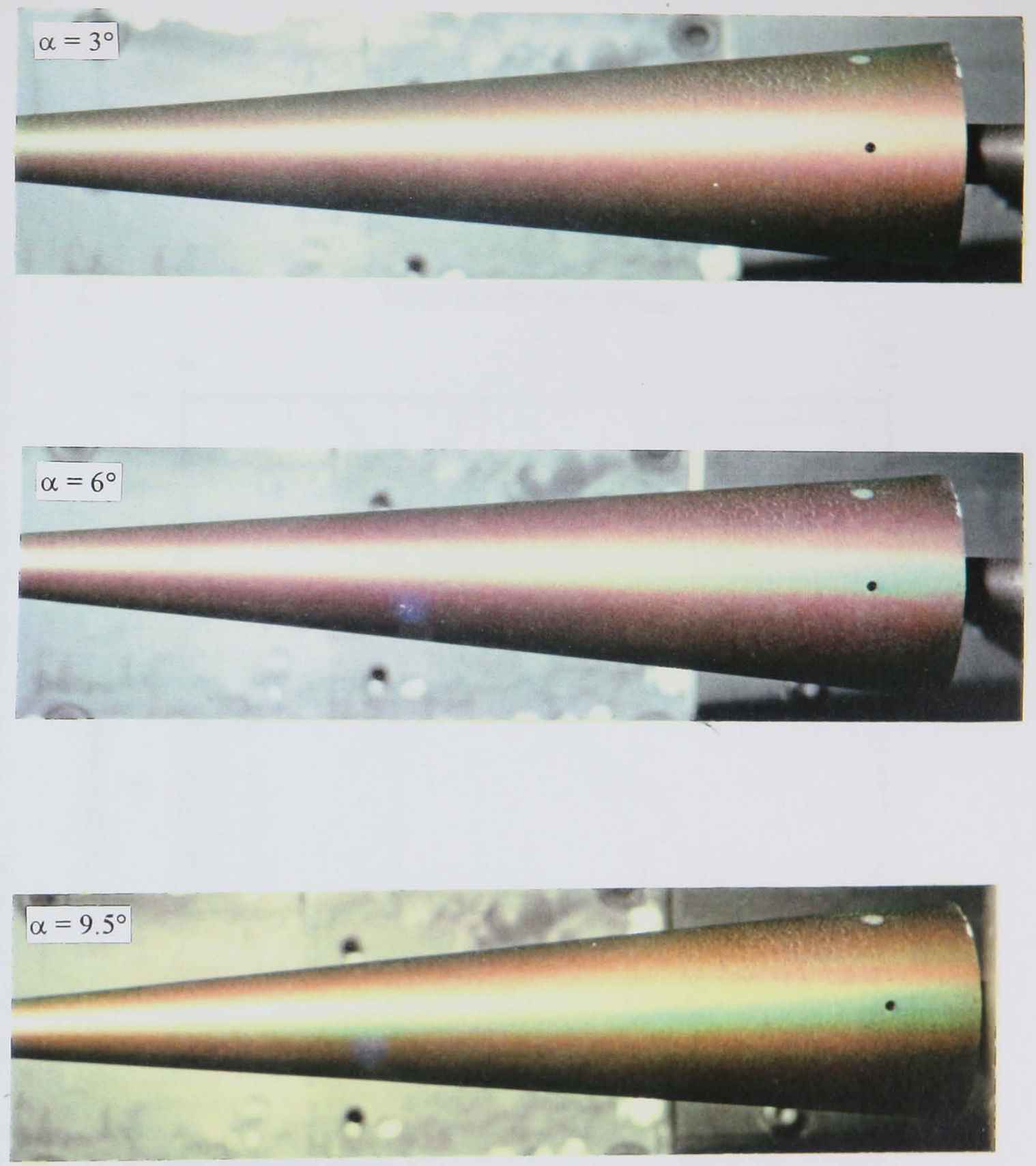

(b) liquid crystal thermographs (plan view)

Figure 9-12 The effect of incidence on the flow structure over a blunt cone ($M_\infty = 8.2$, $Re_\infty/cm = 9.0 \times 10^4$)

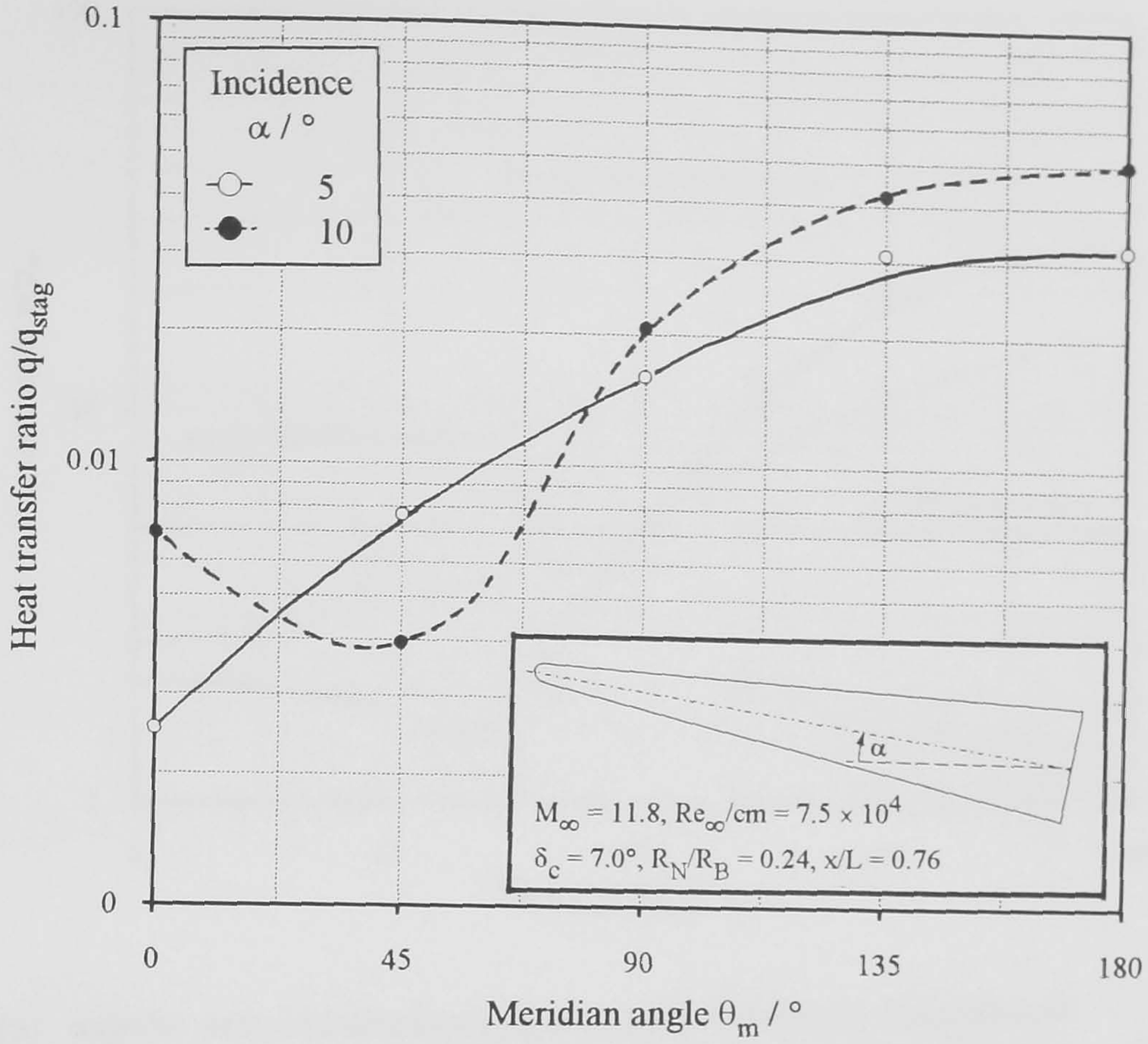

(a) angluar heat transfer distribution on a $\delta_c = 7°$ blunt cone [Wrisdale, 1992]

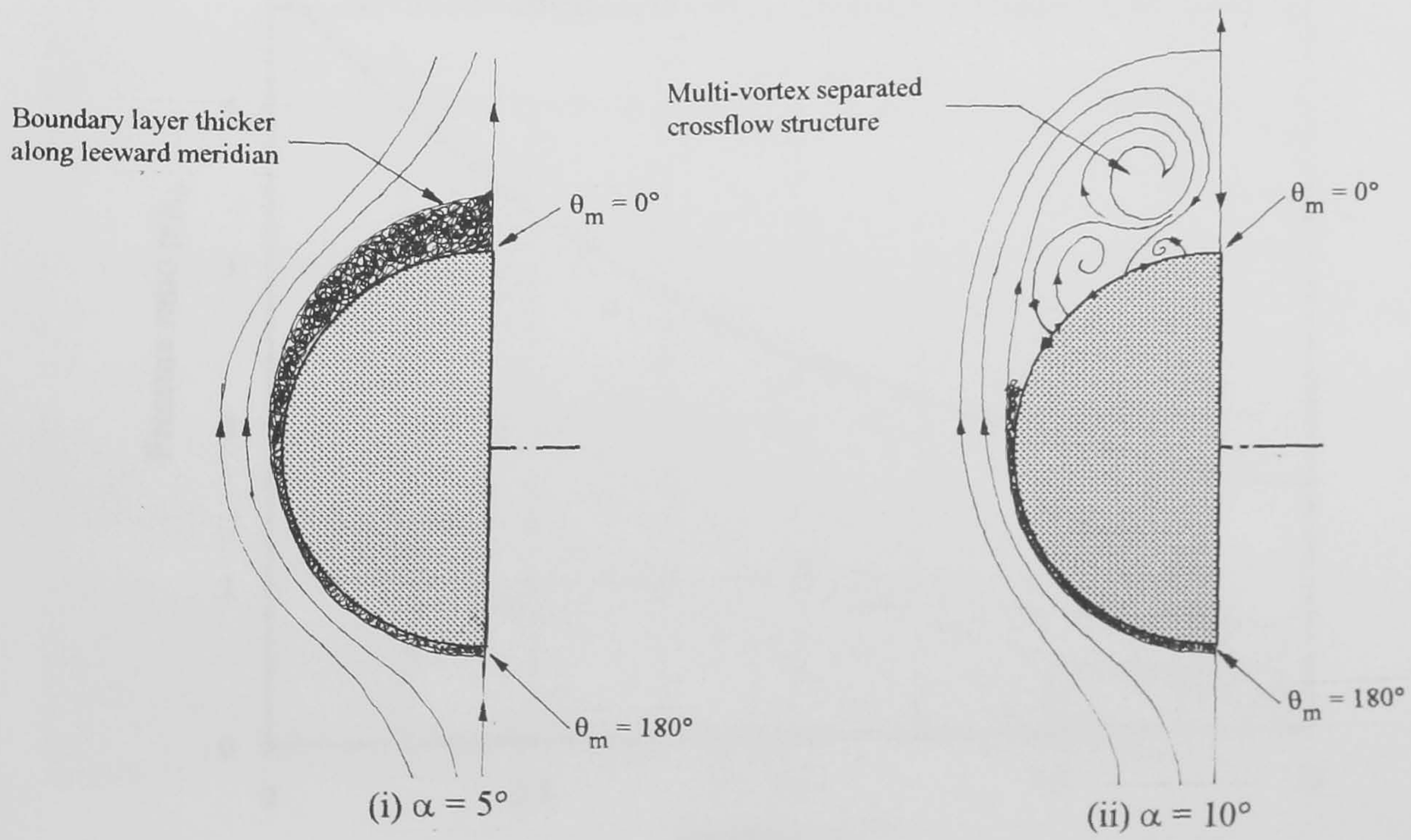

(b) Flow structure in the crossflow plane

Figure 9-13 The effect of incidence on the angular heat transfer distribution and flow structure on a spherically blunt cone in hypersonic flow

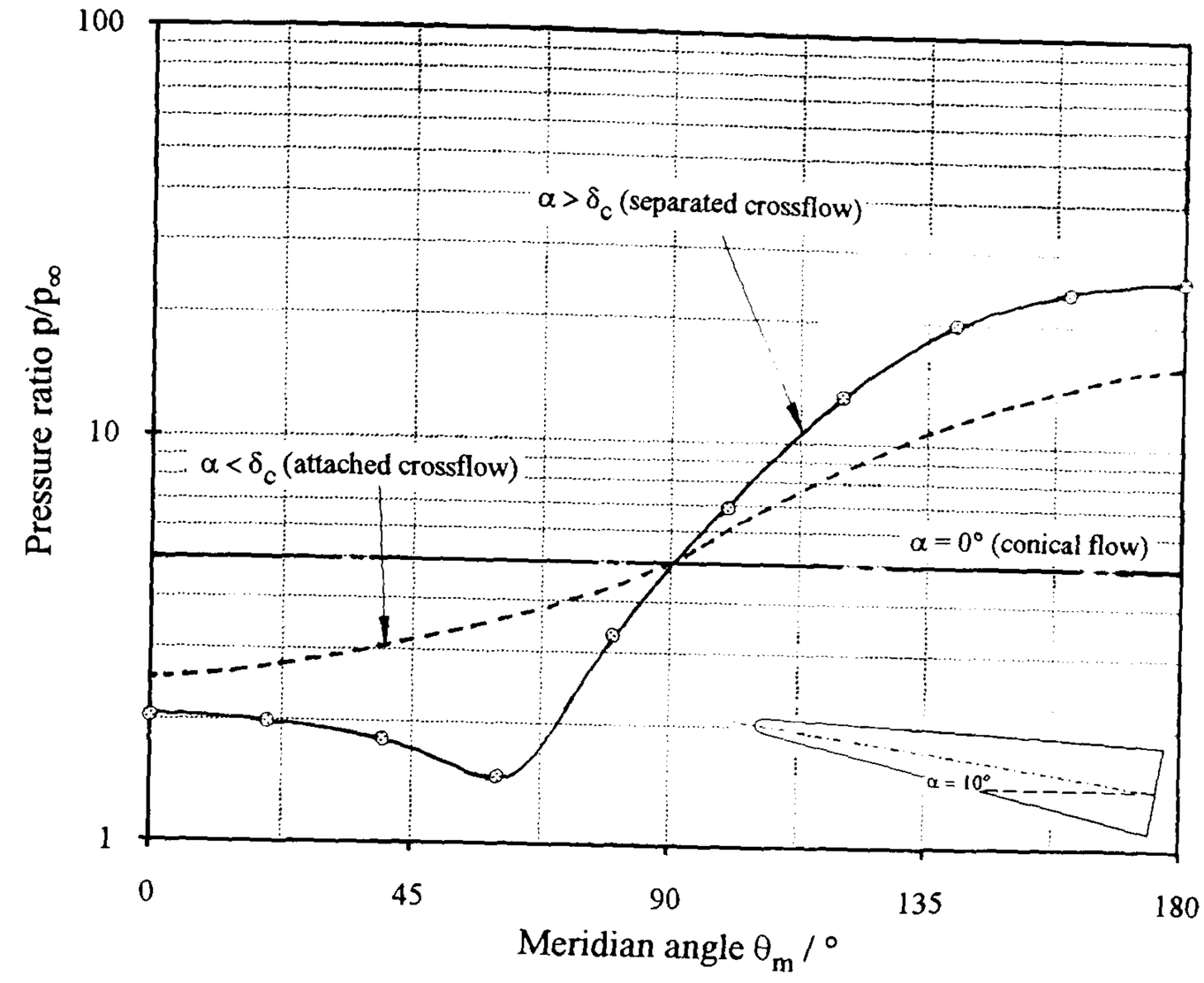

(a) angular pressure distributions on a hemi-spherically blunted cone ($M_\infty = 14.2$, $Re_\infty/cm = 2.0 \times 10^4$, $\delta_c = 5.6°$, $x/R_N = 23.5$, $R_N/R_B = 0.3$, $\alpha = 10°$)

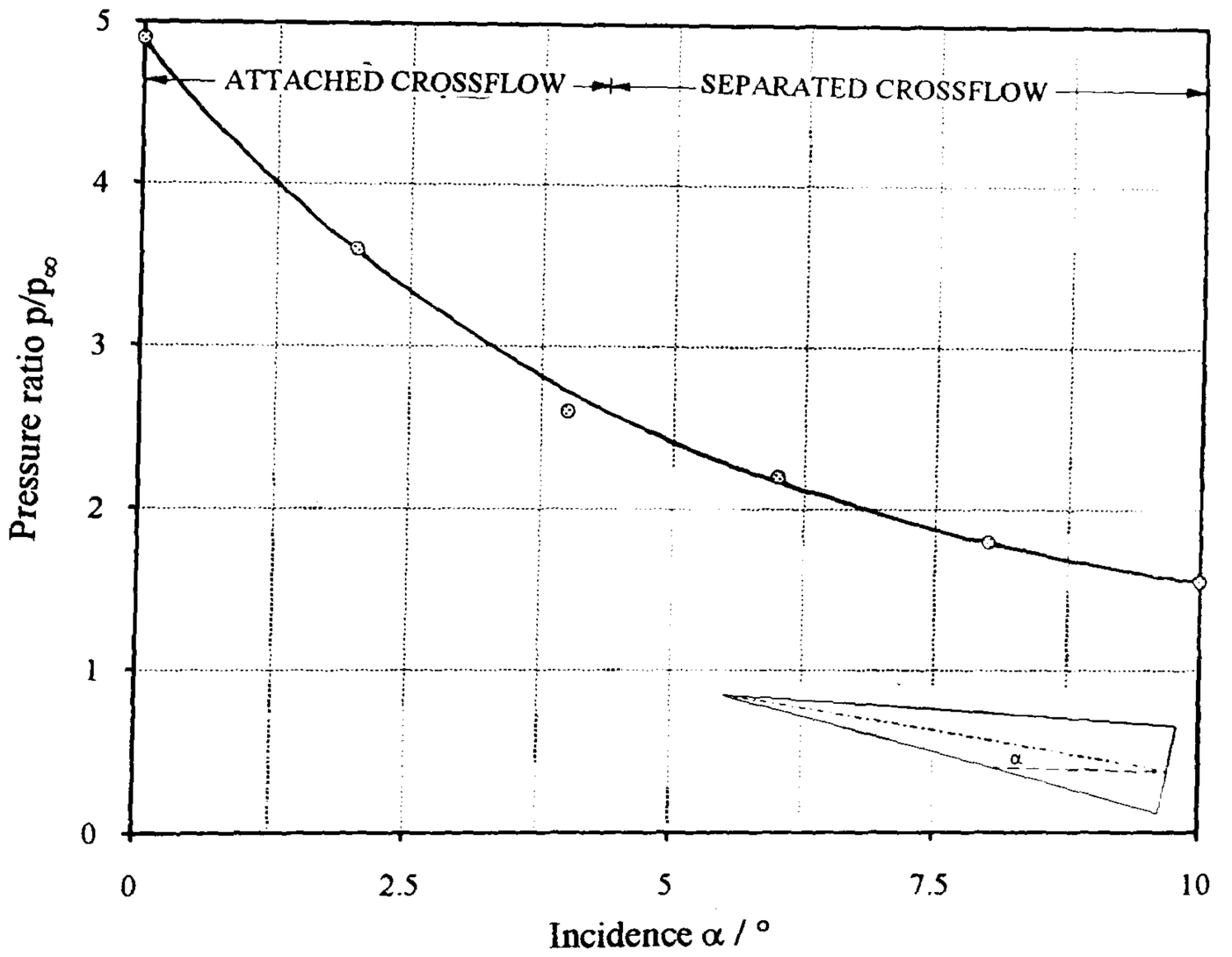

(b) the effect of incidence on the pressure distribution along the leeward meridian of a sharp cone ($M_\infty = 14.2$, $Re_\infty/cm = 2.0 \times 10^4$, $\delta_c = 5.6°$, $x/L = 0.87$)

Figure 9-14 The effect of incidence on pressure distributions over a conical body - Stetson (1972)

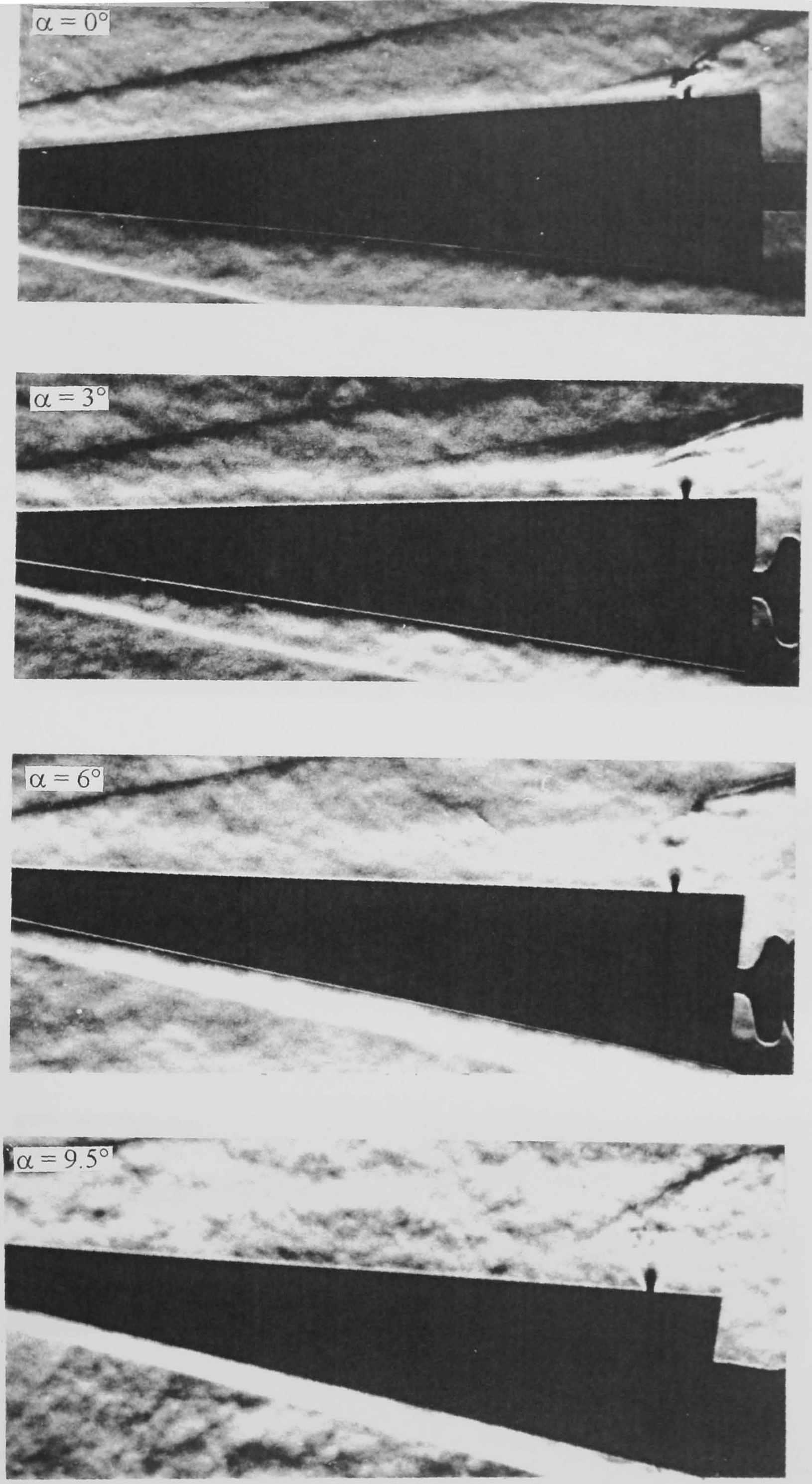

Figure 9-15 The effect of incidence on the interaction of an under-expanded sonic jet with a hypersonic crossflow - schlieren photographs of the side view ($M_\infty = 8.2$, $Re_\infty/cm = 9.0 \times 10^4$, $P_{0j} = 74.7$ psia)

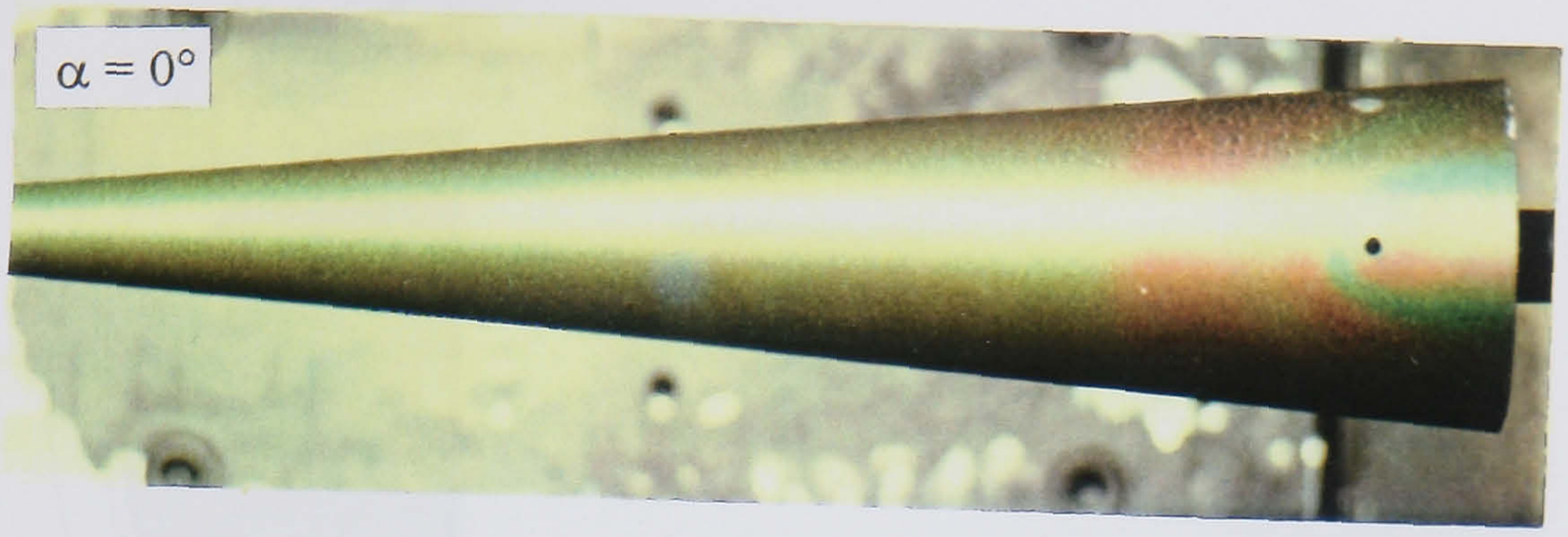

Figure 9-16 The effect of incidence on the interaction of an under-expanded sonic jet with a hypersonic crossflow - liquid crystal thermographs of the plan view ($M_\infty = 8.2$, $Re_\infty/cm = 9.0 \times 10^4$, $P_{oj} = 74.7$ psia)

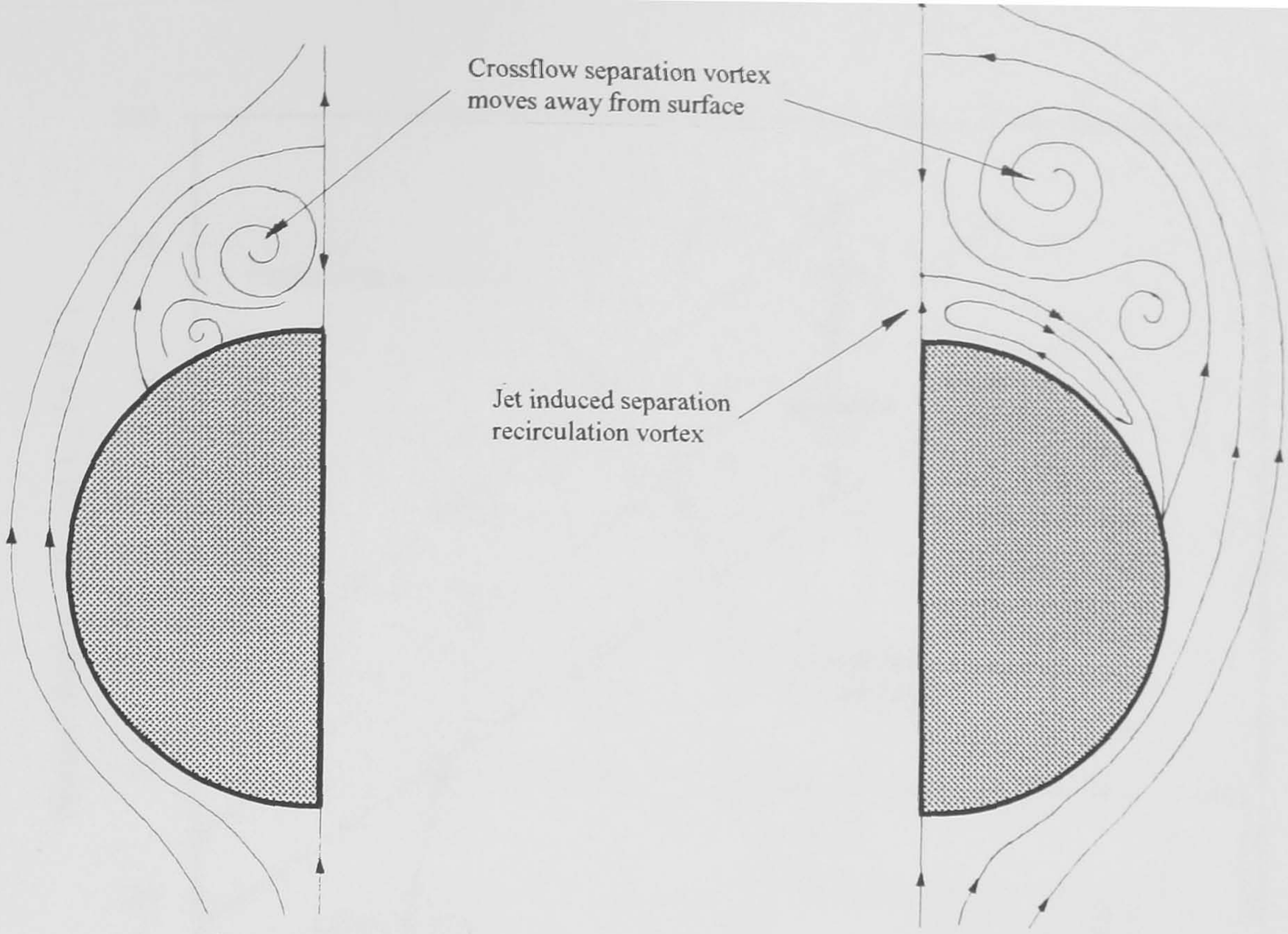

(i) no jet

(ii) with jet

(a) incidence $\alpha = 6°$

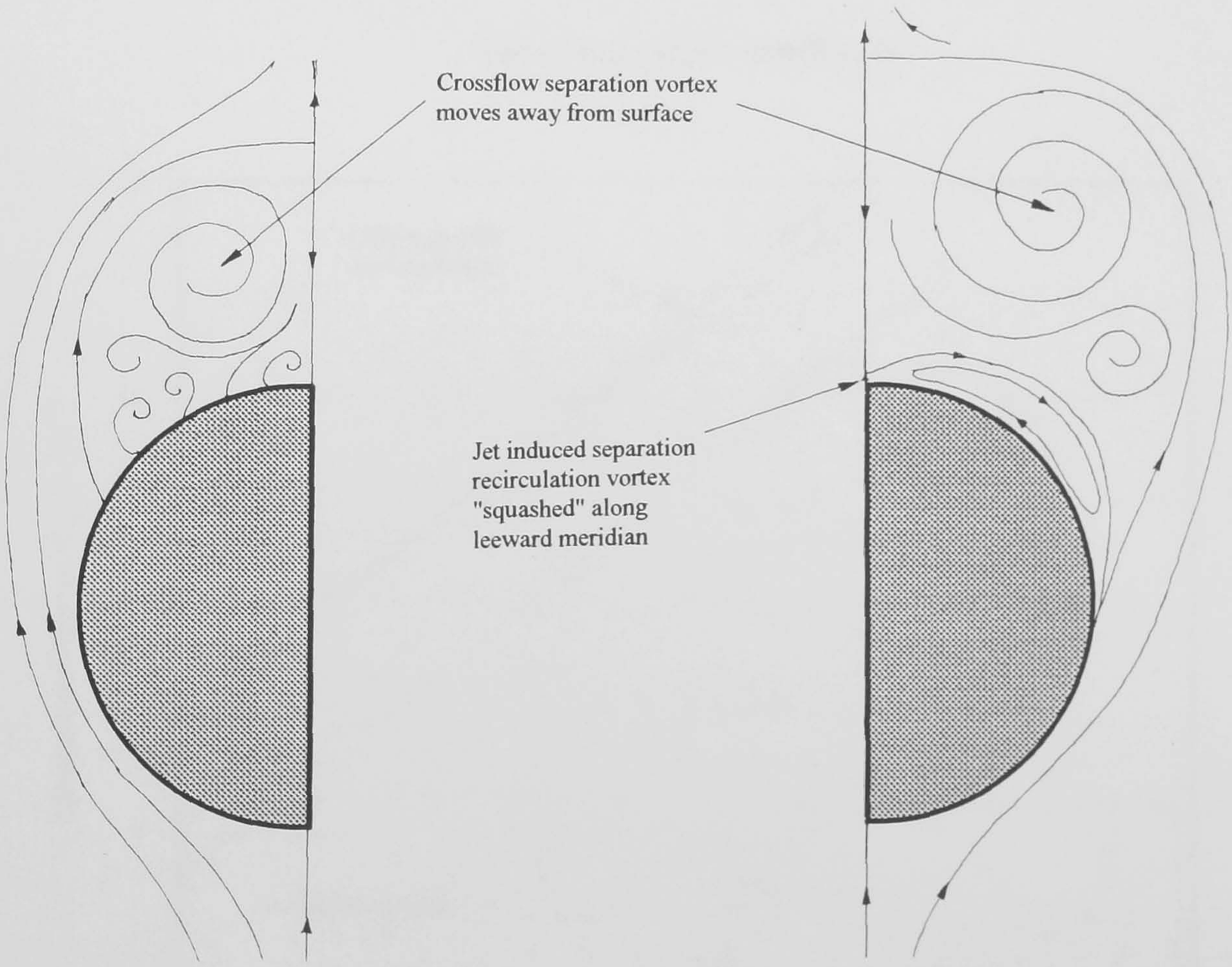

(i) no jet

(ii) with jet

(b) incidence $\alpha = 9.5°$

Figure 9-17 The effect of the interaction of an underexpanded sonic jet on the flow structure in the crossflow plane of a blunt cone at incidence

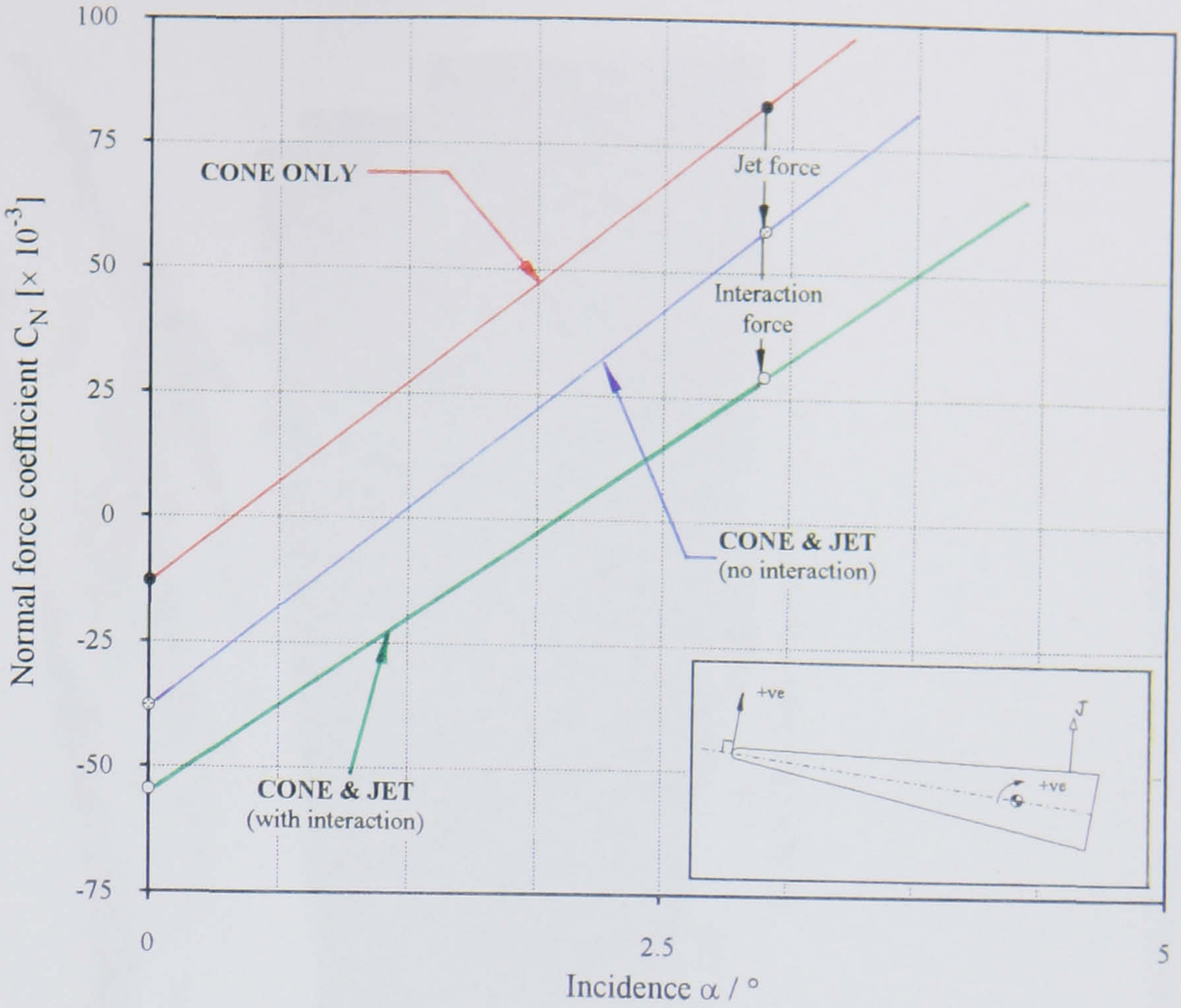

(a) normal force coefficient

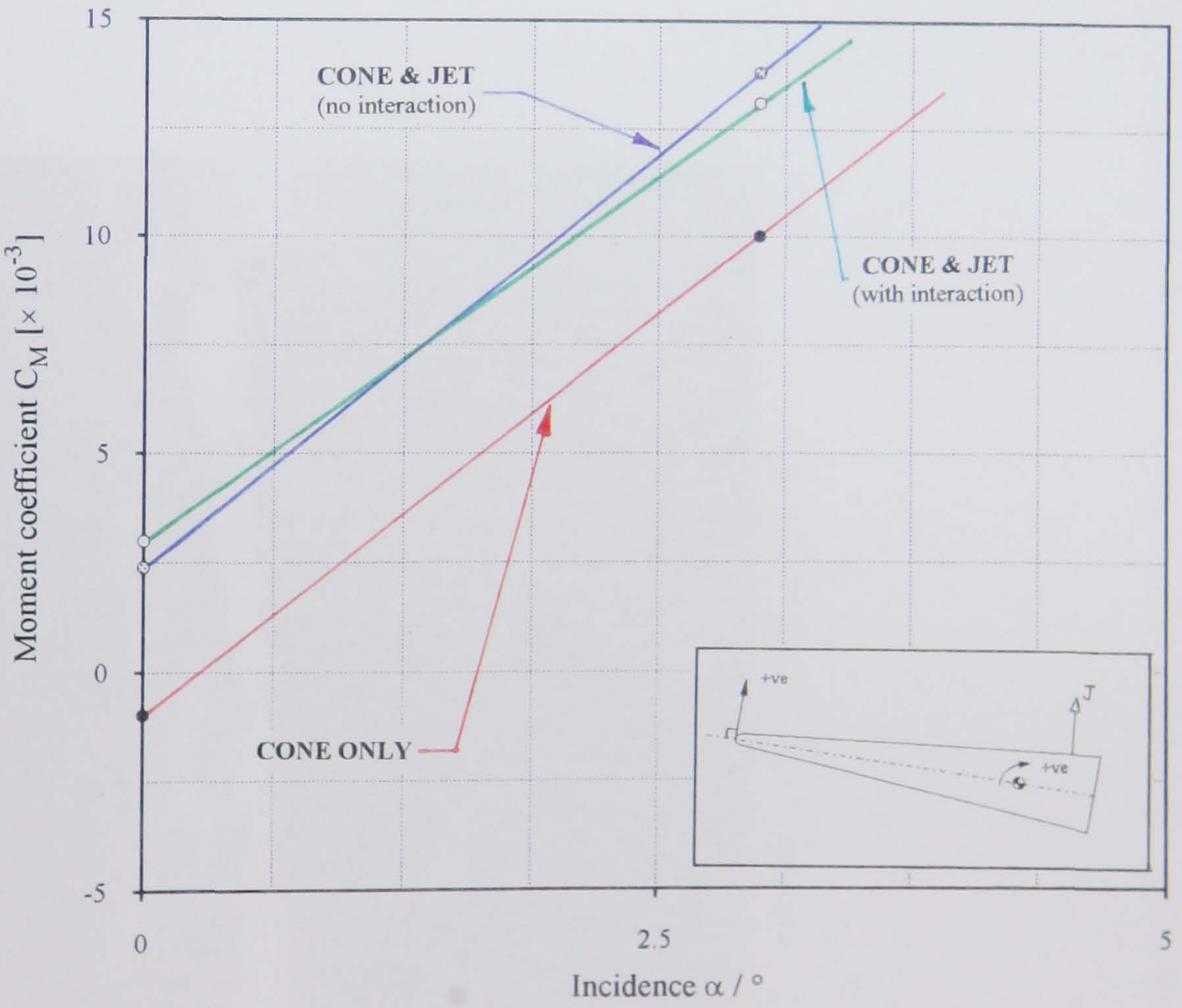

(b) moment coefficient

Figure 9-18 The effect of incidence on the normal force and moment distributions generated by the interaction of an under-expanded sonic jet with a hypersonic crossflow ($M_\infty = 8.2$, $Re_\infty/cm = 9.0 \times 10^4$, $P_{oj} = 74.7$ psia, $p_\infty = 0.13$ psia)

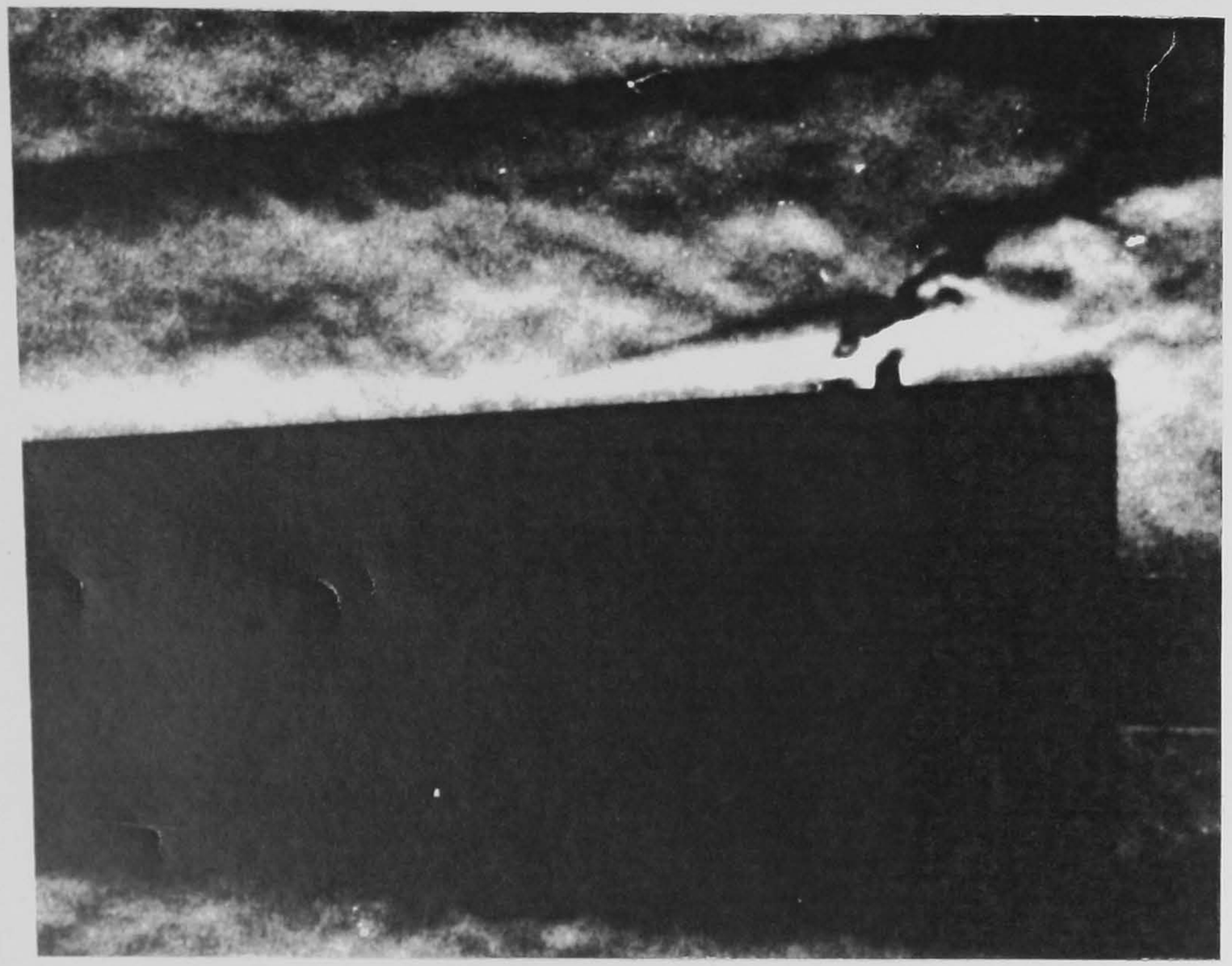

(a) sonic circular jet ($A_{j,\,exit} = \pi$ mm^2)

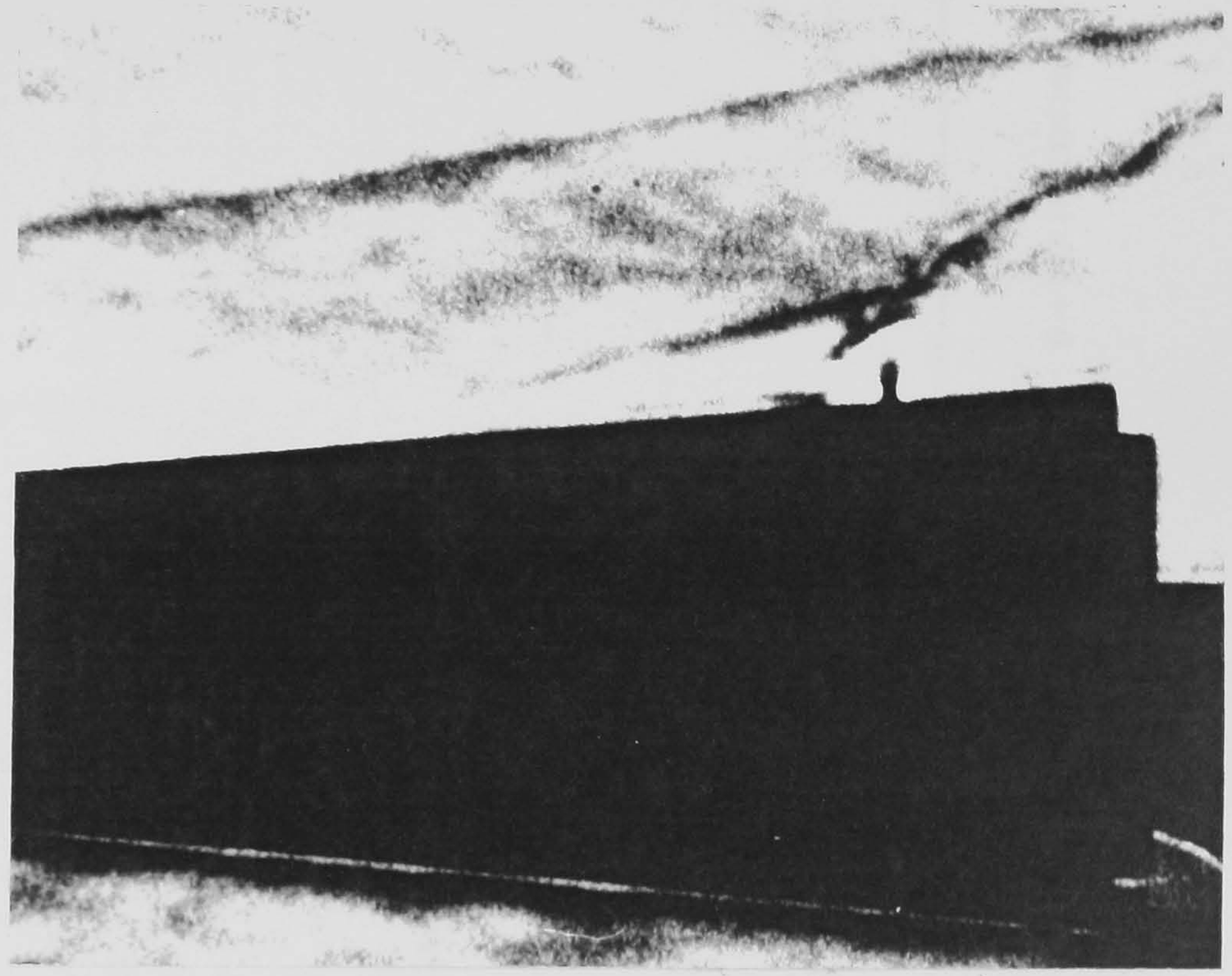

(b) sonic 3:1 transverse slot jet ($A_{j,\,exit} = \pi$ mm^2)

Figure 9-19 The effect of jet nozzle geometry on the interaction of an underexpanded sonic jet with a hypersonic crossflow ($M_\infty = 8.2$, $Re_\infty/cm = 9.0 \times 10^4$, $P_{oj} = 74.7$ psia, $p_\infty = 0.13$ psia)

Note : Jet located at x/d = 0

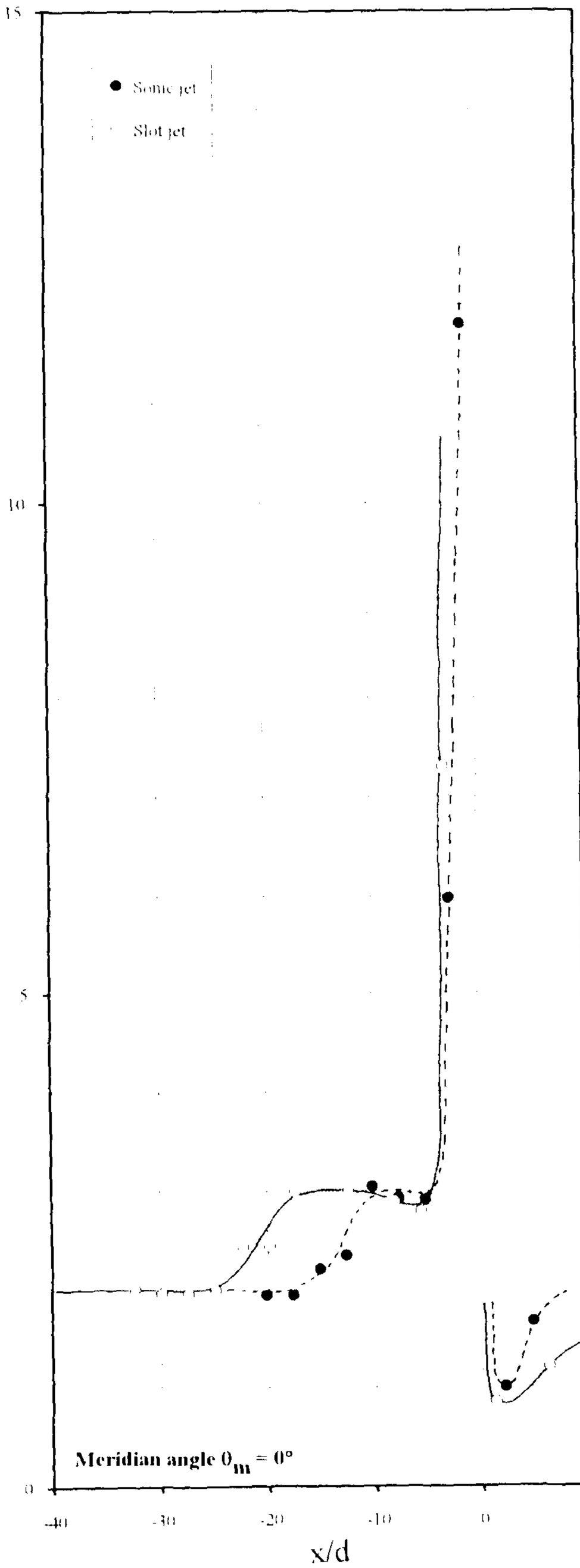

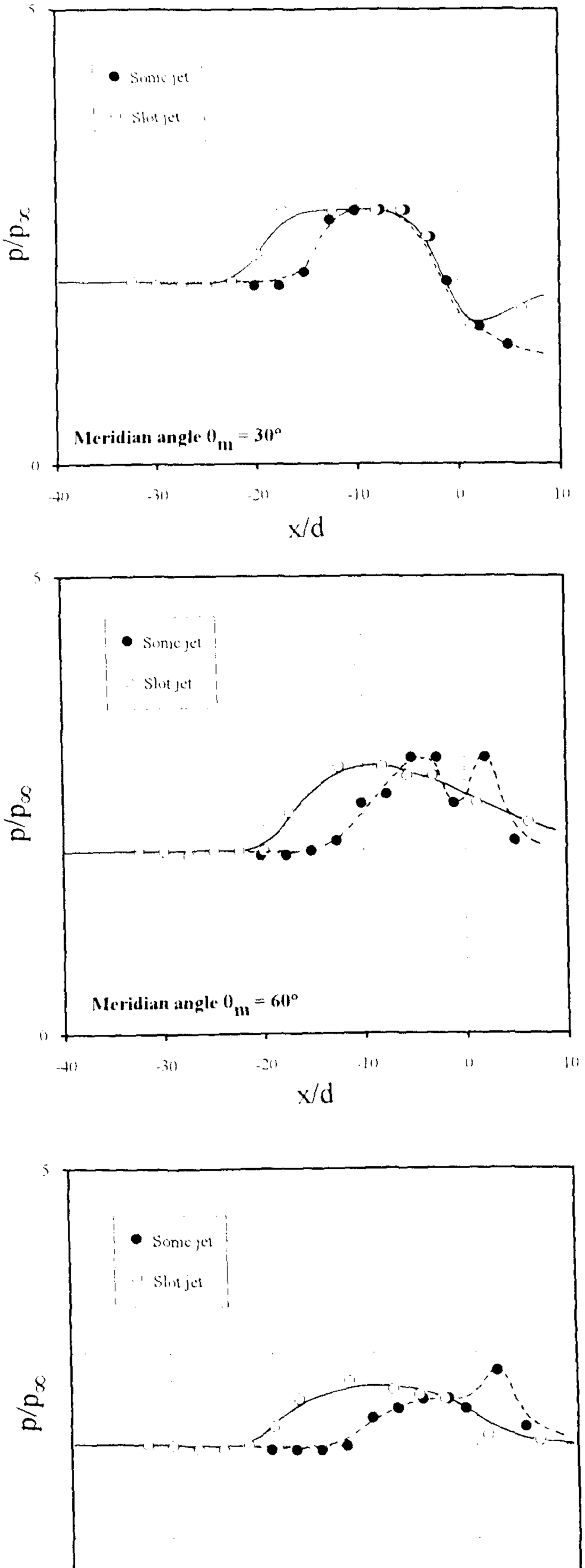

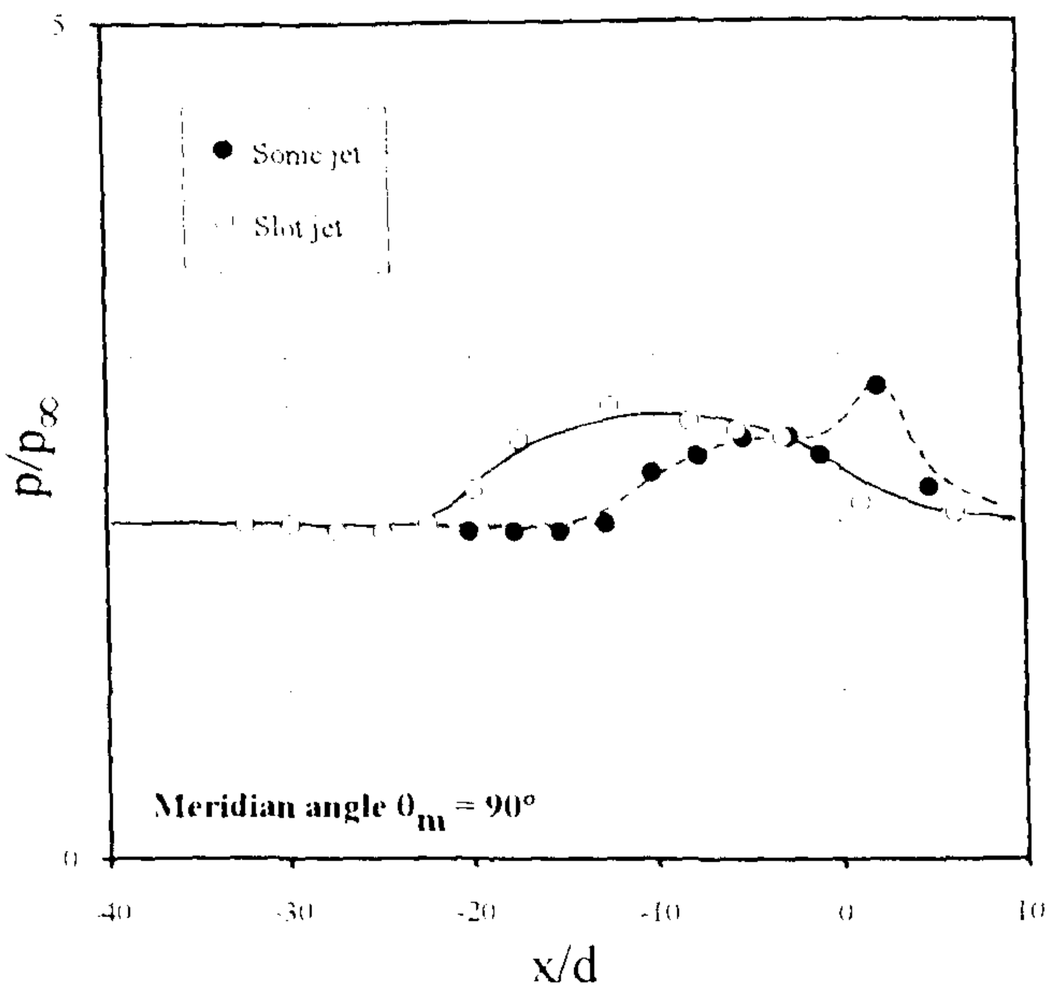

Figure 9-20 The effect of a 3:1 transverse slot jet on pressure distributions along various meridians in the jet interaction region
($M_\infty = 8.2$, $Re_\infty/cm = 9.0 \times 10^4$, $P_{oj} = 74.7$ psia, $\alpha = 0°$, $A_{j,\,exit} = \pi$ mm^2)

(a) Jet exit plane Mach number $M_{exit} = 1.0$

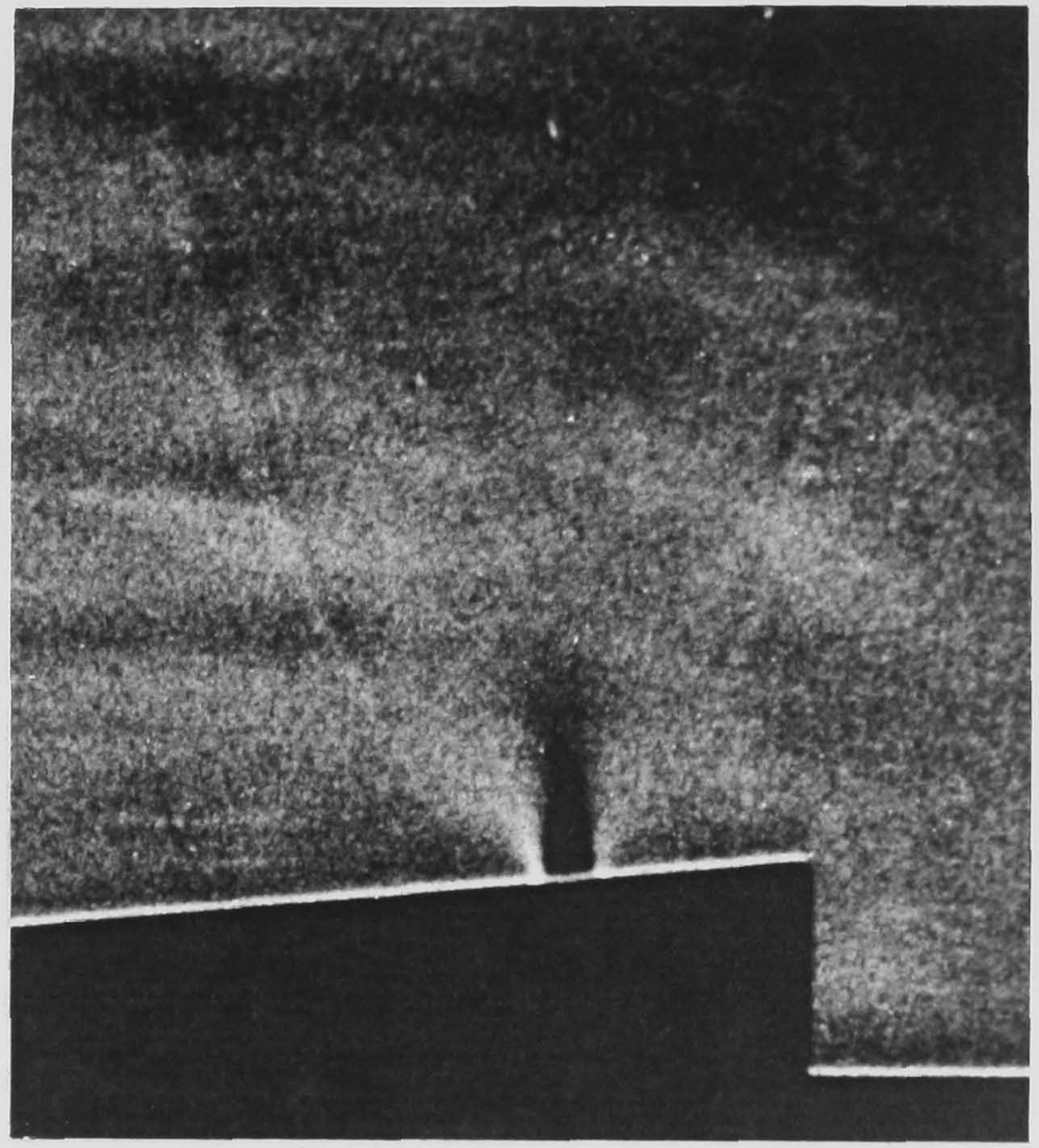

(b) Jet exit plane Mach number $M_{exit} = 3.0$

Figure 9-21 The effect of jet exit plane Mach number on the structure of an under-expanded jet ($P_{0j} = 74.7$ psia, circular nozzle)

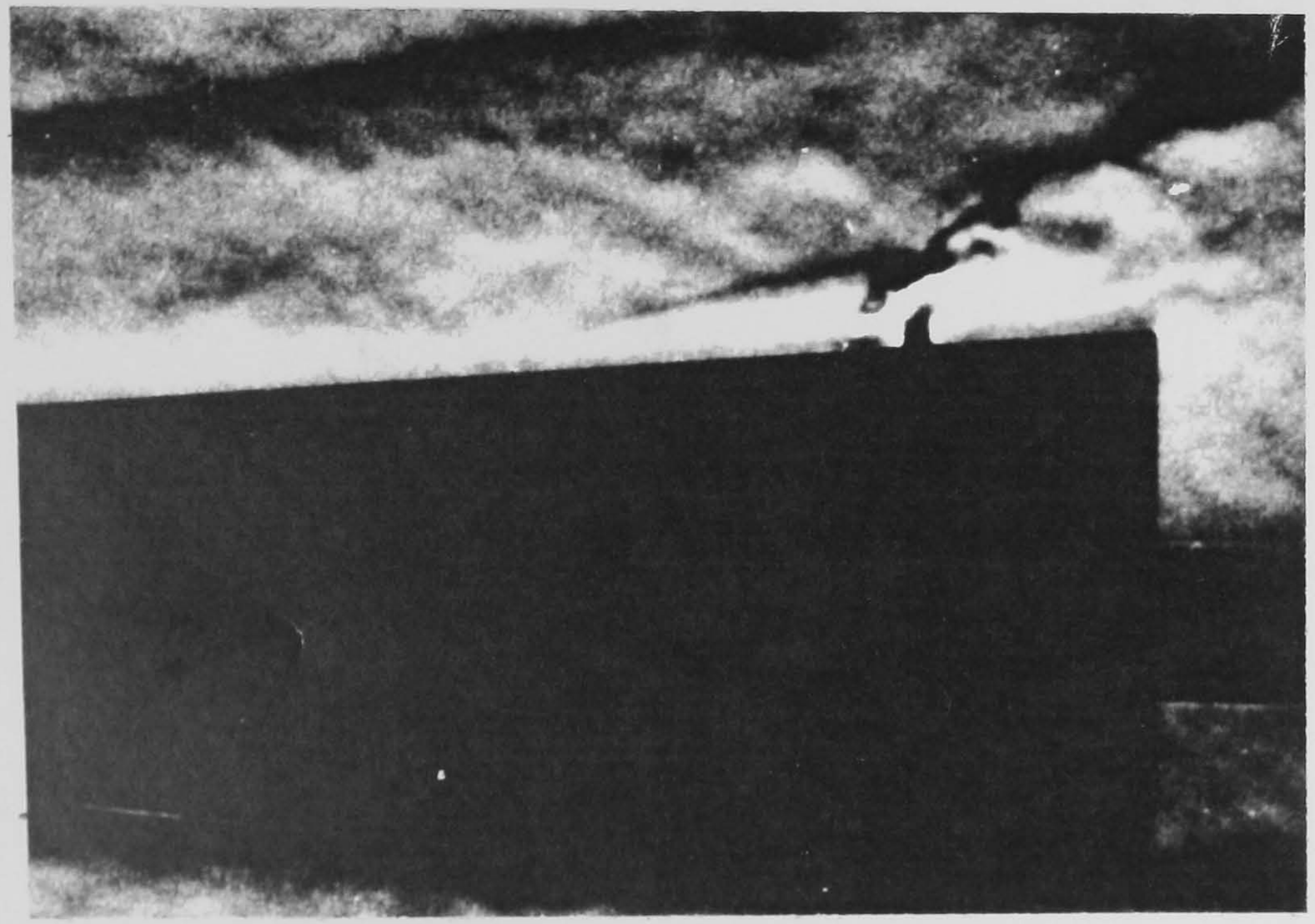

(a) sonic circular jet ($A_{j,\,throat} = \pi\ mm^2$)

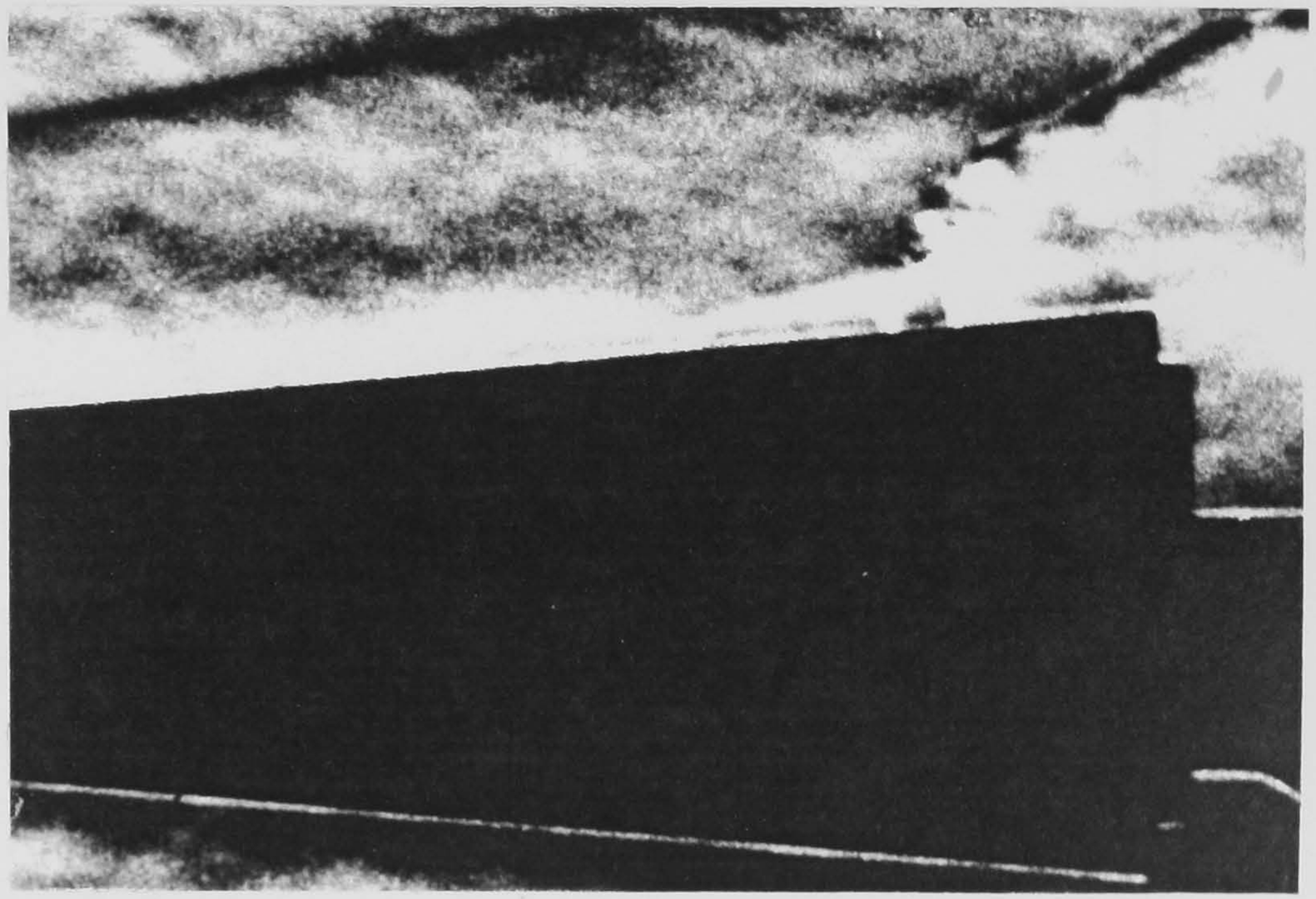

(b) Mach 3 circular jet ($A_{j,\,throat} = \pi\ mm^2$)

Figure 9-22 The effect of jet exit plane Mach number on the interaction of an underexpanded jet with a hypersonic crossflow ($M_\infty = 8.2$, $Re_\infty/cm = 9.0 \times 10^4$, $P_{oj} = 74.7$ psia, $p_\infty = 0.13$ psia)

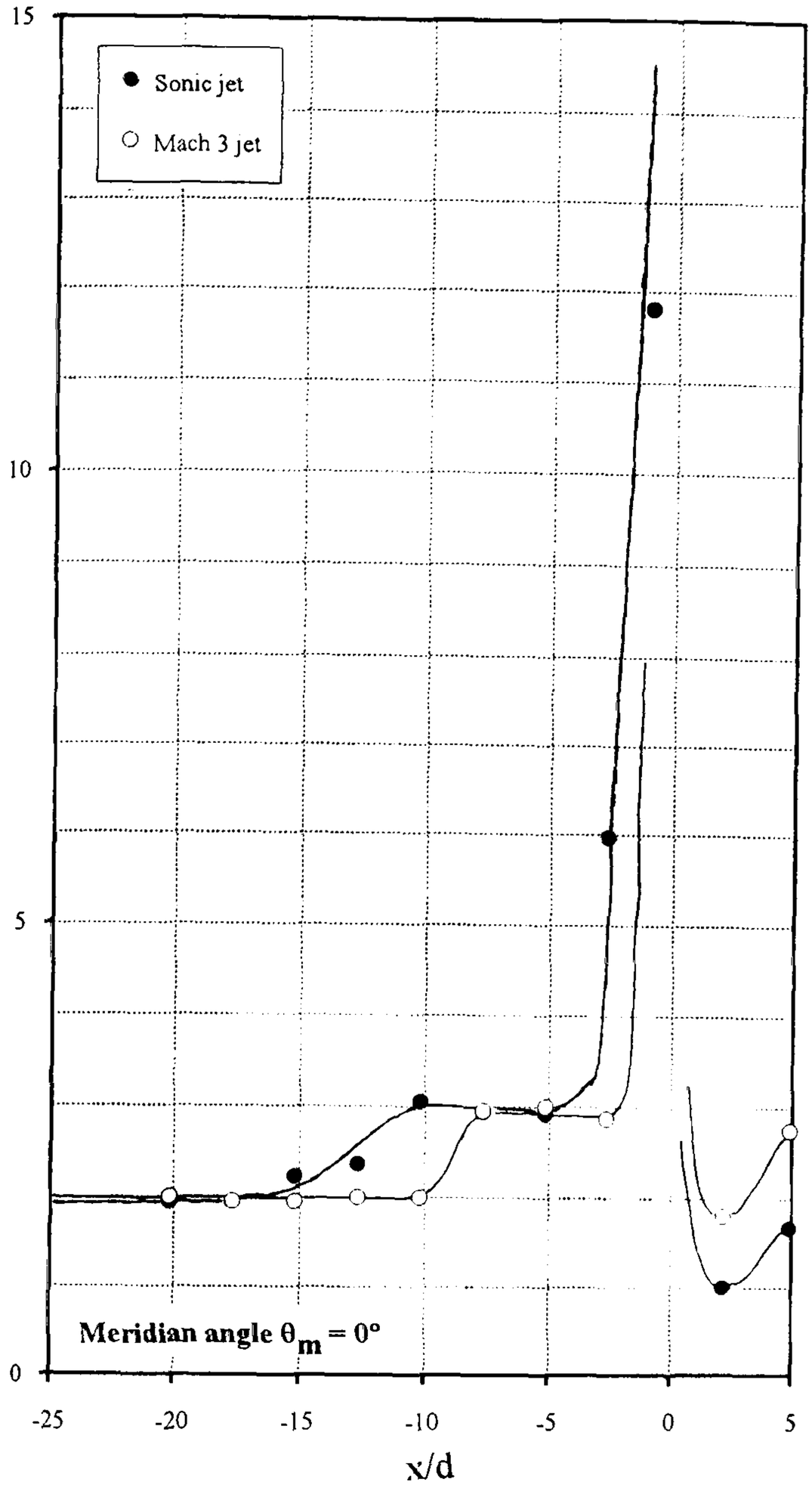

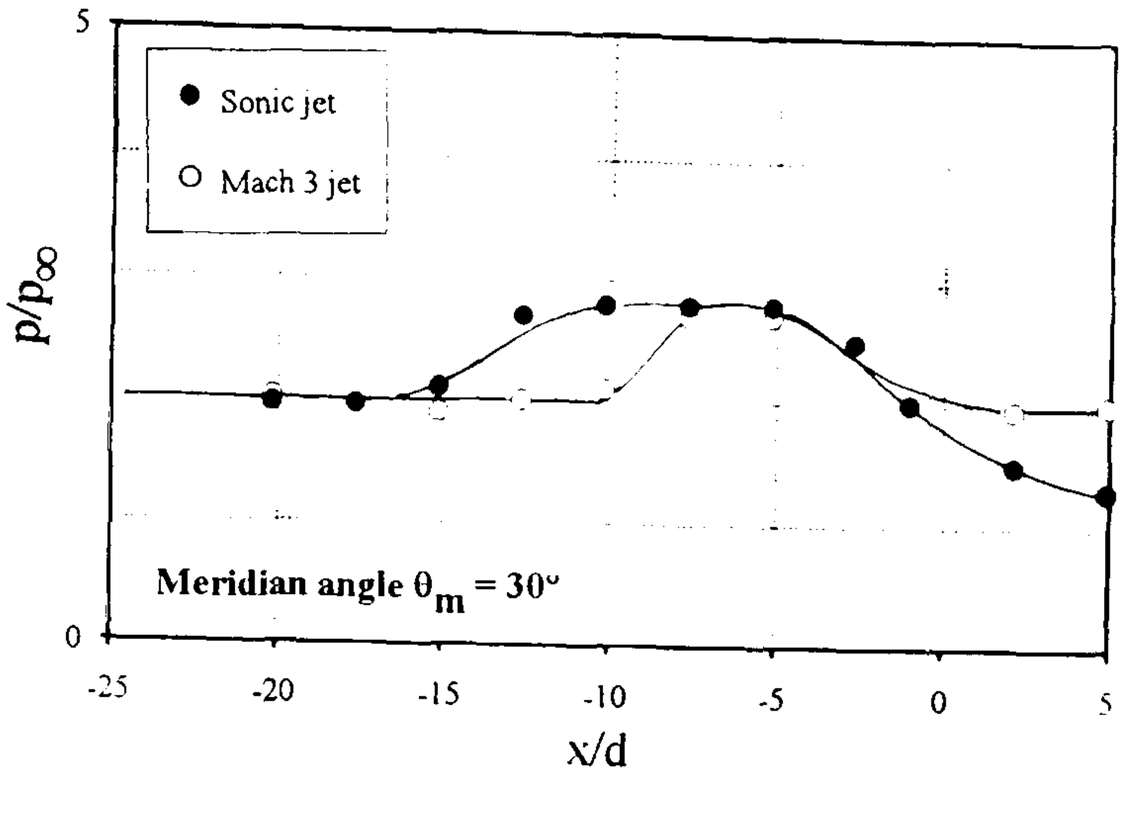

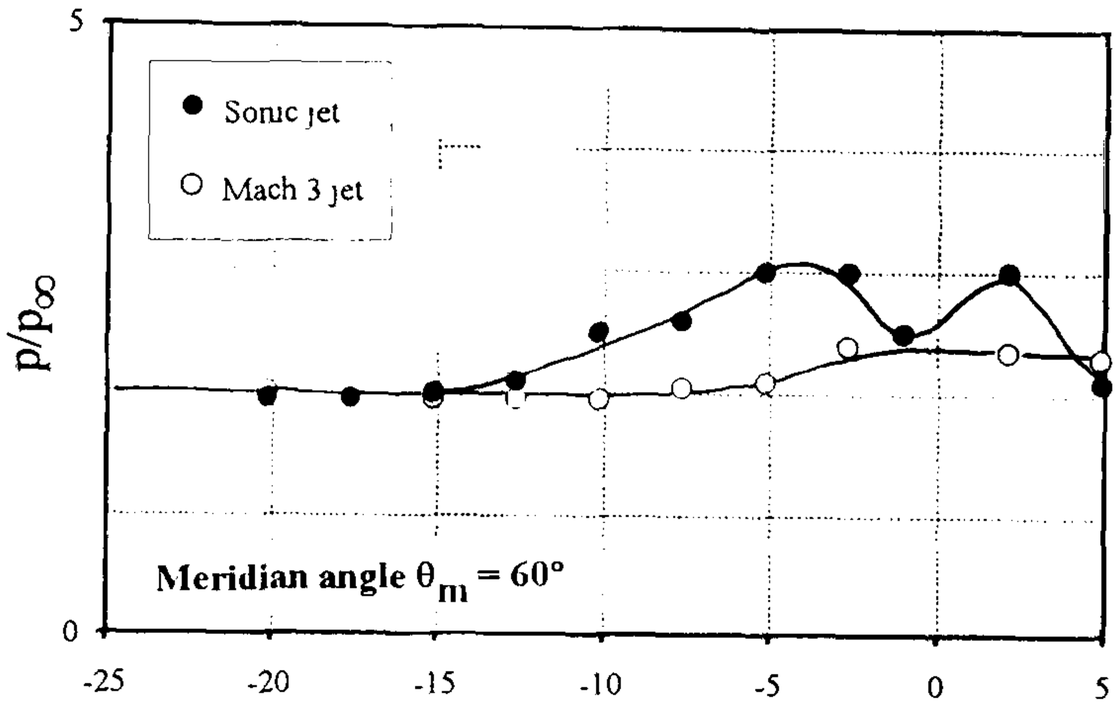

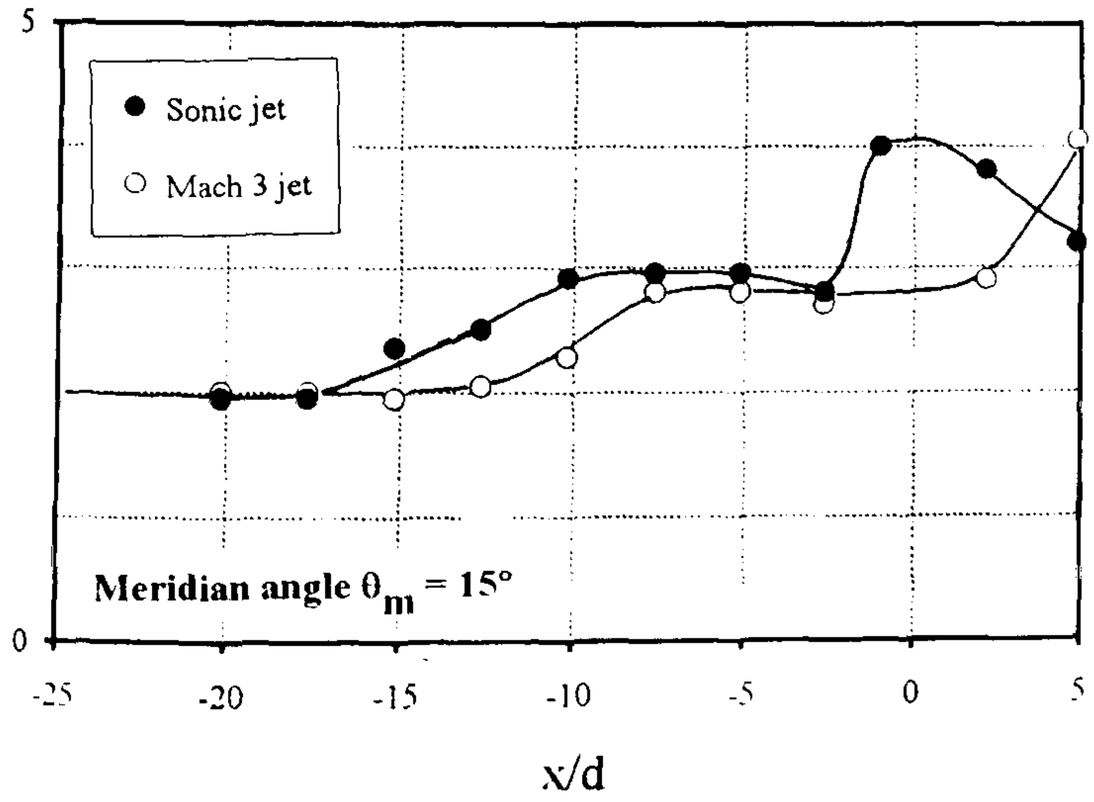

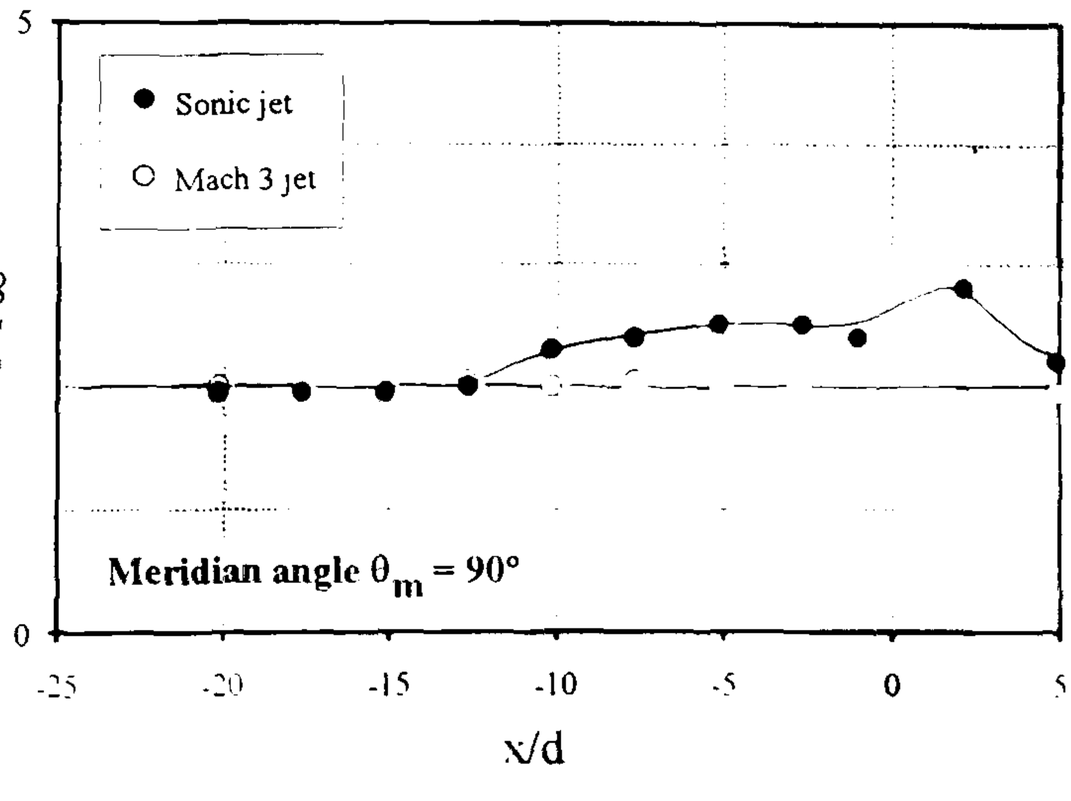

Figure 9-23 The effect of jet Mach number on pressure distributions along various meridians in the jet interaction region ($M_\infty = 8.2$, $Re_\infty/cm = 9.0 \times 10^4$, $P_{oj} = 74.7$ psia)

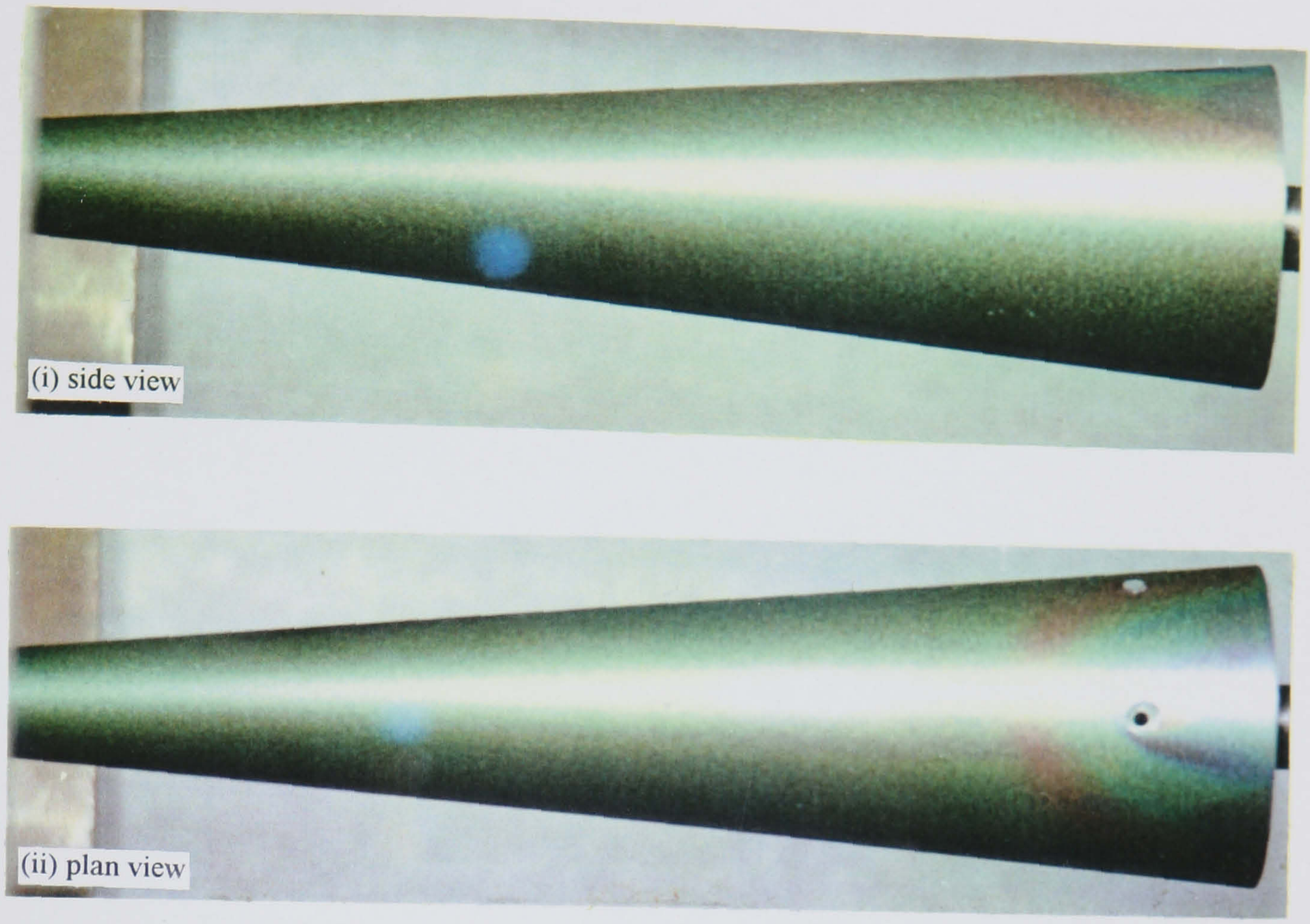

(a) liquid crystal thermographs of the jet interaction region

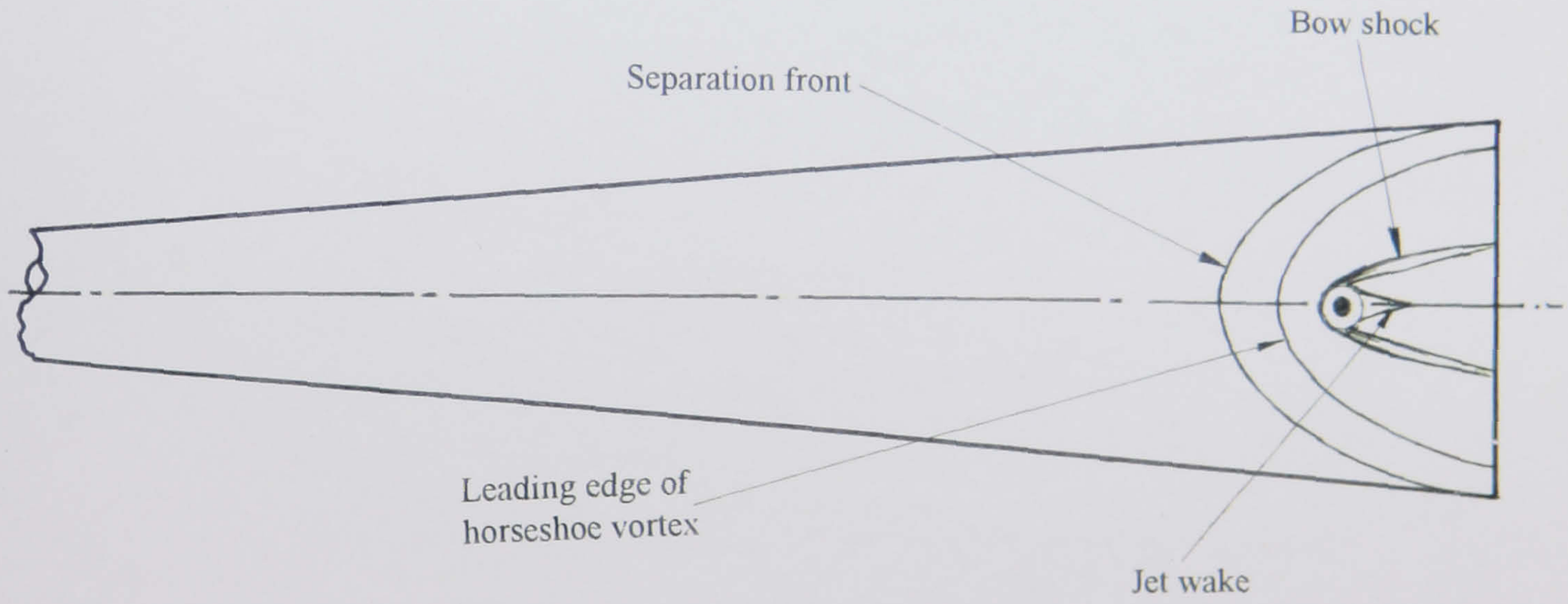

(b) schematic diagram of the jet interaction region (plan view)

Figure 9-24 The effect of jet exit plane Mach number on the interaction of an underexpanded jet with a hypersonic crossflow ($M_\infty = 8.2$, $Re_\infty/cm = 9.0 \times 10^4$, $P_{oj} = 74.7$ psia)